



Università degli Studi di Pavia
Dipartimento di Fisica
Dottorato di Ricerca in Fisica - XXXVIII Ciclo

Development of the HiDRa highly granular dual-readout calorimeter prototype and Search for heavy neutral leptons with the ATLAS experiment

Andrea Pareti

Supervisors:
Prof. A. Negri
Prof. G. Gaudio

A thesis submitted to the Graduate School of Physics
in partial fulfilment of the requirements for the degree of
Doctor of Philosophy in Physics
Dottore di Ricerca in Fisica
at the University of Pavia

Cover: Coloured bubble chamber view of an electromagnetic shower (centre). This has been produced by a muon neutrino (entering from the left) interacting with a neutron at the border of the large circle. Data from the Big European Bubble Chamber (BEBC) at CERN.
Credits: SciencePhotoLibrary

Title: Development of the HiDRa highly granular dual-readout calorimeter prototype and search for heavy neutral leptons with the ATLAS experiment

Andrea Pareti
Ph.D. thesis - University of Pavia

ABSTRACT

This thesis describes the work carried out during the three-year period of my Ph.D. at the University of Pavia, Italy. It is divided into two main sections, corresponding to my work within two collaborations, the RD_FCC project for future accelerators, and the ATLAS experiment at CERN. The first part concerns the development of a dual-readout calorimeter prototype, with a design suitable for the full exploitation of this technology at future Higgs factory facilities. Its most innovative feature is the usage of Silicon Photomultipliers (SiPMs) for the fibre readout, which offers finely segmented information on particle energy deposits inside the calorimeter. The second part of the thesis describes an analysis of the data collected during the Large Hadron Collider (LHC) Run 2 data-taking period from 2015 to 2018 by the ATLAS experiment, searching for heavy neutral leptons (HNLs). These particles are not part of the Standard Model of particle physics, and could provide motivation for several currently open problems, such as dark matter, the baryon asymmetry of the Universe, and neutrino masses.

Contents

Introduction **3**

1 Physics at the LHC and future colliders **5**
1.1 Standard Model searches . . . 5
1.2 The Large Hadron Collider . . . 8
1.3 The Future Circular Collider . . . 11
1.3.1 FCC-hh . . . 17
1.4 Other projects . . . 20
1.4.1 The Circular Electron-Positron Collider . . . 20
1.4.2 The International Linear Collider . . . 21
1.4.3 The Compact Linear Collider . . . 23
1.4.4 The Muon Collider . . . 24

I Development of the HiDRa highly granular dual-readout calorimeter prototype **27**

2 Introduction to calorimetry **29**
2.1 Electromagnetic calorimetry . . . 30
2.1.1 Electrons and positrons . . . 31
2.1.2 Photons . . . 31
2.1.3 Electromagnetic showers . . . 33
2.1.4 Electromagnetic calorimeters . . . 34
2.2 Hadronic calorimetry . . . 38
2.2.1 Hadron showers . . . 39
2.2.2 Hadronic calorimeters . . . 44
2.3 Compensation . . . 48
2.4 Dual-readout calorimetry . . . 49
2.5 Particle-Flow calorimetry . . . 53

3 Design optimisation of the HiDRa prototype **57**
3.1 Calorimetry requirements for future accelerators . . . 58
3.2 The IDEA detector concept . . . 60
3.2.1 Tracking systems . . . 60
3.2.2 Calorimeters and magnet . . . 63
3.2.3 Muon system . . . 65
3.3 Silicon Photomultipliers . . . 66
3.4 Capillary tube calorimeter proof-of-concept . . . 69
3.5 The HiDRa prototype . . . 74

3.6 HiDRa simulation studies . . . 76
3.6.1 Leakage studies . . . 79
3.6.2 Lateral containment . . . 81
3.6.3 Longitudinal leakage . . . 86
3.6.4 Other simulation studies . . . 89

4 High-granularity performances of the HiDRa prototype 97
4.1 Spatial resolution for electromagnetic showers . . . 98
4.1.1 Signal grouping . . . 104
4.2 Application to π^0/γ separation . . . 107

5 Prototype construction and test-beam results 117
5.1 Construction of the HiDRa prototype . . . 118
5.1.1 Final design . . . 124
5.2 Results from the 2024 beam test . . . 125
5.2.1 Calibration . . . 127
5.2.2 Electromagnetic performances . . . 128
5.2.3 Hadronic performances . . . 138
5.3 Conclusions and prospects . . . 157

II Search for heavy neutral leptons with the ATLAS Experiment 161

6 The ATLAS Experiment 163
6.1 ATLAS detector . . . 164
6.1.1 Inner detector . . . 165
6.1.2 Calorimeters . . . 167
6.1.3 Muon systems . . . 168
6.2 Trigger, Data acquisition and processing . . . 169
6.3 Physics objects reconstruction and identification . . . 171
6.3.1 Electrons and photons . . . 171
6.3.2 Muons . . . 173
6.3.3 Hadron jets . . . 174

7 Heavy Neutral Leptons search with prompt signatures 177
7.1 Neutrino physics and Heavy Neutral Leptons . . . 178
7.1.1 Dirac Neutrinos and Oscillations . . . 178
7.1.2 Majorana Neutrinos . . . 181
7.2 Signal model . . . 183
7.3 Background processes . . . 188
7.4 Data and Monte Carlo simulations . . . 189
7.4.1 Monte Carlo samples . . . 192
7.5 Physics objects used in the analysis . . . 194
7.5.1 Variables for event selections . . . 197
7.6 Event selection . . . 198
7.6.1 Pre-selection requirements . . . 198
7.7 Signal regions definitions . . . 202
7.8 Background estimation . . . 205

7.8.1 Standard Model backgrounds 205
7.8.2 Charge-flip background 205
7.8.3 Fake/non-prompt leptons background 209
7.8.4 Background validation 211
7.9 Systematic uncertainties 213

8 HNL Analysis Results **217**
8.1 Statistical framework 217
8.2 Yields in the signal regions 219
8.3 Fit results and limits 221
8.4 Conclusions and prospects 224

9 Conclusions and outlook **229**

INTRODUCTION

In this thesis, the work conducted during the three-year period as Ph.D. student at the University of Pavia, and associate member of the Italian National Institute of Nuclear Physics (INFN), is outlined. Two main topics are discussed, corresponding to the work carried out for two separate projects: the development of a dual-readout calorimeter prototype in the framework of the Future Circular Collider (FCC) and Detector R&D (DRD) collaborations, and a search for beyond-the-standard-model particles named Heavy Neutral Leptons (HNLs) with the ATLAS detector at CERN.

The first project consists of the development, construction and characterisation of a highly granular dual-readout calorimeter prototype, featuring Silicon Photomultipliers (SiPMs) for the readout of optical photons produced by means of the scintillation and Čerenkov processes inside the calorimeter. The main purpose of this prototype is to demonstrate the viability of the dual-readout calorimetry technique, in conjunction with the high granularity feature provided by the SiPMs, for the demanding physics requirements at future collider Higgs factories, such as the Future Circular Collider (FCC) of the Circular Electron-Positron Collider (CEPC). Precise measurements of the Higgs boson are at the core of both projects, and the large multiplicity of hadronic jets in the final state of many interesting Higgs processes requires advanced calorimeters able to correctly reconstruct these kinds of objects. Chapter 1 resumes the current status of particle physics searches at the Large Hadron Collider (LHC) at CERN, and the main target studies at the FCC and the CEPC. In Chapter 2 the concept of calorimetry is presented, with an emphasis on the dual-readout technique on which much of the work in the following chapters is based. Chapter 3 presents the HiDRa calorimeter prototype, with a focus on the performances that must be achieved for the exploitation of its blueprint at the FCC. The Silicon Photomultiplier technology, that represents the salient feature of HiDRa, is also briefly introduced. Geant4 simulation-based studies of the calorimeter's capabilities in terms of electromagnetic and hadronic energy measurements, performed before the actual construction and characterisation of the prototype, are presented. In Chapter 4, applications of the SiPM readout in terms of spatial resolution and particle identification capabilities are studied through the Geant4 simulation. A task of large interest at future colliders, the separation of electromagnetic showers originated by high-energy photons or neutral pions, is also presented. Finally, in Chap-

ter 5 the actual construction of the HiDRa calorimeter is discussed. A first experimental test was made in August 2024 with about half of the calorimeter completed. The analysis of collected data is presented, with a first characterisation of the energy response to electrons and hadrons.

In Part II, the search for HNLs with the ATLAS detector is presented. The ATLAS detector is briefly described in Chapter 6, with the detector subsystems, the trigger and data acquisition chain. The data analysis performed for the HNLs search is presented in Chapter 7. The signal model and the resulting signature are described, as well as the expected backgrounds and the signal regions definitions to perform the search. Background validation and systematics uncertainties are also discussed. Finally, the statistical analysis of the results performed after unblinding the signal regions is presented in Chapter 8, and limits on the HNL mixing parameters are set as functions of the HNL masses.

CHAPTER

1

PHYSICS AT THE LHC AND FUTURE COLLIDERS

The present chapter is devoted to resume the current status of searches in particle physics, open problems and the most important collider projects, both active and under development.

1.1 Standard Model searches

With the discovery of the Higgs boson in 2012 by the ATLAS and CMS experiments [1][2], a fundamental validation of the Standard Model of particle physics, as a powerful theory able to describe elementary particles and their interactions at microscopic level, was obtained. The Standard Model is a quantum field theory invariant under the symmetry group $\mathcal{SU}(2)_L \times \mathcal{U}(1)_Y \times \mathcal{SU}(3)_C$, that considers three out of the four known fundamental forces, namely electromagnetism, the weak and the strong interaction (the last one, gravity, not being considered, as it is non-renormalisable and its contribution to processes studied by currently existing experiments is negligible compared to all others). In this theory, developed in the second half of the twentieth century, matter fields are spin $\frac{1}{2}$ fermions, divided into leptons and quarks, whose interactions are mediated through the exchange of spin 1 gauge bosons. While all fermions interact through the weak force, only quarks are subject to the strong interaction. Neutrinos, being the only leptons with zero electric and colour charge, do not interact through neither the electromagnetic nor the strong forces. A schematic summary of the different elementary particles, divided in quarks, leptons and bosons, is shown in fig. 1.1. Both quarks and leptons are further divided into three families, each representing a weak isospin doublet, with the same quantum numbers and increasing mass. The existence of only three generations of fermions was determined by all four LEP [3] experiments through the measurement of the Z boson width, concluding that only three neutrino

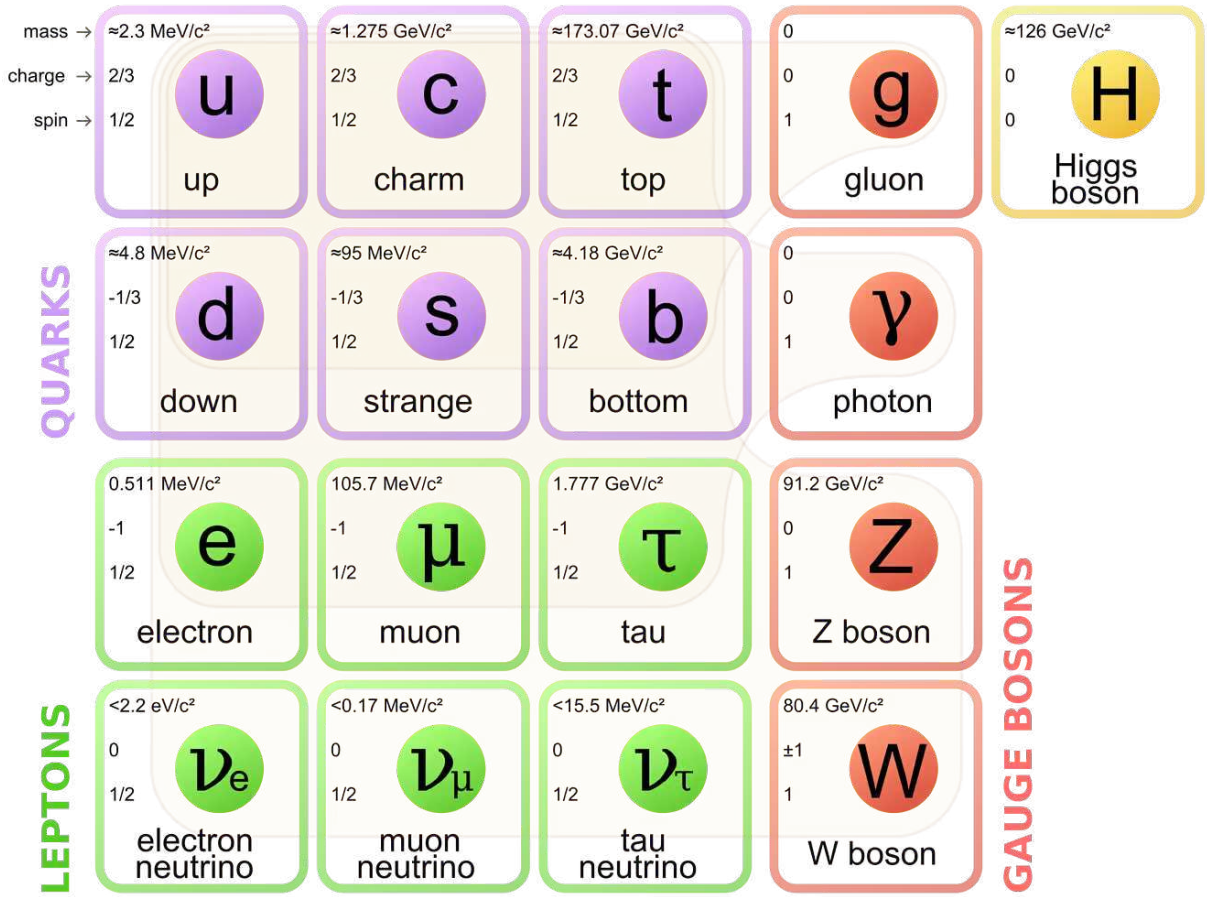


Figure 1.1: Sketch of the Standard Model elementary particles, classified as quarks (purple), leptons (green) and gauge bosons (red), each drawn with the corresponding mass, electric charge and spin. The Standard Model Higgs boson is also shown (yellow). Taken from [6].

species exist, at least with masses below 45 GeV[1] [5].

The Higgs boson plays a crucial role in this theoretical framework. Assigning an explicit mass term to both gauge bosons and fermions in the electroweak Lagrangian would break the local $\mathcal{SU}(2)_L \times \mathcal{U}(1)_Y$ gauge invariance. In the Brout-Englert-Higgs mechanism [7][8] a suitable potential for the Higgs field is introduced, with the form

$$V(\phi) = \frac{1}{2}\mu^2|\phi^2| + \frac{1}{4}\lambda|\phi^4| \tag{1.1}$$

with $\mu^2 < 0$ such that an infinite set of local minima are present, and featuring a vacuum expectation value $\langle 0|\,\phi\,|0\rangle = v/\sqrt{2}$ different from zero. After the spontaneous symmetry breaking one of the degenerate minima is selected, and following Goldstone's theorem a number of bosons, equal to that of broken generators of the symmetry, arises. In the Standard Model the Higgs field is represented by an $\mathcal{SU}(2)$ complex doublet, with a total of four degrees of freedom. Of these, three correspond to broken generators and are absorbed into the $W^{\mu}_{1,2,3}$, B^{μ} gauge bosons to generate the physical $W^{\pm}$ and Z bosons, while the fourth is unbroken so that photons remain massless as they are

[1]The current upper limit on the sum of the three neutrino masses, obtained through cosmological observation, is $\Sigma_{j=1,2,3}\, m_j < 0.115$ eV [4].

experimentally observed. The last degree of freedom is then associated to a spinless and neutral scalar particle, the Higgs boson, the only particle with these characteristics in the Standard Model. Given the vacuum expectation value of the Higgs field v and the electroweak couplings g and g', it is then possible to derive an equation for the W and Z bosons masses

$$m_W^2 = \frac{1}{4}g^2v^2 \qquad m_Z^2 = \frac{1}{4}(g^2 + g'^2)v^2, \tag{1.2}$$

while the mass of Higgs boson itself results

$$m_H = \sqrt{2\lambda v^2}, \tag{1.3}$$

where the parameter λ represents the self-coupling of the Higgs field, therefore weighting the tri-linear and quartic interactions. Fermion masses are then introduced through Yukawa-type interactions with the Higgs scalar field, keeping the theory gauge invariant, and read

$$m_{f_i} = h_{f_i}\frac{v}{\sqrt{2}}, \qquad i = 1, 2, 3 \quad \text{fermion families.} \tag{1.4}$$

A Yukawa coupling matrix h_{f_i} is introduced for up and down components of $\mathcal{SU}(2)$ doublets for quarks and for charged leptons, and must be diagonalised from the interaction basis to the mass eigenstate basis. In the usual Standard Model formulation there are no Yukawa interactions for neutrinos, as these particles are described as massless and no right-handed component ν_R is introduced. The coupling of the Higgs boson to each fermion is directly proportional to the mass of the latter. The highest coupling is to the top quark, with a mass of ~ 173 GeV, resulting in a Yukawa matrix element close to 1. However, since the top mass is higher than the Higgs one, decays of the Higgs boson into a $t\bar{t}$ pair are forbidden at tree level. The second largest coupling is to the bottom quark, with a mass of 4.18 GeV, resulting in a branching fraction of about 58.4% [9]. For the discovery of the Higgs boson, both the ATLAS and CMS experiments focused on the so-called *golden channels*:

$$H \longrightarrow \gamma\gamma$$
$$H \longrightarrow ZZ^*$$

restricting to only electron and muon leptons final states in the second case. Despite the quite small branching ratios (2.27×10^{-3} and 2.62×10^{-2}, respectively), these channels show a much more favourable signal-to-background ratio with respect to all other possible decay modes.

The Higgs boson properties are currently being investigated at the Large Hadron Collider, in order to evaluate how much the new observed particle is compatible with the simplest Standard Model prediction case. There exist several SM extensions that provide additional properties to the Higgs boson, or even additional Higgs-like bosons [10]. Besides the aforementioned golden channels, the Higgs has also been measured in its decay to third-family fermions, namely $b\bar{b}$ quark pairs [11][12], $\tau\bar{\tau}$ lepton pairs [13][14], and with its associated production with $t\bar{t}$ quark pairs [15][16]. Searches for direct measurements of the Higgs couplings to second generations fermions have also been performed, but without definitive results so far. A 3σ evidence for the decay into two muons $H \rightarrow \mu\bar{\mu}$ was found by CMS [17], and only very recently by ATLAS [18], the main difficulty coming from the very small coupling due to the muon mass of only

106 MeV, making this channel hard to observe on top of the remaining SM background processes. Searches for the $H \to c\bar{c}$ decay to charm quarks did not lead to observations, mostly due to very large backgrounds and difficult object reconstruction of displaced vertices with detectors [19][20]. At the time of writing, performed measurements seem to point to a Higgs consistent with its Standard Model prediction. This is especially interesting since there are many evidences of physics not correctly described within the Standard Model, and due to its special role the Higgs boson often enters Beyond-the-Standard-Model (BSM) scenarios. One first example comes from the mass of the Higgs itself. The observation of its mass at 125 GeV means that the Higgs is "light", and should receive quantum corrections that should act to increase its mass value, problem known as *naturalness problem* [21]. This problem could be mitigated assuming some new physics between the electroweak ($\Lambda_{EW} \sim 100\,\text{GeV}$) and the Planck ($\Lambda_{Pl} \sim 10^{19}\,\text{GeV}$) scales, one notable example being Supersymmetry, but no evidences have been found so far. The peculiar properties of the Higgs boson, being a neutral scalar with couplings proportional to particle masses, make it also a candidate to search for BSM models that try to explain other astrophysical and cosmological observations, such as the presence of Dark Matter (DM) and the overabundance of matter with respect to antimatter in the universe. Direct searches for decay of the Higgs into DM candidates such as WIMPs, CP violations or Flavour-Changing Neutral Processes (FCNP), have so far not pointed out significant results.

For all these reasons, the Higgs boson will be extensively studied at the forecoming High-Luminosity LHC project to measure all its possible decay modes, and more interestingly the very rare ones, thanks to the very large datasets that are going to be collected. The recent Update of the European Strategy for Particle Physics [22] poses precise measurement of the Higgs boson as a top priority for particle physics experiments and suggests a multi-TeV collider as the best candidate, with an e^-e^+ collisions phase at its first step. The combined program of the FCC, in its combined lepton and hadron phases, obtained wide consensus during the recent Open Symposium, by fitting precisely the recommendations of European Strategy. The inputs from several European and international institutes were collected by the CERN council, which is expected to take a decision during spring 2026.

1.2 The Large Hadron Collider

The discovery of a scalar boson with characteristics compatible with the Standard Model Higgs was among the main reasons behind the construction of the Large Hadron Collider (LHC)[23], the largest proton-proton collider ever built, in the same underground tunnel previously used for the LEP electron-positron accelerator. The LHC is a 26.7 km long circular collider located at CERN, between 45 m and 170 m underground. Proton beams are accelerated in opposite directions in order to reach energies of 6.8 TeV, corresponding to centre-of-mass collision energies of 13.6 TeV.

Four main experiments are located in the interaction points of the two accelerator rings. ATLAS [24] and CMS [25] are general purpose detectors with nearly full solid angle coverage, to study almost all possible final states originating from the pp collisions. The LHCb [26] experiment has a forward geometry to mainly concentrate on final states comprising b-quarks that are produced at high pseudo-rapidity, in order to search for CP symmetry violations in the quark sector. The last experiment, ALICE [27], mainly focuses on heavy ion collisions for Quark-Gluon Plasma studies. Many other experiments specifically designed for different particle physics topics are also present along

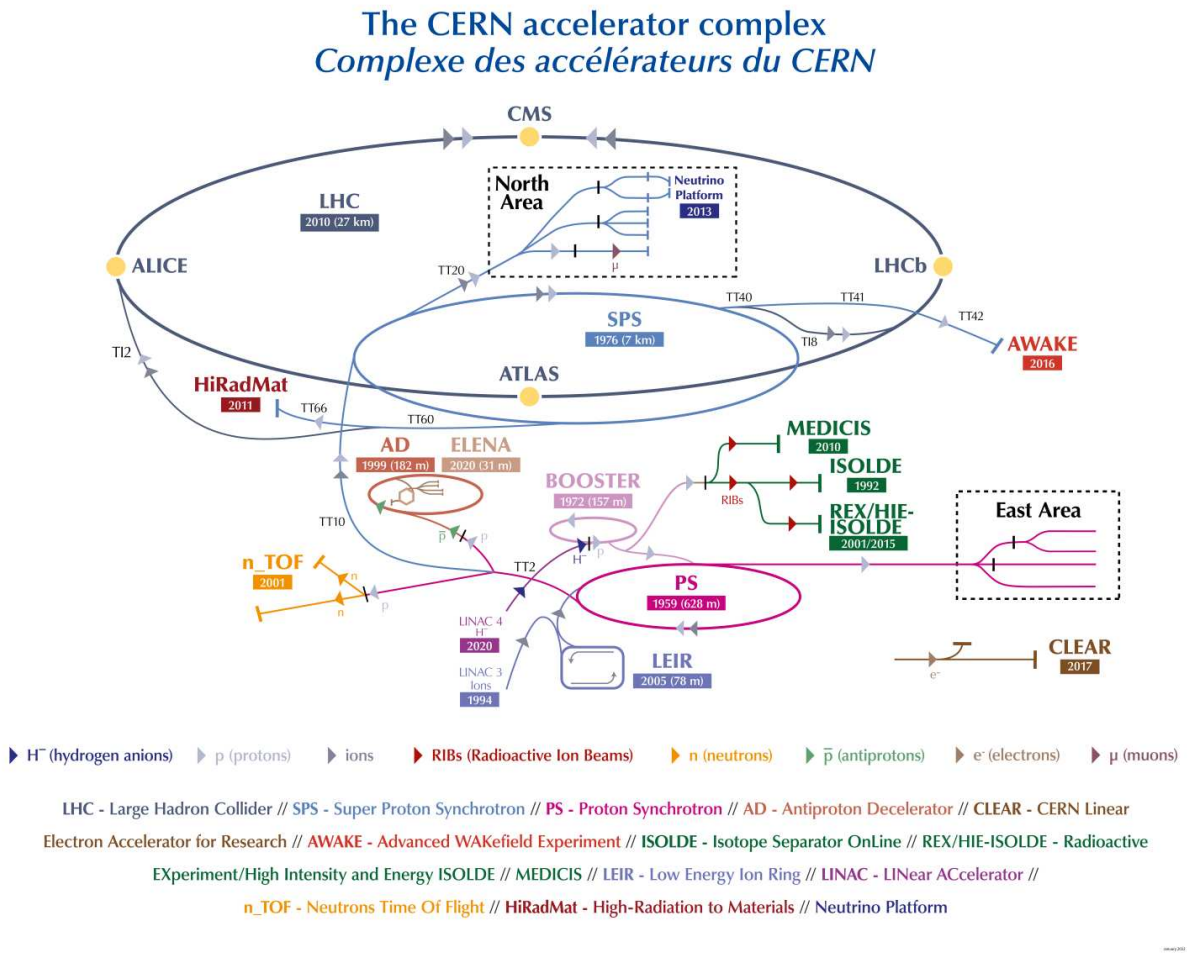


Figure 1.2: Accelerator chain at CERN [32].

the accelerator ring, hosted in caverns close to the interaction points, among which FASER [28], TOTEM [29], LHCf [30] and MOEDAL [31].

The operation of the LHC started with the first data acquisition campaign (Run 1) from 2009 to 2013, and centre-of-mass collision energies of 7 and later 8 TeV. Other two campaigns have been carried out at energy $\sqrt{s} = 13.6$ TeV, Run 2 from 2015 to 2018 and Run 3 which started in 2022 and whose conclusion was postponed to July 2026. Figure 1.2 shows the LHC accelerator chain from the proton extraction up to LHC main ring. After having their electrons stripped from their atoms, the hydrogen positive ions are injected into the Linac4 linear accelerator, which substituted the previous Linac2 in 2020 [33], reaching a momentum of 160 MeV. Different circular synchrotron stages are then used to increase protons energy. The first one is the Proton Synchrotron Booster, able to accelerate protons up to 2 GeV, followed by the Proton Synchrotron (reaching up to 26 GeV) and then the Super Proton Synchrotron (SPS). At an energy of 450 GeV, protons in the SPS are injected into the LHC to be accelerated to the nominal collision energy.

Inside the LHC protons are grouped in bunches, containing up to 10^{11} particles each, with a 25 ns separation between bunch corresponding to about 7 metres [34]. One of the most important parameters in collider physics is the *instantaneous luminosity*, defined

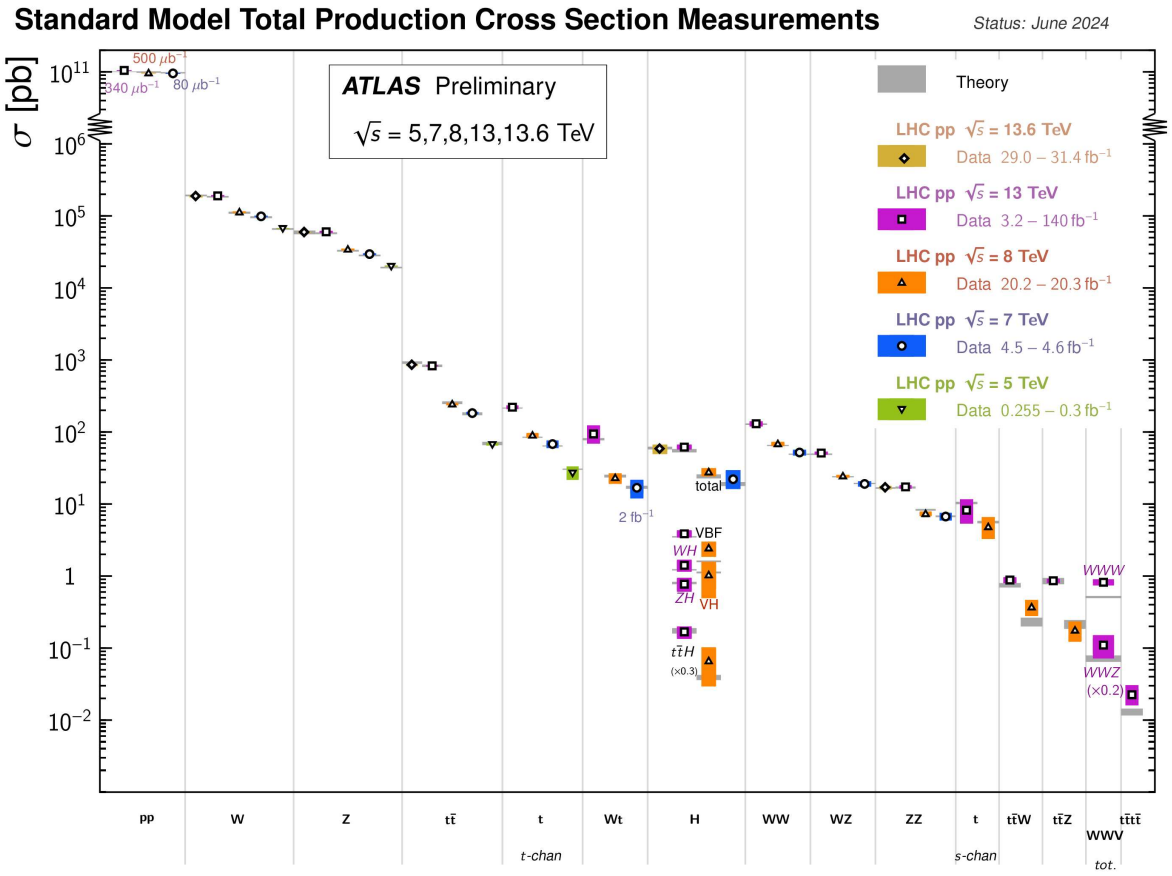


Figure 1.3: Measured cross sections by the ATLAS collaboration, and corresponding theoretical predictions, for different Standard Model processes and centre-of-mass collision energies. Taken from [36].

as

$$\mathcal{L} = \frac{N_b n_1 n_2}{d_X d_Y} f. \tag{1.5}$$

where N_b represents the number of circulating bunches, n_1 and n_2 are the number of proton within each bunch, d_X and d_Y are the lateral dimensions of the bunch (below 20 μm at the LHC), and f is the revolution frequency. More effects can also be taken into consideration to have a more realistic description, such as beam interactions and beam geometry [35]. The rate of events for the process of interest X is then given by its cross section σ_X, that is usually dependent on the collision energy available in the centre-of-mass frame $\sqrt{s}$, and the instantaneous luminosity $\mathcal{L}$, by the relation:

$$R = \frac{dN_X}{dt} = \sigma_X \mathcal{L}. \tag{1.6}$$

Figure 1.3 shows the cross section of different Standard Model processes measured by the ATLAS experiment, and compared with their theoretical prediction, showing excellent compatibility for all of them.

Since σ_X only depends on the physical process of interest, the luminosity is a useful parameter to compare the properties of different colliders. The LHC nominal instantaneous luminosity of 1×10^{34} cm^{-2}s^{-1} is more than an order of magnitude higher than

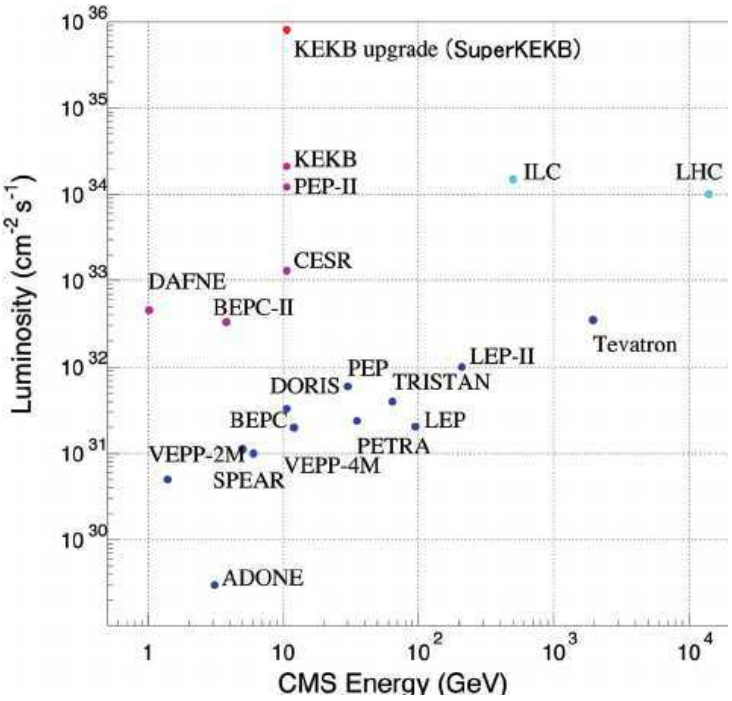
the previous high-energy accelerator, the Tevatron, which was able to reach a luminosity $\mathcal{L} = 4 \times 10^{32}$ cm^{-2}s^{-1}, see fig. 1.4a. During the Run 2 data-taking period, the LHC managed to reach a value of $\mathcal{L} = 2 \times 10^{34}$ cm^{-2}s^{-1}, double than the nominal one, and similar values with higher integrated luminosity were achieved during Run 3.

During the Long Shutdown 3, a three-year period from 2026 to 2028, both the LHC accelerator and experiments will undergo a phase of upgrade in order to sustain substantially higher luminosities. In the following Run 4 and Run 5, foreseen from 2029 to 2041, instantaneous luminosities 5 times higher than the LHC baseline one are expected to be reached, with an integrated luminosity of $L = 3000$ fb^{-1} (see fig. 1.4b). The main hardware upgrades for the accelerator machine consist of new Nb_3Sn magnets able to produce higher magnetic fields with respect to current Nb-Ti magnets, crab cavities to improve the overlapping between colliding bunches, new beam optics and cryogenics systems [39]. The increased amount of bunch interactions comes at the cost of higher pile-up collisions. Pile-up mainly consists of secondary collisions in the same bunch crossing as the hard scattering process, resulting in additional signals in detectors. The number of pile-up events in the two general purpose experiments, ATLAS and CMS, is expected to increase from an average of 40 to 140 per bunch crossing. This dramatic increase in the total number of collisions poses additional requirements on the detector capabilities to identify particles produced in the collision of interest from those coming from soft collisions, such as better performing trigger systems and improved timing resolutions [40][41].

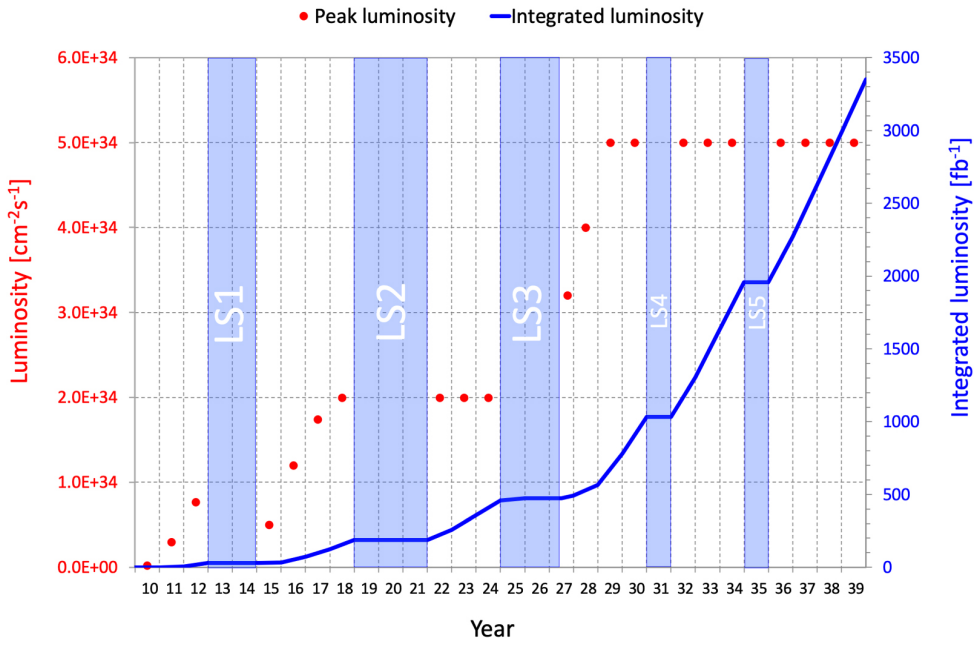
After ~ 15 years of functioning, the most significant result of Large Hadron Collider remains the discovery of the Higgs boson, whose measured properties are, to date, in full agreement with the simplest Standard Model scenario. It it nevertheless impressive how large is the amount of searches performed by the LHC experiments, which found excellent agreement between predictions and observed data spanning over 13 orders of magnitude. Moreover, an incredibly broad campaign of searches for BSM processes has been carried on. Several models have been falsified or disfavoured, therefore revolutionising the theoretical perspective of the pre-LHC era, and increasing the range of tested parameters up to the TeV scale. The huge amount of data that are going to be produced by this machine in the coming decades will allow searching for processes with very low cross sections, that could have passed unobserved during the first runs, and looking for hints of slight deviations from the Standard Model and possibly new particles.

1.3 The Future Circular Collider

Following the Update of the European Strategy for Particle Physics [42], a hadron collider able to reach energies of 100 TeV has been identified as the highest priority collider after the LHC, possibly anticipated by an electron-positron Higgs factory. The integrated project of the Future Circular Collider (FCC) [43] fits precisely in this scenario: a first stage with e^+e^- collisions, the FCC-ee [44], is envisaged for the most precise possible measurements of the W, Z and Higgs bosons and the top quark, followed by a second phase with proton and heavy ion collisions at the highest achievable energy, the FCC-hh [45]. The integrated FCC project would comprise both the FCC-ee and FCC-hh steps, allowing the optimisation of the infrastructure by minimising the amount of work required to switch from one to the other. The currently proposed design, shown in fig. 1.5 for the lepton phase and fig. 1.6 for the hadron one, consists of a 90.7 km long circular accelerator located approximately 200 m underground close to the CERN area,



(a)



(b)

Figure 1.4: (a): Comparison of the instantaneous luminosity, and the corresponding collision energy, for several existing and proposed accelerators, taken from [37]. (b): Total integrated luminosity delivered by the LHC during different years of collisions, image from [38].

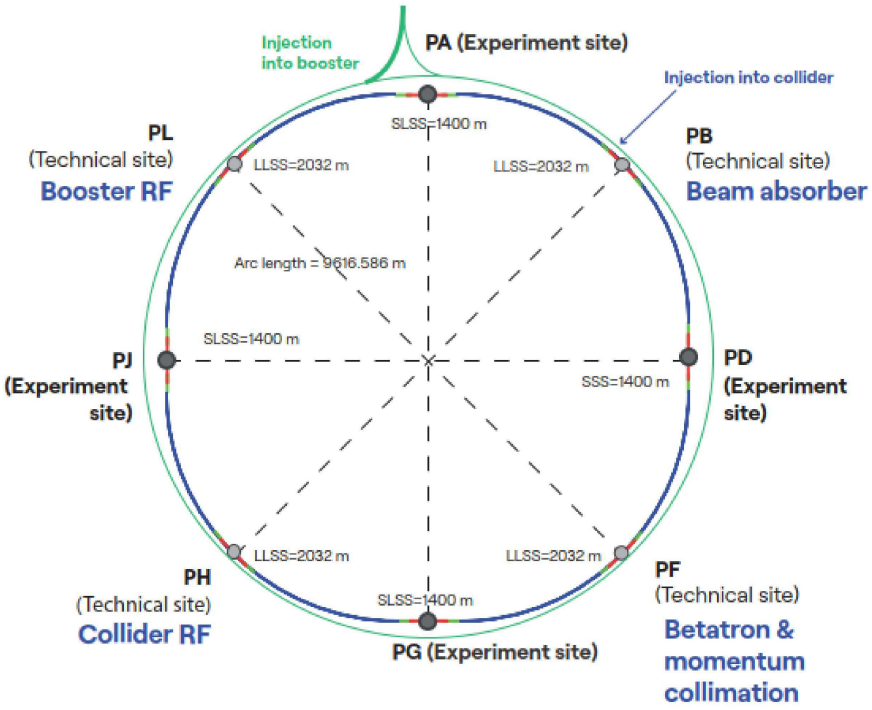


Figure 1.5: Layout of the FCC-ee accelerator machine. The green line represents the accelerator booster, located in the same cavern as the main accelerator. Figure from [46].

between Switzerland and France.

The FCC-ee machine is designed as a very high luminosity collider able to work at different centre-of-mass energy stages from 90 up to 365 GeV, as listed in table 1.1, providing about 6×10^{12} Z bosons, 2×10^{8} $W^{+}W^{-}$ pairs, about 2.5×10^{6} Higgs bosons and 2×10^{6} top quark pairs. While in first baseline concepts two Interaction Points (IPs) were foreseen, more recent proposals point to a four IPs option, hence doubling the amount of events for the analyses, or rather reaching the same statistics in an almost halved amount of time. Three experiments have already been identified in the Feasibility Study Report [47]: the CLD [48], IDEA [49], and the ALLEGRO [50] experiments. The accelerator programme would have a lifespan of about 15 years, before a break for

Table 1.1: Summary of working points and expected event yields at the FCC-ee, assuming four IPs with 185 days of physics data-taking per year and a 75% operational efficiency. Taken from [47].

Working point	**Z pole**	**WW thresh.**	**ZH**	**$t\bar{t}$**	
$\sqrt{s}$ (GeV)	88, 91, 94	157, 163	240	340–350	365
Lumi/IP (10^{34} cm^{-2}s^{-1})	140	120	7.5	1.8	1.4
Lumi/year (ab^{-1})	68	9.6	3.6	0.83	0.67
Run time (year)	4	2	3	1	4
Integrated lumi. (ab^{-1})	205	19.2	10.8	0.42	2.70
Number of events	6×10^{12} Z	2.4×10^{8} WW	2.2×10^{6} ZH + 65k WW $\rightarrow$ H	2×10^{6} $t\bar{t}$ + 370k ZH + 92k WW $\rightarrow$ H	

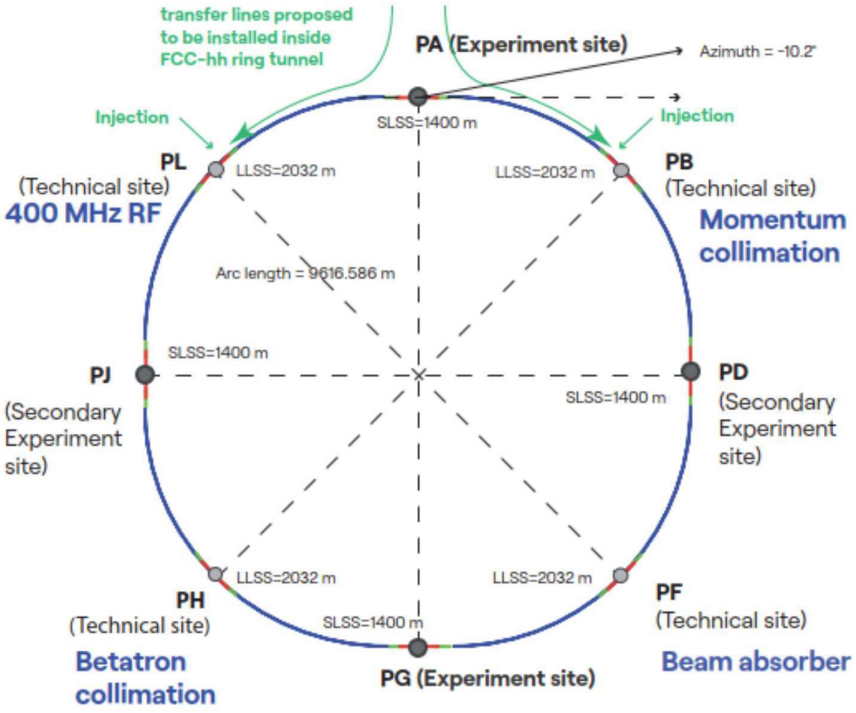


Figure 1.6: Layout of the FCC-hh accelerator machine [46].

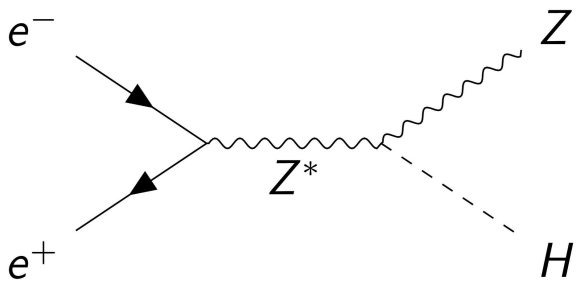


Figure 1.7: Higgsstrahlung process: $e^+e^- \rightarrow ZH$

an hardware upgrade to the $\sim$ 25 years hadron-hadron collisions phase, resembling the successful running of LEP and LHC from 1989 to 2041. The increase from two to four IPs on the beamline also allows to investigate for more diversified detector technologies, and control possible systematics effects that may arise in one or more of the experiments.

The main advantage of the FCC-ee is its extremely high luminosity, and precise knowledge of the beam energy available in the collisions. At the core of the FCC-ee physics programme there is an in-depth characterisation of the Higgs boson properties, that will be explored through sub-percent precision measurements of its couplings with many other Standard Model particles. At $\sqrt{s} = 240$ GeV, the Higgsstrahlung process (see fig. 1.7) allows to measure with sub-percent precision the Higgs boson mass by reconstructing the Z boson mass (which will already be known with even better precision than today, thanks to the previous Z-pole run), and to the exact knowledge of the beam energy and hence centre-of-mass energy available in the collisions (impossible to any hadron collider due to distributions of parton momenta), independently from the Higgs decay channel.

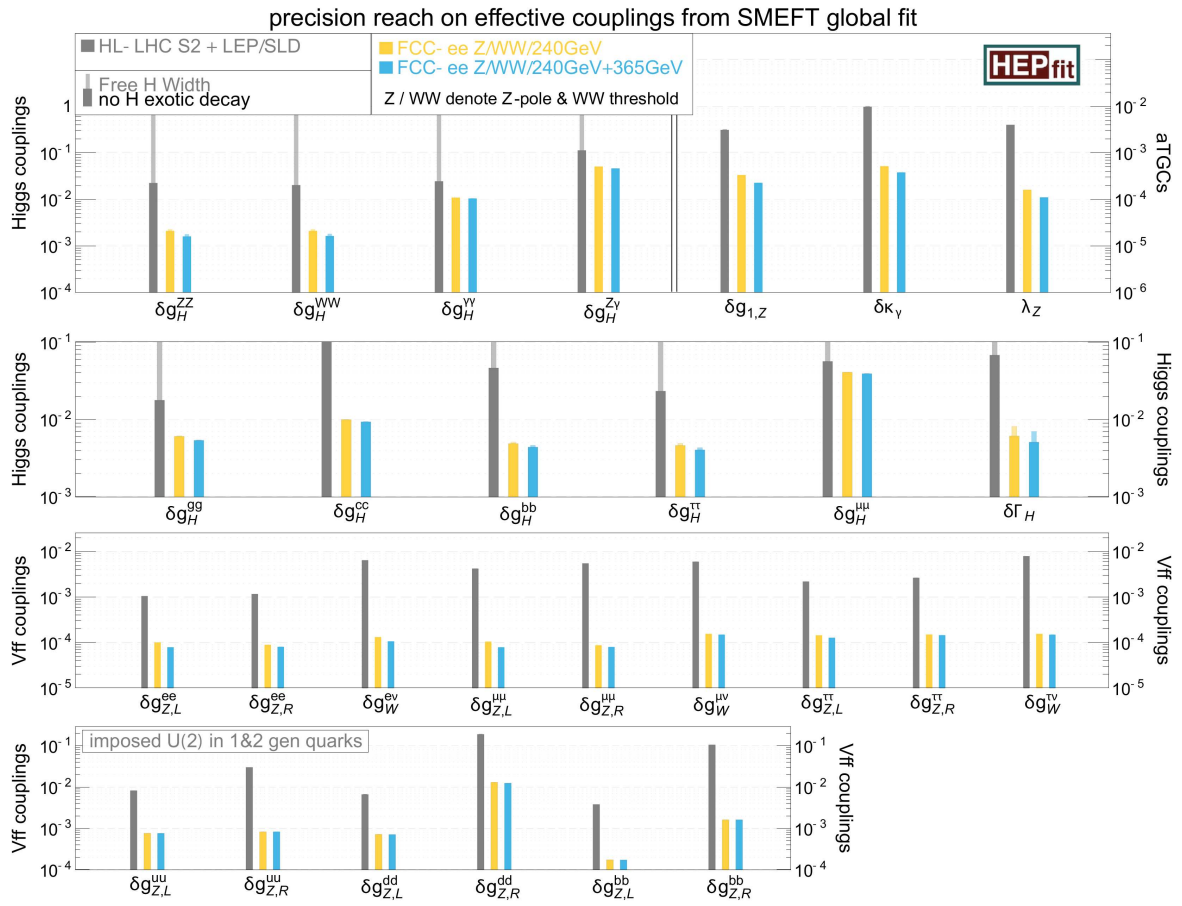


Figure 1.8: Global SMEFT fit results to the full LHC+HL-LHC run operation, and to the FCC, before (yellow) or after (blue) the accelerator upgrade at 365 GeV for the $t\bar{t}$ run. Vertical lines show the uncertainty on the considered parameter. Different dimension-six operators are taken into consideration, affecting electroweak processes (anomalous triple-gauge couplings, aTGCs, and boson-fermions couplings, Vff), or couplings of the Higgs boson [47].

The Standard Model Effective Field Theory (SMEFT) framework is widely used to describe the improvement in sensitivity to deviation in expected processes affecting the Higgs and electroweak sectors for new experiments in a model-independent way. It consists of a global fit of all SM lagrangian parameters and new higher order operators, up to dimension six, to experimental data collected at operating experiments and envisioned future experiments. Possible sources of new physics beyond the Standard Model, up to scales $\Lambda \geq 1$ TeV, may arise through small deviations of lagrangian parameters from their expected values, which are denoted as δg_X where X is the parameter under study, or δg_X^Y if the parameter of interest is the coupling between a particle X and a second particle Y. Figure 1.8 shows the expected improvement of the FCC-ee on the precision upon many of these parameters, which in most cases supersedes previous measurements of LHC and LEP by one (and in some cases even two) orders of magnitudes.

One important measurements that could be in reach at the FCC-ee is the direct measurement of the Higgs self-coupling [51]. The self-interactions of the Higgs boson are fundamental to access the exact shape of the Higgs potential $V(\phi)$, and possible meta-

stable states, therefore understanding the vacuum stability of the Universe. The direct measurement of the tri-linear Higgs coupling at $\sqrt{s} = 240, 365$ GeV is not guaranteed, as the threshold for the leading-order process of tri-linear Higgs vertex production requires higher energies. This process may nevertheless be constrained through higher-order processes contributions, even allowing for close to 5σ discovery significance, turning into one of the main reasons for the increase in the number of IPs. With only two interaction points, a significance of $\sim 2\sigma$ would be expected, and the complete FCC-ee/FCC-hh programme would be required to reach enough precision for this discovery.

One additional interesting analysis related to the Higgs particle would be the direct measurement of the invisible branching fraction, that in the SM only happens through the process $H \to ZZ^* \to \nu\bar{\nu}\nu\bar{\nu}$ with a branching fraction of about 0.1% [52]. A deviation of the predicted branching fraction would point to additional decays, such as the decay of the Higgs into two non-interacting or feebly-interacting particles that, if long-living, could play the role of dark matter candidates.

Before the Higgs run, two sets of data-taking periods are envisioned, the first at the Z pole (around $\sqrt{s} = 91$ GeV), and a second close to the threshold for the production of two W bosons ($\sqrt{s} = 160$ GeV). The exact values of the centre-of-mass energies are given in table 1.1, and allow for scans around the correct mass values to measure the masses and widths of these gauge bosons. The three operation conditions (Higgstrahlung pole, Z pole and W^+W^- threshold) are planned to be run in a quasi-total order flexibility mode, therefore enabling the transition to different centre-of-mass energies with minor delays. This allows to have runs at the Z pole for calibration procedures before taking measurements at other centre-of-mass working points, and also performing the set of measurements at the different energy stages in the preferred order. This flexibility feature does not cover the $t\bar{t}$ threshold run, for which upgrades to the accelerator machine will be required.

The first planned operation stage at the FCC-ee, at the Z boson production pole of $\sqrt{s} = 90$ GeV, will serve for the most precise measurements yet of many Electro-Weak Precision Observables (EWPOs), listed in table 1.2. The improved measurement of the Z boson line shape with respect to the LEP is related to better precision upon several of these observables, such as the Z boson mass m_Z, its width Γ_Z, the peak cross-section for the Z hadronic decay modes, σ^0_{had}, as well as the number of neutrino families, with the LEP combined measurements shown in fig. 1.9. The ratio of Z boson decays into hadrons to leptons, R^Z_ℓ is sensitive to the strong interaction coupling constant $\alpha_s(m^2_Z)$, and is also useful for testing the universality of the Z boson couplings to fermions [53]. An important part of the work to achieve the best measurements in both the Z boson, W boson and possibly even the Higgs boson linewidths is the the beam calibration through beam polarisation at the ~keV level [54]. It can be seen from table 1.2 that the beam energy calibration is, in fact, one of the leading uncertainties for many EWPOs measurements.

Forward-backward asymmetry due to the parity violations in weak interactions will be explored with higher statistics than LEP [55], for all possible final states including b-quarks (A^b_{FB}) and τ leptons ($A^{pol,\tau}_{FB}$). With the very large data samples collected at both the Z pole and W threshold, the FCC-ee will also be a flavour physics factory with about ~ 15 times more events than other B-factories such as Belle-II, producing large amounts of b, c quarks and τ leptons [56]. The τ lepton mass and lifetime will be measured with high precision, and its branching fractions can be detailed with higher

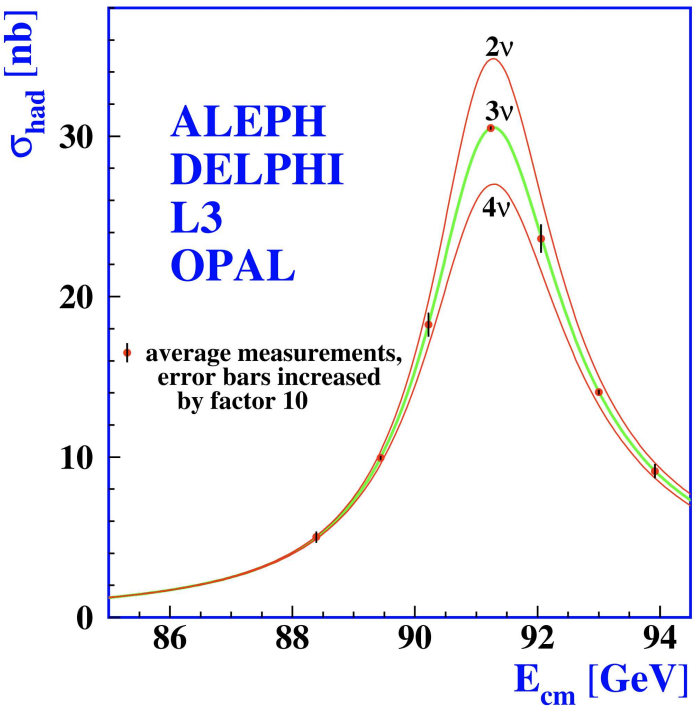


Figure 1.9: Line shape of the Z boson, measured by all four LEP experiments. The three drawn curves represent the theoretical line shape in the case of $\mathcal{N} = 2, 3, 4$ neutrino generations, on which the combined experimental data are superimposed. Image from [53].

accuracy through improved particle identification capabilities of detectors at the FCC, most importantly in the identification of π^0 decays.

The operation stage around the W^+W^- production threshold will complete the set of EWPOs measurements with full detailing of the properties of this boson, including its mass, width, branching fraction and the ratio of hadronic decays with respect to leptons ones. The properties of the W bosons also represent important systematics effects in many BSM searches, therefore this run will be important to fully exploit the wide datasets collected at both the FCC-ee and FCC-hh.

The run at the Z pole, with its extremely large statistics, will also allow to search for feebly interacting particles and very rare phenomena, that could have passed unobserved at the LHC and the Hi-Lumi phase, thanks to the clean experimental conditions. A few examples of these searches involve long-lived particles [57] and axions [58].

Finally, the top quark run, between 340-365 GeV, will serve the purpose of measuring its Yukawa coupling with a precision not in reach at hadron colliders. The outcome will be reducing the uncertainty for several other measurements and also searches for exotic processes, on which the m_{top} variable is one of the largest systematic effects, therefore drastically improving the sensitivity to new physics.

1.3.1 FCC-hh

The second phase of the FCC integrated programme, in agreement with the European Strategy for Particle Physics, involves a hadron-hadron collider machine with the highest achievable energy. Exploiting the same 90.7 km long tunnel already used for the previous FCC-ee stage, centre-of-mass proton-proton collision energies at about 85 TeV

Table 1.2: Summary of electroweak and top observables, with current precision and expected improvements at FCC-ee. All values assume four IPs, with statistical and systematic uncertainties shown separately. The leading uncertainty foreseen at the FCC-ee is briefly described in the right column. Taken from [47].

Observable	**Present value**	**± uncertainty**	**FCC-ee Stat.**	**FCC-ee Syst.**	**Comment and leading uncertainty**
m_Z (keV)	91 187 600	± 2000	**4**	100	From Z line shape scan Beam energy calibration
Γ_Z (keV)	2 495 500	± 2300	**4**	12	From Z line shape scan Beam energy calibration
$\sin^2\theta_W^{\text{eff}} \times 10^6$	231 480	± 160	**1.2**	1.2	From $A_{\text{FB}}^{\mu\mu}$ at Z peak Beam energy calibration
$1/\alpha_{\text{QED}}(m_Z^2) \times 10^3$	128 952	± 14	**3.9** **0.8**	small tbc	From $A_{\text{FB}}^{\mu\mu}$ off peak From $A_{\text{FB}}^{\mu\mu}$ on peak QED & EW uncert. dominate
$R_\ell^Z \times 10^3$	20 767	± 25	**0.05**	0.05	Ratio of hadrons to leptons Acceptance for leptons
$\alpha_S(m_Z^2) \times 10^4$	1 196	± 30	**0.1**	1	Combined R_ℓ^Z, Γ_{tot}^Z, σ_{had}^0 fit
$\sigma_{\text{had}}^0 \times 10^3$ (nb)	41 480.2	± 32.5	**0.03**	0.8	Peak hadronic cross section Luminosity measurement
$N_\nu \times 10^3$	2 996.3	± 7.4	**0.09**	0.12	Z peak cross sections Luminosity measurement
$R_b \times 10^6$	216 290	± 660	**0.25**	0.3	Ratio of $b\bar{b}$ to hadrons
$A_{\text{FB}}^{b,0} \times 10^4$	992	± 16	**0.04**	0.04	b-quark asymmetry at Z pole From jet charge
$A_{\text{FB}}^{\text{pol},\tau} \times 10^4$	1 498	± 49	**0.07**	0.2	τ polarisation asymmetry τ decay physics
τ lifetime (fs)	290.3	± 0.5	**0.001**	0.005	ISR, τ mass
τ mass (MeV)	1 776.93	± 0.09	**0.002**	0.02	Estimator bias, ISR, FSR
τ leptonic BR (%)	17.38	± 0.04	**0.00007**	0.003	PID, π^0 efficiency
m_W (MeV)	80 360.2	± 9.9	**0.18**	0.16	From WW threshold scan Beam energy calibration
Γ_W (MeV)	2 085	± 42	**0.27**	0.2	From WW threshold scan Beam energy calibration
$\alpha_S(m_W^2) \times 10^4$	1 010	± 270	**2**	2	Combined R_ℓ^W, Γ_{tot}^W fit
$N_\nu \times 10^3$	2 920	± 50	**0.5**	small	Ratio of invis. to leptonic in radiative Z returns
m_{top} (MeV)	172 570	± 290	**4.2**	4.9	From $t\bar{t}$ threshold scan QCD uncert. dominate
Γ_{top} (MeV)	1 420	± 190	**10**	6	From $t\bar{t}$ threshold scan QCD uncert. dominate
$\lambda_{\text{top}}/\lambda_{\text{top}}^{\text{SM}}$	1.2	± 0.3	**0.015**	0.015	From $t\bar{t}$ threshold scan QCD uncert. dominate
$t\bar{t}Z$ couplings		± 30%	**0.5–1.5%**	small	From $\sqrt{s} = 365$ GeV run

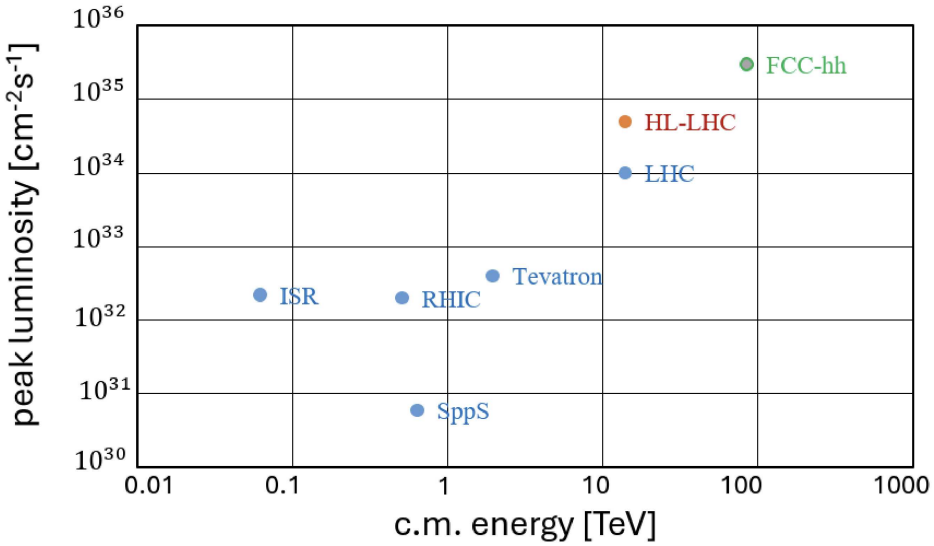


Figure 1.10: Comparison of the energy and integrated luminosity of the FCC-hh and the previous hadron-hadron colliders [45].

are foreseen. Higher energy stages of 100 TeV and 120 TeV could be reached, depending on the available technology at the time of accelerator construction. The main factors limiting the proton beam energies are the technology readiness for accelerating, bending and focusing magnets, and the power consumption of cryogenic cooling system that would be required because of strong synchrotron radiation. The baseline magnet technology used for the FCC-hh are 16 T dipole magnets based on Nb_3Sn superconductors, that should operate at a temperature of 1.9 K. Active research is currently ongoing to increase the maximum operating temperature of these magnets required for their usage. An important line of research is also the development of High-Temperature-Superconductor (HTS) magnets, that are able to achieve superconductivity at higher temperatures of the order of 100 K reaching magnetic fields of 20 T.

The FCC-hh physics programme complements the FCC-ee one, by directly searching for processes that could only be indirectly hinted at the lepton collider. The exploration of the multi-TeV energy scale allows to look for processes well above the electroweak scale, and investigating several BSM models that cannot be directly tested at the LHC. Two important Standard Model processes that can be directly measured at the FCC-hh are the $t\bar{t}Z$ coupling and HH pair production, for which only indirect measurements can be performed at the FCC-ee because of the very high energy required. With the extremely high integrated luminosity of FCC-hh, about 20×10^9 Higgs bosons are expected to be produced, and the sensitivity and precision to specific physics processes measurements drives tight requirements on detectors to reduce drastically the background. As a consequence of the very high luminosities, the mean number of collisions per bunch crossing $\langle\mu\rangle$ (pile-up) is expected to increase to ~1000, almost one order of magnitude higher than the HL-LHC. The large statistics for the production of Higgs bosons allows for direct measurements of small effective H couplings such as muons and $Z\gamma$, that may be statistically limited at the e^+e^- collisions stage. Very high-Q^2 scatterings may be used for heavy resonances searches in the range of tens of TeV, heavy supersymmetric partners (gluinos and squarks), high-energy effective operators and dark matter candidates.

The integrated programme of FCC-ee and FCC-hh shows synergies and comple-

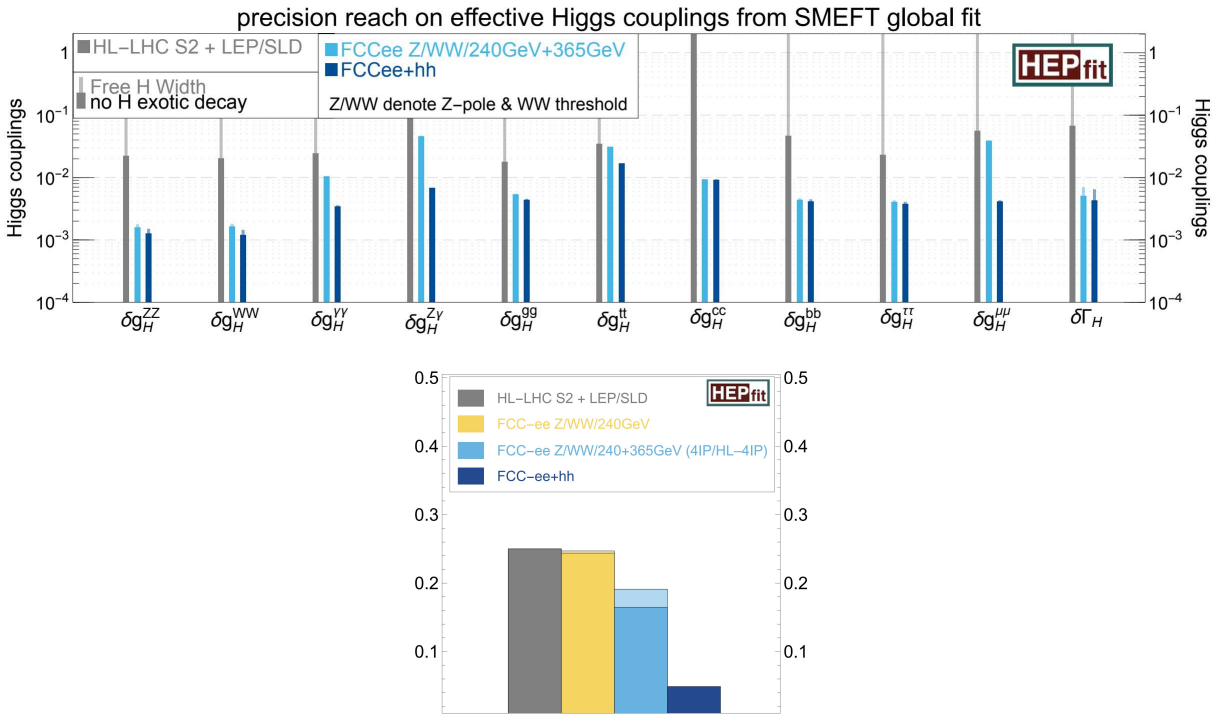


Figure 1.11: Expected improvement in the sensitivity to deviations in Higgs boson couplings in the global SMEFT fit framework, from the complete High-Luminosity LHC to FCC-ee and FCC-hh. On the bottom plot, improvement of the κ_λ Higgs self-coupling parameter from the LHC to FCC-ee and FCC-hh. Both images are from [47].

mentarity both in Standard Model precision measurements and BSM searches. Figure 1.11 shows how beneficial would be the absolute scale determination of several Higgs boson couplings at the FCC-ee, in order to fully exploit the later FCC-hh dataset at higher energies. The precision upon deviations from the Higgs self-couplings κ_λ, whose precision is expected to improve from $\sim 50\%$ to about 28% by the end of HL-LHC, would reach a level of 3% with the combined FCC-ee/hh runs [47]. Hints of new physics, that may manifest as deviations from SM predictions during the precision measurements at the FCC-ee, could later be directly investigated in a much wider energy range during the hadron collision phase. By considering an experimental facility layout similar to the LHC with 4 IPs, two general purpose experiments could be placed along the collider ring. Another detector could focus ion-ion or proton-ion collisions for QCD and Quark-Gluon-Plasma at the highest temperatures ever reached, enriching the landscape of possible measurements with such collider. The fourth large experiment could focus on a specific type of physics searches to be decided, resembling the LHCb experiment at LHC, with a dedicated detector design. Finally, parasitic experiments could be placed along the accelerator for neutrino physics and long-lived and feebly-interacting particles searches, similarly to the FASER and SND experiments at the LHC.

1.4 Other projects

1.4.1 The Circular Electron-Positron Collider

The Circular Electron-Positron Collider (CEPC) [59] is a project that would be hosted in China, and shares similar characteristics with the FCC. A first phase with electron-

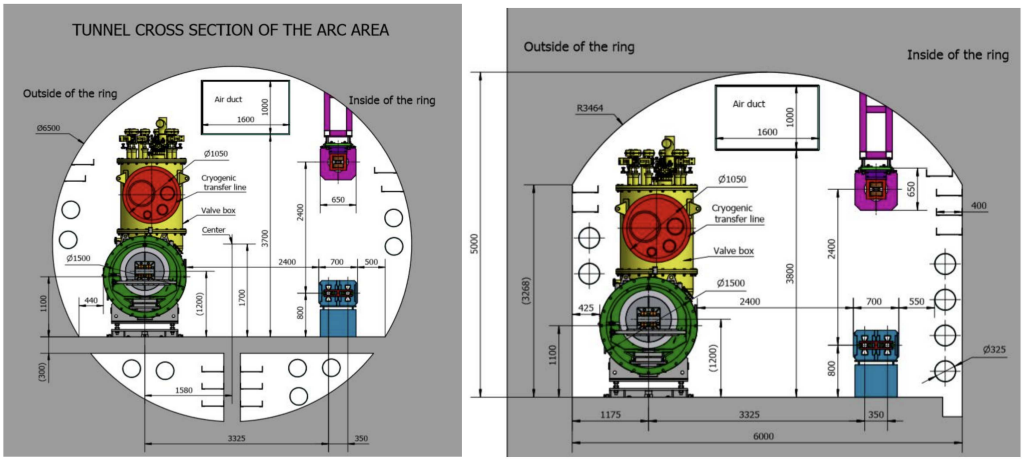


Figure 1.12: Proposed tunnel configurations of the CEPC, including the booster, the electron-positron accelerator, and the proton accelerator [59]. The booster (purple) and electron-positron rings (blue) would be located the inner part of the tunnel, while the proton rings would be placed on the outer side.

positron collision is envisaged, that would subsequentially evolve into a hadron collider, the Super Proton-Proton Collider (SPPC). Both accelerators would be placed in a 100 km long underground tunnel which, differently from the FCC, is large enough to fit both CEPC and SPPC rings at the same time, including also the CEPC booster (see fig. 1.12). Concerning the CEPC, a Linac for electron acceleration up to 30 GeV and a damping ring for reducing the positron emittance would be used before the injection into the underground booster. The baseline CEPC project includes three collision energy stages, $\sqrt{s} = 91, 160$ and 240 GeV (corresponding to Z pole, W^+W^- threshold and ZH), followed after a machine upgrade to a $\sqrt{s} = 360$ GeV stage for top quark measurements. The operation of the machine, and the luminosity it would be able to achieve, are governed by the synchrotron radiation that can be sustained. Two luminosity targets are described in the project Technical Design Report, corresponding to 30 MW or 50 MW synchrotron radiation emitted power, both shown in Figure 1.13. Differently from the FCC-ee operation plan, the CEPC would immediately start collecting data at the $\sqrt{s} = 240$ GeV working point for about 10 years, collecting an integrated luminosity of 21.6 ab^{-1} corresponding to 4.3 million Higgs events, in the hypothesis of 2 interaction points and 50 MW synchrotron radiation power. It would follow 2 years of data taking at the Z pole, collecting 100 ab^{-1}, and one year at the W threshold with 6.9 ab^{-1}. After an upgrade of the accelerator, the centre-of-mass energy could then be increased to reach the $t\bar{t}$ production and collect data for 5 years, reaching 1 ab^{-1}.

1.4.2 The International Linear Collider

The International Linear Collider (ILC)[61] exploits superconducting radio-frequency (SCRF) accelerating technology to achieve high-energy electron-positron collisions using a 31 km long linear tunnel. The concept and accelerator technology discussed in the TDR were already under development during the late 1990s, but the discovery of the Higgs boson at a mass of 125 GeV motivated changes in the operation plan to allow for a set of precision measurements of the newly found particle [62]. The centre-of-mass energies that would be reached are 250 GeV, 500 GeV with a possible upgrade to 1 TeV. In the accelerator chain, electrons are produced by a photocathode gun, while positrons

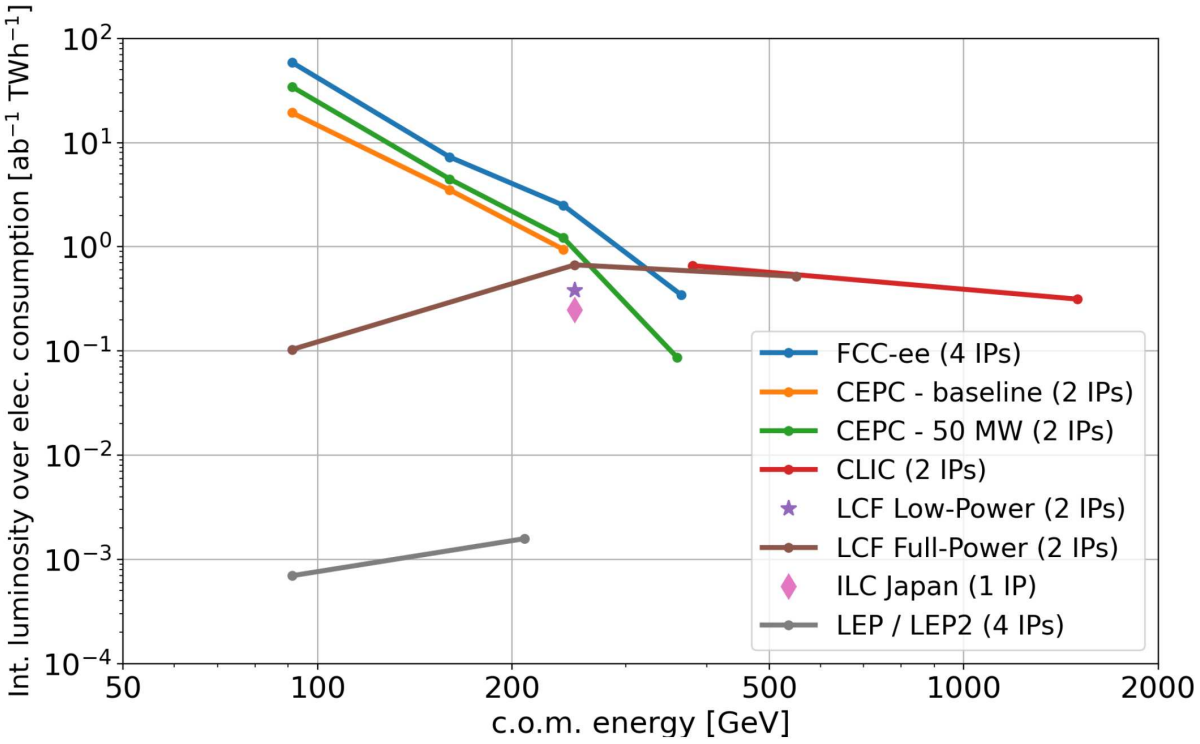


Figure 1.13: Comparison of the instantaneous luminosity of the CEPC with respect to the other proposed Higgs factories [60].

are produced by conversion of high-energy photons produced by letting interact electrons in the main beam through an undulator. After both electrons and positrons are generated, they are injected into two 3.2 km long 5 GeV damping rings and then transported to a two-stage bunch compressor system prior to injection into the main linacs. Each linac uses 1.3 GHz SCRF cavities operating at an average gradient of 31.5 MV/m, provided by ~7000 1 m-long superconducting nine-cell niobium cavities operating at 2 K. One single experimental hall able to host two main experiments in so-called "push-pull" configuration is envisioned, meaning that while one of the experiments it taking data, the other is kept in maintenance mode. Once a target luminosity is reached, the active detector is pushed outside the interaction region and the other is pulled in, with an estimated operation time of the order of just one day, to maximise the overall integrated luminosity of the project.

The proposed operation plan, shown in fig. 1.14, consists of a first $\sqrt{s} = 250$ GeV stage, collecting 2 ab^{-1} in about 12 years of operation, using an electron beam with 80% polarisation and positrons polarised at 30% level. Among the advantages of beam polarisation at e^+e^- colliders are the possibility to increase the rate of interesting physics processes and decreasing the background ones, and a better control of systematic uncertainties. The control of both electrons and positrons polarisations also allows to acquire samples of data with different polarisation configurations, for example exploiting helicity for model discrimination of final state particles consisting of left-handed or right-handed particles.

After an energy upgrade, 0.2 ab^{-1} would be collected at $\sqrt{s} = 350$ GeV to scan at the top quark pairs thresholds, followed by a much longer running time at 500 GeV, collecting 4 ab^{-1} and focusing on ttH and ZHH production. Possible further upgrades of the machine, such as increasing of the collision energy up to $\sqrt{s} = 1$ TeV, can be

achieved at a linear collider by extending it, or increasing the accelerating gradient. The candidate site for the construction and operation of this experiment was identified in the Kitakami region in Japan, which was preferred to others sites because of the optimal geological condition. This region could provide room enough for a 50 km long tunnel, therefore allowing also for the possible 1 TeV upgrade. A second possibility for the construction site, that was proposed very recently as an alternative for Japan, is CERN.

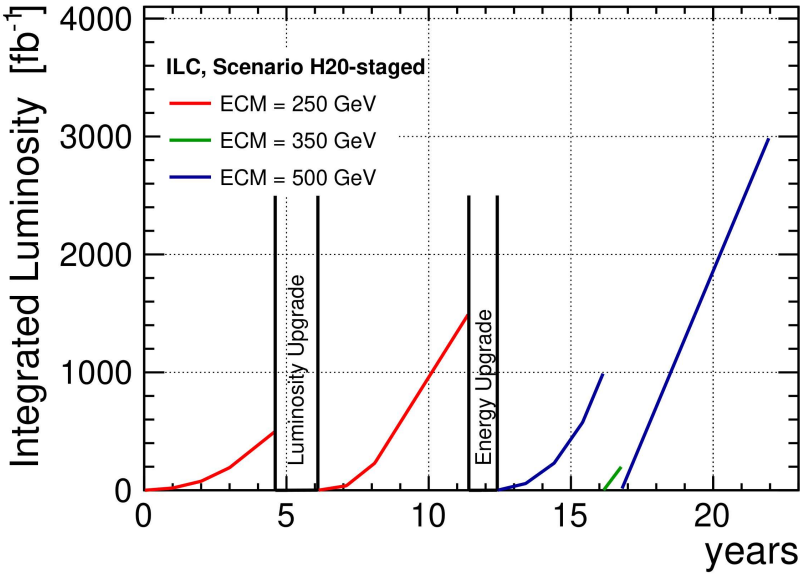


Figure 1.14: Integrated luminosity at the ILC over 20 years of operation [62]

1.4.3 The Compact Linear Collider

The Compact Linear Collider (CLIC) [63] project features a multi-TeV e^+e^- linear collider to be hosted in the CERN area. The main technology under development for its functioning is the novel two-beam acceleration technique, where the power for acceleration is transported to the accelerating structures by a second electron beam, which runs parallel to the main one. Beam power is extracted from the drive beam and converted to RF power in special RF devices called PETS (Power Extraction and Transfer Structures) [64]. The accelerator scheme starts with a radiofrequency injector which produces polarised electrons, whose emittance is reduced through a damping ring. The positron beam is produced through pair production generated by a second electron beam into a target crystal, and later injected into a second damping ring. The two beams are then accelerated to 9 GeV while transported to the main linac, that achieves up to 190 GeV in the first stage through a 100 MV/m accelerating gradient. High energies can be achieved using the same technology by adding accelerating modules and increasing the length of the linac. The first energy stage, with collision energies up to $\sqrt{s} = 380$ GeV, requires a total length of 11.4 kilometers, which would increase to 29 km and 50.1 km at energies $\sqrt{s} = 1.5, 3$ TeV, respectively. High integrated luminosities are in reach over the 30 year lifespan of the project, collecting 1 ab^{-1}, 2.5 ab^{-1} and 5 ab^{-1} at the three energy phases. Of mentioned e^+e^- colliders, the CLIC accelerator is the one able to reach the highest energies, extending the search for new particles with similar mass scales of the LHC, but with the notable advantages of lepton colliders [65]. At the

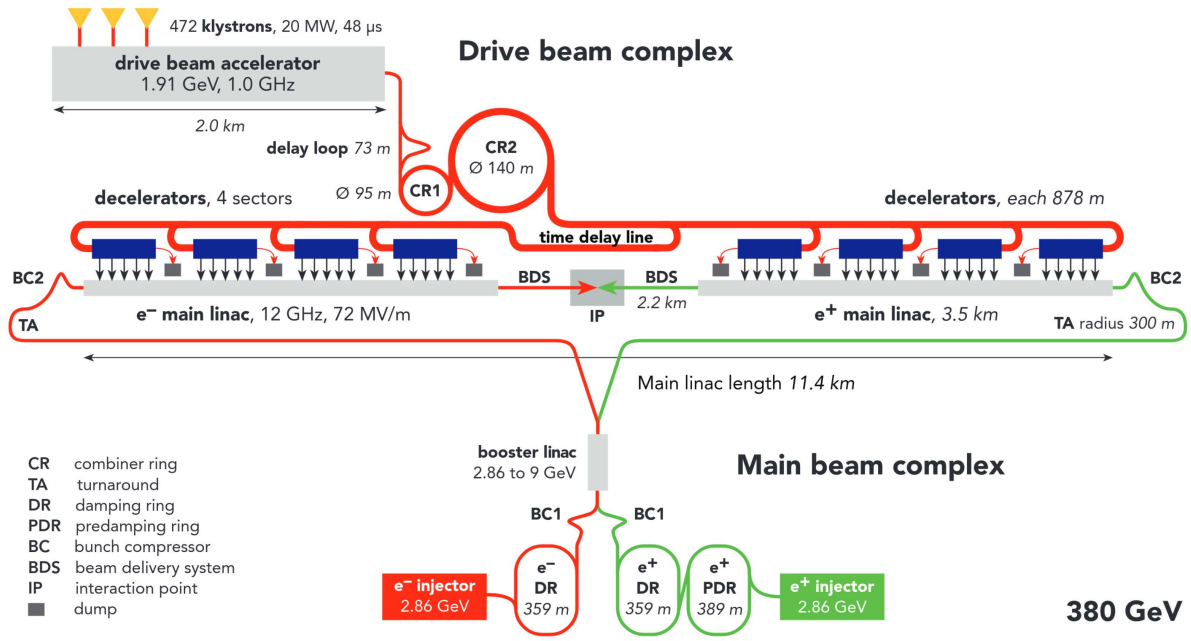


Figure 1.15: The CLIC accelerator complex, image from [63].

380 GeV stage, precision measurements of the Higgs bosons and top quark would be performed. A possible step at $\sqrt{s} = 350$ GeV to investigate the top pair threshold has also been proposed. At higher energy, the most interesting feature of the CLIC is the possibility to explore the double Higgs production through the processes $e^+e^- \to ZHH$ and $e^+e^- \to HH\nu_e\bar{\nu}_e$, therefore directly measuring the Higgs self-coupling.

1.4.4 The Muon Collider

The possibility of colliding muons could offer several advantages over more conventional hadron and electron-positron colliders. At circular accelerators, the emitted power through synchrotron radiation heavily depends on the mass of the accelerated particle, i.e. $P \propto E/m^2$, leading to significant losses by accelerating electrons, and making the reach for very high energies unfeasible. On the other hand, hadrons (mostly protons and anti-protons), due to higher mass with respect to electrons, do not suffer from the synchrotron radiation problem, but being composite particles some well-known issues arise, such as QCD initial state radiation (ISR) and not well known energy in the collision due to parton distribution functions (PDFs). The muon collider project [66] aims at accelerating muons to very high energies, up to the order of 10 TeV, taking the advantage of low synchrotron radiation by these particles and precise knowledge of the energy available for collisions in the centre-of-mass frame. Among the possible physics searches to be performed at a high energy and high luminosity muon collider, are precise measurements of the Higgs boson, including double Higgs production and direct measurements of its trilinear interaction, as well as direct searches for new physics with high precision at scales only available to hadron colliders. The current project for a muon collider follows a two-stage plan with either an energy upgrade, from 3 TeV to 10 TeV, or a luminosity upgrade at a fixed energy of 10 TeV. A comparison of the foreseen instantaneous luminosity of the muon collider, compared with CLIC, are shown in fig. 1.16, showing a large increase in the number of events with the energy in the centre-of-mass frame.

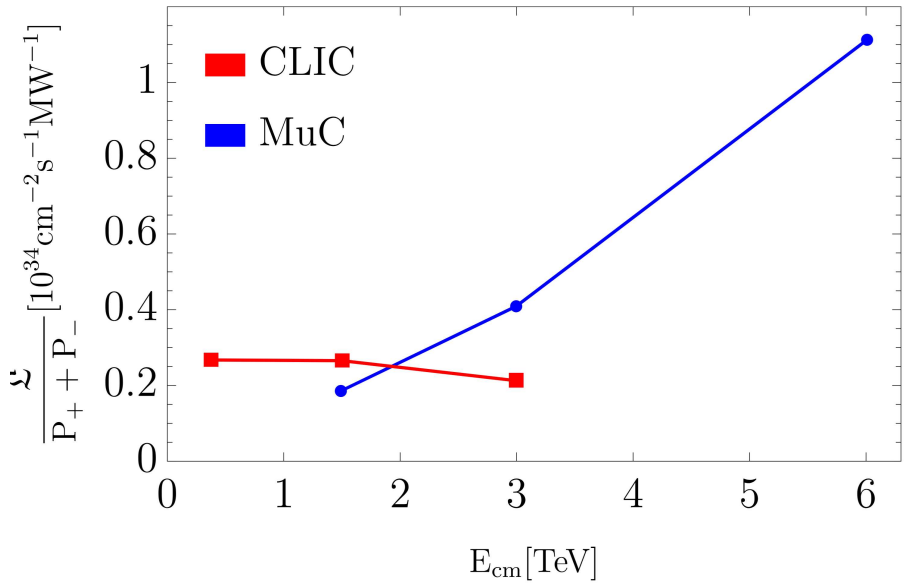


Figure 1.16: Comparison of the instantaneous luminosities of the muon collider and the CLIC linear collier. Figure from [67].

Figure 1.17 shows a picture of the accelerator scheme of the muon collider. Muons are produced through pions decays from a high-intensity proton beam hitting a target. An efficient system for filtering and cooling muons is required to form high intensity bunches with low longitudinal and transverse emittance. A system of linacs then accelerates muons before their final injection into the main collider tunnel. The muon cooling after their production, that is required for the formation of bunches and their injection in the main accelerator, is one of the major technological challenges of the muon collider project. The main difficulty comes from the need to control muons that are produced from pion decays and accelerate them again in an extremely short amount of time, before their decay into electrons. A small-scale demonstrator for the muon cooling technique still has to be built at the time of writing, as it is needed to prove the effectiveness of the muon production for this collider.

From the detector point of view, the most critical issue to address in the identification of a suitable layout is the Beam Induced Background (BIB) due to decaying muons in the region close to the interaction points. For this region, proposed experiments at the muon collider are designed with so-called *nozzles* made of some heavy material, to absorb electron showers produced in the muon decays. Another major requirement on detectors is excellent timing capabilities, in order to only acquire data in a window very close to the bunch crossing and exclude other signals produced at non-collision time stamps. In fact, muons decaying before they reach the interaction point will produce very high energy electrons that generate background signals in most of detectors volume. An excellent timing resolution allows to only select those detector signals that are compatible with particles produced at the very moment of muon collisions in the IPs.

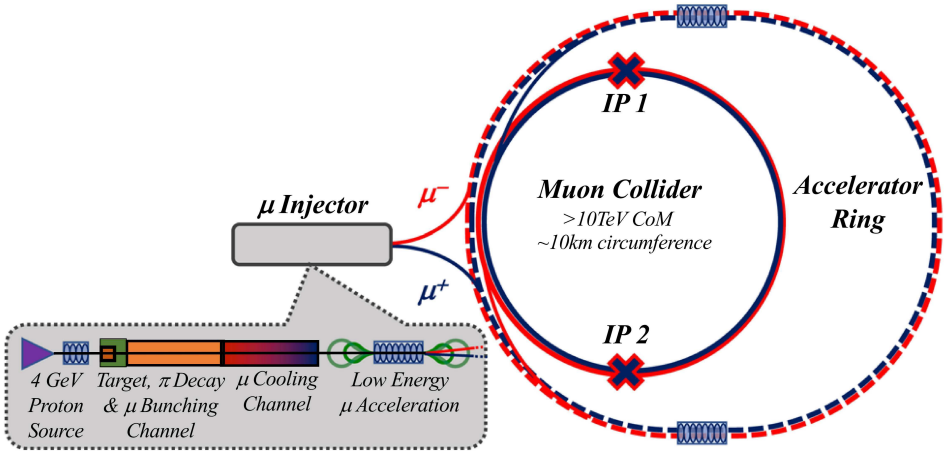


Figure 1.17: Accelerator scheme of the muon collider, showing the muon production and injection infrastructure, the accelerator ring, and the main collider ring. Figure from [67].

Part I

Development of the HiDRa highly granular dual-readout calorimeter prototype

In the following chapters, the development of a dual-readout highly granular calorimeter prototype, called HiDRa, is described, with an emphasis on my own contributions to the project. Chapter 2 provides a short introduction to the complex field of calorimetry in high energy physics. The interactions of different kinds of radiation with matter and the design of calorimeters which measure them are outlined. It follows a presentation of open issues in the calorimetry realm, that limit the performances of currently used detectors at the LHC and other experiments, and methods that have been proposed to overcome these limits, notably the dual-readout method.

Chapter 3 provides a description of the HiDRa prototype. The main features of the SiPM-based readout are briefly introduced. A deep list of studies, performed through Geant4 simulation package, were realised by the candidate during its first year of Ph.D. to identify the best design properties of the calorimeter with the available budget and reported in this chapter.

Chapter 4 describes the analysis of simulated data with the same prototype, consisting of studies concerning high-granularity features provided by the SiPM readout that could not be tested with real data during the three-year doctoral period. Spatial resolution for different particles, particle identification capabilities and other studies are described.

In Chapter 5, the analysis of real data from a partially-completed prototype with PMT-only readout, taken during a 2024 test beam campaign, is presented. The results are compared with a Geant4 simulation replicating the experimental layout, and that is used for validation of the complete HiDRa prototype simulation. The construction technique that is used for the prototype assembly is also described here.

CHAPTER

2

INTRODUCTION TO CALORIMETRY

This chapter provides a short introduction to important concepts in calorimetry that will be used in the rest of the thesis. A much more comprehensive treatment can be found in [68], with other readings in [69][70].

Calorimeters play a central role in many modern particle physics experiments. The working principle of these types of detectors is to (ideally) completely absorb an incoming particle through the development of showers of decreasingly energetic secondary particles. An electronic signal is then produced, that is dependent on the overall absorbed particle energy. Today, calorimeters are used in several fields where one is interested in knowing the energy of some particle, ranging from neutrino detection to space applications. A few examples are the Super-Kamiokande experiment, where high-energy neutrinos interact with atoms in the 50 kiloton water detector and their energy is measured through Čerenkov light emitted by the particles produced in their interactions. In the astrophysics realm, ultra-high energy cosmic rays can be studied by measuring the decay products of their interactions in the Earth's atmosphere as they deposit energy and are eventually absorbed. In medical physics, gamma-rays produced during Positron-Emission-Tomography (PET) medical scans are absorbed and measured for imaging purposes to identify possible diseases, with the same underlying physical processes.

At collider experiments such the LEP, LHC and FCC, calorimeters have a major role in reconstructing the invariant masses of short-lived particles through measurements of their decay products four-vectors. High energy neutrinos can also be identified through reconstruction of the missing energy in the transverse plane of detectors, which is the negative vector sum of all contributions of charged tracks momenta and energy deposits in calorimeters. Detectors for general purpose experiments are required to be hermetic, meaning that they have to cover as much as possible the full solid angle around the point where high-energy particle collisions take place, in order to absorb all decay products. Calorimeters are usually made with dense materials to favour interactions of both charged and neutral particles with the detector nuclei, so that muons

and neutrinos are the only particles with a substantial probability of escaping without being stopped in these detectors. It is common in high energy physics experiments to have calorimeters made of two separate materials with different purposes, usually called *sampling* calorimeters. The first one, called passive material or absorber, is usually built with a high-density element or compound with high atomic number Z, such as steel or brass, lead or even depleted uranium, to favour the interaction of particles and their absorption in a limited volume of the detector. The second material is the active element where the actual signal is produced, such as scintillation light, freed electrons from ionisation, or Čerenkov light. Usually active elements in a calorimeter are lighter than the passive one, for example plastics, noble gases or solid state materials like silicon. There exists, however, cases in which the active material is dense enough to play both the role of active element and absorber, and the resulting calorimeter is called *homogeneous*.

Despite a notable amount of geometries, materials and electronics systems have been used for building and operating calorimeters over the years, most of them have in common a few features. The first one is the quite fast production of signals due to showering particles, that can be almost immediate as in the case of Čerenkov light emission, or in the range of ~few nanoseconds for scintillation and ionisation signals. This property make calorimeters important for triggering systems, for example when identifying electrons or photons.

A second important feature of calorimeters is the resolution on the energy of the absorbed particle, which usually improves with the particle's energy itself, following $\sigma/E \propto 1/\sqrt{E}$. This is very different from tracking systems based on the deviation of charged particles in a magnetic field, where the resolution of the track momenta worsens linearly with the momenta. Furthermore, the longitudinal development of particle showers in a calorimeters scales logarithmically with the energy of the shower-initiating object. This fact allows these instruments to keep working and remain compact even while increasing substantially the centre-of-mass energy. On the other hand, magnetic spectrometer sizes need to increase proportionally with $\sqrt{p}$ to keep unchanged the momentum resolution $\Delta p/p$.

One important property of most calorimeters is the different response, meaning the average observed signal per unit deposited energy, for showers initiated by electrons and photons or hadrons. This is due to the different physical processes taking place within the interactions of showering particles, that only involve electromagnetic interactions in the first case, and include strong interactions with the nuclei in the latter. A common way to take into account the different responses is to have two separate calorimeter systems, an electromagnetic and an hadronic calorimeter, optimised for the two kinds of showers. In the following chapter the physics of electromagnetic and hadron showers development, the main features of calorimeters concerning their performances, and the recent techniques developed to reach state-of-the-art measurements of particle energies at colliders are addressed. A focus will be put on the dual-readout technique, the calorimetry method on which both the HiDRa calorimeter prototype and the IDEA experiment calorimeter are based upon.

2.1 Electromagnetic calorimetry

The interactions of electrons and photons with matter are governed, up to extremely high energies where reactions with nuclei occur, by the electromagnetic force. Several processes are possible or suppressed for both particles, depending on their available

energies.

2.1.1 Electrons and positrons

In the case of electrons and positrons, the main process for depositing energy up to the ~MeV scale is ionisation of the traversed medium atoms, if the transferred energy is sufficient to release the electrons from the atomic Coulomb field. This process is widely used in detectors, where released electrons are collected by means of an electric field and multiplied to produce observable electronic signals. Instead of being ionised, after an interaction with incoming electron, an atom may be left in an excited metastable state. This excited atom will then return to ground state with a characteristic time, dependent on the material, by emitting photons with a process called scintillation (or fluorescence).

At higher energies, the main source of energy losses for electrons is the *bremsstrahlung* process, consisting of the emission of a photon as a result of the interaction of electrons with the electromagnetic field of an atom. The resulting photons have an energy distribution that decreases with energy as $1/E$.

An important parameter that is useful in the description of electromagnetic interactions is the *radiation length* X_0, defined as the distance over which electrons deposit, on average, $(1 - 1/e) \simeq 63\%$ of their energy through emissions of photons. The radiation length value depends on the atomic properties of the traversed medium, namely the atomic number Z and atomic mass A. It can vary from centimetres (5.6 cm in a lead absorber) to tens of centimetres and higher (36.1 cm in H_2O, several tens of metres in air)[71].

The critical energy ε_c is defined as the energy at which the losses due to photon radiation are equal, on average, to the losses for ionisation of the traversed medium. A second definition used in the Particle Data Group considers ε_c as the energy at which the energy losses by means of ionisation equals the electron energy. The two definitions are depicted in fig. 2.1, where the energy loss in a copper material are shown as a function of the incoming electron energy. The critical energy depends, for any charged particle, to the atomic number Z of the medium and mass of the incoming particle. The radiation losses become less and less relevant for higher particle masses with $\varepsilon_c \propto (m/m_e)^2$, so that the critical energy for muons ($m_\mu \simeq 106$ MeV) is over 40×10^3 higher than that of electrons. A useful expression for the critical energy of electrons travelling in a solid or liquid medium with atomic number Z is

$$\varepsilon_c = \frac{610\,\mathrm{MeV}}{Z + 1.24}, \tag{2.1}$$

which shows that the bremsstrahlung losses become more important at lower energies for high Z materials such as lead and uranium.

2.1.2 Photons

The interactions of photons are quite different from that of electrons and positrons because of their absence of electric charge. As a result, photons do not deposit energy continuously along their path ionising the medium they are crossing, but eventually interact with atoms transferring their energy in a single interaction. The most probable interactions to occur are however, in similar ways to electrons ones, dependent on the energy of the incoming photon. At low energies, the most probable interaction process is the photoelectric effect that consists of the absorption of a photons by an atom,

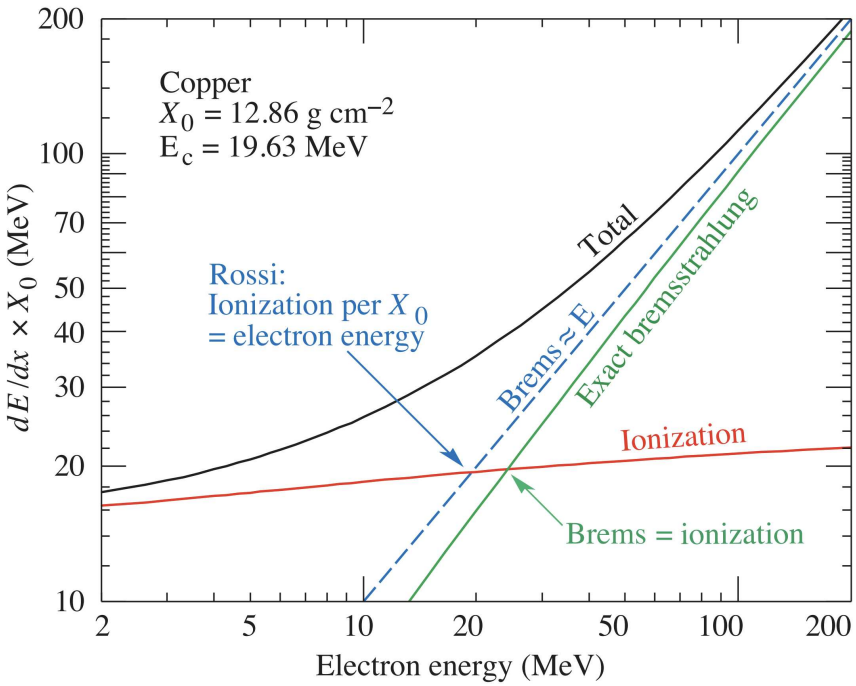


Figure 2.1: Representation of the two critical energy ε_c definitions in a copper absorber. Taken from [71].

that reaches an excited state. The atom will then return to its ground state through the emission of X-rays or Auger electrons. The cross section for the photoelectric effect σ_{pe} heavily depends on the atomic number of the absorber material $\sigma_{pe} \propto Z^n$ with n between 4 and 5. On the other hand, the cross section for this process scales down rapidly with the photon energy, with $\sigma_{pe} \propto E^{-3}$.

At low energies, coherent (Rayleigh) scattering may also happen, with a photon being deflected by its interaction with an electron without exchanging or losing momentum. The result of this process is a change in the spatial distribution of the direction of incoming photons. Incoherent scattering, also called Compton scattering, is favoured at slightly higher energies than photoelectric effect, from ~few hundreds keV up to few MeV, with an electron that is knocked off from its nucleus. A slight preferential direction dependency of the scattered electron with the incoming photon is found, especially at higher energies. This process is important in the physics of electromagnetic shower development, as large part of the overall energy is deposited by particles in the ~MeV range, also motivating the loss of direction of particles in later stages with respect to the primary particle one.

The Compton scattering cross section falls down with the energy as $\sigma_{Compton} \propto 1/E$, and at energies higher than twice the mass of an electron (1.022 MeV) the pair production process becomes kinematically possible and then starts dominating (see fig. 2.2). In this process, a photon interacts with the electromagnetic field of atomic nuclei (with small contributions from atomic electrons), producing an electron-positron pair. It can be found that the mean free path of high energy photons in a medium is related to the radiation length of electrons in the same medium, by the relation

$$\lambda_{Pair} = \frac{9}{7} X_0. \tag{2.2}$$

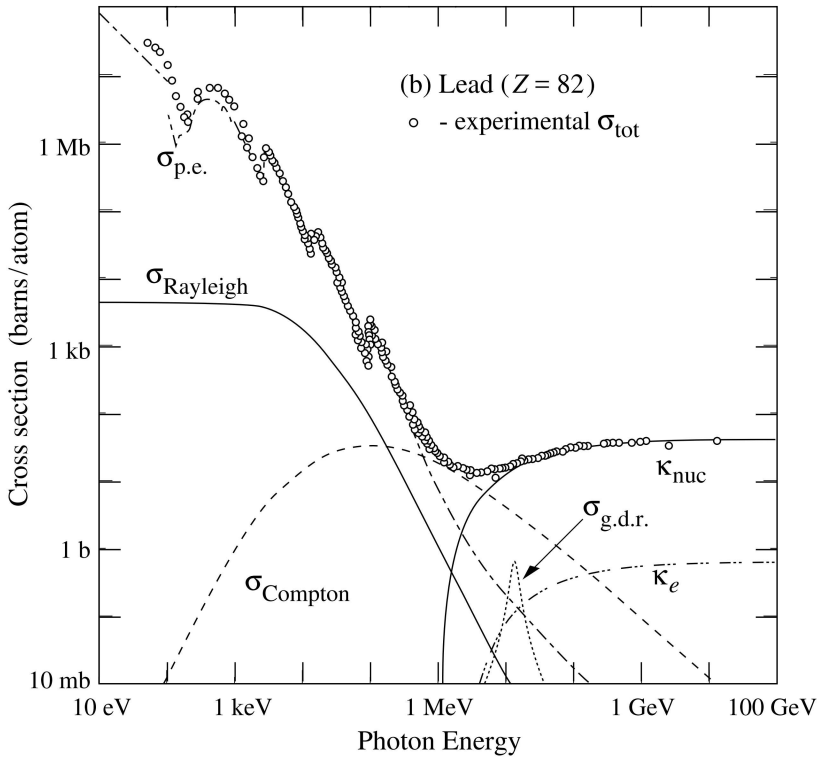


Figure 2.2: Cross section of photon interaction processes with matter over energy, for a lead absorber. The high atomic number (Z=82) makes the photoelectric effect relevant at relatively high energies, where the Compton effect would be dominating in lower Z materials. Image from [22].

2.1.3 Electromagnetic showers

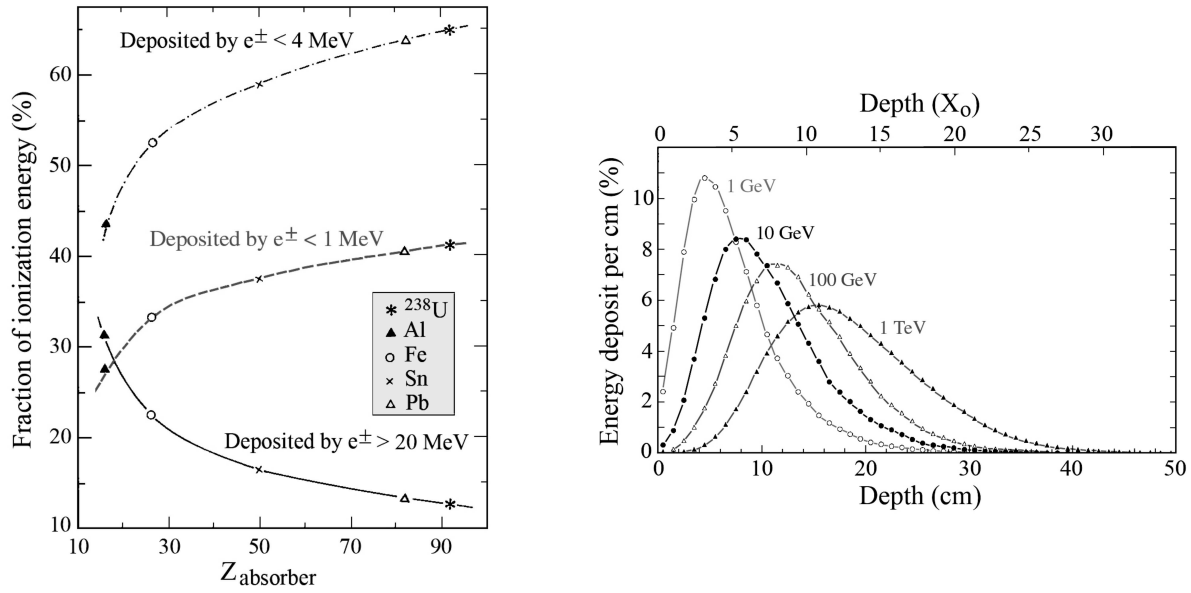
The bremsstrahlung radiation emission from electrons and positrons and the pair production from photons are fundamental ingredients in the development of electromagnetic showers. When a high energy particle enters a detector, both processes occur repeatedly with the emission of new electrons, positrons and photons with lower and lower energies. Electrons and positrons deposit energy both through ionisation of the absorber and radiation of more photons, with different contribution depending on the energy of the particle being higher or lower than the critical energy ε_c. The situation is drawn in fig. 2.3a, which shows the distribution of energy fraction deposited by showering particles in three different ranges, for 10 GeV electromagnetic showers. Only a small amount of energy is deposited by electrons and positrons with more than 20 MeV, while the largest contribution is from particles below 4 MeV. The vast majority of radiated photons already have very low energy, and only those carrying more than $\sim$ few MeV can produce more e^+e^- pairs, while others interact through Compton or photoelectric effect interactions.

The result of the combination of these processes is a very fast (exponential) production of several thousand particles, that eventually stops when all the energy has been shared in the largest number of contributors. When no more photons energetic enough to produce new e^+e^- pairs are present, the shower development stops and particles only deposit energy through other processes, and the total number of particles in the shower decreases. The depth inside the detector at which the maximum number of particles is reached is called shower maximum, and it is found to increase logarithmically with

the energy of the shower-initiating particle, shown in fig. 2.3b. Typical values for the shower maximum of electromagnetic showers with energies between 10 GeV to ~TeV in metal absorbers are tens of centimetres. While the longitudinal development of an em-shower is energy dependent, the lateral size of a shower is not and only depends on the property of the material in which the shower is developed. A useful parameter to describe the lateral dimensions of these object is the Molière radius ρ_M, defined as

$$\rho_M = E_s \frac{X_0}{\varepsilon_c} \tag{2.3}$$

with E_s a characteristic energy equal to 21.2 MeV. About 90% of the total energy is usually deposited in a cylinder with radius ρ_M. The Molière radius is less dependent on the atomic properties of the medium with respect to the radiation length, changing from 16.0 mm in lead to 15.2 mm in copper and 8 cm in LAr [68].



(a) (b)

Figure 2.3: (a): Contribution of particles with different energies produced in electromagnetic showers, to the total energy deposition. (b): Longitudinal development of electromagnetic showers, by means of deposited energy per unit distance inside the absorber, as obtained through simulations. Images from [68].

The lateral spread of electromagnetic showers is mostly due, in the early stages of shower development when particles energies are still high, by multiple Coulomb scattering deviating the particles from their original directions. As the shower develops and the energy decreases, Compton scattering and photoelectric effect, which are way less directional than pair production, become dominant.

2.1.4 Electromagnetic calorimeters

The rather compact profiles of electromagnetic showers seen in section 2.1.3, both in the longitudinal and in lateral directions with respect to the shower axis, make it possible to have calorimeters with limited volume that are sufficient to have good measurements of electrons and photon energies. Homogeneous calorimeters are very effective for these

physics objects, while sampling calorimeters with high density passive elements are also widely used with different designs. For example, the ATLAS experiment uses for its barrel electromagnetic section a sampling calorimeter made of alternating slabs of lead with an accordion geometry interleaved with liquid argon (LAr) active medium, summing up to 22 X_0 radiation lengths with a total depth of 47 cm [72]. CMS conversely adopted a homogeneous electromagnetic calorimeter made of lead Tungstate ($PbWO_4$) crystals, reaching 26 radiation lengths in just 23 centimetres ($X_0 = 0.89$ cm) [73].

One important characteristic of electromagnetic calorimeters is that, when operated correctly, they are usually linear, meaning that the readout signal (whatever is its production mode) is proportional to the energy of the absorbed primary particle. For a linear calorimeter, the response to a particle (in this case, electrons or photons) is independent from the energy of the particle itself. This property comes from the production of a very large number of secondary particles, whose deposited energy in the calorimeter and related signals only depend on the geometry and design of the detector. Possible non-linearity effects may however arise from instrumentation issues, such as saturation of sensors when too many particles are produced in a limited volume, producing a signal too large for the correct working range of the sensitive element. A second problem could concern local variation of the sampling fraction, that is the fraction of energy deposited by *minimum ionising particles*[1] (MIPs) in the active medium of the calorimeter, over the total energy deposit in the whole detector

$$f_{samp} = \frac{E^{\text{mip}}_{\text{active}}}{E^{\text{mip}}_{\text{active}} + E^{\text{mip}}_{\text{passive}}}. \tag{2.4}$$

The request for extracting signals through cables and electronic devices from a full solid angle coverage may require having crack regions or other local changes in the structure of the calorimeter. This could lead to a different sampling fraction and hence to a modified response to the same type of particles. Another example of non-linearity may be caused by the leakage of particles from outside the detector volume, therefore not contributing to the overall signal of the primary particle. If a calorimeter is too short, the longitudinal leakage due to deeper shower maximum will be more effective at high energy, leading to decreasing response as the primary particle energy increases.

When designing a calorimeter, it is important to understand both its average response, meaning its correct dependence of the measured signals on the deposited energy, and its resolution, which concerns the spread of measurements around the mean value that is affected by all the possible fluctuation sources. In general, when multiple sources of fluctuations contribute to the variation in the response of a calorimeter to the same energy particles, the uncertainties related to each source have to be added in quadrature (if they are not correlated between each other). Each fluctuation contribution may depend differently, or even not depend at all, from the energy of the showering particle, as shown in fig. 2.4.

The general formula for describing the energy resolution of a calorimeter is then

$$\sigma_E = \sqrt{\sigma_a^2 + \sigma_b^2 + \sigma_c^2 + \dots} = \sigma_a \oplus \sigma_b \oplus \sigma_c \oplus \dots \tag{2.5}$$

where $\sigma_{a,b,c\dots}$ represent the different sources of fluctuations contributing to the total uncertainty on the energy measurement.

[1] Charged particles characterised by mass and momentum such that the loss of energy through ionisation is at the minimum of the Bethe-Bloch curve.

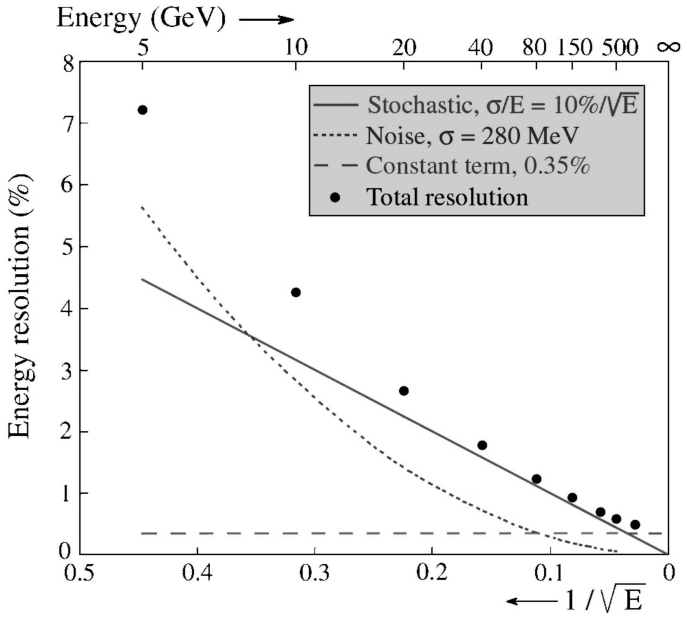


Figure 2.4: Decomposition of the different sources of fluctuations to the total energy resolution of the ATLAS electromagnetic calorimeter. Image taken from [68], experimental data from [74].

In the development of particle showers, with the production of several thousand particles, the measured number of signals follows the Poisson statistics with an average number of particles N proportional to the total primary particle energy E. Even when the exact same number of shower particles are produced, fluctuations in the number of energy carriers, called signal quantum fluctuations, arise. The number of collected carriers may depend, for example, on the spectrum of the associated wavelength in the case of optical photons from scintillation and Čerenkov processes, or from the quantum efficiency of the photon sensors, and others. The standard deviation of a Poisson-distributed value is $\sigma = \sqrt{N}$, which leads to an improving resolution with the total number of produced particles as

$$\frac{\sigma_{stoch}}{E} = \frac{a}{\sqrt{E}}, \tag{2.6}$$

with a being a parameter, called *stochastic*, that describes the statistical nature of the shower development physics and the number of particles depositing signals.

A different source of fluctuations is also present in sampling calorimeters, and leads to the same dependence on energy as eq. (2.6). While for homogeneous calorimeters the entire detector volume is able to generate signals, which is free to fluctuate, in sampling ones only the active material is capable of doing so. It follows that also the amount of energy deposited in the active layers varies event-by-event, and these Poissonian fluctuations contribute to the stochastic term of the calorimeter's resolution. Since a smaller amount of energy is deposited in the active layer, with respect to homogeneous calorimeters, the relative uncertainities due to Poissonian fluctuations are generally larger because of the smaller number of particles N generated in the material.

The stochastic term is found to improve with the sampling fraction of the calorimeter f_{samp} and the dimensions of active layers (examples are the depth of scintillating plates

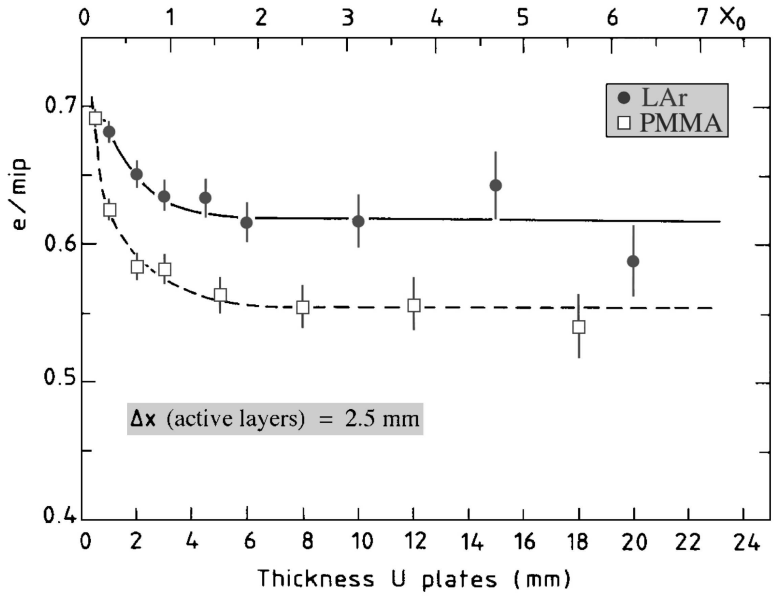


Figure 2.5: EGS4 Monte Carlo simulations of the e/mip response ratio to electrons or MIPs of the same calorimeter with increasing uranium passive absorber plate widths. Two different active mediums with different Z are used, Polymethyl Methacrylate (PMMA) scintillator plastics or Liquid Argon, with a fixed thickness of 2.5 mm.

or diameter of optical fibres), with

$$a = 2.7\% \sqrt{\frac{d}{f_{samp}}}. \tag{2.7}$$

When the sampling fraction is kept fixed, the active medium size d term can be related to the sampling *frequency*, which describes how often a particle shower is sampled while it develops in a material with the same global active/passive percentage densities. This means that better resolutions (smaller stochastic terms) are reached with small sizes of active layers, and high sampling frequencies. Larger sampling frequencies mean that the particles contributing to the detector signals are more efficiently sampled, because even if the largest amount of shower particles (MeV photons) are produced in the passive layers, these manage to reach the active material and produce some signal.

The sampling frequency has an important role in explaining why, in many sampling calorimeters, the response to electrons, positrons and photons, e, is significantly different to the same calorimeter's response to MIPs, so that $e/mip \neq 1$. Figure 2.5 shows the e/mip response ratio of a calorimeter with uranium absorber plates interleaved with either LAr or PMMA active materials. Different absorber depths are used, from less than 1 to 24 mm, therefore changing the sampling frequencies. In both cases the e/mip ratio is lower than 1, and is lower for active materials with an atomic number Z that is much different from that of the passive layer. The reason for this behaviour has to be ascribed to the high dependence of soft gammas over the atomic number Z of the material they are interacting with. As seen in fig. 2.3a, most of the energy in electromagnetic showers is deposited by electrons with less than 4 MeV, that therefore only produce large quantities of low-energy gammas through bremsstrahlung. In this energy range, the interactions of soft photons is dominated by the photoelectric effect, which depends on

Z^5 of the material they are interacting with. In high Z absorber materials, electrons that are freed from photoelectric effect will have very short ranges before they are absorbed again in the same medium, less than one millimetre, and therefore they will not reach the active layer to be sampled. This explains why, in fig. 2.5, for very thin absorber plates and therefore increasing sampling frequency, the e/mip ratio increases, as more electrons freed from photoelectric effect close to the surface will eventually reach the active layer. As should be expected, this problem does not affect homogeneous calorimeters that do not have passive elements, and therefore always have $e/mip = 1$.

Another contribution to the total energy resolution of calorimeters comes from the electronic noise of the readout chain. The origin of electronic noise usually comes from the collection of charge in capacitances during a certain time interval that follows a trigger, called gate time. In scintillation-based calorimeters, and in general when PMTs are used for light conversion into electronic signals, fluctuations of the collected charge during gate time may happen even when no signal is present, causing the appearance of a so-called "pedestal" that has to be subtracted from raw signals during the analysis. The absolute value of the noise term b_{noise}, once converted from ADC counts to an energy value, is estimated as the RMS of the pedestal distribution. Its value is approximately constant and does not depend on the particle energy. When evaluating the relative uncertainty of a calorimeter, the noise term therefore contributes as $\sigma/E = b_{noise}/E$. This term usually dominates the overall resolution at low energies, while becomes less and less relevant with increasing energies, as it can be observed in fig. 2.4.

Other effects that have major contribution in the energy resolution of calorimeters concern local variations of the sampling fraction, and therefore of the calorimeter's response. Sources of dishomogeneities may include structural causes, or the actual design of the calorimeter, such as in the case of accordion geometry calorimeters. Examples of structural dishomogeneities may come from the need to have calorimeters that cover the full solid angle and can end up weighting even several hundred tons, therefore needing mechanical support with different properties than the passive calorimeter material. Some volumes in the calorimeter system is also usually left empty, in order to leave space for cables and readout electronics. Different causes in response variations can also be generated from local changes of the active material properties, or dishomogeneity of signal sensors. By introducing response variations, these additional uncertainties scale linearly with the energy with $\sigma = cE$. Their relative contributions to the calorimeters' energy resolution lead to a constant term $\sigma/E = c$, that therefore has a great impact at high energies, when both the sampling fluctuations and the electrical noise are negligible.

A common way to express the measured energy resolution of calorimeters in order to compare the performances with other detectors, assuming that the different sources of fluctuations are independent and not correlated between each other, is

$$\frac{\sigma}{E} = \frac{a_{stoch}}{\sqrt{E}} \oplus \frac{b_{noise}}{E} \oplus c. \tag{2.8}$$

2.2 Hadronic calorimetry

When highly energetic hadrons enter a medium, a much wider variety of physical processes than with electromagnetic showers occurs. While electromagnetic processes are still present for charged hadrons, strong interactions between the incoming particle and the nuclei of the traversed matter significantly broaden the amount of possible

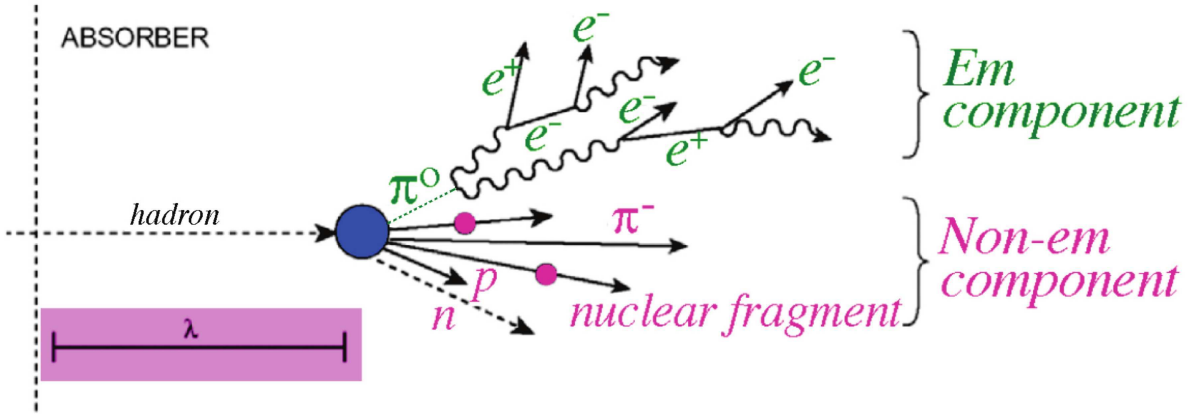


Figure 2.6: Sketch of the development of hadron showers. Image from [68].

processes. For neutral hadrons, strong interactions are the only processes for depositing their energy. The most striking effect of hadron calorimetry, when compared to electromagnetic one, is a missing contribution to the total absorbed energy that is fundamentally not detectable, called *invisible energy*. The origin of this effect comes from the need to overcome the nuclear binding energy in the interactions of hadrons with the nuclei to break them, which adds a contribution not present in electromagnetic showers. The invisible energy severely alters the response of the calorimeter to hadrons, as it results to have large event-by-event fluctuations that are not symmetrical, and also dependent to the shower energy. This results in hardly achievable linear response and limited resolutions on energy measurements, therefore requiring particular care and advanced techniques to achieve optimal hadronic calorimeters.

2.2.1 Hadron showers

In the interactions of hadrons with atomic nuclei, a number of particle with different nature can be produced. The highest percentage of these, about 90% of the total, are pions, followed by protons and neutrons that are freed from their nuclei. Neutral pions play a very interesting role in the development of hadron showers. In nuclear interactions, about $1/3$ of pions are π^0, which decay immediately and almost exclusively into two photons $\pi^0 \rightarrow \gamma\gamma$ with a 99% probability, the remaining 1% consisting of other electromagnetic decays such as $\pi^0 \rightarrow \gamma e^+ e^-$. It follows that the transferred energy to π^0s (and η mesons as well) is used for production of relatively high energy photons and electrons, therefore developing electromagnetic showers. This process is irreversible, as the decay particles will only produce more electrons, positrons and photons that will interact through bremsstrahlung and pair production, respectively, as described before. The fraction of primary hadron energy that is eventually deposited by these particles, the *electromagnetic component*, is hence called *electromagnetic fraction*, f_{em}, sketched in fig. 2.6. We will call *non-electromagnetic component* all remaining contributions from other hadrons. As the hadron shower develops, more and more freed nucleons and charged pions will interact producing more pions, of which on average about one third will again be neutral. At any step n of occurring nuclear reactions in a shower, the

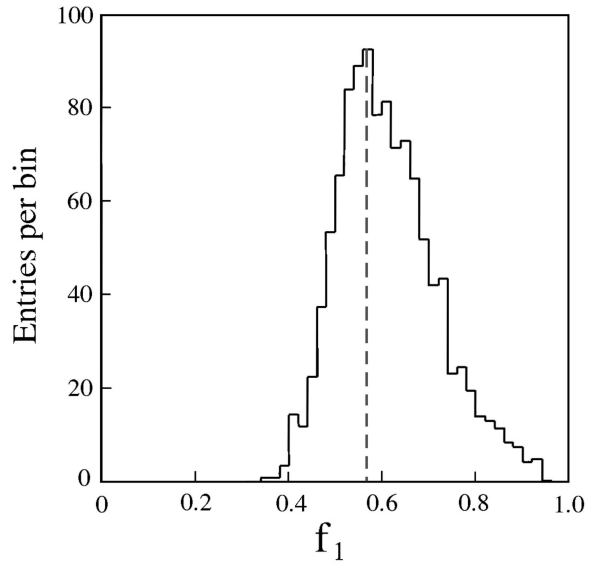


Figure 2.7: Distribution of the measured electromagnetic fraction measured in the SPACAL calorimeter to 150 GeV pion-induced showers. Taken from [68].

electromagnetic fraction carried by π^0s is found to increase as

$$f_{em} = 1 - \left(1 - \frac{1}{3}\right)^n, \tag{2.9}$$

until the available energy falls below the threshold for the production of new pions. The number of generations that contributes to the emission of new π^0s scales, approximately, with the energy of the primary hadron entering the absorber. By taking into account more realistic effects, notably the production of other particles besides pions, the dependence of hadron multiplicities on the nucleus scattering energy, other energy losses through ionisation, a general expression for the dependence of the electromagnetic fraction on the energy is found:

$$f_{em}(E) = 1 - \left(\frac{E}{E_0}\right)^{k-1} \tag{2.10}$$

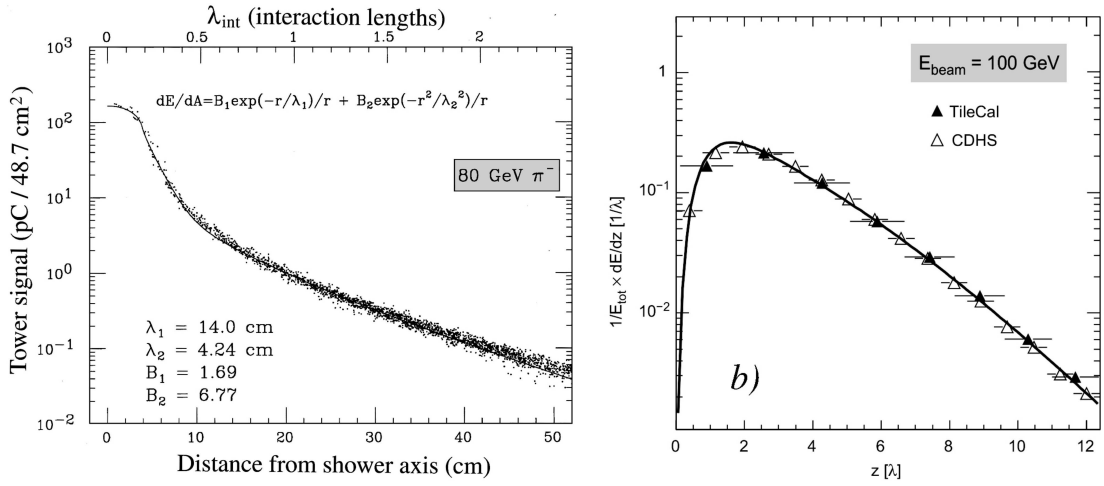
with k parameter value experimentally measured to be close to 0.82. The parameter E_0 is an energy scale which corresponds to the average energy that is needed for the production of a pion and depends on the species of the hit nuclei, with values close to ~ 1 GeV. One also finds that the f_{em} is also significantly lower for proton-induced hadron showers with respect to pion-induced ones, that is commonly interpreted to be due to baryon number conservation effect that is absent for mesons. Figure 2.7 shows the distribution of the measured electromagnetic fraction as measured in the SPACAL lead/fibres calorimeter with 150 GeV pions impinging on the detector. One can observe that the distribution is quite large and asymmetrical, with a tail reaching values close to one. These events with $f_{em} \approx 1$ are produced when a large fraction of the energy carried by the primary particle is immediately transferred in the first interaction to a π^0/η, therefore producing two high-energy photons with following electromagnetic showers.

A second important component in the collection of particles generated by nuclear interaction in hadronic showers is due to spallation protons. In the spallation process,

a rapid intra-nuclear cascade of interactions between quasi-free nucleons takes place, after the momentum transfer from the incoming hadron. The nucleons receiving an energy contribution sufficient to overcome the nucleus potential barrier escape, together with many pions and other unstable hadron that may be produced at this stage, contributing to the hadron shower development. The struck nucleus is left in a highly excited state. In the second stage of the spallation, nuclei decay to their ground state (that could be a different element from the starting one) with the emission of protons and neutrons, usually called evaporation process. Some energy may also be spent with electromagnetic decays through gamma ray emission. The presence of nuclei energy bounds has a crucial role in explaining the different response of a calorimeter to electromagnetic or hadronic showers. In fact, some of the energy carried by incoming hadrons must be spent to free nucleons from their atom, and that energy will not contribute to the production of detector signals - it is therefore *invisible*. The invisible energy has a significant contribution to the composition of energy deposits in hadron showers. In an iron absorber, about 31% of the non-em component energy is invisible [68], while the remaining contribution goes into ionisation from protons and pions, evaporating neutrons and decay γs. In lead, the invisible energy contribution further increases to almost 39%. In the remaining contribution of energy deposit from the non-em component, the major role is played by densely ionising particles, mostly protons and other heavy fragments, usually higher than 30%. Smaller energy deposits contributions are then carried by pions and light hadrons, around 15%. The different ionising power of protons and pions, that can be determined through the Bethe-Bloch equation, results in a shorter range of protons inside a calorimeter than pions, usually few centimetres, before they lose their energy. Only smaller contributions are transferred to the kinetic energy of evaporation neutrons, which are however important for advanced calorimetry techniques such as compensating calorimeters, that are described in section 2.3.

Similarly to the description of electromagnetic shower development, a scaling parameter is introduced to characterise the dimensions of hadron showers, the *interaction length* λ_{int}. This parameter is defined as the average distance that is traversed by an energetic hadron in a medium before a nuclear interaction occurs. Considering the cross sections at nuclear level related to the actual size of nucleons, the available area for scattering scales as the atomic mass number $A^{2/3}$, and the interaction length is then proportional to $A^{1/3}$. The interaction lengths are typically found to be about one order of magnitude larger than the radiation lengths in the same material, therefore tens of centimetres. It should nevertheless be noticed that the interaction length is dependent on the nature of the shower-inducing particle, being about 25% shorter for protons with respect to pions.

The complicated development of hadron showers makes it difficult to define a "typical" profile, both lateral and longitudinal, for these objects. Individual fluctuations of hadron showers concern the position of energetic neutral pions production, which may happen far from the impact point of the primary particle on the calorimeter. Once the electromagnetic component develops, however, it leads to a higher density energy deposit with respect to the non-electromagnetic counterpart. One extreme example in the spectrum of possible hadron processes is the charge exchange process $\pi^- + p \rightarrow n + \pi^0$ in which most of the energy is transferred to the final state neutral pion, which decays in two photons. In a shower where this process occurs early on, the electromagnetic fraction f_{em} will be very close to one, and both lateral and longitudinal profiles will be much more compact that the ones for a non-electromagnetic-like shower. The depen-



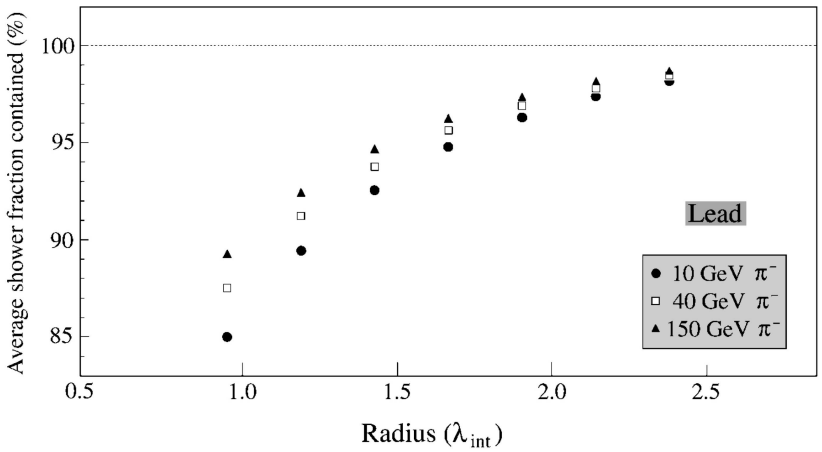
(a) (b)

Figure 2.8: Average lateral (a) and longitudinal (b) profiles of hadron showers, measured with the ATLAS TileCal, the CDHS and the SPACAL hadronic calorimeters. Both images are taken from [68].

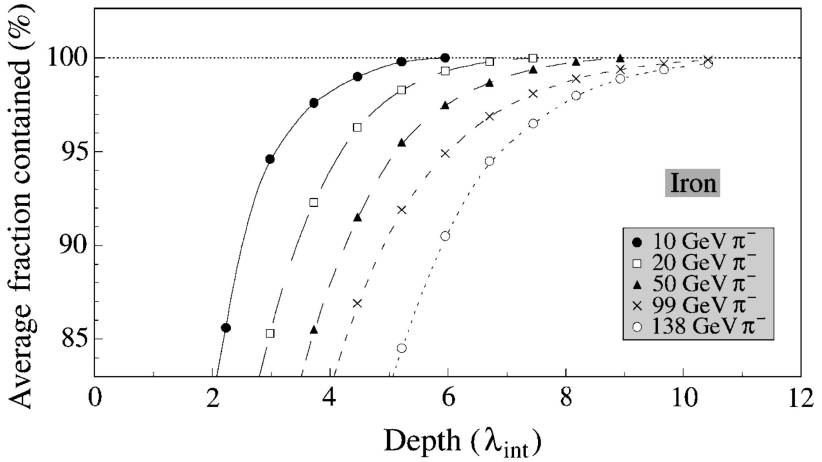
dence of the scattering cross section on the energy also has an impact on the hadron shower shape. This affects especially low-energy pions and kaons that could be part of hadron jets, and may start resembling minimum ionising particles crossing large volume of the calorimeter with small energy deposits.

Figure 2.8 shows the average longitudinal and lateral profiles obtained using charged pions in the ATLAS, CDHS and SPACAL calorimeters, respectively. The longitudinal profile, drawn in fig. 2.8b, has a steep increase up to a peak that depends on the particle nature and energy, followed by a slower decrease. Energy deposits very deep inside the detector can be addressed to very late production of hadrons and decays of these particles into muons. The lateral shower profile, drawn in fig. 2.8a, has a peculiar distribution that is ascribed to a narrow cone in which most of the electromagnetic processes occur (the electromagnetic core), followed by very broad energy deposits at greater distances from the shower axis due to the non-electromagnetic contribution, mostly soft hadrons like evaporation neutrons and protons. The consequence of these results is that a much larger amount of material is needed to completely absorb a high-energy hadron, due to the different scales of hadron interaction lengths and electromagnetic radiation lengths. In order to have the same containment of particles with the same energy, about a factor ~ 10 in material for each spatial direction is required for pions with respect to electrons.

The shape of hadron showers, and consequently the containment of energy inside a calorimeter, are important concepts when developing detector prototypes, as it will be described in chapter 3. For small-scale experiments when one is testing the response of calorimeter prototypes, fluctuations in both lateral and longitudinal containment have a major role in limiting the energy response of the detector, as the measured energy does not correspond to the actual energy of the impinging particle, but rather on the energy that is deposited inside the detector which may vary event-per-event. The ultimate limit in this sense is the instrumented mass of the calorimeter, which scales in some way with the available budget. Figure 2.9a shows how the average fraction of contained energy, with respect to the energy of impinging pions, changes with the lateral



(a) Average fraction of contained energy in a "infinitely" long lead absorber material, over the transverse dimensions expressed in term of nuclear interaction lengths.



(b) Average fraction of contained energy in a "infinitely" large iron absorber material, over the longitudinal dimension expressed in term of nuclear interaction lengths.

Figure 2.9: Experimentally measured profiles of longitudinal and lateral containment for pions of different energies, taken from [68].

size of a cylindrical calorimeter. One can easily see that increasing the instrumental volume of a calorimeter has a great impact on the total contained energy. The increasing containment affects both the measured energy from the calorimeter (linearity response) and on the resolution of the average measured value, through event-per-event fluctuations in the leaked fraction of energy.

Another interesting observation that can be done on the same plot is that the average fraction of contained energy improves for higher energy pions. This is quite different from electromagnetic showers, where the Molière radius does not depend on the energy of incoming electrons or photons. This result can be interpreted by considering the increase in the average electromagnetic fraction $\langle f_{em} \rangle$ with the energy, that results in a larger energy deposit in the electromagnetic core of the shower. Since the energy deposit by neutral pions through $\pi^0 \rightarrow \gamma\gamma$ has a very short range dependent on the radiation length X_0 of the absorber, an increase in the amount of energy transferred to π^0s will lead to better contained hadron showers. It should be noticed that this effects is only valid when considering the fraction of contained energy with respect to the

total one carried by the shower-inducing particle. The absolute scale of lost energy will nevertheless increase for higher energy incoming hadrons.

The second major source of leakage from calorimeters is the longitudinal one. Figure 2.9b shows the average fraction of contained energy from pions in an "infinitely large" iron calorimeter. The amount of material required to completely absorb the hadrons increases with the energy itself, passing from $\sim 6\ \lambda_{int}$ for 10 GeV pions to $\sim 10\ \lambda_{int}$ for 138 GeV pions. In the longitudinal direction, an opposite dependence is found with respect to the lateral leakage, with higher energy showers that require more material to be equally contained as lower energy showers. Longitudinal leakage is however a larger source of event-by-event fluctuations than the lateral one. This happens because of the large number of low-energy nucleons that populate the lateral tails of hadron showers, consisting mostly of evaporation neutrons and protons, some of which may randomly escape from the detector volume. On the other hand, longitudinal leakage fluctuations are caused by very few highly energetic hadrons that travel very deep inside the detector before interacting, causing larger contributions to the missing energy.

2.2.2 Hadronic calorimeters

The response of calorimeters to hadrons is a combination of its response to the electromagnetic component e, that is mostly produced through the $\pi^0/\eta \rightarrow \gamma\gamma$ process, and the response to the non-electromagnetic component h. The response h describes the average signal generated by spallation protons, evaporation nucleons and the contribution of invisible energy, that is the response to the non-electromagnetic component. This value is found to be constant and does not depend on the showering hadron energy, but only on the signals generated by these secondary particles. Due to the missing contribution of the invisible energy, most calorimeters have a lower response to hadron showers than for electromagnetic ones, so that $e/h > 1$, and they are said to be *undercompensating*. Techniques have been developed to have calorimeters with the same response to both components, and calorimeters featuring $e/h = 1$ are called compensating, while in the case $e/h < 1$ are called overcompensating. The compensation technique, that was developed specifically to achieve $e/h = 1$, will be described in section 2.3. Figure 2.10 shows examples of the average response to pions of undercompensating (WA, $e/h > 1$), compensating (HELIOS, $e/h = 1$) and overcompensating (WA78, $e/h < 1$) calorimeters.

While the responses e and h to the electromagnetic and non-electromagnetic components can be considered energy independent, the response of a calorimeter to hadrons is not, as the sharing between the two components changes with the primary particle energy with a weight that is described by the electromagnetic fraction f_{em}. The response to single charged pions π is therefore

$$\pi = e\, f_{em} + h(1 - f_{em}). \tag{2.11}$$

Because of the dependence of f_{em} on the primary energy E seen in eq. (2.10), the energy response of non-compensating calorimeters to hadron showers in not constant and changes with increasing energy, and these calorimeters are therefore non-linear. A second effect that contributes to non-linearity, that is also present in compensating calorimeters, takes place as low energies, for hadrons with $E \lesssim 1$ GeV. Nuclear interaction for pions in this energy range become secondary with respect to ionisation and excitation of the traversed medium, and therefore these particles start resembling minimum ionising particles. For sampling calorimeters, that are always characterised by

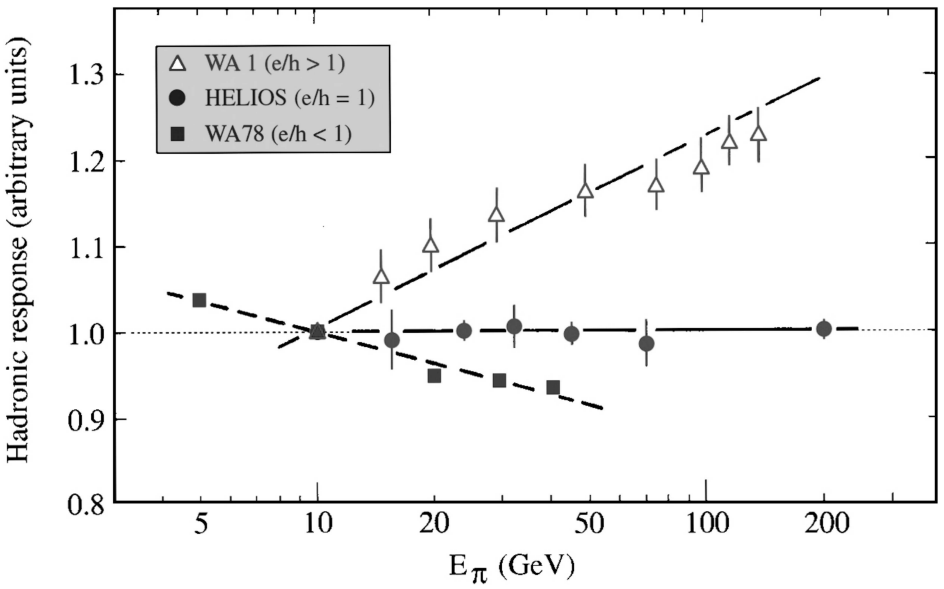
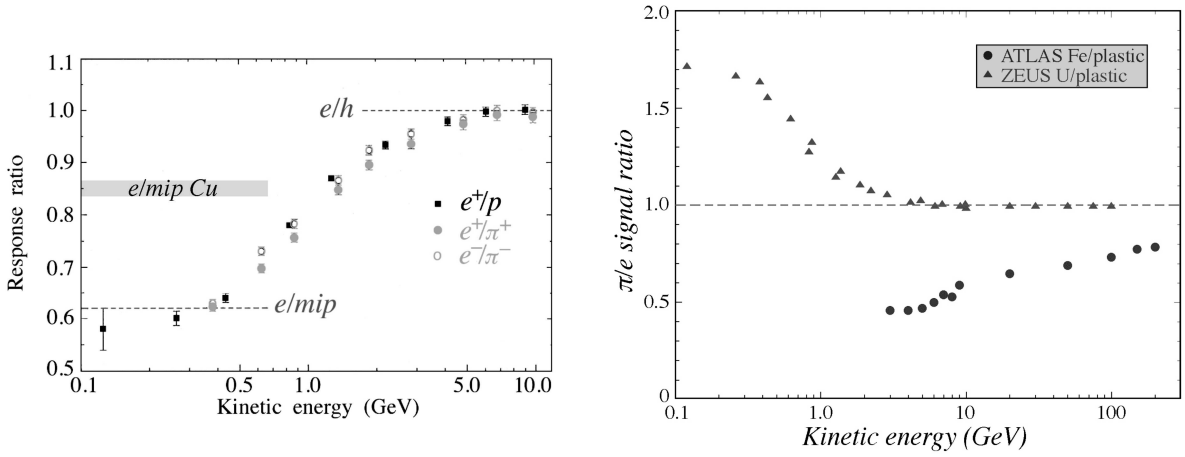


Figure 2.10: Dependence of the response to pions for calorimeters with different e/h ratios [68].

$e/mip \neq 1$, this effect leads to non-linear response independently from the compensating (or non-compensating) behaviour at higher energies, as shown in fig. 2.11a for the ZEUS (compensating) calorimeter. The result in the combination of these two peculiarities in the response to hadrons is shown in fig. 2.11b. In the ZEUS calorimeter, the decrease of the e/mip response ratio at low energy, combined with the mip-like behaviour of pions in the same energy range, leads to a π/e ratio larger than one. As the energy increases, however, the ratio of the responses to the two particles flattens out because of the compensating behaviour of this calorimeter. For the ATLAS calorimeter only data at energies higher than 3 GeV are available, and the under-compensating properties of this detector leads to an increasing response to pions, that remains however always lower than the electron one. The e/mip and e/h response ratios are important when evaluating the performance of calorimeters to hadron jets energy measurements. These objects are produced at colliders through the fragmentation of final state quarks and gluons, with the production of several lower energy pions and kaons, as well as photons from the decay of neutral pions. Calorimeters with e/mip very different from 1 would systematically reconstruct the incorrect energy if the incoming hadron behaves more like a minimum ionising particle. Active element and absorber materials are therefore an important choice to be taken in the design of hadron calorimeters, as high-Z absorbers have smaller e/mip with respect to lower-Z ones, despite showing better containment for high energy showers.

In order to measure the response e to electromagnetic showers, it is in first principle sufficient to test the calorimeter under study with an electron or positron beam with known energy. The average collected signal, in terms of integral of some voltage distribution, the pulse height or some other parameter dependent on the used electronics, is linked to the energy of incoming electrons for calibrating the response of the detector. Measuring the response to hadrons, h, is conversely much more complicated, as one would need to know both the response to pions or protons, and the value of electromagnetic fraction f_{em} event-by-event, and repeat the measurement for several energies.



(a) (b)

Figure 2.11: (a): Response of the ZEUS compensating calorimeter to hadrons in the low-energy range (experimental data from [75]). (b): Response to pions (normalised over the electron response) of the ZEUS and ATLAS calorimeters [68]. See text for details.

The vast majority of calorimeters used in particle physics experiments cannot access the value f_{em} of every showering hadron. A particular technique for calorimeter construction and operation, the dual-readout calorimetry technique (see section 2.4), works precisely by measuring the electromagnetic fraction event-by-event. It is nevertheless possible to measure the response ratio to hadrons and electrons (h/e), by studying the dependence on the energy of the average electromagnetic fraction, $\overline{f_{em}(E)}$. One can then take the ratio of the responses to pions at two different energy points, given by

$$\frac{\pi(E_1)}{\pi(E_2)} = \frac{\overline{f_{em}(E_1)} + [1 - \overline{f_{em}(E_1)}]h/e}{\overline{f_{em}(E_2)} + [1 - \overline{f_{em}(E_2)}]h/e} \tag{2.12}$$

to obtain information on the (h/e) ratio, even without knowing the exact dependence of the f_{em} on energy.

Limits on energy resolution in hadronic calorimetry

The additional sources of fluctuations on the electromagnetic fraction, combined with the invisible energy ones, affect the energy resolution of hadronic calorimeters. The same sources of fluctuations that were described for electromagnetic calorimeters are present as well. Sampling fluctuations also have even larger impact on hadronic calorimeters, as in these object the energy is not evenly distributed. In hadron showers, most of the signals is deposited by protons and pions with ~tens of MeV that travel longer distances, in the order of λ_{int}. In most calorimeters these particles end up depositing signals in more than just one active element, and therefore the overall calorimeter signal is generated by few particles with high energy. This is quite different from electromagnetic showers, where as seen in fig. 2.3a, most of the energy is carried by ~MeV (and lower) particles with very short range. Other experimental sources of fluctuations that are more notable in hadron than in electromagnetic showers, and concur to worsening the energy resolution of calorimeters, is leakage of particles outside the detector volume. This is of particular relevance for smaller-scale prototypes, where one of the important features of collider experiments, hermeticity, is missing.

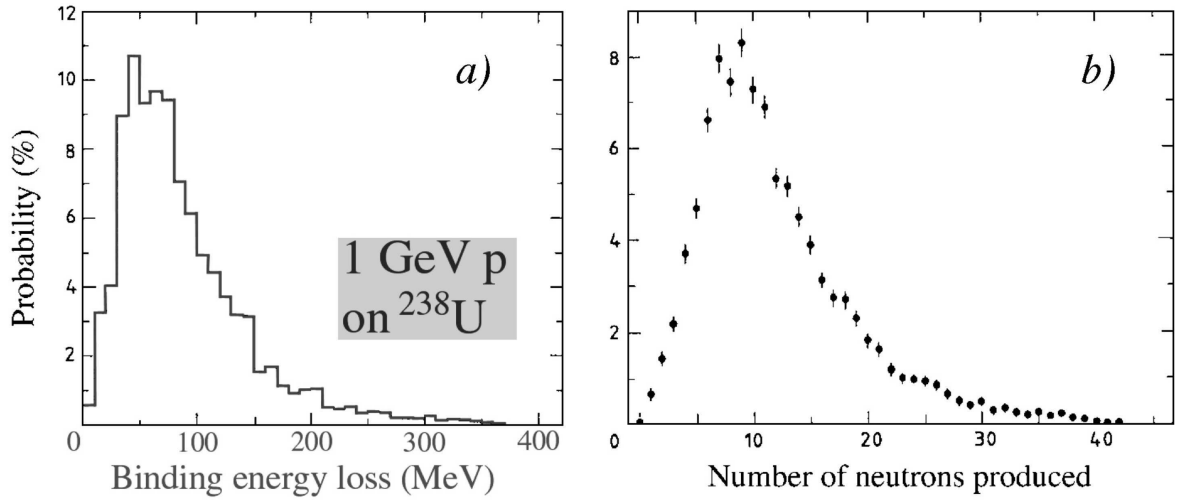


Figure 2.12: Left: nuclear binding energy losses produced through spallation reactions of protons on an uranium target. Right: number of neutrons produced in the same reactions. [68].

In non-compensating calorimeters, event-by-event fluctuations in the electromagnetic fraction are often the largest contributions to the energy resolution. As previously discussed, the f_{em} depends on the energy and the type of impinging particles, and are also large and non-Poissonian, comprising tails in its distribution to high values close to 1 (see fig. 2.7). Because of the energy dependence of the electromagnetic fraction, the effects of f_{em} fluctuations on the resolution have to be energy-dependent, and cannot be added in quadrature as a constant term to the sampling one. The term that was found to better represent the contribution of f_{em} fluctuations to the energy resolution (see ref. [68]) is

$$\frac{\sigma}{E} = \frac{a_1}{\sqrt{E}} \oplus a_2 \left[\left(\frac{E}{E_0} \right)^{l-1} \right] \tag{2.13}$$

with $E_0 = 0.7$ GeV, $l = 0.72$ and a_2 a parameter that depends on the degree of non-compensation, varying between 0 and 1. The behaviour described by Equation (2.13) is however found, in a wide energy range up to hundreds of GeV, to be in good agreement with

$$\frac{\sigma}{E} = \frac{c_1}{\sqrt{E}} + c_2 \tag{2.14}$$

which should not however be interpreted as a complete correlation between the two contributions to the sources of fluctuations previously described. One should notice that the parameters $a_{1,2}$ are different from $c_{1,2}$, and the two equations should not be used for a direct comparison. Equation (2.14) is, nevertheless, often used to describe the energy resolution dependence on primary particle (or jet) energy for non-compensating calorimeters.

The second important contribution to fluctuations in the response of calorimeters to hadron, that is absent in electromagnetic showers, is due to fluctuation in the visible (or rather, invisible) energy. The relative fraction of invisible energy in an hadron shower, with respect to the primary hadron, will be denoted as f_{inv}. The origin of this effect, described in section 2.2.1, is ascribed to the energy lost to overcome the nuclear bounds

for the release of nucleons, that does not contribute to the calorimeter's signals. The invisible energy sums up to 30-40% of the energy carried by the non-em component, but is subject to large event-by-event fluctuations. This effect is not present in electromagnetic showers, where nuclear reactions are not part of the shower development. The relative contribution of binding energy fluctuations around the mean value E_B, shown in fig. 2.12 and estimated through Monte Carlo simulations, point to contributions of the order $\sigma/E_B \sim 15 - 20\%/\sqrt{E_B}$. One could argue that fluctuations in f_{inv} must be, in some way, correlated to the fluctuations in f_{em}, as the larger is the electromagnetic component of a shower, the smaller is the number of released neutrons and protons generated through spallation and evaporation processes in the same shower event. In Ref. [76] the correlations between f_{inv} and f_{em} are studied, in order to compare two calorimetric techniques, the compensation and the dual-readout methods, that were developed to address each one of the two fluctuation sources and addressed shortly. One important result that should already be mentioned is that the non-complete correlation between the two effects has a notable impact on the performance of calorimetric resolution on energy measurements. Even when the electromagnetic fraction fluctuations are addressed, the remaining fluctuations on the invisible energy make the hadron energy measurements less precise with respect to electromagnetic ones.

2.3 Compensation

The *compensation* method in calorimetry was developed to correct for the different response of many calorimeters to the electromagnetic and non-electromagnetic components of a showers, $e/h \neq 1$. The underlying idea was to increase the calorimeter signals produced by showering hadrons, therefore compensating for the missing contribution of the invisible energy, hence cancelling the different responses for different particles. Historically, the first concept for compensating calorimeters was to exploit nuclear fission generated by hadron interactions within a very heavy ^{238}U absorber, to produce extra contributions from nuclear de-excitation products. Early studies made with uranium/LAr [77] and later uranium/plastic [78] materials showed that e/h ratios very close to one could in fact be achieved. However, it turned out that ^{238}U absorbers were not necessary nor sufficient to achieve linear response to hadrons, as depending on the proportion between active and passive materials different e/h behaviours could be observed. The underlying phenomenon that was actually being exploited, and that was used for the construction of other compensating calorimeters, was the increase of the response to neutrons, that are freed in large quantities from very heavy absorbers. The response to hadrons by calorimeters can be decomposed through the response to the different particles that are generated in hadron showers. A general way to express the different contributions, relative to the mip response, is

$$\frac{e}{h} = \frac{e/mip}{f_{rel} \cdot rel/mip + f_p \cdot p/mip + f_n \cdot n/mip} \tag{2.15}$$

with f_{rel}, f_n and f_p representing the fraction of energy carried by relativistic charged particles (pions, kaons ecc.), spallation protons and evaporation neutrons. The fraction of energy carried by neutrons in hadronic showers f_n, is usually quite low, below 10%, but it was found that their relative contribution to the total calorimeter signal can be increased widely. The fundamental ingredient for boosting the response to neutrons in compensating calorimeter is a very light active material rich in hydrogen, that is the case of scintillating plastic materials. For low-energy evaporation neutrons, the most

probable process for depositing energy is elastic scattering with atomic nuclei. The transferred energy from a neutron to a target nucleus through this process is

$$f_n = \frac{2A}{(A+1)^2}, \tag{2.16}$$

and is largely dependent on the atomic number A of the hit nucleus. The fraction of transferred energy ranges from ~ 0.5 with collision to atomic hydrogen, to less than ~permil for lead and uranium. It follows that neutrons will lose almost all their energy, up to 90%, interacting with the nuclei in the active layer, that will produce signal through recoil of the scattered nucleus. Conversely, protons and relativistic particles deposit most of their energy in passive layers, depending on the calorimeter sampling fraction that is usually at percent level. By identifying the correct sampling fraction, one could fine tune the n/mip ratio until the neutron contribution is large enough that the response to hadrons becomes equal to that of electrons, satisfying the compensation criteria. The advantages of compensating calorimeters in removing the response dependence on f_{em}, and the effects of its fluctuations on the energy measurements precision, allow to build detectors with excellent performances. The ZEUS and SPACAL calorimeters, both designed to achieve compensation through tuning of plastics/absorber sampling fraction, obtained energy resolutions of $\sigma/E = 35\%/\sqrt{E}$ and $\sigma/E = 32\%/\sqrt{E} \oplus 1\%$, respectively. For comparison, the ATLAS hadronic (non-compensating) calorimeter resolution, measured at beam tests with pions, is reported to be $\sigma/E = 52.9/\sqrt{E} \oplus 5.7\%$ [79]. The CMS calorimeter resolution, obtained through reweighting between the electromagnetic and hadronic calorimeters also during test beams, is $\sigma/E = 112\%/\sqrt{E} \oplus 3.6\%$ [80]. The ultimate limit on energy resolution that is found in compensating calorimeters is then the degree of correlation between the total energy carried by neutron component in hadron showers, f_n, and the invisible energy of the same shower f_{inv}.

Despite the clear advantages in using compensating calorimeters, a number of limitations arise when designing detectors that operate through neutron signal boosting. The first issue is that, in order to achieve compensation, a very precise sampling fraction is required, and it cannot be increased as desired. This ultimately limits the electromagnetic performances, as sampling fluctuations cannot be reduced beyond the restraint imposed by fluctuations in the fraction of energy deposition in the passive layer. The same limit ultimately works for hadron energy resolution as well. The possible choices for active and passive materials are also few, being restricted to hydrogen-rich active layers, and very heavy absorbers that minimise the neutron energy deposition. A second problem of operating compensating calorimeters is the large volume of integration to collect signals generated by neutrons. These particles travel further from the shower axis with respect to protons and pions, and generally populate the lateral tails of the shower profile distribution. For the same reasons, a long integration time between 50 - 100 ns is required, that would make it difficult to use this method at collider experiments with very short colliding bunch intervals.

2.4 Dual-readout calorimetry

Another way of addressing the additional sources of fluctuations in showers generated by hadrons is to measure f_{em} event-by-event, and exploit this information to correct the calorimeter signal. In this way, the fluctuations of f_{em} are removed, and it is possible to restore the calorimeter response to the electromagnetic scale, also for hadrons.

This procedure is followed by the *dual-readout* calorimetry approach [81], that works by measuring the same hadronic shower using two different signals. A method that has been widely tested is to use a scintillator light signal (S), and Čerenkov light emission (C). The latter process is particularly important because Čerenkov light is emitted almost only by electrons and positrons while depositing their energy, until they reach ~ 200 keV, therefore it allows to measure the electromagnetic component of hadrons showers. The first signal, usually scintillation, provides information on the total energy deposition in the calorimeter material, which is often non-compensating and that is eventually corrected through the f_{em} measurement.

Assuming a calibration of the calorimeter with electrons of known energy E has already been taken, so that $\langle S \rangle = \langle C \rangle = E$, when tested with an hadron beam the calorimeter signals in the two channels are

$$\begin{aligned} S &= E\left[f_{em} + \frac{1}{(e/h)_S}(1 - f_{em})\right] \\ C &= E\left[f_{em} + \frac{1}{(e/h)_C}(1 - f_{em})\right]. \end{aligned} \tag{2.17}$$

In Equation (2.17) the observed signal in each of the two channels is the sum of the electromagnetic component of a shower, weighted with f_{em}, and the non-em one, with a detector response for hadrons h/e and a weight $(1 - f_{em})$. An important requirement for the dual-readout method to work correctly is for the $(e/h)_S$ and $(e/h)_C$ to be different. The two ratios can be measured by taking data with hadrons on known energy E and knowing the dependence of the electromagnetic fraction on the energy $\langle f_{em}(E) \rangle$, as described in section 2.2.2.

The two-equation system in eq. (2.17) can then be solved event-by-event, with the known parameters $(e/h)_{S,C}$ for the energy E and the value of f_{em}

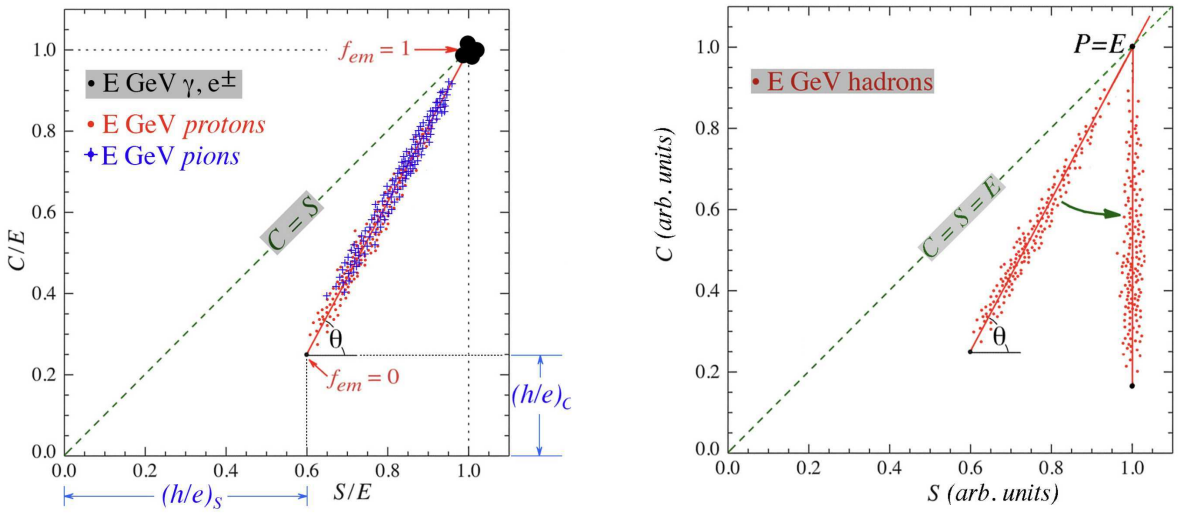
$$E = \frac{S - \chi C}{1 - \chi}, \qquad \text{with} \qquad \chi = \frac{1 - (h/e)_S}{1 - (h/e)_C} \tag{2.18}$$

and

$$f_{em} = \frac{(h/e)_C - (C/S)(h/e)_S}{(C/S)[1 - (h/e)_S] - [1 - (h/e)_C]} \tag{2.19}$$

with the measured S and C signals detected by the calorimeter.

A representation of the dual-readout approach is shown in fig. 2.13, where a scatter plot of the scintillating and Čerenkov signals, generated by electrons (black dots), pions (blue crosses) and protons (red dots) is drawn. As expected, all electron-originated showers are concentrated at the point $f_{em} = 1$, located along the diagonal line representing equal signals in the two channels, $S = C$. The missing contribution from the invisible energy in the non-em component of hadron showers manifests itself in the lower S and C signals, located along a line with the two endpoints $f_{em} = 1$ (completely electromagnetic event) and $f_{em} = 0$ (hadronic-only signal contributions, with responses $(h/e)_S$ and $(h/e)_C$. It can be noticed that pions and proton events populate differently this line, with pions usually having larger f_{em}, because of baryon number conservation effects affecting proton-originated showers. The effect of eq. (2.18) is analogous to a rotation of the same scatter plot around the $S/E = C/E = 1$ point of an angle θ such that $\chi = \cot\theta$, which depends the $(h/e)_{S,C}$ properties of the calorimeter. The result of this rotation, as observed in fig. 2.13b, is that the points are then aligned on the vertical



(a) (b)

Figure 2.13: Graphical representation of the dual-readout method. (a): After calibrating with electrons, electromagnetic showers are centred around the point with $f_{em} = 1$ and $S = C = E$. Hadron showers are located along a line which connects the points $((h/e)_S, (h/e)_C)$, with $f_{em} = 0$, and $(1, 1)$, $f_{em} = 1$. (b): The dual-readout method can be geometrically interpreted as a rotation around the point P (where $f_{em} = 1$) of an angle $\frac{\pi}{2} - \theta$. After this rotation, the projection of the points along the X axis (S signal channel) are distributed as a gaussian, and the f_{em} fluctuations have been removed. Taken from [76].

line described by $S/E = 1$, i.e. the electromagnetic scale. The resulting distribution is gaussian-distributed, since the non-poissonian fluctuations of f_{em} are no longer present. This is true for both protons and pions, but also for all different kinds of particles, hence cancelling the effect of different responses depending on the nature of the impinging hadron. The fact that the $(h/e)_C$ response is larger than zero means that some signal is still generated by the non-electromagnetic component, through relativistic contributions of mostly pions and kaons with relatively high energy. If $(h/e)_C$ was zero, the C channel would only sample the electromagnetic component of hadron showers, and therefore directly provide the measurement of f_{em}. Conversely, if the two responses $(h/e)_S$ and $(h/e)_C$ were equal, then the two components would be equally sampled by both scintillating and Čerenkov signals, and therefore no f_{em} measurement could be possible. The best case for a dual-readout calorimeter would therefore be a low $(h/e)_C$ and high $(h/e)_S$, which means a small χ factor as calculated by eq. (2.18).

The fact that, after applying the dual-readout method, the measured signal is scaled to the electromagnetic scale means that a linear response is recovered and, since $e/h = 1$, the calorimeter is therefore compensating. The response of the detector becomes symmetric and is distributed as a gaussian around the correct energy value of the hadron beam. The dual-readout technique offers several advantages with respect to compensating calorimeters. The first one is that the sampling fraction is not forced to assume one specific value necessary to achieve compensation, but can be increased depending on the experiment needs. This allows dual-readout calorimeters to offer good performances for electromagnetic showers, competitive with dedicated electromagnetic calorimeters. The Čerenkov light component is also produced immediately

as the particles in the hadron shower deposit energy, making this signal extremely fast. Electrons and positrons, the main sources of Čerenkov light, are produced in a region close to the shower development axis, the electromagnetic core of the shower. In this way, both the problems of long integration time and volume of compensating calorimeters are solved. The original DREAM (Dual-Readoud Module) [82] calorimeter prototype exploited scintillating fibres and clear optical fibres (for Čerenkov photons collection) inserted in copper rods to separate the contribution from the two physical processes. The same technique was also followed for the RD52 dual-readout calorimeter prototype [83], for the HiDRa prototype presented in this thesis [84], and for the proposed IDEA dual-readout calorimeter system [49]. The measured performances concerning the energy resolutions for single pions of the DREAM prototype pointed to an excellent scaling with $E^{-1/2}$, with $\sigma/E = 64\%/\sqrt{E} + 0.6\%$ [85]. The RD52 prototype also reports comparable resolutions [86].

It has also been demonstrated that the two signals can be separated also through different methods. Homogeneous dual-readout calorimeters based on BGO crystals [87], designed to improve the electromagnetic performances, were tested as well. The working principle would be separating the contribution of "prompt" Čerenkov light from the remaining scintillation photons, by means of different time gates. Active research on the possibility of using crystals is being pursued [88] to identify better material components such as LYSO crystals and optical filters to remove scintillating component from the Čerenkov channel. More recent versions of the IDEA calorimeter system proposal include a dual-readout calorimeter section based on crystals, located before the fibre-based hadronic one, to further improve on electromagnetic performances.

In order to understand how much can the energy resolution for single hadrons and jets improve using the dual-readout technique, one needs to investigate the correlations between the measured electromagnetic fraction of each event, and the value of the invisible energy that has been lost in the same event. Both the dual-readout and the compensation method exploit different quantities - the f_{em} or the neutron kinetic energy f_n - to account for the invisible energy losses. Figure 2.14 shows the result of a Geant4 Monte Carlo study, performed in Ref. [76], concerning the correlations between the electromagnetic fraction (or neutrons kinetic energy) and the total nuclear binding energy losses, produced from 100 GeV charged pions entering a large block of lead. In the same figure, the ratio of the same variables (the quantity $1 - f_{em}$ was used instead of f_{em}) over the binding energy is also shown, to better appreciate the degree of correlation between the two quantities. A tighter correlation is found using the electromagnetic fraction, proving the effectiveness of the dual-readout technique. However, while both techniques effectively work in removing the signal dependence over f_{em}, fluctuations in the invisible energy are still present, conspiring to worsen the energy resolution for hadrons with respect to that of electrons. Because of non-perfect correlation, invisible energy fluctuations, f_{inv}, represent the ultimate limit on dual-readout calorimeters, even for 100% contained events. Further development on new calorimetric techniques, aiming to pose further constrains on invisible energy fluctuations by measuring both Čerenkov light and neutron component signal, is being investigated through use of multiple readout systems [89].

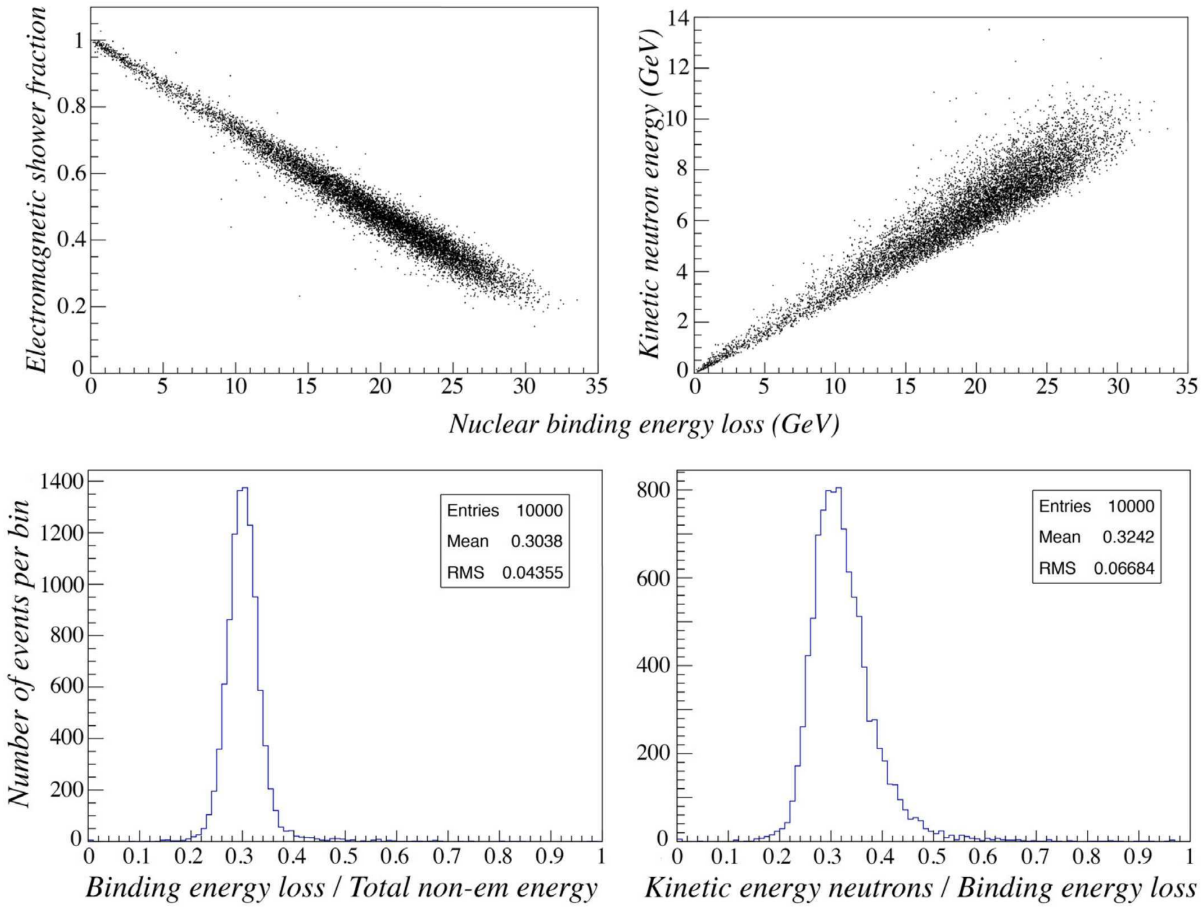


Figure 2.14: Upper row: correlations between the electromagnetic fraction f_{em} (left) or the energy carried by evaporation neutrons f_n, with the total nuclear binding energy loss produced by 100 GeV pions impinging on a lead target. The information was provided by a Geant4 simulation. Lower row: ratio between the variables shown in the upper plot. For a clearer comparison between the two different information, which are anti-correlated, in the left (lower) plot the reciprocal of $1 - f_{em}$ variable was used, instead of f_{em}. All images are taken from [76].

2.5 Particle-Flow calorimetry

A completely different calorimetric technique is offered by the Particle-Flow Analysis (PFA) method [90], which focuses on an holistic approach of using the entire detector system information, rather than the calorimeter alone to reconstruct the four-momentum of each final state particle.

After the fragmentation of decaying quarks and gluons, about 27% of the energy is carried by relatively high energy photons, 10% by neutral hadrons, and the remaining component (with the exception of neutrinos) is carried by charged particles, most of which are hadrons. The underlying idea of particle-flow is that, by identifying with excellent accuracy each of the particles in the jet composition, the detector system providing the most precise measurement can be used. For low-momentum charged particles, the best measurement is provided by an inner tracker through the track bending inside a strong enough magnetic field. For most (non-compensating) calorimeters, the energy resolution for hadrons scales as $aE^{-1/2}$ with $a \gtrsim 55\%$, while the tracker performance

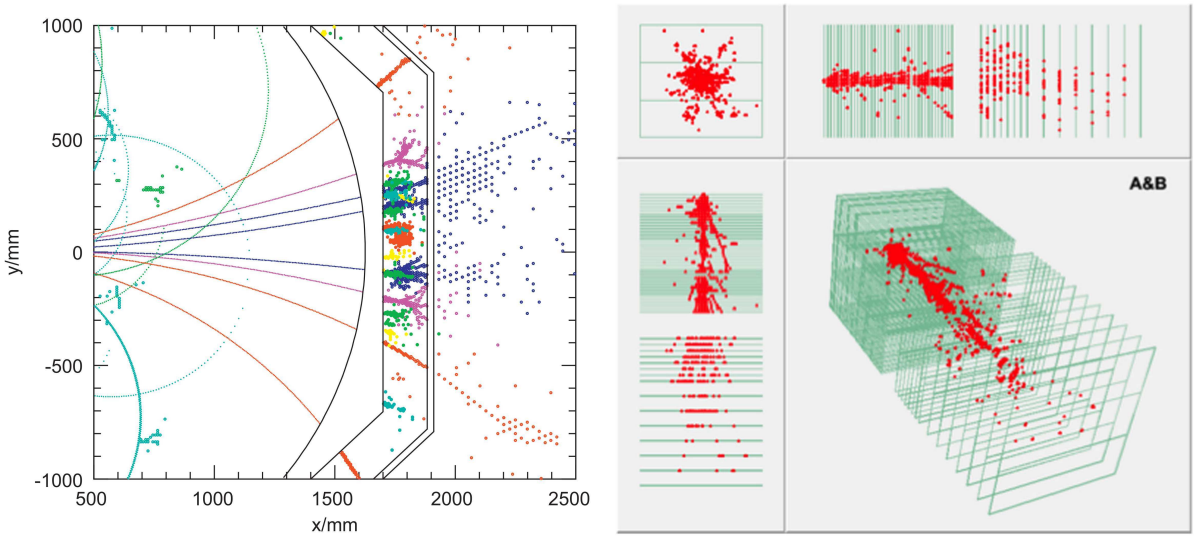


Figure 2.15: Examples of energy depositions in a finely segmented calorimeter optimised for particle-flow application. Images from [90] and [91], respectively.

degrades linearly with the track momentum, and stronger magnetic fields are required to keep untouched the momentum measurement precision. For high energy photons and neutral hadrons, that are not measured by the inner tracker, only the information provided by electromagnetic and hadronic calorimeters can be used. Once the momentum of a track has been provided by the tracker, its contribution to energy deposits in the calorimeter system must be removed to avoid double counting. Calorimeters optimised for particle-flow (see fig. 2.15) are therefore required to be highly granular, in order to better separate very close energy deposits in the calorimeter, and match them to the correct track reconstructed by the vertex detector.

Particle-flow was first used by the LEP experiments to improve on the limited performances of available calorimeters. The OPAL experiment used a simpler technique, called the Energy-Flow technique, that allowed to improve the energy resolution for jets by removing the energy deposits in calorimeter based on the momentum of associated tracks. Also at other experiments, such as the H1 experiment at HERA and D0 experiment at Tevatron, adopted a similar technique. The ALEPH experiment used actual PFA to measure the four-momentum of the particles entering the detector in the same event [92]. The calorimetric improvement obtained by ALEPH allowed to reach a quite good energy resolution for jets of $\sigma/E = 59\%/\sqrt{E} + 0.6$ GeV, resulting in a 6 GeV uncertainty at $\sqrt{s} = m_Z = 90$ GeV. Such performance was however still limited by the very coarse granularity of the calorimeters. In fact, neutral hadron contributions could not directly be separated, and had to be identified as energy deposition excesses from the remaining charged hadron contributions.

The PFA approach is also being used at the LHC experiments, with applications in the ATLAS [93][94] and CMS [95] experiments. It is interesting to notice that the largest improvements on energy resolution are found when applied on detectors whose calorimeter shows moderate performances, while only slight benefits are observed when more performant calorimeters are used, as shown in fig. 2.16. The largest improvement is found at low transverse momenta, with charged particles being more easily bent under magnetic fields and hence separated, and pions starting to resemble minimum ionising particles. This technique is also going to be extensively used

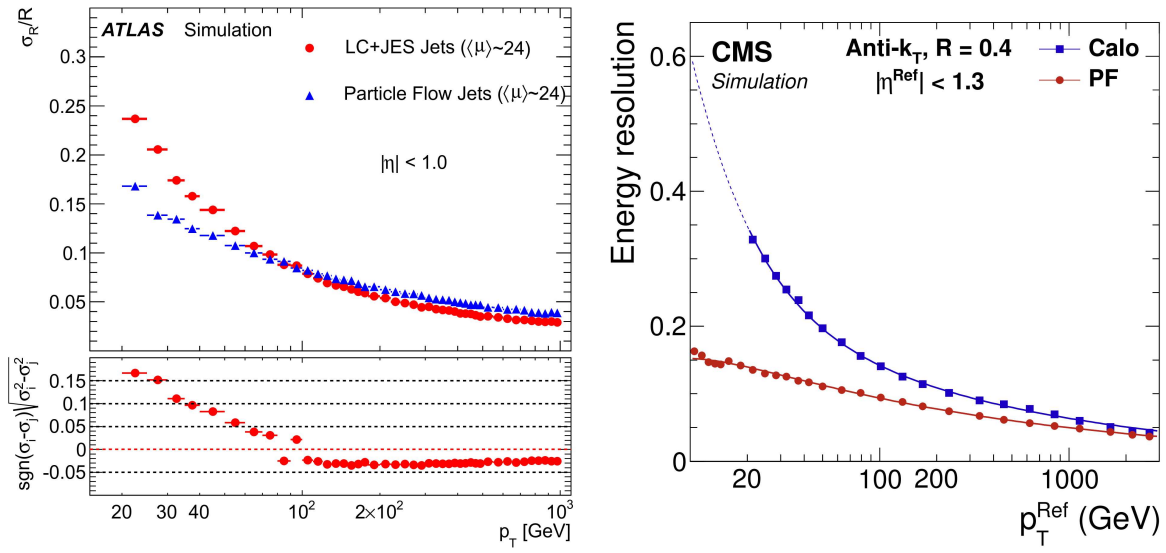


Figure 2.16: Jet Energy Resolution (JER) parameter measured through Monte Carlo simulations, with or without the application of particle-flow algorithm, for the ATLAS (left) and CMS (right) experiments [94][95].

during Run 4 and Run 5 of the LHC, with the CMS experiment undergoing a large upgrade of the forward calorimeter [96] to replace the current crystal calorimeter that would become unusable at the High Luminosity phase due to radiation damage, with a High Granularity Calorimeter (HGCAL). It was also found that a second important advantage of PFA is also pile-up mitigation, most importantly at very high luminosities.

Particle-Flow-based calorimetry is part of almost every detector concept for future lepton collider, both e^+e^- and $\mu^+\mu^-$. The effort in developing suitable calorimetric systems for these experiments has been led, since many years, by the CALICE collaboration, which realised and tested prototypes to validate the simulations with real data [97]. These types of calorimeters have a first electromagnetic section based on Silicon-based sensors and Tungsten passive material, which allows a good separation between electromagnetic and hadron showers. The tungsten absorber is particularly interesting because of its very small radiation length ($X_0 = 0.35$ cm) and Molière radius ($\rho_M = 0.93$ cm), that make electromagnetic showers very compact, while at the same time offering small absorption for hadrons ($\lambda_I = 9.6$ cm). The hadronic calorimeter section would consist of stainless steel absorbers interleaved with active elements, that may be plastic tiles with SiPM readout, Resistive Plate Chambers or other Multi-Pattern Gaseous Detectors (MPGDs), in any case able to cope with the fine segmentation requirement.

Two detectors based on highly granular calorimeters, the ILD [98] and SiD [99] experiments, were designed to operate at the ILC collider. The detector operating at CLIC [100], being an evolution of the two previous concepts, follows the same high-granularity criteria. At the FCC-ee, all three proposed detector concepts plan to apply particle-flow algorithms, despite different layouts and lower magnetic fields available in the experiment regions with respect to linear colliders. The CLD (CLIC-Like-Detector) [48] was designed by adapting the CLIC detector concept to the circular collider requirements, mainly the continuous operation and smaller bunch crossing intervals. The ALLEGRO detector [50] exploits finely segmented ECAL (based on LAr/W

or LAr/Pb) and HCAL (scintillator plastic/steel) to complement a much more granular ATLAS-like calorimeter with additional tracking information from a silicon vertex detector and drift chamber. The IDEA experiment [49], which focuses on a dual-readout calorimeter based crystals ECAL and optical fibres/absorber HCAL and is discussed in detail in section 3.2, plans to exploit at some level particle-flow techniques through single-fibre readout using Silicon Photomultipliers providing excellent transverse segmentation. Longitudinal segmentation would be provided by a two-section ECAL and a third section consisting of the fibre-based HCAL, with possible additional information provided by timing.

CHAPTER

3

DESIGN OPTIMISATION OF THE HIDRA PROTOTYPE

HiDRa (High Resolution, Highly Granular Dual-Readout demonstrator) is a project, funded by CSN5 (Commissione Scientifica Nazionale 5) of the Italian National Institute for Nuclear Physics (INFN), for the construction and testing of a dual-readout calorimeter prototype. Aside from the application of the dual-readout method, its main feature is the very fine lateral segmentation. Silicon Photomultipliers (SiPMs) are the driving technology for this high-granularity feature, making it possible to (potentially) readout each optical fibre independently from the others.

I joined the HiDRa project soon after its approval, and one of the major tasks during the first year of my Ph.D. period was studying the optimal design for the construction of the calorimeter that could be achieved with the available funding. These optimisation studies were performed by means of a Geant4 simulation package, previously developed in the same group for an already existing smaller-scale prototype[1], and tailored and expanded to the needs of the study. This chapter starts with a short resume on the performance needs that are posed on calorimeters at future colliders to match the physics goals that should be accomplished. The layout of the IDEA experiment at the FCC, which uses a dual-readout calorimeter for particle energy measurements, is then presented. The driving technology for the innovative readout system, Silicon Photomultipliers, are briefly described. The calorimetric requirements set the target for the optimisation of the HiDRa calorimeter design, on which the geometry of the dual-readout fibre calorimeter of the IDEA conceptual experiment is based. The HiDRa prototype is then presented, with Geant4 simulation studies performed before the actual construction of the detector and that guided its geometry and design.

[1] Results from the testing of this smaller-scale prototype with particle beams, to whom I participated, will be presented throughout the chapter.

3.1 Calorimetry requirements for future accelerators

In order to measure with high precision the properties of the Higgs boson, and successfully perform the set of refined Standard Model measurements planned at both the FCC and CEPC projects, highly performant detectors must be built and operated.

In events comprising W, Z and Higgs bosons, final states consisting of hadron jets have the largest branching ratios, with $\Gamma(W \rightarrow \text{hadrons}) \simeq 67\%$ and $\Gamma(Z \rightarrow \text{hadrons}) \simeq 70\%$. At the LHC most measurements involving the properties of the Higgs are carried on through the $H \rightarrow ZZ^* \rightarrow 4l$ and $H \rightarrow \gamma\gamma$ processes comprising leptons and photons as final state particles, with little branching ratio when compared to the total number of permitted Higgs boson decays. At future Higgs factories it will conversely be important to perform analyses sensitive to all possible final states. For a "SM-like" Higgs boson with a mass of 125 GeV, the main decay channels are to b-quarks ($\Gamma(H \rightarrow b\bar{b}) \simeq 58\%$), W bosons ($\Gamma(H \rightarrow WW^*) \simeq 21\%$), tau leptons ($\Gamma(H \rightarrow \tau\bar{\tau}) \simeq 6\%$) and Z bosons ($\Gamma(H \rightarrow ZZ^*) \simeq 2.6\%$), all having hadron jets as most probable final state. Remaining branching fractions to other fermions are much smaller, being proportional to their respective masses.

At the $\sqrt{s} = 240$ GeV working point the main production channel of the Higgs particle is the Higgstrahlung process (fig. 1.7), with an associated Z boson. The combined final state will include, on average, 2 jets about 32% of the times from $Z \rightarrow 2j$ and $H \rightarrow 0j$, $Z \rightarrow l\bar{l}, \nu\bar{\nu}$ and $H \rightarrow jj$, $Z \rightarrow l\bar{l}, \nu\bar{\nu}$ and $H \rightarrow WW/ZZ$ with semileptonic decays. Approximately 55% of events will comprise four jets final states, including $Z \rightarrow jj$ and $H \rightarrow 2j$, $Z \rightarrow l\bar{l}, \nu\bar{\nu}$ and $H \rightarrow WW/ZZ \rightarrow 4j$. The remaining 11% of events will averagely include 6 jets, from $Z \rightarrow 2j$ and $H \rightarrow WW/ZZ \rightarrow 4j$ with fully hadronic decays.

One of the crucial benchmark requirements on calorimetry for future accelerators is the capability to distinguish processes involving Higgs boson decays to hadron jets, $H \rightarrow WW^* \rightarrow 4j$ or $H \rightarrow ZZ^* \rightarrow 4j$, from other background processes involving electron-positron scattering, $e^+e^- \rightarrow WW^* \rightarrow 4j$ and $e^+e^- \rightarrow ZZ^* \rightarrow 4j$. To achieve this, it will be important to reconstruct the mass of the on-shell W or Z boson in the di-jet decays, with sufficient precision to distinguish it from the other vector boson. For particles of masses 80 GeV and 90 GeV, the Rayleigh criterion for clearly distinguishing the two di-jet invariant mass distributions poses a relative resolution on the invariant mass of about 3 GeV. Assuming a negligible constant term, a stochastic one of

$$\frac{\sigma}{E} = \frac{30\%}{\sqrt{E}}$$

would be required for achieving a good separation between W and Z bosons. Figure 3.1 shows an example of the di-jet mass distributions of hadronically decaying W, Z and Higgs simulated events through a previous version of the IDEA dual-readout calorimeter full simulation, described in detail in [101].

Besides good energy resolution for hadrons, the complete set of precision measurements of both FCC and CEPC also poses demands on excellent measurement for electrons and photons. While for most Higgs-related processes, such as $H \rightarrow \gamma\gamma$, a stochastic term $\sigma/E = 15 - 20\%/\sqrt{E}$ is generally considered sufficient, other physics studies require much better precision for these particles. One example of application where exquisite electromagnetic calorimetry would play a role is flavour physics [102]. In-depth measurements of B baryons decays are of particular interest for CP-symmetry

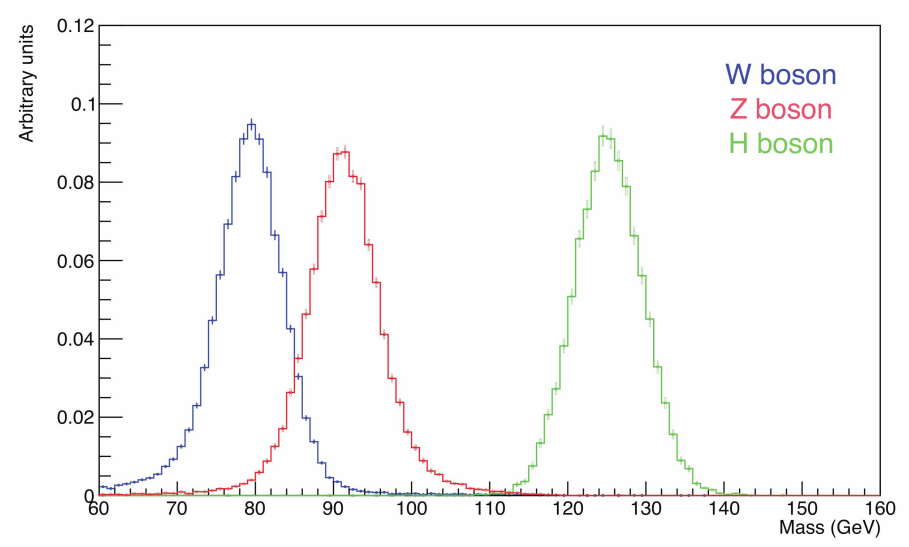


Figure 3.1: Jet-jet invariant mass distributions for final states consisting of W, Z, and H bosons decaying hadronically in a dual-readout calorimeter with $\sigma/E = 38\%/\sqrt{E}$ for hadron jets [101].

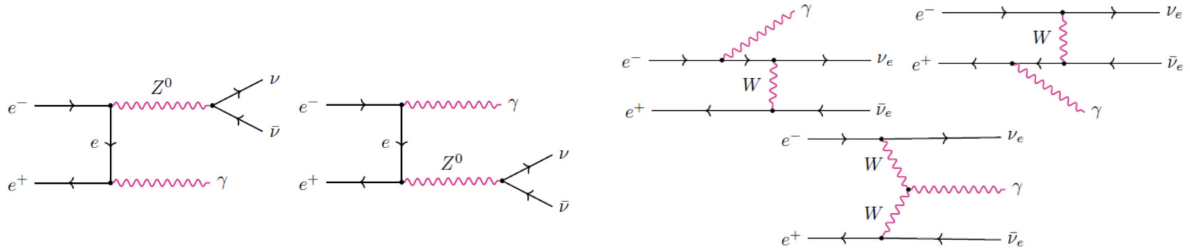


Figure 3.2: Processes involving neutrino production in association with a high-energy photon γ, through W or Z vector bosons. On the left, processes involving the Z boson, in which the neutrino flavour is not tagged. On the right, processes with the same final state but involving W boson exchange in the t-channel, in which the neutrino flavour can be tagged because of the original e^+e^- initial state, causing interference terms [103].

violation searches in the quark sector. Final states comprising multiple π^0s with rather low energy would greatly benefit from an energy resolution better than $5\%/\sqrt{E}$. Another measurement that would take advantage of excellent electromagnetic resolution would be the precise measurement of the Z boson coupling to electron neutrino, which is today poorly known, through the $e^+e^- \rightarrow Z\gamma$ process with the following $Z \rightarrow \nu_e\overline{\nu}_e$ decay. Interference contributions with the t-channel W boson exchange process, depicted in fig. 3.2, would modify the energy spectrum of the outgoing photon [103]. An asymmetric deformation of the Z boson lineshape, measured through the $\nu\overline{\nu}$ invariant mass $M^2_{\nu\overline{\nu}} \simeq s - 2\sqrt{s}E_\gamma$ at $\sqrt{s} = 161$ GeV, would then be observed when compared to the 3 neutrino case, with a relative effect of up to 8%. In order to perform percent-level measurements of this lineshape variation, very high luminosities of $10 - 20$ ab^{-1} and electromagnetic energy resolution as close as possible to 1% for detecting the associated photon should be achieved.

Finally, very good electromagnetic energy resolution can be exploited to recover bremsstrahlung radiation contributions from electrons [88]. In fact, final states includ-

ing electrons such as $e^+e^- \rightarrow Z(\rightarrow e^+e^-)H$ would have non-negligible contribution of final state radiation from electrons under experiments' solenoidal magnetic fields. With a good enough clustering algorithm able to associate calorimetric deposits to the correct (deviated) electron, it was found that an energy resolution for electrons about 80% to that of muons of the same energy of $M_Z/2$ could be found, if a stochastic term of $\sigma/E = 3\%/\sqrt{E}$ was reached.

3.2 The IDEA detector concept

The Innovative Detector for Electron-positron Accelerators (IDEA) [49] experiment is one of the three main detectors proposed to be operated at the FCC-ee. It features a number of advanced detector technologies, combined in a single collider experiment targeting the broad FCC physics programme. The layout of IDEA is drawn in fig. 3.3. From the interaction point going outwards, the current proposal envisages a silicon-based pixel detector with very high spatial resolution, followed by an ultra-light drift chamber for an improved tracking and particle identification purposes. The tracking system is completed by a wrapper based on silicon sensors which may also provide timing information for time-of-flight measurements. A crystal-based dual-readout calorimeter that features excellent energy resolution for electrons and photons is located before a thin superconducting solenoid that provides the magnetic field for the tracker. Outside the solenoid, the calorimetric system is completed by a fibre-based dual-readout calorimeter, with excellent energy resolution and lateral granularity for further particle identification purposes and possibly apply particle-flow techniques. Finally, the detector is completed by a muon system based on μ-Rwell micro-pattern gaseous detectors for the momentum measurement of muons and their identification. In the following, a brief description of the employed technologies for each sub-detector is given.

3.2.1 Tracking systems

The vertex detector of IDEA features two main subsystems, an inner and an outer vertex detector. For the inner vertex detector, two proposals are currently being developed. The baseline one features three concentric barrel layers supported by a carbon fibre structure, both shown in fig. 3.4. The main design parameters are listed in table 3.1. It is located very close to the accelerator beam pipe, between 13.7 mm for the inner layer and 35.6 mm for the outer one. The basic unit has a size of 32×8.4 mm^2 in the $z \times (r - \varphi)$ plane, with silicon pixels having an area of 25×25 μm^2. The total length of each barrel layer varies from 96.5 mm to 257.5 mm, covering $|\cos\vartheta| < 0.99$. Each layer contributes to the material budget to 0.25% X_0 in the normal incidence direction.

The second inner vertex proposal is based in the ALICE ITS3 curved sensor technology for the Long Shutdown 3 detector upgrade [104]. This latter option provides a self-supporting structure from the silicon sensors, resulting in an ultra-light vertex detector. The sizes of the silicon sensors varies between layers, and optimisation of the parameters are being performed. Each layer only contributes to 0.075% X_0 with almost uniform distribution in φ, because of the missing supporting structure, therefore drastically reducing the required material budget.

In both configurations, the tracker detector is completed by an outer vertex, which comprises two further barrel layers, and three endcap disks. Silicon sensors with size $40.6\,(\mathrm{z}) \times 42.2\,(r - \varphi)$ mm^2 and 150×50 μm^2 pixels would be used for both outer tracker systems.

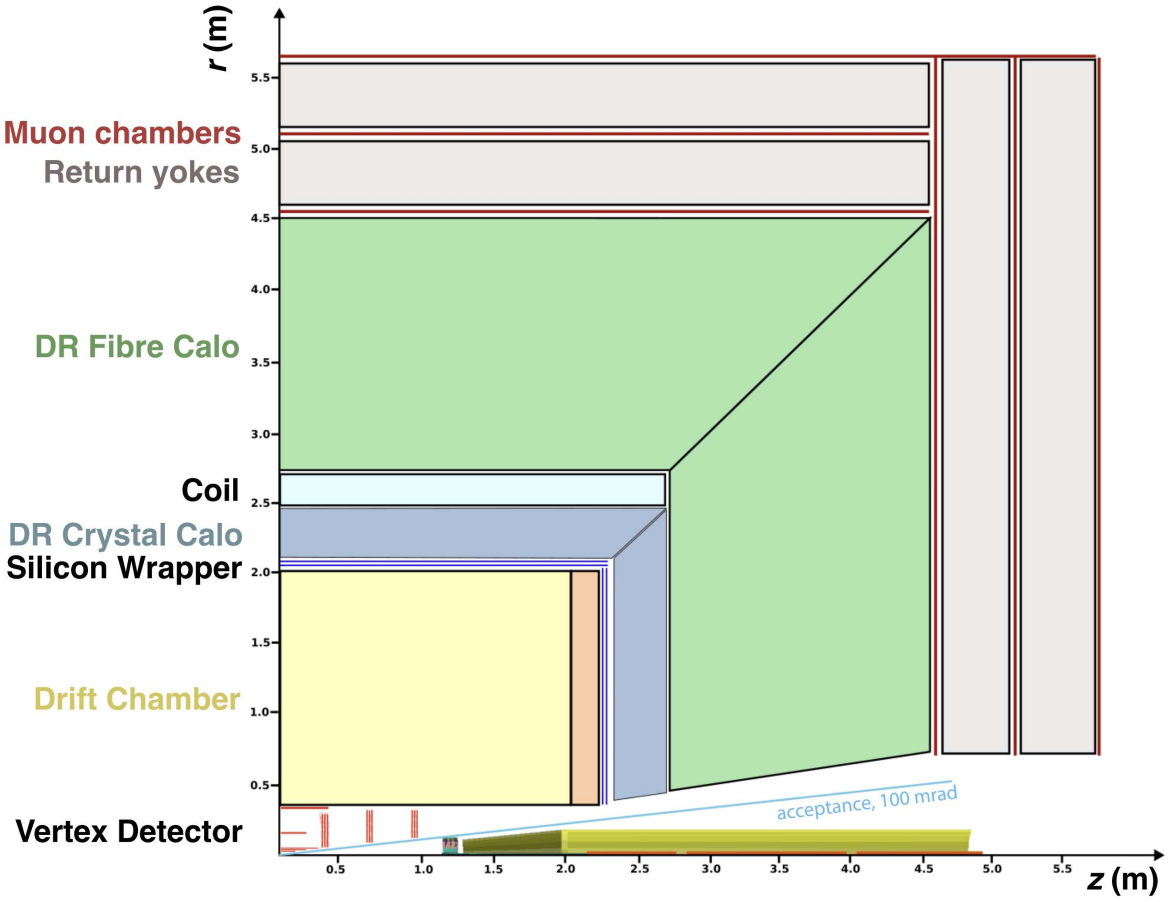


Figure 3.3: Sketch of the IDEA experiment layout [49].

Table 3.1: Main parameters of the baseline vertex detector.

Subsystem	Layer ID	Radius [mm]	$\|z\|$coverage [mm]	Power [W]
Inner barrel	1	13.7	< 96.5	12
Inner barrel	2	23.7	< 160.9	32
Inner barrel	3	34 and 35.6	< 257.5	77
Middle barrel	1	130	< 163.1	316
Outer barrel	2	315	< 326.3	1400
Disks	1	$34.5 < r < 275$	304.7	135
Disks	2	$70 < r < 315$	620	420
Disks	3	$105 < r < 315$	930	370

The largest component of the IDEA tracking system volume is occupied by the drift chamber, shown in fig. 3.5 (left). This detector exploits the innovative cluster counting technique [106] to provide excellent particle identification, beside precision tracking and tracks momentum measurements. Its main feature is a very high transparency, which allows to minimise multiple scattering of particles in the hundreds of MeV range up to several GeV. Other advantages are the reduction of high-energy photons conversions and minimisation of hadron interactions in this volume. The drift chamber consists of a single cylindrical volume filled with a very light gas mixture, being 90% He

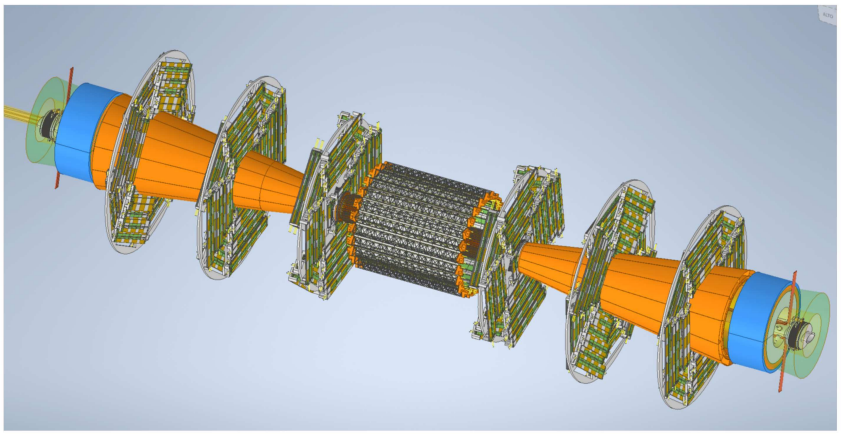


Figure 3.4: Drawing of the baseline vertex detector middle layer, and the three outer wheels. Taken from [49].

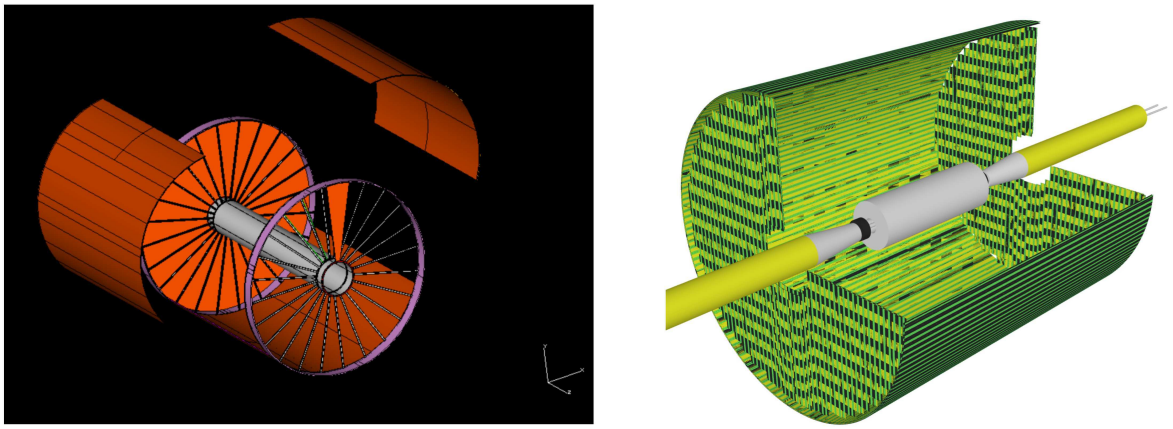


Figure 3.5: DD4hep [105] renderings of the IDEA drift chamber (left) and silicon wrapper (right) [49].

and 10% CH_4. Isobutane was chosen because of excellent quenching properties, its low cost, and the relatively low environmental impact. The chamber has an internal radius of 350 mm and an outer one of 2000 mm, and has a length of 4 m, covering up to $\vartheta \simeq 13°$. The wires that compose the chamber are co-axial with the magnetic field, and grouped into 14 co-axial *super-layers*, each comprising 8 layers. The wires in each layer are arranged with small stereo angles with respect to the beam line, from 50 to 250 mrad, to also recover longitudinal coordinates information. With this gas and wire design, the full chamber only sums up to 1.6% X_0 in the radial direction, mostly coming from the outer end of the chamber. In the longitudinal direction, the material budget increases to 5% X_0, with a large contribution from the front-end electronics located in this region.

The performances of this type of chamber, with different drift distances, sense wire sizes and gas mixtures were tested with muon beams at CERN for their evaluation. Preliminary studies show that a factor 2 improvement in the particle identification could be found with the dN/dX cluster counting technique, over the traditional dE/dX ionisation measurement, for a wide range of particles momenta. Excellent spatial resolutions of less than 100 μm are in reach, when also combining timing information.

The IDEA tracking system is completed by a silicon wrapper, which surrounds the drift chamber, with an area of ~ 100 m^2 covering up to $|\cos\vartheta| < 0.99$. A baseline tech-

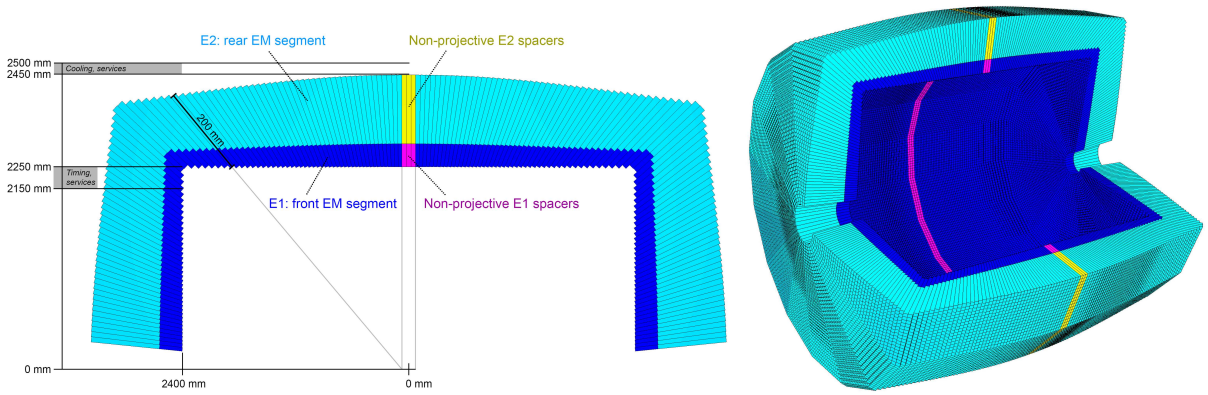


Figure 3.6: Sketches of the IDEA crystal ECal [49].

nology for this layer has not yet been fixed. The current proposal foresees Monolithic Active Pixel Sensors (MAPS) technology for a last track position measurements, with spatial resolution of 10 μm over the widest coverage possible, mostly for cross-section measurements. Alternative solutions are based on Low-Gain Avalanche Photodiods (LGAD), which also provide excellent timing resolutions at a level of 100 ps that would be used for time-of-flight measurements and further improving k/π separation. If the MAPS technology was accepted, a timing layer before the electromagnetic calorimeter would be added with the same purpose, consisting of a LYSO crystal layer.

The entire tracking detector should allow excellent momentum measurements for charged particles at a level of $\sigma(1/p_T) \leq 3 \times 10^{-5}$ (GeV/c)$^{-1}$ for 45 GeV muons, representing the requirement for precise Higgs boson measurements [107].

3.2.2 Calorimeters and magnet

The calorimetry system of IDEA was designed to enable precise measurements of hadronic final states, at a level currently not in reach at present hadron colliders. The benchmark process for the IDEA calorimeters was a good statistical separation of $W \rightarrow 2j$ and $Z \rightarrow 2j$ events, as mentioned in section 3.1, leading to a target energy resolution of $30\%/\sqrt{E}$ with small constant terms. To achieve this, the dual-readout technique was chosen as a good candidate to improve the calorimetric performances. In a first layout proposal, a dual-readout fibre calorimeter was designed as a standalone calorimeter system, offering both electromagnetic performances ($10 - 15\%/\sqrt{E}$) and excellent hadronic ones. An electromagnetic calorimeter based on crystals was later added to further improve the electromagnetic energy resolution, with a stochastic term of $3\%/\sqrt{E}$ as target. Since a non-dual-readout crystal section would spoil the hadronic energy resolution of the following dual-readout calorimeter, by losing information on the f_{em} of incoming hadrons, the dual-readout method was also considered for the ECal.

The electromagnetic calorimeter section of IDEA, shown in fig. 3.6, extends from about 2150 mm from the IP, to 2400 mm, depending on the azimuthal position of each tower. Each crystal tower has a trapezoidal shape oriented along the radial direction, and is longitudinally segmented. The total depth of this calorimeter is 22 X_0, with the first layer contributing to $6X_0$ and the second to $16X_0$. The front face of each crystal in the first layer has an area of 10×10 mm^2. Different types of crystals are currently being investigated, including $PbWO_4$, BGO and BSO. The double readout is obtained by

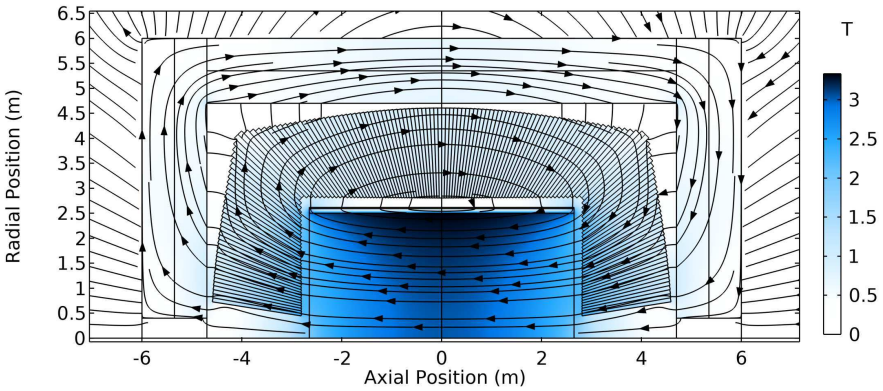


Figure 3.7: Magnetic field lines produced by the 3 T HTS superconducting solenoid [49].

applying two SiPMs to each crystal in the second layer, with size $6{\times}6$ mm^2, one of which having a thin optical filter on its surface to filter out photons with a wavelength inside a window around the scintillation peak. A second strategy, also being developed, is to separate the scintillation and Čerenkov light components through their different time profile. In both cases, a single SiPM would be used for the readout of the first crystal section. This choice was guided by the very small energy deposits from hadrons in this first lightweight section, which only contributes 0.25 λ_I.

Between the electromagnetic and the hadronic calorimeters of IDEA, a superconducting solenoidal coid is inserted to provide the magnetic field for charged tracks momentum measurements. In previous detector designs, a 2 T magnet based on NbTi technology was chosen to operate at very low temperatures, for all beam energies from 90 GeV at the Z pole up to 365 GeV at the $t\bar{t}$ run. Recent advancements in superconducting coil technologies, however, made it possible to conceive the usage of a high-temperature superconducting (HTS) solenoidal coil, operating at temperatures higher than 20 K, and providing a magnetic field up to 3 T (see fig. 3.7).

The hadronic section of the IDEA calorimeter is based on a design constituted of two types of optical fibres, scintillating and clear ones, embedded into a passive absorber material. Different construction methods are being investigated, one being described in detail in the following chapters, consisting of absorber capillary tubes in which the optical fibres are inserted. Alternative methods for the passive absorber construction and calorimeter assembly were tried out by the RD52 collaboration, with groups from Korea and US. Among these, are the holes drilling in a metal slab, 3D printing, and optical fibres placed into a metal skiving fin heat sink geometry. Among the most interesting features of this calorimeter is the readout system based on Silicon Photomultipliers (SiPMs), solid-state optical sensors which enable the independent readout of each optical fibre, and therefore providing excellent lateral granularity. More information on these photodetectors, which are used in the HiDRa calorimeter prototype discussed in the following of this thesis, are reported in section 3.3. The current calorimeter layout used in the simulations exploits tubes arranged in towers forming symmetrical staves along the φ direction, shown in fig. 3.8. A total of 72 staves are used to define the granularity in the φ direction, each comprising 45 towers in the ϑ direction in the barrel, and 35 towers in the endcaps. The coverage of each tower results in about 1° on the ϑ direction, and 5° in the φ one. Considering the capillary tube layout under study in this thesis, with 2 mm outer diameter tubes and 1 mm outer diameter optical fibres, the

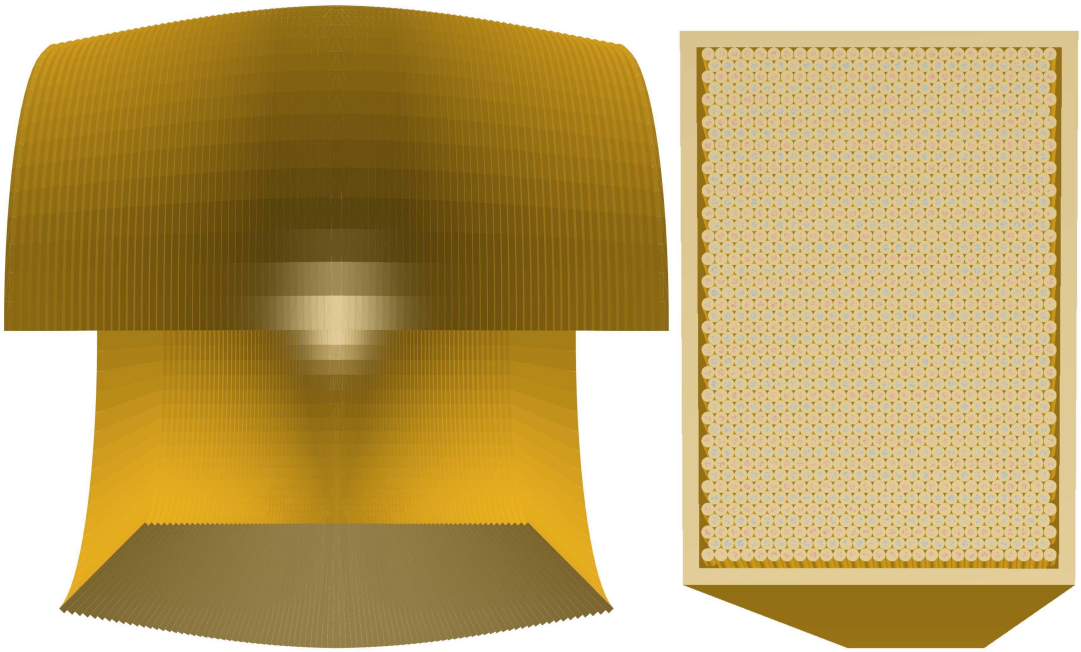


Figure 3.8: Section of the IDEA barrel fibre calorimeter, with some towers removed for visualisation purposes, and zoom on the backside of one tower with its mechanical support [49].

hadronic calorimeter would comprise about 80 million fibres, of which 60 in the barrel and 20 in the two endcaps. With the insertion of the electromagnetic calorimeter, the total length of the towers composing the hadronic one were shortened from 2 m to 1.8 m, extending from 2.8 m to 4.6 m from the interaction point. It should be noted, however, that the mentioned geometry with very high lateral segmentation was proposed before the additional proposal of an electromagnetic calorimeter section before the hadronic one. A very fine lateral segmentation would be helpful, for example, in separating electromagnetic showers originated by high-energy photons or neutral pions, as will be described in chapter 4. Additional important features of the high granularity would be the implementation of other particle identification purposes, and providing more information to neural networks during data analyses. If the current design with an electromagnetic calorimeter was accepted, a change in the hadronic calorimeter layout would probably be required, following the lower need for lateral segmentation at the millimetre level.

3.2.3 Muon system

The muon system of the IDEA experiment, located outside of the calorimeter volume, comprises three or more layers of gas chambers covering the entire solid angle. The muon chamber layers would be located inside the iron yoke, which confines the solenoidal magnetic field. A spatial resolution of $\sim$ 100 μm was estimated to be required on the muon hits position, to achieve optimal performances in Standard Model precision measurements, as well as long-lived particles decays into muons inside the calorimeter. μ-Rwell gaseous detectors [108], drawn in fig. 3.9, being compact single-stage MPGDs, currently are the proposed option to achieve the target spatial resolution. These detectors are constituted by a Printed Circuit Board (PCB) layered on top with a thin copper layer, which acts as a cathode, and a second multi-layer PCB. This

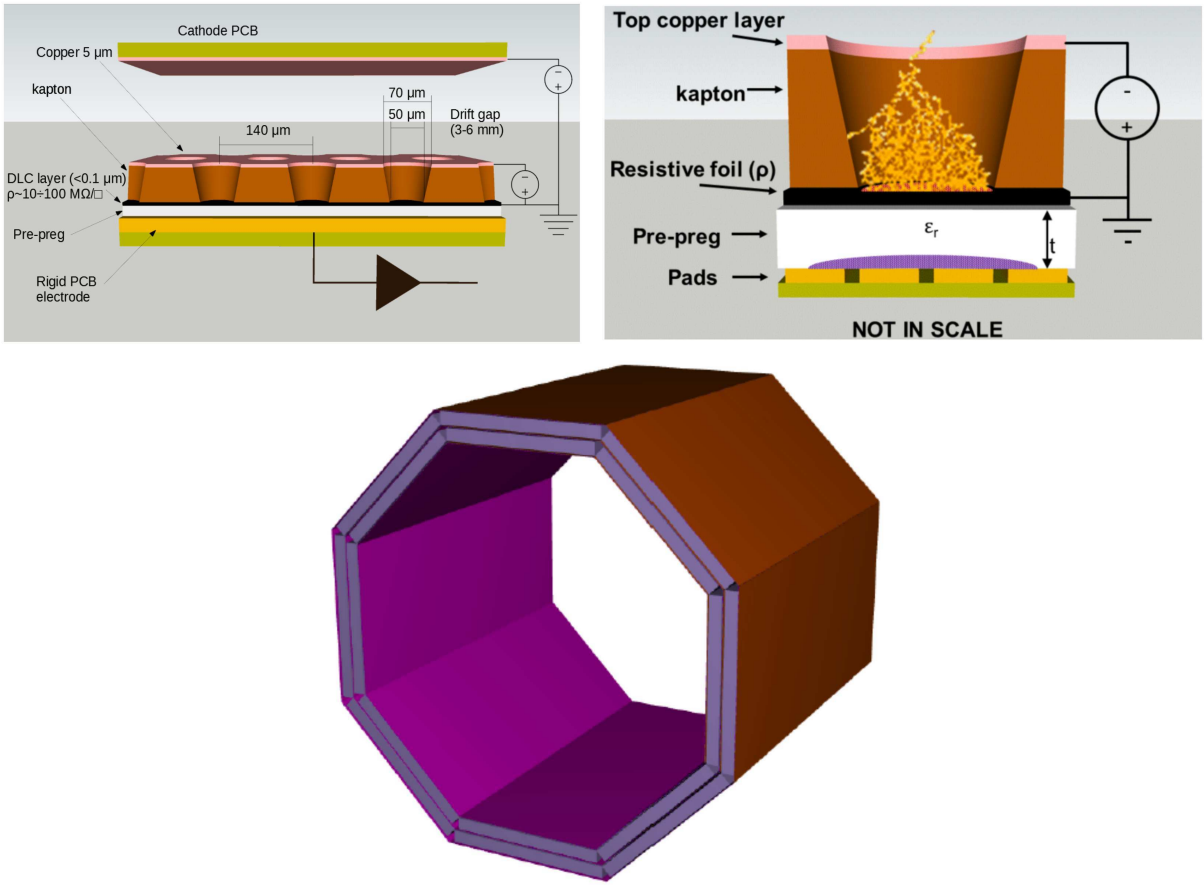


Figure 3.9: Drawing of the µ-Rwell gaseous detectors used for the IDEA muon system, and DD4hep simulation of barrel section [49].

second PCB is produced through photo-lithography methods to present a pattern of wells in the copper-polyimide multi-layer foil. A resistive layer made of Diamond-Like Carbon (DLC) completes the amplification stage, with the wells providing gaps for the charge multiplication. This stage is used for the signal amplification in a way that resembles GEM gaseous detectors [109], when a suitable voltage is applied between the copper layer and the DLC. The other layers of the bottom PCB are a resistive layer for discharge limitation, and a readout plane for the readout, that is segmented into strips in the case of the muon system. The µ-Rwell chamber module currently envisaged for the IDEA experiment would be based on 50×50 cm^2 tiles with strip readout. The general layout of their disposition to form the barrel section of IDEA is also shown in fig. 3.9 through the DD4hep simulation framework. A strip pitch of 0.4 mm to 1.5 mm would be adopted to provide spatial resolutions of 100-500 µm. Dedicated optimisation is being performed to compromise between current industrial production capabilities, the detector capacitance than can be tolerated by front-end electronics, signal-to-noise ratio, spatial resolution and total costs.

3.3 Silicon Photomultipliers

A different type of requirement that is almost ubiquitous in calorimeters development for future colliders is very fine detector segmentation, both lateral and longitudinal. As discussed in section 2.5, disentangling very close energy deposits in the calorimeter al-

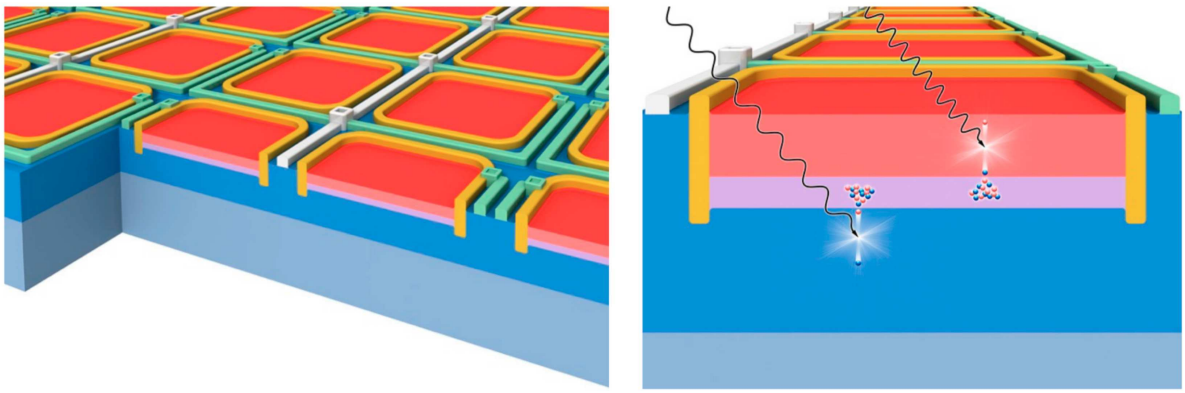


Figure 3.10: Drawing of a Silicon Photomultiplier. Image from [101].

lows for their better association to the incoming tracks, whose momenta was measured in the inner tracker detector, and enables a better performing particle-flow algorithm application. A widespread instrument envisaged for the readout of calorimeters light signals, which is produced in most cases from scintillation emission (and Čerenkov light for dual-readout calorimeters) are Silicon Photomultipliers (SiPMs). SiPMs, pictured in fig. 3.10, are solid state light sensors consisting of matrices of Single-Photon Avalanche Diode pixels, all operated in Geiger mode. Each photo-diode is a pn-junction operated a few volts above the breakdown voltage, V_{BD}. Upon the absorption of an optical photon, the charge from freed electron-hole pair undergoes avalanche multiplication due to the high local electric field, until the total charge overcomes a set threshold, inducing a quenching resistor to lower the voltage below V_{BD}. Very high gain, of the order of $\sim 10^6$, can be produced with these devices, allowing the detection of single photons impinging on their surface. While the use of digital photosensors may not seem appealing for calorimeters, where a linear response is important, an analogical response can be partially recovered by reducing drastically the size of each pixel, and reading out the total charge produced by an array of pixels. Modern SiPMs have typical pixel widths ranging from $10\ \mu\text{m}^2$ to $100\ \mu\text{m}^2$ and total size of one or more millimetres, therefore reducing the probability of multiple photons impinging on the same cell.

Figure 3.11 shows an example of the integrated response of a Silicon Photomultiplier from Hamamatsu, when exposed to differently populated bunches from a light source. When more then one cell is fired, the total collected charge is the sum of the charge deposited in each pixel, leading to the shown equally-spaced multiple peak behaviour. With a correctly set gain, and sufficient control over the system noise, each peak correspond to a different number of photons hitting more pixels in the SiPM, therefore providing a direct counting of the total number of impinging optical photons. The first peak at zero ADC counts, which corresponds to the case where no photons were detected, provides a direct measurement of the electronic noise of the instrument. The peaks width increases with the square root of the total number of detected photons, causing an upper limit on the maximum number of optical photons that can be resolved in the same SiPM.

Among the advantages of SiPMs, when compared with previous generations of light sensors such as Photomultiplier Tubes, are the possibility to be operated in magnetic fields and with lower voltages, higher PhotoDetection Efficiency (PDE), robustness and, depending on the use cases, lower prices [111]. Excellent timing capabilities through

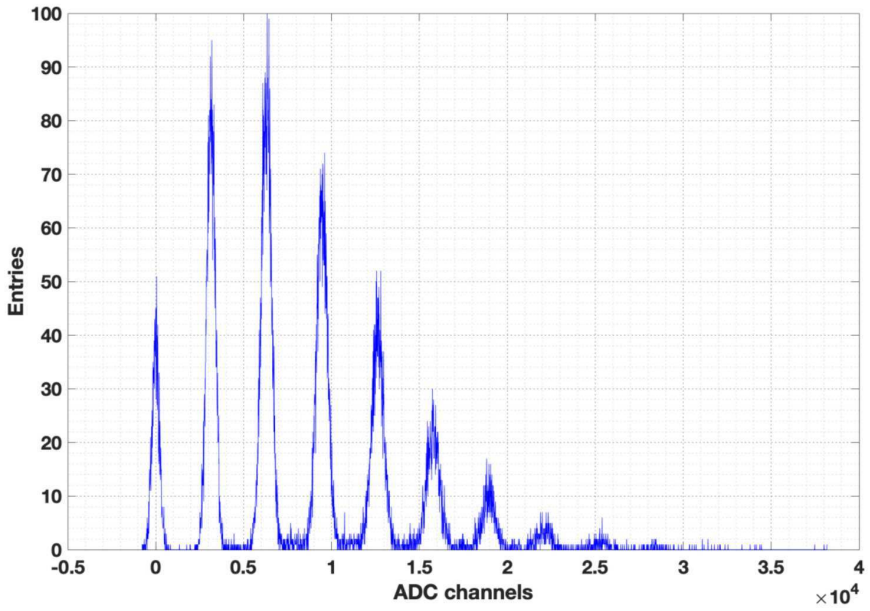


Figure 3.11: Multi-photon spectrum of the Hamamatsu SiPM model 13360-1350CS, having a 50 μm pixel pitch and total dimension of 1.3×1.3 mm^2. Taken from [101].

time-of-arrival measurement, at the level of tens of picoseconds, can also be reached. The PDE parameter describes the probability for a light sensor to generate a signal when hit by an optical photon. It is straightforwardly defined as the ratio between the average numbers of fired pixels N_F over the one of photons impinging on the surface area N_γ,

$$PDE = \frac{\langle N_F \rangle}{\langle N_\gamma \rangle} = FF \times QE(\lambda) \times P_T(\lambda, V_{OV}, T), \tag{3.1}$$

and can be expressed as the product of the Filling Factor (FF), the Quantum Efficiency (QE), and the probability of triggering an avalanche P_T. The photodetection efficiency depends, in general, on both geometrical and physical properties of the sensor in use. The Filling Factor represents the fraction of sensor area that can generate some signal over the total SiPM area. As shown in fig. 3.10, some surface between the cells is not active, and is used to separate two adjacent pn-junctions and reduce cross-talk between cells. While a larger number of pixels in the same SiPMs leads to better linearity, it has the effects of reducing the PDE because of larger non-active area in between pixels. This is shown in fig. 3.12: for similar SiPM sensor (Hamamatsu S13360 series), smaller cell pitch (25 μm, left image) has a lower total PDE for any photon wavelength when compared to a larger cell pitch sensor (50 μm, right image). The Quantum Efficiency describes the probability for a photon of wavelength λ, entering in the SiPM sensitive area, to create an electron-hole pair. It depends on the photon frequency and on the thickness of the different layers in the pn-junction of which the SiPM is made. It is therefore possible, by designing apposite sensor geometry, to optimise the PDE for different wavelengths such as the one emitted by a specific scintillator material, or from Čerenkov light. Finally, the avalanche trigger probability P_T is the probability for a charge carrier avalanche to be generated when a photon is converted into an electron-hole pair in the depletion region. This probability depends on the depth of photon absorption in the silicon pixel, which varies with the wavelength λ, the applied electric field through the applied over-voltage V_{OV}, and the temperature T.

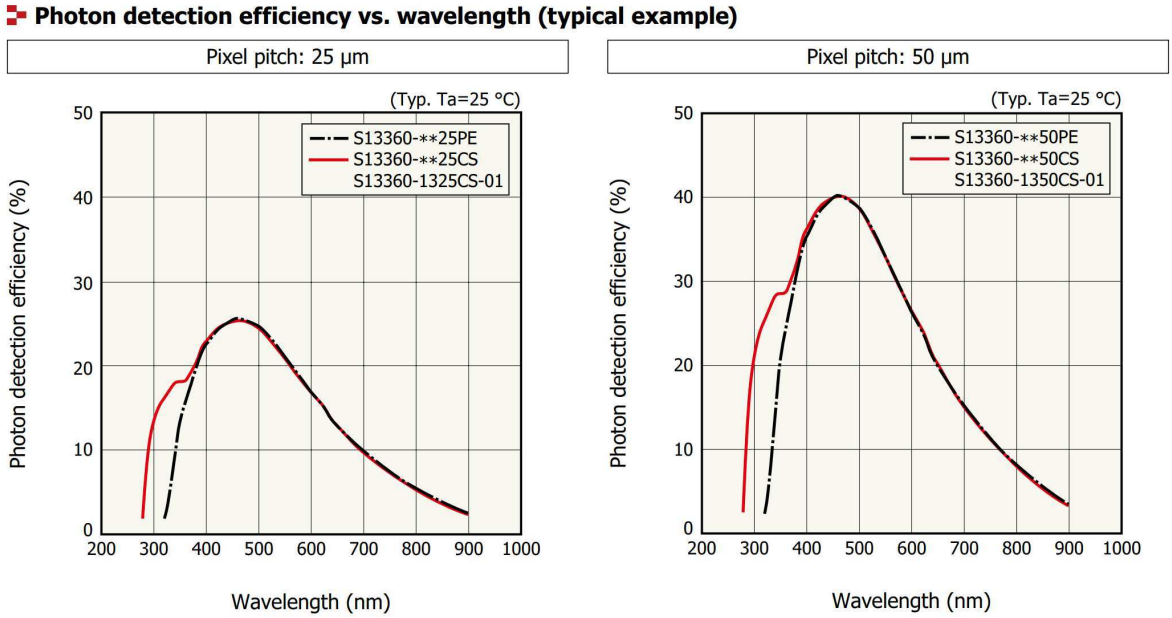


Figure 3.12: Example of photodetection efficiency dependence on the wavelength of impinging photons, for two SiPMs from Hamamatsu S13360 series with different cell pitch. Image from [110].

Silicon photomultipliers are today largely used in several operating particle physics experiments and future upgrades. Notable examples are the liquid-Xenon calorimeter upgrade for the MEG experiment [112], the LHCb scintillating fibre tracking detector [113], and the CMS high granularity calorimeter upgrade (HGCAL) for the Hi-Lumi LHC [96].

The usage of SiPMs for calorimetry readout was pioneered by the CALICE collaboration, which developed prototypes based on SiPM-on-tile technology [114]. The Analogue Hadron Calorimeter (AHCAL) is based on 3×3 cm^2 scintillating tiles interleaved with 20 mm steel absorber plates, with a total volume of 1 m^3. Scintillation light from each tile was individually read with a SiPM, reaching in total 21888 readout channels.

A further line of research on more advanced SiPM technology are digital SiPMs (dSiPMs) [115]. These devices are designed to improve the scalability of photosensors for very large projects. Each cell is equipped with its own readout circuit, and digitised signals from pixel counting are directly provided from each dSiPM. This step allows to remove the signal amplification and digitisation through dedicated readout chips as for common SiPMs, with much better integration capabilities.

3.4 Capillary tube calorimeter proof-of-concept

A preliminary prototype of a dual-readout calorimeter with silicon photomultipliers included in the readout system was built in 2020, as a proof-of-concept for a novel construction technique based on optical fibres inserted in metal capillary tubes. A major effort was put on the identification of a scalable construction technique to overcome previous difficulties encountered during the construction of RD52 modules, namely limited assembly precision due to copper plates hardness, or lead plates softness making the structure unable to be sustained correctly when used for a 4π experiment calorimeter. A modular design was chosen, based on multiple identical units called towers, as a preliminary step to identify a suitable assembly method for larger scale detectors.

Details on the exact construction procedure can be found in [116].

The front and lateral faces of the prototype are shown in fig. 3.13. A tower consists of 320 brass capillary tubes aligned in 20 rows, with 16 tubes each. All capillary tubes have an outer diameter of 2 mm and an inner one of 1.1 mm. Two different types of optical fibres, scintillating and clear (Čerenkov) ones, are alternatively inserted row-after-row, with an outer diameter of 1 mm. Scintillating fibres are Saint Gobain BCF-10, with polystirene core and polymethyl-methacrylate (PMMA) cladding, while Mitsubishi SK-40 with PMMA core and fluorinated polymer cladding are used for Čerenkov fibres. The total volume of the detector, made of nine towers, is $\sim 10 \times 10 \times 100$ cm^3, enough to contain electromagnetic showers at a level of about 94%. The main feature of this prototype is the SiPM readout of the central module, (M0 in fig. 3.13), instrumented with Hamamatsu model S14160-1315PS with 1.3×1.3 mm^2 sensitive area and 15 mm pitch, for both scintillation and Čerenkov photons. Since the size of the sensor with its packaging is larger than the fibre diameter, optical fibres are extracted from the calorimeter rear side to be connected to one SiPM each through optical grease. The remaining eight towers (M1-M8 in fig. 3.13) are equipped with Photomultiplier Tubes from Hamamatsu, model R8900 for scintillating fibres and R8900-100 for Čerenkov ones. A yellow optical filter (Kodak Wratten 2 #3 [117]) was also used in between scintillating fibres and optical sensors, to cut out higher photon wavelengths that are more heavily attenuated.

The performances of this prototype were assessed during two consecutive tests with particle beams, in 2021 [118] and 2023 [119], to the latter of which I directly participated. In both cases, the detector was tested at the SPS H8 beamline located in the North Area, at CERN. Positron beams with energy in the range 10-120 GeV were used, with a selection obtained by means of upstream Čerenkov counter detectors. A preshower ancillary detector was also used to remove minimum ionising particle contributions (mostly pions and muons) when Čerenkov counters were not considered sufficiently reliable.

Among the most interesting results from the first beam test, is the measurement of electromagnetic showers lateral profile, made possible by the fine segmentation provide by independent fibre readout. The same measure was performed separately for the scintillation and Čerenkov channels, by calculating for each event the energy-weighted barycentre coordinates as

$$X_{CALO} = \frac{\sum_i x_i E_i}{\sum_i E_i}, \qquad Y_{CALO} = \frac{\sum_i y_i E_i}{E_i} \tag{3.2}$$

where x_i, y_i are the coordinates of each SiPM (with index i) in the calorimeter, and E_i is the energy contribution by that SiPM after the calibration. The lateral profile was then obtained by calculating the fraction of energy deposited in a fibre with coordinates (x, y) at a radius r from the shower axis, calculated as

$$r = \sqrt{(x - X_{CALO})^2 + (y - Y_{CALO})^2}, \tag{3.3}$$

with respect to the total energy of the event. The observed profile for both channels is shown in fig. 3.14 (left), also compared with Geant4 simulations, to whom excellent agreement was found. Interestingly, different profiles are found between scintillation and Čerenkov signals, the motivation being ascribed to early em-showers components being collimated with the primary particle direction, causing optical photons from Čerenkov radiation to fall out of the numerical aperture of the fibre. This effect is not seen in the scintillation component, due to the isotropic nature of scintillation light emission.

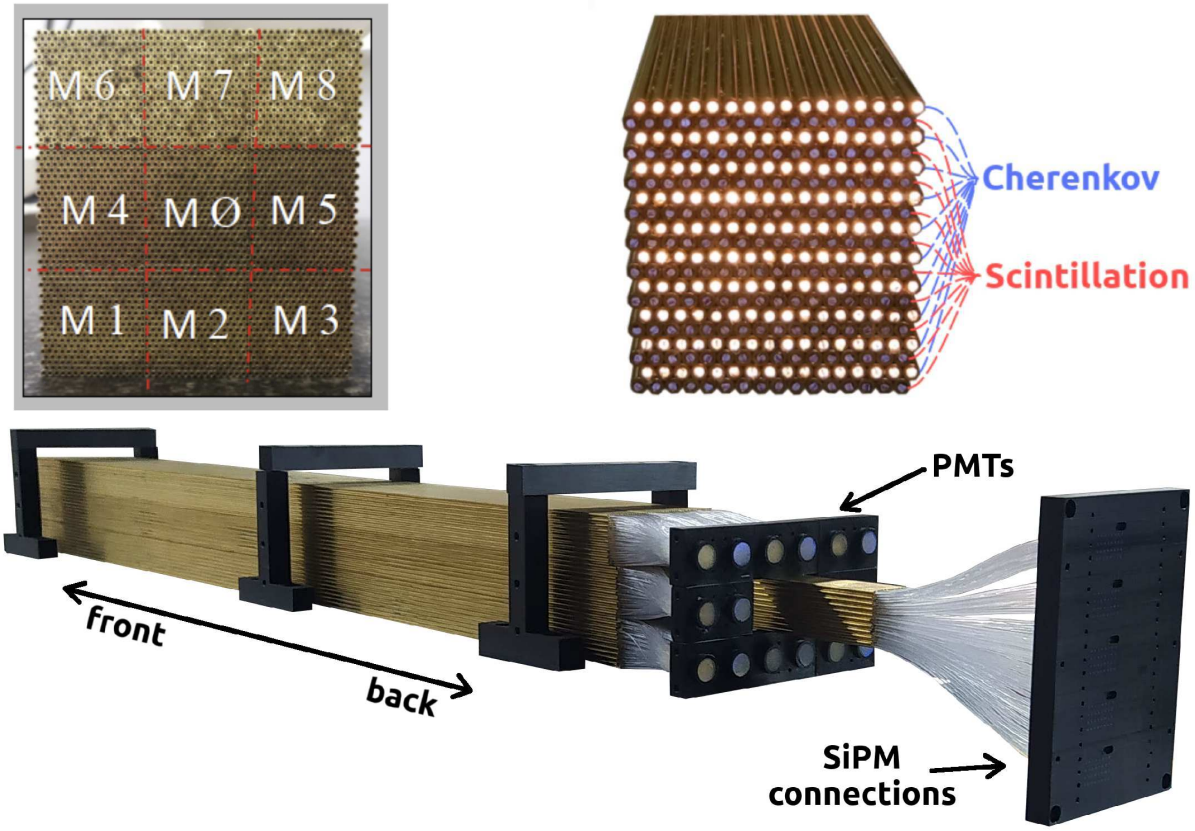


Figure 3.13: Pictures of the "electromagnetic shower-size" prototype. On the upper left, the nine towers composing the calorimeter, with a 10×10 cm^2 area, are shown before inserting the fibres. On the upper right, a zoom on one of the $\sim 33 \times 33$ mm^2 towers showing the fibre disposition, consisting of alternating scintillating and clear (Čerenkov) fibre rows. Below, back-side view showing PMTs and SiPMs connections to rear end of the optical fibres.

The impact point position reconstruction by means of SiPM information also proved highly useful to understand a periodical modulation of the signal, observed in both scintillation and Čerenkov channels, on the vertical coordinate Y_{CALO} (fig. 3.14 (right)). This effect was caused by channeling effects due to the absence of a vertical tilting angle between the positron beam direction and the fibre/capillary tubes. Consequently, larger or lower calorimeter signals, depending on the beam impact point on the calorimeter being an optical fibre or the brass capillary tube respectively, were measured. This effect was also well described by the Geant4 simulation, which also suggested that an increase of such angle could reduce, and eventually cancel, the modulation effect. While geometrical higher-level variable used during the analysis of the 2021 test beam data were found to mitigate this problem, other issues concerning very high beam contamination and issues with ancillary detectors along the beamline made it difficult to express the optimal energy resolution of this prototype's response to electrons. For this reason, a second campaign taken in the same beamline in 2023 was carried out. Based on the previous experience, several issues also concerning ancillary detectors were solved, and positron beam data were taken with a calorimeter oriented with a 2.5° vertical angle and a 1.5° horizontal one, sufficient to remove modulation effects.

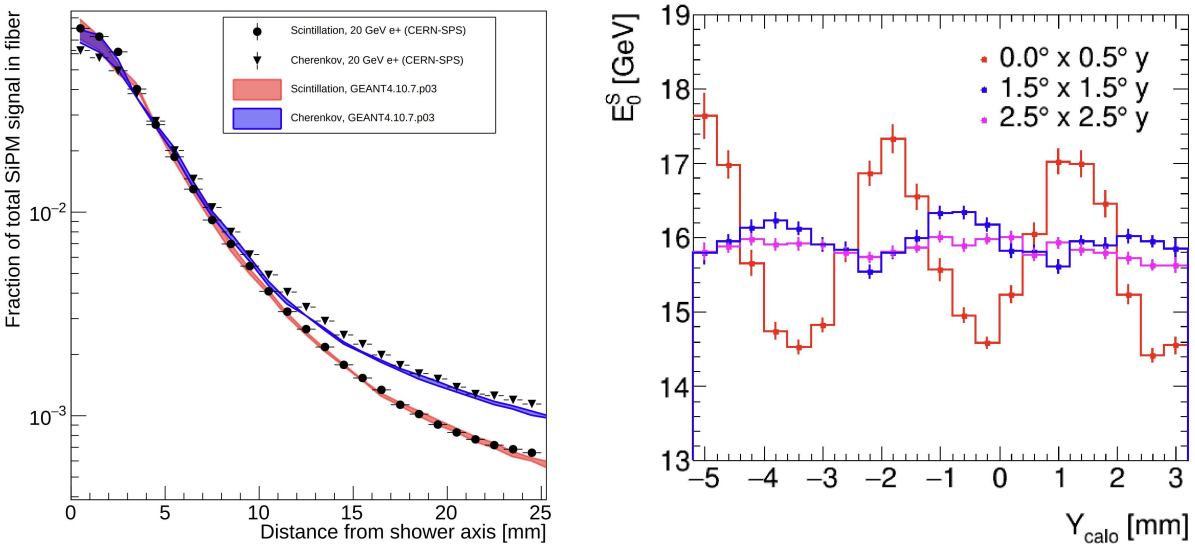


Figure 3.14: On the left, scintillation and Čerenkov lateral profile of electromagnetic showers. On the right, simulation-based modulation of scintillating signal in tower M0 depending on the Y_{CALO} coordinates for different calorimeter tilting vertical angles. See text for details. Plots taken from [118].

Figure 3.15 shows the reconstructed energy, taken as the mean of the scintillation (E_S) and Čerenkov (E_C) energies after the calorimeter calibration, as

$$E = \frac{E_S + E_C}{2}, \tag{3.4}$$

for different beam energies. The distributions are then fitted with a gaussian function to express the average response as the mean of this function, μ, and the energy relative resolution as the fraction of the gaussian standard deviation and the truth beam energy $\frac{\sigma}{E}$. The fit range was bounded from below, considering a limit of $\mu - 1.8\sigma$, to exclude from the fit events not completely contained in the calorimeter volume, and reject beam impurities of particles different from positrons which were not properly selected with ancillary detectors.

The energy response figures of merit, linearity and energy resolution, are shown in fig. 3.16. Apart from the energy data point at 10 GeV, which is probably affected by incomplete noise removal during the analysis, reconstructed energy points are well inside a $\pm 1\%$ range from the nominal beam energy. For the S and C channels separately, stochastic terms of 20% and 22.7% are found. These close values suggest that the main contribution to the stochastic term is due to sampling fluctuations caused by limited sampling fraction, with minor contribution to fluctuations in the number of optical photons carrying the actual calorimeter signal. About ~ 250 photoelectrons per GeV were measured for the scintillation channel through the SiPM multiphoton spectra, and ~ 55 for the Čerenkov one. A stochastic term of $15\%/\sqrt{E}$ is found by combining the scintillator and Čerenkov information. This improvement has to be addressed to the larger total sampling fraction which is doubled with respect to one independent channel, therefore reducing the sampling fluctuations. The total stochastic term is in excellent agreement with the Geant4 simulation reproducing the test beam conditions, which suggests $\sigma/E = 14.8\%/\sqrt{E}$. One of my main contributions in this activity was

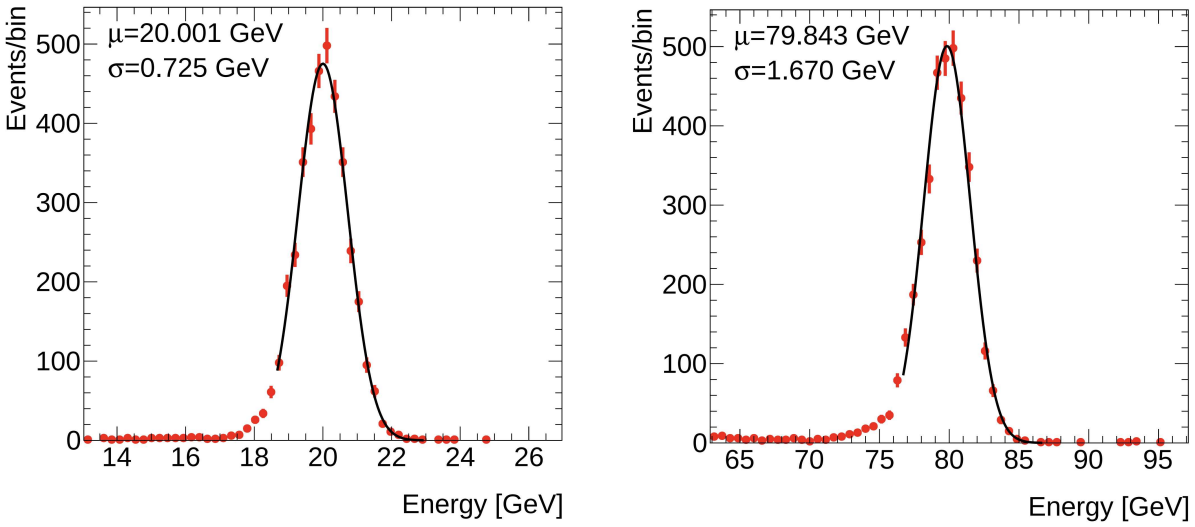


Figure 3.15: Measured energy from the electromagnetic-size prototype, taken as the mean of scintillation and Čerenkov signals event-by-event, and gaussian fit superimposed on the observed data. Shown are 20 GeV and 80 GeV nominal beam energies. Taken from [119].

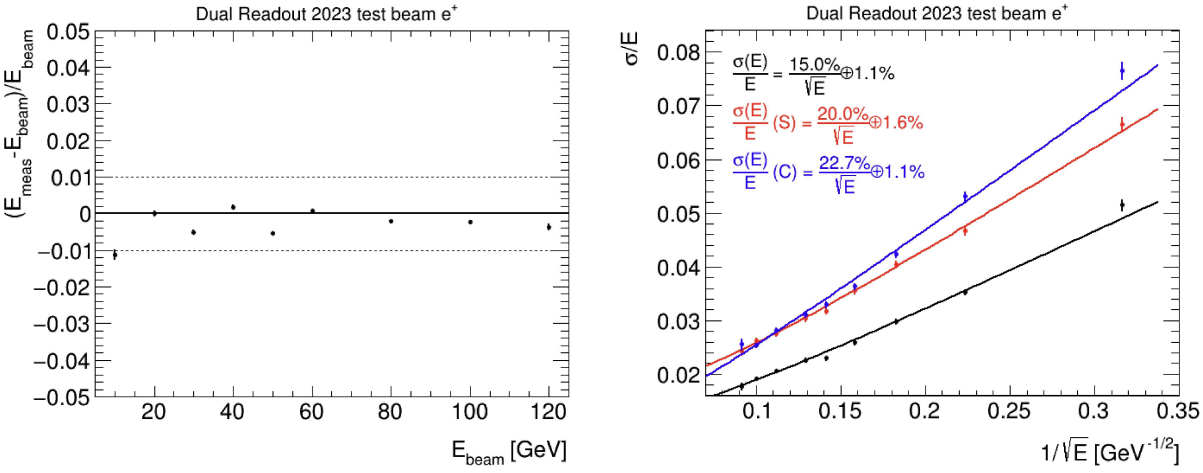


Figure 3.16: Left: response of the calorimeter to positron beams in the range [10-120] GeV. Shown is the relative difference of the mean reconstructed energy, taken as the mean value of a gaussian fit, with respect to the nominal beam energy. On the right, measured relative energy resolution taken from the RMS of the same gaussian fit. Taken from [119].

showing, using dedicated simulations, that the residual constant term in the calorimeter energy resolution arises mainly from the beam energy spread around its nominal value. With a total measured constant term of 1.1%, an energy spread of 1% introduced in the simulation correctly recovered the observed value, also being in agreement with information provided by SPS beam physicists.

3.5 The HiDRa prototype

Because of the relatively large interaction length λ_I governing the development of hadron showers, the construction of calorimeter prototypes large enough to effectively contain these objects requires large material quantities and considerable budget. The HiDRa project was funded to build and characterise a dual-readout calorimeter prototype able to contain to a sufficient level hadron showers, with a SiPM-based readout system providing very fine lateral segmentation. Of particular interest is to demonstrate the possibility for the assembly technique to allow room for SiPMs on the immediate back of the calorimeter, and therefore proving the SiPM readout solution to be scalable for a full azimuthal coverage detector. HiDRa is a collaboration of a number of INFN groups (units from Bologna, Catania, Milano, Pavia, Pisa and Roma) and abroad universities and institutions, including CERN.

Similarly to the smaller prototype, a modular design consisting of multiple iden-

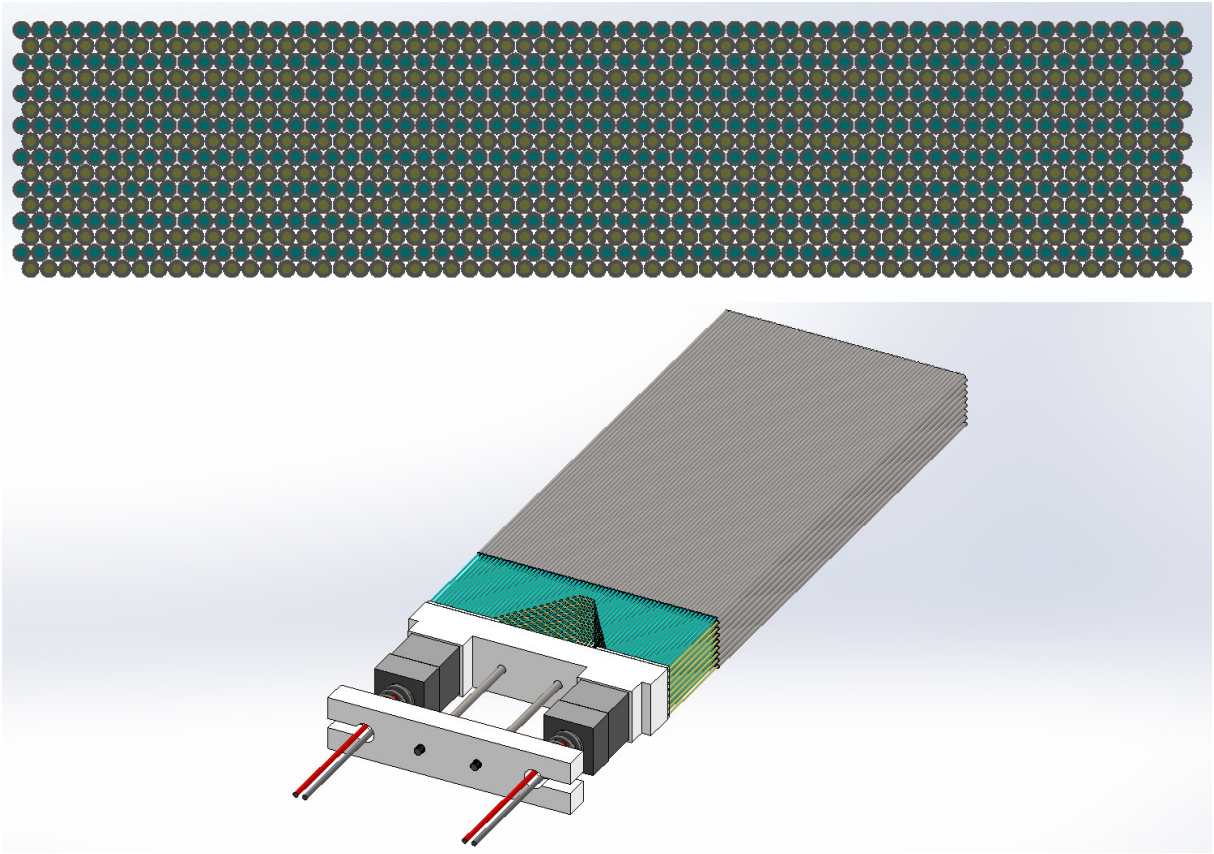


Figure 3.17: 3D rendered image of one HiDRa modules. In the above image, the fibre disposition from a frontal view is shown, with scintillating fibres (yellow) and clear ones (blue), inserted in metal capillary tubes. Below, not-to-scale image of the back of one module, with different types of fibres coupled to PMTs mechanical supports.

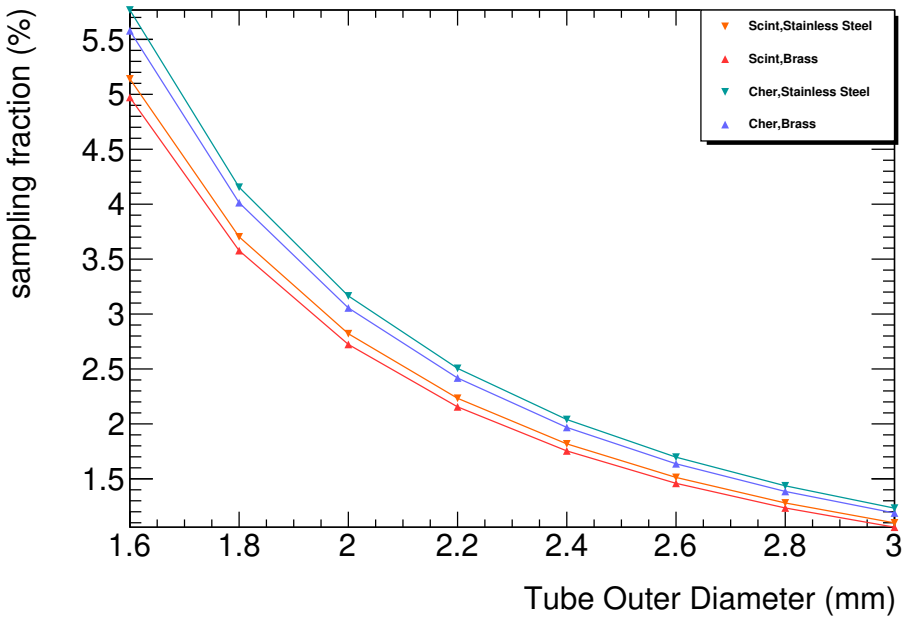


Figure 3.18: Analytical calculation of the sampling fraction, separated between scintillation and Čerenkov channels, for different capillary tubes outer diameters. The inner diameter was fixed to 1.1 mm [84].

tical units was adopted. The modules arrangement, as well as the geometry of the single module layout, varied during the initial phases of the project. The fundamental unit, used in the prototype optimisation as well as in the final construction, is shown in fig. 3.17. Sixteen rows of capillary tubes, each comprising 64 tubes, are alternatively inserted with scintillating or Čerenkov fibres. The same tubes dimensions of the previous prototype, with external diameter of 2 mm and internal diameter of 1.1 mm, are used. An hexagonal-based arrangement is used to minimise empty volume between capillary tubes. With these parameters, the lateral dimensions of one module are approximately 128×28.2 mm^2.

Since containing hadron showers requires large volumes, several tens of these modules were to be built. Considering $16 \times 64 = 1024$ fibres per each module, reading out each fibre with a Silicon Photomultiplier for all modules appeared unfeasible already at initial stages of the project. The main challenges in this regards were identifying a solution for the integration of these sensors on the calorimeter, beside limited budget and the complexity of the acquisition system, for a relatively small collaboration. It was therefore decided to have, similarly to the electromagnetic shower-size prototype, a mixed readout solution consisting of 10 modules with SiPM-based readout, and the remaining ones coupled to PMTs. Some sensors from the previous RD52 calorimeter (36 PMTs for S and C channels each) could also be reused, allowing to further reduce the total cost of the prototype integration.

As a baseline absorber material for geometry studies, stainless steel (68% Fe, 20% Cr, 12% Ni) was considered. This allowed to use capillary tubes manufactured by industrial companies instead of custom ones, lowering the total costs. An alternative option, that was already used for the electromagnetic prototype and tested through Geant4 simulations, was brass (70% Cu, 30% Zn). The sampling fractions for the scintillation and Čerenkov active media, considering separately both passive materials, are shown

Table 3.2: Specifications of the two scintillating fibres considered for measurements.

Characteristics	**SCSF-78 Kuraray**	**BCF-12 Saint Gobain**
Color	blue	blue
Peak (nm)	450	435
Attenuation length (m)	> 4.0	> 4.0
Decay time (ns)	2.8	3.2

Table 3.3: SK-40 Clear optical fibre specifications

Specification	**Unit**	**Min.**	**Typ.**	**Max.**
Core Material	–	Polymethyl-Methacrylate Resin		
Cladding Material	–	Fluorinated Polymer		
Core Refractive Index	–	1.49		
Refractive Index Profile	–	Step Index		
Numerical Aperture	–	0.5		
Core Diameter	μm	920	980	1040
Cladding Diameter	μm	940	1000	1060
Approximate Weight	g/m	1		

in fig. 3.18 as a function of the tube outer diameter. Concerning the scintillating fibres, two different manufacturers were considered, SCSF-78 from Kuraray and Saint-Gobain (Luxium) BCF-12. Some important parameters for a comparison between the two candidates are listed in table 3.2. After laboratory tests, and useful discussions with the producer for improving the attenuation length parameter close to ~ 4 m, Saint-Gobain optical fibres were chosen for the HiDRa construction. For the Čerenkov fibres, laboratory measurements are not possible because of the need for relativistic particles emitting light. Therefore, the same clear optical fibres model that was already used for previous prototypes, including DREAM, RD52 and the em-size prototype were selected, being Mitsubishi ESKA-SK40 fibres.

3.6 HiDRa simulation studies

A Geant4 simulation of the HiDRa prototype, shown in fig. 3.19, was originally developed in 2021 within the Pavia dual-readout group and before the actual start of my own doctoral period, as a direct evolution of the electromagnetic shower-sized prototype simulation. Data available by that period, e.g. the first characterisation at the 2021 test beam, were used for the parametrisation of the simulation to reproduce, as faithfully as possible, the measured signal distributions.

Similarly to the actual prototype design, the simulation also features a modular implementation, with multiple identical units placed iteratively to fill the calorimeter volume. The stainless steel (or brass) capillaries, alternatively filled with plastics and PMMA fibres to replicate the actual optical fibres under use, are inserted as daughter volumes of each tower. The material density and refractive index, which allowed to replicate the Čerenkov light production and transport, were used to replicate the actual fibre properties. Accurate positioning was realised by disposing an hexagonal polygon with a capillary tube occupying the geometrical centre of each hexagon, and precisely placing the towers to lay beside the next one. The number of capillary tubes

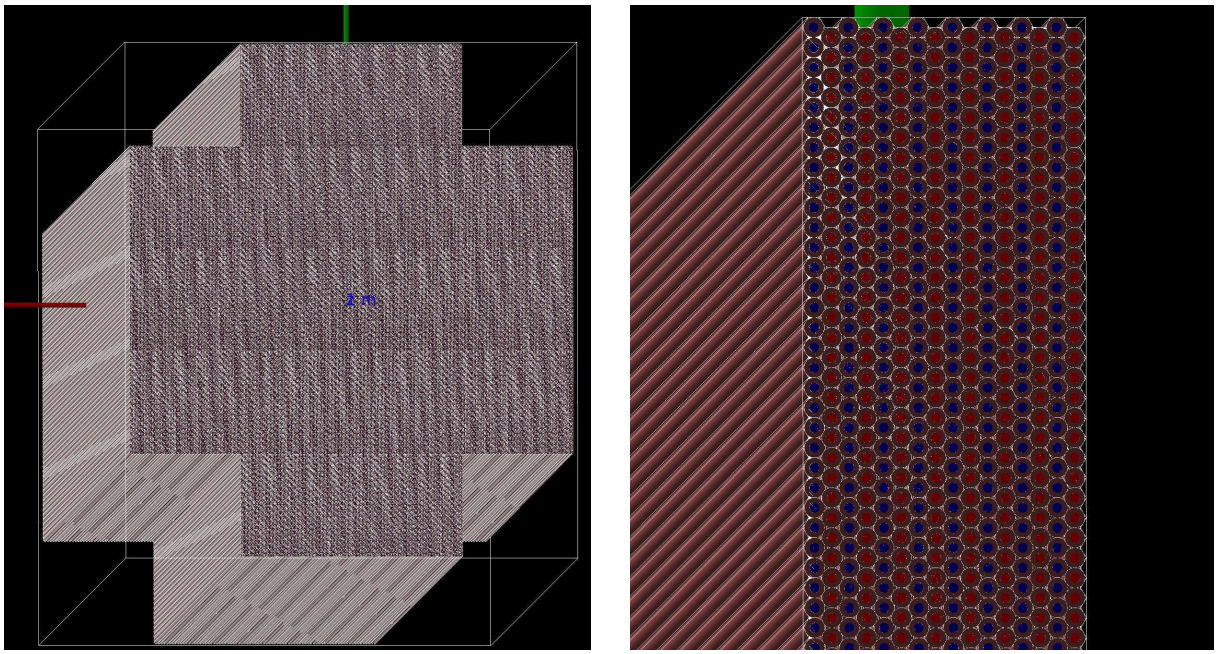


Figure 3.19: Frontal view of the HiDRa prototype simulation, consisting of 80 modules, and detailed view of one of the modules. In the original layout, a 90° rotation along the $\hat{z}$ axis was implemented, and later changed.

and optical fibres was increased from the electromagnetic prototype to the hadronic one, passing from 320 (with 16 fibres per column and 20 rows) to 1024 (64 fibres per column and 16 rows). The simulation was implemented using the `Geant4.10.07_p03` version of Geant4 released in late 2021. It was later adapted to the `Geant4.11` version, without any significant change in the simulated performance of the detector.

Of particular interest in this simulation is the way scintillation and Čerenkov signals are handled, from their production to visible signals to be used in the analyses. Because of the very large scintillation photon yield, about 10^4 optical photons per MeV of deposited energy, the transmission of each optical photon from the point of production until the fibre end would be too computationally demanding, as it would require calculating, at each step, if the optical photon has an angle that satisfies the total internal reflection conditions. When optical photons production and tracking were tried in the simulation, the large amount of light generated in scintillating fibres resulted in a quite large amount of time, up to several minutes per event with ~ 20 GeV impinging electrons on the calorimeter. Full optical photon transportation was therefore abandoned in favour of a semi-parametrised signal production model.

Optical photons produced in scintillating fibres are tracked through a Geant4 method and removed. The signal is obtained by applying the Birk's saturation effect and a Poissonian-distributed smearing term, applied to the truth deposited energy by ionising particles. The resulting quantity is interpreted as the number of collected photoelectrons by the SiPM and added to the simulation output instead. The smearing term therefore allows to weight the sensors photodetection efficiency, the optical connection from the fibres to the sensors, and other experimental effects that might affect the detector's response.

For the Čerenkov light signal a different procedure is applied, to take into account the different properties of this process. In this second case the light yield is much lower,

and the direction of the emitted photon depends on the direction of the charged particle from which it is emitted. Optical photons in clear fibres are tracked and requested to satisfy total internal reflection criteria through the Geant4 optical physics package. A very detailed simulation would require reproducing all the different optical surfaces impacting internal reflections. Since this is not feasible, also in this case a parametrisation through a Poissonian smearing term is applied on those photons reaching the end of the fibre through total internal reflection. This smearing parameter, similarly to the scintillating case, was tuned on data targeting the Čerenkov channel and the resulting smeared value is added to the simulation output. Optical photons not satisfying total reflection inside the fibres are removed, and no signal production through Poissonian smearing is applied. Good agreement between Monte Carlo simulations and observed data were found, despite the technical difficulties encountered during the 2021 test beam experience. Figure 3.20 shows two examples of reconstructed energy, observed and measured, for 20 GeV positrons entering the calorimeter. The energy resolution for actual data could only be estimated below 30 GeV due to ancillary detector issues limiting the beam purity. It was nevertheless possible to reproduce the energy resolution in this range through Geant4 when considering the experimental setup, with significant contribution coming from insufficient rotation angle of the calorimeter with respect to the incoming beam.

The `FTFP_BERT` physics list, commonly used in several high-energy physics experiments among which LHC ones, was used as reference model for the description of physics processes. It uses the Fritiof parton model for inelastic hadron-nucleus interactions in the range $[3, +\infty]$ GeV, and the Bertini model for interactions between 0 and 6 GeV. In the intermediate $[3 - 6]$ GeV energy range, a linearly decreasing probability, from 1 to 0, is associated to the Bertini model interactions, while the complementary probability is associated to the Fritiof one. All common electromagnetic interactions are also described in the same physics list, with the exception of optical photon production and transportation, which require a dedicated Geant4 package.

The output information concerns the number of optical photons produced in each optical fibre for those modules having SiPM-based readout. For the towers with PMT readout, all optical fibres in the same modules are summed, and only the total number is stored as an array with size equal to the number of calorimeter towers implemented at the time of simulation running. The truth energy deposit in the calorimeter volume, consisting of optical fibres and absorber tubes, is also stored, together with the truth energy deposit in each type of optical fibre. This allowed to cross-validate the sampling fraction of the calorimeter with analytical calculations when modifying design parameters. A second advantage of these variables was to estimate the amount of invisible energy for hadron-induced showers by taking the difference of the total energy deposited in the calorimeter, the truth leaked energy outside the calorimeter volume, and the primary particle energy originating each event.

In the remaining part of this chapter, a number of results I obtained by means of this simulation, aimed at characterising the HiDRa calorimeter's response to different particles, are described. The work included modifications to the detector geometry and to the underlying Geant4 code to implement new features, record additional observables, and refine the detector response model. Further development of the simulation is still ongoing.

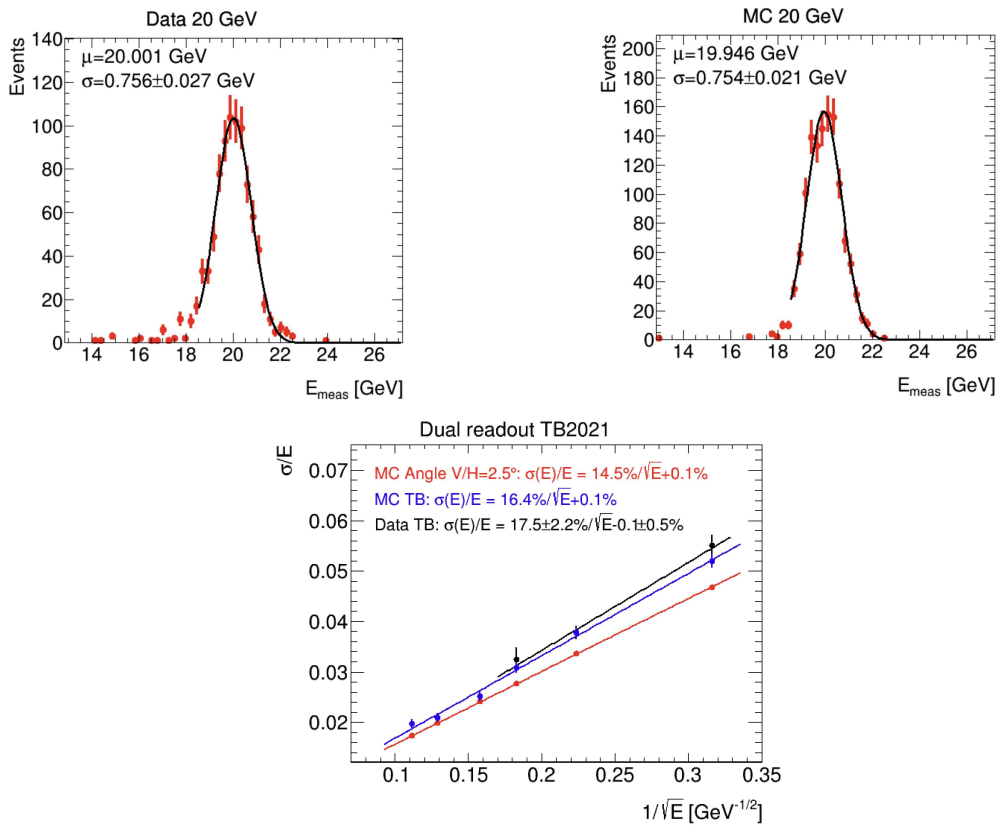


Figure 3.20: Measured (left) and simulated (right) energy distributions with the 2021 electromagnetic-size prototype with 20 GeV impinging positrons. Below, observed resolution (black) is compared to the simulated one (blue) mimicking the beam test setup for energies lower than 30 GeV. The red line represent the ideal beam test conditions obtained through simulation, by increasing the vertical tilting angle.

3.6.1 Leakage studies

Leakage of particles may arise during the particle showers development, with secondary particles escaping outside the detector volume. It severely affects the detectors' energy measurements by introducing large fluctuations that do not depend on the design (and response) of the calorimeter. This is a major problem during the development of smaller-scale prototypes, particularly for hadron showers, as the random behaviour of hadron interactions greatly varies event-by-event the deposited energy in the active volume, making it difficult to assess from this the performance of a similar full-scale detector that covers the entire solid angle.

In order to better understand the impact, and preferential direction, of leaking particles outside the detector volume, additional volumes were added in the simulation, shown as green volumes in fig. 3.21. Using the truth Geant4 information, particles escaping from the calorimeter volume and entering these "leakage" volumes were stopped, and the information related to their total energy were added to the simulation output.

A cylinder surrounding the detector, and able to rotate rigidly with it, was used to obtain information on leakage in the transverse direction. The back end of this volume, opposite to the direction of incoming particles, was closed through an endcap volume that measures longitudinal leakage. The backsplash leakage, or albedo, was calculated

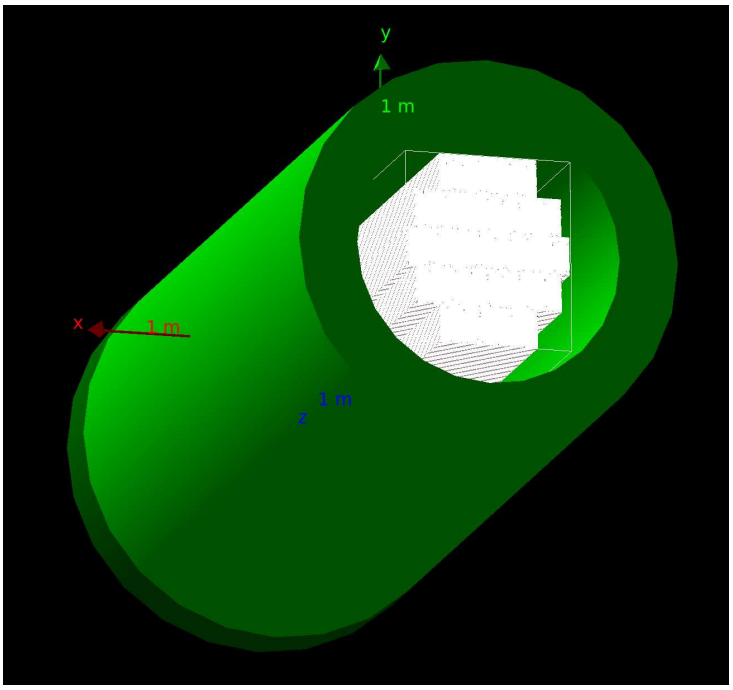


Figure 3.21: Cylindrical (light green) and endcap (dark green) additional volumes for lateral and longitudinal leakage studies.

for electrons and positrons as the difference between the truth Monte Carlo particle energy, and the sum of the total energy deposit in the calorimeter and the two leakage volumes. It was always found to be almost negligible, with contributions only at permil level. For hadrons, the same method would eventually include also the invisible energy component, as it contributes to the missing total energy deposit in the calorimeter. Placing another endcap volume in front of the calorimeter to estimate the amount of escaping energy from the front of the detector would have prevented incoming particles to enter the calorimeter. On the other hand, albedo effects are only expected to contribute for very low energy particles, that would need to be scattered at large angles already at the first interactions with the calorimeter. Therefore, backsplash leakage was not investigated further.

Figure 3.22 shows the two leakage components, lateral and longitudinal, produced by 40 GeV pions entering the HiDRa calorimeter, divided by the primary particle energy. In both cases, 10^4 events were generated. Two possible calorimeter lengths were simulated, with 2 m ($8.4\ \lambda_I$) or 2.5 m ($10.5\ \lambda_I$) long capillary tubes made of stainless steel. Different behaviours are found when comparing the two components, showing how, on average, a significant component of hadron shower energy losses occurs in the lateral direction, with average contributions around 7-8% for most events. Conversely, longitudinal leakage is almost negligible for the vast majority of events, for two tested calorimeter lengths of $8.4\ \lambda_I$ or $10.5\ \lambda_I$. Nevertheless, few permil event fluctuations may extend even up to almost the primary particle energy, meaning that in some cases particles barely interacted inside the calorimeter before escaping. Extending the total depth of the calorimeter allows to better contain also those showers that develop very deep, therefore reducing the tail of events with very large longitudinal leakage.

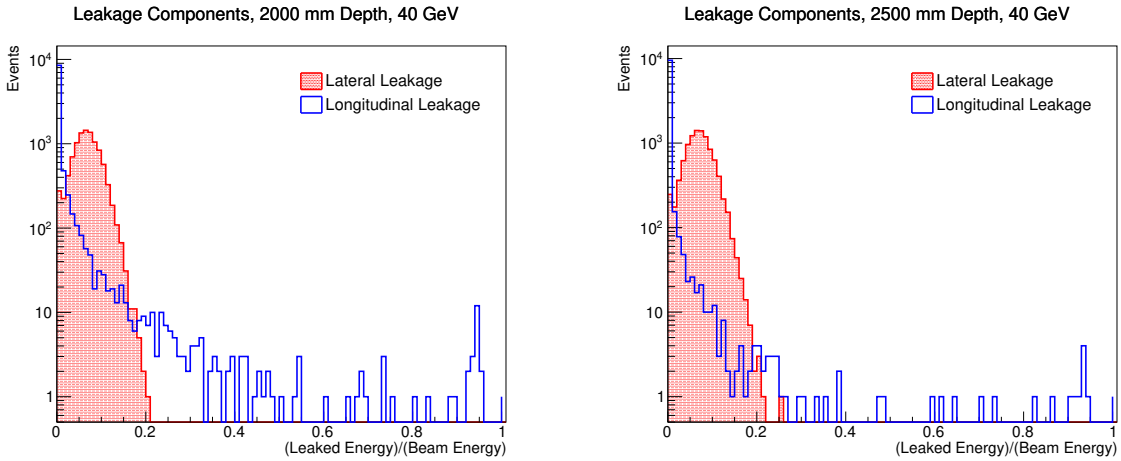


Figure 3.22: Comparison of lateral and longitudinal leakage information for two geometry options. On the X axis, the fraction of each type of leaked energy over the primary particle energy is shown. In both cases, the calorimeter consisted of 80 modules, with a length of 2 metres (left) or 2.5 metres (right) [120].

3.6.2 Lateral containment

The design of the HiDRa prototype, consisting of capillary tubes and optical fibres running almost parallel to the incoming particles direction, makes the choice of the calorimeter cross section shape important for optimal lateral shower containment. Once this is set, longitudinal containment can be changed by making the capillaries and fibres longer or shorter. Initial design ideas were having modules with sizes of about 13×13 cm^2, large enough to contain completely electromagnetic showers. For mechanical and structural stability reasons, however, it was preferred to have flatter modules, each with two PMTs for the readout. Super-units consisting of multiple modules, up to five, were considered, which may have required iron structures to keep the modules in place. In Figure 3.23, the image on the top left shows a geometry consisting of 80 modules, which has been considered for some time the baseline design of the HiDRa prototype. The choice of the arrangement was originally thought to be assembled as 16 identical copies of a macro-unit made of 5 modules. Because of the different horizontal and vertical sizes of one single module (128×28.2 mm^2), five towers would have allowed to completely contain electromagnetic showers. Examples of simulated prototype geometries that were tested are shown in fig. 3.23, with a varying number of towers from 80 up to 104. The corresponding fraction of contained energy, deposited by impinging charged pions with different energies, are shown in fig. 3.24. A much more massive simulated prototype is also shown, comprising 480 modules and consisting of a $\sim 1.3 \times 1.3$ m^2 square cross section calorimeter. This latter geometry was used to evaluate the performance of the calorimeter to single hadrons with a close to fully containing detector. It was useful, for example, to predict the energy resolution of a capillary-based IDEA detector calorimeter when changing the design parameters.

As can be observed in fig. 3.24, the average containment is observed, in most cases, to increase at higher energies. While being at first counter-intuitive, as the shower maximum moves to deeper positions, the reason lies in the increasing average electromagnetic fraction f_{em}. When neutral pions are produced in a strong interactions, the two decay photons start interacting immediately in the calorimeter, producing elec-

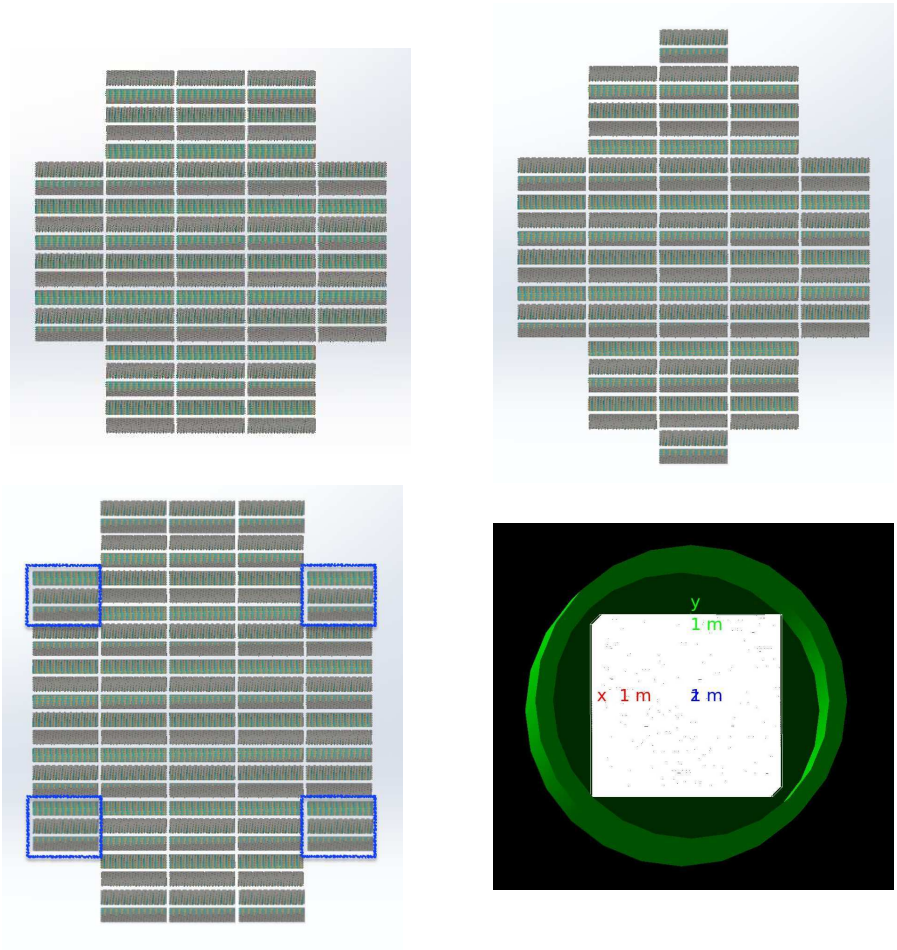


Figure 3.23: Examples of tested geometries, obtained by arranging different number of modules to estimate the variation of lateral containment. From the upper left going clockwise, 80, 84, 480 and 104 modules are shown.

tromagnetic showers which are much better contained than charged pions. Following eq. (2.10), the f_{em} increases with the energy of the primary particle, as the production of neutral pions that carry considerable energy becomes favoured ($\sim 1/3$ in any strong process at any step of hadron shower development). This behaviour reaches a plateau for large enough calorimeters, where showers are efficiently contained at any energy. With 480 modules, a 98% containment is found at any energy, with only very small deviation at lower values. For other tested geometries of the prototype, the average containment is estimated between 92-94%. While being far from fully containing, these results seemed sufficient for estimating to a good approximation the performances of a hadronic calorimeter based on capillary tube technology.

Lateral leakage introduces an additional source of fluctuations that may spoil the energy resolution of calorimeters. In Ref. [68], the author found these fluctuations to be reasonably described by a term that depends on the energy as $E^{-1/4}$, that should be added in quadrature to the stochastic term $aE^{-1/2}$. For the preliminary studies shown in this chapter, however, it was preferred to not disentangle the two contributions when citing the observed energy resolutions for different prototype geometries. Distributions of lateral leakage for two tested geometries with different containment, 80 and 104 modules, are shown in fig. 3.25 at two energy working points of incoming pions, 20 GeV or

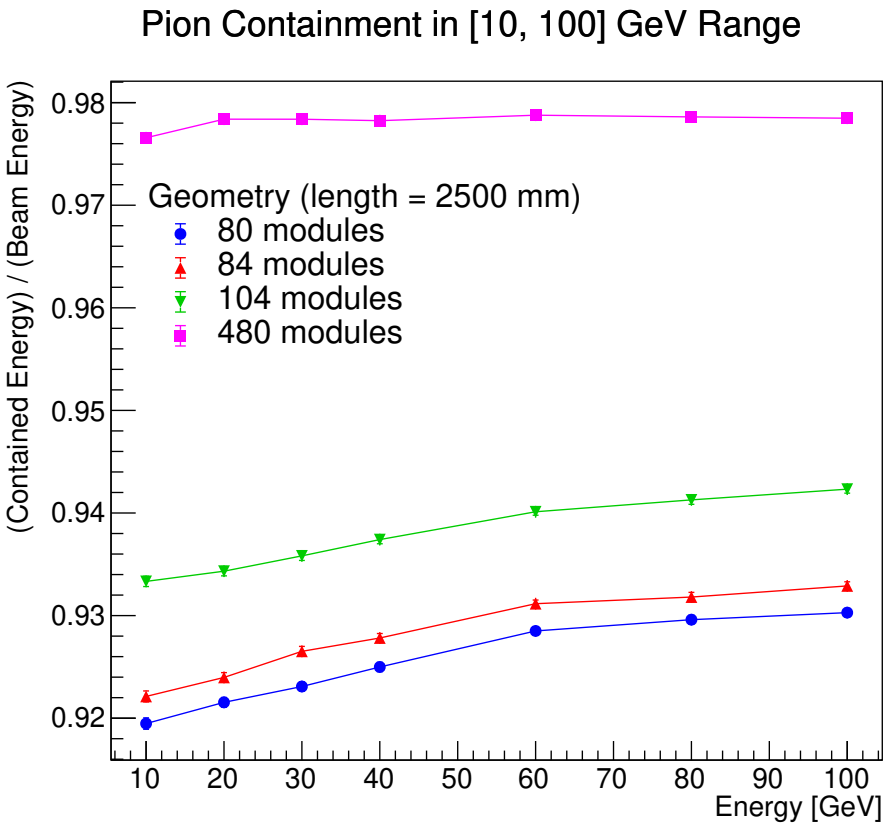


Figure 3.24: Fraction of contained energy for different calorimeter geometries (and number of used modules.)

100 GeV. As expected, the larger prototype results in smaller lateral leakage, also being characterised by smaller fluctuations around the mean value. In both cases, the two distributions shrink at higher energies, and the mean of the distributions moves towards lower values, therefore providing better containment as shown in fig. 3.24.

In order to estimate the energy resolution in each tested configuration, the same approach was followed repeatedly. A beam of electrons, with energies between 10 GeV and 100 GeV, was simulated (10^4 events per energy point). These datasets were used for the calibration of the calorimeter in terms of number of collected photoelectrons per GeV of deposited energy. To obtain these values, the sum of collected photoelectrons by all modules in the calorimeter was taken, and divided by the truth energy of incoming electrons. As electrons-originated are well contained in few modules, and the response of all tower is the same in the simulation, the same phe/GeV ratio was used for all tested configurations. The two parameters amounted to 226 photoelectrons per GeV in the scintillation channel, and 55.2 for the Čerenkov one. Very similar results were obtained during the 2021 test beam period, providing a cross-check of the electromagnetic performances. An energy resolution of $\sigma/E = 13.9\%/\sqrt{E}$ with a negligible constant term was obtained, compatible with the smaller scale prototype results, when considering the negligible leakage fluctuations (more than 99% of containment for electromagnetic showers, compared to 94% for the smaller prototype).

With the known conversion parameters from number of photoelectrons to signals in GeV, it was then possible to obtain the measured energy distribution for the scintillation and Čerenkov channels for impinging pions, in the same energy range, with

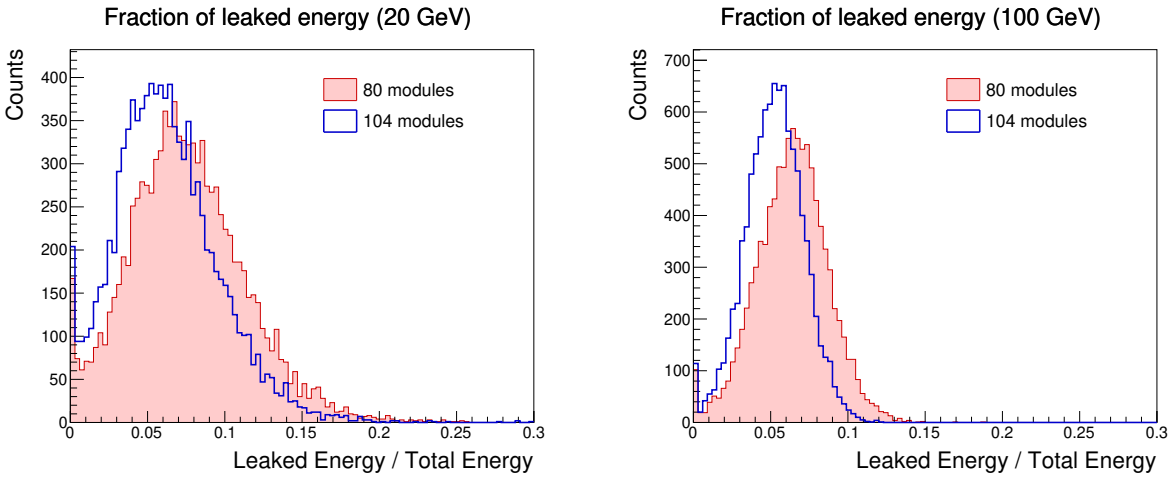


Figure 3.25: Fraction of lateral leakage, over the total energy of the primary particle, for 20 GeV of 100 GeV pions.

an example shown in fig. 3.26. In order to test the linear response of the dual-readout corrected energy measurement, a correction procedure for the varying containment at different energy points was implemented. Without considering a correction for the leakage, the mean value of the measured energy would increase with the average f_{em}, therefore spoiling the expected linear behaviour of the dual-readout technique.

The points in fig. 3.24 were fitted with an inverse logarithmic curve to obtain an expected level of containment at each energy value of the impinging hadron. The dual-readout formula was then modified by multiplying for the inverse of the expected containment at that energy E_0:

$$E_{DR} = \frac{1}{\text{exp. containment}(E_0)} \times \frac{S - \chi C}{1 - \chi}. \tag{3.5}$$

While this procedure is certainly not correct to be used at a real collider experiment, where the true energy of incoming particles is not known[2], it can be applied to a test beam situation with particles of known momenta. In the case of the largest tested geometry, with 480 modules, the values applied for the correction are at the level of 2% and almost constant, which is expected when looking at the relative points in fig. 3.24.

The energy distributions obtained through eq. (3.5) were fitted with gaussian functions to extract, in each case, the mean value and the RMS. A lower bound was set on the fit, taken as the mean value of the raw energy distribution μ minus two standard deviations σ, $\mu - 2\sigma$, to exclude from the fit the low energy tails produced by badly contained events that may alter the distribution. An example of this procedure is shown in fig. 3.26, which is built applying eq. (3.5) event-by-event on scintillation and Čerenkov data.

Once the correction for containment is applied, a scan on the possible values of χ, to be applied in the dual-readout formula, is performed. This search is intended to obtain the parameter that minimises the distances between the reconstructed energy and the nominal value over a full energy scan, therefore improving the linearity in the response. Figure 3.27 shows the mean values of these gaussians, and their associated

[2]Such a correction would not be required in a 4π experiment calorimeter, as lateral leakage should not be an issue.

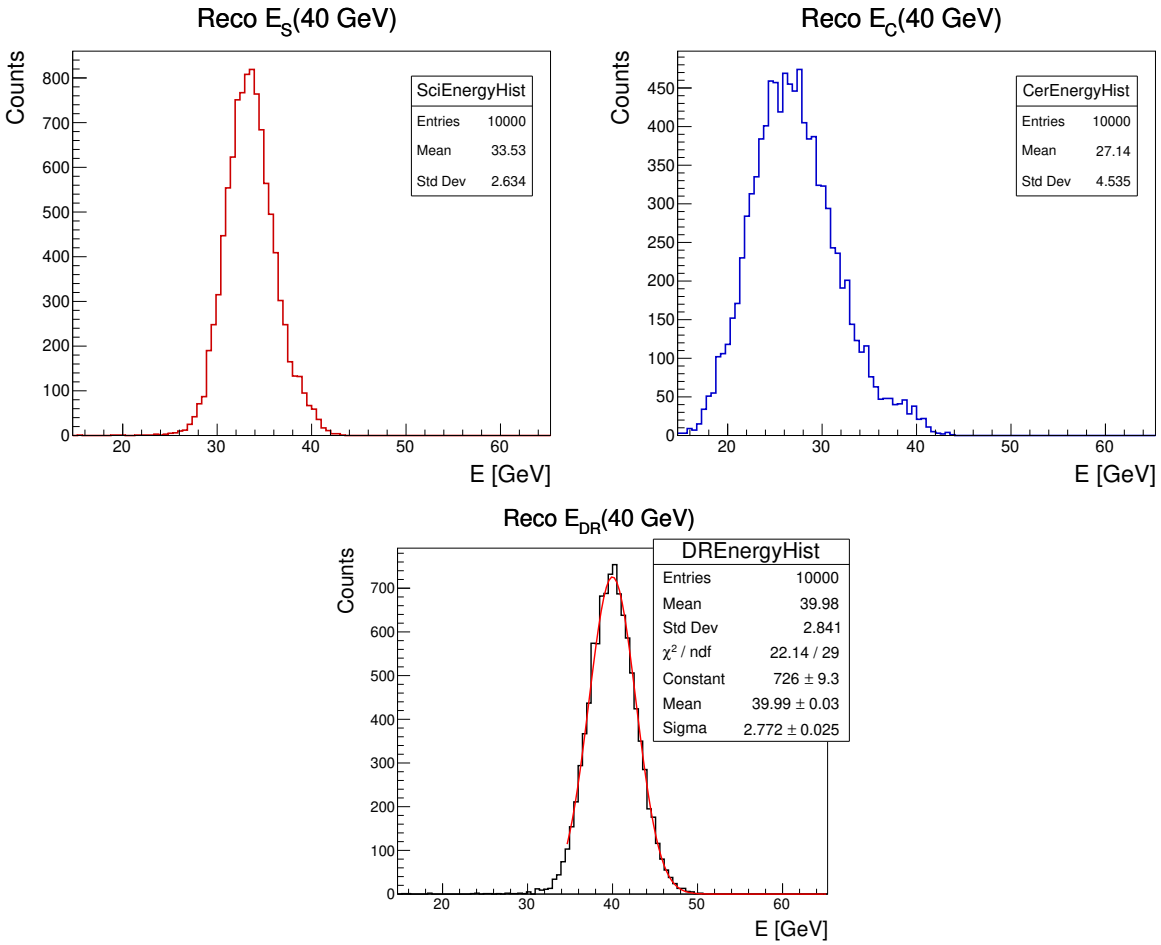


Figure 3.26: Scintillation, Čerenkov and dual-readout corrected energy distributions for 40 GeV pions entering the simulated HiDRa calorimeter. The simulated prototype consisted of 80 modules with a 2.5° tilting both horizontal and vertical, and a χ factor of 0.352 was used in the dual-readout formula.

errors given by the fit, compared to the nominal beam energy values. For each tested prototype setup, the value of χ that was used is reported. Interestingly, the χ values are found to decrease with larger prototypes, and therefore more efficiently containing calorimeters. In all cases, an excellent linear response is found, suggesting that in an ideal situation (not considering electronical issues, high noise, ecc.), the dual readout method effectively works in measuring on average the correct incoming hadron energy. A systematic increase in the measured energy is however found at low energies, which is probably due to particles originated by hadron showers that start behaving as minimum ionising particles, changing the e/mip ratio.

The energy resolutions for each simulated setup, and taken from the gaussian fit together with its associated uncertainty, are shown in fig. 3.28. A linear sum between the stochastic and constant terms is reported, as it was found to better describe the obtained values than a quadratic one. With increasing calorimeter lateral sizes, fluctuations arising from lateral leakage decrease, and the overall energy resolution improves. Relatively small improvements were found when extending the prototype geometry from 80 modules to 104, with differences of 1-2% in the stochastic term. It was therefore decided to keep the HiDRa prototype with the smaller number of modules, as the

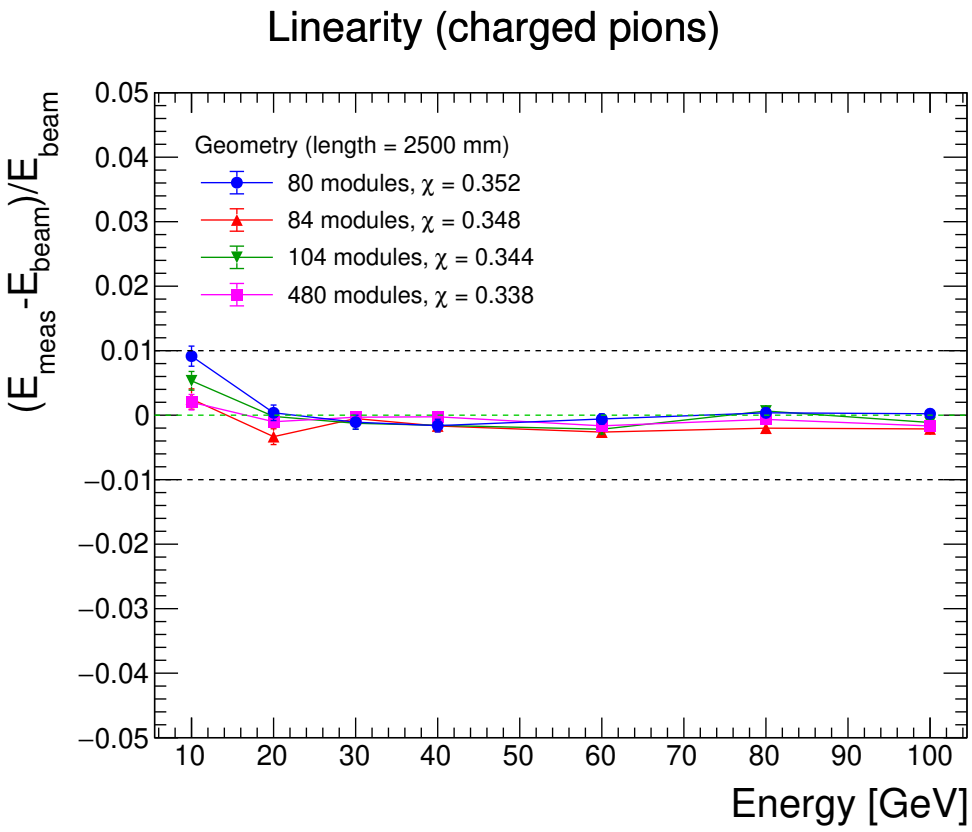


Figure 3.27: Relative difference between measured and truth particle energies, for the tested simulated geometry configurations.

difference was considerated not sufficient to motivate a 30% increase in the cost of the prototype.

Based on the geometrical parameters chosen for HiDRa, consisting of optical fibres with a 1 mm diameter inserted in 2 mm outer diameter tubes made with stainless steel, an energy resolution of $\sigma/E = 33.7/\sqrt{E} + 0.3\%$ was estimated for the largest tested geometry, that can be considered a raw estimate of the IDEA dual-readout calorimeter performances for single hadrons. This result, if confirmed by experimental data, would already be very close to the calorimetric performances required at the FCC, described in section 3.1. More advanced techniques, notably neural networks, could further improve energy reconstruction capabilities of the calorimeter alone [121], and even better results could be achieved when including tracks information through particle-flow methods.

3.6.3 Longitudinal leakage

As shown in fig. 3.22, particles leakage in the longitudinal direction leads to a completely different type of energy losses from the calorimeter, compared to lateral one. The latter component is characterised by significant missing contributions, at a level of some percent, with relatively small fluctuations around a mean value, that impact the resolution of energy measurements. Conversely, leakage in the longitudinal direction gives rise to tails of poorly contained events, with a significant contribution of the total energy that escapes from the detector. If a calorimeter is built too short, these losses would not appear as very unlikely, but instead as an important issue to consider when estimating the total energy deposit in the calorimeter, making it hardly usable. The

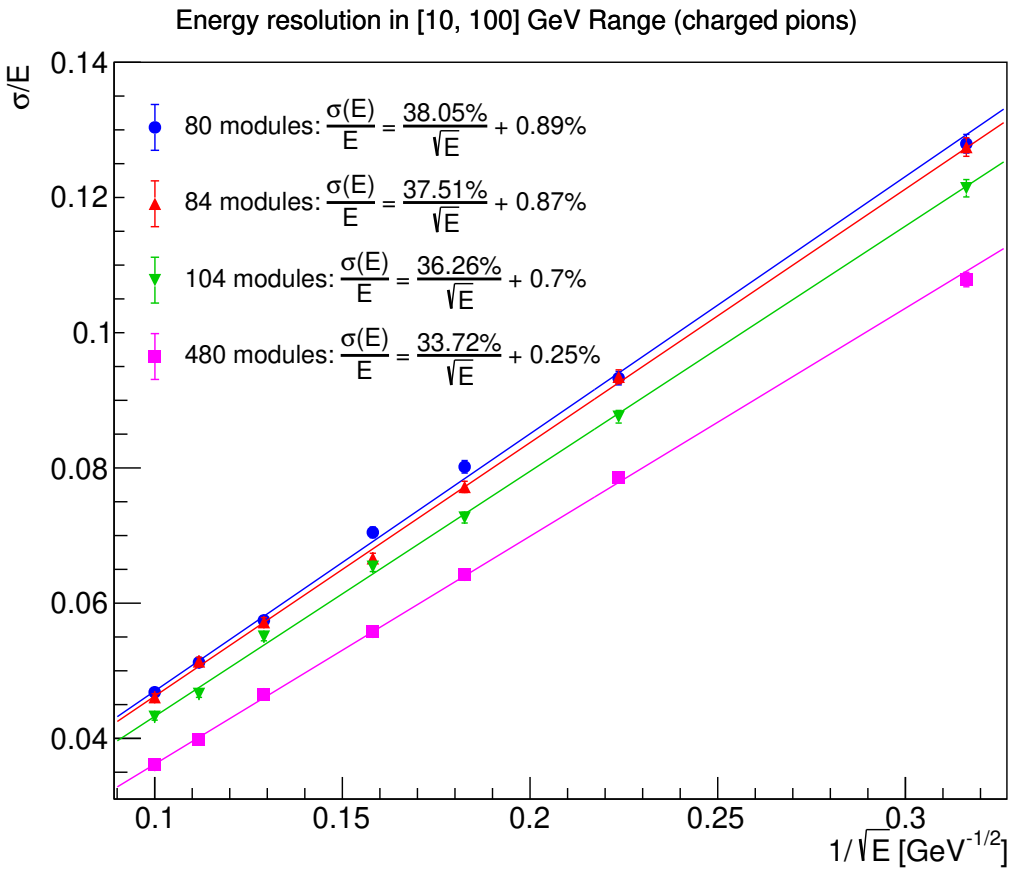


Figure 3.28: Energy resolution obtained through the dual-readout method, for different simulated prototype geometries. The χ value was chosen such as the one that improved the linearity of the response.

different properties of these two components directly derive from the different nature of particles production in hadron showers. In nuclear interactions, pions and energetic protons from spallation processes are produced close to the incoming hadron direction, therefore moving deeper inside the calorimeter (and in worst cases, outside of it). These particles carry large fractions of the primary particle energy, explaining the large missing contributions shown in fig. 3.22. Lateral leakage is mostly produced from evaporation neutrons and protons, that are emitted isotropically from the decays of excited nuclei of the calorimeter. If the lateral size is too small, these particles (which usually have ~MeV energies or lower) escape before being reabsorbed inside the active volume.

To study the impact of longitudinal leakage on the performances of the HiDRa prototype, two options were simulated, consisting of a 2 m long calorimeter, or a 2.5 m long one. With an estimated interaction length $\lambda_I = 238$ mm, these two parameters correspond to about 8.4 λ_I and 10.5 λ_I deep calorimeters. The design selected in section 3.6.2, with a total of 80 modules, was used. Figure 3.29 shows two examples of the reconstructed energy through the dual-readout method, using 40 GeV or 100 GeV pions, with the procedure described in the previous section to identify the value of χ that optimised the linear response. In both cases, the average reconstructed energy is within 1% the primary particle energy. In these plots, a gaussian fit is superimposed on each of two distributions corresponding to one of the two length options, with a lower bound of $\mu - 2\sigma$, as described before. The reduction of the total length had little impact

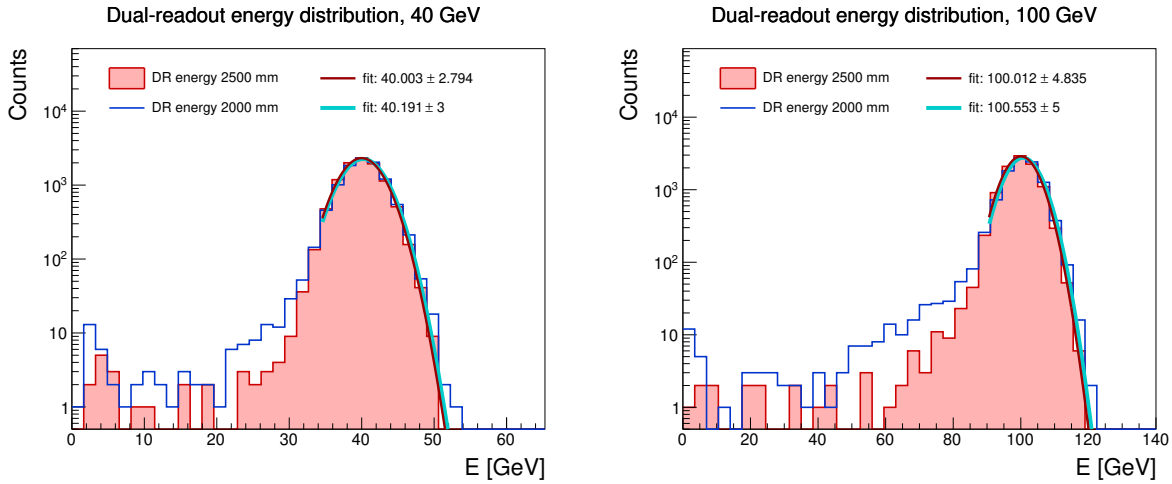


Figure 3.29: Comparison of low-reconstructed-energy events for two calorimeter length options, 2 m or 2.5 m. A logarithmic scale was set on the Y axis, to better distinguish the tails at low values. In both cases, the prototype consisted of 80 modules.

on the obtained resolutions measured through the fit, which are reported in the plots. On the other hand, one can observe a significant increase in the number of events populating the low-energy tails. In real collider experiments, the missing contribution of energy deposits due to significant longitudinal leakage would severely spoil the energy measurement of physics objects from the calorimeter, limiting the effectiveness of otherwise excellent energy resolution for well-contained hadron showers. Figure 3.30 shows the relative amount of mis-reconstructed hadron showers for different energies on the primary hadron. On the left plot, all events with an observed energy lower than $\mu - 2\sigma$, that are excluded from the gaussian fit, are counted, and their number is compared to the total number of simulated events. It is found that, with an increasing energy of the primary hadron, the low energy tail becomes more populated for the shorter calorimeter, as expected for a deeper developing hadron shower. On the right side, events with very low measured energy are shown, with less than half of the nominal beam energy. While no significant dependence on the beam energy is observed, probably due to the quite low statistics, a $\sim 2\lambda_I$ longer calorimeter allows to reduce by a factor 2-3 the number of very badly measured showers.

Finally, in fig. 3.31 the observed energy resolutions estimated through the gaussian fits previously described are shown. As already mentioned, the shorter calorimeter option does not lead to a significant worsening of the fit RMS, and this results in a comparable energy resolution between the two options. Two fit possibilities are explored, where the constant term is added linearly or in quadrature to the stochastic one. The reduced chi square are also reported, showing a slightly better agreement for the linear term. In both cases, the fit procedure suggests a slightly larger contribution to the constant term for the shorter calorimeter.

Based on these results, both possibilities looked viable for the construction of the HiDRa prototype. In order to ensure optimal containment, and minimise the risks of shower mis-measurements, it was decided to choose the longer calorimeter prototype option of 2.5 metres.

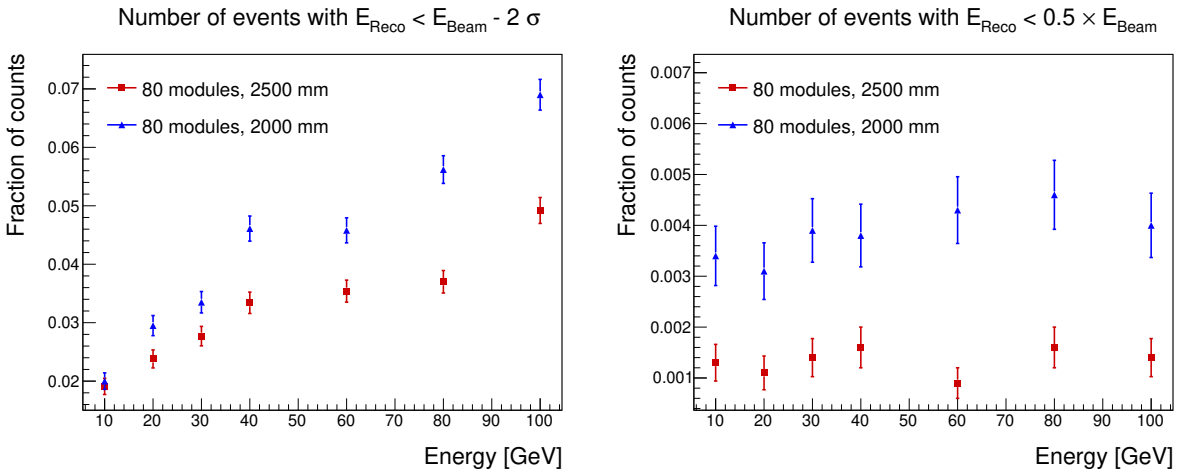


Figure 3.30: Fraction of simulated events, in which the reconstructed energy through the dual-readout method is significantly lower than the nominal one. On the left, the fraction of events with reconstructed energy lower than the nominal energy minus two times the RMS of the dual-readout energy distribution, therefore excluded by the gaussian fit. On the right, the very low energy tails are considered, where only less than half of the nominal energy is reconstructed. A total of 10^4 pions entering the HiDRa prototype were simulated.

3.6.4 Other simulation studies

With the described studies on the effects of particles leakage on the calorimetric performances of the HiDRa calorimeter, which guided the final geometrical parameters, the design of the prototype could be considered established at a good level. Nonetheless, it was considered interesting to estimate the impact on the performances of the calorimeter when changing other parameters, that were until now considered fixed. These included the choice of the material used as absorber, and the inner and outer radii of the capillary tubes on which the HiDRa design is based.

Absorber material

A second absorber material that was considered for the capillary tubes of the calorimeter was brass, which was also already exploited for the electromagnetic-size prototype build in 2020. Other heavier absorbers, such as lead, were also tested by the DREAM/RD52 collaborations, but eventually proved difficult to use in conjunction with optical fibres for larger scale experiments due to its malleability and deformation risks under its own weight. When compared to stainless steel, brass is slightly denser (8.4-8.7 g/cm^3 for brass versus 7.8-8 g/cm^3 for steel), resulting in smaller radiation length, Molière radius and interaction length, making showers more compact. This effect can be appreciated in fig. 3.32, where two calorimeters with the same overall geometries (80 or 480 modules) are simulated using stainless steel or brass as absorber materials for the capillary tubes. For both simulated calorimeters, the brass version has a slightly better containment (estimated through both lateral and longitudinal leakage), which allows to reduce leakage fluctuations.

Figure 3.33 shows the corresponding energy resolution for incoming pions for all different cases. For each material, a corresponding simulation is also run with an electron beam to extract the photoelectron to GeV conversion factors, followed by a simu-

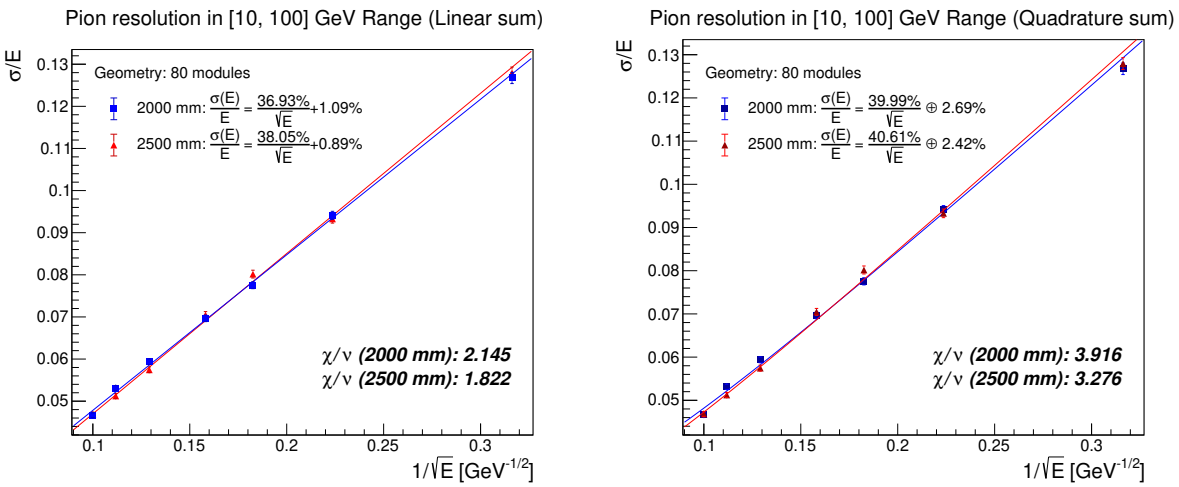


Figure 3.31: Energy resolution for 2.5 or 2 metres long HiDRa prototype. On the left, the stocastic and constant terms are linearly added. On the right, the two terms are added in quadrature.

lation with pion beams to obtain the value of χ in the dual-readout formula to improve linearity. Interestingly, while the electromagnetic performance do not change substantially when comparing the two materials (both estimated close to $13.9\%/\sqrt{E}$ with negligible constant terms), the brass absorber seems to perform better than steel for hadron shower measurements. For the smaller geometry consisting of 80 modules, an initial guess could be addressing the improvement on energy resolution to the smaller leakage fluctuations obtained by the denser material. On the other hand, for the larger geometry with 480 modules, that is a square of 1.3×1.3 m^2 cross section, the improvement in containment is very small. The reduced fluctuations in the hadron signal must therefore be addressed to the different component breakdown of energy depositions in nuclear processes when different nuclear species are involved, and the corresponding calorimeter's response to each species, also including different invisible energy fluctuations.

To my knowledge, an in-depth evaluation of the impact of different absorber materials on dual-readout calorimeters has not been realised yet, if not for structural considerations. In this thesis the topic is not investigated further, but an investigation with dedicated simulation studies could be made in the future.

Capillary tube diameter

The chosen design parameters for the HiDRa prototype, consisting of 2 mm steel capillary tubes inserted with a 1 mm optical fibre each, were selected to push the detector's granularity to an unprecedented level. By reading out each of the fibres with a SiPM, an extremely well-detailed information on hadron jets showering in the calorimeter could be associated to the one from the tracking detectors. On the other hand, this degree of segmentation poses several issue on the construction and operation of highly granular calorimeters. For the HiDRa prototype, custom SiPMs from Hamamatsu were used to have very compact sensor packaging, and a grouping of eight adjacent silicon photomultipliers, coupled to same-type fibres, was performed through an analogical summation of the collected currents generated by each sensor.

When the calorimeter to equip shifts from a test beam-like geometry to a collider

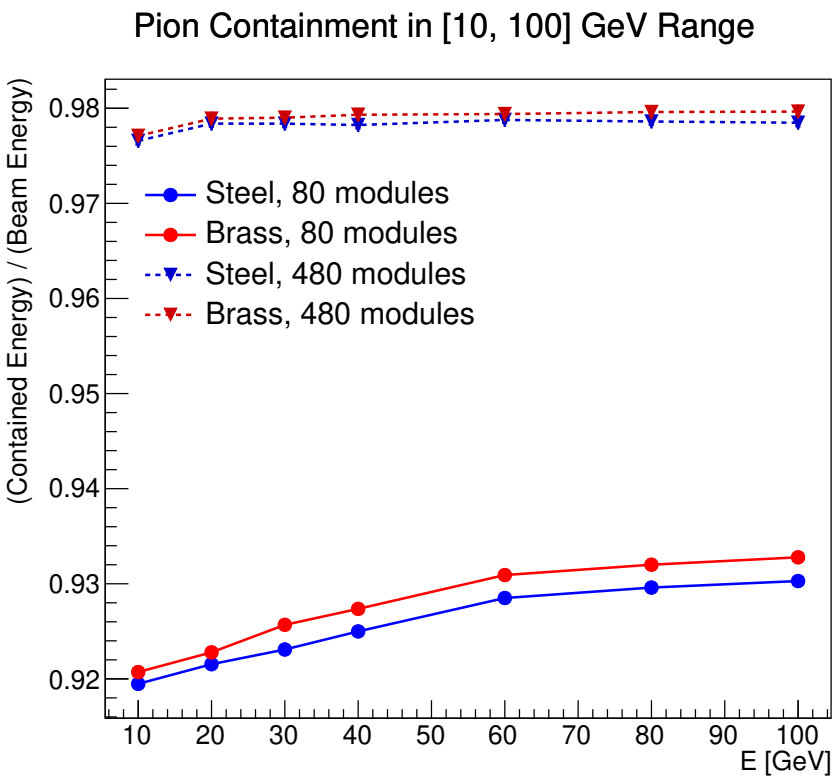


Figure 3.32: Average containment dependence on the primary pion energy, for different calorimeter sizes and absorber materials.

experiment one, several new difficulties arise. Assuming one is able to cover the entire solid angle with capillary tubes pointing to the interaction point (or with small offsets from it), it was estimated that about 3×10^8 tubes similar to the HiDRa ones would be necessary for building such a calorimeter. Reading out such a large number of signals, possibly including also timing information for longitudinal shower development measurements, would pose tight demands on the electronic systems and reconstruction software frameworks. One could then think of reducing the total number of capillaries by increasing their total size, therefore covering the same solid angle with a smaller number of optical fibres. Changing the geometrical settings of the calorimeter would hence alter the sampling fraction and sampling frequency of the calorimeter, therefore modifying its performances. Furthermore, if the IDEA experiment option which exploits a crystal section for improving the electromagnetic shower measurements is accepted for the final proposal, it would make little sense to push for extreme granularity in the hadronic section at a level of 2 mm, if the sizes of the crystals in front of them is at few cm^2.

Figures 3.34 and 3.35 show how the energy resolution for single hadrons changes when different inner and outer radii for the stainless steel capillaries are modified in the simulation. The radius of optical fibres is changed accordingly, to fill the space in the inner capillary diameter with the same amount of air used for the HiDRa prototype. In each case, the calibration procedure using both electrons and pions for the phe/GeV ratios and χ values are used, in all cases observing excellent linear response to both electromagnetic and hadron showers.

In fig. 3.34 the inner diameter of capillaries is kept fixed to 1.1 mm and the optical

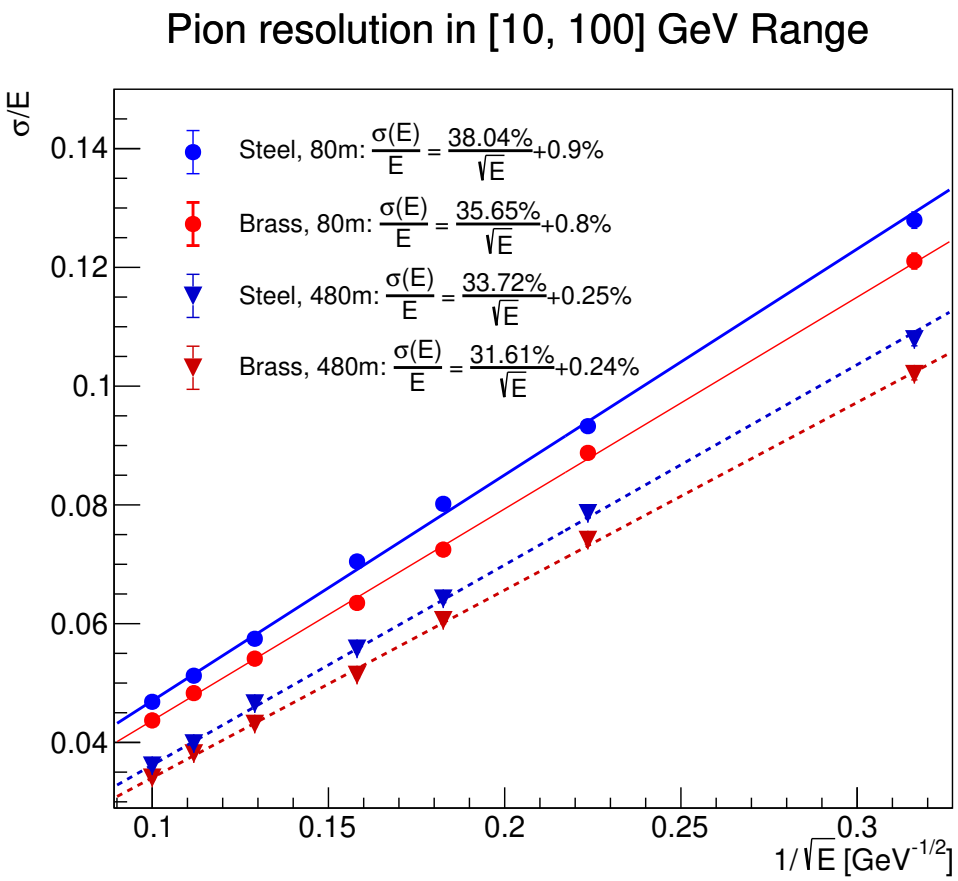


Figure 3.33: Energy resolution for charged pions, for stainless steel or brass simulated calorimeters. Two geometries were tested, with 80 or 480 modules.

fibres one is 1 mm. By increasing the outer radius, also the distances between two fibres increases with the same scaling, therefore reducing both the sampling fraction for both scintillating and Čerenkov channels, and the sampling frequency. For the calorimeter option with the largest outer diameter of 3 mm, the estimated sampling fractions are 1.1% for the scintillating fibres, and 1.2% for the clear ones which are slightly denser. These low values lead to much larger sampling fluctuations, increasing the resolution for electron-originated showers up to 23% for the stochastic term. The related hadron energy resolution is estimated around $51\%/\sqrt{E} + 1\%$ which would be comparable to several operating hadron calorimeters, therefore not providing significant advantages from using the dual-readout method, except for the response linearity.

In fig. 3.35, the same outer diameter of 3 mm is instead kept fixed, and the inner one is let change from 1.6 mm to 2 mm. The combined effect of increasing the active volume of the fibres, and reducing the passive one of the capillary tubes, increases the sampling fraction to about 6.3% for S fibres and 6.9% for C fibres in the 2 mm fibres case, with a substantial improvement in the energy resolution performances. This improvement in the overall resolution comes at the cost of a lighter calorimeter with a longer interaction length $\lambda_I \simeq 29.2$ cm. While longitudinal leakage did not affect drastically the 2.5 m long simulated prototype, a shorter calorimeter under use at IDEA may possibly suffer from incomplete containment of all particles belonging to hadron jets. This effect should therefore be taken into consideration when designing the final IDEA calorimeter. Figure 3.36 shows the two leakage components for the simulated 480

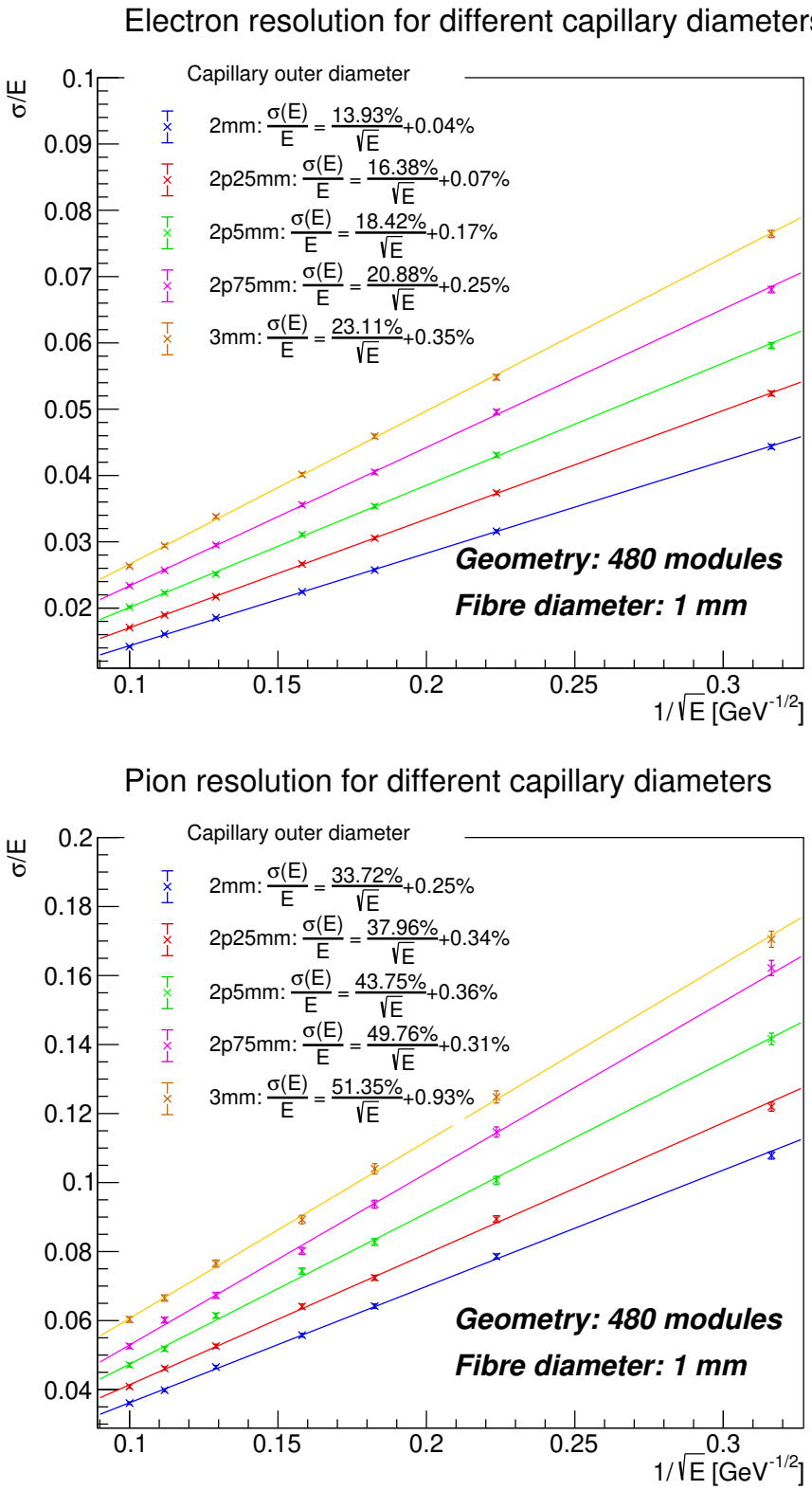


Figure 3.34: Energy resolution for electrons (upper plot) and pions (lower plot), by changing the capillary outer diameter and keeping the inner one fixed.

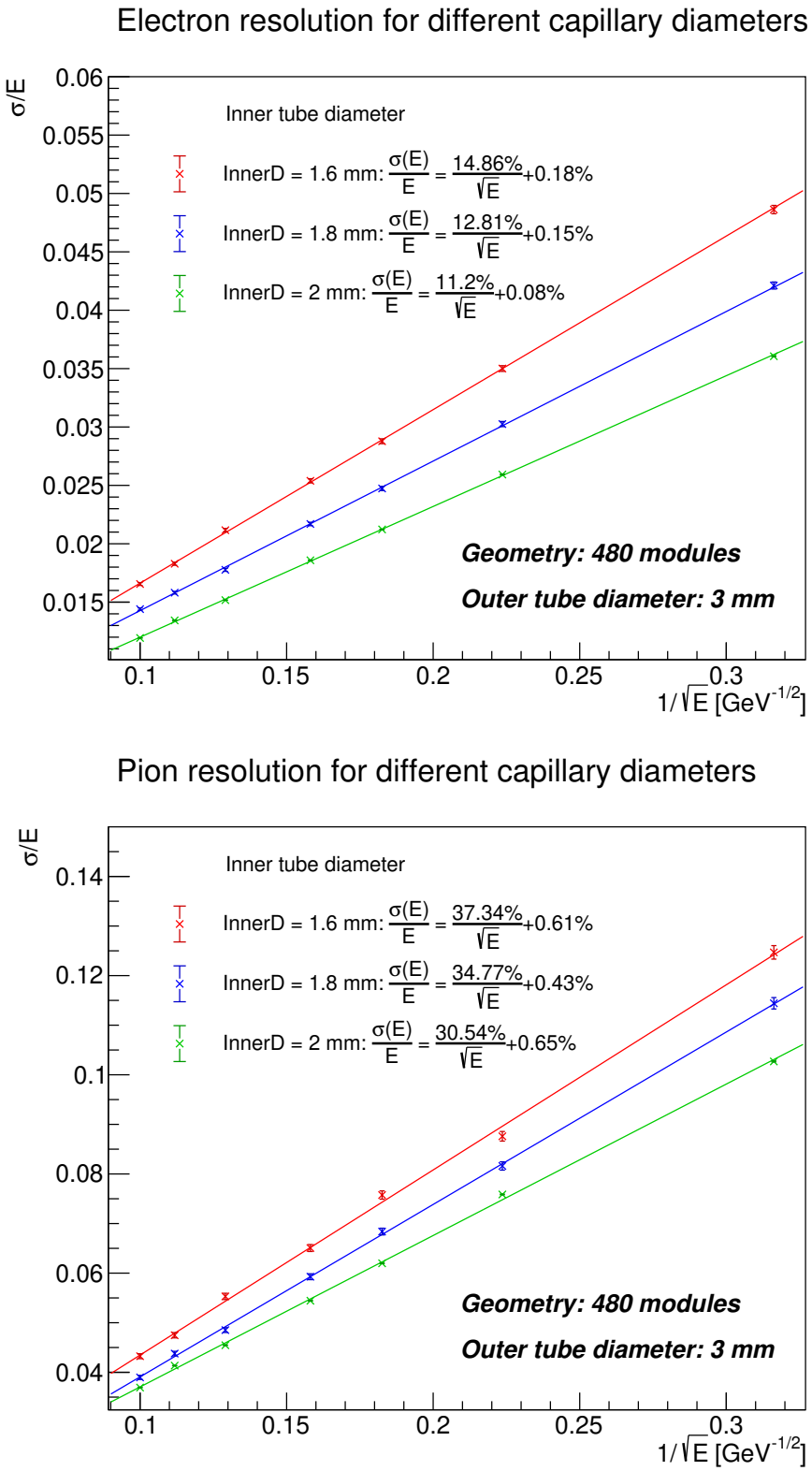


Figure 3.35: Energy resolution for electrons (upper plot) and pions (lower plot), by changing the capillary inner diameter and keeping the outer one fixed.

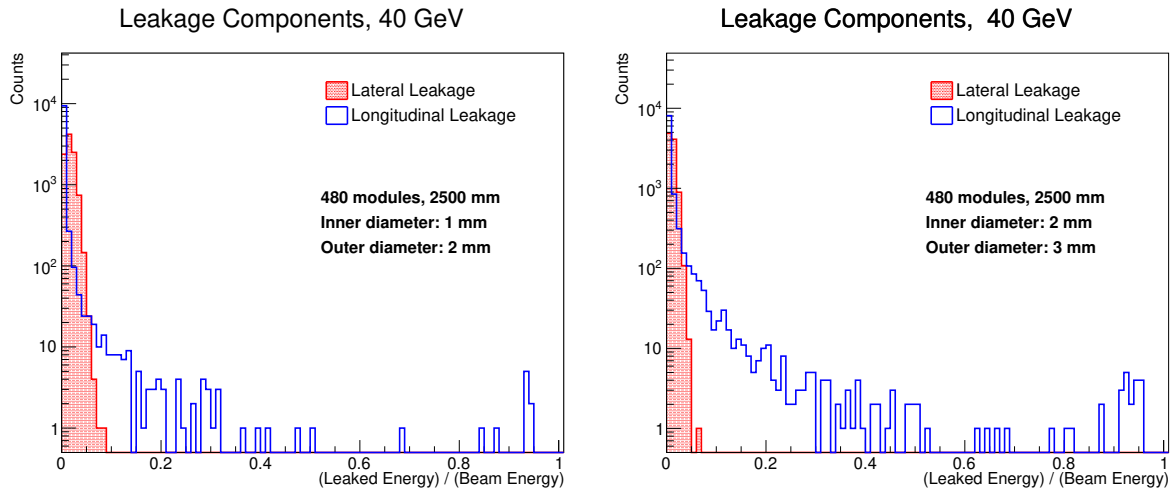


Figure 3.36: Lateral and longitudinal containment, estimated through the Geant4 simulation, for a 480 modules calorimeter. On the left, the HiDRa prototype capillary parameters are used, with an inner tube diameter of 1 mm and an outer one of 2 mm. On the right, the inner one is increased to 2 mm, and the outer diameter is set to 3 mm. The optical fibre radius is adjusted accordingly, to fill the inner tube volume.

modules geometry, with the HiDRa parameters for the capillary tubes, or by increasing the outer diameter of the capillaries to 3 mm and the inner one to 2 mm, which has a higher sampling fraction but a longer interaction length.

CHAPTER

4

HIGH-GRANULARITY PERFORMANCES OF THE HIDRA PROTOTYPE

The silicon photomultiplier technology, which allows the readout of optical photons produced in each fibre, opens to a variety of studies concerning the spatial distribution of the showering particles. For an effective particle-flow approach, energy deposits in the calorimeter must be well separated and clusterised, in order to be correctly associated to tracks or eventually be removed. A good separation between very close energy deposits requires excellent spatial resolution to be distinguished correctly.

An example where good spatial resolution has been important in recent particle physics searches is the measurement of the Higgs boson mass in its $H \rightarrow \gamma\gamma$ decay channel. The invariant mass of the two-body final state is

$$m^2_{\gamma\gamma} = 2E_1E_2(1 - \cos\theta), \tag{4.1}$$

where along the resolution on the energy $E_{1,2}$ of each photon by the calorimeter, a role is also played by the measurement of the angle θ between the two photons. By improving the spatial resolution, this angle can be measured with better precision and therefore refine the invariant mass resolution [122].

Other applications that are interesting for calorimeters, beside correct and accurate energy measurements, are particle identification capabilities. While this task is often performed by other subdetectors in the inner tracker, with some notable examples being Čerenkov ring detectors and transition radiation detectors, calorimeters with very fine granularity can also play a role in separating the species of different particles. Approaches for separating particle species using calorimeters' information, concerning features like particle shower shape, energy deposition in the first layers and others, have been used since many years [123][124].

Modern analyses techniques, for example different architectures of neural networks like Convolutional Neural Networks (CNNs) and Graph Neural Networks (GNNs), are able to exploit at a level never reached before the finely segmented information of calorimeters. In ref. [125], the authors managed to reach τ lepton identification at an excellent level using standalone calorimeter information, through a previous version of Geant4 IDEA calorimeter full simulation (not using capillary tubes) and using a more evolved GNN model.

While a fully working particle-flow approach exploiting the capillary tube design of the proposed IDEA calorimeter is out of the scope of this thesis, a few studies exploiting the finely segmented readout of the HiDRa prototype are presented in this chapter. All results were obtained by means of dedicated Geant4 simulations. The spatial resolution for electromagnetic showers is firstly studied, followed by a tentative approach of separating π^0 originated showers from single photons ones.

4.1 Spatial resolution for electromagnetic showers

Finely segmented calorimeters offer the advantage of measuring with good precision the position of energy deposits produced by particles interacting inside the detector. For electromagnetic showers, which are very compact and whose development is well understood, the deposition of energy very close to the shower axis allows to measure the impact point position on the calorimeter's surface of the incoming electron or photon.

The specific geometry chosen for the HiDRa calorimeter, based on optical fibres running almost parallel to the incoming particles, allows to sample very finely the lateral disposition of energy deposits and hence the lateral shower profile. Conversely, the absence of longitudinal segmentation of the optical fibres, which run from the front face directly to the photodetector, does not allow to measure the longitudinal profile of particles showers. Attempts to recover this kind of information through measurement of optical photon time arrival on the sensor's surface are being actively pursued, both within the HiDRa group, and other dual-readout calorimeters groups [126][127].

Given a calorimeter with a lateral segmentation provided by some separation into different cells, the position of an incoming particle entering the detector can be reconstructed through the centre-of-gravity method:

$$X_{CALO} = \frac{\sum_i x_i E_i}{\sum_i E_i}, \qquad Y_{CALO} = \frac{\sum_i y_i E_i}{E_i}. \tag{4.2}$$

The coordinates (x_i, y_i) represent the position of each calorimeter cell, and E_i is the total energy (calibrated signal) deposited in that cell. The $(X, Y)_{CALO}$ coordinates provide the energy-weighted position of deposited signal in the calorimeter, which can then be associated through geometrical considerations to the impact point position on the calorimeter, and eventually linked to reconstructed tracks.

Figure 4.1 shows the map of energy deposits in the two different types of fibres produced by 40 GeV electrons showering in the centre of the simulated HiDRa prototype. In the Geant4 simulation each fibre is associated with an identifier number, which is only later converted to actual spatial coordinates as would happen with an experimental setup. The resulting coordinates in millimetres are reported on the plot axes. For the studies reported in this chapter, the truth longitudinal position of each optical photon production point (or energy deposit in the case of scintillating fibres) is stored. This allowed to evaluate the effect of varying time resolution on the optical photon arrival time measurement, by applying offline smearing effects on this truth information.

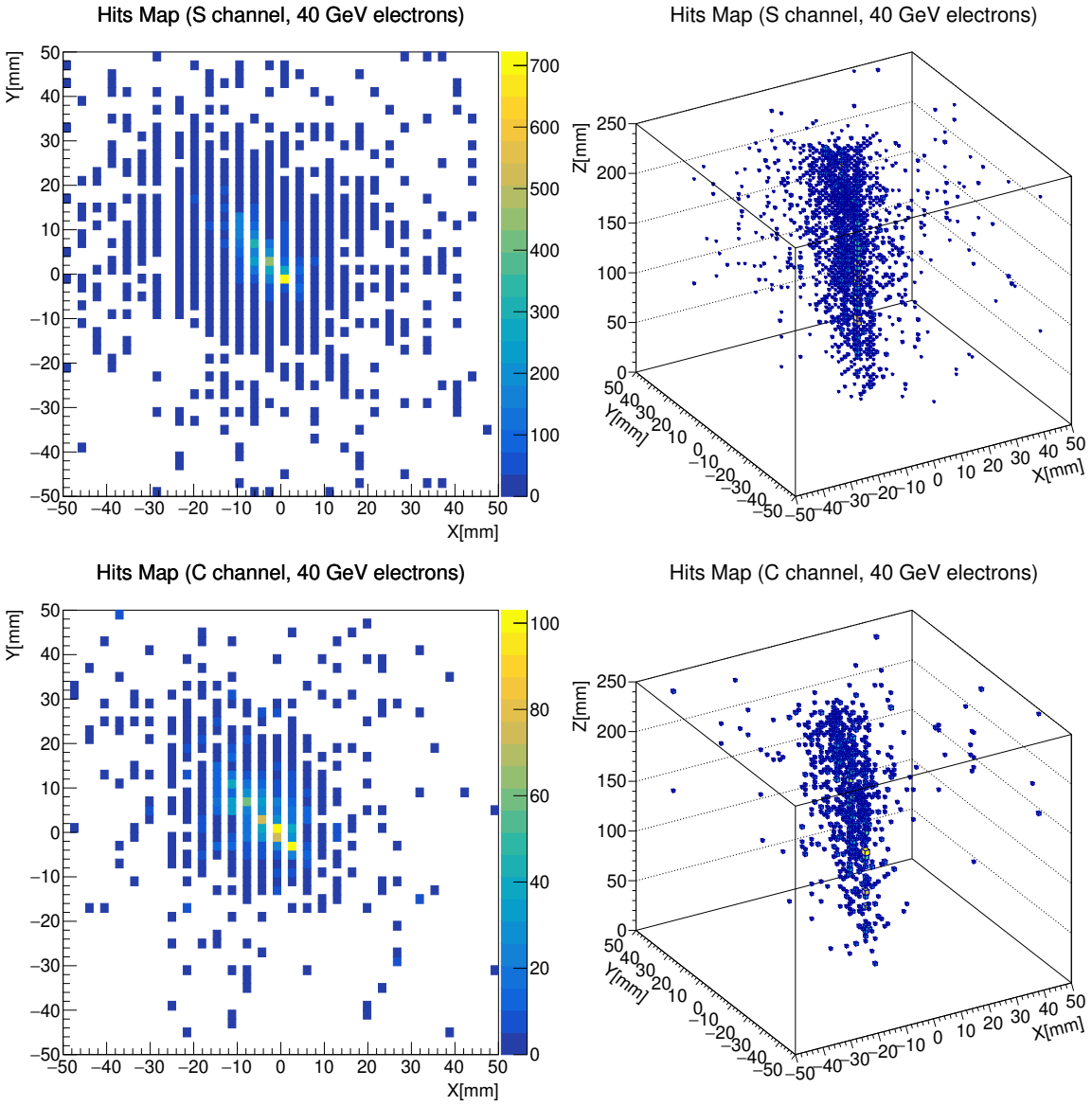


Figure 4.1: Example of one simulated electromagnetic shower, originated by a 40 GeV electron moving towards positive $\widehat{z}$, as seen in the scintillation (upper row) and Čerenkov (lower row) channels. On the right the truth z coordinate of each hit is also shown.

One should notice that, for the studies reported here, the Geant4 simulation was rotated by 90° around the $\widehat{z}$ axis with respect to the final prototype geometry. This can be seen, for example, on the left plots of fig. 4.1, where signals in same-type fibres are shown vertically aligned, and so are also the missing contribution from the different type of fibres. The subsequent change, however, does not affect any result, except when explicitly mentioning the spatial resolution along the $\widehat{x}$ (horizontal) or $\widehat{y}$ (vertical) axes.

In order to estimate the resolution on the measurement of the impinging particle position, 10^4 events consisting of electrons with different energies were simulated. A beam distributed uniformly with a circular shape, with a radius of 1 cm, was directed along the $\widehat{z}$ axis, representing the longitudinal axis of the calorimeter. As in chapter 3, the calorimeter was rotated by 2.5° in both horizontal and vertical direction. For each event, the centre-of-gravity coordinates are reconstructed and compared with the true

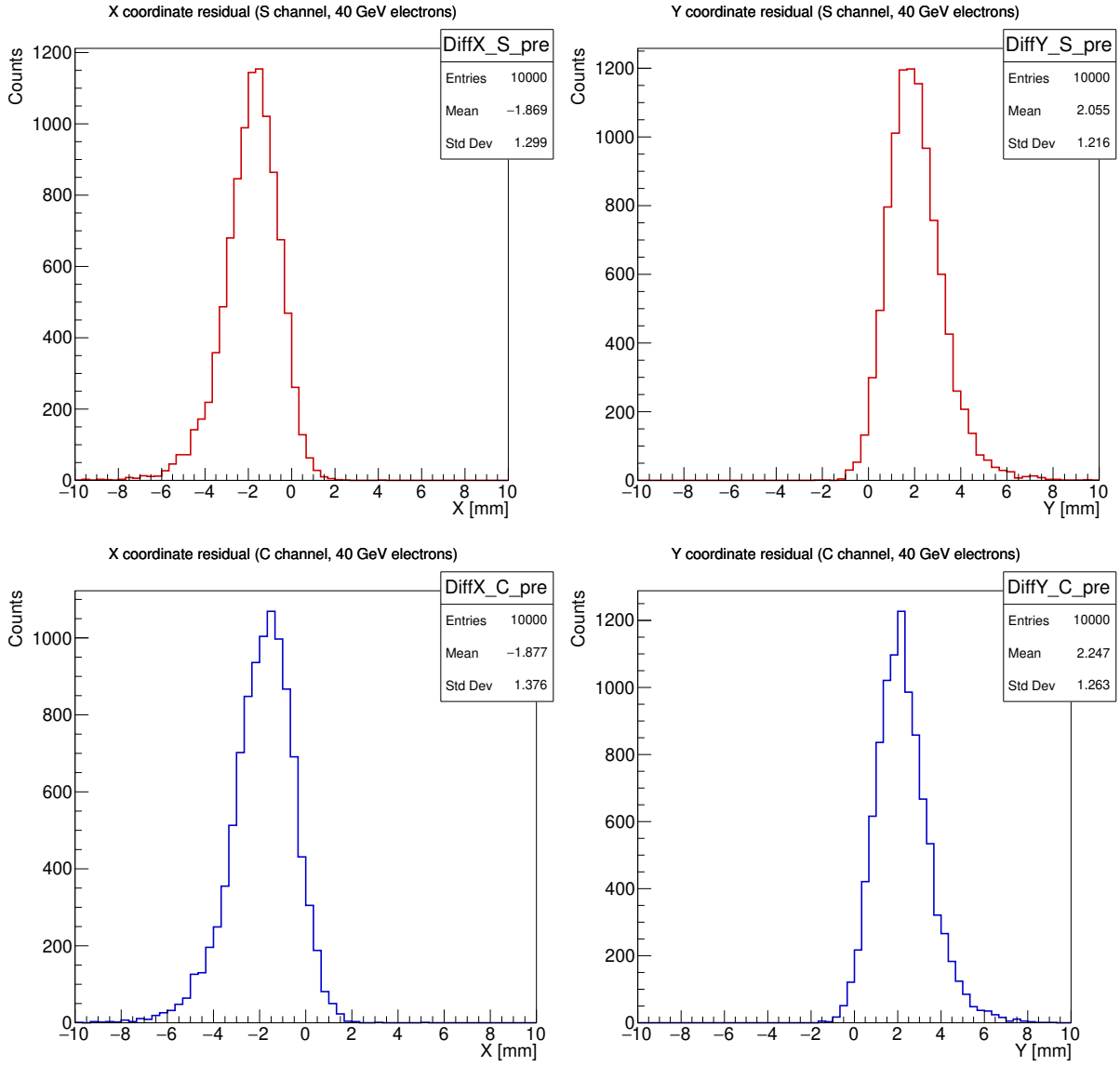


Figure 4.2: Difference between true beam impact point position, and reconstructed one through the centre-of-gravity method. The upper line shows the x (left) and y (right) coordinates for the scintillating channel, while the lower line shows the Čerenkov ones.

ones provided by the simulation, with the distributions in fig. 4.2 showing the difference between the two values. These distributions are visibly skewed in either positive or negative residuals that result from the calorimeter tilting, with a most probable value that is different from zero by few millimetres. The reason for these tails are signals deposited in later stages of the electromagnetic showers, that by developing deeper in the calorimeter are more displaced from the impact point on the surface.

For simple geometrical setups, like the one used for prototype beam tests, these distributions can be corrected through geometrical considerations, if one is able to measure the shower barycentre in the longitudinal direction Z_{Reco}. By knowing with a certain precision the average depth at which the signal was produced, and the calorimeter ro-

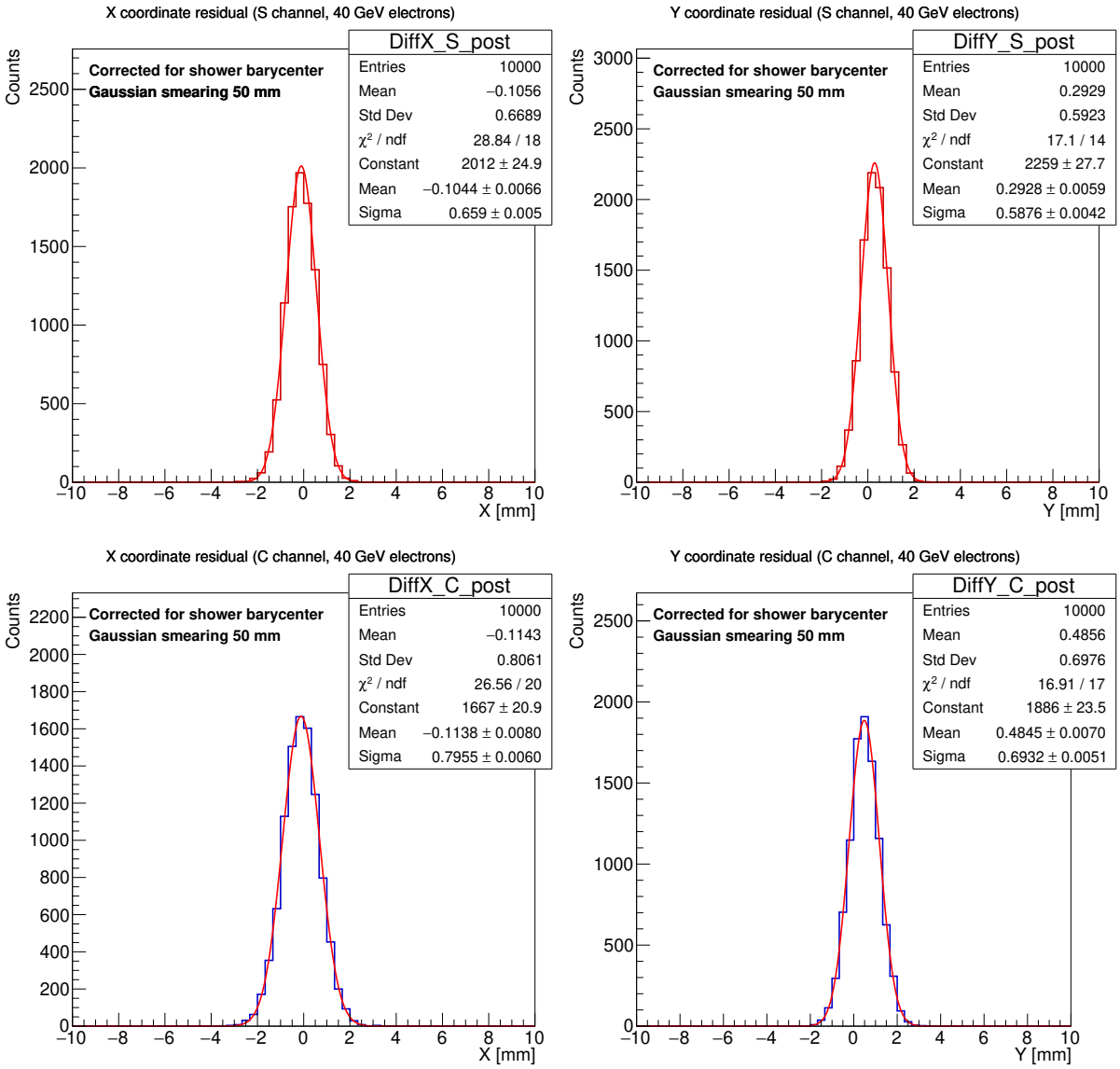


Figure 4.3: Difference between true beam impact point position, and reconstructed one through the centre-of-gravity method. A correction for the calorimeter horizontal and vertical rotation angles of 2.5°, described in the text, was applied. The upper line shows the x (left) and y (right) coordinates for the scintillating channel, while the lower line shows the Čerenkov ones.

tation angles, one can adjust the observed coordinates through

$$X_{\text{Corrected}} = X_{\text{Reco}} + Z_{\text{Reco}} \times \tan(\theta_{\text{Horz}})$$
$$Y_{\text{Corrected}} = Y_{\text{Reco}} + Z_{\text{Reco}} \times \tan(\theta_{\text{Vert}}).$$

Figure 4.3 shows the same distributions after this correction was applied on both coordinates (for each channel). The Z_{Reco} coordinate was here measured once again through the centre-of-gravity method, by weighting the longitudinal position of each calorimeter hit with its energy deposit. A gaussian smearing on the truth deposit longitudinal position, with the truth z coordinate of the hit as mean and a 5 cm standard deviation, was in this case applied to replicate the uncertainty given by sensors' signal properties and electronics timing resolution. This level of longitudinal spatial resolution, while being quite optimistic, is potentially in reach with very fast SiPM rising signals and time resolution on photons time of arrival of few tens of picoseconds. Different smearing parameters were nevertheless tested to evaluate the worsening of the correction method. A different procedure, consisting of correcting for the average shower barycentre depth at a certain energy instead of the event-by-event one, was also tested and applied. These shower barycentres varied from 20 cm for 10 GeV electrons to about 24 cm for 100 GeV ones, consistent with a longer longitudinal shower development at higher energies. In the second case, the distributions in fig. 4.2 are found to shift until the most probable value is located at a zero residual, meaning that, on average, the beam impact position is properly reconstructed. On the other hand, the missing correction for the deeper energy deposits results in distribution tails that are still present, worsening the spatial resolution.

The spatial resolution is here parametrised with the same analytical expression as the energy resolution one, $\sigma^{spatial}/E = a/\sqrt{E} \oplus b$. The underlying reasoning is that the reconstructed position through the centre-of-gravity algorithm depends on the energy deposits in each calorimeter cell, which are subjected to Poissonian fluctuations. The same sources of uncertainty of the energy resolution also affect, very similarly, the spatial one.

We studied the spatial resolution improvement when taking advantage of excellent timing measurements. The two methods are compared in fig. 4.4 with their dependence on the electron energy E. In the upper line, the resolution $\sigma_{X,Y}$ is taken as the RMS of the histograms in fig. 4.2, where the only correction is considering the average shower depth at each energy point. In the lower row, the shower barycenter Z_{Calo} was calculated event-by-event from the smeared position of each calorimeter deposit, and used for correcting the (X_{Calo}, Y_{Calo}) coordinates. The corresponding resolution is obtained through the standard deviation of a gaussian fit imposed on the distributions in fig. 4.3. In this second case, the obtained resolutions from the scintillation and Čerenkov channels were also used to obtain a weighted combination of the two information through

$$X_{Combined} = \frac{\frac{X_S}{(\sigma_{S,X})^2} + \frac{X_C}{(\sigma_{C,X})^2}}{\frac{1}{(\sigma_{S,X})^2} + \frac{1}{(\sigma_{C,X})^2}}, \qquad Y_{Combined} = \frac{\frac{Y_S}{(\sigma_{S,Y})^2} + \frac{Y_C}{(\sigma_{C,Y})^2}}{\frac{1}{(\sigma_{S,Y})^2} + \frac{1}{(\sigma_{C,Y})^2}} \tag{4.3}$$

to take advantage of the channel with the smaller uncertainty, that was found to be the scintillation one. The most interesting result from the comparison of the two methods is a $\sim 1\%$ reduction in the constant term to a negligible level, also complemented by a slight decrease in the stochastic one.

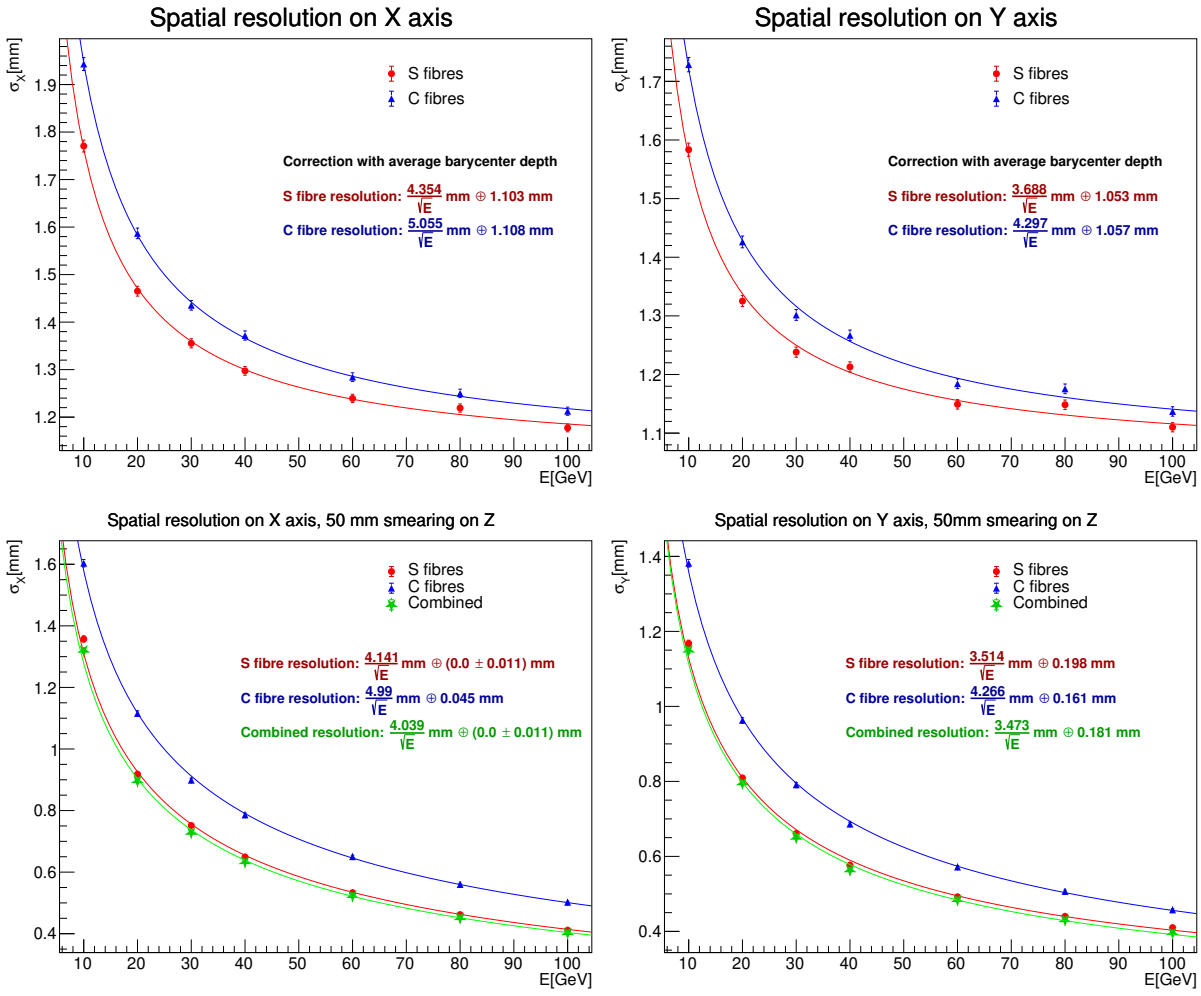


Figure 4.4: Spatial resolution along the $\widehat{x}$ (left) and $\widehat{y}$ (right) directions obtained for an electron beam with energies between 10 GeV and 100 GeV. In the upper row, a correction for the calorimeter rotation based on the average shower barycentre depth Z_{Calo} in the calorimeter was used for all events. In the lower row, the Z_{Calo} variable was computed for each event. The RMS of the gaussian fit on the corrected S and C distribution was used, using eq. (4.3), to combined the two channels. 10^4 events were simulated for each energy point.

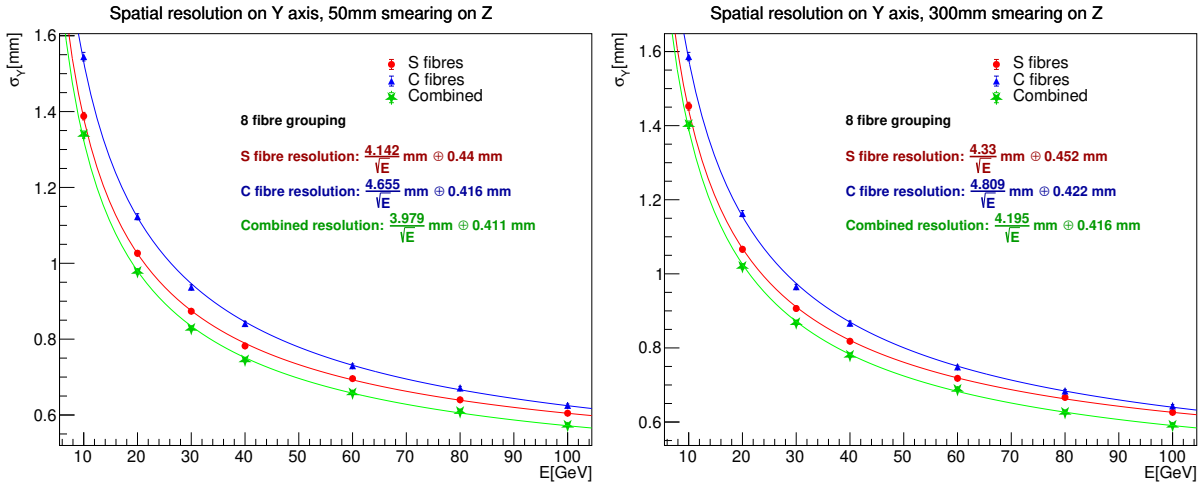


Figure 4.5: Spatial resolution for electrons on the $\widehat{y}$ direction for the scintillation, Čerenkov channels and combined through eq. (4.3), when different gaussian smearing parameters are applied. In both cases, the signal from 8 adjacent same-type fibres are added into one channel, to reproduce the HiDRa readout grouping.

From the obtained spatial resolutions, it is possible to extract, at conceptual level, what the IDEA calorimeter angular resolution would be if it had the same design as HiDRa. Assuming that the calorimeter is located at a distance $d = 2$ metres from the interaction point, and not considering other experimental effects, the angular resolution is $\sigma_\theta = \arctan(\sigma_X/d)$. For 40 GeV electrons, considering a spatial resolution $\sigma_X \simeq 0.6$ mm, an excellent angular resolution of $\sigma_\theta \simeq 3$ mrad is found.

4.1.1 Signal grouping

As it will be better detailed in chapter 5, during the development of the HiDRa prototype readout system it was decided to reduce the amount of channels from the calorimeter modules instrumented with SiPMs. This was achieved by using front-end boards directly connected to 8 SiPMs coupled to same-type neighbour fibres, and performing an analogical summation of their electronic signals. The result is a reduction of the effective granularity of HiDRa along the direction on which same-type fibres are aligned, from 1024 to 128 channels (64 for scintillating and 64 for Čerenkov channels) despite the calorimeter's actual geometry being unchanged.

To reproduce the effect of signal grouping on the spatial resolution performances, also considering different number of fibres packed in one readout channel, the signals from adjacent fibres were summed offline, with the assumption that the analogue sum would not lead to signal losses. The corresponding coordinate of one channel was taken as the centre of the grouped fibres, so that, with an eight-fibre grouping, the signal would be placed between the fourth and fifth capillaries. Because of the initial rotation of the calorimeter simulation, this channel grouping only affects the granularity on the $\widehat{y}$ axis. The spatial resolution along the $\widehat{x}$ axis is unaffected with respect to the single fibre readout case, as each energy deposit corresponds to the same x coordinate when calculating the event centre-of-gravity.

Figure 4.5 shows the spatial resolution along the fibre-grouping direction, when all (smeared) photoelectron signals produced in eight fibres are summed before the construction of the shower barycentre. The results must be compared to the lower-

right plot in fig. 4.4, where no grouping was applied and all fibres provided their own energy and spatial information. To estimate the effect of different time resolution on the shower barycentre correction, two gaussian smearing parameters are used, 5 cm or 30 cm. Interestingly, despite the quite large difference in the z coordinate precision of each energy deposit, the global spatial resolution is not severely worsened. This is probably due to the energy deposits in the tails being considerably deeper in the calorimeter and sufficiently separated from the rest of the shower, even with the less precise longitudinal information smearing, therefore allowing a good correction. As expected, the reduced granularity leads to a slightly worse spatial resolution, as a larger percentage of the total signal is deposited in one channel, and a lower amount in the neighbourhood. The smaller energy weight associated to close cells therefore reduces the detector's capability to interpolate correctly the centre-of-gravity.

A completely different result is obtained when the number of fibres comprised in simulated grouping is increased further. Figure 4.6 shows the difference between the true and reconstructed coordinate from the same set of events, consisting of 40 GeV electrons entering the centre of the HiDRa calorimeter, with 8 or 16 fibres gathered in one readout channel. A double structure appears in the latter case, with two clearly separated peaks. The understood reason for this effect to appear only for sufficiently large amount of fibres in one readout channel is that the size of the readout cell (32 mm for 2 mm capillary tubes) becomes larger that the Molière radius of electromagnetic showers, which was estimated to 24.6 mm. Consequently, only very small signals are produced in the nearby cells, and if some signal is produced in the upper cell, almost none will be produced in the lower one, shifting the centre-of-gravity in the positive vertical direction. Only events in which an electron enters the boundary region between two cells, and a significant amount of signal is deposited in both readout channels, will have a barycentre correctly reconstructed.

To evaluate the spatial resolution that would be obtained in this extreme case, since a gaussian fit is not possible, the RMS of each distribution is used. Correction procedures to improve the resolution, while certainly possible, were not investigated as for the HiDRa prototype an 8 fibre grouping was chosen, therefore not manifesting this issue. The obtained spatial resolution dependence on the shower energy are shown in fig. 4.7. A significant worsening of both stochastic and constant terms is observed as expected. A fit considering a linear sum between the two terms is found to describe slightly better the simulated resolutions, suggesting 3.1% and 2.6% constant terms for the scintillating and Čerenkov channels, respectively.

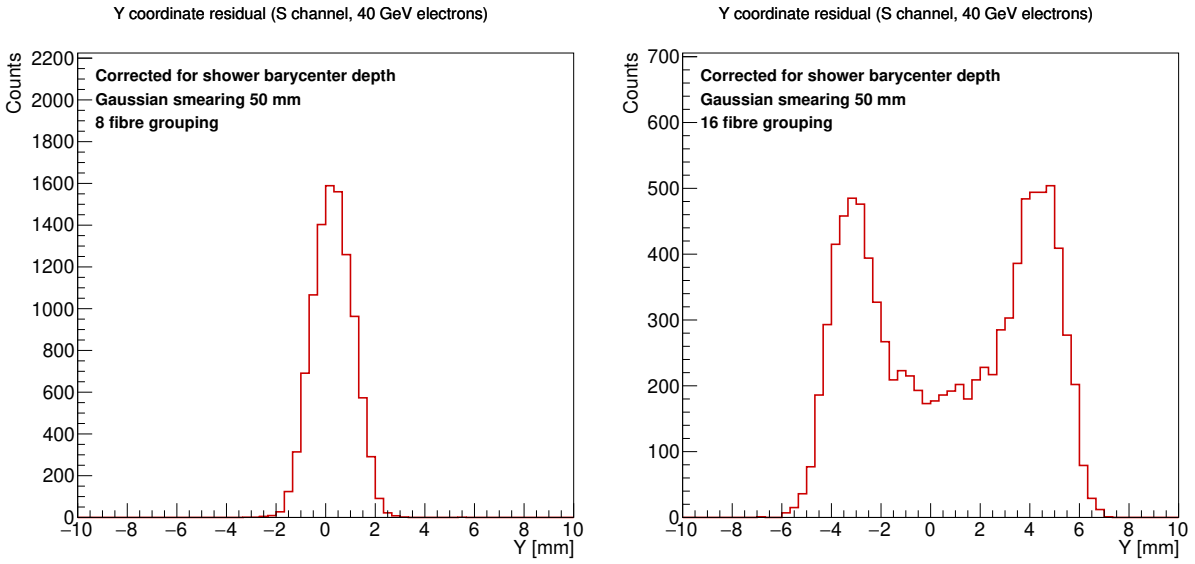


Figure 4.6: Comparison of the reconstructed shower barycentre, along the $\widehat{y}$ direction where the fibres are grouped, for a 40 GeV electron beam. On the left, photoelectrons from 8 adjacent fibres are summed together. On the right, the sum is taken from 16 adjacent fibres. See text for details.

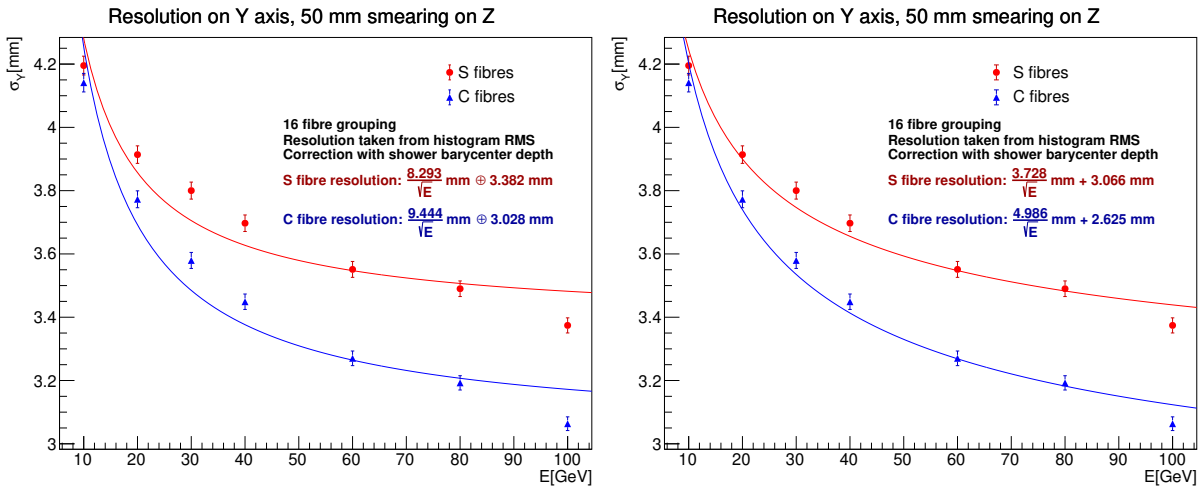


Figure 4.7: Spatial resolution for electrons with different energies, using 16 fibre grouping. Two fit trials were tested, where the stochastic and the constant terms are linearly added or in quadrature. Much worse resolution terms are obtained when compared to the grouping of eight fibre case, as expected because of the loss in lateral granularity.

4.2 Application to π^0/γ separation

An interesting application of very fine calorimeter granularity is the possibility to separate electromagnetic showers produced by single high-energy photons, or similar events originated by neutral pions. Examples of relevant cases where such a feature would be important are identification of π^0s produced from τ lepton decays for polarisation measurements, flavour physics, and recovery of bremsstrahlung radiation photons from final state particles for an improved particle-flow reconstruction. The origin of possible mis-identification of π^0 originated showers lies in the kinematics of π^0 decays into two high-energy photons. With a mass $m_{\pi^0} = 135$ MeV, neutral pions are produced with very high boost already at energies of few GeV. While in the decaying pion's reference frame the two photons are produced back-to-back, in the laboratory frame they are observed to be very close because of the large relativistic boost. The relative aperture angle between the two photons decreases at higher Lorentz boosts γ of the π^0, making them less distinguishable as the energy increases. The minimum angle between the two photons from π^0 decay in the laboratory frame is found when both particles are produced with an angle $\theta = \frac{\pi}{2}$ with respect to the neutral pion's direction, with transverse momentum $p_T = m_{\pi^0}/2$ and longitudinal one $p_L = \sqrt{E_{\pi^0}^2 - m_{\pi^0}^2} \simeq E_{\pi^0}$. It follows that the minium angle α_{min} between the two photons is approximately

$$\tan(\alpha_{min}) = \frac{m_{\pi^0}}{E_{\pi^0}} \simeq \frac{1}{\gamma} \approx \alpha_{min} \tag{4.4}$$

and the related distance D between the two energy deposit in the calorimeter, located at a distance $d = 2$ m from the interaction point in the case of IDEA, is

$$D(\alpha_{min}) = d \times \tan(\alpha_{\min}) = \frac{2\,\mathrm{m}}{\gamma}. \tag{4.5}$$

The minimum opening angle, calculated for a 135 MeV π^0, varies from $\alpha_{min} \approx 270$ mrad for $E_{\pi^0} = 1$ GeV (about 15.5°) to $\alpha_{min} \approx 27$ mrad at 10 GeV (1.55°) and 5.4 mrad at 50 GeV (0.31°). These angles are compatible, for a range of energies accessible to the final state particles produced at the FCC, with the estimated spatial (angular) resolution through the HiDRa simulation results. With increasing energy of the neutral pion, the minimum angle separating the energy deposits from the two photons decreases. Eventually, this distance becomes smaller than the Molière radius value of the calorimeter, and the two showers become undistinguishable.

Two examples of energy deposits in the scintillating channel of the HiDRa simulated calorimeter, assuming individual readout of each fibre, are shown in fig. 4.8 for 40 GeV photon and pion originated showers. The showers initiated by π^0s feature a greater variability event-by-event, depending on the emission angle of the two photons and their different Lorentz boosts (and the related energies). The calorimeter's capability to disentangle very close energy deposits, each one contributing differently to the total energy measured by the detector, depends on how finely segmented is the detector and on its capability to measure even very small energy contributions. The spatial resolution for single-photon showers of different energies, obtained through the procedure described in section 4.1, is reported in fig. 4.9. It shows quite good agreement with those of electrons showers, as expected because of the same processes involved in electromagnetic showers development, despite the different properties of the particles from which they are produced [128].

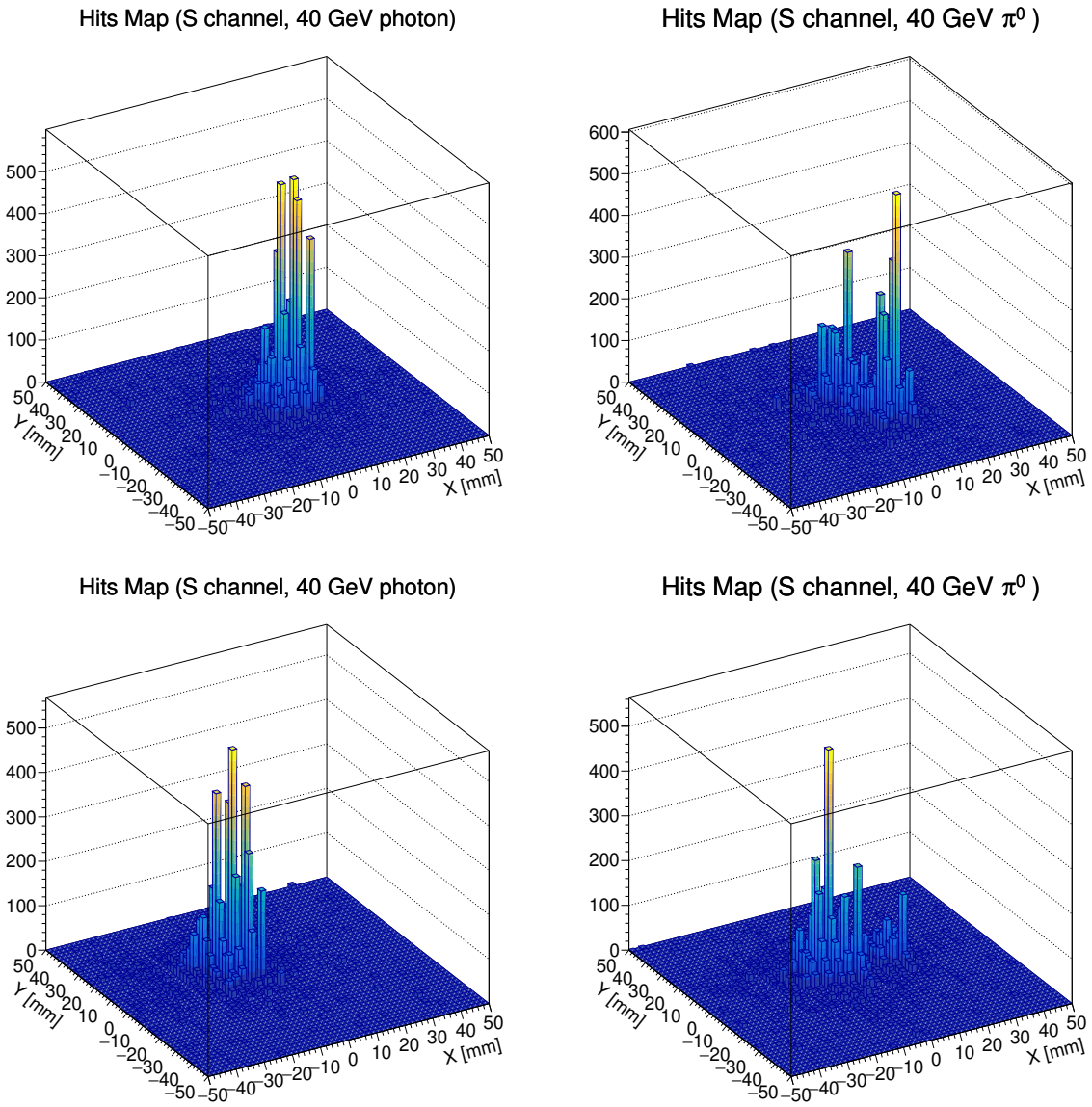


Figure 4.8: Examples of energy deposits from electromagnetic showers in the scintillating channel of the calorimeter, originated by 40 GeV photons (left) or neutral pions (right).

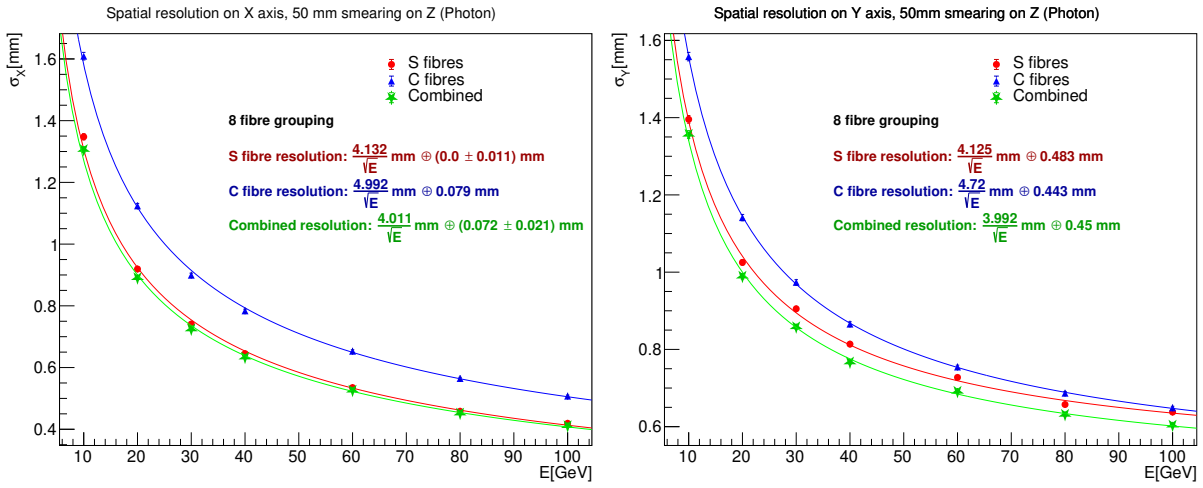


Figure 4.9: Spatial resolution in the $\widehat{x}$ and $\widehat{y}$ directions obtained for photons of different energies in the HiDRa simulated calorimeter. An eight-fibre grouping was performed offline, and a 5 cm smearing on each energy deposit was applied when correcting for the calorimeter's rotation in horizontal and vertical directions.

In order to classify electromagnetic shower events with unknown origin into one of the two possible classes, γ or π^0, several approaches are possible. A procedure presented in ref.[129] was followed, by introducing a set of discriminant variables able to describe the shape of these showers, which is expected to show different structures or broader lateral profile in the case of two merging photons. Starting from a set of N cells, each one with coordinates (x_i, y_i) and an energy deposit e_i, the first three variables that are introduced are the elements of the 2×2 spread matrix S along the two lateral directions:

$$S_{XX} = \frac{\sum_{i=1}^{N} e_i (x_i - x_{Calo})^2}{\sum_{i=1}^{N} e_i}, \qquad S_{YY} = \frac{\sum_{i=1}^{N} e_i (y_i - y_{Calo})^2}{\sum_{i=1}^{N} e_i}, \tag{4.6}$$

$$S_{XY} = S_{YX} = \frac{\sum_{i=1}^{N} e_i (x_i - x_{Calo})(y_i - y_{Calo})}{\sum_{i=1}^{N} e_i} \tag{4.7}$$

with (x_{Calo}, y_{Calo}) the usual barycentre coordinate measured through the shower centre-of-gravity algorithm. Based on these variables, new features to describe the shower shape are introduced. The first one is the second order momenta $r2$, related to the cluster size

$$r2 = \langle r^2 \rangle = S_{XX} + S_{YY} = \frac{\sum_{i=1}^{N} e_i [(x_i - x_{Calo})^2 + (y_i - y_{Calo})^2]}{\sum_{i=1}^{N} e_i}, \tag{4.8}$$

followed by a second variable, named $r2r4$, which parametrises the contribution of the lateral tails of each shower

$$r2r4 = 1 - \frac{\langle r^2 \rangle^2}{\langle r^4 \rangle}, \quad \text{with} \quad \langle r^4 \rangle = \frac{\sum_{i=1}^{N} e_i [(x_i - x_{Calo})^4 + (y_i - y_{Calo})^4]}{\sum_{i=1}^{N} e_i}. \tag{4.9}$$

A different variable, denoted as k, is obtained as the ratio of the spread matrix eigenvalues, and describes the ratio between the two semi-axes of the ellipse representing the

2D image of the calorimeter energy deposits

$$k = \sqrt{1 - 4\frac{S_{XX}S_{YY} - S_{XY}^2}{(S_{XX} + S_{YY})^2}} = \sqrt{1 - 4\frac{\det S}{\mathrm{Tr}^2 S}}. \tag{4.10}$$

Another variable, $asym$, describes the correlation of ellipse between the two X and Y coordinates

$$\mathrm{asym} = \frac{S_{XY}}{\sqrt{S_{XX}S_{YY}}}. \tag{4.11}$$

The last two variables that can be used are the ratios between the largest energy deposit in one cell over the total energy deposit, $E_{Seed} = E^1_{Cell}/E_{Tot}$, and the ratio that also included the second largest cell contribution, $E^{2nd}_{Seed} = (E^1_{Cell} + E^2_{Cell})/E_{Tot}$. Examples of the distributions of these variables, when computed for 40 GeV photons and neutral pions, are drawn in figs. 4.10 and 4.11.

The shown distributions may seem at first difficult to separate based on some selection on each variable. In order to obtain a preliminary classification between the two different samples, a multi-variate analysis based on the XGBoost [130] Python software package was used. The advantage of this Machine Learning (ML) method, which is not described in detail here, is the possibility to take into account the correlations between different variables to improve the classification power by introducing sets of boosted decision trees (BDT). Each BDT associates a score to each sample of a dataset, depending on feature requirements that were learned during the model training. The score from many BDTs is then summed, and the overall output is interpreted as a probability, for each sample, to belong to one of the two possible γ or π^0-induced shower classes. Figure 4.12 shows the output probability of the tested XGBoost classifier model for a 3.6×10^4 sample of simulated photons and neutral pions equally populated, which were excluded from the training set. It is common, when describing the performance of a classifier, to establish a working point on its output. The figure of merit could either be the efficiency for the desired signal, or the rejection factor of the background, and several others. As the only purpose of the study here described is to evaluate the possibility of rejecting neutral pions by taking advantage of the highly granular design of the dual-readout calorimeter, a simple selection on the output probability $P_{XGB} > 0.9$ is used. Examples of few variables of interest that were used for the training, drawn after imposing the output probability cut, are drawn in fig. 4.13. The obtained efficiency for photons with the selected requirement is $\varepsilon_\gamma = 9694/(1.8\times10^4) \approx 54\%$, while the one for pions is $\varepsilon_{\pi^0} = 416/(1.8\times10^4) \approx 2\%$.

The results shown until this point represent my own preliminary work for a very simple classification task on simulated samples of photons and pions in the HiDRa calorimeter. The effort of further improving this work, including more advanced algorithms among which Convolutional Neural Networks (CNNs), was undertaken by a Master student in the Pavia dual-readout group under my supervision, with very interesting results that can be found in [131]. An immediate improvement was the introduction of a clustering algorithm to take into account those events with two well-separated photons from the π^0 decay. The high-level variables previously defined are more effective when one single cluster is identified, with a broader shape generated by two-photons events with respect to single-photon ones. A second well-separated peak, on the other end, could end up with misleading variables computation, therefore reducing the classification performances. Another correction, which was effective at

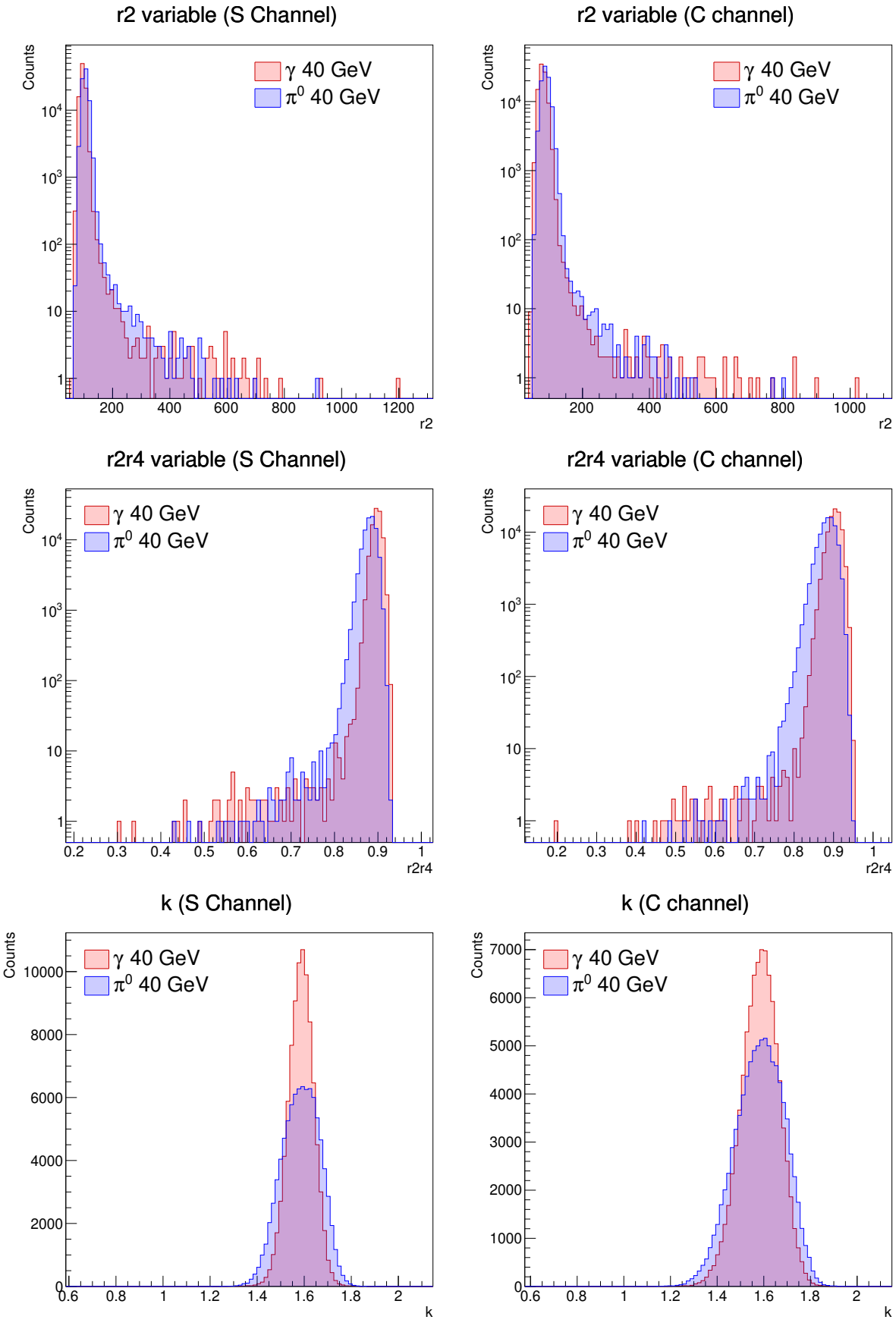


Figure 4.10: Distributions of variables used for separating γ electromagnetic showers from π^0 ones. In each row the same variable is shown, as observed by scintillating fibres (left) and Čerenkov ones (right).

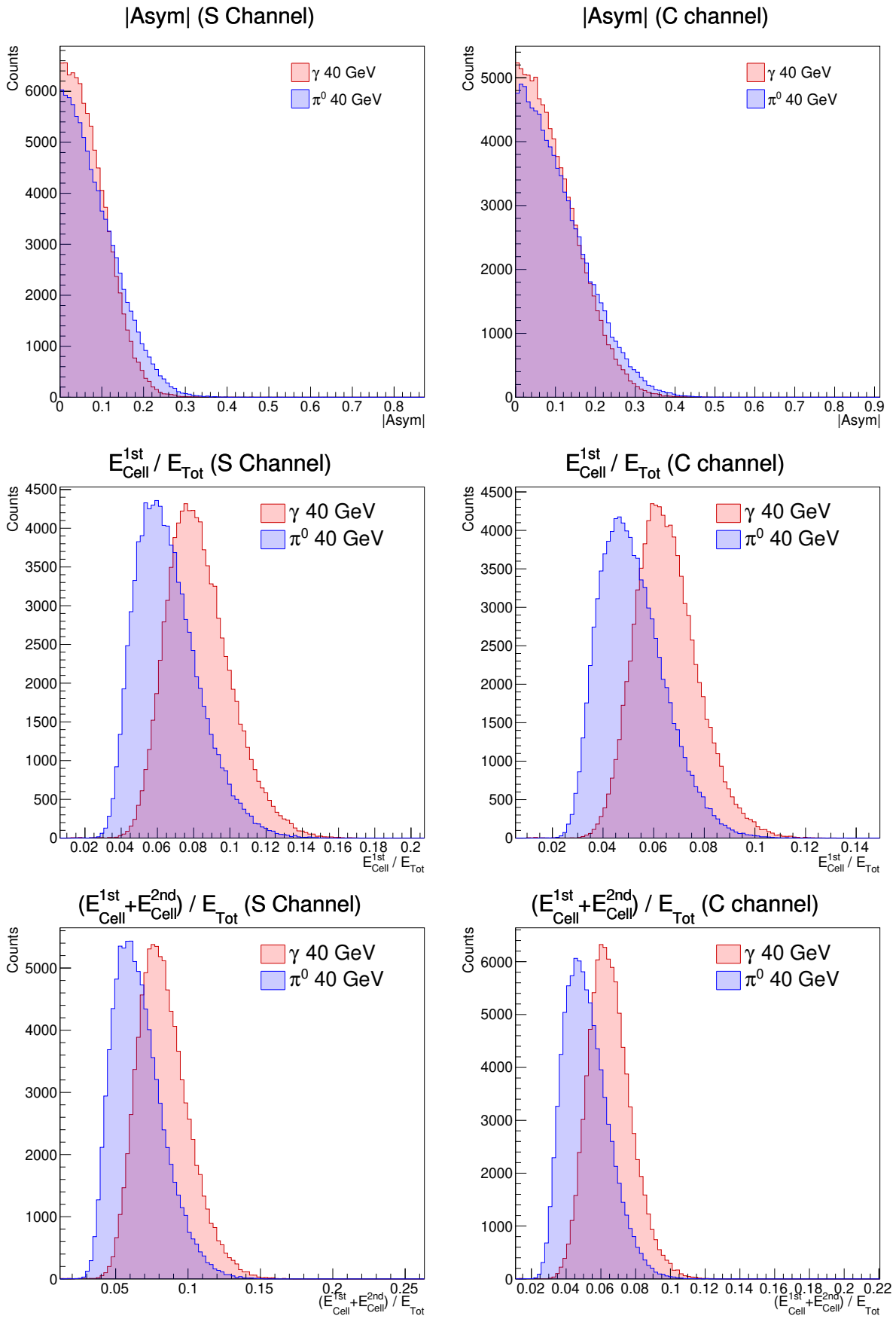


Figure 4.11: Distributions of variables used for separating γ electromagnetic showers from π^0 ones. In each row the same variable is shown, as observed by scintillating fibres (left) and Čerenkov ones (right).

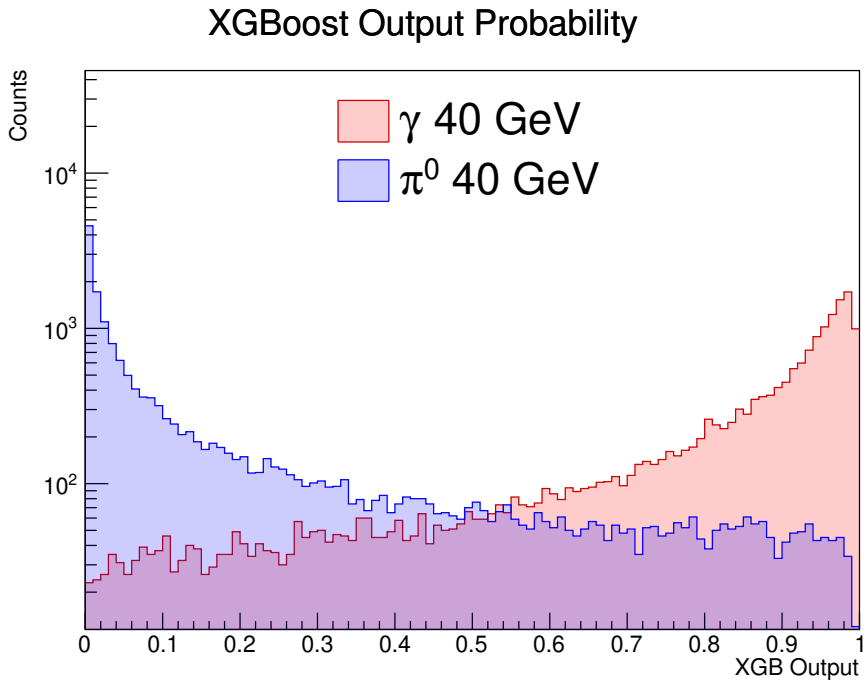


Figure 4.12: Output of the XGBoost model, for the two tested samples of photons and neutral pions.

lower π^0 energies, was removing those events with one of the two photons produced with very low transverse momenta, therefore missing the calorimeter with a test-beam geometry (which would otherwise be measured with a 4π detector). Finally, another excellent improvement was found by using CNNs architectures, which were originally designed for image recognition problems. By using as input the event-based energy deposition in each fibre as a two-colour image (for scintillating and Čerenkov channels) instead of custom variables, the networks were let free to identify their own shower patterns, resulting in significant improvements in the classification performances.

The results of the study are reported in fig. 4.14, which shows the background rejection (defined as the reciprocal of the False Positive Rate at a fixed efficiency for the photon signal) for several tested energy points. Good improvements are found by firstly including the clustering algorithm for both XGBoost and Deep Neural Networks, and even better ones with CNNs, in the energy range 10-60 GeV. For higher energies, the two photons from π^0 decays become more and more collimated, until they can hardly be distinguished.

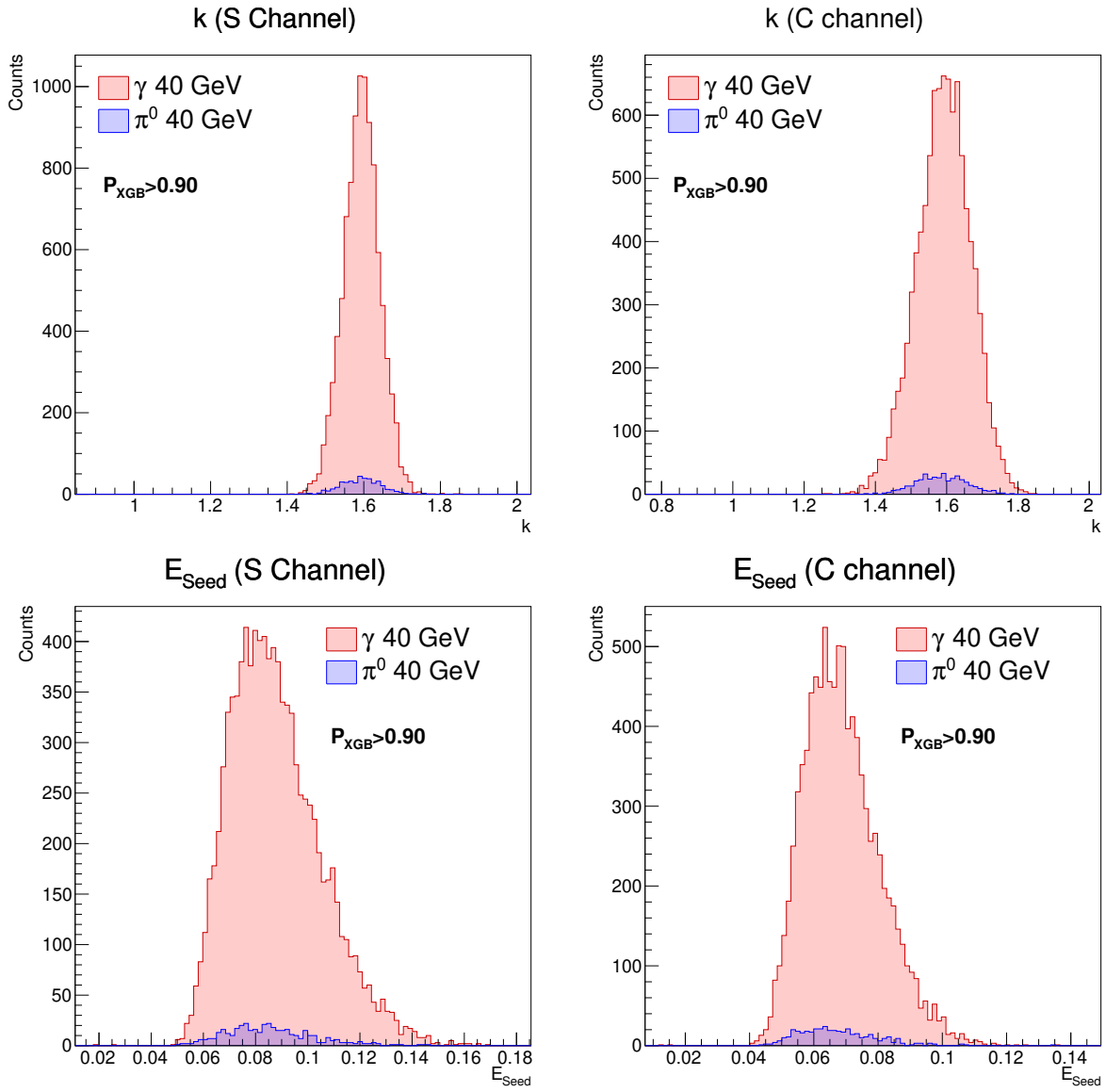


Figure 4.13: Examples of high-level variables distributions, obtained after imposing a cut on the XGBoost output probability to remove π^0 contributions.

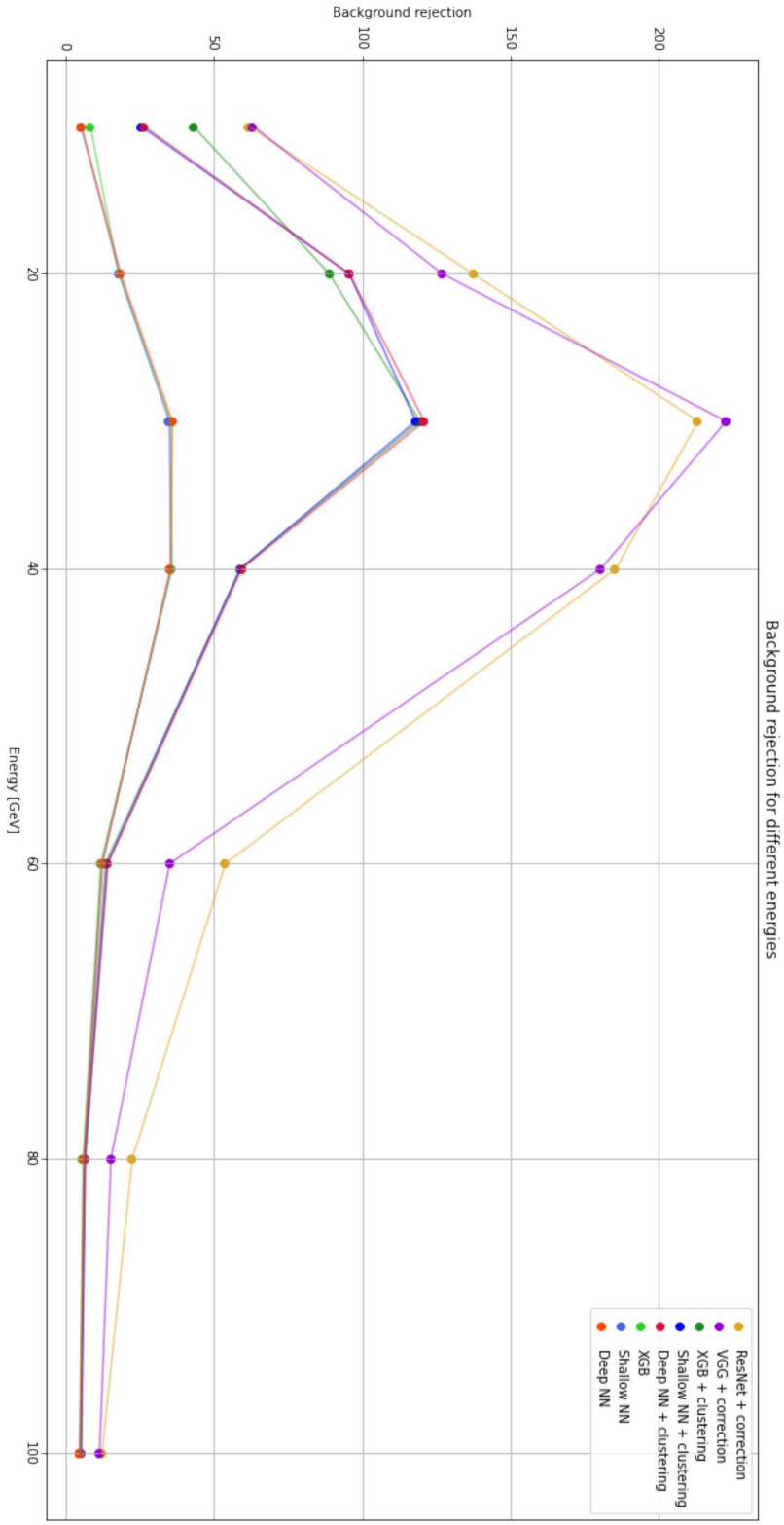


Figure 4.14: Comparison of the background rejection performances for different machine learning algorithms, and application of clustering methods, for different particle energies. Image taken from [131].

CHAPTER

5

PROTOTYPE CONSTRUCTION AND TEST-BEAM RESULTS

This chapter presents the current status of the HiDRa project at the time of this thesis' writing. The construction procedure, encountered challenges and the prototype's final design are here described. While only a brief discussion on the actual assembly of the calorimeter is presented, I was extensively involved in the laboratory work required for the construction of the detector. Since these efforts are primarily technical in nature, they are not documented in detail in this thesis. A first test with particle beams was undertaken during August 2024 with an only partially-completed calorimeter prototype, in order to have a first direct characterisation with real data before the detector completion. My own analysis of collected data will be reported. The presented results are still preliminary, as several topics are still work in progress. A second beam test was also done in early September 2025, but the data analysis is being performed at the time of writing and is not discussed here.

Figure 5.1 outlines the HiDRa prototype concept. It is based on a modular design consisting of 80 identical units, each made of 1024 fibres inserted in 2.5 m long stainless steel capillary tubes. Ten of these modules, shown inside the red area located in centre of the calorimeter, are instrumented with silicon photomultipliers, while, for the remaining ones, two PMTs are used to readout the two types of optical fibres separately.

The most innovative element of the project is the SiPM readout, that required a very careful study and precise implementation for the integration (see fig. 5.2). The capillary tubes for Čerenkov fibres were 2 cm shorter in the SiPM-instrumented modules, in order to avoid cross-talk between different type fibres. Two types of boards for the SiPM readout were designed. A "micro-pcb" board containing 8 SiPMs was used for Čerenkov fibres. Outgoing cables are guided through holes located in the second front-end "macro-pcb" board, which supports 128 SiPMs for the readout of scintillating fibres. In both cases, the signal grouping of eight fibres described in chapter 4 is performed analogically on the output of the SiPMs. For each HiDRa module, a total

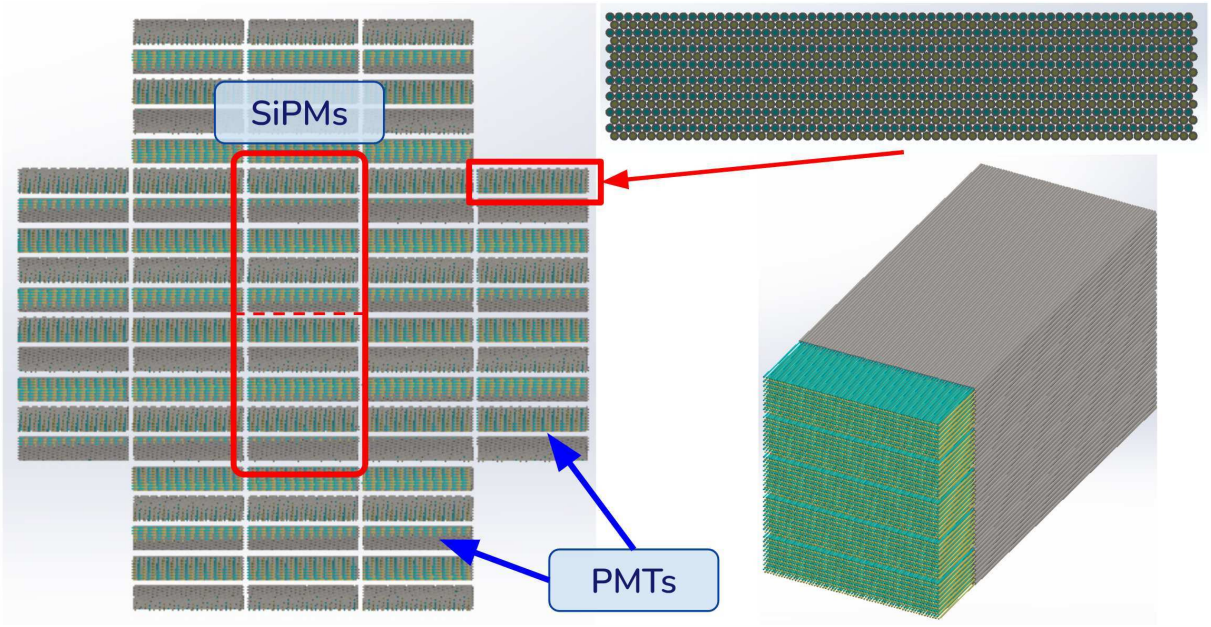


Figure 5.1: Rendered image of the HiDRa prototype modules, and their arrangement to form the entire calorimeter.

of 64 micro-pcb and 4 macro-pcb are used for the readout of all optical sensors. All these cables are then guided to a patch panel, simplifying the cable routing outside the calorimeter. The readout makes use of CAEN FERS A5202 [132] readout boards based on Citiroc 1A chips [133] for signal integration, connected to a PC for data storage and analyses. Each FERS system is able to collect 64 channels, therefore two FERS boards are used for each HiDRa module.

5.1 Construction of the HiDRa prototype

The actual construction of the HiDRa calorimeter started in November 2023, and took place for the entire duration of the project at the INFN laboratories in Pavia, Italy. Front-end boards for the SiPM readout were designed and assembled at the University of Insubria (Como, Italy) laboratories, before being transported for their integration in Pavia.

The scintillating and clear optical fibres described in chapter 3 were ordered and shipped to CERN in the form of few kilometres long spools. Help from the Bologna and Pisa groups was given for cutting them into 2.9 metres long pieces, ready to be inserted in the capillary tubes with enough fibre left for their coupling to optical sensors. Considering 80 towers for the construction of the HiDRa prototype and 1024 fibres for each tower, more than 237 km of optical fibres were used for the entire calorimeter, excluding spare fibres and those that were discarded for other issues. The stainless steel capillary tubes were ordered from Eastern Metal Industrial Co. (Hong Kong) [134] and shipped to the laboratory for initial measurements of the inner and outer radii (shown in fig. 5.3). Measurements were performed through a semi-automatic system installed on a 3D-movement machine, which measured the outer diameter of randomly sampled capillary tubes to ensure the correct size. An excellent uniformity was found for all measured capillary tubes, with just 4 μm RMS.

The construction of one module, depicted in fig. 5.4, starts with the selection of cap-

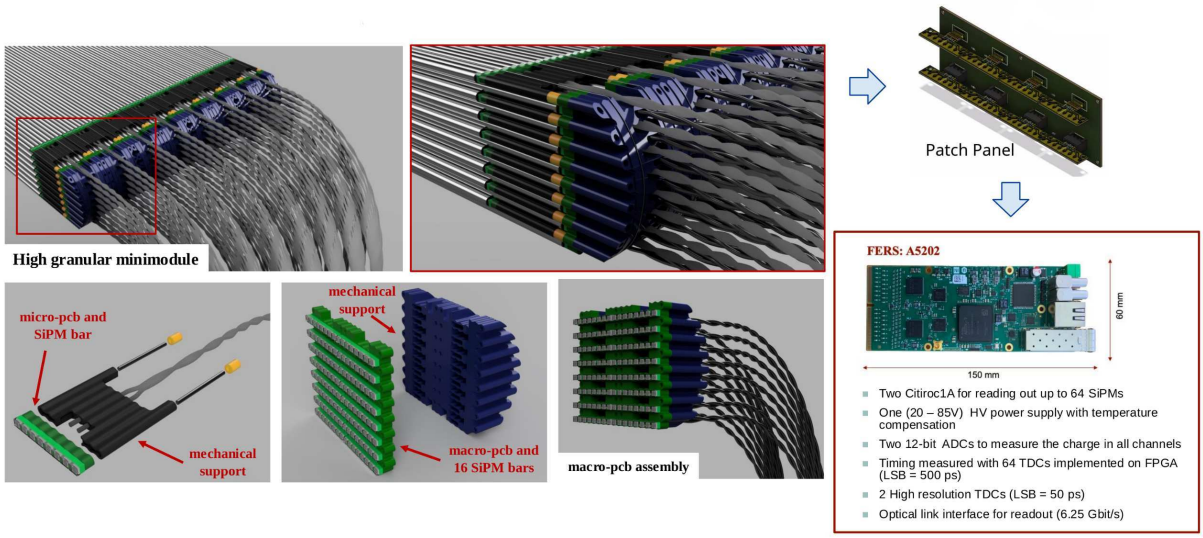


Figure 5.2: Rendered images of the SiPM readout system, including the two types of front-end boards, the patch panel for gathering all the cables, and the CAEN FERS readout system for acquiring the data.

illary tubes, which are simply rolled one-by-one on a dedicated plane surface. Those exhibiting kinks and other issues will have a less smooth movement, which makes them recognisable, and are therefore discarded. Of the remaining capillaries, 64 are aligned on a dedicated granite table instrumented with reference tools pointing to the correct module length and width for further checks that no tube would spoil the module's structure. The capillaries are here simply cleaned by wiping them with an alcoholic solution. Other procedures for the cleaning were evaluated, including NGL detergent [135] in hot water or ultrasonic cleansing, but they proved too costly and with little to no advantages, and were eventually dropped.

The rigid movement of the 64 aligned capillary tubes, that would form one module's row, was handled with a vacuum system installed on an overhead crane. The first row is simply positioned on a second granite table instrumented with other reference tools. All the other rows, from the second to the sixteenth, are first flipped and cleaned, and subsequently an adhesive layer of bi-component glue[1] is deposited on their surface. The row is then flipped again and moved on top of the previous layer with an half-tube offset to obtain the desired hexagonal-like tube disposition. The module thus fabricated is then pressed with aluminium plates for one night to ensure the correct curing of the glue over the entire capillary surfaces. About 4 people are needed for the construction of one module, with one session taking ~3 hours.

Once the module is completed, the semi-automatic measurement system is again used to evaluate the tower's height in several positions across its entire area, to ensure the integrity of its structure. An example of these measurements, consisting of an iterated scan with 9 points along the module's length and 10 on its width, is shown in fig. 5.5a. These measurements were performed to evaluate the consistency of the assembly procedure over the entire lifespan of the construction period. After an initial learning phase, the developed method proved very effective, allowing to reach a precision of the order of 10 μm over the entire towers area. Measurements of the av-

[1] Araldite 2011.

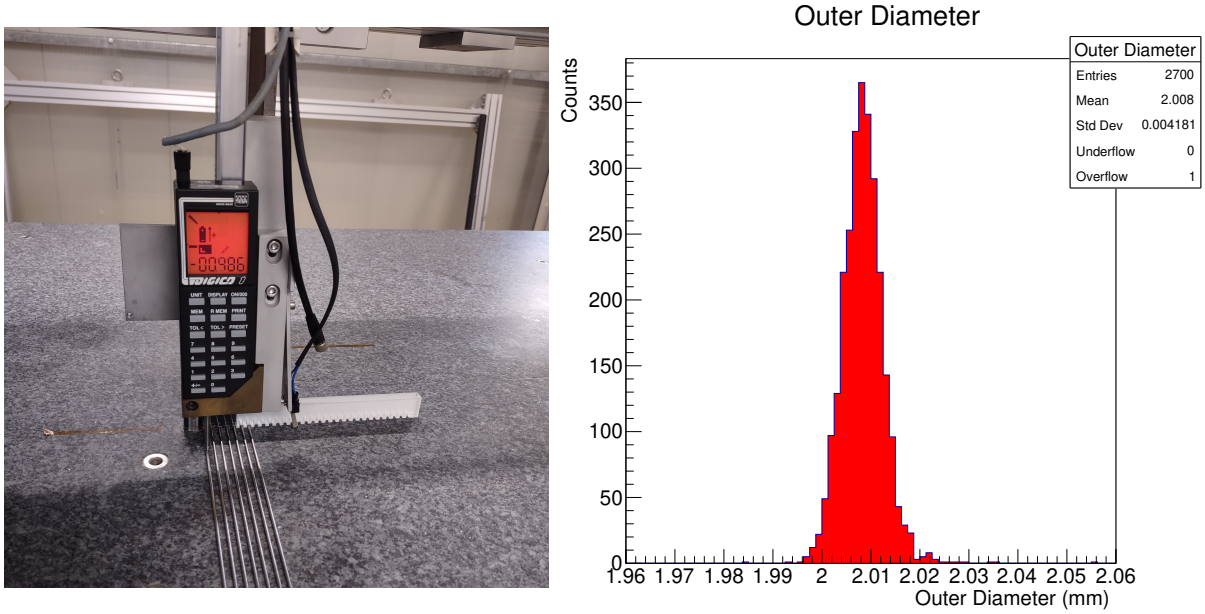


Figure 5.3: Semi-automatic measurement system used for the capillaries and modules qualification. On the right, example of measured sample of tubes.

erage module thickness, the minimum and maximum values, and the RMS of these measurements are reported in fig. 5.5.

A slightly different procedure was followed for the last ten modules, that were to be instrumented with SiPMs. A set of capillary tubes 20 mm shorter than the others were ordered, with the idea of separating the tubes rear ends to limit cross-talk between different-type fibres.

Once a module has been assembled, it is moved to a second room for the insertion of optical fibres, starting from the bottom with scintillating ones. This phase proved to be the most time consuming, as several issues were encountered. Some capillaries were found to be partially obstructed with industrial cleaning residuals, and had to be freed with iron wires. In a few cases, however, it was not possible to insert the fibres because of their fragility, and therefore some tube were occasionally left empty. The situation improved with a capillary tube treatment consisting of a compressed air gun system, which was used to remove the internal dust that would otherwise cluster when pushing the optical fibres inside. Also, obstructed tubes were discarded. A second problem was found with the scintillating fibres, that were observed to randomly show local bulges that prevented the insertion in capillaries, because of the very small difference between the fibre diameter and the inner capillary tube one. This issue made the actual fibre insertion much slower, as a significant amount of fibres from some spools manifested this problem, while others had excellent uniformity. The problem was reported to the fibres manufacturer, which proceeded to partially replace the missing items and revised the internal production chain.

Even for cases where the described issues did not manifest, the process of fibre insertion was generally found to be the most critical one, because of the very large amount of time needed to load the fibres. At least 10 hours of person-power were required for completing one module, with large operator-to-operator variations, posing a critical difficulty for such a small collaboration. Automatic insertion systems were not considered for limited budget reasons, and also because of the described encountered problems.

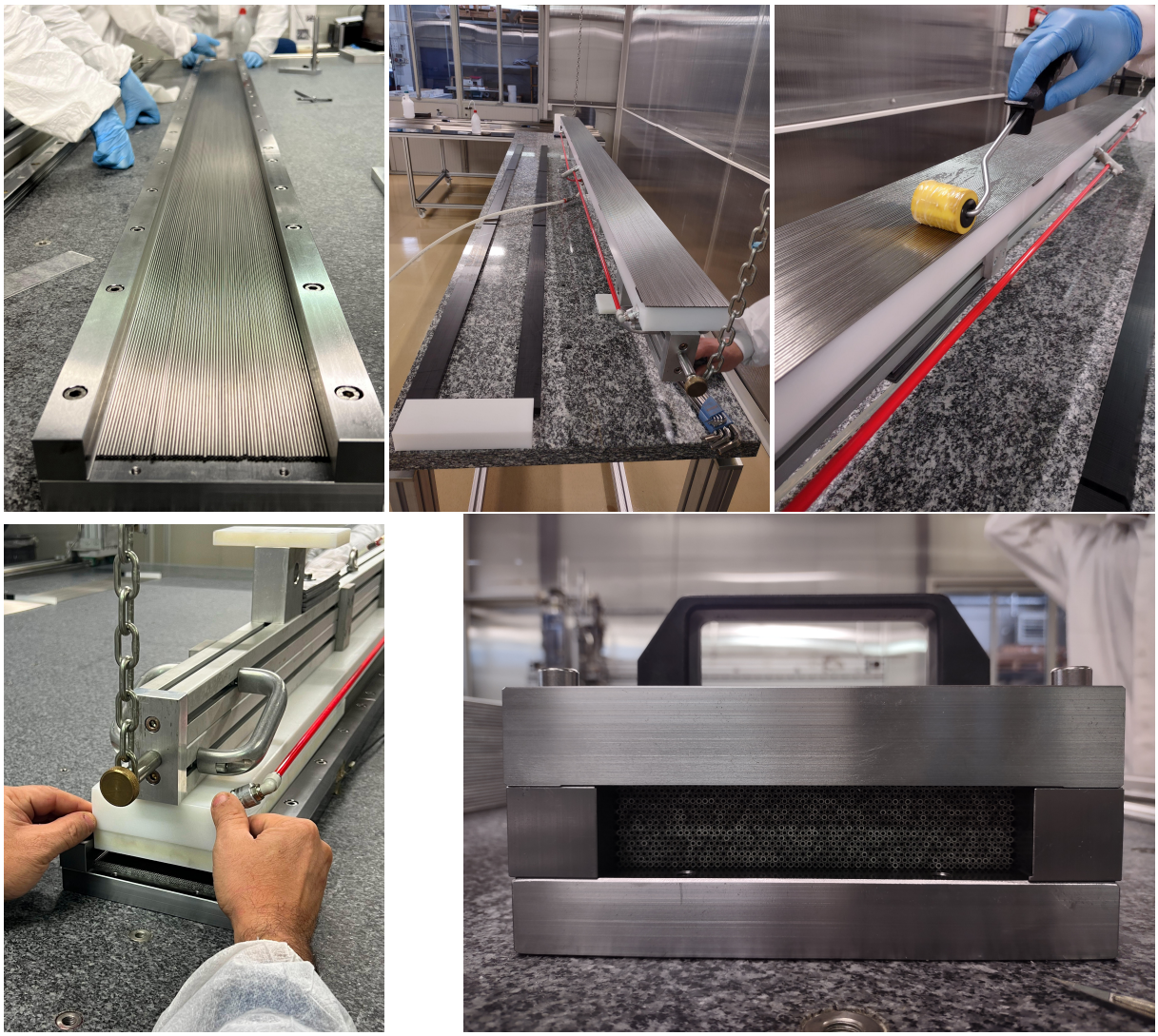
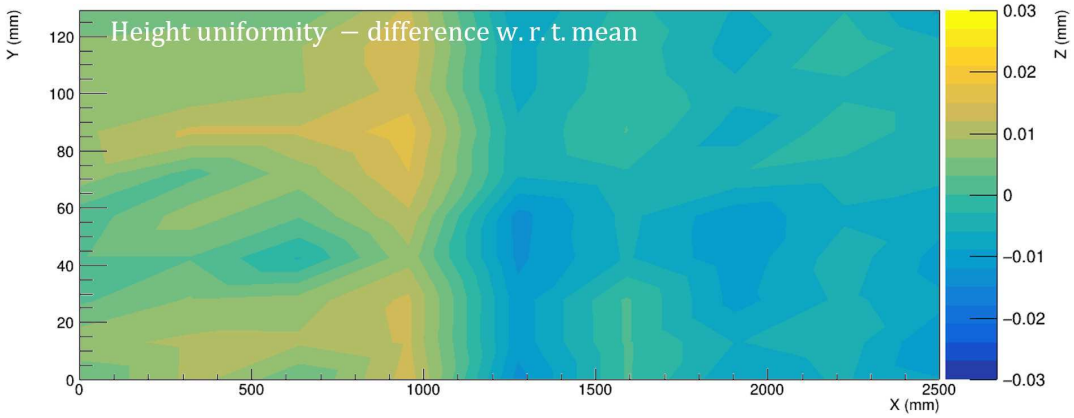


Figure 5.4: Steps of the HiDRa modules construction.

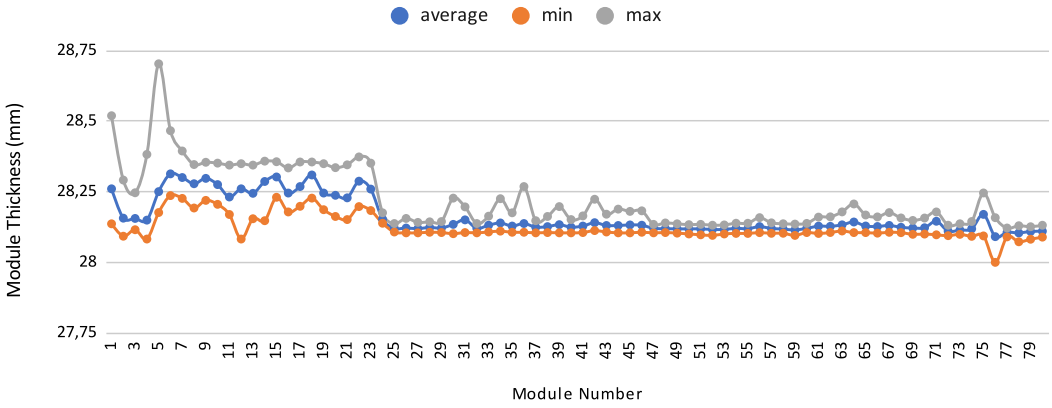
If the capillary-based design had to be chosen for the IDEA detector, some automatic method will nevertheless have to be implemented for such a large scale detector construction.

Concerning the light sensors integration, for the 70 PMT modules with PMT readout, the scintillating and clear fibres are extracted from the rear end of the calorimeter and separated into two different bundles. The fibres are also glued at the opposite end, in front of the calorimeter, to avoid any further movement inside the tubes. Each bundle of fibres is first glued to a mechanical support to keep them fixed (shown in fig. 5.6), followed by mechanical polishing. A transparent optical grease is then put between the fibres end and the PMTs which are connected to the mechanical support. A yellow optical filter (Kodak Wratten 2 #3 [117], also used in the previous prototype) is also placed before the PMTs for the scintillation channel, between two layers of optical grease.

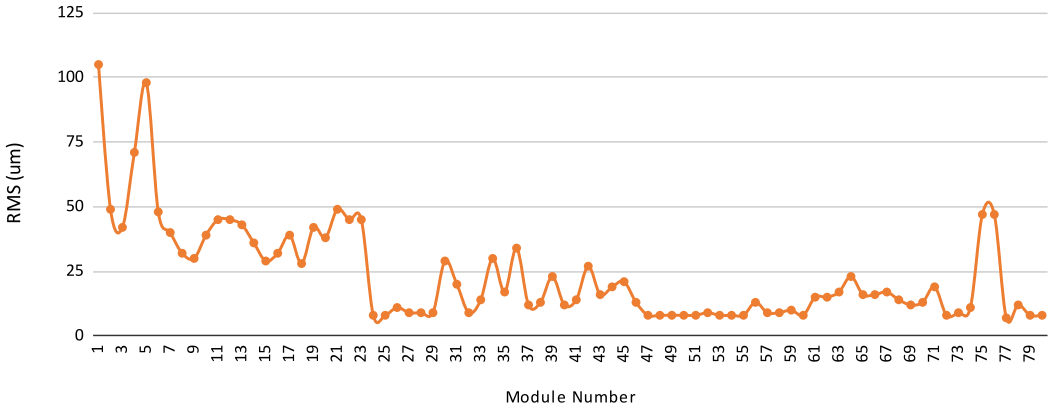
For the SiPM-based readout towers, a different method is followed, because of the 2 cm length difference making it difficult to access the rear volume of the shorter tubes. Scintillating fibres, that are placed in the longer capillaries, are firstly inserted until they are sticking out for about 1 mm. Some glue is then deposited on the other side, to prevent the fibres from moving out. The rear ends of the fibres are then polished



(a) Example of planarity measurement scan of one module, taken from [136].



(b) Average, maximum and minimum measured thicknesses of each built HiDRa module.



(c) RMS of the measurement scan taken on each module.

Figure 5.5: Measurements of the HiDRa modules' structural uniformity.

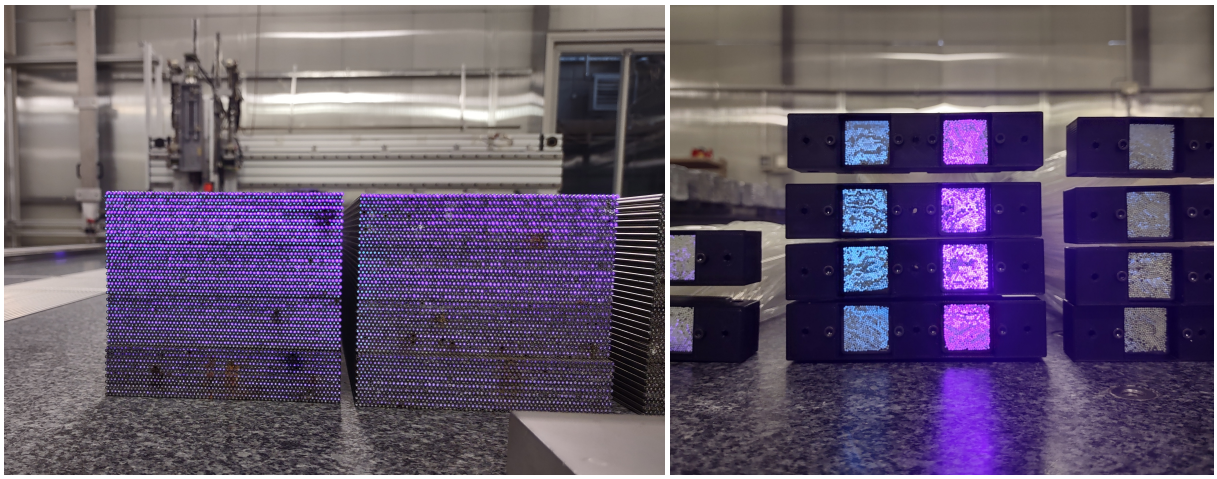


Figure 5.6: Front and back of HiDRa modules with PMT readout. An UV lamp was placed on the opposite side, to distinguish between scintillating (light blue) and transparent clear fibres (violet).

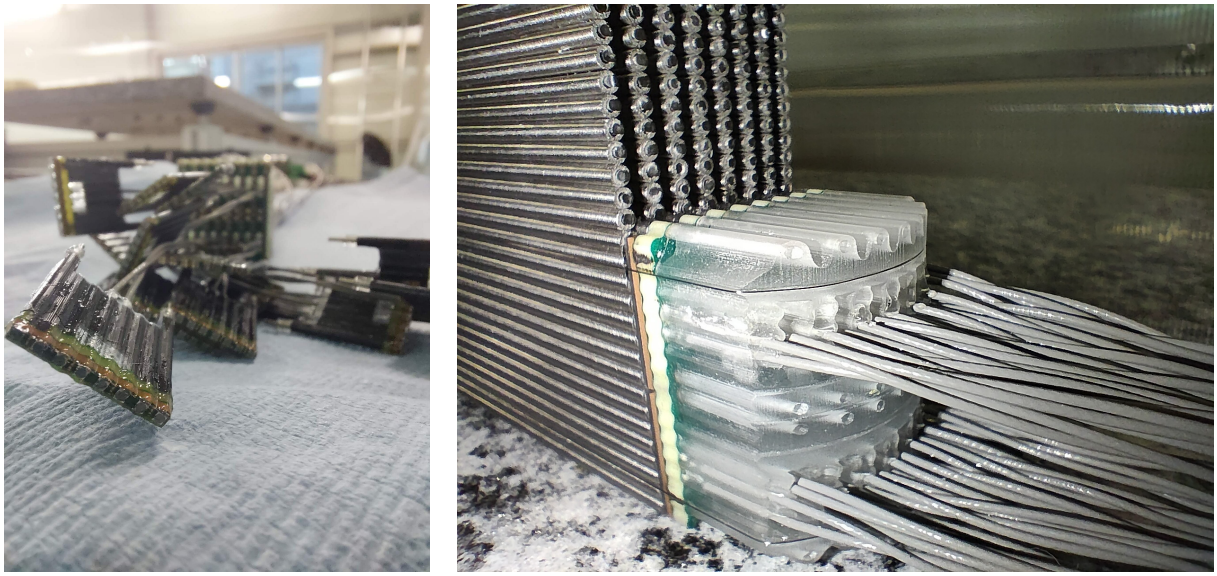


Figure 5.7: Details of the mini-frontend boards (8 SiPMs each) and large ones (128 SiPMs) integration on the ten modules with SiPM readout.

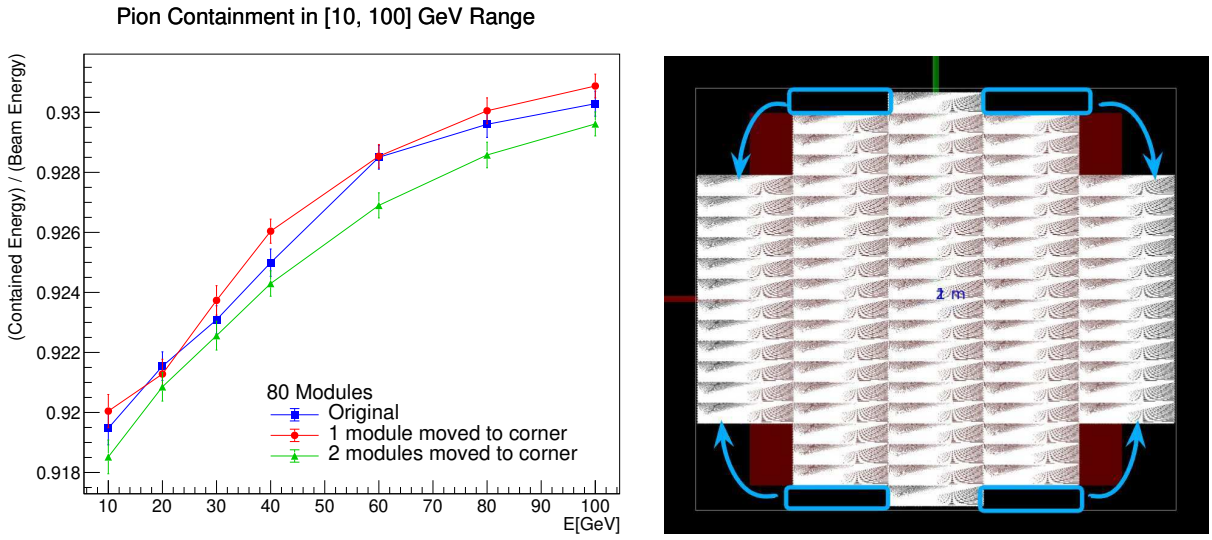


Figure 5.8: Average containment for pions of different energies, when moving 1 or 2 modules to the corners of the HiDRa prototype. On the right, the alternative option with one relocated module is shown.

until they reach the edge of the capillary. Čerenkov fibres are conversely inserted immediately in the capillaries, and then polished once they are fully inserted. A 2 cm aluminium spacer is pushed in the gap between the upper and lower tubes, to align the clear fibres to the capillaries in the middle. Also in this case, some glue is deposited on the other side. Finally, iron wires are crimped on the front of the module and run along the entire module's length, in order to fasten the macro-pcb boards and their SiPMs to the optical fibres.

5.1.1 Final design

With the advancement of the HiDRa prototype construction, the identified construction method proved very reliable from the structural point of view. The build towers were found to be solid, with the tube disposition making it possible to joint adjacent modules without any cracks. The achieved construction precision is such that it is indeed difficult to distinguish by eye the edge between two modules, which should allow minimising the constant term in the energy resolution, having a regular sampling fraction over the entire calorimeter surface.

In the initial design ideas of HiDRa, five modules would have been tied into a macro-unit, in order to keep the entire tube geometry stable. The whole prototype would have therefore consisted into sixteen macro-units, with the geometry shown in fig. 3.23 with 80 modules. Because of the effective assembly technique, the modules could instead be precisely handled as independent units. Figure 5.8 shows the average expected containment for pions of different energies, obtained by means of the Geant4 simulation, by moving one or two modules to a different place. The general guiding rule was obtaining a shape which resembled as much as possible a circular one, with the constraint of the different horizontal and vertical modules sizes. A very slight improvement was found by moving one module from the first and last rows to the nearby corner, which was the closest point from the interaction point left empty. On the other hand, moving two towers to that location made the HiDRa calorimeter sizes along the $\widehat{X}$ and $\widehat{Y}$ directions too uneven, with a slight reduction of the overall containment. The first of the



Figure 5.9: Prototype assembled for test beam in 2025.

two alternative geometries was therefore selected as the final one for the construction of the prototype. A picture of the construction status taken at the end of August 2025, before shipping the calorimeter to CERN for a beam test, shown in fig. 5.9. At the time, 70 modules were used, 8 of which being instrumented with SiPMs.

5.2 Results from the 2024 beam test

A first experimental test of the HiDRa calorimeter was done in summer 2024, with the modules that were completed and available at the time. Of the built 40 modules, 36 were used for testing. Additional PMTs had not been ordered yet, so the 72 PMTs used for the RD52 calorimeter were mounted, 36 for scintillating and 36 for Čerenkov fibres. The high-granularity feature was still under development at the time, as the SiPMs had not been shipped yet, and the readout boards were not finished. The so-formed prototype was therefore colloquially called DRAGO (Dual-Readout Almost Granular Object). This prototype had a square-like shape, consisting of a 3×12 matrix of modules, with dimensions 38.7×33.9×250 cm^3 (see fig. 5.10).

The beam test took place at the H8 beamline of the SPS North Area, at CERN. Before

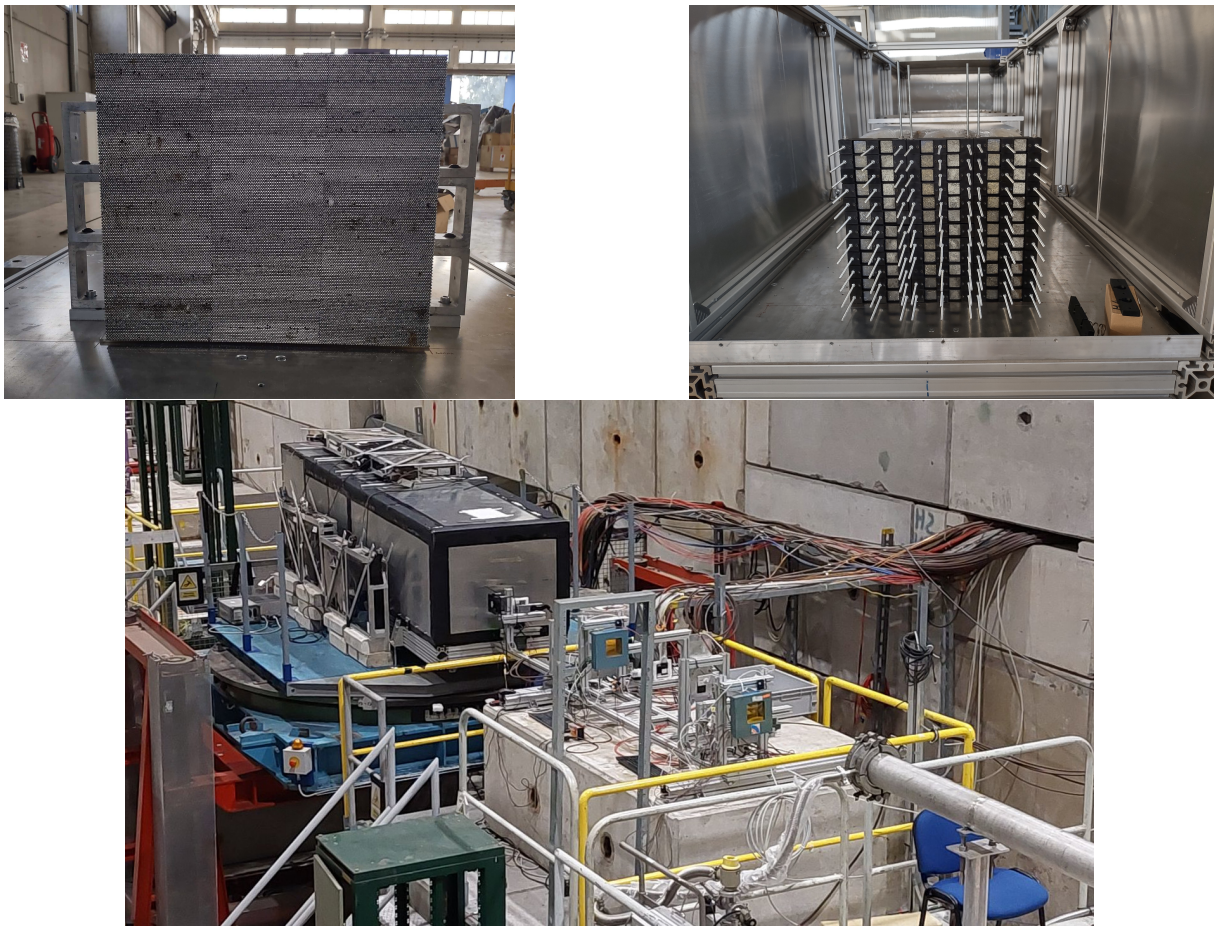


Figure 5.10: Front and rear faces of the DRAGO prototype, and its position in the box located along the H8 beamline with ancillary detectors.

being shipped, the calorimeter was put in a box able to blacken out the inside volume, and avoid any source of light contamination. Dedicated patch panels were used for extracting signals from the PMTs to the cabling and the data acquisition systems located in the nearby control room. The experimental setup is shown in fig. 5.10. Three upstream Čerenkov threshold counters were available, with either He or CO_2 gases whose pressure was set to optimise the particle identification capabilities depending on the beam particles momenta, mainly at the threshold between electron and pion Čerenkov production. Two delay wire chambers (DWCs) were used to measure the impact point position of incoming particles on the calorimeter's surface, with a ~mm precision. Two 4×4 cm^2 scintillator plastic tiles were placed between the DWCs, and used for triggering purposes, by requiring a logical AND on their signals. Finally, a preshower detector consisting of 5 mm lead plate and a scintillator was located 15 cm from the front face of the calorimeter. Muon contamination inside the beam was identified through a scintillator counter located downstream the beamline, after about 20 m of concrete walls to absorb all other particle contributions. The calorimeter was vertically tilted by $2.5°$ using dedicated support of the box. Different horizontal rotations around the $\widehat{y}$ axis were tested by moving the rotating platform on which the calorimeter was placed. The following analysis focuses on data taken with a $2.5°$ angle in the horizontal plane, which was also used for calibrating the detector.

Additional ancillary detectors were added to measure the contribution of shower

particles escaping from the calorimeter volume. A set of 15 leakage counters, consisting of $50 \times 50 \times 12$ cm^3 plastics scintillator, were positioned on the sides of the calorimeter, 4 per side (three on the upper side, as one leakage counter was broken). An additional scintillator volume was positioned about 50 cm behind the rear face of the calorimeter box, and was intended to measure the longitudinal leakage contributions.

5.2.1 Calibration

The reconstruction chain, from the raw data to fully calibrated events, required several intermediate steps. Signals from the calorimeter and ancillary detectors passing the trigger system were first filtered and digitised, in order to be stored in the form of ADC counts in simple text files. These files were later converted into a first set of ROOT files containing the information from each subdetector. Among my contributions to this data acquisition campaign was taking care of extracting the correct equalisation and calibration of the modules, and analysing the preliminary results to spot possible issues.

A first equalisation run with 20 GeV positrons was performed by shooting particles at the centre of each of the 36 calorimeter towers. It was estimated through simulations that about 70% of the energy deposited by electromagnetic showers was contained inside the central module, and the remaining 14% into the modules immediately above and below the central one. Only contributions at percent level would be deposited in the remaining calorimeter towers. The PMTs voltages were set by looking at charge distribution histograms from an online monitoring framework, by requiring that the peaks of the distributions were low enough to stay well inside the overflow limit when scaled to the maximum expected particles energy to be used of 120 GeV. An equalisation constant for each channel was then taken by imposing a first gaussian fit on the raw signal distribution to identify the peak value (in ADC counts). A second fit within a more strict range, taken as the mean value minus 1.5 times the RMS of the first fit, was used to obtain a more precise value of the peak position by excluding contributions from pions and muons contamination which may have altered the first fit.

In previous test beam experiences, pedestal data were saved using a random trigger being acquired every ten "physics" ones (meaning events with a real beam particle causing the trigger to be activated). This allowed to access pedestal event information per each run of data acquisition, imposing a mask requirement, with the exact detector conditions of physics data used in the analysis. However, problems with the software framework were found during this campaign, and therefore dedicated runs without beams were taken from time to time to study the pedestal values and their variations over time. With the obtained pedestal values p_i and peak values q_i for 20 GeV positrons, the equalised signal for any event e was then taken as

$$E_{e,i}^{Eq} = \frac{A_{e,i} - p_i}{q_i - p_i} \tag{5.1}$$

for each calorimeter tower i (both scintillating and Čerenkov), and given signal in ADC counts, $A_{e,i}$, in that tower.

Two final calibration constants for the entire calorimeter, $c^S_{adc\to\, GeV}$ and $c^C_{adc\to\, GeV}$, used to set the electromagnetic scale responses for the scintillation and Čerenkov channels, were obtained by dividing the nominal beam energy for the sum of the equalised

Table 5.1: Ancillary detectors requiremets for positron selection.

Anc. Detector	Cut value [ADC counts]	Comments
C2	> 160	
Preshower	> 550	Used for calibration
Muon counter	< 200	
Tail catcher	< 300	
Leakage counters	$\sum_i^{i\neq 20} L_i < 5000$	
Delay wire chambers	$\lvert XDWC2 - XDWC1\rvert < 5$ [mm] $\lvert YDWC2 - YDWC1\rvert < 5$ [mm] $\lvert XDWC2\rvert < x, \quad \lvert YDWC2\rvert < y$	x, y set run-per-run

responses of the fifteen innermost towers of the calorimeter

$$c^{S,C}_{adc\rightarrow\, GeV} = \frac{20\,\mathrm{GeV}}{\sum_i E_i^{Eq}}. \tag{5.2}$$

For any event in the physics runs, the energy contribution from each tower is therefore calculated as the product of the equalised signal in ADCs and the obtained calibration constants.

5.2.2 Electromagnetic performances

In order to estimate the energy response of the DRAGO calorimeter to electrons, a beam of positrons with energies from 10 GeV up to 120 GeV was steered into the centre of the prototype. Positrons were selected, out of other particles which may contaminate the beam composition, through a set of requirements posed on the ancillary detectors data, listed in table 5.1. A first cut was posed on the minimum ADC value produced by the C2 Čerenkov counter, $C2 > 160$, which allowed to reduce heavier particles contributions, mostly muons and other hadrons. The other two Čerenkov counters proved not to be useful. The Helium chamber could not reach the needed gas pressure to obtain correct particle identification, and the other CO_2 chamber did not improve the selection once the cut on C2 was already set. A lower cut on the preshower detector signal was initially set during the calibration procedure, in order to exclude events contributing less than the average signal deposited by three MIPs produced in the lead plate absorber (the primary positron and the e^+e^- pair produced in the first conversion). However, it turned out during the following analysis that a significant amount of electrons were not showering in this detector and were therefore removed. Since a more efficient selection could be reached through other ancillaries, it was then decided to not use the preshower further.

An efficient selection from muon contamination was obtained by requiring an absence of signal in the muon counter located downstream after the concrete walls. Similarly, a cut on the tail catcher allowed to remove pion events in which a significant amount of energy was deposited well inside the calorimeter. In both cases, only events in which the ADC count was very close to the pedestal was selected.

Another useful cut to remove pions from the final positron samples was set on the total signal deposited inside the leakage counters. As will be better detailed in section 5.2.3, the average containment for pions inside the DRAGO prototype is 88%, which means that a significant amount of energy escapes laterally. By setting an upper limit

on the total signal from these ancillary detectors, pion events could be efficiently removed. From the total signal, one particularly noisy leakage detector, located below the calorimeter opposite from the beam direction, was removed.

Finally, sets of requirements were posed on the DWC information. Firstly, once they were calibrated, a limit of 5 mm from the coordinates differences provided by both detectors was set, to remove events with large beam divergence. Furthermore, the beam position was found to shift for different beam particles momenta. It was therefore decided to adapt a series of cuts on the coordinates of the second DWC, closest to the calorimeter, to remove lateral tails of the beam. These cuts were set by keeping a fixed efficiency of 95% on the remaining number of events after all previous cuts had been applied.

Examples of the effects of presented cuts on the total energy measured by the calorimeter for two beam energy samples, at 20 GeV or 100 GeV, are shown in fig. 5.11. While the proposed selection proves able to remove most of remaining muon and pion components, that can be clearly seen at higher beam momenta, the shown distributions are far from gaussians, with a shape distortion that becomes clearer as the energy increases. In order to understand the reason of this behaviour, the measured energy dependences over several variables were investigated. The clearest dependence was found with respect to the Y coordinate, which was provided by the second delay wire chamber, the closest to the calorimeter. Examples of these dependences, obtained for both calorimeter channels, are reported in fig. 5.12 for 100 GeV positrons entering the detector. The double peak observed in the scintillation channel at higher energies, and not in the Čerenkov one, could be explained by the better resolution in the first channel and with improving relative resolution at higher energy.

Several approaches were followed to understand the reason for the observed distributions. A first set of checks was done on the equalisation and calibration procedure. These were hence repeated by restricting to a tighter range on the vertical axis, in order to only consider those electromagnetic showers that were well centred inside the tower under test. However, minimal changes were found. The possible mis-calibration of the three towers producing most of the signal (Towers T00, T11 and T15 as shown in fig. 5.13) was also disfavoured by a further test, which consisted in assigning a different weight to each tower's signal until a flat response over the Y axis could be obtained. However, it turned out that these weight could be significantly different from 1, and shifted to higher or lower values the measured energy for more peripheral showering particle positions in the upper and lower modules.

In order to study in detail the response of each tower, a scan on the profile of measured energy over the Y coordinate was performed, with two examples shown in fig. 5.14. In each plot, the nominal hit tower and the two modules next to it are drawn. In addition, the sum of the three towers under study, and the total energy measured by the calorimeter are reported. Interesting results were found, as in the central tower T00, as well as in several others, a strong dependence on the Y position was observed. On the other hand, some other towers featured a flat response when profiled over the Y coordinate. In general, a flat response was found when the hit tower featured a well-defined "pleateau", that should be expected in cases where electromagnetic showers are located in the exact centre of the cell. The same study was also performed when profiling over the horizontal X coordinate, but any of these features was found, also because of the significantly larger size of the calorimeter modules along that direction. A study on the different batches of optical fibres being used in each tower of the calorimeter was

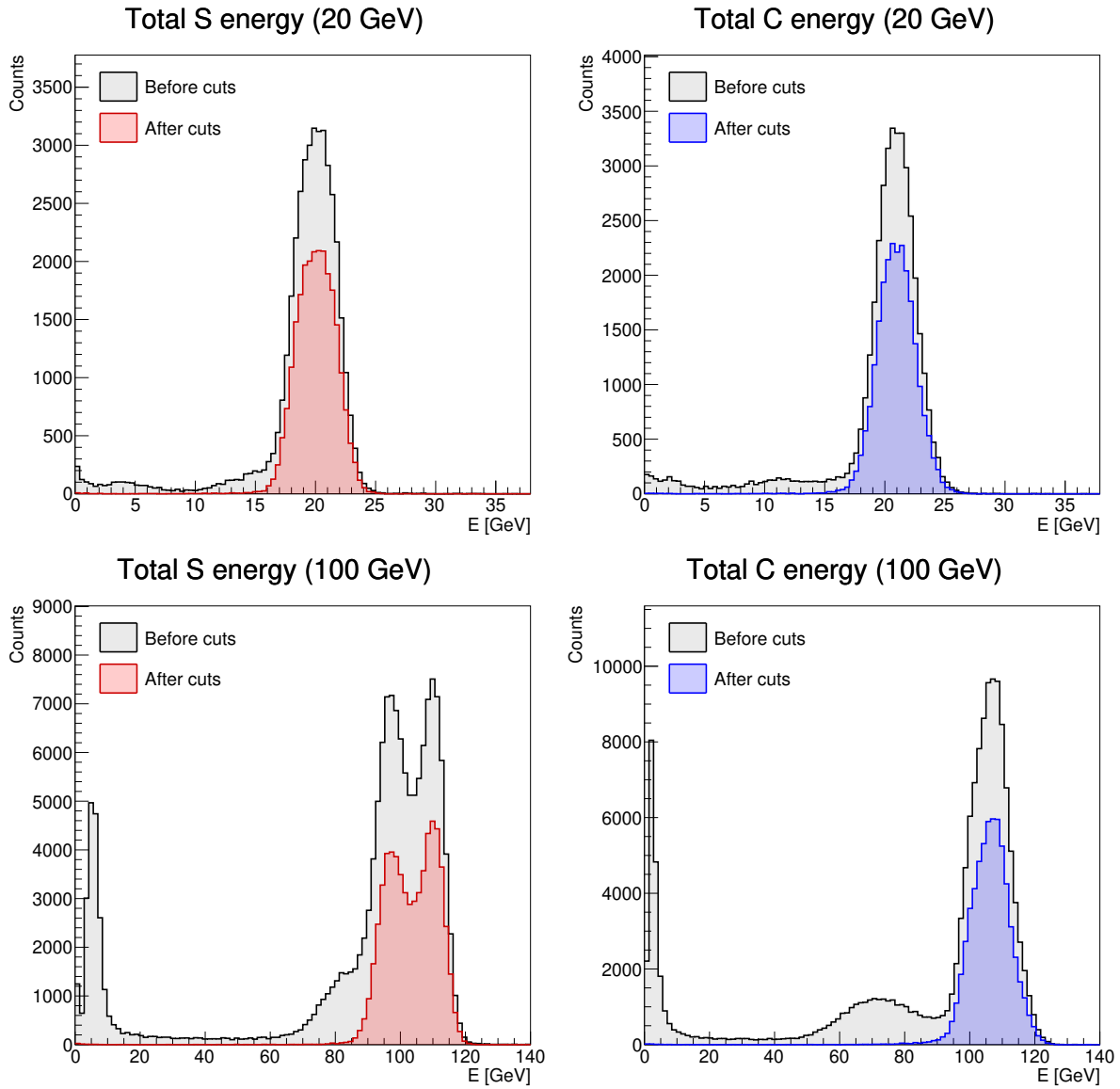


Figure 5.11: Total measured energy in the scintillation and Čerenkov channels using electron beams. Distributions are shown before and after applying the selections from table 5.1.

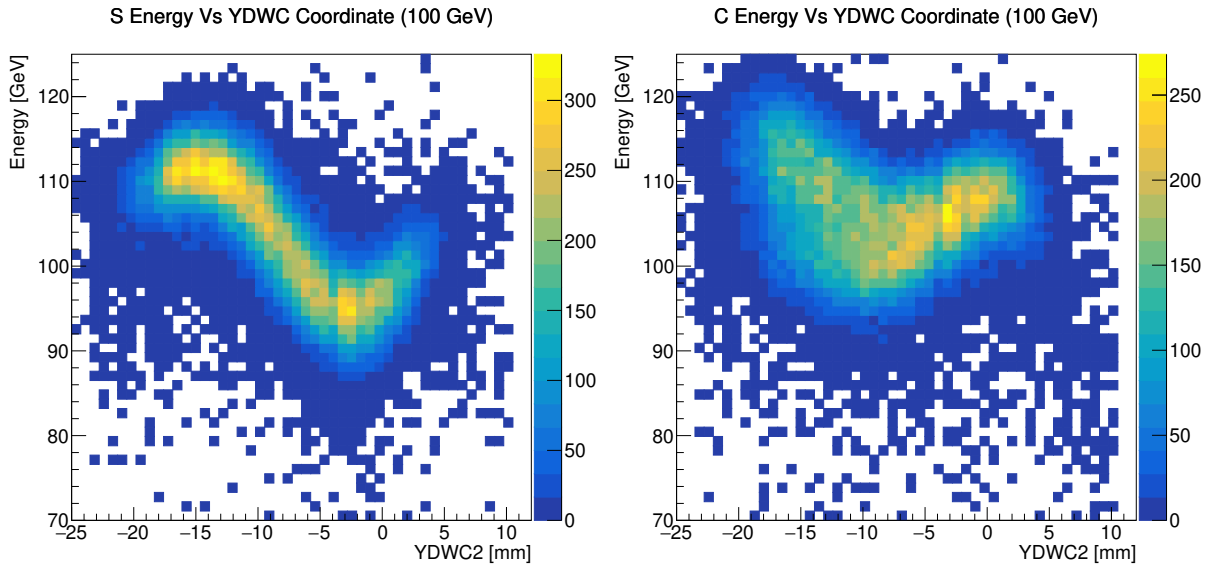


Figure 5.12: Dependence of the energy in the scintillation or Čerenkov channels, on the vertical coordinate provided by the DWCs.

TS55	TC55	TS54	TC54	TS53	TC53
TS45	TC45	TS44	TC44	TS43	TC43
TS35	TC35	TS34	TC34	TS33	TC33
TS25	TC25	TS24	TC24	TS23	TC23
TS16	TC16	TS15	TC15	TS14	TC14
TS17	TC17	TS00	TC00	TS13	TC13
TS10	TC10	TS11	TC11	TS12	TC12
TS20	TC20	TS21	TC21	TS22	TC22
TS30	TC30	TS31	TC31	TS32	TC32
TS40	TC40	TS41	TC41	TS42	TC42
TS50	TC50	TS51	TC51	TS52	TC52
TS60	TC60	TS61	TC61	TS62	TC62

Figure 5.13: Ordering scheme for each tower of the DRAGO prototype. Scintillating and Čerenkov PMTs belonging to the same tower have the same number.

performed as well, but later excluded as a possible cause for the different localised response. In fact, fibres from the same batch were found to have been placed in towers showing very different behaviours, disfavouring this hypothesis.

The remaining hypothesis that was proposed was the presence of local dishomogeneities in some PMTs responses. These local non-uniformities may spoil the resulting energy measurements if the activated optical fibres are directed to a position of the PMT windows producing a lower or higher signal than the rest of their surfaces. An attempt to replicate the possible effect of PMT response differences was also performed through the Geant4 simulation. The test consisted in reducing the probability of optical photons to reach the end of optical fibres with a varying parameter, from 5% up to 25%, for the fibres in the first and last two or three rows of each module. The underlying assumption was a reduced PMT sensitivity in the regions close to the borders of the sensor window, and that the optical fibres sticking out from the calorimeter modules kept, approximately, their location after being bundled. While this simulation effectively produced a varying response with the Y coordinate, being lower in the re-

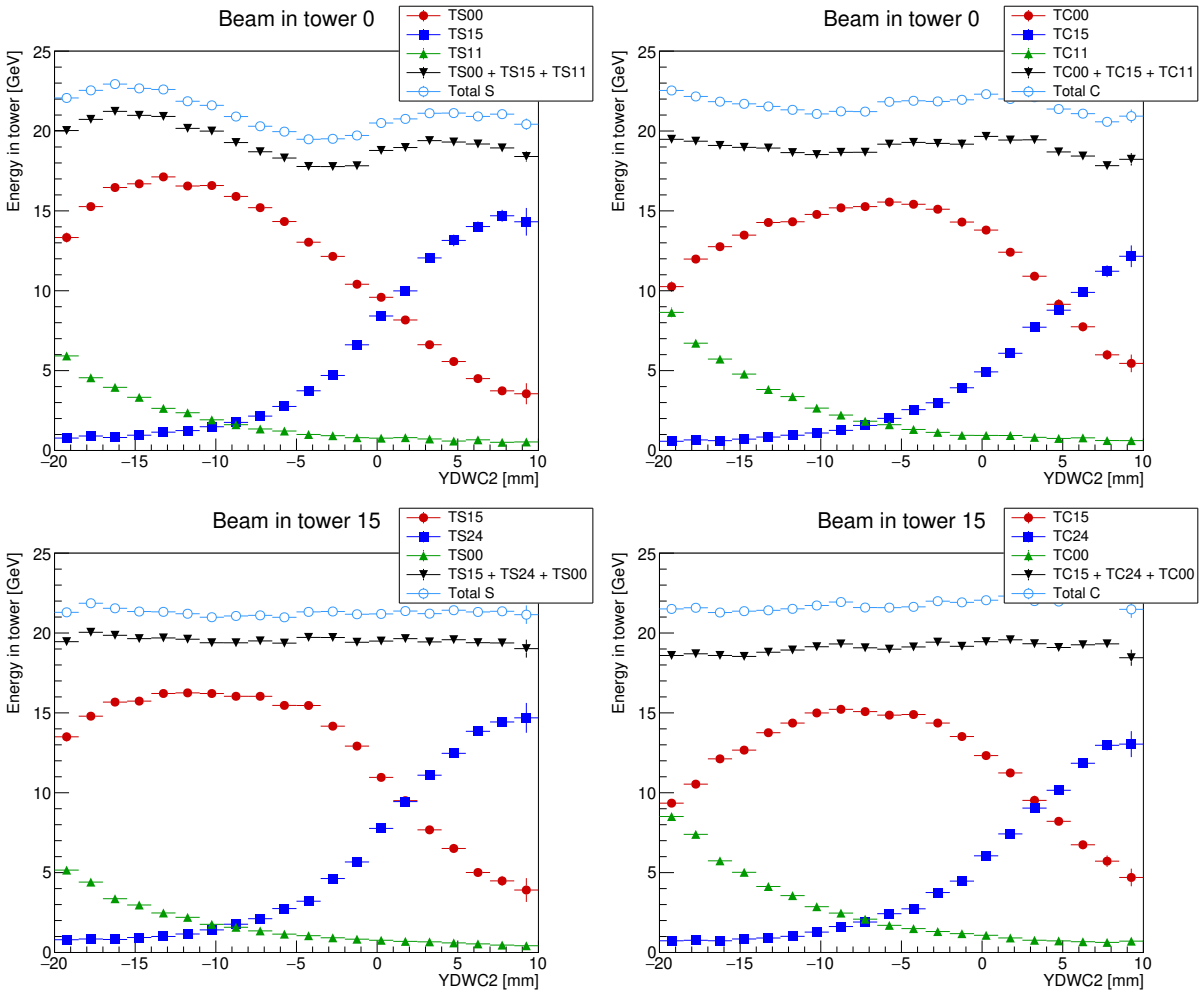


Figure 5.14: Profiles of two different towers responses over the Y coordinate. Data were taken with a 20 GeV electron beam steered into tower T00 (the nominal centre of the calorimeter) and tower T15. The scintillation channel is drawn on the left, while the Čerenkov one is shown on the right.

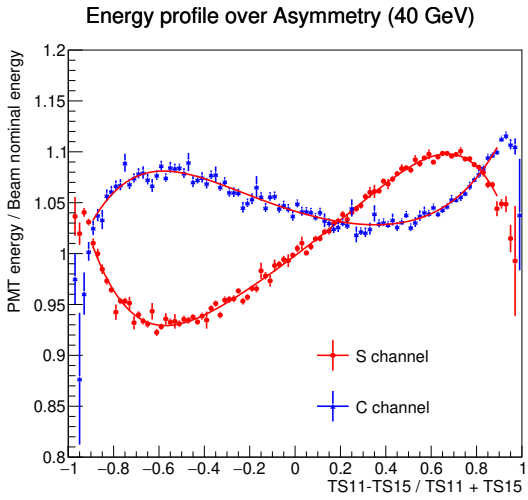
gions between the edges of two towers, it did not manage to reproduce correctly the observed data.

Correction procedure

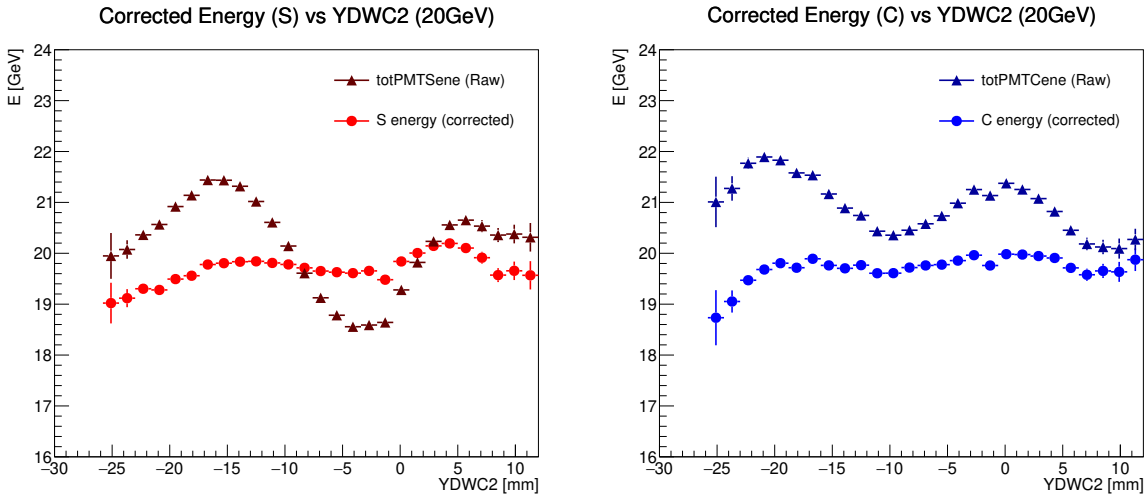
In order to restore faultless energy measurements and evaluate the electromagnetic performances of the DRAGO prototype, a correction procedure was established. This correction allowed to evaluate the linearity response of the detector, and its resolution on the particle energies, by trying to remove the dependence on the impact point position, or at least reducing it as much as possible. An auxiliary variable called asymmetry (A) was introduced to describe the local dependency of the signal over the vertical coordinate,

$$A_S = \frac{TS11 - TS15}{TS11 + TS15} \quad A_C = \frac{TC11 - TC15}{TC11 + TC15} \tag{5.3}$$

with TS and TC the energy contribution in the scintillating and Čerenkov signals respectively, in the corresponding tower. For particles entering at higher coordinates, the tower above the central one (see fig. 5.13) will measure a higher fraction of the total



(a) Five-degree polynomial fit on the energy profile over the asymmetry variable.



(b) Profiles of measured energy over the y coordinate, before and after the correction.

Figure 5.15: Correction procedure of the measured electromagnetic showers energies.

energy with respect to the one below. By measuring this asymmetry, a local description of the energy dependence at different coordinates could be obtained. Figure 5.15a shows the normalised energy dependence, obtained for 40 GeV positrons, on the asymmetry variable for both channels. Different dependences were found in the two cases, in agreement with the different behaviours obtained by the towers responses. As the dis-homogeneity effects are expected to be energy-independent, these profiles were fitted with a 5-degree polynomial $f_{S,C}^{40\ GeV}$, at a fixed working point with 40 GeV positrons. The obtained functions were then used to correct the measured signal at all remaining energy working points by applying

$$E_S^{\text{Corrected}} = \frac{E_S^{\text{Raw}}}{f_S^{40\text{ GeV}}(A_S)}, \quad E_C^{\text{Corrected}} = \frac{E_C^{\text{Raw}}}{f_C^{40\text{ GeV}}(A_C)} \tag{5.4}$$

for the measured asymmetry values (A_S, A_C) calculated event-per-event.

The described correction's effect can be seen in fig. 5.15b for 20 GeV positrons in scintillation and Čerenkov channels. In both cases, the corrected data are shifted towards

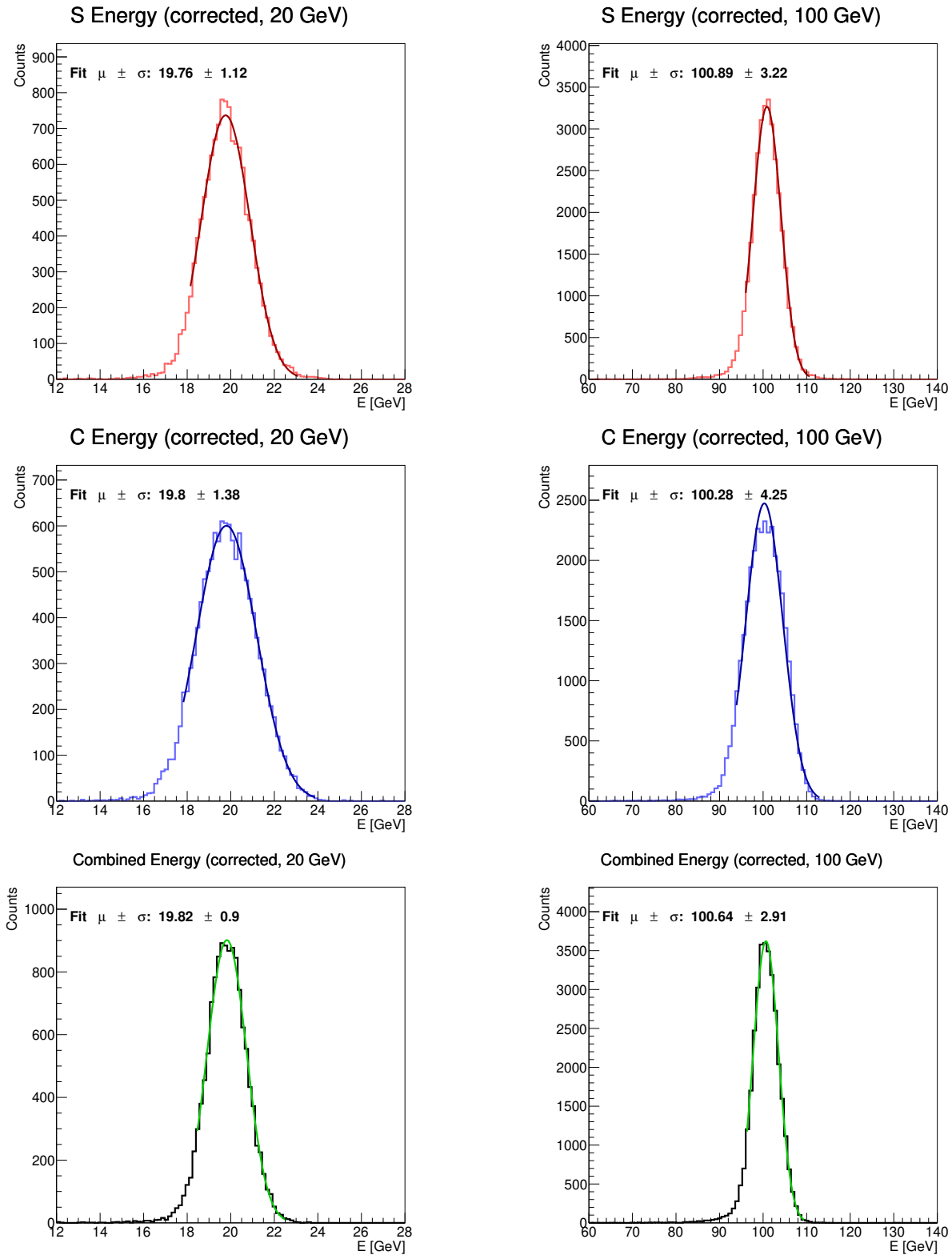


Figure 5.16: Corrected measured energy for 20 GeV and 100 GeV positrons, in the scintillation and Čerenkov channels, and combined.

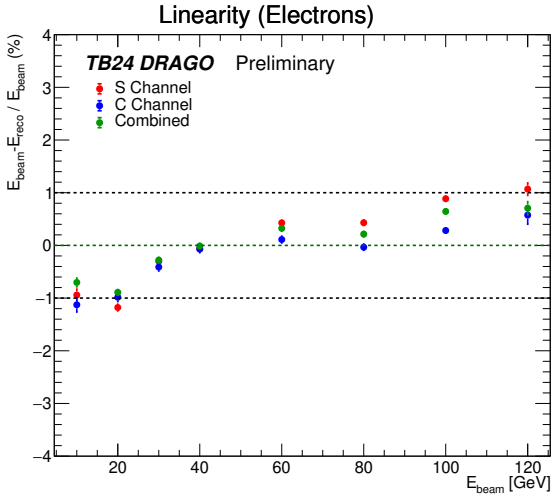


Figure 5.17: Difference, in percentage, between the nominal beam energy and the reconstructed one. Scintillation, Čerenkov and the combined measurements are drawn.

the nominal beam position also for those energies different from the 40 GeV working point, which was used for the asymmetry parametrisation. The main advantage, however, is that the new distributions are much less dependent on the Y position, despite some feature still remaining at more displaced events. Examples of the corrected scintillation and Čerenkov signals are shown in fig. 5.16. The combination of the two channels, taken event-by-event as the mean of each measured energy $E = (E_S + E_C)/2$, is also reported. These distributions are obtained by imposing a further cut on the asymmetry value, $|A_{S,C}| < 0.7$, to only consider those events almost centred in the T00 calorimeter tower. A double gaussian fit is then performed, also shown in fig. 5.16, such that the second fit's range is $(\mu - 1.5\sigma, \mu + 3\sigma)$ with μ, σ the mean and RMS parameters of the first fit.

The results are shown in fig. 5.17 and fig. 5.18. The fit mean lies within a 1% range from the nominal beam one, despite an increasing measured energy pattern can be observed. All the three measurements are centred at 40 GeV, as a result of choosing this point for the correction procedure. The resulting relative energy resolution (fig. 5.18) is parametrised with two possible fits, considering or not the noise term, which is measured as the total energy observed by the PMTs in pedestal runs that were taken in time periods close to the energy scan runs. The run with 120 GeV positrons was in this case excluded because of a very small amount of events passing the selection cuts. If the noise term is not considered, a stochastic term of $18.3\%/\sqrt{E}$ is found, which improved to $15.3\%/\sqrt{E}$ by including it. In both cases, a significant constant term of 2% is obtained. This term can be partially motivated by imperfect correction procedure, with a small contribution from the beam momentum spread, evaluated around 1%. Nevertheless, by accounting for the encountered issues during the beam test time, the obtained stochastic term is compatible with the one previously obtained with the smaller-scale prototype. A $1\%/\sqrt{E}$ difference is then found, when compared to the results measured through the best-case scenario represented by the Geant4-based simulation of the same prototype.

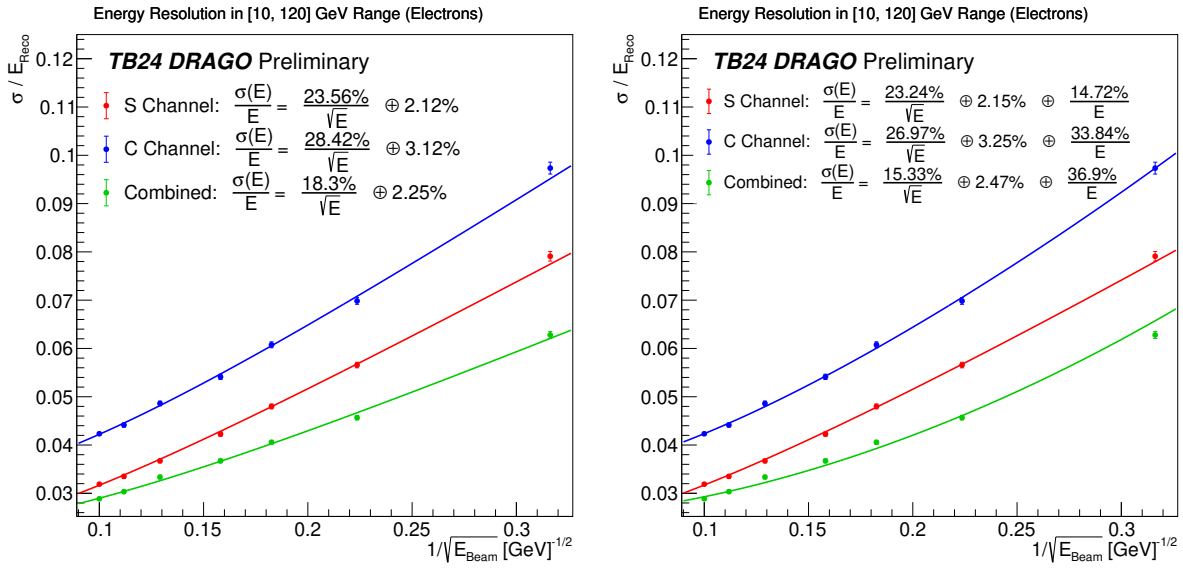


Figure 5.18: Energy resolution for the three considered channels. Two fits are considered, with or without a noise term contribution added in quadrature to the stochastic and constant ones.

Light attenuation measurements

A completely different type of measurement, that was also performed during the 2024 beam test, was the estimate of light attenuation within the optical fibres. Attenuation of light may arise for several possible reasons, including intrinsic material self-absorption, impurities in the fibres core and cladding materials, or micro-damages to the fibre's structure. In general, light intensity $I(z)$ in an opaque medium is subject to an exponential decay, which depends on a parameter λ called attenuation length as

$$I(z) = I_0 e^{-\frac{z}{\lambda}}. \tag{5.5}$$

Higher values of λ lead to smaller impact of light attenuation across the point where light is generated, to the fibre's end. Light attenuation may represent a significant problem for the correct measurement of hadron showers, which can develop across the entire length of the calorimeter. For shorter attenuation lengths, light produced by hadrons showering very deep inside the detector would be significantly less attenuated than the one generated, for example, by electrons which are absorbed in the first tens of centimetres (which are used for calibration of dual-readout calorimeters).

The light attenuation in both types of fibres was previously measured both during the 2023 beam test with the smaller-scale prototype, but also at laboratory measurements performed in Pisa, reaching surprisingly different results. In the first case, the measurement consisted in rotating horizontally the platform upon which the calorimeter was placed, and shifting it along the $\widehat{x}$ axis, therefore changing the impact point position of particles along the calorimeter's length. The measurement was performed independently for the scintillating and Čerenkov fibres, resulting in attenuation lengths of ~ 2 m and 3.9 m, respectively. In the laboratory measurement case, a lamp emitting UV light was put upon different positions along the optical fibre, and the resulting attenuation length was calculated by inverting eq. (5.5) for two different positions z_0 and

z_1, such that

$$\lambda = \frac{z_1 - z_0}{\ln \frac{I_0}{I_1}}.$$

An attenuation parameter of 6.7 m was measured for the scintillating fibres, with a large distribution spread with 3 m RMS. A significant reduction of this parameter was observed for optical fibres that were found to have micro-fractures, and were therefore left out of the measurement. After this observation, a test with fibres that were first put in the calorimeter capillary tubes and then extracted to be measured again, did not lead to a reduction of the attenuation length.



Figure 5.19: Picture of the calorimeter positioned on the 90° degree rotated platform for light attenuation measurements.

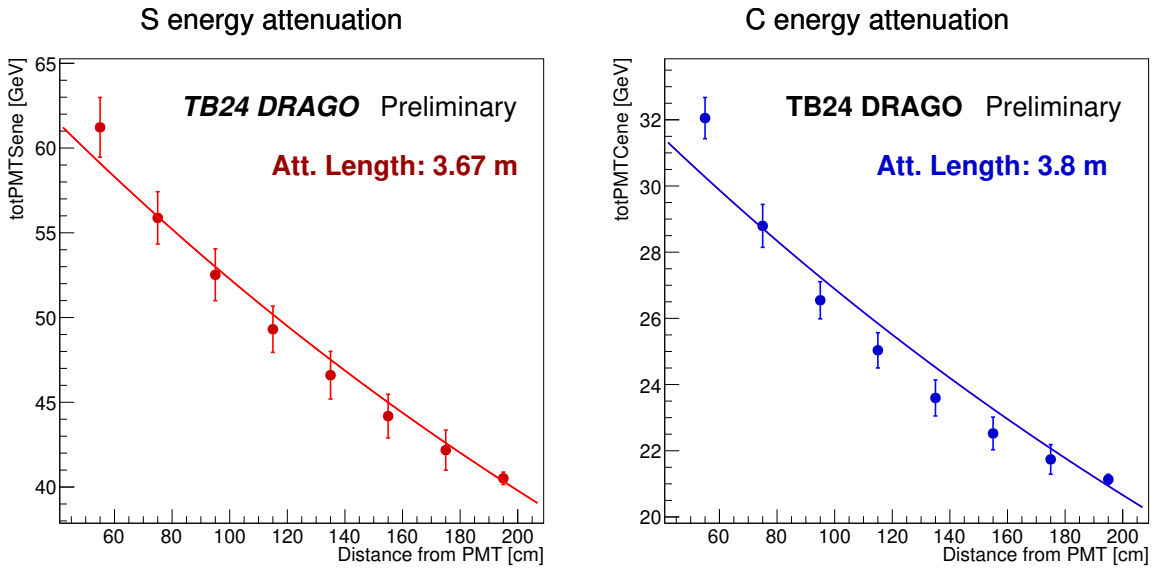


Figure 5.20: Light attenuation measurements in the two types of optical fibres, with 40 GeV electrons impinging on the side of the DRAGO calorimeter.

In order to address the incompatibility between these two sets of measurements, the same procedure used for the previous prototype was repeated also with the DRAGO prototype. The platform upon which the calorimeter was positioned, that allowed vertical and horizontal shifting, was rotated by 90°, as shown in fig. 5.19. A set of runs with 40 GeV positrons was used for measuring the signal deposited in the calorimeter at different distances from the readout, located at the rear end of the prototype. A total of eight measurements were taken, shifting horizontally the calorimeter with a 20 cm step between each run. The lateral size of the calorimeter, almost 39 cm, is enough to contain electromagnetic shower almost completely. The selection of positrons was kept the same as the one reported in table 5.1, minus the per-run cuts on individual delay wire chambers, and the request for the total leakage counter signals, which were removed to allow the complete platform rotation. The average measured signal, in both scintillation and Čerenkov channel, is reported in fig. 5.20. The large difference of values on the vertical axes were addressed to the different amount of Čerenkov light emission entering the acceptance angle in the early shower component for a $90°$ rotated calorimeter, while scintillating signal is not affected because of the isotropic light emission. The main limitation of this study comes from the limited statistics, as these measurements were taken at the end of the available beam time. The exponential fit superimposed on the measured values suggests $\lambda_S = 3.67$ m for the scintillation channel, and $\lambda_C = 3.8$ m for the Čerenkov one. The latter measurement is approximately compatible with the one observed during the previous beam test of the smaller prototype, while the scintillating fibres attenuation length improved by a factor $\sim 75\%$. Nevertheless, both results are in large disagreement with both laboratory measurements, and values suggested by the manufacturers. An additional point of uncertainty is that both types of fibres have a surprisingly similar attenuation parameter, while the Čerenkov ones was expected to be much larger than the scintillating one because of missing self-absorption from the organic scintillating material. Additional studies are currently planned, for example using radioactive sources along different places of the module, to shed light on this currently unexplained effect.

5.2.3 Hadronic performances

Similarly to the case of electrons, a first selection on the output of ancillary detectors is used to identify pions and estimate the response of the calorimeter to these particles. The applied requirements are listed in table 5.2. Two cuts are imposed on the preshower detector signal, in order to remove pedestal events and other events contributing with more than one mip, which is the expected signal deposited by these particles. The muon counter detector is required to not see more signal than the average pedestal, as muons were found to be the largest source of contamination in the pion beam. Both lower and upper cuts were also imposed on the tail catcher, to remove pedestal events and outliers with very high energy deposits in this detector. For similar reasons, an upper limit on the total signal by the leakage counters is posed, which only removes very high energy tails in these detectors at 100 GeV and 120 GeV runs, at this preliminary level. Finally, a selection on the delay wire chambers is set to remove beam divergence, and to remove very largely displaced particles. Distributions of measured energy in the scintillation and Čerenkov channels, obtained for 20 GeV or 100 GeV pions entering the DRAGO prototype, are shown in fig. 5.21 before and after applying these requirements.

The resulting distributions, typical of non-compensating calorimeters, are skewed towards lower values than the nominal energy, with a tail that extends at higher en-

ergies. These observations are in agreement with the missing contribution from the invisible energy, and higher energy tails generated by events with randomly large electromagnetic fraction f_{em}. For small prototypes like the one under study, incomplete containment of hadron showers in the calorimeter volume plays an important role in the overall energy measurement capabilities. In order to better understand how leakage affects obtained measurements, the Geant4 simulation of the HiDRa prototype was updated to replicate the used geometry, shown in fig. 5.22. Sixteen plastics leakage counters, plus the rear tail catcher, were added to the simulation, before the truth leakage volumes discussed in chapter 3. A parametrisation for the light attenuation in the two types of optical fibres was also added to the simulation, in order to replicate the observed effect. To achieve this, for each hit in the calorimeter producing optical photons through the Poissonian smearing function, the distance from the fibre end is calculated, and an exponential decay function to the signal is applied. This method was previously introduced in the 2023 beam test, with the attenuation lengths measured at the time, providing an excellent description of the measured data.

The total containment for hadron showers originated by pions, with energy from 20 GeV up to 120 GeV and estimated through the simulation, is shown in fig. 5.23, with one example of the two main leakage components at 40 GeV. The fraction of contained energy is again found to increase, inside the simulated energy range, by more than 2%. Such a variation would be translated into a clear increase in the observed energy also through the dual-readout method, whose main advantage is the response linearity to any hadron. In order to account for this effect, eq. (3.5) was used again to obtain the dual-readout correction, by accounting for the missing energy contribution. The idea behind this procedure was to first correct for the known leakage contribution, to evaluate the presence of other possible issues in hadrons energy measurements.

Figure 5.24a shows the obtained dual-readout distribution, with a value of $\chi = 0.35$ which was set to have the reconstructed energy approximately close to the nominal one, and an expected containment of 88%. A quite large distribution is found, with leakage fluctuations conspiring to produce tails at both low and high energies, depending if shower particles escape out of the calorimeter, or if they are well contained. This effect is clear in fig. 5.24b, where events in which a large amount of energy is deposited in the leakage counters are mostly located below the nominal 40 GeV energy (which should be ideally the peak position, after the containment correction). On the other hand, well-contained events, in which a small signal is deposited in the leakage counters, are clustered at higher energies.

The mean values of the reconstructed energy response from the three channels (scin-

Table 5.2: Ancillary detectors requirements for pion selection.

Anc. Detector	**Cut value [ADC counts]**
Preshower	> 350 & < 450
Muon counter	< 160
Tail catcher	> 170 & < 400
Leakage counters	$\sum_i L_i < 6500$
Delay wire chambers	$\lvert XDWC2 - XDWC1\rvert < 5$ [mm]
	$\lvert YDWC2 - YDWC1\rvert < 5$ [mm]
	$\lvert XDWC2\rvert < 20$ [mm]
	$-20 < YDWC2 < 5$ [mm]

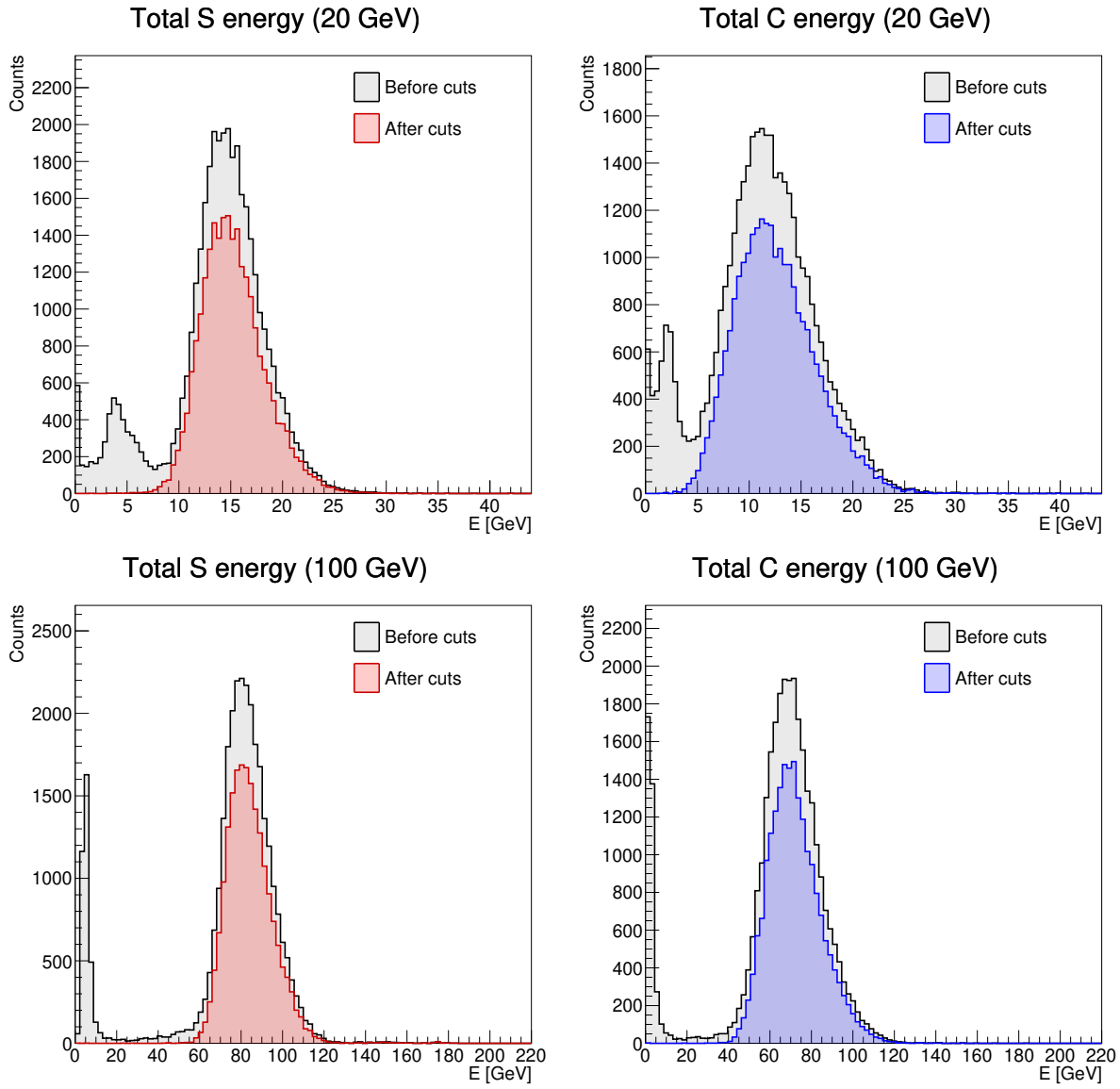


Figure 5.21: Examples of scintillation and Čerenkov energy distributions before and after the pion selection cuts listed in table 5.2.

tillation, Čerenkov and dual-readout) are plotted in fig. 5.25. A shaded area is superimposed on the measured energy points, to better appreciate how the reconstructed energy changes with the nominal one. While for both the scintillation and the Čerenkov channels an increase of the average signal with the beam energy is expected because of the increasing f_{em} (with the Čerenkov one being lower, as it mostly samples the electromagnetic component of the shower), the dual-readout would be expected almost constant, inside the drawn $\pm 1\%$ range. Instead, a clear shift towards lower values is observed as well. Furthermore, the expected dual-readout energy distribution should have a gaussian-like shape, while the observed one also features a larger tail towards high energies.

Among the possible reasons for this behaviour, the one that drawn the largest attention was the light attenuation problem, as the longer longitudinal development of hadron shower at higher energies would result in less attenuated light and higher signals. This result was also observed with preliminary simulations in which the light

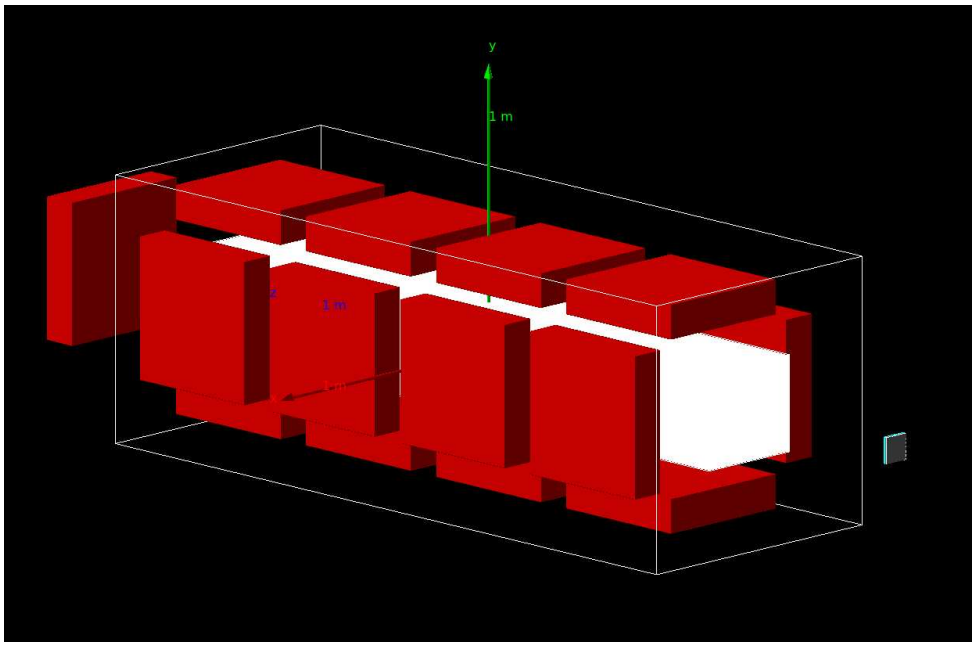


Figure 5.22: Geant4 simulation of the 2024 DRAGO prototype, with preshower, tail catcher and leakage counters ancillary detectors.

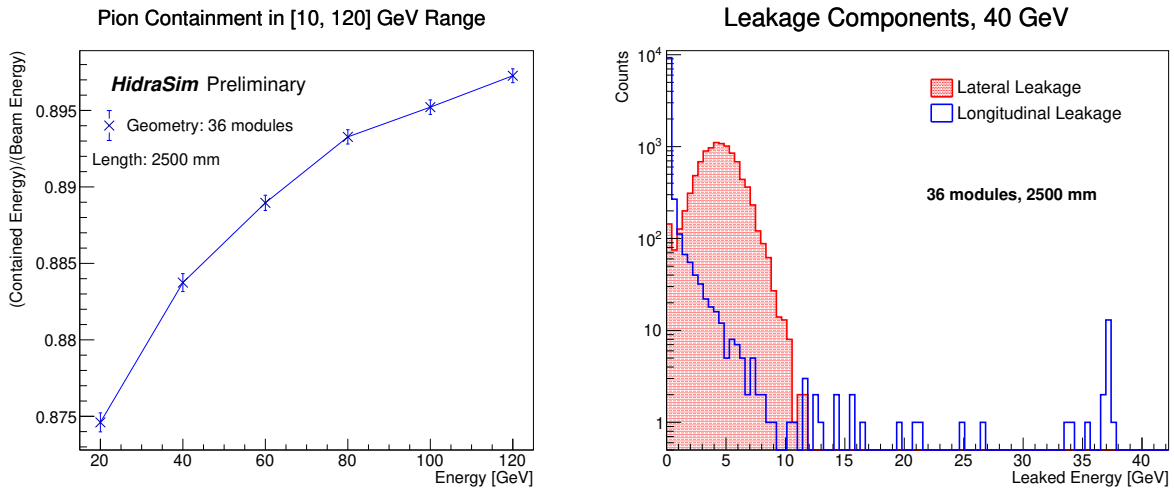
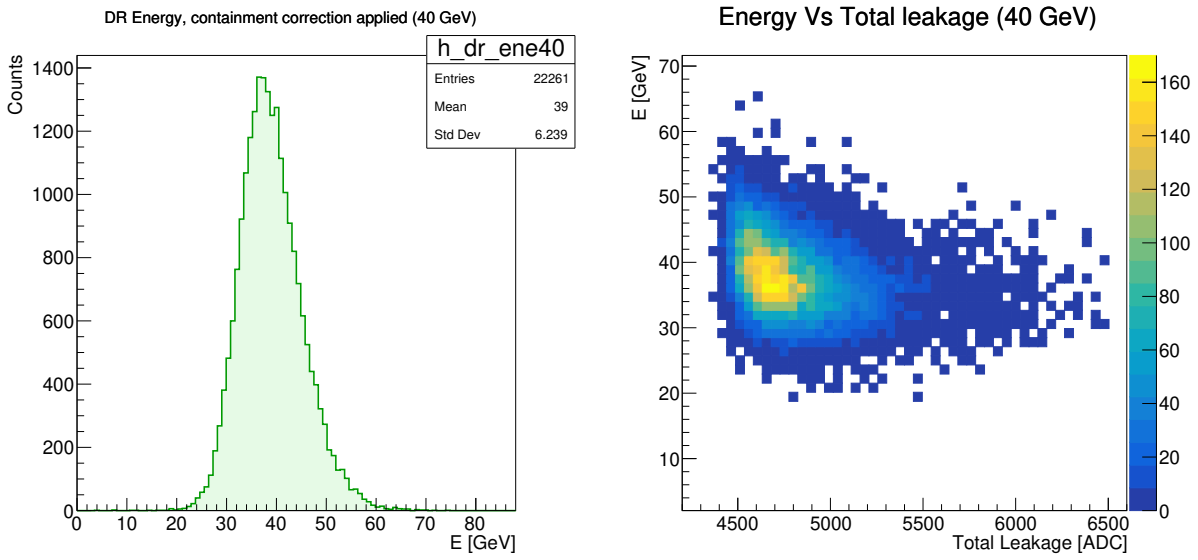


Figure 5.23: Expected containment with 36 modules geometry in the tested range during the 2024 beam test, obtained through the Geant4 simulation. On the right, one example of truth leakage breakdown into the two lateral and longitudinal components, for 40 GeV pions.



(a) (b)

Figure 5.24: Dual-readout energy distribution for 40 GeV pions (a) corrected for the average expected containment through simulation, and (b) its dependence on the total signal from the leakage counters.

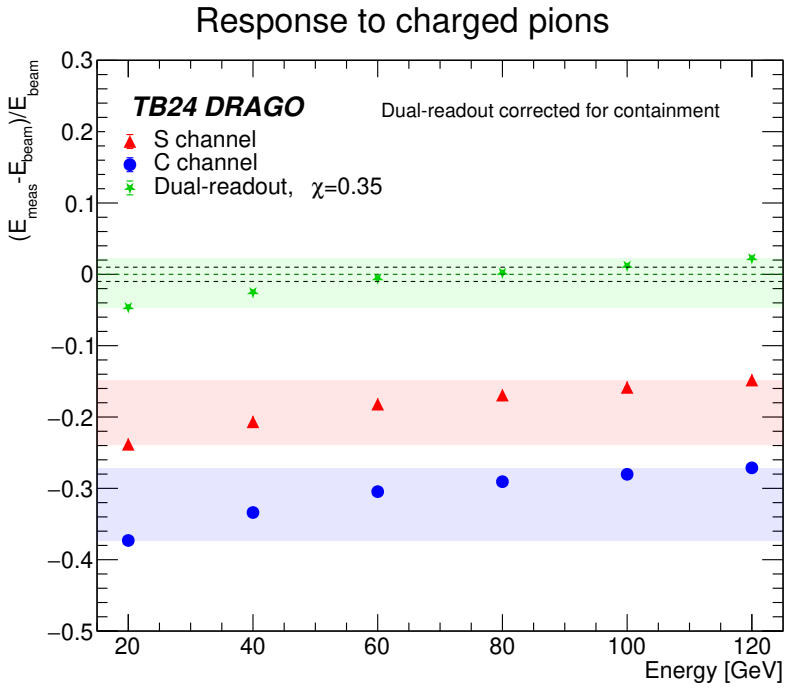


Figure 5.25: Responses to pions in the [20-120] GeV energy range of the DRAGO prototype.

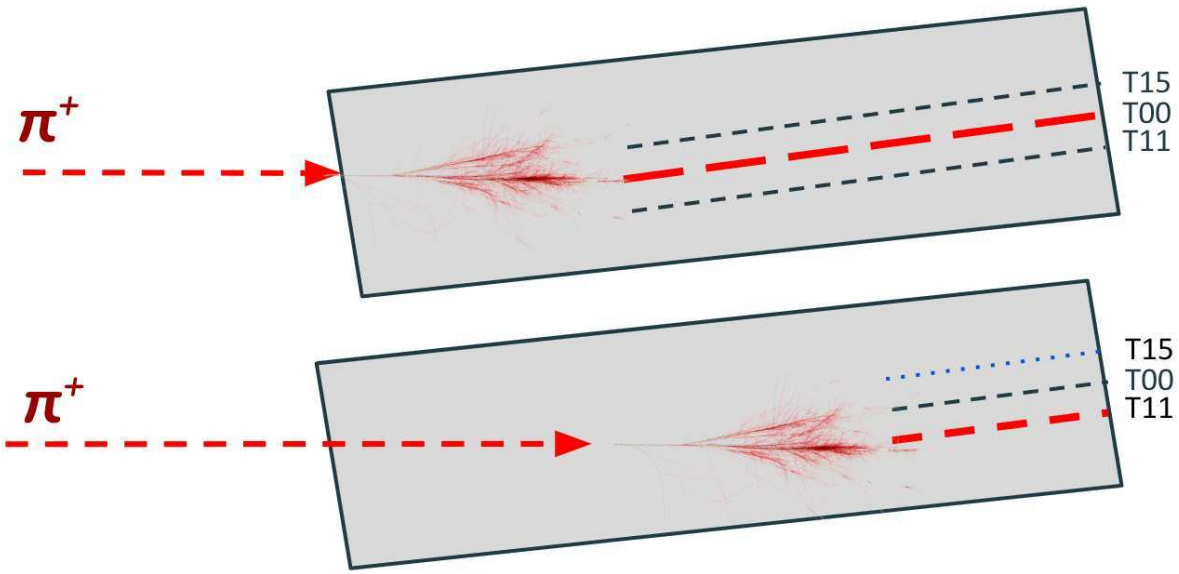


Figure 5.26: Sketch showing the energy asymmetry produced by hadron showers developing deeper inside the rotated calorimeter.

attenuation function was added, confirming it as a motivation for the observed non-linearity. Several approaches were therefore tested to address this issue, with the most important points outlined in the following.

Correction for asymmetry

One first attempt for correcting the attenuation problem was performed by re-applying the asymmetry variable, previously defined for correcting the electromagnetic shower dependence on the impact point position, and defined in eq. (5.3). The underlying idea was that, for a calorimeter with sufficient vertical rotation, hadron showers developing deeper inside the calorimeter (and therefore producing less attenuated light) would deposit a larger fraction of signal in the lower half of the calorimeter, with respect to the upper one. A simple drawing representing the tilted calorimeter, with an angle larger than the one actually used of $2.5°$, is shown in fig. 5.26. A similar procedure as the one previously described was followed, constructing two asymmetry variables using scintillation or Čerenkov energy deposited in different towers. A reasonably good result was obtained by taking the energy from towers in the second ring from the central module where the beam was impinging, namely towers T24 and T21. Other tests were performed by summing more signals in the same rows, and from more than one row of the calorimeter, without appreciable improvements on the simplest considered case.

The dual-readout energy was, for the study under discussion, treated as an independent channel. It was firstly estimated event-per-event from the energies in the two types of fibres, and then corrected by considering its own dependence over the asymmetry variable. The dependence of the measured energy in the three considered channels, scintillation, Čerenkov and dual-readout, is shown for 40 GeV positively charged pions in fig. 5.27. Data taken at this corrected energy were, once again, used for fitting a 5-degree polynomial function that was used for correcting the total energy variables. The dual-readout dependence was obtained for both the asymmetry variables obtained through the scintillation and Čerenkov channels, but minimal differences were found, so only the scintillation case is further discuss, but valid for the other one.

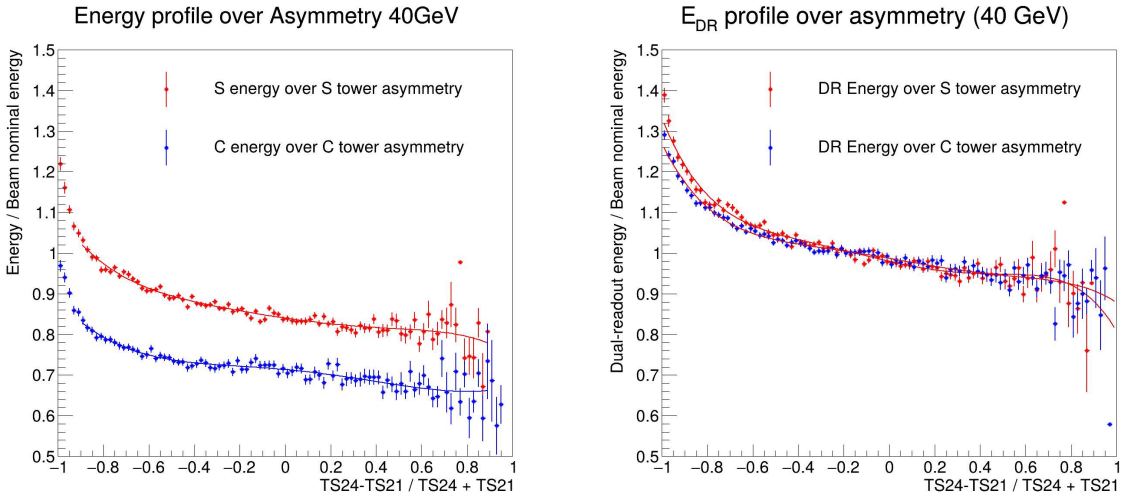


Figure 5.27: Profiles of the measured energy in the scintillation, Čerenkov and dual-readout channels, over the asymmetry variable. See text for details.

Despite not completely being gaussian-distributed, the corrected energy distributions were then fitted with a first gaussian function for estimating the peak position, and the width of the distribution in the region where most of the signal lies. A second fit is reapplied in the range of $\pm 1.5\sigma$ from the peak of the first fit. Examples of some of these results are reported in fig. 5.28, where one can observe a shift towards higher energies and a slight modification of the initial shape. The new responses are shown in fig. 5.29: similarly to the case of electromagnetic showers, the imposition of the fitting at 40 GeV pushes the three curves to cross close to this energy value. On the other hand, a clear non-linearity is visible, with the measured energy increasing for all three channels, and most importantly the dual-readout one, even if in a moderately smaller range than the non-corrected one.

Because of the insufficient improvement on correcting the response dependence on the hadrons' energy, this method was not investigated further. A possible reason for the described method not working correctly, could be non-sufficient tilting of the calorimeter of just 2.5° making the differences between upper and lower modules too small to be used to be relied on for corrections.

Correction through timing

Exploiting time information was not part of the initial scheme for the experimental setup planned for the beam test under discussion. Nevertheless, Time-to-Digital Converters (TDCs) were being used for the measurements of signal delays in the delay wire chambers. We therefore decided to use six available free channels to test the possibility of exploiting the time information in signal reconstruction and correction. These channels were used, during the last few days of data taking, for reading out the three central towers (T00, T11 and T15 in fig. 5.13), with two channels each for both scintillation and Čerenkov fibres. However, because of other issues during the data-taking, the settings for their usage were adjusted run-by-run, and some effort was later spent during the data analysis to merge all the information and make it usable.

The time information may be useful for correcting the issue of light attenuation, because light emitted by very deep energy deposits in the calorimeter, close to the readout on the rear of the detector, takes less time to travel across optical fibres before reaching

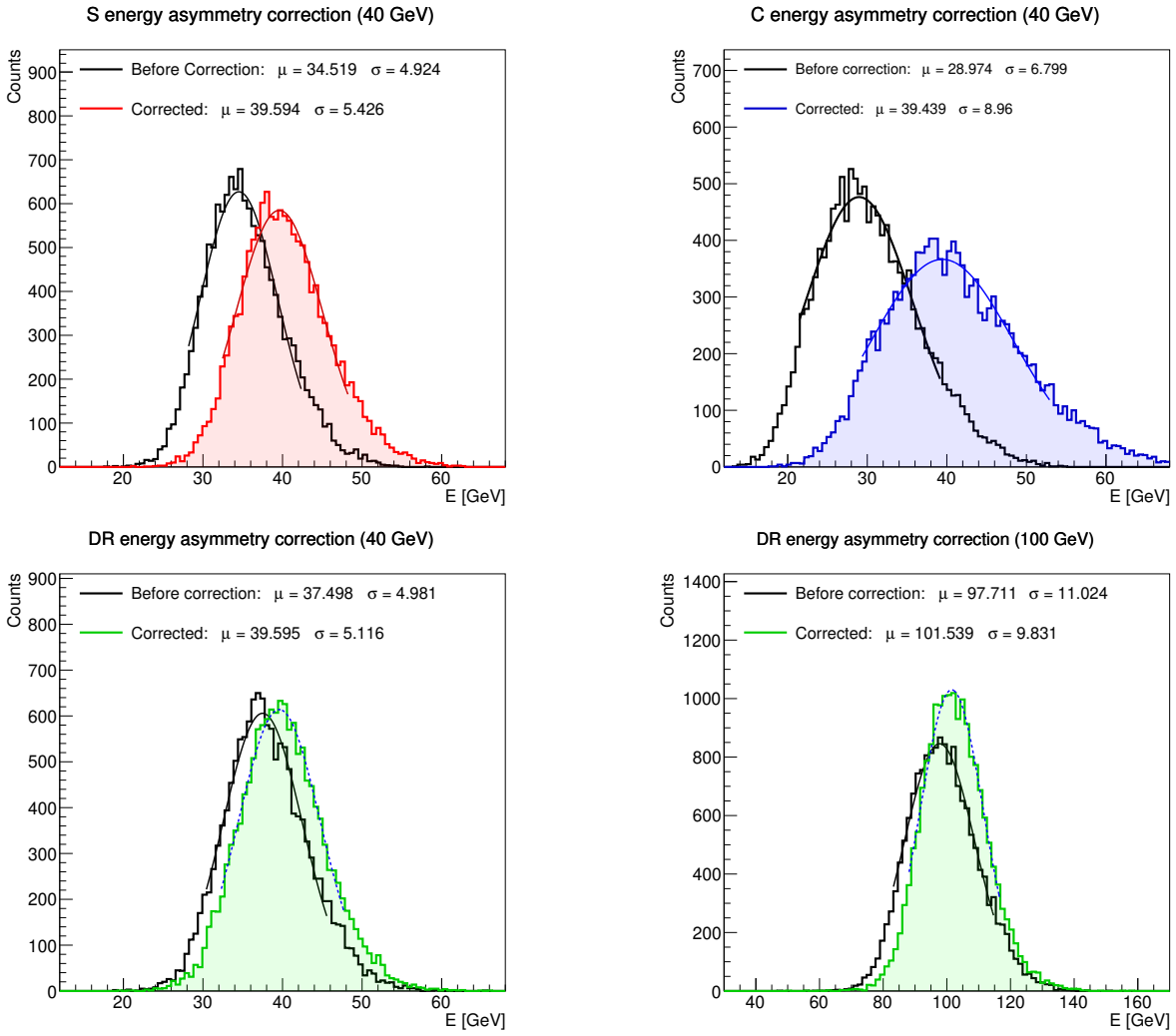


Figure 5.28: Examples of the original and corrected energy distributions from 40 GeV pions, and one example also at 100 GeV for dual-readout corrected energy.

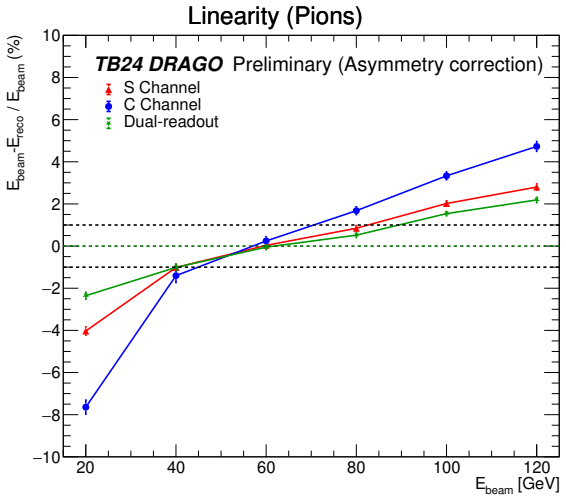


Figure 5.29: Responses of the two calorimeter channels, and dual-readout one, after the correction for the asymmetry variable.

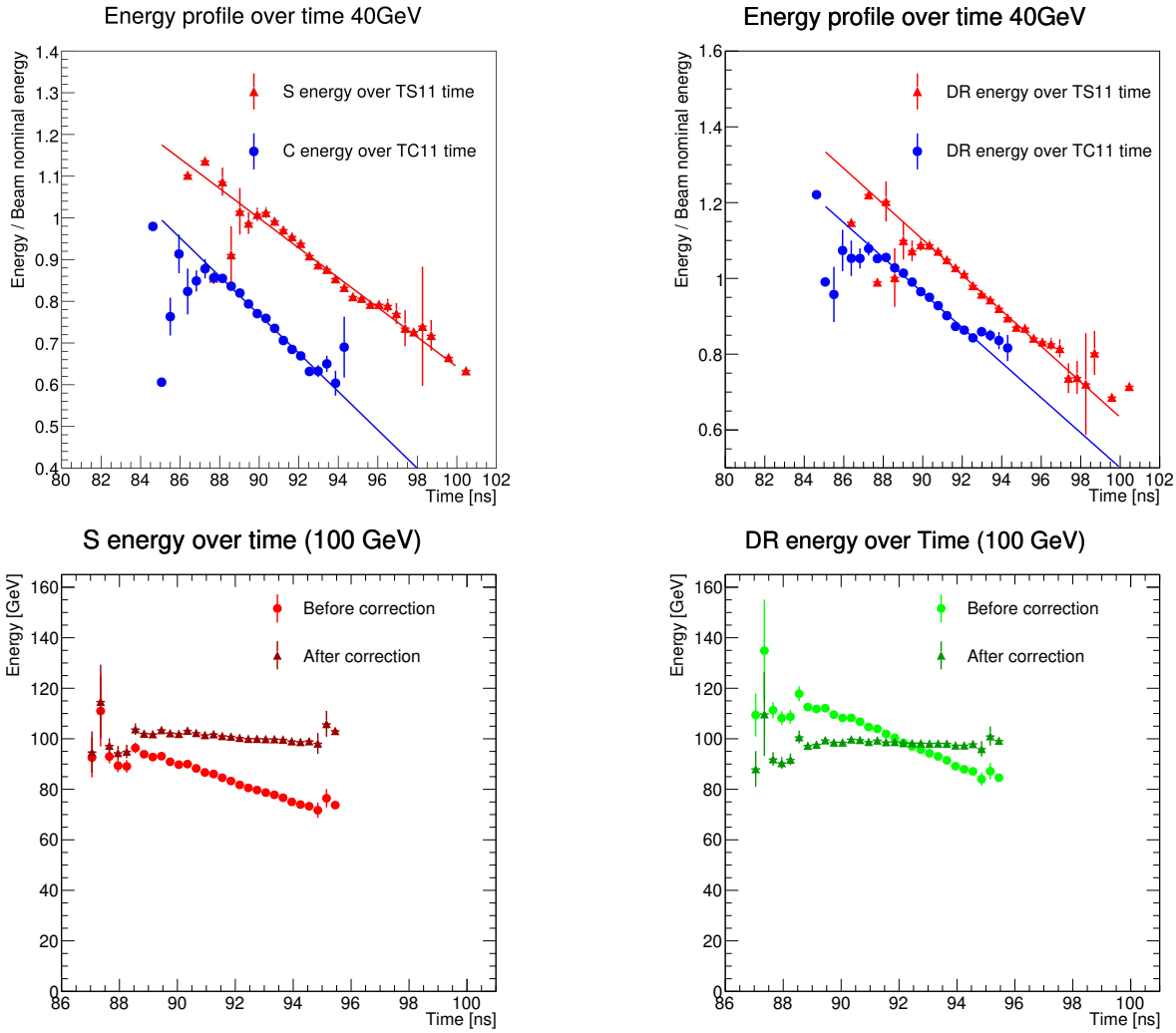


Figure 5.30: Time dependency of the scintillation, Čerenkov and dual-readout corrected energies, and the effect of the relative correction to different energy data.

the sensors. At the same time, these deep energy deposits are also the less attenuated ones, for which the difference between a same-energy signal produced by electromagnetic showers during calibration are the largest. The exploitation of timing measurement from SiPMs, such as rising time, time-over-threshold and other features, are planned in the future for imaging purposes. If optical fibres with long enough attenuation parameters were not available for the construction of the final IDEA calorimeter, an additional usage of the time information could be the correction of light attenuation fibre-per-fibre.

The only timing information used in the following is the measurement of the delay time from the initial trigger to the instant at which the PMT's signal overcomes a defined threshold. In this case, the signal generated by each PMT is the sum of all 512 fibres, and therefore provides a much less granular information about the instant in which a large enough signal is deposited in the related tower. Despite this limitation, a clear dependence of the total signal in the calorimeter on the time information provided by one tower is shown in fig. 5.30. On the X axis, the measured time interval from the trigger is shown, also including cables and electronics hence motivating the large values. The time information used in this analysis only exploits the T11 tower, that

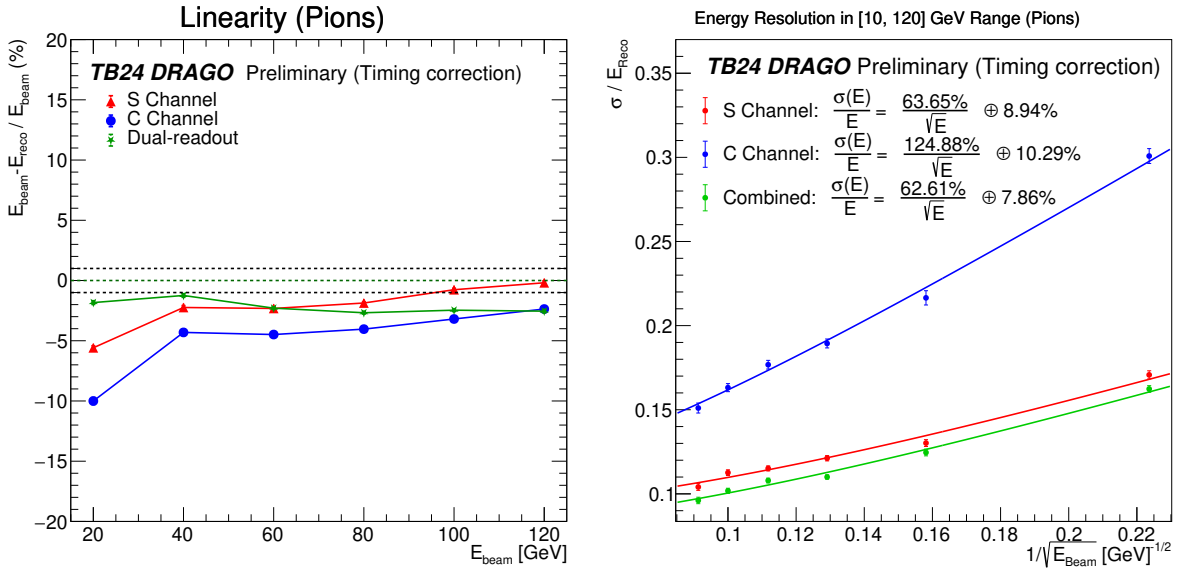


Figure 5.31: Energy measurement linearity and resolution for the scintillation and Čerenkov channels, and dual-readout.

received a significant amount of signal from hadron showers because of the calorimeter vertical rotation. The other two towers with available TDC channels did not show a clear enough dependency, and were therefore not considered. Other variables were also tried, including the time barycentre built as eq. (3.2) using time instead of the spatial coordinates, without improvements. The measured time by the TC11 channel used to readout the Čerenkov signals anticipates the scintillation one by few nanoseconds, in agreement with the prompt light emission of the first production process. As expected, an increase of the measured energy is found for early-produced signals.

In order to evaluate the hadron energy response parameter, a correction procedure was performed again by taking a linear fit on the distributions in fig. 5.30, obtained for 40 GeV pions. Once again the dual-readout measured energy is fitted using both the time information provided by the scintillation and Čerenkov channels, and the first one is then reported. The energy distribution are corrected by dividing event-per-event the measured energy for the value of the fit corresponding to the event's time information. The so-built distributions are then fitted with a gaussian in the $\pm 1.5\sigma$ region close to the peak, excluding remaining high and low energy tails.

The resulting gaussian mean and RMS values, with their associated errors, are shown in fig. 5.31. The dual-readout energy, despite being about 1-2% lower than the correct energy value, remains almost constant inside the entire energy range. The other two distributions are also reported in the same plot: they are shifted towards higher values, because of the described post-calibration procedure, and the overall range is compressed with only the 20 GeV set remaining drastically lower. A slight increase of the response at higher energies is however still present, possibly due to the increasing f_{em}. While the described method allows to recover an almost linear dual-readout response, once both the corrections for the containment and the one for light attenuation are applied, it only affects minimally the widths of the resulting distributions. The obtained energy resolution shows a stochastic term of $\sigma/E = 63\%/\sqrt{E}$ with a very large constant one of 8%. Similar terms were also obtained through the previously described method which made use of the asymmetry variable.

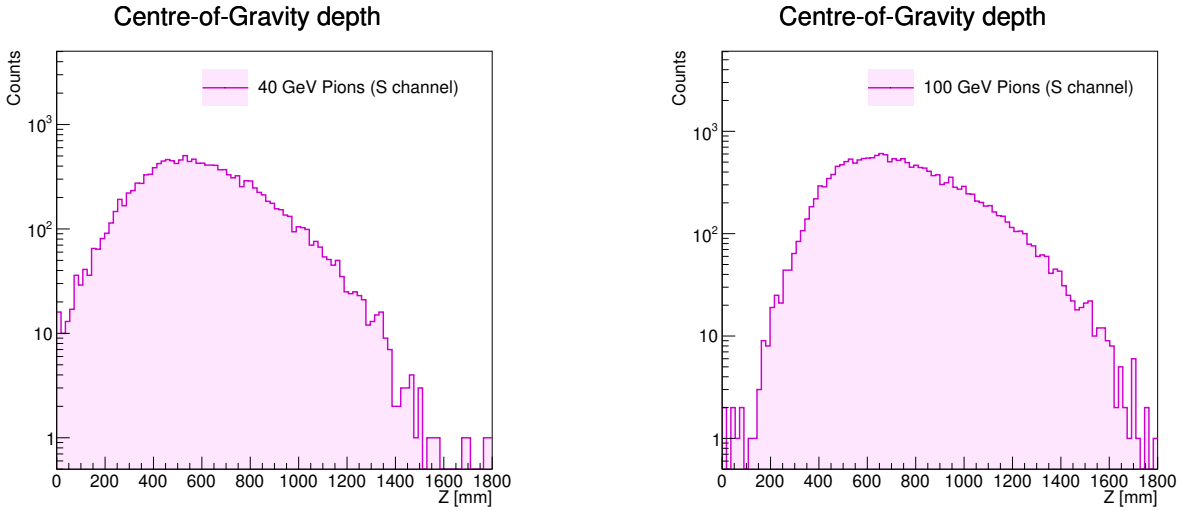
Other tests were also performed and not reported here, for example correcting the scintillation and Čerenkov energy distributions first, and only later applying the dual-readout correction on the two resulting measurements. Since in both cases the applied procedure shifts to drastically different variables both the scintillation and Čerenkov signals, it was tried to take as normalisation factor for the fit the Most Probable Value (MPV) of each energy distribution instead of the truth energy of the beam. As a consequence, the scintillation and Čerenkov energies were not shifted towards the nominal energy value, and could be used within the dual-readout formula of eq. (3.5). It was found, on the other hand, that the MPV is not a stable parameter for describing the underlying distribution when using the same fit on different energy working points, and the so-built dual-readout energy was far from linear.

While the proposed method showed that a correction for the light attenuation through timing measurements is possible, it still required a drastic modification of the underlying measured energy distributions, by fitting a function on data of known energy and extrapolating it towards different values. These methods were then abandoned, and a different method, that did not require any additional information besides the ones provided by the calorimeter and ancillary detectors, was preferred.

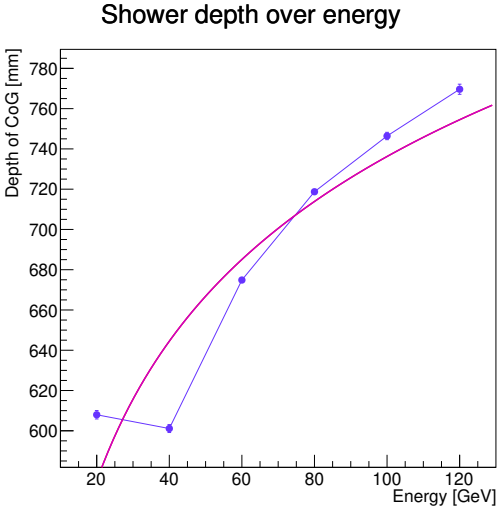
Correction through Centre-of-Gravity depth measurement

With the known attenuation length parameters measured in section 5.2.2, it would be conceptually possible to correct the measured signal in each optical fibre, by measuring the depth at which the light was emitted. An additional source of fluctuations would be introduced, that would be absent if light attenuation was negligible. Correcting for the depth of signal emission would nevertheless allow to rescale the less-attenuated hadron signals to the correct electromagnetic scale. Since the measurement of longitudinal emission point was not effective during the 2024 beam test, a backup solution was found by projecting the measured Centre-of-Gravity (CoG) of any hadron shower onto the front face of the calorimeter. With a known prototype rotation of $\vartheta_y = 2.5°$, the vertical displacement of the barycentre with respect to the impact point position made it possible, through geometrical considerations, to obtain a measurement of the depth in the calorimeter where the CoG was located event by event. This depth information was used as a variable to describe the energy deposition of the entire hadron shower along the longitudinal direction.

The precision on the barycentre position reconstruction depends on the available granularity of the calorimeter, which was very limited in the DRAGO prototype. Since there were only three towers in the horizontal direction and twelve in the vertical one, the reconstruction of the CoG along the $\widehat{y}$ axis was preferred to estimate the CoG longitudinal position, with a 2.8 cm cell size. The scintillation channel was used in all cases for the reconstruction of the shower barycentre depth. The resulting distributions of hadron shower barycentre depths are shown in fig. 5.32a for 40 GeV and 100 GeV charged pions. Most of the energy is deposited in a range from 40 cm to 80 cm inside the calorimeter, with a significant amount of events that develop even after 1 m. Figure 5.32b shows the average barycentre depth increase with the energy of the showering hadron. A logarithm curve was fitted on the evaluated points, despite the agreement not being very good. Among the possible underlying reasons could be a bad energy resolution at low energies making it difficult to estimate correctly the shower barycentre, spoiling the later reconstructed shower depth, together with limited detector granularity.



(a) Measured depth of the centre-of-gravity for 40 GeV or 100 GeV positively charged pions.



(b) Measured average shower barycentre depth for pions of different energies. A tentative logarithmic fit was superimposed on data.

Figure 5.32: Measurement of longitudinal depth of hadron showers in the DRAGO calorimeter.

The following correction for the light attenuation consisted in rescaling both scintillating and Čerenkov measured signals for a depth-dependent weight, to obtain the equivalent signal that would have been emitted at the depth of 20 GeV positron showers, which were used for calibrating the calorimeter:

$$\begin{aligned} E_S &= E_S^0 \times e^{-(z_{\text{eff}} - 18\text{ cm})/\lambda_S} \\ E_C &= E_C^0 \times e^{-(z_{\text{eff}} - 18\text{ cm})/\lambda_C}. \end{aligned} \tag{5.6}$$

A depth of 18 cm, equivalent to about $7X_0$, was set as electromagnetic depth scale. The dual-readout formula was then applied to the corrected energy values applying eq. (3.5). In order to evaluate the correction technique, the scintillation, Čerenkov and dual-readout energy distributions were plotted as a function of the shower depth in fig. 5.33, before and after having applied eq. (5.6). An over-correction is observed in all three considered channels, being mostly evident in the scintillation one, and being

therefore carried on also through the dual-readout formula. Different tests with varying parameters were tested to address this observation, and it was found that using values of approximately double the measured attenuation parameters allowed to have an almost constant response over the barycentre depth position. However, it turned out that such modification resulted in non-linear response when considering the dual-readout measurement, and the baseline parameters were therefore preferred. Little impact was found when varying the average shower depth instead, with tested values between 15-30 centimetres. Further optimisation of the correction method is still ongoing.

Two examples of the resulting energy distributions, corrected through the dual-readout technique, are shown in fig. 5.34. Once again, a high-energy tail is still present. A gaussian fit between $\pm 2\sigma$ from the peak was also tested to estimate the peak position and the width of its peak, but was not used as it did not describe correctly the underlying distribution. Therefore, the mean and RMS of the histograms are used for the following energy response characterisation. The two main parameters, the energy response and the relative resolution, are shown in fig. 5.35. While the dual-readout observed curve is nicely linear in the measured range within less than 2%, all measured energy values are widely underestimated, by using a "standard" value for the dual-readout parameter $\chi = 0.35$. With the set value of χ, a stocasthic term of $\sigma/E = 71\%/\sqrt{E}$ is found for the energy resolution, plus a very large constant one of more than 8%. Once again, the applied correction technique allows to partially recover a linear response for the dual-readout method, but cannot improve the very poor resolution. The corrected energies could be found by increasing its value to about $\chi = 0.63$, which means associating a much larger weight to the Čerenkov signal in eq. (2.18). Since the Čerenkov energy is the one with the worst energy resolution, applying a larger value of χ would mean spoiling even more drastically the dual-readout energy resolution.

The effect of the applied correction procedure can also be observed in fig. 5.36, which shows the scatter plot of the scintillator and Čerenkov energies, normalised for the beam energy. A marker was set on the point $(S/E, C/E) = (1, 1)$, which sets the electromagnetic scale of the calorimeter. In non-compensating calorimeters, the entire distribution produced by showering hadrons should be located along a line connecting the values $((h/e)_S, (h_e)_C)$ and (1, 1), without any event having an energy fraction larger than one, because of the missing invisible energy contribution. Events with randomly large f_{em} should at most be located close to the drawn marker, while in the shown plot a significant fraction of events have both a larger scintillator and Čerenkov signals. The effect of the applied correction is therefore to shift these distribution to lower values, until almost all events are roughly located in the expected range. On the other hand, the newly obtained scatter plot is not significantly narrower than the original one, in line with the minor energy resolution improvement after the correction.

Monte Carlo studies

Because of the poor energy resolution parameters obtained even through all three proposed correction procedures, a campaign of Monte Carlo simulation studies was done to spot possible issues that could be addressed before the completion and following beam test of the HiDRa prototype. While light attenuation was fairly well reproduced by the Geant4 simulation, once the correct parameters were experimentally measured, the observed response dishomogeneity issues encountered during the prototype characterisation with electrons could not be easily reproduced. As it was shown in sec-

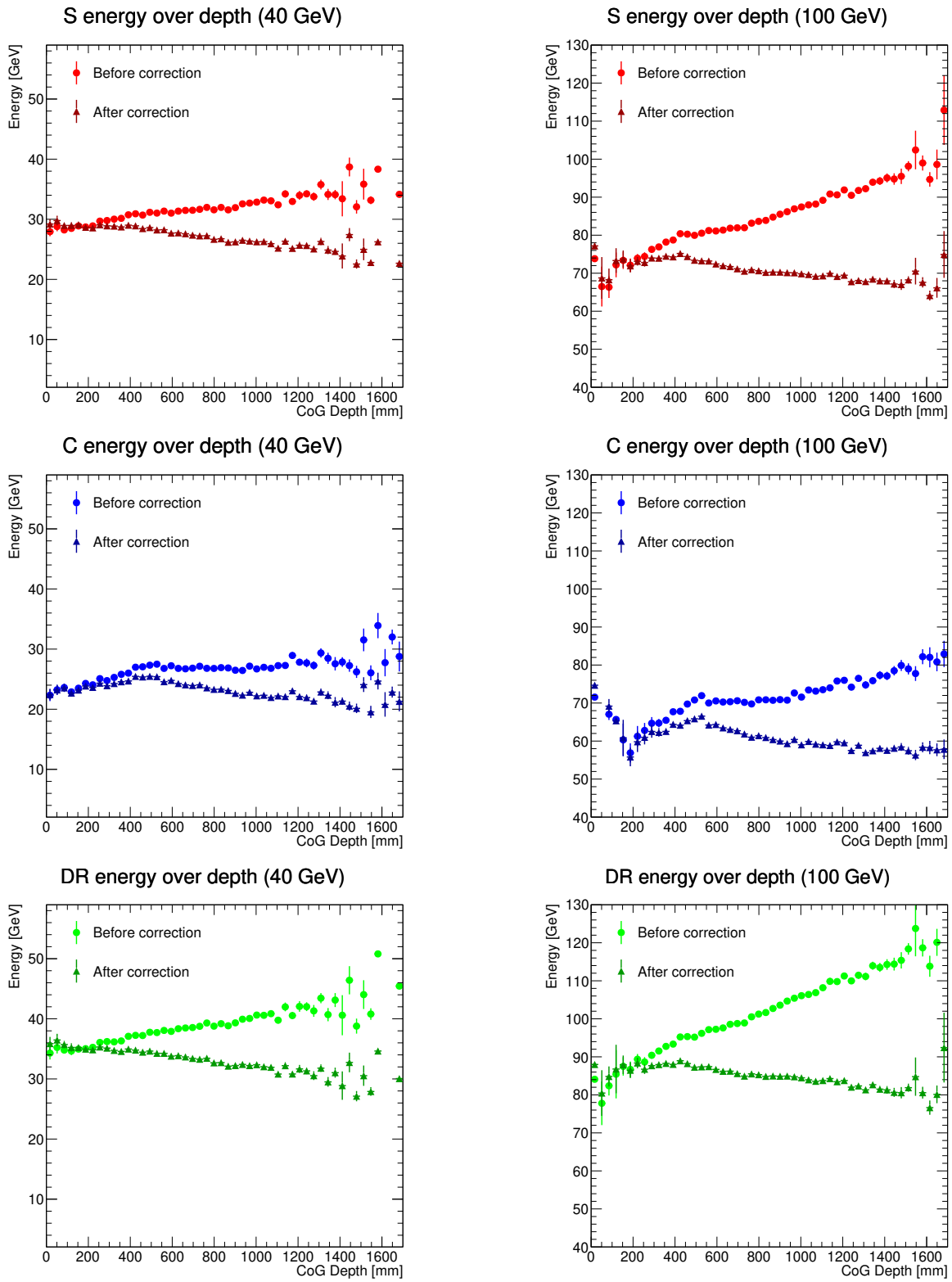


Figure 5.33: Effect of the correction of the measured shower depth on the energy measurements in the three channels.

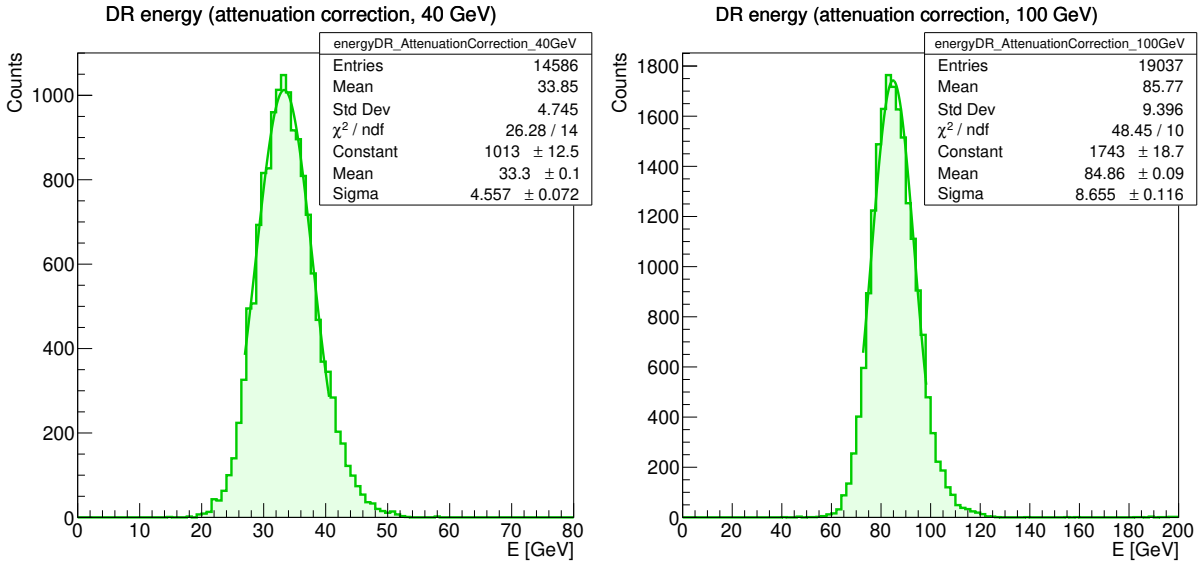


Figure 5.34: Energy distribution, obtained through the dual-readout method, applying eq. (3.5) on the scintillation and Čerenkov signal corrected for light attenuation.

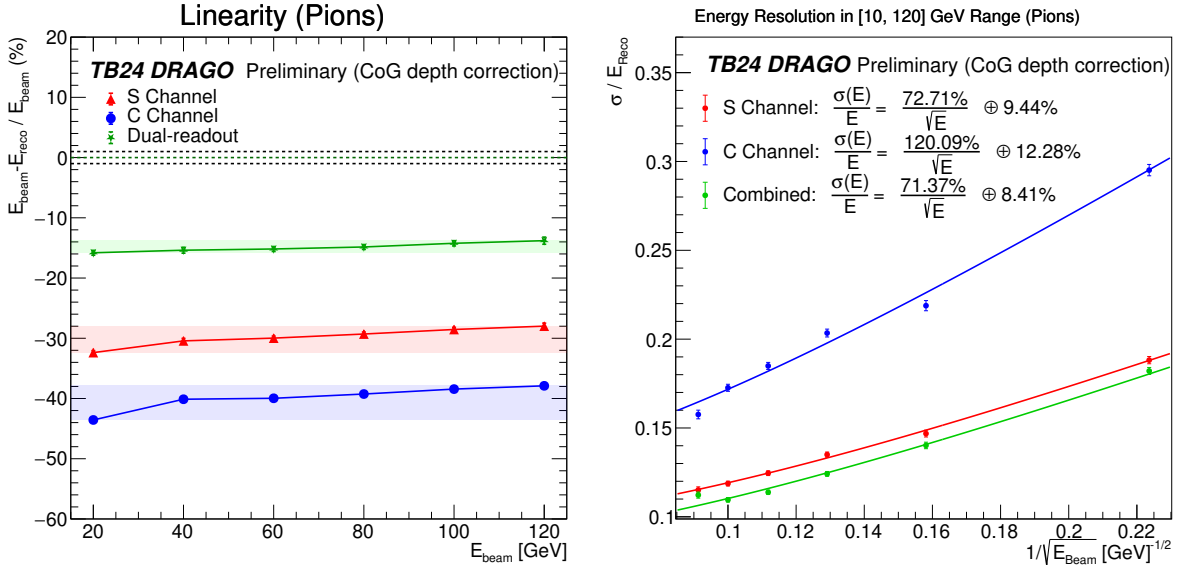


Figure 5.35: Response dependence of the scintillation, Čerenkov and dual-readout channels on the impinging pion energy, and resulting relative energy resolution.

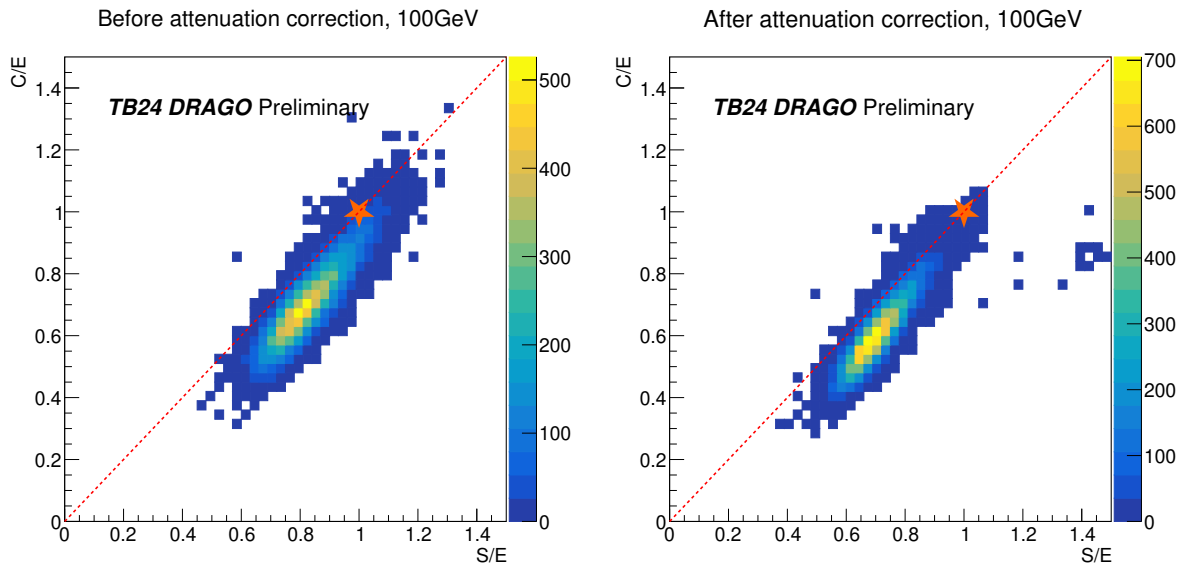


Figure 5.36: Measured scintillator and Čerenkov responses to positive pions, before and after applying the light attenuation correction procedure.

tion 5.2.1, the local calorimeter response varied significantly within each tower, resulting in a some-percent level mis-calibration of each calorimeter tower. For electromagnetic showers, only very few calorimeter towers produced a quantitative amount of signal. Conversely, for hadron showers the entire calorimeter contributes in some way to the energy reconstruction, with each tower adding a small source of uncertainty. Among the tested ways to reproduce this source of uncertainty into the simulation, besides the application of local tower dishomogeneity mentioned in section 5.2.2, an uniformly-generated random parameter to weight the signal deposited in each tower was introduced. So far, a good simulated description of electromagnetic showers response to reproduce measured data has not been found.

In order to better understand the position-dependent response of the different modules, laboratory measurements are planned at the Pavia laboratories. Tests with light mixers, consisting of transparent plastic elements used to diffuse light on a wider area, could not be performed yet because of encountered hardware issues. However, with the usage of per-fibre granular readout with SiPMs, the local non-uniformity problem should not be reproduced, unless a different source of dishomogeneity exists. If light mixers were not to be used, the described problem might nevertheless affect the remaining 70 PMT-instrumented calorimeter towers.

Despite the described challenge, the simulated beam-test geometry allows to estimate the performances of an ideally performing calorimeter, that allows to isolate experimental effects. Figure 5.37 shows a comparison of the total energy in the scintillation and Čerenkov channels, originated by 40 GeV pions, between measured data and that predicted by the Geant4 simulation. For the present study, sources of tower non-uniformity were removed, such that all calorimeter modules have the same response to electrons, and only the reproduced light attenuation was added. This effect can be observed in the high-energy tails of both distributions, with a non-negligible tail that extends over the truth pion energy. The distributions observed in data have a wider shape that extends to lower vales than the simulated ones, contributing to the total signal width of both channels.

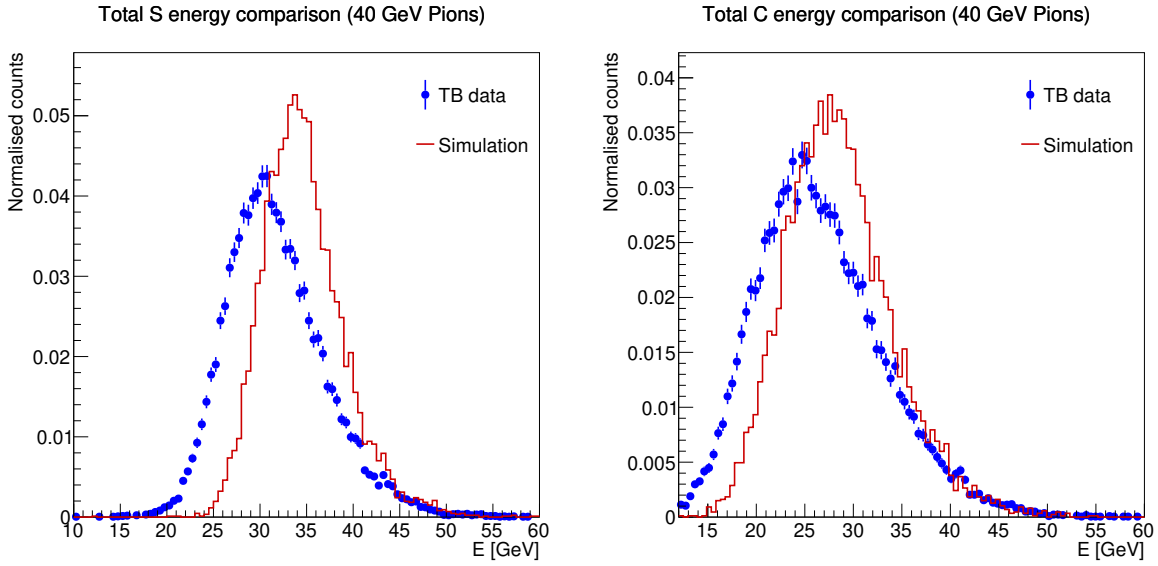


Figure 5.37: Comparison of the simulated and measured total energies in the scintillation and Čerenkov channels.

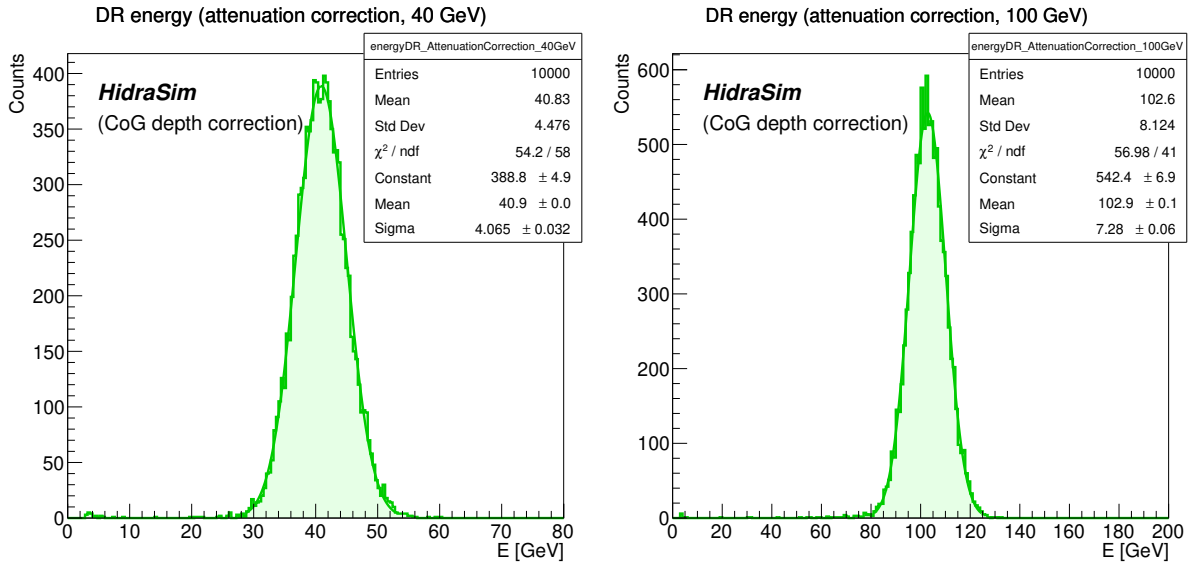


Figure 5.38: Simulated dual-readout energy distributions, obtained by applying the same procedure used for analysing the test beam data. Light attenuation parameters were set to reproduce the observed one.

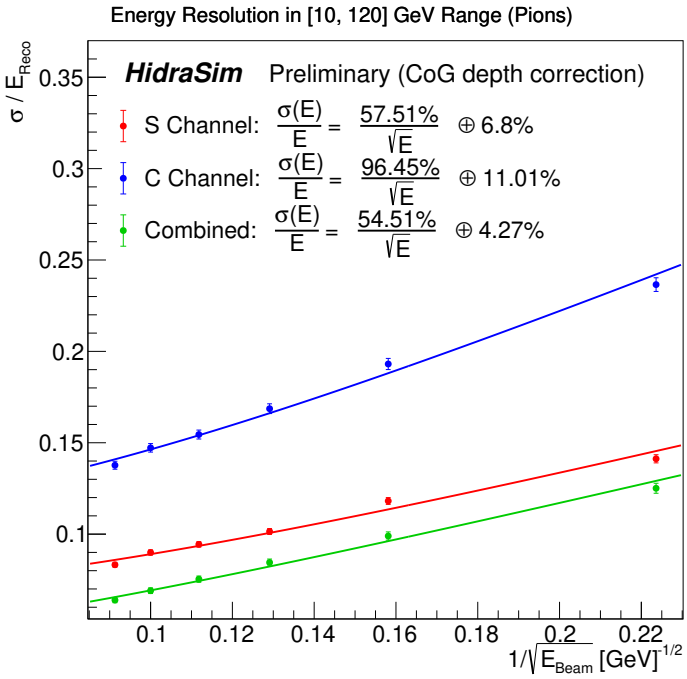


Figure 5.39: Energy resolution obtained through the Geant4 simulation, applying the same correction procedure that was used for test beam data.

Since both the calorimeter limited containment and the light attenuation were corrected through the procedure described in section 5.2.3, the same method could also be applied to the simulation output. Figure 5.38 shows two examples of dual-readout energy distributions, that were computed by applying the usual dual-readout formula on the scintillation and Čerenkov signals, previously corrected for their own light attenuation. These resulting distributions are far better described by gaussian functions than the ones measured through test beam data (fig. 5.34), also being more compact and distributed around the true hadron energy with a value of $\chi = 0.32$. This result proves that, in a situation with only the light attenuation being the major calorimeter problem besides small containment, the followed procedure works correctly in restoring the dual-readout method advantages. The resulting energy resolutions, represented as the RMS of the scintillation and Čerenkov energies, and the gaussian fit one for the dual-readout energy, are shown in fig. 5.39. All three resolution curves show some improvement in both stochastic and constant terms. The slightly more reliable Čerenkov energy resolution also makes it possible to obtain a small improvement of the dual-readout curve over the scintillation alone, while these two curves were very close to each other in all previously obtained results because of large Čerenkov signal fluctuations. The usage of dedicated SiPMs with improved photon detection efficiency for Čerenkov light could make it possible to sample a larger amount of optical photons produced through this process, hence improving the total resolution of both the Čerenkov and the dual-readout energies.

A final observation that was done while evaluating the scintillator and Čerenkov responses of the DRAGO simulated calorimeter, was that the profile shown in fig. 5.36 lies very close to the diagonal line, suggesting very similar $(h/e)_S$ and $(h/e)_C$ responses of the two active media. The underlying idea behind the dual-readout technique is that the two ratios should be as different as possible, to correctly exploit the complemen-

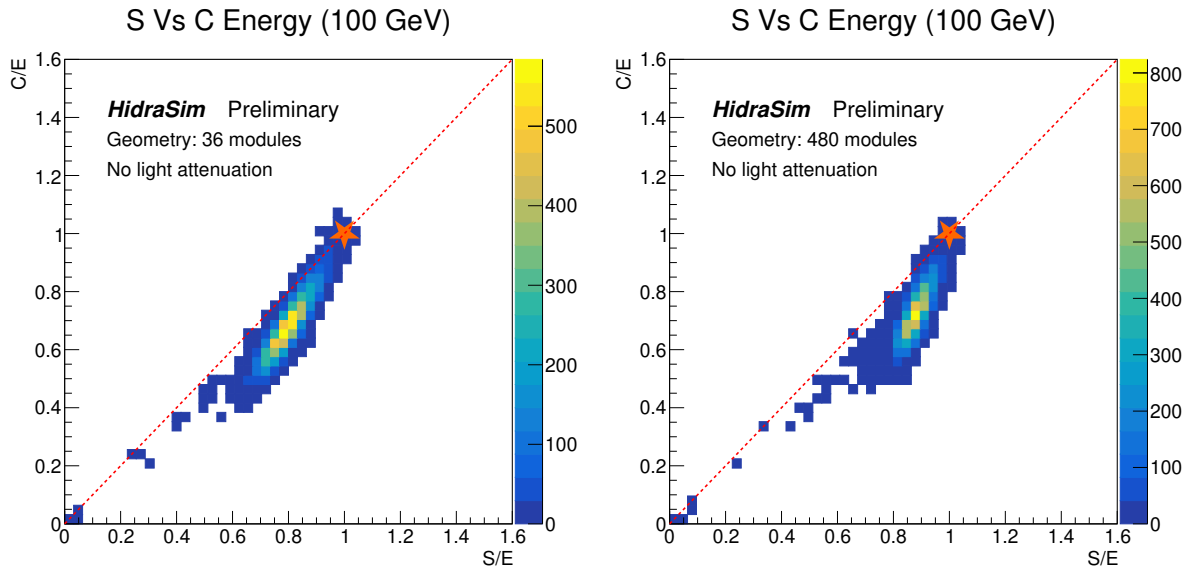


Figure 5.40: Simulated scintillator and Čerenkov responses (normalised for the beam energy) for two tested geometry, the DRAGO prototype one, and a fully-containing calorimeter. Light attenuation was in this case switched off.

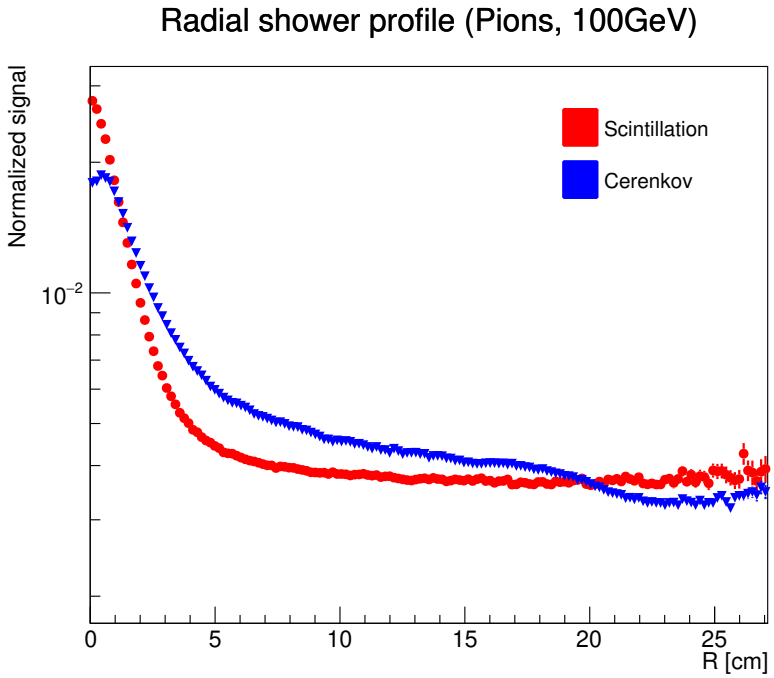


Figure 5.41: Simulated radial profile of 10^4 hadron showers, originated by 100 GeV positive pions, assuming the readout of each fibre independently.

tary information provided by the considered physics processes. In order to evaluate if light attenuation is playing any role in this regard, the simulation was run again with this effect being suppressed, with the result shown in fig. 5.40. A second simulation is also run with a much larger prototype, being the one with 480 modules described in chapter 3. The resulting distribution reproducing the DRAGO geometry, despite a slightly higher total signal in both the scintillating and Čerenkov channels (as could also be observed in fig. 5.37), reproduces fairly well the profile orientation found in data (see fig. 5.36), after the correction for light attenuation. The much larger prototype with almost complete hadron shower containment, on the other hand, is located further from the diagonal, suggesting different responses to the two components of hadron showers. Since the value of the dual-readout parameter χ is directly obtained from the mentioned responses as

$$\chi = \frac{1 - (h/e)_S}{1 - (h/e)_C}, \tag{5.7}$$

one possibility for the different values of this parameter during the optimisation procedure of the HiDRa calorimeter could be different containment of the total hadron shower energy, when evaluated separately for the two channels. Figure 5.41 shows the simulated lateral profile of 100 GeV pions entering the DRAGO calorimeter, as it would be measured if all fibres in the prototype were readout with silicon photomultipliers. Different profiles are found for the two kinds of signals, with a larger Čerenkov profile that deposits a larger fraction of signal within a radius that is compatible with the calorimeter being tested. One should however keep notice that the resulting distribution only shows an average distribution of hadron showers, which are very complex object subject to large event-by-event fluctuations. The result here briefly presented should therefore be deepened with more detailed studies, both through simulations and with real data, when they will be available.

5.3 Conclusions and prospects

While the development of HiDRa approaches its conclusion, with the almost finished integration of SiPMs in the readout of the core modules, some preliminary conclusions can be pointed out. Identifying a cost-effective construction technique for fibre calorimeters, that could be scaled up for full coverage experiments, was among the main objectives of the project. The capillary-based design goes precisely in this direction, with the built modules showing excellent structural results at moderate costs. The next step in this regard is identifying a solution for automatic insertion of optical fibres in the capillaries, which was found to be the major issue in the calorimeter construction. This second part of the project has been funded with 10 k€ for the investigation of possible methods, and will be carried out in the Pavia laboratories with remaining spare tubes and fibres.

Concerning the actual physics performances of the tested prototype, a significant amount of work is still required to fully characterise the built calorimeter. The response to electromagnetic showers was found to be reasonably well described by simulations, but tower-by-tower response dishomogeneities, combined with the uneven tower sizes, made the equalisation and calibration procedures difficult. Dedicated studies are planned to understand the origin of these effects and solve them, to reduce at negligible level the constant term of the obtained energy resolution. Laboratory tests with LED pulses and light mixers are envisaged, but could not be performed before the 2025 beam test, the first test of this prototype with SiPMs readout. If they were

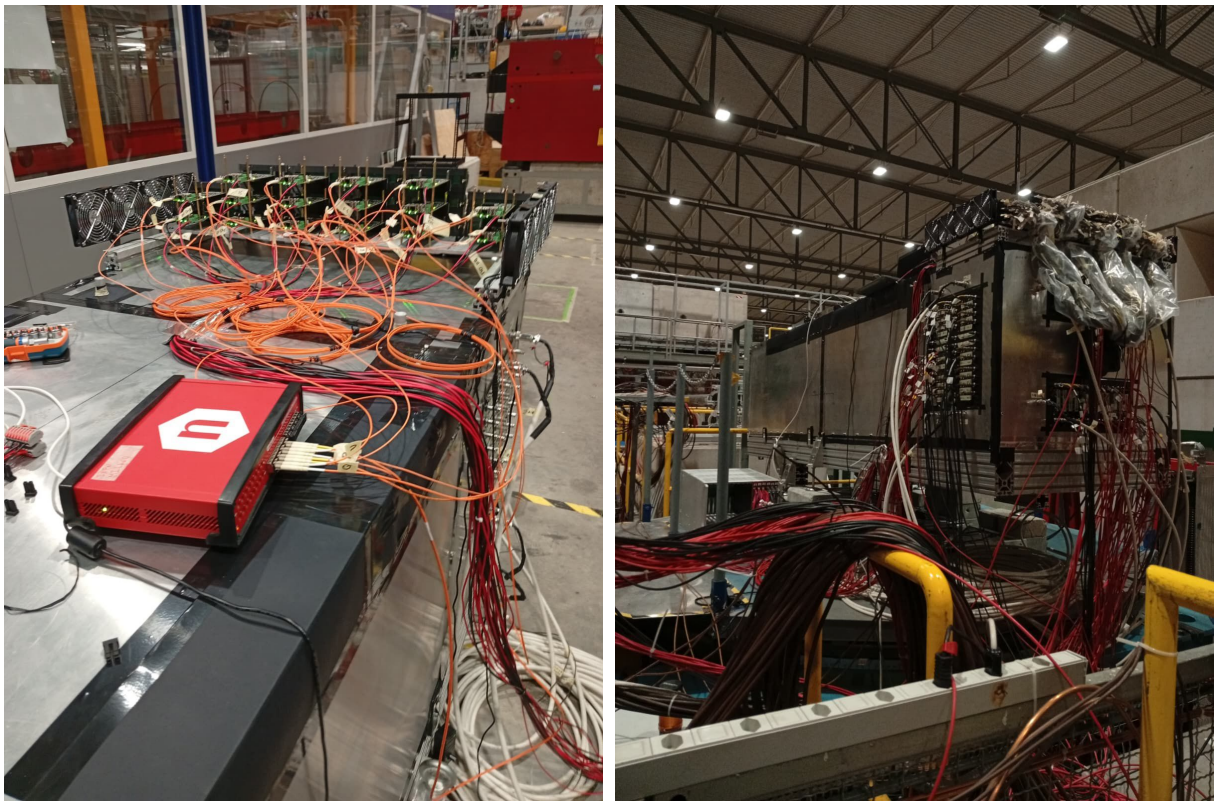


Figure 5.42: Pictures from the 2025 beam test at CERN North Area. On the left, preparation of the SiPM readout system before the calorimeter transportation in the experimental area. The CAEN FERS boards were located on top of the calorimeter box, with dedicated fans for cooling. The signals are collected through a daisy chain from the data concentrator system, also from CAEN [137]. On the right, calorimeter cabling for the readout of PMTs and SiPMs.

found to guarantee significant improvement in the homogeneity of towers responses, light mixers should be added in between the optical fibres and PMTs, and the mechanical supports should be modified accordingly. Additional sources that could explain the described detector response are nevertheless being investigated with the newly collected data.

An open point being investigated is attenuation of light in the optical fibres. This effect may play a significant role in spoiling the hadronic performances of fibre calorimeters, and currently available measurements are not pointing to a clear result. This is mostly true for clear fibres, which are expected to provide large attenuation length parameters, in agreement with laboratory measurements but disfavoured by test beams data. Disagreement between different measurements are also observed for scintillating fibres, despite smaller attenuation lengths with respect to Čerenkov ones are expected.

The performance of the calorimeter regarding the response to hadrons is far from being completely comprehended. Despite the small containment of the tested prototype during the 2024 beam test, leading to large leakage fluctuations in the lateral direction, significant deviations from the simulation and measured data have to be understood. One possible reason, that was later discovered during the latest beam test campaign in 2025, was related to the high voltage settings of PMTs. In the previous year run, a limited dynamic range of the PMTs amplifier boards forced the team to reduce the high

voltage of PMTs to not saturate the signals. This issue was observed later during the data taking, when looking at signal linearity for electrons. To overcome this problem, all the PMT high voltage settings were reduced to avoid saturation when looking at the entire energy range of interest. The lower gain, however, may have reduced too much the sensitivity to small signals emitted by pions in PMTs far from the core of the shower energy deposition. This issue would mostly contribute at lower pion energies, where signals in other towers would not deviate significantly from the pedestals, while at higher pion energies the deposition would still be sufficient to be measured. This effect still has to be completely comprehended, and the inclusion of a digitiser module in the simulation is planned to try reproducing the electronics and readout impact on the actual resolution to hadrons. Naively, one may interpret that an effect that reduces the sensitivity at lower energies would contribute to the stochastic term of the resolution, by increasing fluctuations on the deviations over the threshold over which the signal is actually read out, partially explaining the significant differences between the simulated and measured energy resolutions for pions.

The saturation issue should have been partially addressed during the 2025 beam test with the inclusion of SiPMs in the core of the HiDRa prototype. The dynamic range of the amplifier boards was increased, and the high gain of the PMTs was set to higher values, enhancing the sensitivity to lower energy deposits. For the SiPMs, that receive most of the total energy deposition from particle showers, two spectra are collected with both high gain and low gain, therefore enhancing the sensitivity to a wider energy range than for PMTs. Figure 5.42 shows pictures of the readout system used for the data taking, concerning both types of photosensors. The major effort is currently being posed on the equalisation of all PMT and SiPM channels, which has never been done for this types of calorimeters, particularly using SiPMs to readout optical fibres. The grouping of eight SiPMs signals into one readout channel, including electronic noise, made the identification of multi-photon spectra not feasible in early stages of the data analysis, so alternative solution are being investigated, using both electrons and also muons. Figure 5.43 shows an event display of a 60 GeV pion entering the HiDRa calorimeter, after the alignment of the two readouts. After this important preliminary step, it will be extremely interesting to finally evaluate the energy responses of this detector to different particles. This will allow having a complete characterisation of this new type of calorimeters, targeting future collider experiment studies based on real detector performance measurements.

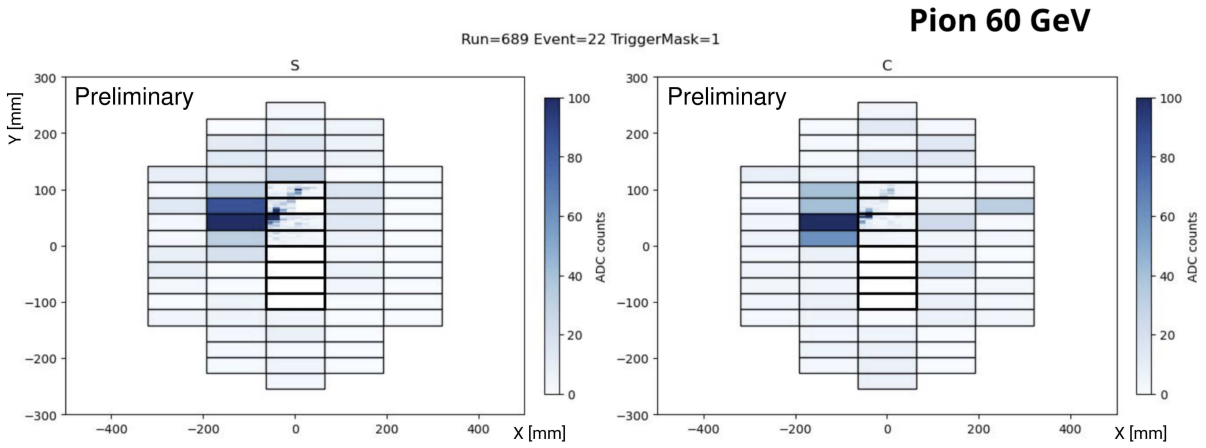


Figure 5.43: Preliminary event display, before all channels equalisation, for a 60 GeV pion event from the 2025 test beam with the combined PMT and SiPM readout.

Part II

Search for heavy neutral leptons with the ATLAS Experiment

In the following chapters, a search conducted as a member of the ATLAS collaboration for new particles outside of the Standard Model, the heavy neutral leptons (HNLs) is outlined. I participated to this analysis in two different time periods, during my Master thesis, with a preliminary search using Machine Learning techniques for improving the sensitivity of the experiment to HNLs [138], and during my doctoral period at a later stage of the analysis. In this activity, I was mainly involved in the setup of the TRExFitter [139] software framework for the statistical data analysis, which was used for the fits inside the defined signal regions and obtain the limits on the heavy neutral leptons mixing parameters. I also had the chance of working on the definition and optimisation of some signal regions, which resulted in a significant improvement over the ones in use previously. Other roles I was mainly involved with were studies on the validation of the different sources of background of the analysis, which will be presented in the following. The paper describing the main results of this analysis has been accepted for publication by Eur. Phys. J. C, and is currently available as pre-print in Ref. [140].

CHAPTER

6

THE ATLAS EXPERIMENT

The ATLAS experiment [24] is the largest scientific collaboration active at CERN, involving 6113 members from 262 institutes in 46 countries, at the time of this thesis' writing. The collaboration was first formed in 1992, and the experiment was later approved in 1996, with the first data collected in 2008. Besides the search and discovery of the Higgs boson, the range of measurements performed by ATLAS spans from search of new phenomena beyond the Standard Model, to precision QCD and electroweak studies, and flavour physics. The ATLAS detector was in fact designed to allow a broad research program by exploiting various subdetectors covering almost the entire solid angle. In this chapter, the ATLAS experiment is presented, including the different subsystems that constitute the detector, and the data pipeline from the particles interactions to reconstructed events that can be used in the analyses. Particular care is put on the reconstruction of those physics objects that will be later used in the analysis presented in chapter 7.

In order to better describe the characteristics of the detector, a set of geometrical and kinematic variables in use at ATLAS must be first introduced, being the rapidity y, the transverse momentum p_T and azimuthal angle φ. ATLAS uses a right-haded coordinates system, shown in fig. 6.1, with the $\widehat{z}$ axis defined along the beam direction and pointing to the following LHCb experiment, and the $\widehat{x}$ axis pointing towards the centre of the LHC ring. It is then possible to pass from Cartesian coordinates to polar ones defining a radius r as the distance from the experiment beamline in the $x-z$ plane, and the polar angle ϕ as the angle between the radius r and the x axis. The azimuthal angle is then the angle between the radius r and the $\widehat{z}$ axis. From this set of coordinates, the four-momentum p^μ of a particle with mass m can be defined as

$$\begin{aligned} p^\mu &= (E, p_x, p_y, p_z) \\ &= (m_T \cosh y, p_T \sin \varphi, p_T \cos \varphi, m_T \sinh y), \end{aligned} \tag{6.1}$$

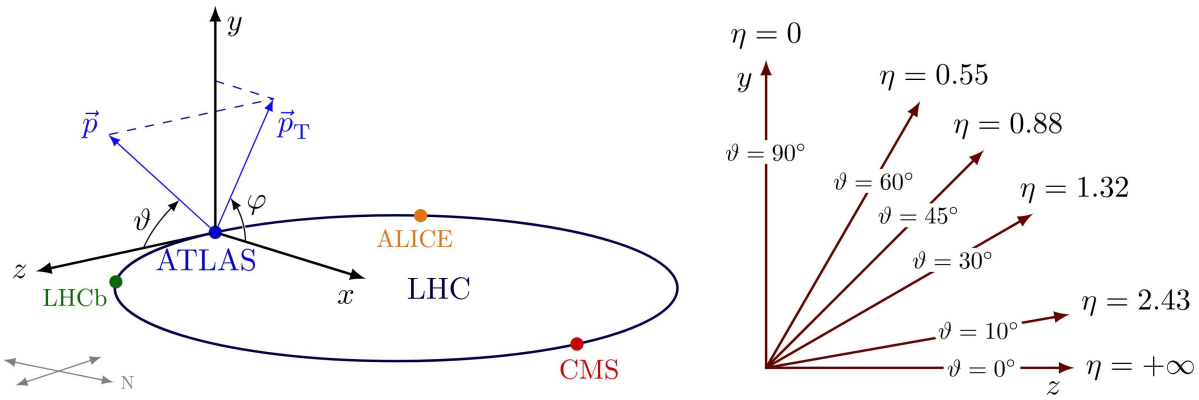


Figure 6.1: ATLAS coordinate system and pseudorapidity as a function of the polar angle. Both images taken from [141].

with the transverse momentum p_T and transverse mass m_T defined as

$$p_T = \sqrt{p_x^2 + p_y^2}, \quad m_T = \sqrt{p_T^2 + m^2} \tag{6.2}$$

and the rapidity y:

$$y = \frac{1}{2} \ln \left(\frac{E + p_z}{E - p_z} \right). \tag{6.3}$$

A widely used approximation of the rapidity, valid for small particles masses, is the pseudorapidity η, defined as

$$\eta = -\ln \left(\tan \frac{\vartheta}{2} \right). \tag{6.4}$$

While neither the rapidity nor the pseudorapidity are Lorentz-invariant quantities, the differences between two vectors' rapidity is invariant under Lorentz transformation, but pseudorapidity differences are not. Pseudorapidity is nevertheless useful for converting particle-level information into more simple geometrical azimuthal angle coverage of detectors, as shown in fig. 6.1 (right). Pseudorapidity is also used to define angular separation between two close particles, $\Delta R = \sqrt{(\Delta\eta)^2 + (\Delta\varphi)^2}$, which is Lorentz invariant under boosts along the longitudinal $\hat{z}$ direction.

6.1 ATLAS detector

The ATLAS detector is the largest of the four main experiments currently active at the CERN Large Hadron Collider. A cut-view drawing of the detector and its different subsystems is shown in fig. 6.2. It features a forward-backward cylindrical symmetry, with a 44 m long structure and 25 m height, summing up to about 7000 tonnes of weight.

The detector was designed to fulfil a list of benchmark requirements posed both on the physics goals, and on the need to operate at the most powerful accelerator ever built, the LHC. Among these concepts behind the experiment design were fast and radiation-hard detector elements, including electronics and sensors, to withstand the high activity of the LHC, and detectors granularity to reduce multiple particle overlapping in the same cell. Detector acceptance until very large pseudorapidities, and with almost complete azimuthal angle coverage, were required to maximise the reconstruction efficiencies and to fully exploit the large number of produced collisions data. Concerning

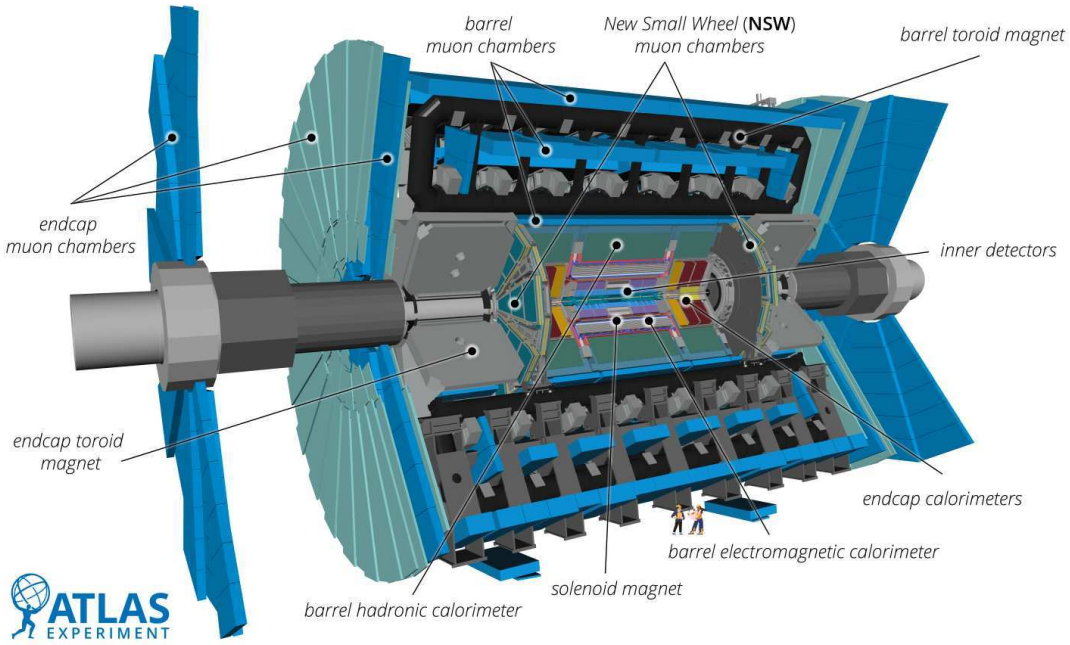


Figure 6.2: Schematic rendering of the ATLAS detector, taken from [142].

individual subdetector performances, good tracking systems working close to beamline were required for the tagging and reconstruction of b-quark hadrons and τ leptons. Both excellent electromagnetic calorimetry and muon momenta measurements were required for the search of the Higgs boson into the $H \rightarrow \gamma\gamma$ or $H \rightarrow 4l$ decays, and electroweak processes studies. A reasonably good hadronic calorimeter would have allowed better reconstruction of events including hadronic jets as final states, and improved missing transverse momentum reconstruction. Finally, an important requirement on such a complex system is efficient triggering capabilities to select interesting events from a large amount of background processes that have to be rejected, and an advanced data acquisition chain to collect such an impressive amount of data. The magnetic field, required for bending charged tracks and the measurement of their momenta, is provided by a thin superconducting coil located around the inner tracker detector, that produces solenoidal field lines. It is complemented by other three large superconducting magnets providing a toroidal magnetic field, two of which located in the detector end-caps and the third one placed in the barrel. A brief description of each ATLAS subdetector, and its performances on particle measurements that impact physics analyses, is reported in the following. Table 6.1 reports a summary of the individual resolutions on particles momenta or energy, and their azimuthal angle coverage for both particles measurements and triggering purposes.

6.1.1 Inner detector

The inner detector (ID) is the ATLAS subdetector closest to the interaction point. It allows the measurement of the position of each particle produced after pp (or ions) collisions, about 1000 per event every 25 ns, when they cross one of the ID layers. The individual hit positions are then used for the reconstruction of each track, from the IP to the outer layers of ATLAS. For this reason, an extremely fine granularity is required, to minimise multiple tracks crossing the same tracker cell, and improve the position resolution. The ID comprises three detector technologies, with decreasing granularity

Table 6.1: Main performance requirements for the different ATLAS subdetectors [24].

Detector component	Required resolution	η coverage	
		Measurement	**Trigger**
Tracking	$\sigma_{p_T}/p_T = 0.05\% \, p_T \oplus 1\%$	± 2.5	
EM calorimetry	$\sigma_E/E = \frac{10\%}{\sqrt{E}} \oplus 0.7\%$	± 3.2	± 2.5
Hadronic calorimetry (jets)	$\sigma_E/E = \frac{50\%}{\sqrt{E}} \oplus 3\%$ (barrel & end-cap)	± 3.2	± 3.2
	$\sigma_E/E = \frac{100\%}{\sqrt{E}} \oplus 10\%$ (forward)	$3.1 < \lvert\eta\rvert < 4.9$	$3.1 < \lvert\eta\rvert < 4.9$
Muon spectrometer	$\sigma_{p_T}/p_T = 10\%$ at $p_T = 1$ TeV	± 2.7	± 2.4

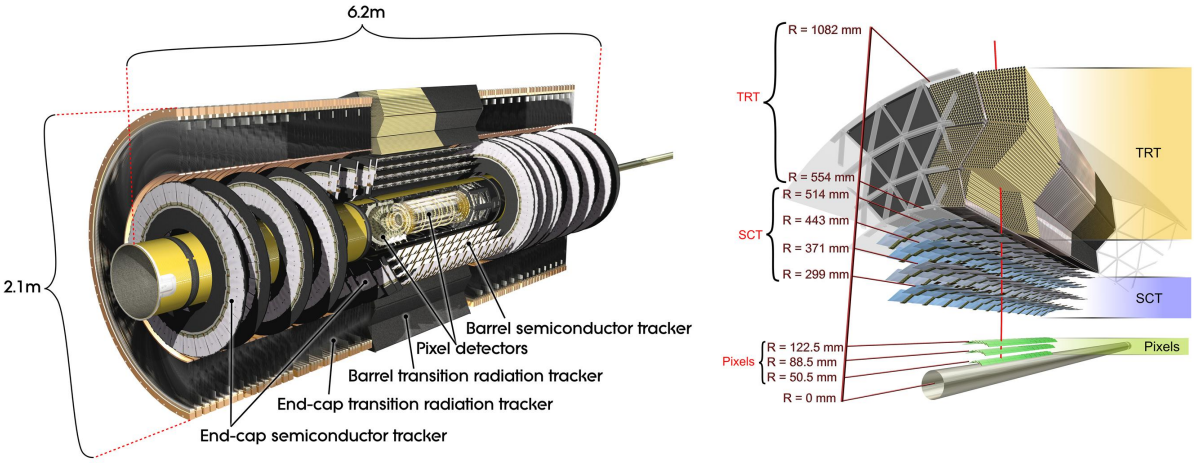


Figure 6.3: Cut-view images of the ATLAS inner tracking detector [24].

from the inner to the outer layers. From the innermost layer, these are silicon pixel, silicon microstrips (SCT), and Transition Radiation Tracking (TRT) detectors, shown in fig. 6.3. All three systems cover the pseurodapidity range up to $|\eta| < 2.5$, having a total length of 6.2 metres, and are immersed in a 2 T solenoidal magnetic field provided by the inner magnet coil.

The silicon pixel system comprises three layers, arranged as concentric cylinders in the barrel and disks perpendicular to the beamline in the end-cap regions. All pixel sensor cells cover the same area of 50×400 μm^2, being oriented along $(r - \varphi) \times z$ in the barrel and $(r - \varphi) \times r$ in the end-caps, summing up to a total of 80.4×10^6 channels for the readout. An additional pixel layer, the Insertable Barrel Layer (IBL) [143], was inserted during Long Shutdown 1 between the previous innermost pixel layer and the beam pipe to cope with the increasing luminosity.

The SCT system consists of a total of eight layers of silicon strips, providing four measurements of traversing particles positions, since each strip provides measurement of only one coordinate. Each strip has a length of 6.4 cm and a pitch of 80 μm, adding approximately 6.3×10^6 channels.

Finally, the outermost system is a transition radiation detector, which besides particle identification, also acts as a tracker by providing information of particles positions in the $(r - \varphi)$ plane, with an accuracy of 130 μm. It consists of 4 mm diameter straw tubes arranged in 73 layers in the barrel and 160 in the end-caps [24][144], providing on average about 36 hits per track up to $|\eta| < 2$, providing 3.5×10^5 channels. The straw tubes run parallel to the beamline in the barrel, with a length of 144 cm, while the ones in the end-caps are arranged radially in wheels and are 37 cm long.

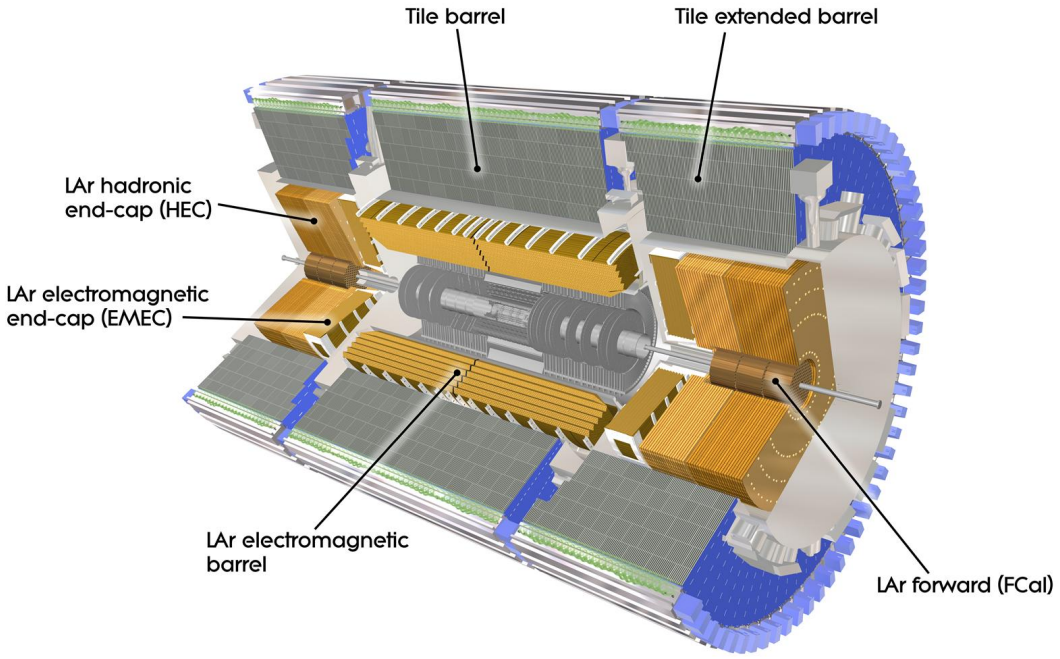


Figure 6.4: Computer rendering of the ATLAS calorimeters [24].

6.1.2 Calorimeters

The ATLAS calorimetry system, shown in fig. 6.4, is divided into an electromagnetic section, followed by a second one for hadron energy measurements, covering a pseudo-rapidity range $|\eta| < 4.9$. Both calorimeters feature some degree of non-compensation, and exploit different technologies for the measurements of particle energies. The electromagnetic section consists of a lead-liquid argon (LAr) sampling calorimeter featuring an accordion-shaped geometry. It is divided into a barrel section ($|\eta| < 1.475$), and two end-cap section further divided into two components, an outer wheel with $1.375 < |\eta| < 2.5$ and an inner one with $2.5 < |\eta| < 3.2$. The total depth of this calorimeter is equivalent to $22X_0$ in the barrel, and $24X_0$ in the end-caps.

The hadronic calorimeter section exploits different sets of materials, both active and passive, at increasing pseudorapidity values. One central barrel region and two extended barrels cover the range $|\eta| < 1$ and $0.8 < |\eta| < 1.7$ respectively, and are based on steel absorber and plastics scintillating tiles, and are therefore called tile calorimeter. The azimuthal angle is divided into 64 modules, each further divided into three longitudinal layers that are $1.5\ \lambda_I$, $4.1\ \lambda_I$ and $1.8\ \lambda_I$ deep in the barrel and $1.5\ \lambda_I$, $2.6\ \lambda_I$ and $3.3\ \lambda_I$ in the extended barrels. Each scintillating tile is read out on two sides by wavelength shifting fibres for the coupling to PMTs.

At increasing pseudorapidity values, $1.5 < \eta < 3.1$, the Hadronic End-cap Calorimeter (HEC) features once again LAr technology associated to copper plates as absorber materials. Each side of the HEC is subdivided into two wheels containing two modules each, extending from 0.475 m to 2.03 m from the beamline. A total depth of $9.7\ \lambda_I$ is obtained by summing all four layers of each end-cap.

Finally, the Forward Calorimeter (FCal) is used to cover the very-high pseudorapidity region up to $3.1 < |\eta| < 4.9$. It is divided into three sections, all using LAr as active medium and being located into the same cryostat as the HEC calorimeter. The first

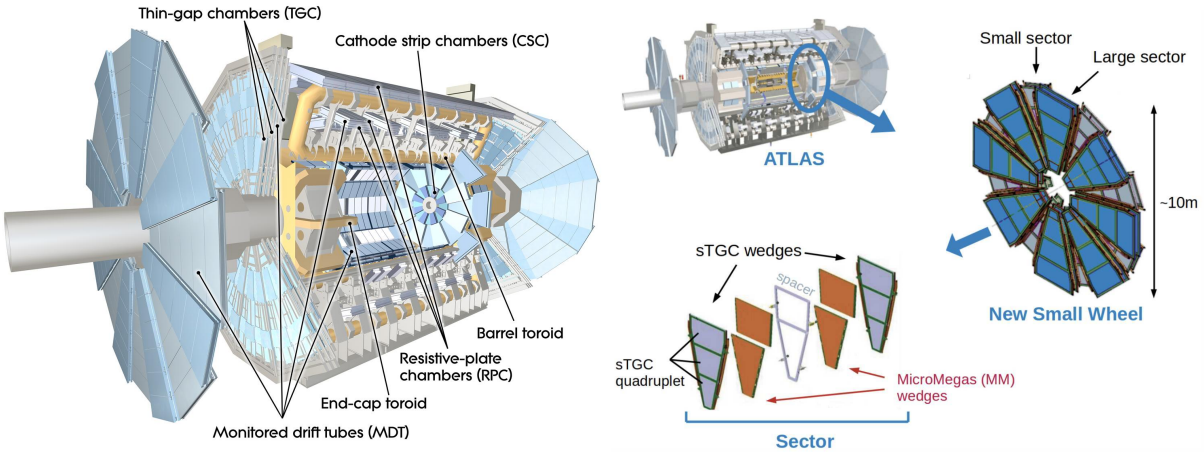


Figure 6.5: Image of the ATLAS muon systems until the end of Run 2, and the New Small Wheel installed in 2020 [145].

layer features a copper passive absorber and is designed for improved electromagnetic showers measurements, while the other two layers use a heavier tungsten absorber for hadronic ones. The design of each layer is based on a metal matrix in which equally spaced longituidinal rods filled with LAr and the relative tubes and electronics are inserted, parallel to the beamline. The total depth of the FCal, summing all three layers, reaches $\sim 10\ \lambda_I$.

6.1.3 Muon systems

The outermost system of the ATLAS experiment is the muon spectrometer, which allows the identification and momentum measurement of muons through the bending inside the toroidal magnetic field provided by the superconductive coils. These particles are, in fact, the only species that are expected to escape from the calorimetric system, with the exception of neutrinos which are measured through the missing transverse momentum, $p_{\mathrm{T}}^{\mathrm{miss}}$, and punch-through jets leaking out of the calorimeters. The layout of the muon spectrometer is shown in fig. 6.5, which was used until the end of the Run 2 of the LHC. The spectrometer was then updated during the LHC Long Shutdown 2 before the start of Run 3 with the inclusion of the New Small Wheel (NSW). A first description of the muon system before the NSW inclusion is given, as it was the detector layout for the data taking campaign used for the analysis presented in chapter 7. The detector upgrade with the NSW from Run 3 is then outlined. The barrel toroids produce a magnetic field in the $|\eta| < 1.4$ region, which is extended for $1.6 < |\eta| < 2.7$ by end-cap toroids. In the "transition" region with $1.4 < |\eta| < 1.6$, the magnetic field is a combination of the two remaining fields provided by the two toroid systems.

The layout of the muon spectrometer system is based on triple detector layers, having a cylindrical geometry in the barrel and radial one on each side of the ATLAS end-caps. An optical alignment system is also used to monitor the relative positions of the different subsystems and their deformations. Monitored Drift Tubes (MDTs) are used for precise tracks position measurements over the entire pseudorapidity range covered by the muon spectrometer, $|\eta| < 2.7$. The sizes of the MDTs, including the tube radii and their length, vary with their positions in the barrel or end-caps, and the subdetector layer they are located in. In the higher pseudorapidity region $2 < |\eta| < 2.7$ of the end-caps, cathode-strip-chambers (CSCs) were used until Run 2 to cope with the very

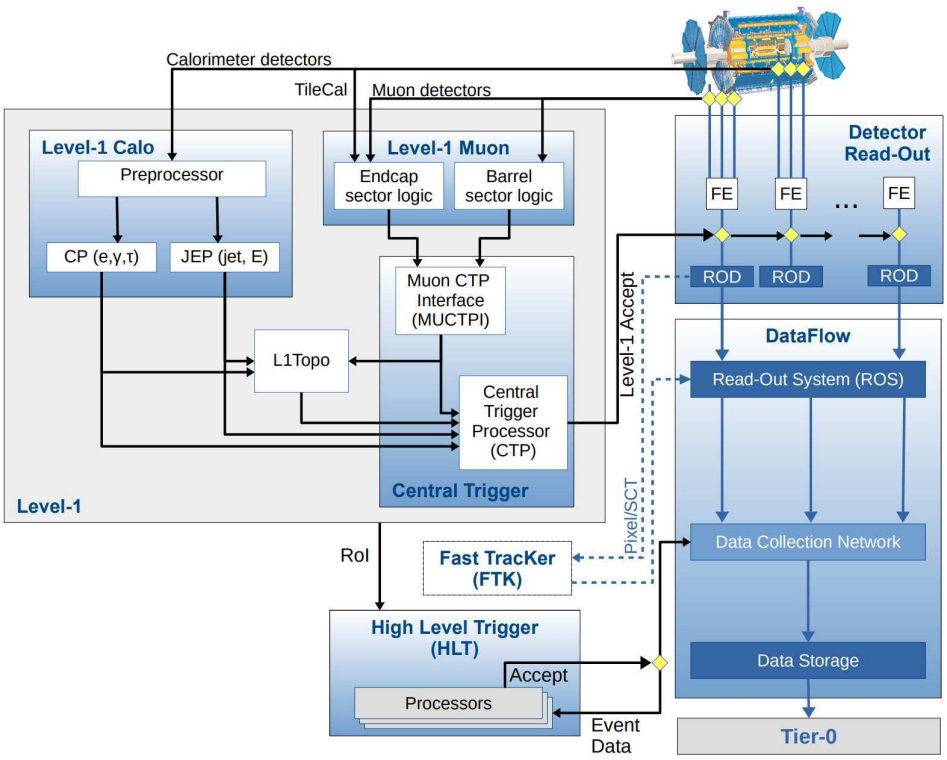


Figure 6.6: Scheme of the ATLAS trigger system [146].

high fluxes present in those regions, because of their finer segmentation.

The other two main muon detector systems are used for the triggering of interesting events, and mainly focus on very fast signal production which is used for bunch crossings identification. They also provide a measurement of the second coordinate, orthogonal to that measured by the other high-precision chambers. These systems are Resistive Plate Chambers (RPCs), used for the barrel region, and Thin-Gap Chambers (TGCs) in the end-caps, covering up to $|\eta| < 2.4$.

The New Small Wheel muon system was included in ATLAS in 2021, replacing the "old" wheel based on MDTs and CSCs, in prevision of the much higher luminosities of the LHC Run 3, and more importantly, the following High-Luminosity phase. Two detector technologies are used, the MicroMegas (MMGs)[1] for precision tracking and small-strip Thin Gap Chambers (sTGCs) for triggering. Both detectors are nevertheless able to supply the other type of information for redundancy. Each NSW consists of a total of 16 layers, which are arranged into two multi-layers. One multi-layer comprises four MMG and four sTGC layers, with the sTGC ones on the external sides of the multi-layer, as shown in fig. 6.5.

6.2 Trigger, Data acquisition and processing

Because of the large amount of detector channels to readout, and the very high rates of particles interactions provided by the LHC, the ATLAS experiment must rely on efficient and highly performant triggering and data acquisition (TDAQ) systems. These

[1]During my Ph.D. I also took part to the development of the online monitoring framework of the MMGs system, which is not described in this thesis. I was mainly involved on algorithm development and preparation of histograms and plots to be shown in the ATLAS Control Room by shifters, to check the correct working of detectors.

systems allow passing from an event rate of 40 MHz, produced by the 25 ns spacing between LHC bunches, to about 1 kHz, that is a sustainable rate for the storing of the acquired data. Once the data from the different subsystems of the detector have been collected, they need to be processed, in order to be transformed from raw electronic signals to calibrated data, to reconstruction of high-level information on final state particles that can be used in the physics analyses. In the following, a brief description of the different steps of the data-flow chain are given.

ATLAS uses a two-level trigger system, the first one called Level-1 (L1) trigger, being hardware-based, and the second one based on software, the High-Level Trigger (HLT). A further selection is then applied on events passing both levels, the event filter. A drawing of data flow between the three systems is shown in fig. 6.6. The L1 trigger is designed to look for events containing muons with high transverse momenta in the MS, electrons and photons in the ECal, jets and hadronically decaying τ leptons in the HCal. Additional event features that would activate the trigger are large missing transverse momentum or large total transverse energy. A subset of information from individual subdetectors is used to switch on the L1 trigger, in order to keep it as fast as possible, by using only the trigger-dedicated subdetectors information from the muon spectrometer and reduced granularity information from the calorimeters. A list of requirements on this kind of information, called menu, is applied by a central trigger processor which takes decisions based on individual triggers. The L1 trigger is also used to define, for any event, one or multiple Regions-of-Interest (RoIs), being coordinates regions (η, φ) where some interesting objects were identified, that is later used by the HLT. The first level of trigger allows to decrease the event rate, from the starting 40 MHz, down to 100 kHz and with a 2.5 μs latency. For the accepted events, data from the Front-End (FE) readout electronics of each detector is processed and formatted through ReadOut Drivers (RODs), and later collected by the ReadOut System (ROS), in order to be further processes by the HLT.

The second trigger level, being software-based, applies a light and fast reconstruction process through specific algorithms, that resemble those later applied offline but with less precision. Some event features are usually extracted from the selected ROI and used in the reconstruction, but the entire detector information is also available for building the trigger decision, including the inner tracker detector. The execution is applied in a dedicated farm with approximately 40000 Processing Units, and requires few hundred milliseconds to take a decision on the entire event.

The selected events from these two levels of trigger are then passed to the Tier-0 facility for the complete event reconstruction, drawn in fig. 6.7. The "raw" formatted data are stored, after the Trigger and Data Acquisition (TDAQ) steps, in the form of data *streams* representing low-level collections of event fragments. The main types of streams type are *calibration*, comprising non-complete events for calibration and alignment tasks, *express* which uses only a partial set of physics triggers, and *main*, from which most events used for the physics analyses are taken [148]. The first two data streams are fast processed by the Tier-0 farm, which is located in a room close to the experiment at CERN, to obtain a first calibration parameters that would be used for the main stream. Events from the main stream are processed in bulk usually about 48 hours after their acquisition. A further reprocessing of the reconstructed events is later performed in the Tier-1 grid, which consists of several computing farms located over the world. The reprocessing allows to obtain fully calibrated events with well-understood data, and also when passing to different reconstruction software releases. A hierarchi-

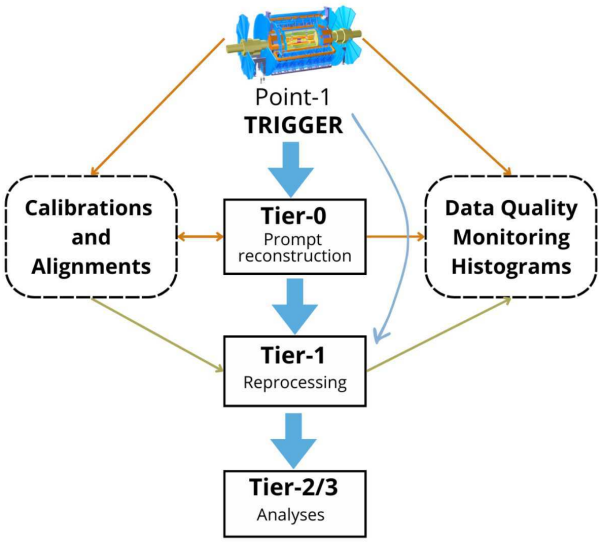


Figure 6.7: Data processing of the ATLAS experiment, from selected events by the trigger to reconstruction and analyses. Image taken from [147].

cal grid model was designed, to share the computing needs required to process very large amounts of data, consisting of multiple levels, from Tier-1 to Tier-3 facilities. These facilities are also used for the production of Monte Carlo simulated events and their reconstruction, obtaining the same data format as real data.

6.3 Physics objects reconstruction and identification

The reconstruction process is a fundamental step which allows passing from digitised detector readouts into physics objects to be used in the analyses. After pp and ions collisions in the LHC beam pipe, several short-lived particles are produced and decay before being detected, and their properties must therefore be inferred from the signatures of their decay products. In the following, the reconstruction and identification steps of stable particles (or particles with a half-life long enough such that they can be considered stable while traversing the ATLAS detector) are described. A focus is put on electrons and muons, which are the most important physics objects for the analysis presented in chapter 7, but also including hadron jets and photons which may enter as possible background sources. The reconstruction technique of several physics objects has been refined over the years, since the beginning of LHC Run 1. The information prodided in the following mostly refers to the 2015-2018 period of Run 2, whose data has been used in the later analysis.

6.3.1 Electrons and photons

Electrons are searched through signatures consisting of clusters of energy deposits in the electromagnetic calorimeter, that can be matched to a track in the inner detector which points to the calorimeter cluster in the (η, φ) plane [149]. Their reconstruction is closely related to that of high-energy photons, which are characterised by similar deposits in the ECal, but usually missing an associated track. In fact, energetic γs can convert into e^+e^- pairs while passing through the inner detector, or even the beam pipe, and in that case they are denoted as *converted* photons. Otherwise, if no conversion vertex was reconstructed or associated to the cluster, these photons are called *unconverted*.

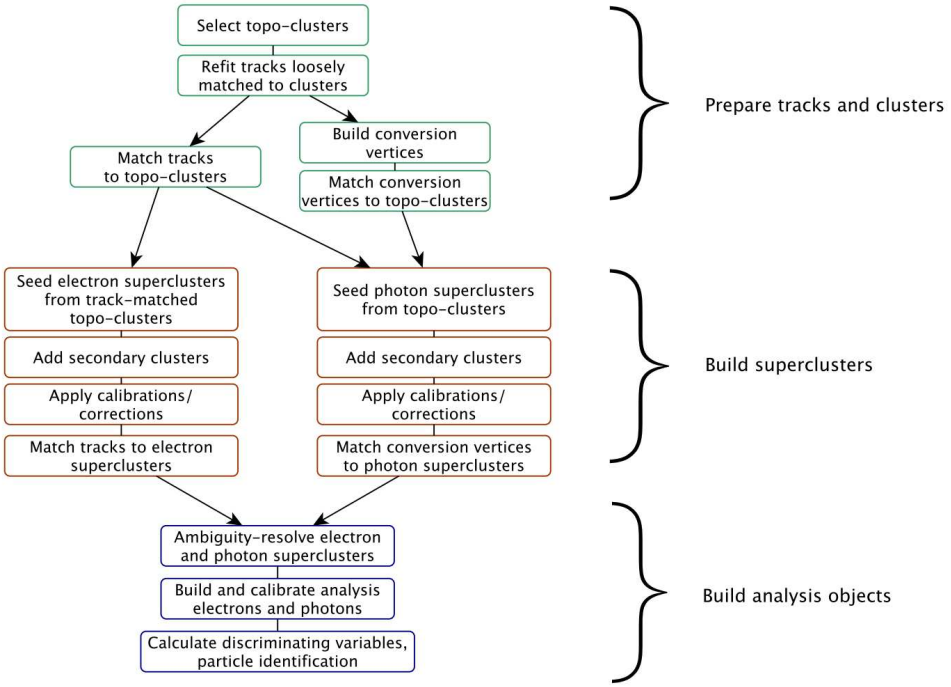


Figure 6.8: Reconstruction process of electron and photon candidates, taken from [149].

Furthermore, energetic electrons can also emit photons through the bremsstrahlung process while traversing the materials composing the beam pipe or the inner tracking layers, which may convert back into an e^+e^- pair and produce multiple tracks. A step in the electron and photon reconstruction process is therefore dedicated to resolving these ambiguities which may spoil the correct particle identification.

The reconstruction algorithm of both electrons and photons starts with the search for clusters in the calorimeters and tracks in the inner detector. For calorimeter clusters, ATLAS uses a dynamical topological cell clustering algorithm [150], which is an evolution of the previously used sliding-window algorithm [151] that used fixed-size windows, in order to account for electrons radiative emission. It starts with the identification of multiple seeds, consisting of calorimeter cells with a significant energy deposit over a noise threshold. Topological clusters are then built by aggregating neighbouring cells, some eventually being merged. Tracks reconstruction starts by aggregating individual hits in the layers of silicon tracking detectors, followed by a series of algorithms for pattern-recognition, solving ambiguities and track extension to the TRT subdetector. Radiative losses from electrons are also considered in these steps through dedicated techniques [152] to account for varying track curvature under the tracker's magnetic field. The two kinds of object are then matched, through their (η, φ) coordinates (based on the barycentre position of the cluster and extrapolated coordinates given by tracks). A track selection method is performed, if multiple tracks are matched to the same cluster. Both bremsstrahlung energy losses and photon conversion are taken into account by re-fitting tracks to the superclusters [153] to form an electron or photon candidate, associating conversion vertices to the topo-clusters. For both electron and photon candidates, the reconstruction is performed through the building of calorimeters *super-clusters*. This step takes into account secondary "satellite" clusters, and applies calibration corrections and clusters' position and total energy. In a second step, tracks

and conversion vertices are once again matched to super-clusters to form electron or photon candidates. The reconstruction of electron and photon super-clusters happens in parallel, so that a same cluster seed can be associated to both types. A method for solving possible ambiguities is therefore applied, which can produce an electron or a photon candidate if the ambiguity has been solved, and both types of object otherwise. Discriminating variables of the produced object, mostly regarding the shower shape and additional subdetectors information, are also calculated for the following particle identification purposes.

Depending on the role played by electrons in each analysis, different working points on the correct identification of these particles are applied in the ATLAS workflows. This process allows to define multiple purity selections, for example increasing the amount of electron objects but at the same time accepting other misidenfied particles such as photons or jets, or reducing to a limited sample of electrons with very low remaining contaminations. These working points used by the ATLAS framework are denoted as *loose*, *medium* or *tight*, and correspond to a certain requirement on the value assumed by a likelihood discriminant, which is a function of the variables introduced during the candidate object reconstruction and described in [150]. The likelihood function is further binned in pseudorapidity and transverse energy E_T, in order to keep track of the varying reconstruction efficiency.

Additional requirements that are also used in ATLAS analyses are posed on the isolation of individual physics objects, which concerns the presence of other tracks or energy deposits close to the ones identified as the particle under study. For electrons, a calorimeter isolation variable is built by considering the sum of individual topological clusters that are present in a cone centred around the identified electron. Other corrections, including energy leakage and pile-up contributions are also considered. Similarly, for tracks another variable is introduced by taking the sum of the transverse momentum of other tracks falling in a cone around the identified electron track. Isolation criteria are then defined by setting requirements on these variables, the most important ones used in the following being *Loose* and *Tight*. The values of the different selections are listed in [149].

6.3.2 Muons

The reconstruction of muons is accomplished through the combination of individual information provided by the inner detector and the muon spectrometer. Offline reconstruction first builds tracks independently in the ID and in the MS, and then combines them into one of the possible muon object classes, depending on the subdetectors that are used, being Combined (CB), Segment-tagged (ST), Calorimeter-tagged (CT), and MS-extrapolated (ME) [154]. Track reconstruction in the MS begins by forming straight-line *segments* within individual tracking chambers, either MDTs or CSCs (MMGs after the introduction of the New Small Wheel). An algorithm based on Hough transform [155] is used to search for aligned hit patterns in the bending plane. These segments from multiple stations are then matched and fit to form MS tracks. Requirements typically include at least two MS stations, or a single high-quality one in the barrel–endcap transition region. Energy loss in the calorimeters is accounted for when extrapolating MS tracks to the interaction point [154]. Tracks in the inner detector are reconstructed similarly to those of section 6.3.1, with algorithms operating on silicon tracking detectors and TRT hits. Combined (CB) muons are built by a global refit that uses hits from both ID and MS. An *outside-in* path is the default choice for the reconstruction of

CB muons, starting from MS segments and combining them to ID ones. Individual hits in the MS may also be removed to improve the global fit quality. A complementary search in the opposite *inside-out* direction is also performed, from the ID segments and their extrapolation to the MS. Segment-tagged (ST) muons are used for low-p_T muons or in regions with low detector acceptance, and consist of ID tracks matched to at least one MS segment, used when only a single MS layer is crossed. Calorimeter-tagged (CT) muons are ID tracks matched to a minimum-ionizing signature in the calorimeter, improving acceptance where MS coverage is limited. MS-extrapolated (ME) muons rely on MS tracks, with only loose requirements on tracks originating from the IP, and extend acceptance to $2.5 < |\eta| < 2.7$ [154]. Possible overlaps between multiple classes are resolved by preferring CB muons, followed by ST and then CT ones. Overlaps between MS or ME muons is solved through a comparison of fit quality and number of subdetectors hits.

Different reconstruction quality selections are then introduced, to suppress backgrounds from hadron decays-in-flight and hadron punch-through while preserving high efficiency, depending on the needs of each physics analysis. The selection requirements are posed on discriminating variables including on the individual charges and momenta of the two ID and MS tracks, and the χ^2 of the combined track fit. The standard working points are *Loose*, *Medium*, *Tight*, and *High-p_T*, and are designed such that all Tight muons are included into the Medium category, and all also belong to the Loose set. The Medium category is the default WP, as it minimises systematics uncertainties due to muon reconstruction and calibration, and only exploits CB and ME muons. The Loose category maximises reconstruction efficiency and includes all muon types, while restricting to the $|\eta| < 0.1$ for CT and ST muons. The Tight muons working point is used to obtain a set of high-purity muons, eventually reducing the total reconstruction efficiency. Only CB muons are used, with requirements on the number of subdetector hits, the fit quality and ID–MS consistency. Finally, the High-p_T working point targets improved resolution at high muon momenta, targeting very high-mass resonances such as W' and Z' hypothetical particles, by requiring at least three hits in three MS stations.

Also for muons, analyses often apply isolation and primary-vertex association requirements, depending on the process of interest involving electroweak processes, or muons from semileptonic decays close to hadron jets. The isolation of muons is assessed through two variables, that define a cone around the muon ID track, and a cone containing calorimeter topo-clusters surrounding the muon (and excluding those energy deposits associated to the reconstructed muon itself). Association of the two types of information through particle-flow methods is also performed [156]. Multiple working points are also introduced to describe the muons isolation, also applying multivariate analysis techniques, to consider the total acceptance, inclusion or rejection of non-prompt muons, and others. The different working point selections, that will also be used in the heavy neutral lepton analysis presented in chapter 7, are listed in [156].

6.3.3 Hadron jets

Hadronic jets are reconstructed in ATLAS with the anti-k_t algorithm [157] (typically $R = 0.4$) as implemented in FastJet [158], using either calorimeter topological clusters, inner detector tracks, or a particle-flow combination of both [94].

The different steps of the reconstruction procedure, from calorimeter energy deposits to fully-calibrated jets used in the analyses, are shown in fig. 6.9. Topological clusters of calorimeter cells (both ECal and HCal) are built from significant energy de-

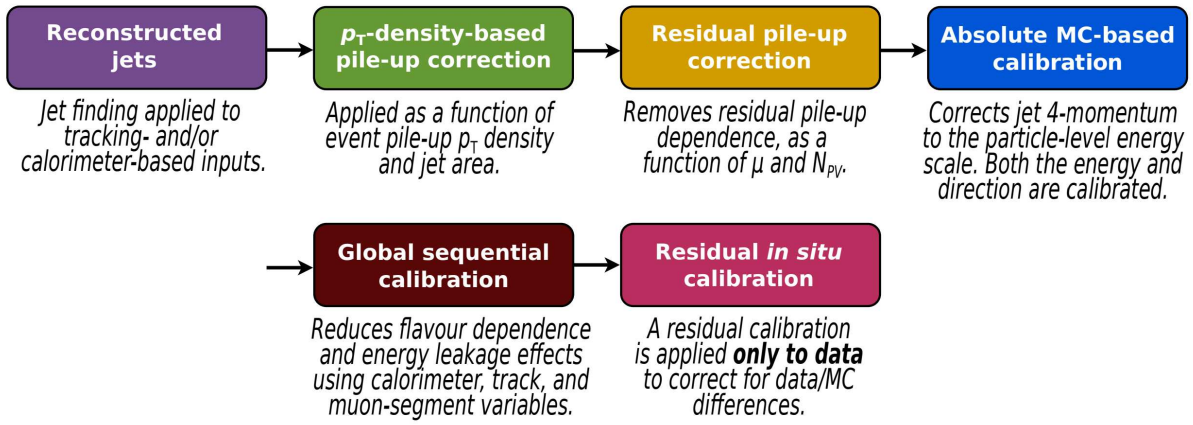


Figure 6.9: Steps of hadron jet reconstruction and energy correction in ATLAS [94].

posits over a certain threshold, to suppress noisy cells [159], which are merged through a nearest-neighbour algorithm [160]. The energy of resulting topo-clusters is at this level defined at the electromagnetic scale, which is known to be not correctly estimated because of the non-compensating behaviour of both electromagnetic and hadronic ATLAS calorimeters. Jet calibration then applies an area-based pile-up correction and an origin correction, followed by a Monte-Carlo-derived jet energy scale (JES) calibration. A Global Sequential Calibration (GSC) reduces residual dependencies on jet structure and flavour, and residual *in situ* corrections align data and simulation using γ+jet, Z+jet and multijet balance. A jet energy resolution (JER) smearing is applied in simulation to match the data resolution [159].

b-jet identification. A special role in hadron jet measurements is played by jets originated by b-hadrons. Top quarks decay almost exclusively to these particles, and therefore their correct identification is fundamental for studying the properties of the heaviest Standard Model particle. Furthermore, semi-leptonic b-hadrons decays produce electrons and muons that may be incorrectly identified as leptons from the primary interaction vertex, therefore introducing significant sources of backgrounds for BSM searches. The identification of b-jets, called b-tagging, exploits the long b-hadron lifetime, high mass and decay multiplicity [161]. Multiple b-tagging algorithms have been implemented and used by ATLAS during Run 1 and 2, with significantly increasing complexity. An extensive description of the different algorithms is reported in Ref. [162].

Low-level taggers introduce discriminating variables to separate b-jets from c and light jets, exploiting tracks information such as impact-parameter significance of tracks, secondary-vertex reconstruction, and topological multi-vertex fitting methods. High-level taggers combine these with multivariate classifiers. The analysis presented in chapter 7 used the DL1r series of taggers, which exploit fully-connected feed-forward neural networks. During Run 3, even more advanced taggers were introduced, exploiting transformer neural network for improved performances [163]. The DL1r algorithm is applied with standard single-cut operating points at 60%, 70%, 77% and 85% b-efficiency. A calibration of the DL1r tagger is performed using likelihood-based methods for each jet flavour [161], with correction factors to account for differences between Monte Carlo simulations and data.

CHAPTER

7

HEAVY NEUTRAL LEPTONS SEARCH WITH PROMPT SIGNATURES

Heavy neutral leptons (HNLs) are hypothetical particles with zero electric and colour charge, whose allowed mass range may span several orders of magnitude. A particularly interesting motivation for introducing HNLs into the Standard Model is their potential connection to the Majorana nature of neutrinos: in the Type-I see-saw mechanism (presented in section 7.1), heavy partners to neutrinos arise with large masses and weak interactions suppressed by a factor $\Theta = m_D M_R^{-1}$, where m_D and M_R are the Dirac mass term and Majorana mass of right-handed neutrinos, respectively. Such a model provides a natural explanation for the very small masses of active neutrinos, which would be inversely proportional to their partners' masses. At least two right-handed neutrino states are required to explain current neutrino oscillation data, while a massless lightest neutrino remains allowed.

In a model with three additional sterile neutrinos, $N_{i=1,2,3}$, the νMSM can also accommodate a dark matter candidate and a source of CP violation in the lepton sector. To achieve these further possibilities, small mixing angles between left and right-handed states are needed. Depending on the mass of each HNL and its mixing couplings with active neutrino states, which describe their production and decay properties, these particles may be observed as short-lived or long-lived, the difference lying in the identification of a decay vertex different from the production one by the experiments' trackers. Lepton Number Violating (LNV) processes, arising because of the Majorana nature of HNLs, would be permitted giving rise to specific final state signatures that are not allowed, or strongly suppressed, in the Standard Model. Heavy neutral leptons may nevertheless exist as purely Dirac particles, consisting of right-handed states N_R, and acquiring mass through their Yukawa couplings to the Higgs boson. In the absence of a see-saw mechanism, the Yukawa couplings of active neutrinos would need to be

extremely small, and only Lepton Number Conserving (LNC) processes would be allowed.

The analysis presented in this and following chapters outlines a search, performed with the ATLAS detector, for heavy neutral leptons in their leptonic decays, through prompt (short-lived HNLs) signatures. The main results are described in Ref. [140]. Data collected during the full Run 2 of the LHC between 2015 and 2018, reaching a total integrated luminosity of 140 fb^{-1}, were used for this search. A previous analysis, looking for the same final state, was also performed with partial Run 2 data, with a total integrated luminosity of 36 fb^{-1}, and a more limited HNL mass range than the one shown here [164]. A recent ATLAS analysis focused on displaced vertices signatures [165], both leptonic and semi-leptonic, not resulting in significant excesses over the Standard Model background. This analyses focused on masses below 20 GeV, in which the HNL could travel a significant distance from the pp interaction vertex before decaying.

7.1 Neutrino physics and Heavy Neutral Leptons

The observation of neutrino oscillations by the Super-Kamiokande [166] and SNO [167] experiments provided a definitive evidence that, out of the three known neutrino species, at least two have a non-zero mass. The oscillation process allows a neutrino generated with an initial flavour $\alpha = e, \mu$ or τ, to be later observed with a different flavour $\beta \neq \alpha$. This important observation is currently the only direct evidence of physics beyond the Standard Model at the microscopic scale, as neutrinos are described as massless particles in the theory and no right-handed singlet states ν_R are present. Two main ways of introducing neutrino masses in the Standard Model are currently largely accepted, differing for the nature of the neutrino itself as a Dirac or a Majorana-type particle [71]. Neutrinos are, in fact, the only known neutral fermion, and either of the two possibilities could be possible depending on the identification of the neutrino with its own anti-particle state.

7.1.1 Dirac Neutrinos and Oscillations

Dirac neutrino masses can be introduced by adding a right-handed *sterile* neutrino state for each of the three flavours of active neutrinos, ν_R^e, ν_R^μ and ν_R^τ. Following the same procedure that is used to give mass to quarks and charged leptons, neutrino mass terms in the lagrangian are found through Yukawa interactions of fermions with the Higgs field:

$$\mathcal{L}_D^\nu = -\frac{v}{\sqrt{2}} \sum_{\alpha,\beta=e,\mu,\tau} \left(\bar{\nu}_{\alpha L} Y^\nu_{\alpha,\beta} \nu_{\beta,R} + h.c. \right). \tag{7.1}$$

By diagonalising the Yukawa matrices with bi-unitary transformations, explicit kinetic and mass terms for neutrinos are obtained

$$\mathcal{L}^\nu_{Kin} = \sum_{i=1,2,3} \bar{\nu}_{i,L} i \not{\partial} \nu_{i,L} \qquad \mathcal{L}^\nu_{Mass} = -\sum_{i=1,2,3} \frac{v y_i'^\nu}{\sqrt{2}} \left(\bar{\nu}_{i,L} \nu_{i,R} + h.c. \right) \tag{7.2}$$

with the convention of using Greek letters for indexing flavour eigenstates and Latin letters for mass eigenstates used in eq. (7.1) and eq. (7.2). Differently from the quark and charged lepton sectors, flavour eigenstates are in general different from the mass

eigenstates, and the states in the two basis and can be related by

$$\nu_L^\alpha = \sum_{i=1}^{3} V_{\alpha i}^{PMNS} \nu_L^i \qquad \alpha = e, \mu, \tau \tag{7.3}$$

where V^{PMNS} is the Pontecorvo-Maki-Nakagawa-Sakata matrix. In matrix form eq.(7.3) becomes

$$\begin{pmatrix} \nu_e \\ \nu_\mu \\ \nu_\tau \end{pmatrix}_L = \begin{pmatrix} V_{e1} & V_{e2} & V_{e3} \\ V_{\mu 1} & V_{\mu 2} & V_{\mu 3} \\ V_{\tau 1} & V_{\tau 2} & V_{\tau 3} \end{pmatrix} \begin{pmatrix} \nu_1 \\ \nu_2 \\ \nu_3 \end{pmatrix}_L .$$

Unitary matrices with dimensions N can in general be parametrised using $\frac{N(N-1)}{2}$ angles and $\frac{(N-1)(N-2)}{2}$ complex phases. The PMNS matrix therefore only requires a total of three angles and a complex phase, and can be expressed as

$$V^{PMNS} = \begin{pmatrix} c_{12}c_{13} & s_{12}c_{13} & s_{13}e^{-i\delta_{CP}} \\ -s_{12}c_{23} - c_{12}s_{23}s_{13}e^{i\delta_{CP}} & c_{12}c_{23} - s_{12}s_{23}s_{13}e^{i\delta_{CP}} & s_{23}c_{13} \\ s_{12}s_{23} - c_{12}c_{23}s_{13}e^{i\delta_{CP}} & -c_{12}s_{23} - s_{12}c_{23}s_{13}e^{i\delta_{CP}} & c_{23}c_{13} \end{pmatrix}$$

with $c_{ij} = \cos\theta_{ij}$, $s_{ij} = \sin\theta_{ij}$, and δ_{CP} is the imaginary phase that, if different from zero, could account for CP symmetry violations.

Once they are generated with flavour α, freely propagating neutrinos can be described as plane waves that evolve over time with

$$|\nu_\alpha(t)\rangle = \sum_{i=1,2,3} V_{\alpha i}^* |\nu_i(t)\rangle. \tag{7.4}$$

In general, each one of the three mass eigenstates ν_i has eigenvalues m_i and will travel with energy E_i, according to

$$|\nu_i(t)\rangle = e^{-iE_i t} |\nu_i(0)\rangle, \tag{7.5}$$

and with the experimentally motivated assumption of very relativistic neutrinos with masses negligible with respect to their propagation momenta ($m_i \ll p_i$), one obtains

$$E_i = \sqrt{p_i^2 + m_i^2} \simeq p + \frac{m_i^2}{2E}. \tag{7.6}$$

Following [71] and references therein, one can finally express the probability of a neutrino oscillating after having travelled for a distance $L \simeq ct$ as

$$P_{\nu_\alpha \to \nu_\beta} = \left|\langle \nu_\beta | \nu_\alpha(t)\right|^2 = \left| \sum_{i=1}^{n} \sum_{j=1}^{m} V_{\alpha i}^* V_{\beta j} \langle \nu_j | \nu_i(t) \rangle \right|^2 = \tag{7.7}$$

$$= \delta_{\alpha\beta} - 4 \sum_{i<j}^{n} \mathrm{Re}[V_{\alpha i} V_{\beta i}^* V_{\alpha j}^* V_{\beta j}] \sin^2 X_{ij} + 2\mathrm{Im}[V_{\alpha i} V_{\beta i}^* V_{\alpha j}^* V_{\beta j}] \sin 2X_{ij}$$

with

$$X_{ij} = \frac{(m_i^2 - m_j^2)L}{4E} \simeq 1.267 \frac{\Delta m_{ij}^2}{\mathrm{eV}^2} \frac{L/E}{m/MeV}.$$

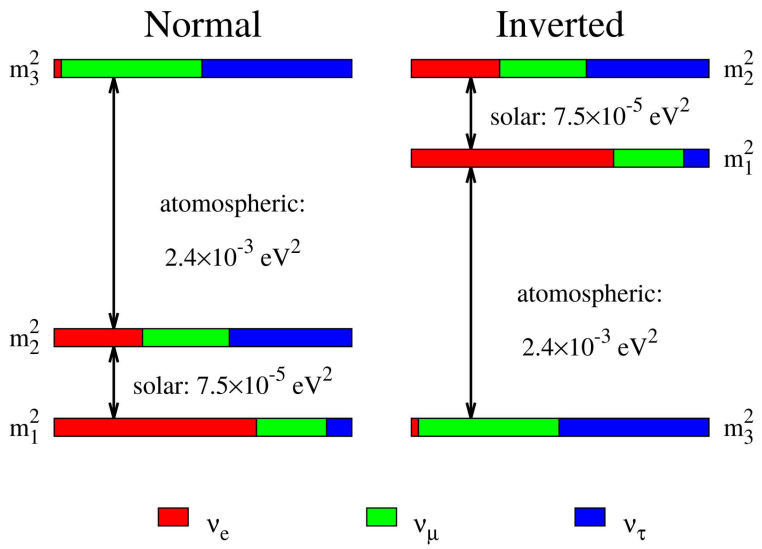


Figure 7.1: Normal (left) and inverted (right) neutrino mass hierarchies. Image taken from [168].

After the observation of neutrino oscillations, an extensive programme of neutrino oscillation parameters measurements has been carried out. This process allowed, for example, to explain the solar neutrino problem, that consisted in a much lower flux of electron neutrinos produced in the sun's core with respect to the theoretically predicted one. Equation (7.7) shows that the oscillation probability has itself an oscillatory behaviour with an amplitude that depends on the matrix elements, and a damping parameter consisting of the difference of the squared neutrino masses and the travelled distance between the production and observation positions. Several of these parameters have been measured in the last twenty years, through solar and atmospheric neutrino observatories and nuclear reactor and accelerator experiments, by fine-tuning the neutrino energies or the source-detector distances. As the oscillation probability only depends on the neutrino squared mass differences, it does not allow to directly access information on the scale of neutrino masses. Current measurements point out that one of the squared differences is much smaller that the other two, namely $\Delta m^2_{21} \ll \left|\Delta m^2_{31}\right| \simeq \left|\Delta m^2_{32}\right|$. Accounting for this observation, two possible ways of ordering the mass eigenstates can be used, shown in fig. 7.1, depending on which mass state is put at the bottom mass value. Given the smallest mass difference as Δm^2_{12}, it is common to refer as normal hierarchy of neutrino masses the case where $m_1 \lesssim m_2 \ll m_3$, and inverted hierarchy the one with $m_3 \ll m_1 \lesssim m_2$, both shown in fig. 7.1.

Current best fit values for neutrino oscillations parameters, as listed in [71] and separated in mixing angles and mass splittings, are reported in table 7.1.

Measurement performed by the T2K experiment [169] hint to a non-zero (and possibly even maximal) δ_{CP} phase, introducing CP violations in the lepton sector of the Standard Model. This fact generates a new source of CP violations, together with the one already observed in the quark sector, in studies of $B^0 - \overline{B^0}$ and $K^0 - \overline{K^0}$ mesons decays [170][171]. Further studies at proposed experiments such as DUNE, NOνA and the T2HK with the Hyper-Kamiokande detector upgrade will drastically improve the sensitivity on the CP violating parameter in the neutrino sector that would motivate baryon asymmetry in the early Universe.

Parameter	Value	Mass Ordering
$\sin^2\theta_{12}$	0.307 ± 0.013	—
$\sin^2\theta_{23}$	0.546 ± 0.021	Normal
$\sin^2\theta_{23}$	0.539 ± 0.022	Inverted
$\sin^2\theta_{13}$	$(2.20 \pm 0.07) \times 10^{-2}$	—
δ_{CP}	1.36 ± 0.2	—
Δm^2_{12}	$(7.53 \pm 0.18) \times 10^{-5}\,\text{eV}^2$	—
Δm^2_{23}	$(2.453 \pm 0.033) \times 10^{-3}\,\text{eV}^2$	Normal
Δm^2_{23}	$(-2.536 \pm 0.034) \times 10^{-3}\,\text{eV}^2$	Inverted

Table 7.1: Neutrino oscillation parameters for different mass orderings.

While the Dirac neutrino model with the introduction of SM singlets ν_R is viable to explain the oscillation process and neutrino masses, it fails to motivate the smallness of neutrino masses when compared to all other elementary particles. In fact, to obtain ~meV neutrino masses, the corresponding Yukawa matrix elements $Y^{\nu}_{\alpha,\beta}$ should be several order of magnitudes lower than all other elements for both quarks and charged leptons. Moreover, the hierarchy of neutrino family masses and mixing matrices is found to be largely different with respect to the ones observed in the quark sector.

7.1.2 Majorana Neutrinos

A second way of introducing neutrino masses to the Standard Model is to consider neutrinos as Majorana particles. A wide literature on the topic exists, and the following section will largely follow, as example, refs. [172][173][174]. Majorana fermions satisfy the property

$$\psi^C = C\overline{\psi^T} = \psi, \tag{7.8}$$

where C is the charge-conjugate operator that transforms a particle in its own antiparticle state. A novel mass term in the Lagrangian of the type

$$\mathcal{L}^{\nu_L}_M = -\frac{M_L}{2}(\bar{\nu}_L \nu^C_L + h.c.) \tag{7.9}$$

can be introduced, that interestingly only requires one Weyl spinor, and could therefore account for a neutrino mass term without explicitly introducing right-handed states. The lagrangian term described in eq. (7.9) breaks lepton number conservation by two units, and is not gauge-invariant under $\mathcal{U}(1)$ symmetry, therefore it is only suitable to describe electrically-neutral particles such as neutrinos. Unfortunately, this term also breaks the Standard Model electroweak gauge symmetry and is consequently not suitable for introducing a neutrino masses. A similar term for right-handed neutrinos with no electric charge and weak hypercharge ν_R can nevertheless be added, without breaking any gauge symmetry, as

$$\mathcal{L}^{\nu_R}_M = -\frac{M_R}{2}(\bar{\nu}_R \nu^C_R + h.c.). \tag{7.10}$$

With the newly added right-handed neutrino states, Dirac mass terms generated through Yukawa interactions

$$\mathcal{L}_D = \frac{y_\nu v}{\sqrt{2}}(\bar{\nu}_L \nu_R + h.c.), \tag{7.11}$$

as derived from eq. (7.2), can also be considered. The most general case will have to take into account these two possible sources of neutrino mass generation that do not break any gauge symmetry, and in the first case of a single neutrino generation can be expressed in the compact form

$$\mathcal{L} = \begin{pmatrix} \bar{\nu}_L & \bar{\nu}_R^C \end{pmatrix} \begin{pmatrix} 0 & m_D \\ m_D & M_R \end{pmatrix} \begin{pmatrix} \nu_L^C \\ \nu_R \end{pmatrix}. \tag{7.12}$$

The mass matrix in eq. (7.12) can be diagonalised with a 2×2 orthogonal matrix that only depends on one angle θ such that

$$\tan(2\theta) = \frac{2m_D}{M_R}. \tag{7.13}$$

The mass eigenstates, that arise after the matrix diagonalisation, are

$$\begin{pmatrix} \nu \\ N \end{pmatrix} = \begin{pmatrix} \cos\theta & -\sin\theta \\ \sin\theta & \cos\theta \end{pmatrix} \begin{pmatrix} \nu_L^C \\ \nu_R \end{pmatrix}. \tag{7.14}$$

Considering the limit $m_D \ll M_R$ so that $\tan\theta \approx \theta \approx \frac{m_D}{M_R}$, and $\cos\theta \approx 1$, the first of the two mass eigenstates $\nu \simeq \nu_L^C - \frac{m_D}{M_R}\nu_R$ is closely aligned to the left-handed neutrino ν_L, while the second eigenstate N, also called Heavy Neutral Lepton, almost corresponds to the right-handed neutrino state $N \simeq \frac{m_D}{M_R}\nu_L + \nu_R \approx \nu_R$. The mass eigenvalues of the two states are $m_1 \approx \frac{m_D^2}{M_R}$ for the lighter neutrino ν, while the heavier mass eigenvalue results $m_2 \approx M_R$ for the state N that is close to the sterile state ν_R.

The *see-saw mechanism* here described provides a natural explanation for the smallness of neutrino masses, as the lightest eigenstate corresponds to the experimentally observed active state and its mass is pushed to lower values for higher Majorana masses M_R. The second state $N \approx \nu_R$ potentially has very high masses that range over several orders of magnitudes, and its weak interactions, only mediated by the little ν_L component coupling, are highly suppressed by a factor $\frac{m_D}{M_R}$.

While the presented results are already valid by including a single new singlet state ν_R and postulating Majorana neutrinos, it is natural to take into account a number of new particles equal to the number of families of both quarks and leptons. The full lagrangian that generates the masses of neutrinos including both Dirac and Majorana states is

$$\mathcal{L}_M^\nu = -y_{ij}\overline{L_i}\phi^C\nu_{Rj} - \frac{M_R^{ab}}{2}\overline{\nu_{Ra}^C}\nu_{Rb} + (h.c.) \tag{7.15}$$

with $i, j = 1, 2, 3$ the flavour indexes and $a, b = 1, 2, 3$ the three heavy right-handed states. In this more general model, the matrix of light neutrino masses is

$$\begin{aligned} m^\nu &\approx -m_D M_R^{-1} m_D^T \\ &\approx V_{PMNS}\text{diag}(m1, m2, m3)V_{PMNS}^T. \end{aligned} \tag{7.16}$$

The model provided in eq. (7.15), called ν *Minimal Standard Model* (νMSM [175]), requires a total of 18 new parameters in the assumption of $\mathcal{N} = 3$ new families, consisting of three Dirac neutrino masses, three Majorana masses, 6 mixing angles and 6 CP-violating phases. This large parameter space can already be partially limited by taking into account neutrino oscillation and cosmological data. The request for at least a

third family is already motivated by the two measured squared mass differences Δm^2_{12} and Δm^2_{23} observed in atmospheric and solar neutrino oscillations, unless the lightest neutrino is allowed to be exactly massless. The remaining space of free parameters of the model is surprisingly interesting as it could explain several open problems related to both particle physics and cosmology. Although mass ranges much higher than the TeV scale, and even up to the Planck scale are possible and also allow for simple explanation of the neutrino small masses, they have the disadvantage of not being testable at current and even reasonably future experiments. Several low-scale see-saw models have been proposed to account for the same unexplained phenomena, while keeping the mass range of heavy neutral leptons close to the one available at colliders and event lower energy experiments [173].

The different scale of the two squared mass differences could suggest that one of the three heavy neutrino states N_I is lighter than the others, and could play the role of a stable dark matter candidate if having a mass in the range O(keV-MeV), due to its feebly interacting nature. Besides the explanation of neutrino masses and possibly new particles compatible with dark matter signatures, a third consequence of this model is the possibility to explain the baryon asymmetry problem, that could be achieved through rapid oscillations of the two remaining HNLs in the early Universe [176][177]. In 1967 Sakharov [178] discussed the conditions to achieve an asymmetry in the density of baryons n_b with respect to their CP-conjugates $n_{\bar{b}}$. From cosmological observations [179], the value of asymmetry between the two densities is

$$\eta = \frac{n_b - n_{\bar{b}}}{n_\gamma} = (6.12 \pm 0.04) \times 10^{-10}, \tag{7.17}$$

with n_γ being the density of photons from the cosmic microwave background. These conditions consisted of i) violation of baryon number (B) conservation , ii) C and CP symmetries violation, and iii) an out-of-equilibrium state such as the one that could have happened during a first-order phase transition in the early Universe. According to several models [180], heavy neutral leptons could have favoured Baryogenesis through a Leptogenesis process [181][182].

As a consequence of all these problems the existence of heavy neutral leptons would help to address, these particles have been searched for by many experiments. In order to set limits on the excluded parameters ranges where the HNLs have not been found, it is common by many collaborations to use a simple benchmark model in which the HNL is produced and decays through the mixing with one single neutrino flavour. This allows to look for specific channels that are extremely rare and select the related events from all other Standard Model processes with much higher probabilities to occur. It is possible, nevertheless, to account for HNL mixings with different flavour neutrinos in more realistic scenarios [172]. The available parameter space excluded by currently running experiments, and also including projections from already accepted projects such and SHiP [183] and DUNE [184], are shown in figures 7.2, 7.3 and 7.4 for the exclusive mixing with a single neutrino flavour.

7.2 Signal model

For masses below 80 GeV, the main production channel for HNLs is through the decays of W bosons due to $W^\pm \to \ell^\pm N$ in association with a charged lepton. The HNL is generated through its mixing with active neutrinos, with all three possible active couplings in the most general case. The production of these particles is also possible

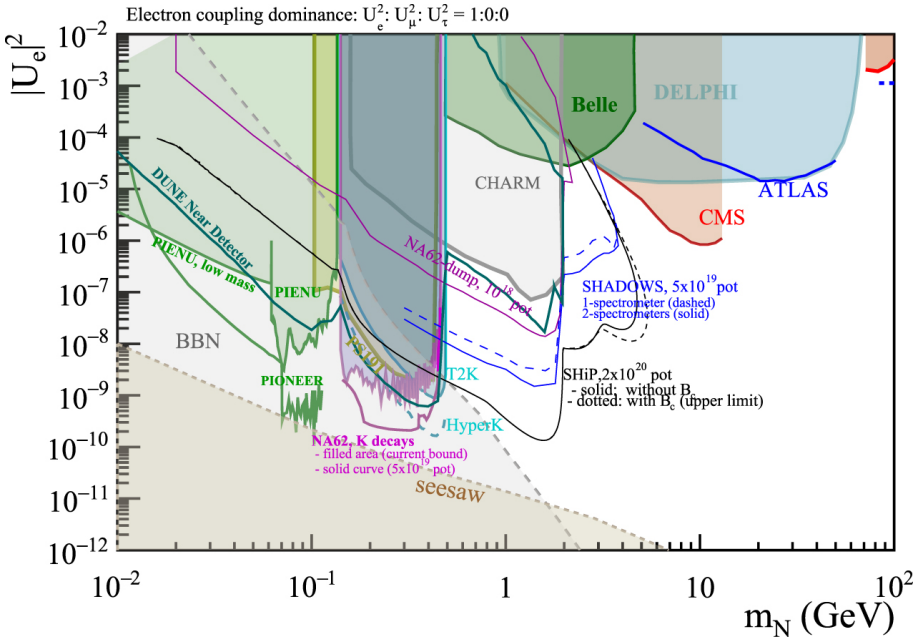


Figure 7.2: Current (and foreseen) limits on HNL mixing with electron neutrino $|U_e|^2$ [173].

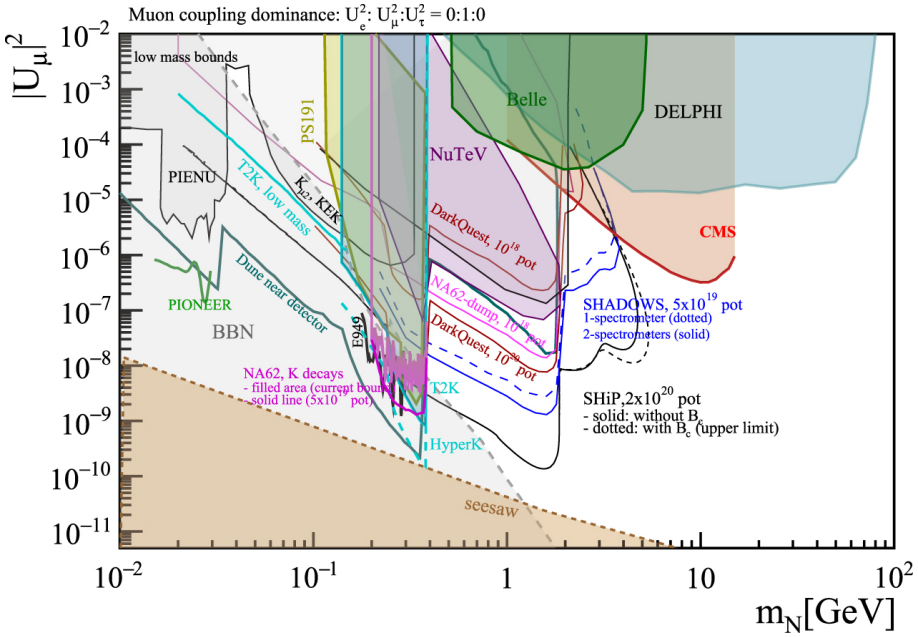


Figure 7.3: Current (and foreseen) limits on HNL mixing with muon neutrino $|U_\mu|^2$ [173].

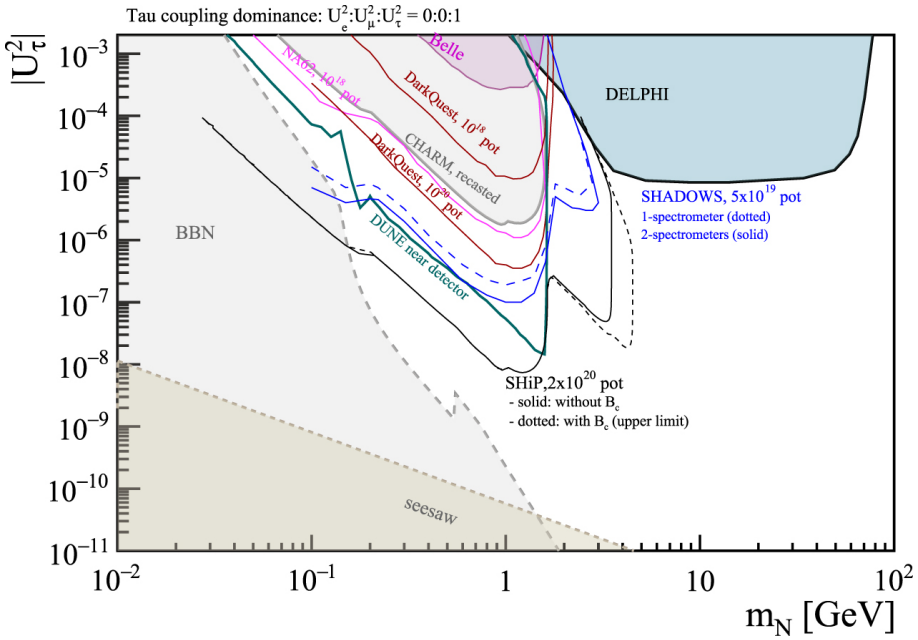


Figure 7.4: Current (and foreseen) limits on HNL mixing with tau neutrino $|U_\tau|^2$ [173].

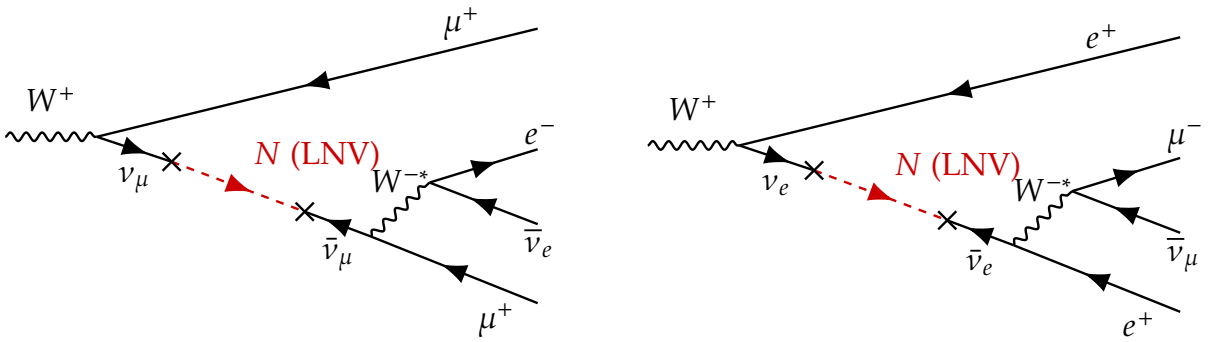


Figure 7.5: Lepton number violating (LNV) processes mediated by a heavy neutral lepton N, involving only one active mixings, either with muon (left) or electrons (right) neutrinos.

through Z boson decays through $Z \rightarrow N\nu$, but it would happen is association with a second neutrino, making the following search more complicated at pp colliders such as the LHC. The HNL decays through its mixing with active neutrinos into a second charged lepton and an off-shell W boson, which is only searched in its leptonic decays. Hadronic decays of this boson are not considered, in order to only search for very well reconstructed final states and reduce as much as possible the large amount of other Standard Model processes. Only electron and muon flavours are considered, both for the charged leptons and active neutrino mixings. The final states therefore consist of three charged leptons, and the missing transverse momentum from the neutrinos produced in off-shell W bosons decays. The off-shell W boson decay is not constrained by the HNL flavour, and therefore the three charged leptons in the final state could have the same flavour. Nevertheless, the analysis focuses on events in which the W^* boson decays into a different flavour lepton with respect to the other two, featuring a better signal-to-background ratio.

Other selections on events entering the analysis are related to the Majorana proper-

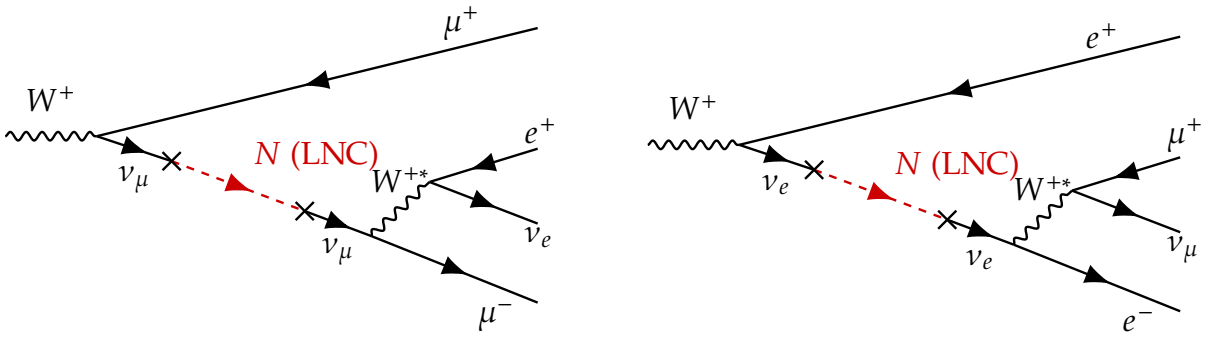


Figure 7.6: Lepton number conserving (LNC) processes, involving only one active mixings, either with electrons or muon neutrinos.

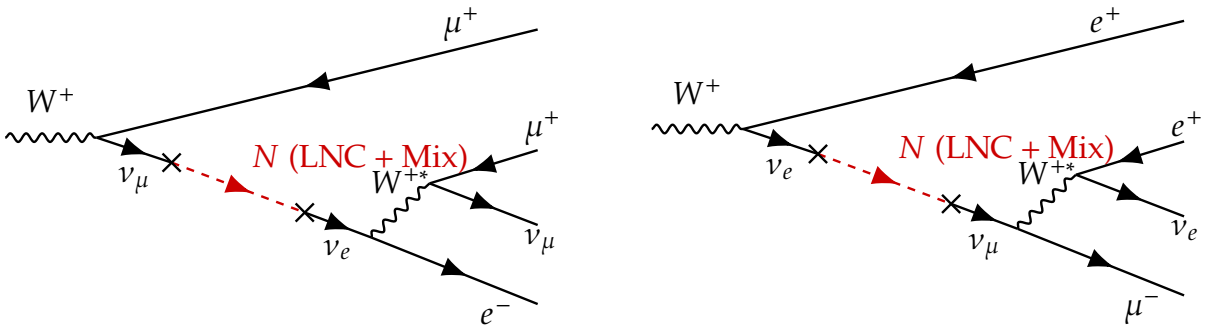


Figure 7.7: Lepton number conserving (LNC) processes mediated by a heavy neutral lepton, N. Processes involving two considered active mixings, with electrons or muon neutrinos, are drawn.

ties of heavy neutral leptons, and the possible mixings between light and heavy neutrinos. As in several previous analyses, both by ATLAS [164] and CMS [185], a simplified signal model in which a single HNL, either Dirac or Majorana, only couples to one neutrino flavour is used. The Feynman diagram related to the process of interest for this analysis is drawn in fig. 7.5. For short-lived HNLs searches, the most favourable signature is the one exploiting Lepton Number Violating (LNV) processes, in which the two neutrino states through which the HNL is produced and decays have opposite helicities, therefore exploiting Majorana particles' properties. Assuming only one lepton flavour coupling, this process leads to two Same-Flavour, Same-Charge (SFSC) charged leptons that drastically reduces Standard Model backgrounds. The HNL then decays through $N \rightarrow W^{*\pm}\ell^{\mp}$ into the off-shell boson. Only events in which the third lepton, produced in the W^* decays, has a different flavour from the previous leptons are considered, hence only selecting $\mu\mu e$ or $ee\mu$ final states, and excluding three same-flavour final states eee and $\mu\mu\mu$.

Other HNL-related processes, that do not exploit LNV and are not used in this analysis, are shown in fig. 7.6 and fig. 7.7. In the first case, only one active mixing between SM neutrinos and HNLs is considered. Consequently, the two Same-Flavour (SF) leptons have opposite electric charge, and the resulting final states would be overwhelmed by other SM backgrounds such as diboson production ($pp \rightarrow WZ$) or bosons plus hadronic jets. This kind of process would be best probed exploiting displaced vertices signatures, with HNLs travelling a significant distance from the production vertex before decaying into two Different-Flavour, Opposite Charge (DFOC) leptons and miss-

ing transverse momentum, drastically reducing SM backgrounds. In the latter case, if HNLs are allowed to mix with more than one lepton flavour, a final state compatible with the LNV one is found. While this kind of process leads to clean fully-leptonic final states with two SFSC leptons, more oscillation parameters would have to be included, complicating the analysis optimisation and results interpretation, and were therefore not considered, preferring the simpler one-flavour scenario. The results from single active mixing may nevertheless be reinterpreted into realistic HNL scenarios with more than one flavour [172].

When considering only one active mixing between left and right-handed neutrino states, the kinematics of the process of interest and its cross section only depends on two parameters, being the mixing matrix element $U_{\alpha N}$ and the HNL mass m_N. The expression that describes the cross section of HNL production and decay into the final state presented in fig. 7.5, which depends on these two parameters, is

$$\begin{aligned}\sigma(pp \to \ell_\alpha^\pm \ell_\alpha^\pm \ell_\beta^\mp \bar{\nu}_\beta) = \sigma(pp \to W^\pm) \cdot \mathrm{BR}(W \to \ell_\alpha^\pm \nu_\alpha) \\ \cdot |U_{\alpha N}|^2 \cdot \left(1 - \frac{m_N^2}{m_W^2}\right)^2 \left(1 + \frac{1}{2}\frac{m_N^2}{m_W^2}\right) \\ \cdot \mathrm{BR}(N \to \ell_\alpha^\pm \ell_\beta^\mp \bar{\nu}_\beta), \qquad \alpha \neq \beta\end{aligned} \tag{7.18}$$

for two leptons with flavour α, a third one with flavour $\beta \neq \alpha$, and a HNL only coupling to α-flavour leptons. The factors appearing in the first line of eq. (7.18), related to the total $W^\pm$ boson production cross section and its branching ratio into leptons and neutrinos, were taken by previous ATLAS measurements [186][187]. In the second line, the quadratic dependence of the cross section on the mixing angle parameter is expressed, together with phase-space factors resulting from the decay of a W boson into a heavy particle N. The same phase-space factors involving the electron or muon masses were not taken into account, as they are negligible with respect to the other particle. Finally, the branching ratio in the third line represents the partial width fraction for the decay $N \to \ell_\alpha^\pm \ell_\beta^\mp \bar{\nu}_\beta$, over the total width Γ of the HNL, being the sum of all partial widths $\Gamma = \sum_i \Gamma_i$. Each partial width depends linearly on $|U_{\alpha N}|^2$, while the dependence on the HNL mass, m_N is more complicated and described in detail in [188]. The actual calculation for eq. (7.18) is therefore left to the `MadGraph` (MG5) matrix element calculator software package, which estimates the total HNL width and the different branching ratios starting from a grid of m_N values and a fixed mixing parameter $|U_{\alpha N}|^2 = 1$. The HNL width Γ is therefore rescaled by $|U_{\alpha N}|^2$ to obtain lifetimes, and the BRs from the $|U_{\alpha N}|^2 = 1$ calculation are used for the signal yield. The obtained values for each mass point used in the following analysis are listed in table 7.2.

With the given branching ratios and the resulting total heavy neutral lepton widths, the proper decay length $c\tau$ of these particles is obtained through the relationship

$$c\tau = \frac{\hbar c}{\Gamma} \tag{7.19}$$

and hence depends on m_N and the active neutrino mixing. Good approximations for the dependence of the HNL lifetime on its mass and mixing, within 2% for $m_N \leq 50$ GeV,

Table 7.2: MadGraph calculation of the total HNL width, and branching ratio of the process of interest, for the considered masses in the analysis. The total width in GeV was estimated by setting $|U_\mu|^2 = 1$, and branching ratio is also valid for the charge conjugate process.

Mass [GeV]	**Width [GeV]**	**BR** $(N \to \mu^+ e^- \nu_e)$
8	1.5809×10^{-8}	4.8045×10^{-2}
10	5.2253×10^{-8}	4.4547×10^{-2}
15	4.0738×10^{-7}	4.4153×10^{-2}
20	1.7701×10^{-6}	4.3496×10^{-2}
30	1.4333×10^{-5}	4.2806×10^{-2}
40	6.5355×10^{-5}	4.2671×10^{-2}
50	2.2203×10^{-4}	4.2827×10^{-2}
60	6.4349×10^{-4}	4.3286×10^{-2}
65	1.0680×10^{-3}	4.3551×10^{-2}

were proposed in [189]:

$$\begin{aligned} \tau(N_e) &= \frac{1}{2}(4.15 \times 10^{-12}\text{s}) \cdot \left(\frac{m_N}{1\text{GeV}}\right)^{-5.17} \frac{1}{|U_e|^2} \\ \tau(N_\mu) &= \frac{1}{2}(4.49 \times 10^{-12}\text{s}) \cdot \left(\frac{m_N}{1\text{GeV}}\right)^{-5.19} \frac{1}{|U_\mu|^2} \end{aligned} \tag{7.20}$$

where a factor $\frac{1}{2}$ was added to also include LNV decays of the HNL from the original reference, and the subscript α in N_α indicates the active coupling flavour.

7.3 Background processes

Several types of physics processes may give origin to final states entering the signal regions (SRs) which will be defined for selecting signal events. These sources of background are usually classified into irreducible or reducible categories. The first class usually contains the same types of prompt leptons that are used to search for heavy neutral leptons, but originated by Standard Model processes. The most relevant contributions for the present analysis are WZ and ZZ diboson processes. Leading-order diagrams representing these processes with leptonic decays of each boson, resulting in three of four lepton final states, are drawn in fig. 7.8. WZ and ZZ processes can result in the same signal signature of HNLs when one of the final state particle is a τ lepton that decays leptonically. Other rare but irreducible processes entering the analysis at preselection level, or event in the SRs, are triboson events and top+X with X being a vector or a Higgs boson (fig. 7.9).

The second class of background processes are detector (reducible) backgrounds. Events produced through these types of processes contain different types of physical objects with respect to signal ones, but may nevertheless enter the signal regions if one or more object is not correctly reconstructed by the ATLAS detector. Detector backgrounds are further divided into two classes, charge-flip and fake/non-prompt backgrounds. Charge-flip background is mostly relevant for final state electrons whose electric charge was misidentified, or having radiated a high-energy γ that converted into an

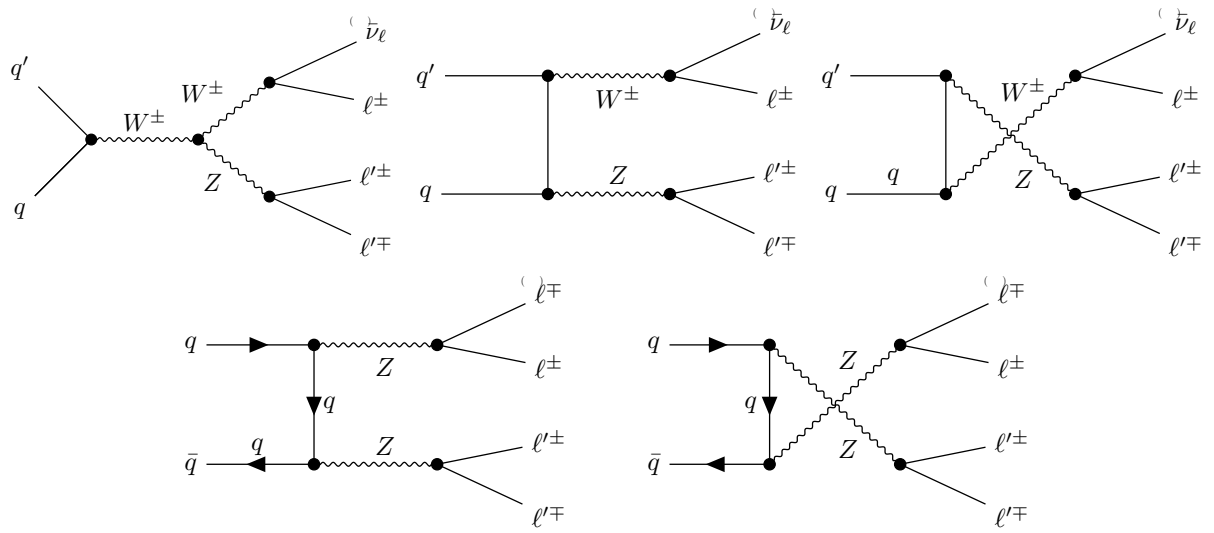


Figure 7.8: Diagrams for Standard Model processes involving WZ and ZZ diboson production that may be incorrectly identified as signal events.

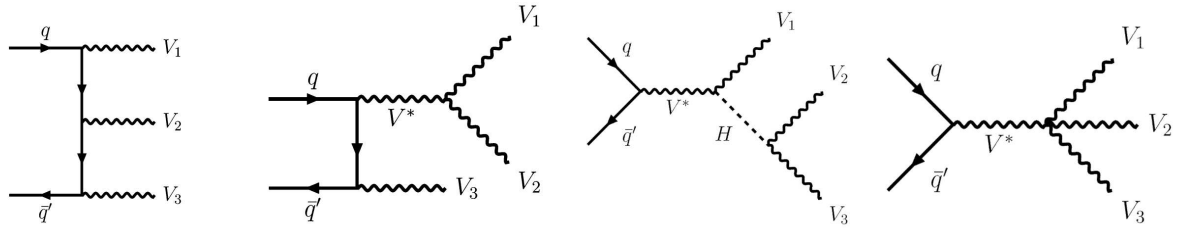


Figure 7.9: Standard Model processes involving the production of triboson events [190].

e^+e^- pair within the beam pipe or the tracker material. In some cases, one of the converted electron or positron may be preferred in the track reconstruction fit over the primary track, therefore leading to a charge mis-reconstruction. Fake/non-prompt backgrounds consist of events with leptons produced from decays of heavy-flavour mesons or other hadrons, photon conversions or other sources of electrons and muons not produced in the primary vertex, which is defined as the vertex with the largest sum of associated charged tracks momenta, $\sum(p_T^{track})^2$. These sources of background events, related to detector inefficiencies, mis-reconstruction and other effects, are specifically important for the presented analysis because of the specific desired final state consisting of SFSC leptons, which are extremely rare in the Standard Model. Detector-related backgrounds, on the other hand, may produce electrons and muons with any electric charge, forming a SFSC pair with other leptons in the underlying event. Because of their relevance for the analysis, different techniques were used to estimate the respective sources of background. They are described in detail in section 7.8.3. Finally, other contributions may come from $t\bar{t}$ and $t\bar{t}+X$ processes with multiple leptons in the final state, with an example shown in fig. 7.10, and leptons from b-jets.

7.4 Data and Monte Carlo simulations

Data used in this analysis were recorded during the four years of LHC Run 2, from 2015 to 2018, at a centre-of-mass energy of $\sqrt{s} = 13$ TeV. The experimental conditions under which data were being collected evolved significantly over the years, with a peak

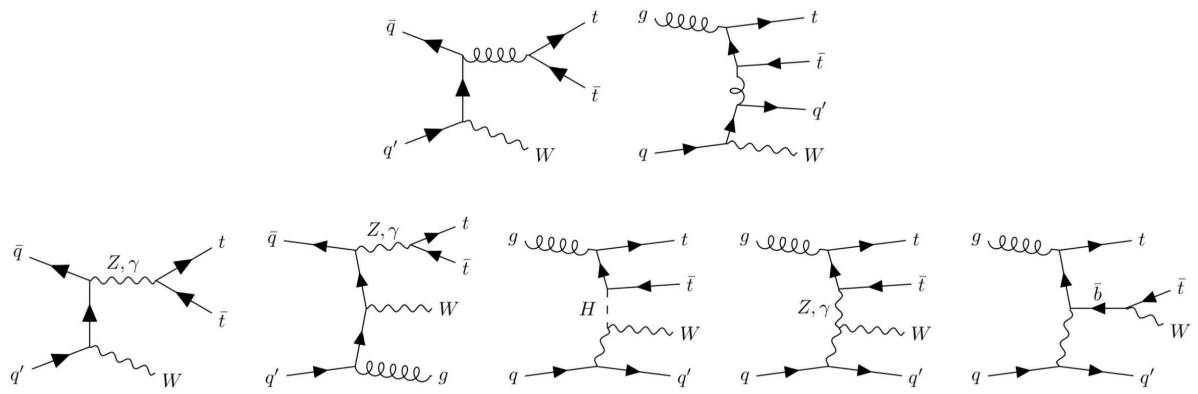


Figure 7.10: Feynman diagrams for the production of $t\bar{t}W$ final states [191].

instantaneous luminosity $\mathcal{L}_{peak}$ passing from 5 to 19×10^{33} cm^{-2}s^{-1} and an increase in the number of colliding bunches n_b from 2232 to 2544 over the Run 2 period, with 25 ns bunch spacing. From the entire set of collected events, samples corresponding to pp collisions with stable beam conditions and all ATLAS subdetectors operational were selected. In ATLAS, samples corresponding to about one minute of data taking and without substantial instantaneous luminosity changes, called *lumiblocks*, are prepared by dedicated groups. Those lumiblocks passing data quality checks are inserted in the ATLAS `GoodRunLists` to be used for the analyses. The following lists of lumiblocks, separated for years of data-taking and taken from the GoodRunList for Run 2, are used in this analysis:

- `data15_13TeV.periodAllYear_DetStatus-v89-pro21-02_Unknown_PHYS_StandardGRL_All_Good_25ns.xml`
- `data16_13TeV.periodAllYear_DetStatus-v89-pro21-01_DQDefects-00-02-04_PHYS_StandardGRL_All_Good_25ns.xml`
- `data17_13TeV.periodAllYear_DetStatus-v99-pro22-01_Unknown_PHYS_StandardGRL_All_Good_25ns_Triggerno17e33prim.xml`
- `data18_13TeV.periodAllYear_DetStatus-v102-pro22-04_Unknown_PHYS_StandardGRL_All_Good_25ns_Triggerno17e33prim.xml`

with the corresponding integrated luminosities, collected each year, listed in table 7.3. The uncertainty on the total integrated luminosity combined over the four years, measured through the LUCID-2 detector [192] dedicated to luminosity measurements, is 0.83%.

Table 7.3: Integrated luminosities of each year of data taking during Run 2, for the selected datasets.

Year	**Integrated luminosity [fb^{-1}]**
2015	3.24454
2016	33.4022
2017	44.3074
2018	58.7916

The several petabytes of data collected by the LHC must be then filtered during the reconstruction process, before obtaining data usable for the analysis. Different event-level information may be considered interesting for one analysis and discarded by others, and therefore different *derivation* procedures are used to reduce the total required

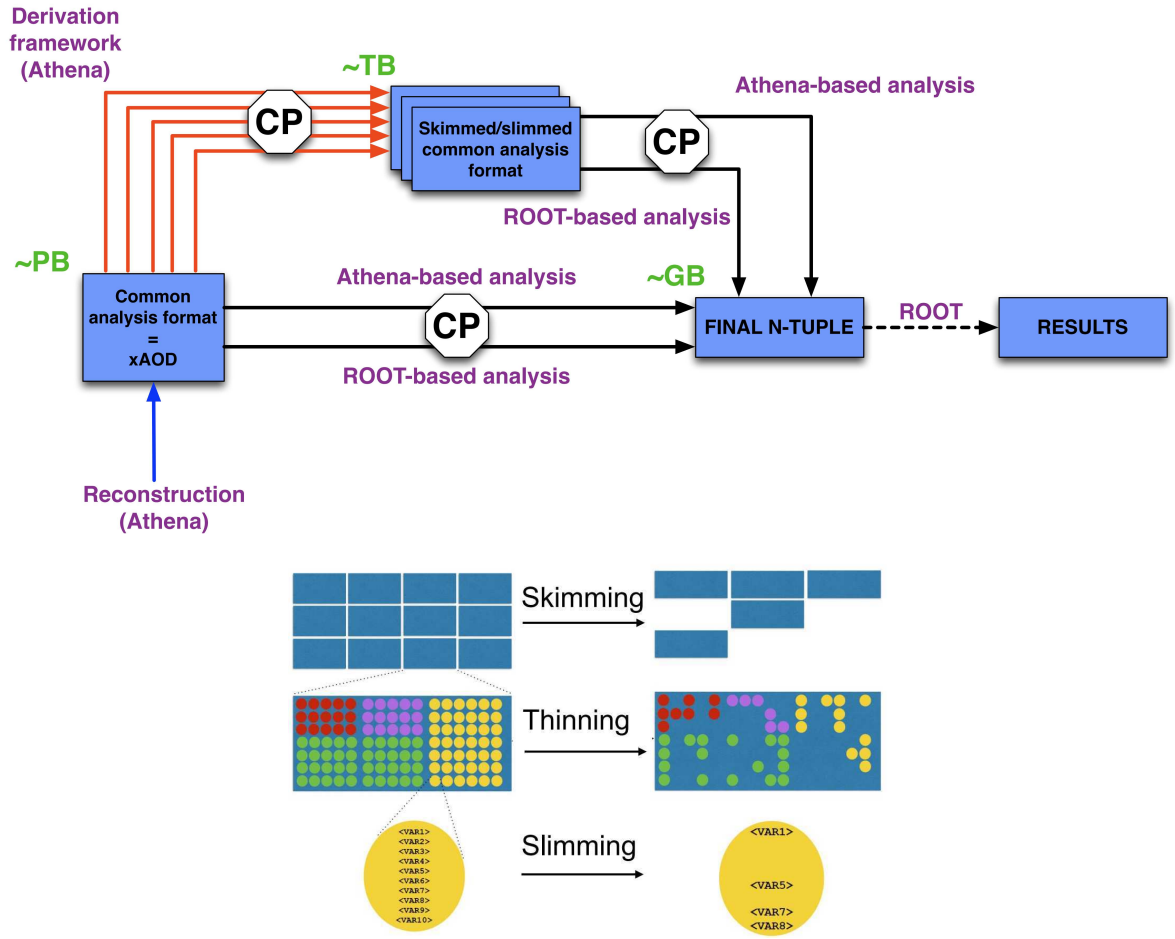


Figure 7.11: Drawing of the derivation framework process used by ATLAS, taken from [193]. On the bottom, picture showing the steps of derivation [196].

data size to a reasonable one. A derivation framework [193], shown in fig. 7.11, was introduced by ATLAS during Run 2 to reduce the information obtained after event reconstruction, called Analysis Object Data (AOD). This framework is based on the xAOD data structure, and can be directly read by the analysis framework. The derivation framework allows passing to a derived-AOD (DxAOD) which contains a subset of information required for the analysis, or groups of analyses with similar final states. It is based on the ATHENA reconstruction suite [194], which in turn is based on the GAUDI framework [195] used in many experiments, among which ATLAS, LHCb, and the FCC. A set of operations are performed during the derivation process, mostly consisting of filters on the amount of information from the input data to the output:

Skimming: removal of entire events depending on event-level features criteria.

Thinning: removal of objects within an event, based on their features.

Slimming: removal of object variables, uniform for all objects of the same type.

Augmentation: addition of variables to existing objects, for example from combined performance criteria.

For the analysis discussed here, the release 21 of Athena was used, version 2.2.79.0 (p4190 with v01 containers). The SUSY2 DxAOD derivation was used for the anal-

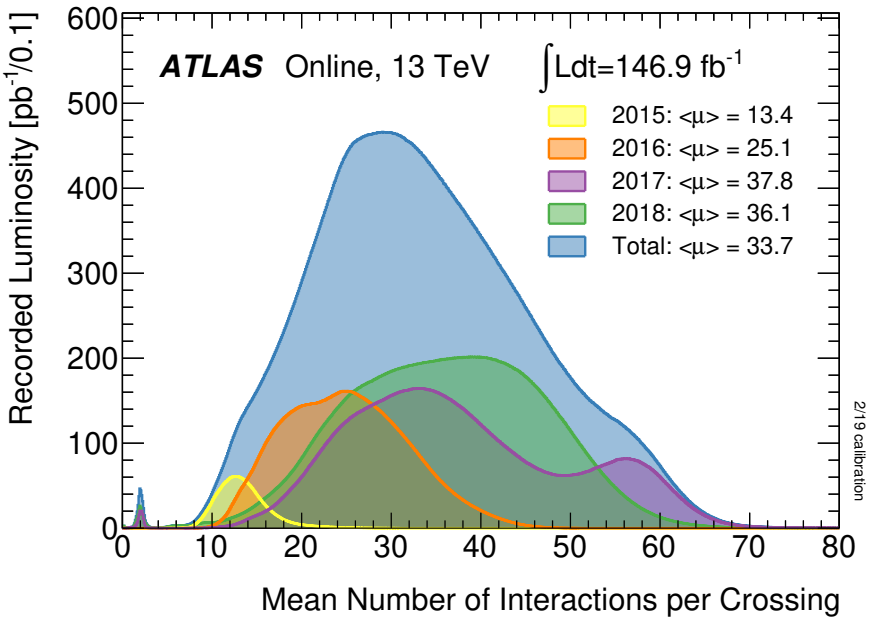


Figure 7.12: Measured pile-up profile for each year of the Run 2 in ATLAS [203].

ysis, which was previously made for other SUSY-related analyses by ATLAS groups targeting multi-lepton final states. At least two lepton objects were required during the derivation step to enter the final ROOT flat ntuples used in the following.

7.4.1 Monte Carlo samples

Signal and Standard Model (background) sources are modelled using Monte Carlo simulated samples. All samples are passed through the simulation of the ATLAS detector, to reproduce the experiment's response. Either the GEANT4-based full simulation of ATLAS [197], or a fast simulation are used to this purpose. In the latter case a parametrised response of the electromagnetic and hadronic calorimeters, which are the systems requiring the largest computational resources, is used, while the GEANT4 simulation is used for all other subdetectors [198]. Additional minimum-bias simulated interactions were run and added to each Monte Carlo event containing hard scattering processes, in order to account for additional pp interactions in the same bunch crossing, called *in-time pile-up*, and from adjacent bunch crossings (*out-of-time pile-up*) [199]. The pile-up profile was configured to replicate the one observed in data (fig. 7.12), with an average number of additional interactions per each bunch crossing, $\langle\mu\rangle$, extending from 0.5 to almost 80. The simulated pile-up samples were produced using PYTHIA 8.186 [200] with the NNPDF2.3LO [201] set of parton distribution functions and the A3 tune parameters [202].

A list of the generators used to produce the SM processes comprising background events are listed in table 7.4, including the parton shower algorithms, the selected sets of tuned parameters (if they are not the default ones), and the parton distribution functions. Bottom and charm hadrons decays were simulated through the EVTGEN [204], in cases where PYTHIA was used as generator. Events originated from diboson processes may contain two to four leptons through $pp \to 3\ell\nu/4\ell/\ell^{\pm}\ell^{\mp}\nu\nu$, up to order α^4 of the fine-structure constant, both resonant and non-resonant. Contributions from Higgs bosons and vector-boson scattering (VBS) and vector-boson fusion (VBF) pro-

cesses are included as well, reaching order α^6. Diboson events are generated with SHERPA 2.2.2 [205], using OPENLOOPS [206] for one-loop virtual amplitudes, with NLO accuracy for 0–1 jets and LO for 2–3 jets. The Catani-Seymour parton shower [207] is used for these events, as well as the ATLAS full simulation. Triboson events may reach up to six charge lepton in the final state, through resonant and non-resonant processes. These events are processes with SHERPA 2.2.1 only at LO, with the same remaining settings as diboson events. Remaining samples of $t\bar{t}W$ or $t\bar{t}Z$ were produced with SHERPA or MADGRAPH [208], with dilepton invariant masses down to 1 GeV in the case of $t\bar{t}Z$ containing SFOC leptons. The recommended version of SHERPA for each sample, proposed by the dedicated Physics Modelling Group in ATLAS, was used. Furthermore, samples of $t\bar{t}$ and single-top events were also produced, using the diagram removal scheme [209] to account for overlaps between the two sets of samples. Other processes that were simulated for their estimates as background events, but not listed in the table, are $4t$, tH, tWH, $t\bar{t}ZZ$, $t\bar{t}WH$ and $t\bar{t}HH$. For all these samples, the ATLAS fast simulation was used for the production.

Table 7.4: Monte Carlo generators, and the used settings, for the simulated Standard Model processes. LO and NLO refer to the relative calculation accuracy in the strong coupling α_s, being Leading-Order and Next-to-Leading-Order, respectively.

Process	Generator	Computation order	Parton shower	Cross-section normalization	PDF set	Set of tuned parameters
Diboson	SHERPA 2.2.2 [205] + OPENLOOPS [206]	NLO 0-1j + LO 2-3j	CSSHOWER [207]	NLO	NNPDF3.0NNLO [210]	default
Triboson	SHERPA 2.2.1	LO 0-1j	CSSHOWER	NLO	NNPDF3.0NNLO	default
$t\bar{t}W$	SHERPA 2.2.10 + OPENLOOPS	NLO 0-1j + LO 2j + LO $O(\alpha^3\alpha_s)$	CSSHOWER	NLO	NNPDF3.0NNLO	default
$t\bar{t}\ell^\pm\ell^\mp$, $m_{\ell\ell} > 5$ GeV	SHERPA 2.2.1	NLO	CSSHOWER	NLO	NNPDF3.0NNLO	default
$1 < m_{\ell\ell} < 5$ GeV	MG5_AMC@NLO 2.3.3 [208]	NLO	PYTHIA 8.212	NLO	NNPDF3.0NLO	A14[202]
$t\bar{t}H$	POWHEG BOX v2 [211]	NLO	PYTHIA 8.230	NLO	NNPDF3.0NLO	A14
$t\bar{t}$	POWHEG BOX v2	NLO	PYTHIA 8.230	NNLO	NNPDF3.0NLO	A14
Single top (s-, t-channel)	POWHEG BOX v2	NLO	PYTHIA 8.230	NNLO	NNPDF3.0NLO	A14
(tW)	SHERPA 2.2.7	NLO	CSSHOWER	NNLO + NNLL [212]	NNPDF3.0NNLO	default
$W \to \ell^\pm\nu$, $Z/\gamma^* \to \ell^\pm\ell^\mp$	SHERPA 2.2.11	NLO 0-2j + LO 3-5j	CSSHOWER	NNLO	NNPDF3.0NNLO	default

Monte Carlo samples for heavy neutral leptons signal events were produced using MADGRAPH 2.9.3, with NNPDF2.3LO PDF set and the HEAVYN model [213] at LO in QCD, permitting the emission of up to two additional partons. The parton shower, hadronisation and underlying event modelling were performed through PYTHIA 8.245 with the A14 set of tuned parameters. The matching between matrix element in the hard scattering and soft QCD radiation from parton showers were realised with the CKKW-L prescription [214]. The ATLAS fast simulation was used for all signal samples. At the time the analysis was performed, a bug in the MADGRAPH NLO production of HNL samples was found, and therefore only LO samples were used. The W bosons were set to only decay into a charged lepton, either an electron or a muon, and a HNL through $W^\pm \to \mu^\pm N$ or $W^\pm \to e^\pm N$. The only simulated HNL decays were the ones included in this analysis, hence $N \to \mu^\pm e^\mp \bar{\nu}_e$ or $N \to e^\pm \mu^\mp \bar{\nu}_\mu$, therefore decays into τ leptons and hadronic decay modes were not considered. The set of produced HNL samples featured different masses $m_N \in [8, 10, 15, 20, 30, 40, 50, 60, 65]$ GeV and two possible mean proper decay lengths of $c\tau_N = 0.1$ or 1 mm. The longer lifetime was only produced for m_N below 15 GeV. For each sample, 10^5 events were simulated, each divided into three samples to account for different pile-up conditions. The produced samples corresponding to different HNL masses and lifetimes are drawn in fig. 7.13, compared to previous limits obtained by ATLAS, for both prompt and displaced HNL signatures. Since the production cross section for heavy neutral leptons with different

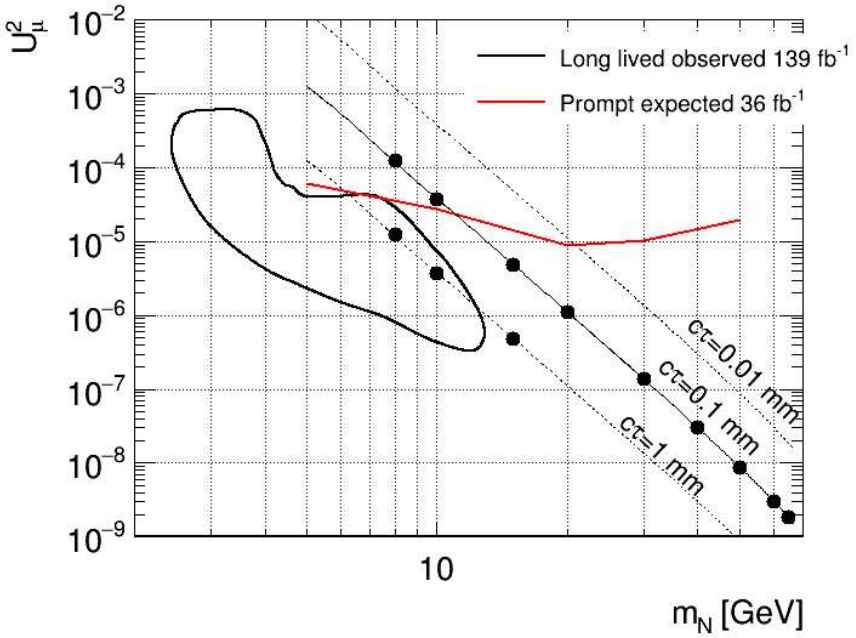


Figure 7.13: Position of the produced samples in the $(m_N, |U_\mu|^2)$ plane. Limits obtained through the previous partial Run 2 analysis focusing on the same prompt final state (red line), and the other ATLAS analysis focusing on displaced vertices (black line) are shown as well.

masses ranges over several order of magnitudes (see table 7.5), they were normalised during the analysis by scaling them until a value for $|U_e|^2 = |U_\mu|^2 = 1$ was found. The obtained limits were then scaled back to the original values later during analysis when discussing the actual results in terms of expected and observed limits on $(m_N, |U|^2)$.

7.5 Physics objects used in the analysis

Because of the specific final states enriched in multiple leptons with different flavours, the reconstruction and correct identification of electrons and muons plays a significant role in this analysis. Nonetheless, hadron jets, and specifically b-jets are also important, as leptons produced from their decays may be misidentified and associate to the primary interaction vertex, therefore giving rise to sources of background.

Electrons are reconstructed, as described in section 6.3.1, from the matching of clusters built with energy deposits in the ATLAS ECal, and ID tracks. Their identification is performed through a likelihood-based method, whose output depends on variables such as track-cluster matching compatibility, information from the TRT, and EM-shower shape. This technique provides five different working points, that can be used depending on the role of these particles in each analysis. Two electron identification classes are used in the following, one being a subset of the other. All pre-selected electrons, called *baseline* in the following analysis, must pass the `LooseLHBLayer` identification criteria, have a transverse energy $E_T > 8$ GeV and pseudorapidity $|\eta| < 2.47$. Those electrons measured in the crack region of the LAr calorimeter, $1.37 < |\eta| < 1.52$, are rejected in order to decrease the background coming from fake/non-prompt electrons. Further requirements are set on the transverse impact parameter, $|d_0/\sigma(d_0)| < 5$ where d_0 is

Table 7.5: Cross-sections for the signal samples, as obtained from each value of HNL mass and lifetime.

DSID	M_N (GeV)	$c\tau_{HNL}$ (mm)	final state	U^2	XS (pb)
537203	8	0.1	$\mu\mu e$	1.25e-04	1.22e-01
537205	8	0.1	$ee\mu$	1.25e-04	1.22e-01
537207	10	0.1	$\mu\mu e$	3.78e-05	3.39e-02
537209	10	0.1	$ee\mu$	3.78e-05	3.39e-02
537211	15	0.1	$\mu\mu e$	4.84e-06	4.18e-03
537213	15	0.1	$ee\mu$	4.84e-06	4.18e-03
510529	20	0.1	$\mu\mu e$	1.11e-06	9.08e-04
510531	20	0.1	$ee\mu$	1.11e-06	9.08e-04
510533	30	0.1	$\mu\mu e$	1.38e-07	9.64e-05
510535	30	0.1	$ee\mu$	1.38e-07	9.64e-05
510537	40	0.1	$\mu\mu e$	3.02e-08	1.69e-05
510539	40	0.1	$ee\mu$	3.02e-08	1.69e-05
510541	50	0.1	$\mu\mu e$	8.89e-09	3.52e-06
510543	50	0.1	$ee\mu$	8.89e-09	3.52e-06
537215	60	0.1	$\mu\mu e$	3.07e-09	6.87e-07
537217	60	0.1	$ee\mu$	3.07e-09	6.87e-07
537219	65	0.1	$\mu\mu e$	1.85e-09	2.64e-07
537221	65	0.1	$ee\mu$	1.85e-09	2.64e-07
537223	8	1.0	$\mu\mu e$	1.25e-05	1.22e-02
537225	8	1.0	$ee\mu$	1.25e-05	1.22e-02
537227	10	1.0	$\mu\mu e$	3.78e-06	3.39e-03
537229	10	1.0	$ee\mu$	3.78e-06	3.39e-03
537231	15	1.0	$\mu\mu e$	4.84e-07	4.18e-04
537233	15	1.0	$ee\mu$	4.84e-07	4.18e-04

the distance in the transverse plane from the electron track to the primary vertex, and $\sigma(d_0)$ is the associated uncertainty. This requirement allows reducing the contribution from charge misidentification of secondary tracks produced through interactions with the detector material. Another requirement is also posed on the longitudinal impact parameter $|z_0 \cdot \sin\vartheta| < 0.5$ mm, which is used to reduce fake electrons produced from pile-up jets.

The second class of electrons used in the analysis, called *signal*, satisfy tighter requirements on their identification and isolation. This allows to further reduce fake/non-prompt electrons from misidentified jets and hadrons decays. Signal electrons must pass the `MediumLH` identification requirement and be well-separated from other jets or muons in the event. Electron candidates are required to not have a displaced vertex reconstructed at a radius $r > 20$ mm, where the electron track was associated to that vertex during its reconstruction. A *photon conversion veto* is set, by imposing a lower limit of 100 MeV on the invariant mass of the system comprising the electron track and the closest track in the primary or conversion vertex. The `Loose_VarRad` iso-

lation working point is applied as isolation criteria. It is defined as a fixed cut on a track isolation variables, which uses as input the track cone size

$$\Delta R = \min\left(\frac{k_T}{p_T}, R\right) \tag{7.21}$$

with fixed $k_T = 10$ GeV, R being the maximum cone size set to $R = 0.3$, and the electron track momentum p_T.

A correction procedure with dedicated tools is applied for two very-close leptons in events with two overlapping isolation cones, therefore degrading the selection efficiency. It identifies other objects in the neighbour of the selected track and cluster and removes them, then recalculating the electron isolation variable to check if it passes the selected criteria. A further selection is applied to reduce reconstructed signal electrons with incorrect assigned charge. A BDT classifier combines electron cluster and track properties to calculate a single output score [149]. The selection is performed through the `ElectronChargeIDSelector` (ECIDS) tool, and is used with the `Loose` working point that guarantees a 9.17 rejection factor for electron with an incorrectly assigned charge, and an efficiency of 97.77%.

Muon objects are reconstructed through iterative track fits applied on hits in the inner tracker and the muon spectrometer (see section 6.3.2). Also for these particles, two identification and isolation classes were defined, baseline and signal. Baseline muons are required to pass the `Medium` identification working point. They must have $p_T > 8$ GeV, $|\eta| < 2.5$ and satisfy the longitudinal impact parameter requirement $|z_0 \cdot \sin\vartheta| < 0.5$ mm, to remove fake muons produced from pile-up jets. For signal muons, the `TightTrackOnly_VarRad` isolation working point is used to suppress those leptons produced from pile-up jets. This working point is defined through a fixed cut on the track isolation variable with a variable cone size. A selection on the transverse impact parameter, $|d_0/\sigma(d_0)| < 3$ was also applied for signal muons. The same electron isolation correction procedure for the removal of other objects in neighbourhood of the selected tracks was also applied for signal muons.

Hadron jets are reconstructed from particle-flow objects combining information from the inner detector and both ECal and HCal. The combined information allows to improve the jet energy resolution and also the reconstruction efficiency for low-p_T jets. After their reconstruction, both in-situ and simulation-based corrections are applied. Only *signal* jets featuring $p_T > 20$ GeV and $|\eta| < 2.8$ are stored in the analysis workflow after the derivation step. Jets originating from other sources, ranging from calorimeter noise, non-collision backgrounds and pile-up, are removed through the `JetVertexTagger` track-based discriminants. A veto condition is set on events containing a `LooseBad` working point jet, in order to reject events produced from non-collision backgrounds. Signal jets are required to pass the `JVT signal` working point. The identification of b-jets is performed through the `DL1r` flavour tagging algorithm. The same p_T and η selections are applied as for all other jets. The selected working point on the identification of b-flavoured jets guarantees an average efficiency of 85%, which was measured in a sample enriched in $t\bar{t}$ events.

For all defined physics objects, an overlap removal method is applied to remove those entering more than one possible definition, in order to avoid double counting. One simple example are electrons being reconstructed also as jets. Jets found inside an electron or a muon cone, within $\Delta R = 0.2$, are discarded to reject those originating from electromagnetic showers or bremsstrahlung from energetic muons. From the remain-

ing objects, electrons and muons in the neighbourhood of remaining jets are discarded, to reject non-prompt leptons and those coming from hadron decays.

The missing transverse energy ($E_{\mathrm{T}}^{\mathrm{miss}}$) and momentum $\mathbf{p}_{\mathbf{T}}^{\mathrm{miss}}$ are reconstructed based on all objects, leptons, jets and reconstructed photons satisfying $p_{\mathrm{T}} > 25$ GeV and $|\eta| < 2.37$, and passing their corresponding `signal` identification criteria. A *soft term*, calculated from ID tracks which were associated to the primary vertex but not matched to any of the reconstructed object of that event, is added to the previously defined quantities. An overlap-removal technique, specifically targeting the $E_{\mathrm{T}}^{\mathrm{miss}}$ reconstruction, has been implemented and used for its correction [215].

7.5.1 Variables for event selections

From the reconstructed objects described before, a list of variables later used for defining regions used to study and validate the expected background and to optimise the signal selection were defined. These variables are:

- The transverse momentum of the leading lepton, being the charged lepton with the highest $p_{\mathrm{T}}^{\ell_1}$.
- The transverse momenta of the sub-leading lepton $p_{\mathrm{T}}^{\ell_2}$, the second lepton with the highest momentum, and the third leading lepton $p_{\mathrm{T}}^{\ell_3}$.
- The scalar sum of all signal leptons in the event, $\sum p_{\mathrm{T}}^{\mathrm{lep}}$
- The minimum invariant mass of the Different Flavour Opposite Charge (DFOC) signal lepton pair, $m_{\mathrm{DFOC}}^{\mathrm{min}}$, for events containing one such object. This variable is used as a proxy for the HNL mass m_{HNL} with the missing momentum of one neutrino. For each value of m_{HNL}, the $m_{\mathrm{DFOC}}^{\mathrm{min}}$ distribution has an end-point value of m_{HNL} (corresponding to almost negligible neutrino momentum).
- The invariant mass of a Same-Charge (SC) signal lepton pair, $m_{\mathrm{SC}}^{\ell\ell}$.
- The invariant mass of the three-signal-lepton system $m_{\ell\ell\ell}$.
- The transverse mass, computed based on the leading signal lepton and missing energy, and defined as $m_{\mathrm{T}} = \sqrt{2p_{\mathrm{T}}^{\ell_1} E_{\mathrm{T}}^{\mathrm{miss}}(1 - \cos(\Delta\varphi(\ell 1, \mathbf{p}_{\mathrm{T}}^{\mathrm{miss}})))}$.
- The inclusive effective mass, m_{eff}, that is defined as the scalar sum of the measured p_{T} from all jets and leptons, and the $E_{\mathrm{T}}^{\mathrm{miss}}$.
- The distance, in the (η, φ) plane, between the two SC signal leptons in the event $\Delta R(\ell_1^{\pm}, \ell_2^{\pm})$.
- The azimuthal distance between the two leading and sub-leading leptons, and the missing transverse momentum $\Delta\varphi((p_{\mathrm{T}}^{\ell_1} + p_{\mathrm{T}}^{\ell_2}), \mathbf{p}_{\mathrm{T}}^{\mathrm{miss}})$.
- The number of baseline leptons in the event, $N_{\mathrm{lep}}^{\mathrm{base}}$.
- The number of signal leptons in the event, $N_{\mathrm{lep}}^{\mathrm{sig}}$.
- The number of b-tagged jets in the event, $N_{\text{b-jets}}$.

- The interval of assumed W boson mass, computed from the tri-lepton and $\mathbf{p}_{\mathrm{T}}^{\mathrm{miss}}$ system, for which no real solution exists for the kinematics of the reconstructed event, $m_W^{\mathrm{max}} - m_W^{\mathrm{min}}$. This variable allows to evaluate the compatibility of the event to be originated by the decay of a W boson. Assuming the W boson mass equal to the PDG value [71], the missing component of the neutrino, p_{Z}, can be calculated. The resulting calculation leads to a quadratic equation, whose discriminant has to be larger than zero to obtain real solutions. By selecting events for which a solution exists, however, a significant amount of signal is removed, possibly due to the m_W in the event being higher than the PDG value, or because of leptons and $E_{\mathrm{T}}^{\mathrm{miss}}$ mis-measurements. The discriminant is nevertheless a quadratic function of m_W. It is therefore possible to calculate the two values, m_W^{max} and m_W^{min}, for which the discriminant is positive. The $m_W^{\mathrm{max}} - m_W^{\mathrm{min}}$variable hence defines the interval between these two values for which the resulting equation has a solution.

7.6 Event selection

From the indicated data samples and produced Monte Carlo events, additional cleaning of the dataset and initial selections were performed. Two sets of ROOT ntuples were obtained for different types of studies. A first set, derived through the SS3LDEV framework, only contained light ntuples with events passing a set of additional pre-selection requirements, triggers and final state events compatible with the analysis target (e.g. at least two SC leptons). These sets of ntuples also contained all sources of considered systematic uncertainties, and were used for the yields estimates in the different analysis regions. A second set of ntuples, obtained through the SS3LANALYSIS framework, contained more detailed object information without application of overlap removals nor isolation cuts. These datasets were used for studies related to detector backgrounds, such as fake lepton rates studies, estimate of non-prompt lepton backgrounds, charge-flip studies and others. Because of the much larger size of these ntuples, they did not include systematic uncertainties, and were used to validate the yields in the different analysis regions obtained with the other framework.

Several combinations of dilepton triggers were used for selecting events with leptons in the final states with sufficient p_{T}. A logical `or` was applied on each trigger. Offline electrons were required to have a $p_{\mathrm{T}} > 18$ GeV to pass the di-electron trigger, while for muons the same requirement was set to 15 GeV in the case of symmetric trigger between two leptons, or 9 GeV and 19 GeV for asymmetric muon pairs. For events triggered by electron-muon pairs, the p_{T} thresholds were set to 8 GeV and 25 GeV, or 18 GeV and 15 GeV, respectively. Trigger matching between online and offline lepton objects was performed through a dedicated software package, only considering signal leptons with p_{T} higher than the mentioned values, in a plateau region of the trigger efficiency. Trigger scale factors were applied to Monte Carlo samples to replicate the ATLAS trigger efficiency. Individual factors were computed for each event, based on the fired triggers in that event, and the actual physics object content, therefore concerning the number of leptons, their flavour, and the corresponding triggering efficiency.

7.6.1 Pre-selection requirements

Before the actual definition of signal regions for the search of heavy neutral leptons, a first set of pre-selection cuts was posed on all samples, in order to obtain a subset of events compatible with the desired final states. These events were also used to study

the background composition, and to validate the detector background estimates that were obtained through dedicated data-driven methods.

The list of cuts applied on all events is listed in table 7.6. The first set of requirement was posed on the lepton's momenta, with a cut of 20 GeV on the lepton with the highest p_{T}, regardless of its flavour. The remaining two lepton were selected to have a transverse momentum of at least 15 GeV for the sub-leading lepton, and 8 GeV for the third one. Only events containing at least two signal leptons and at most three signal leptons were retained, and the same request was also set on baseline leptons. These cuts allows to remove backgrounds with multiple leptons in the final states, such as $t\bar{t}Z$ and $t\bar{t}H$ processes. Events with three same-flavour leptons were rejected, while those including Different-Flavour, Same-Charge (DFSC) leptons were retained for background validation. At least one SFSC lepton pair was required in each event, in order to suppress multi-boson background processes, mainly $pp \to ZZ$. A minimum value of 5 GeV was set on the invariant mass of the DFOC lepton pair, reducing the background produced from W+jets and Z+jets and diboson events, and also a lower cut on $m_{\mathrm{SC}}^{\ell\ell}$ of 20 GeV was set with the same purpose. The scalar sum of the signal leptons, $\sum p_{\mathrm{T}}^{\mathrm{lep}}$, was required to be above 50 GeV to suppress backgrounds arising from fake/non-prompt leptons produced with low momenta. The remaining selection cuts were posed on the effective mass, $m_{\mathrm{eff}} > 250$ GeV, to suppress W/Z+jets, WZ ant $t\bar{t}$ background sources, and on the missing transverse energy $E_{\mathrm{T}}^{\mathrm{miss}} < 100$ GeV to reduce remaining backgrounds that include a leptonic decay from W bosons, mainly $t\bar{t}$.

Table 7.6: The pre-selection requirements applied in the analysis to study the background composition, as well as validate the background estimations with the data-driven methods.

Variable	**Selection**
$p_{\mathrm{T}}^{\ell_1}$	> 20 GeV
$p_{\mathrm{T}}^{\ell_2}$	> 15 GeV
$p_{\mathrm{T}}^{\ell_3}$	> 8 GeV
$N_{\mathrm{lep}}^{\mathrm{base}}$	2 or 3
3 signal SF ℓ	$= 0$
ee SS pairs	kept
$\mu\mu$ SS pairs	kept
$e\mu$ SS pairs	only for validation
$m_{\mathrm{DFOC}}^{\mathrm{min}}$, when $N_{\mathrm{lep}}^{\mathrm{sig}} = 3$	> 5 GeV
$m_{\mathrm{SC}}^{\ell\ell}$	> 20 GeV
$\sum p_{\mathrm{T}}^{\mathrm{lep}}$	> 50 GeV
m_{eff}	< 250 GeV
$E_{\mathrm{T}}^{\mathrm{miss}}$	< 100 GeV

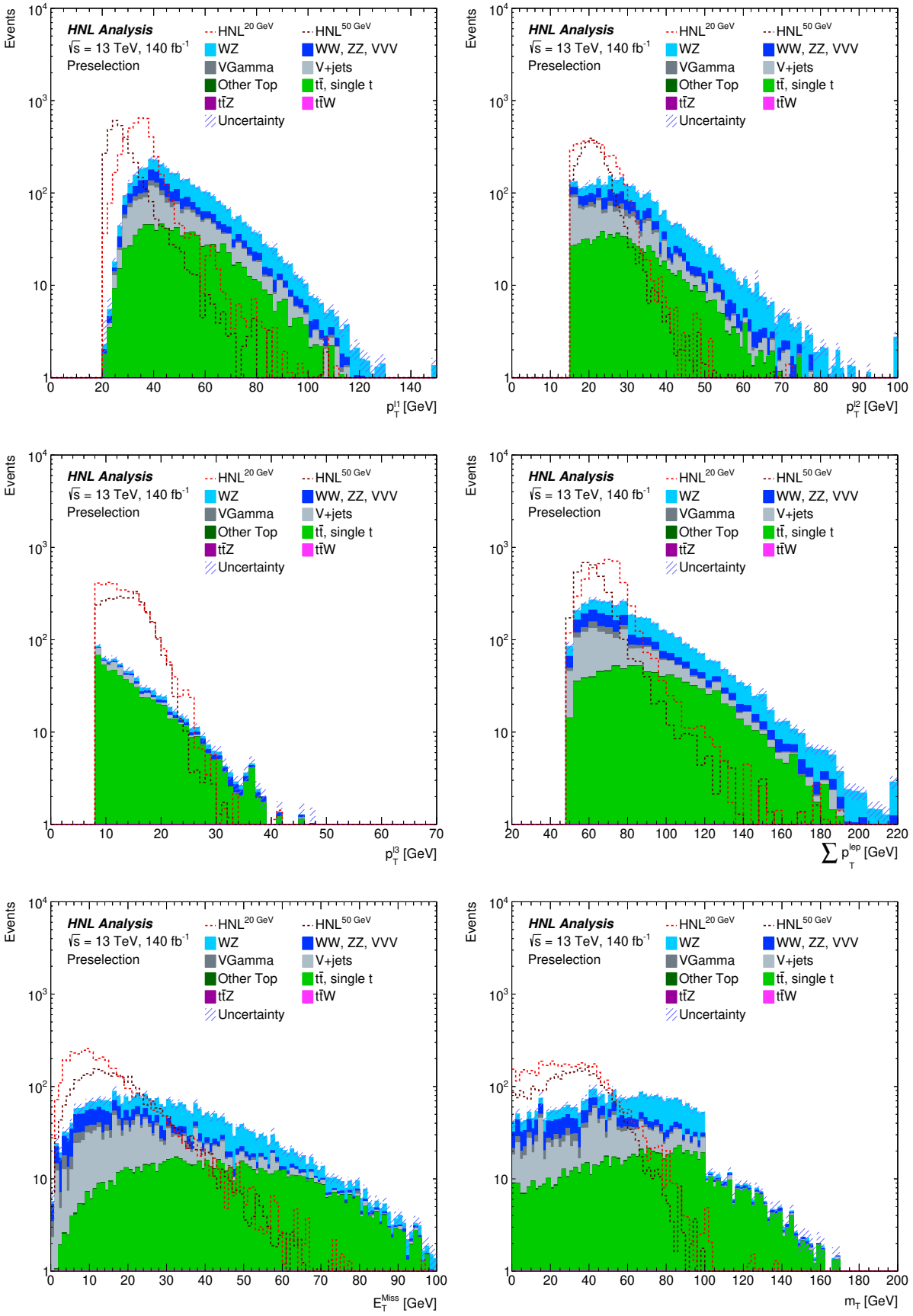


Figure 7.14: Distributions of signal and background samples for variables presented in section 7.5.1. See text for details.

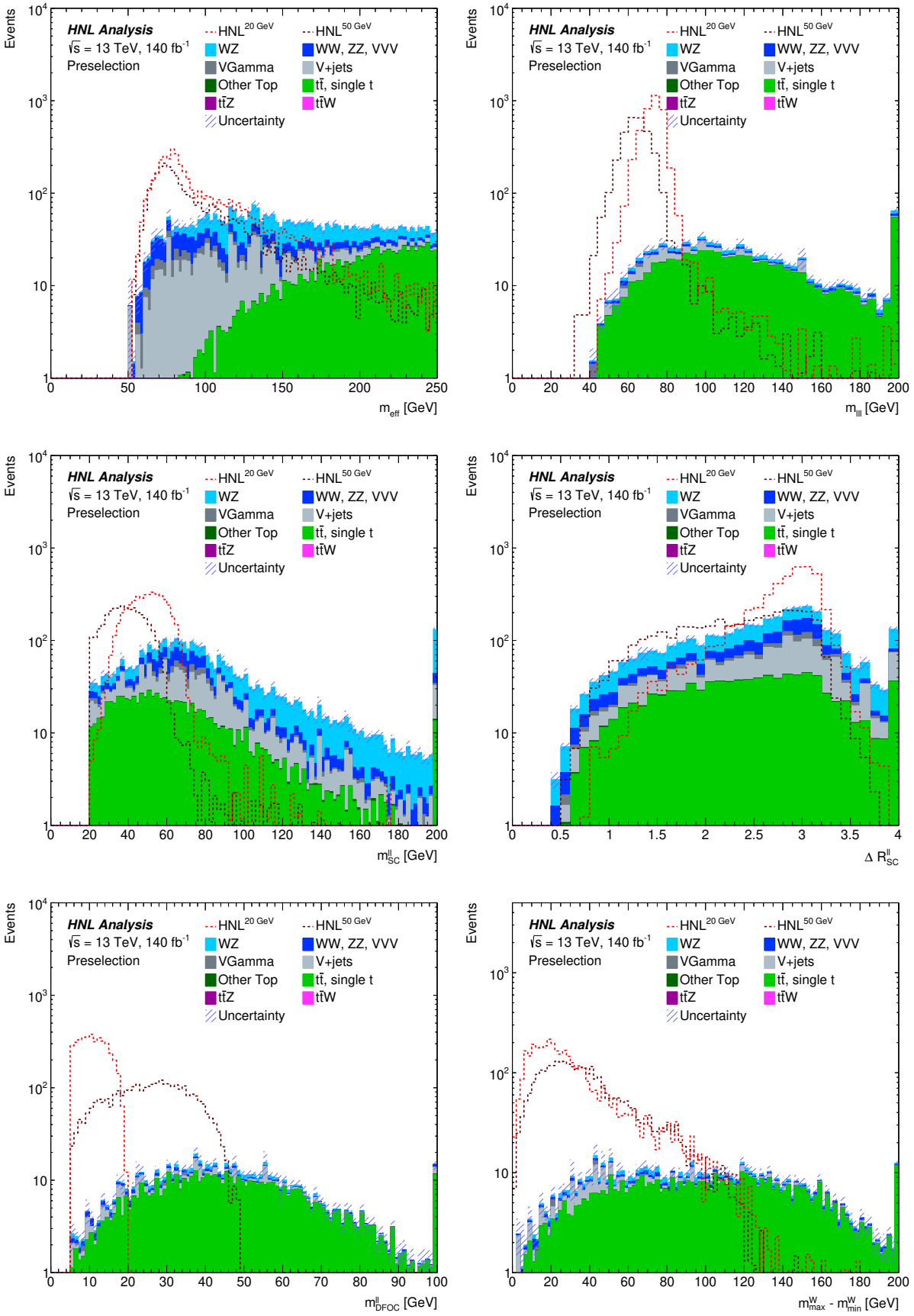


Figure 7.15: Distributions of signal and background samples for variables presented in section 7.5.1. See text for details.

Figures 7.14 and 7.15 show the distributions of some of the presented variables, for events passing the pre-selection step. The dashed red histograms show two examples of signal distributions for different masses, $m_{\mathrm{HNL}} = [20, 50]$ GeV, not stacked on the background and scaled up by a factor 100. Only Monte Carlo samples were used at this preliminary level. For the $p_{\mathrm{T}}^{\ell_3}$, $m_{\ell\ell\ell}$, $m_{\mathrm{DFOC}}^{\mathrm{min}}$ and $m_W^{\mathrm{max}} - m_W^{\mathrm{min}}$distributions, the additional requirement of exactly three signal leptons was posed, as they were not calculated for events for which the third lepton did not pass the tight selection criteria.

The expected contamination of signal events inside the so-formed pre-selected regions is drawn in fig. 7.16, for two examples with $m_{\mathrm{HNL}} = [20, 50]$ GeV and $\mu\mu e$ or $ee\mu$ final states. The simulated background is dominated, at this level, by events with one or more top quarks. For this reason, most signal regions, defined in section 7.7, exploit signal cuts on the number of b-tagged jets, effectively removing a significant amount of such source of background. The remaining largest source of backgrounds are detector-related events, which may only reach the final state configuration through fake/non-prompt leptons. In fact, in these plots the $V\gamma$, V+jets and several t-quark events may only enter the selection through detector effects, because of the SC lepton pair requirement. These kinds of processes are however subject to simulation mis-modelling, which makes their obtained yields unreliable for the correct background estimation inside SRs. For this reason, dedicated techniques were implemented, described in section 7.8.

7.7 Signal regions definitions

A number of Signal Regions (SRs) were defined from sets of kinematic requirements and cuts applied on variables defined in section 7.5.1, with the purpose of identify regions with very low background contamination, while keeping the signal efficiency as high as possible. The statistical significance Z, calculated through the formula given in [216][217]

$$Z = \pm\sqrt{2} \times \sqrt{n \ln \frac{n(b+\sigma^2)}{b^2+n\sigma^2} - \frac{b^2}{\sigma^2} \ln \frac{b^2+n\sigma^2}{b(b+\sigma^2)}}, \tag{7.22}$$

was used as an estimator for the SR optimisation. In eq. (7.22), b is the number of expected background events, and n represents the total number of entries in the region, being $n = s + b$ with s expected HNL signal events. The uncertainty on the number of background events, σ, was taken as the combination of the statistical uncertainty plus a flat 30% systematic uncertainty associated to all samples. By requiring Z to be as high as possible, an iterative procedure consisting of an automatic scan on different sets of kinematic variables to separate signal and background was performed. All available signal mass samples were individually used during this procedure, with both $c\tau_{\mathrm{HNL}} = 0.1$ mm and $c\tau_{\mathrm{HNL}} = 1$ mm. Additional requests were posed during this optimisation procedure, for example requiring a minimum number of signal or background events entering the SRs after cuts, or requiring the resulting statistical uncertainty to be lower than a set threshold. While in most cases the resulting SR only considered final states with three signal leptons, a set of signal regions was specifically obtained targeting final states including only two SC signal leptons, and allowing the third one to be a baseline lepton. This choice was taken aiming at very low mass signal points, where low-p_{T} leptons may not have passed the signal lepton identification and isolation criteria.

From the results of the iteration over several millions variable configurations, only using Monte Carlo background samples, a subset of 30 signal regions was obtained. In order to select the final regions to be used in the analysis, the full background estima-

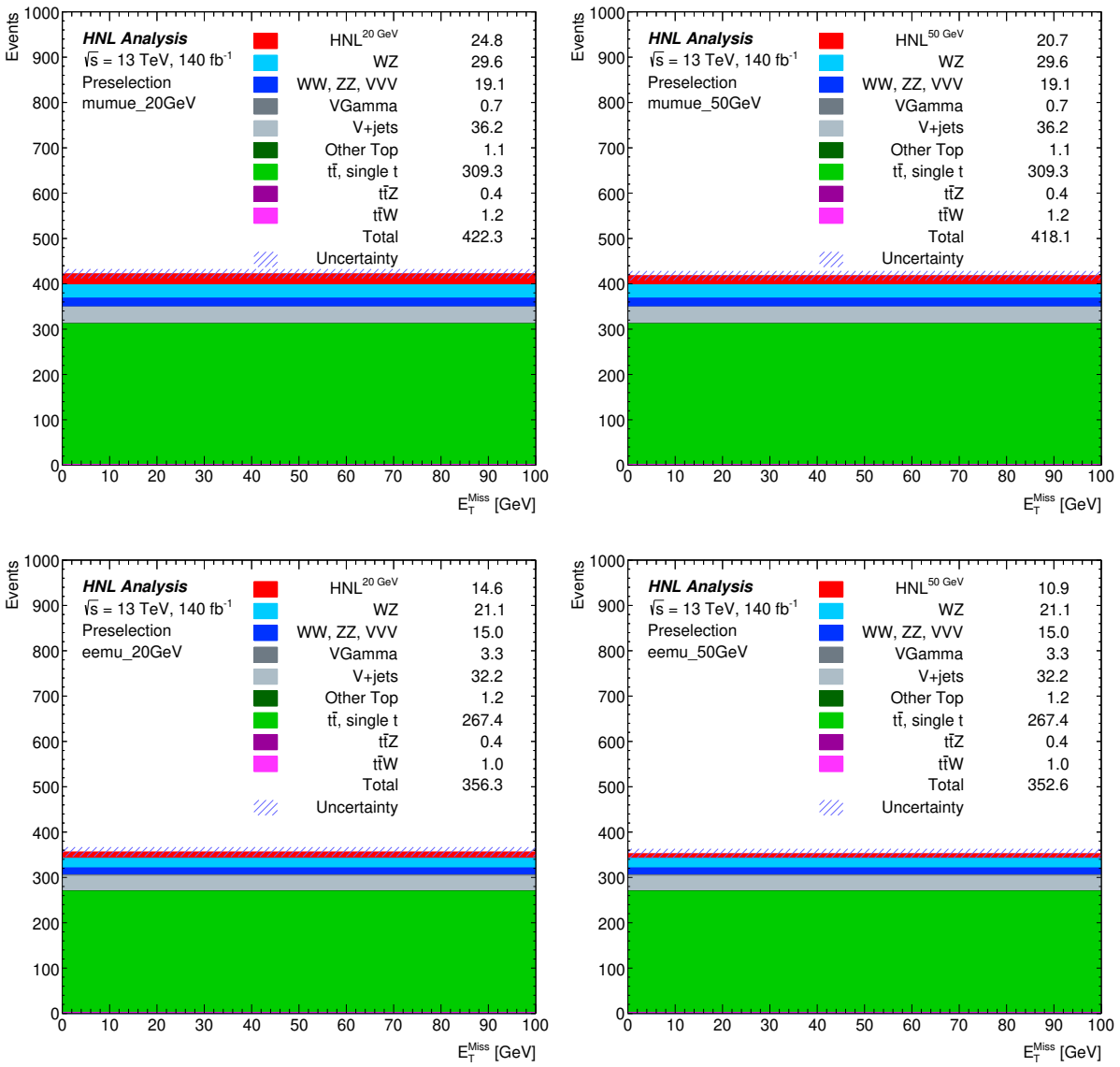


Figure 7.16: Contamination of signal at pre-selection level, using only Monte Carlo background samples. The "Other" sample groups most top-related backgrounds, including single top, $t\bar{t}$, and events with more than two top quarks. A further separation was applied on pre-selected samples, requiring three signal leptons. The final states were then separated into the $\mu\mu e$ (upper row) and $ee\mu$ (lower row) channels. For each channel, two HNL mass samples were used, corresponding to $m_{\mathrm{HNL}} = 20$ GeV (left) and $m_{\mathrm{HNL}} = 50$ GeV (right).

tion in each region, including data-driven techniques that are described in section 7.8, was performed. A merging of remaining signal regions showing good results for close m_{HNL} samples was also done, to reduce the number of regions. As a result of this optimisation procedure, however, the signal regions may present overlaps. Therefore, when presenting the results of the analysis, only the regions featuring the highest expected sensitivity were used.

Table 7.7: Signal regions considered in the analysis.

SR name	$N_{\text{lep}}^{\text{sig}}$	m_{T} [GeV]	m_{eff} [GeV]	$\Delta R_{\text{SC}}^{\ell\ell}$	$m_{\text{DFOC}}^{\text{min}}$ [GeV]	$m_{\text{SC}}^{\ell\ell}$ [GeV]	$m_W^{\text{max}} - m_W^{\text{min}}$ [GeV]	$N_{\text{b-jets}}$	Additional requirements
Three-signal-lepton SRs									
SRE1	= 3	< 70	< 250	> 2.0	< 20	< 75	< 60	= 0	-
SRE2	= 3	< 65	< 200	–	< 25	< 65	< 60	= 0	-
SRE3	= 3	< 50	< 150	> 1.5	< 35	< 60	< 70	= 0	-
SRE4	= 3	-	< 250	–	< 50	-	< 70	= 0	$m_{\ell\ell\ell} < 80$ GeV, $p_{\text{T}}^{\ell_1} < 30$ GeV
SRM1	= 3	< 70	< 120	> 2.0	< 25	< 70	< 70	= 0	-
SRM2	= 3	< 45	< 120	–	< 40	< 65	< 70	= 0	$\Delta\varphi((p_{\text{T}}^{\ell_1} + p_{\text{T}}^{\ell_2}), \mathbf{p}_{\text{T}}^{\text{miss}}) > 1.0$
Two-signal-lepton SRs									
SRM3	= 2 (SC)	< 60	< 120	> 2.5	–	< 75	-	-	-
SRM4	= 2 (SC)	< 55	< 150	> 2.0	–	< 70	-	= 0	-
SRM5	= 2 (SC)	< 70	< 120	> 2.0	–	< 75	-	-	-

The obtained set of SRs used in the following analysis is listed in table 7.7, and separated for final state configurations. Regions SRE1-4 target events with three signal leptons with two SC electrons, namely $e^{\pm}e^{\pm}\mu^{\mp}$, while SRM1-2 target $\mu^{\pm}\mu^{\pm}e^{\mp}$ final states, also with three signal leptons. The remaining three signal regions, SRM3-5, also target $\mu^{\pm}\mu^{\pm}e^{\mp}$ final states, but also baseline electrons may enter the SR, while the two SC muons are required to have passed the signal identification criteria. The reciprocal set of events, with two SC signal electrons and the remaining baseline OC muon, were not considered, because of the much larger background from charge-flip processes. The veto on b-jets, present in most selected regions, suppresses the background originated by one or more top quarks. The selection on $\Delta R_{\text{SC}}^{\ell\ell}$ allows to overall reduce remaining contributions from W/Z+jets, in some cases in conjunction with cuts on the transverse mass variable, m_{T}. The $m_W^{\text{max}} - m_W^{\text{min}}$ variable, which was used as an estimator of the compatibility of the event to be originated from an on-shell W boson, was found to have good rejection capabilities mostly for $t\bar{t}$ and VV backgrounds, for which larger values than signal were observed.

Figures 7.17 to 7.20 show a few examples of the impact of different variable cuts on the rejection of backgrounds from the SRs. In each plot, the entire set of pre-selection and the corresponding SR requirements were applied, with the exception of the one on the plotted variable. The name of the signal region under study is written on the upper side of each plot, while the legend reports the yields of each signal and background process in that region. For each plot, only one signal at the time is drawn, while in several cases the same region was used to search for more than one HNL mass point. The signal sample was randomly selected from the subset of signal samples with m_{HNL} targeted by the corresponding region. A vertical dashed line was drawn, corresponding to the value on which the SR cut from table 7.7 was applied. For these plots, only

Monte Carlo samples were used to demonstrate the correct results of the optimisation procedure, and only statistical error bars were drawn. On the lower pad, an approximation of eq. (7.22), $Z \simeq S/\sqrt{S+B}$, was drawn to better visualise the regions with the highest signal sensitivity. Because of the very limited number of entries, the defined SRs are not binned in any variable, and therefore all entries in these histograms below the set cut were to be added to obtain the final SR yields.

7.8 Background estimation

Background sources that may produce final states consistent with those presented in section 7.2 can be grouped into three main categories. The first one are SM processes originating multiple (prompt) leptons. The second are SM processes producing an opposite charge lepton pair, with one of them being reconstructed with the incorrect electric charge, therefore forming a SFSC pair. This is almost exclusively the case for electrons, because of the much smaller interaction cross section of muons with the detector material. Finally, the third source of background are SM processes resulting in SFSC pairs due to additional fake/non-prompt leptons in the same event incorrectly associated to the same vertex. In the following, the applied procedure for the estimation of each background sources is discussed.

7.8.1 Standard Model backgrounds

Standard Model processes entering the signal regions comprise events with multilepton final states with one SFSC pair. Most signal regions feature a veto on b-jets which, in combination with the low $E_{\mathrm{T}}^{\mathrm{miss}}$ and m_{eff} cuts, allows to remove almost completely top-related backgrounds. In fact, processes due to $t\bar{t}H$, $t\bar{t}Z$, $t\bar{t}W^+W^-$, $t\bar{t}WZ$, $t\bar{t}HH$, $t\bar{t}WH$ $t\bar{t}ZZ$, tWZ, tZ, $3t$ and $4t$ are found to have no any contribution inside the SRs. The remaining largest sources of prompt SM backgrounds are multiboson events, mainly from WZ and then from W^+W^-, ZZ and VVV processes. The only expected way for ZZ and VVV processes to produce SFSC lepton pairs, and therefore enter the SRs, is through decays into τ leptons and their following decays into light leptons. The τ-related origin of these events was evaluated using a dedicated software, called `MCTruthClassifier`, that exploited generator-level information to check that none of the produced events contributed to SRs yields with fake/non-prompt leptons, leaving the τ origin the only remaining alternative. Since the remaining sources of backgrounds are detector-related, simulated samples containing fake/non-prompt leptons were removed through the same software package to avoid double counting. In order to estimate the contributions from remaining SM processes giving rise to prompt leptons, the Monte Carlo samples are normalised to replicate their corresponding theoretical cross sections.

7.8.2 Charge-flip background

The charge of electrons is reconstructed in the ATLAS inner detector through their track's curvature under a solenoidal magnetic field. Charge mis-measurement mostly arises because of bremsstrahlung radiation from electrons, with converted high-energy γs producing additional tracks, one of them possibly being selected during the track fitting with an opposite charge with respect to the original electron. Errors in the charge assignment of electron tracks, without any additional radiation, are possible but were evaluated to be much rarer. As bremsstrahlung radiation mainly occurs while particles traverse the ID material, these effects are almost negligible for muon reconstruction,

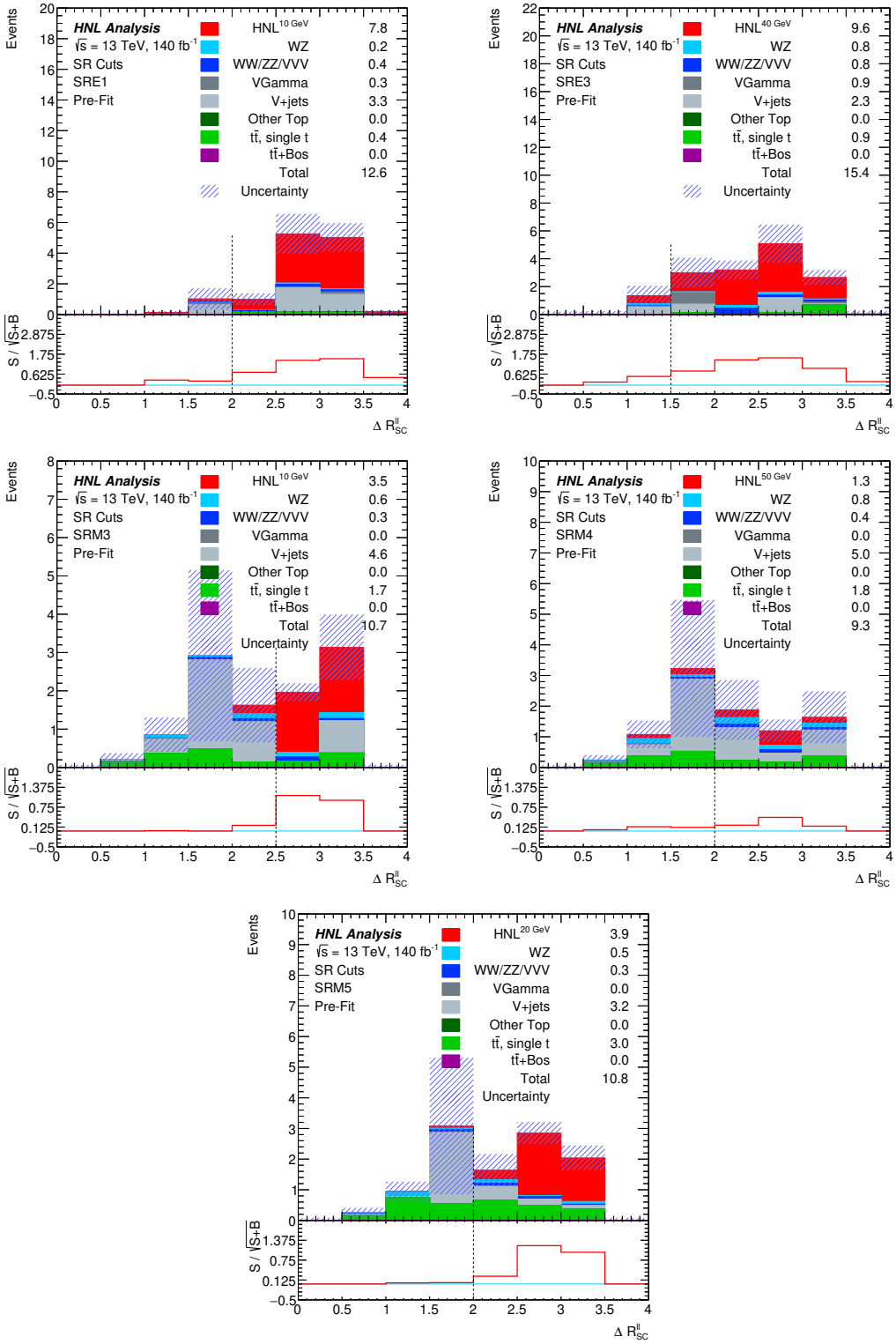


Figure 7.17: Examples of HNL signal and background yields in the SRs, where the $\Delta R^{\ell\ell}_{\mathrm{SC}}$ cut was removed.

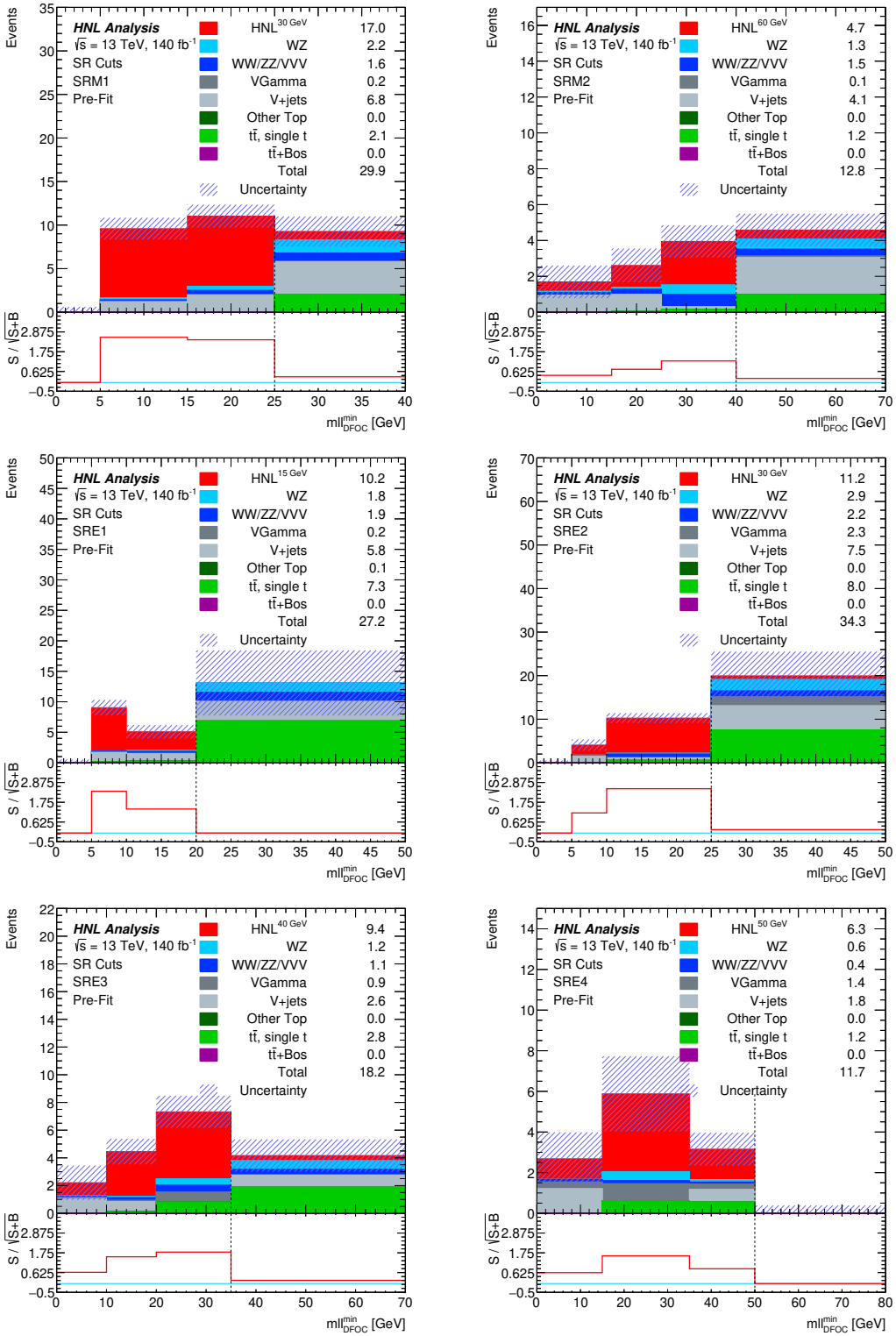


Figure 7.18: Examples of HNL signal and background yields in the SRs, where the $m^{\text{min}}_{\text{DFOC}}$ cut was removed.

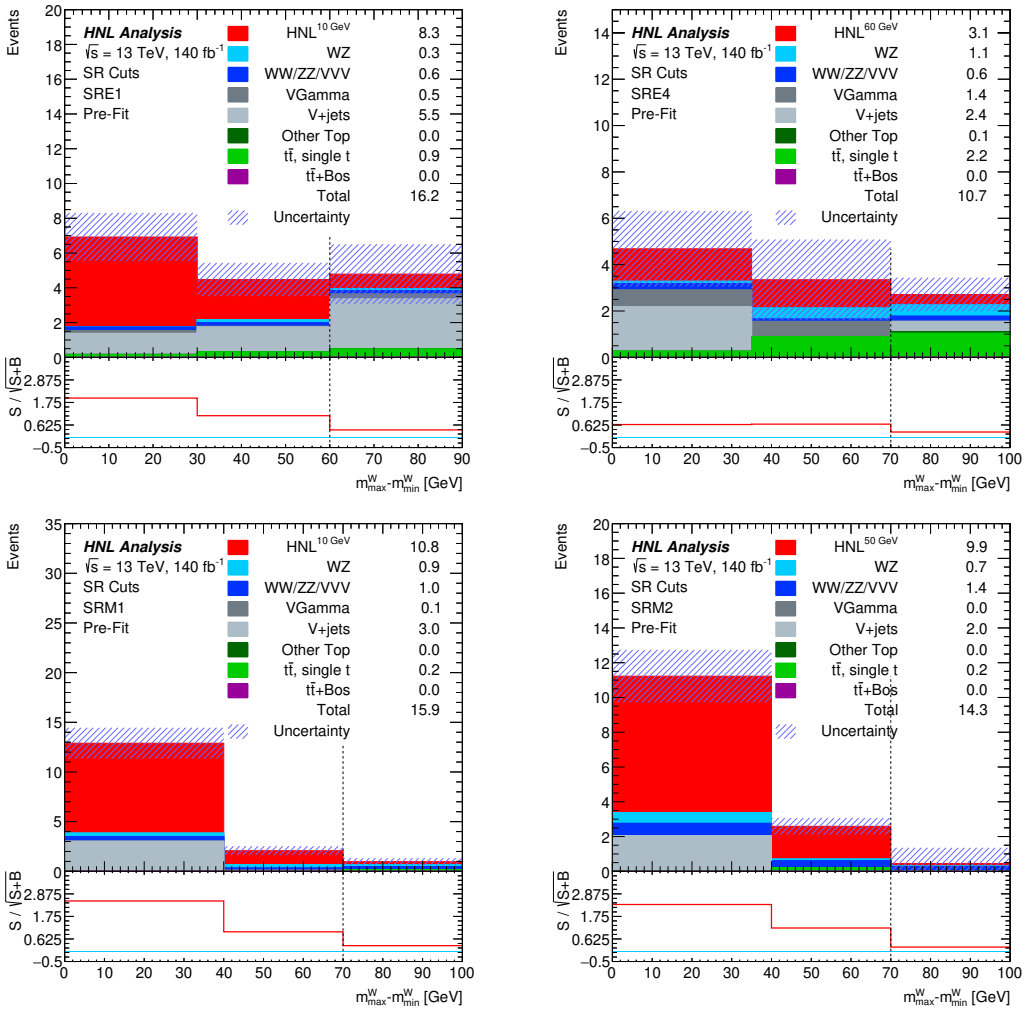


Figure 7.19: Examples of HNL signal and background yields in the SRs, where the $m_W^{\max} - m_W^{\min}$ cut was removed.

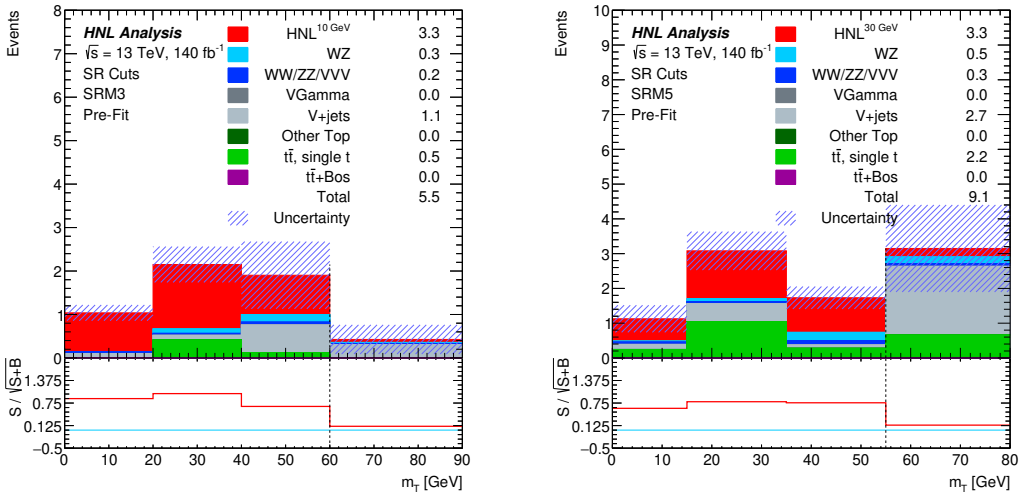


Figure 7.20: Examples of HNL signal and background yields in the SRs, where the m_{T} cut was removed.

since they feature a smaller cross-section for this process. This kind of background, commonly named "charge-flip", mainly affects analyses sensitive to the charge of leptons to target SC pairs. A data-driven approach was used in the analysis to estimate the event yields due to charge mis-assignment inside SRs.

The procedure for evaluating these yields consisted in associating events featuring OC lepton pairs (e^+e^- or $e^\pm\mu^\mp$) and weighting them for a *charge-flip rate*, $\xi(\eta, p_\mathrm{T})$, that is a function of leptons' pseudorapidity and transverse momentum. Assuming these flip rates are known, the weight for each OC event to be charge-flip is given by

$$w_\mathrm{flip} = \frac{\xi_1(1-\xi_2) + (1-\xi_1)\xi_2}{(1-\xi_1)(1-\xi_2) + \xi_1\xi_2} \tag{7.23}$$

with ξ_1, ξ_2 being the probability for each of the two leptons to have been assigned the wrong charge. The probability ξ_i given to muons was set to zero. These factors were measured through dedicated simulated $Z \to e^+e^-$ samples, with correction factors obtained through real data to account for mismodelling. After applying the corresponding corrections, an agreement within a 20% range was obtained for the charge-flip rates in this sample. This kind of background is not discussed in more detail here, as it was found not to have contributions in the SRs yields. The main uncertainties in the estimate of the charge-flip yields are the correction factors measurements, which are statistically limited because of the low charge-flip probability. A second contribution to the large uncertainty on these factors is a non-negligible background contamination during their estimate procedure. These two effects lead to a $\sim 40\%$ uncertainty on the predicted electron charge-flip yields.

7.8.3 Fake/non-prompt leptons background

As discussed in section 7.3, fake/non-prompt background comprises any kind of event with reconstructed lepton objects that are not produced in the primary vertex. Examples of possible mechanism for their production are non-prompt leptons from heavy-flavour mesons decays, tracks from converted high-energy γs, light hadrons being reconstructed as electron showers, or leptons from $K^\pm/\pi^\pm$ decays. Usually these kinds of objects are effectively rejected through identification criteria, larger impact parameter than "real" leptons, or also isolation requirement from neighbouring jets. Nevertheless, some of these objects may pass the baseline or even signal lepton criteria, and therefore form a SFSC pair with other leptons in the event. The most relevant source of fake/non-prompt leptons, evaluated from Monte Carlo samples, are V+jets events with minor contributions from $t\bar{t}$ processes. When evaluating the event yields in the SRs, these Monte Carlo samples were removed, and the yields obtained through a dedicated data-driven approach, the *matrix method* [218], were use instead to avoid double counting.

The matrix method allows to estimate the amount of fake leptons in a certain parameter region, based on the different numbers of real and fake leptons passing certain requirements on identification quality, isolation and other variables inside a second auxilliary region. Real leptons have, in general, a higher probability to pass good quality reconstruction/isolation criteria than fake ones. Given the fractions of real and fake leptons passing the tighter selection criteria, $\varepsilon_\mathrm{real}$ and $\varepsilon_\mathrm{fake}$, the number of observed signal and loose leptons obtained from a set of events containing only one lepton in the final state is

$$\begin{pmatrix} N^\mathrm{signal} \\ N^\mathrm{loose} \end{pmatrix} = \begin{pmatrix} \varepsilon_\mathrm{real} & \varepsilon_\mathrm{fake} \\ 1-\varepsilon_\mathrm{real} & 1-\varepsilon_\mathrm{fake} \end{pmatrix} \begin{pmatrix} N^\mathrm{base}_\mathrm{real} \\ N^\mathrm{base}_\mathrm{fake} \end{pmatrix} \tag{7.24}$$

where *loose* leptons are defined as those that pass the baseline selection criteria, but not the signal one. In a shorter form, the previous equation can be written as

$$\mathbf{N}_{\text{sl}} = \mathbf{M}_{\varepsilon}\mathbf{N}^{\text{b}}_{\text{rf}}.$$

The number of fake leptons passing the tighter criteria selection, the one of largest interest for the analysis, can be obtained by reverting the matrix and solving for $N^{\text{signal}}_{\text{fake}}$ through

$$N^{\text{signal}}_{\text{fake}} = \frac{\varepsilon_{\text{fake}}}{\varepsilon_{\text{real}} - \varepsilon_{\text{fake}}}\Big[(\varepsilon_{\text{real}} - 1)N^{\text{signal}} + \varepsilon_{\text{real}}N^{\text{loose}}\Big]. \tag{7.25}$$

The values for real and fake lepton efficiencies are usually obtained through dedicated MC samples and eventually corrected for data/MC differences. The presented method can be extended by considering the efficiencies $\varepsilon_{\text{real}}$ and $\varepsilon_{\text{fake}}$ as functions of leptons properties, such as flavour and event kinematics. Fake leptons estimates for final states comprising more than one lepton can be calculates as well, by extending and inverting the presented matrix, which will have dimensions $2^{n_\ell} \times 2^{n_\ell}$. The result is, however, a system of linear equations that can be solved event-by-event, with as coefficient the efficiency functions $\varepsilon_{\text{real}}(|\eta|, p_{\text{T}})$ and $\varepsilon_{\text{fake}}(|\eta|, p_{\text{T}})$.

The additional sample of loosely selected leptons, that was used for the fake/non-prompt estimation as input to the matrix method, comprised baseline leptons satisfying additional demands. For electrons, the photon conversion veto was applied, which required tighter cuts on the impact parameters and on the p_{T} of tracks associated to their origin vertex, and they were also required to pass the ECIDS charge identification tool requirements (discussed in section 7.5) to reduce charge-flip contributions to the fake electron estimate. For muons, an additional requirement on the impact parameter of $|d_0/\sigma(d_0)|$ was posed, being looser than that for signal muons. This additional subset of baseline leptons allowed to obtain an ensemble of objects similar to those that could have wrongly passed the signal leptons criteria, with a large enough statistics.

The real prompt leptons efficiencies $\varepsilon_{\text{real}}(|\eta|, p_{\text{T}})$ were calculated through dedicated $t\bar{t}$ Monte Carlo samples with semileptonic decays, that were later corrected with apposite scale factors to account for known mismodelling. For fake/non-prompt lepton efficiencies, $\varepsilon_{\text{fake}}(|\eta|, p_{\text{T}})$, dedicated control regions enriched in such processes were defined. These regions were designed to contain one or two prompt leptons, plus a fake/non-prompt lepton that would form a SC pair with one of the others. These regions were built requiring $m^{\text{min}}_{\text{DFOC}} > 30\,\text{GeV}$ to minimise eventual signal contaminations, and $8\,\text{GeV} < p_{\text{T}} < 75\,\text{GeV}$ for electrons and $8\,\text{GeV} < p_{\text{T}} < 40\,\text{GeV}$ for muons. The efficiencies estimates were performed separately for events with two SC signal leptons and those with three signal leptons, in order to account for the two kinds of defined signal regions.

Conservative systematic uncertainties were used to account for incorrect modelling of real and fake leptons efficiencies. These may arise from prompt (real) SC leptons in the defined measurement regions, and the extrapolation of these factors to different analyses regions. The results are varying uncertainties depending mostly on leptons p_{T}, ranging from 20% at low values to 50% for high momentum objects, both electrons and muons. The corresponding systematic uncertainties, combined with statistical ones for the fake leptons efficiency measurements, were used as systematic uncertainties on the fake/non-prompt leptons yields in the signal regions, ranging from 28% to 43%.

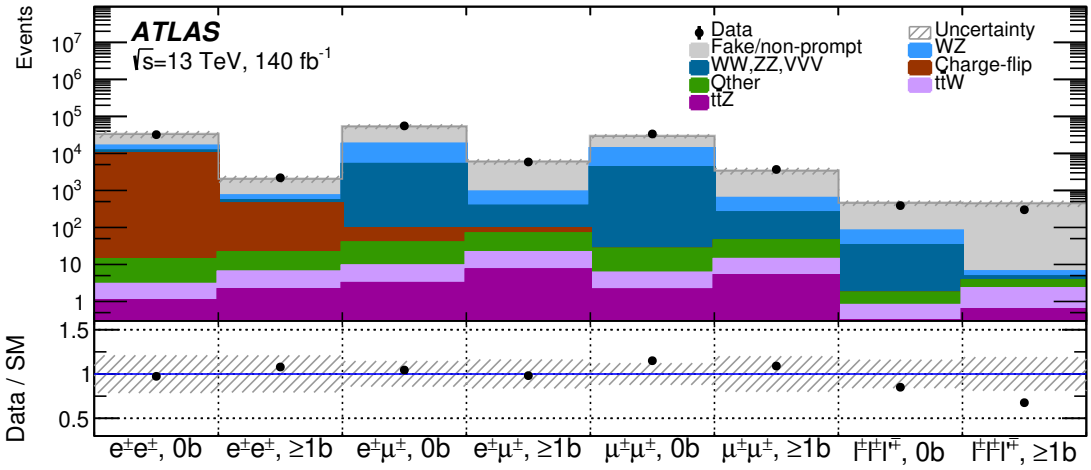


Figure 7.21: Comparison between data and estimated background with both Monte Carlo and data-driven estimates, at pre-selection level. Additional requirements were posed to remove events entering the SRs, and to classify events based on the different final states with two or three signal leptons, and number of b-jets [140].

7.8.4 Background validation

In order to cross-check that the proposed methods for evaluating the different sources of background were working correctly, different selections were applied to compare the observed data yields with the expected total background, in regions increasingly closer to the defined SRs. In all cases, a veto on events entering the SRs was set, by imposing a logical `or` between the different SR requirements. This allowed to drastically reduce possible signal contaminations in regions defined to only evaluate Standard Model processes (or detector-related backgrounds).

Figure 7.21 shows the data/background comparison for all events passing the "pre-selection + SR veto" cuts, classified for different final states including number of b-tagged jets, and number and flavour of signal leptons. A good agreement was found overall in all channels, showing the validity of the charge-flip and fake/non-prompt leptons estimates, that constituted the largest background components. As mentioned in section 7.8.1, Monte Carlo events resulting in fake/non-prompt leptons were removed through generator-level information, to avoid double counting. The signal contamination in each of the selected channels was found to be below 7% in the bin containing events with three signal leptons (two forming a SFSC pair) and zero b-jets, and much lower in all remaining cases. In this plot, only statistical uncertainties were considered for Monte Carlo samples, while the full statistical and systematic uncertainties were applied to data-driven background estimates.

As will be discussed in chapter 8, the fit performed to search for excesses over the expected background did not make use of any Control Region to modify the shapes or normalisation of the backgrounds, differently from several other analyses. Therefore, dedicated regions were used to check the correct background estimates in regions very close to the SRs. Backgrounds from prompt leptons produced in SM processes, for which Monte Carlo samples were used, were evaluated through a dedicated region enriched in WZ and other multiboson events. Besides the already mentioned pre-selection and the veto on SR events, additional cuts were posed, being the request for

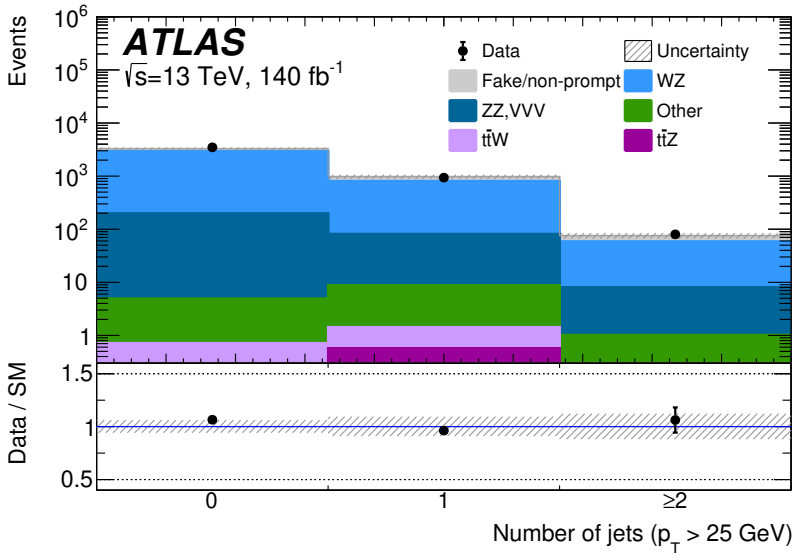


Figure 7.22: Data/background comparison in a region dedicated to evaluate Standard Model processes, mostly di- and tribosons. Pre-selection requirements plus additional cuts for selecting these SM processes were applied. See text for details.

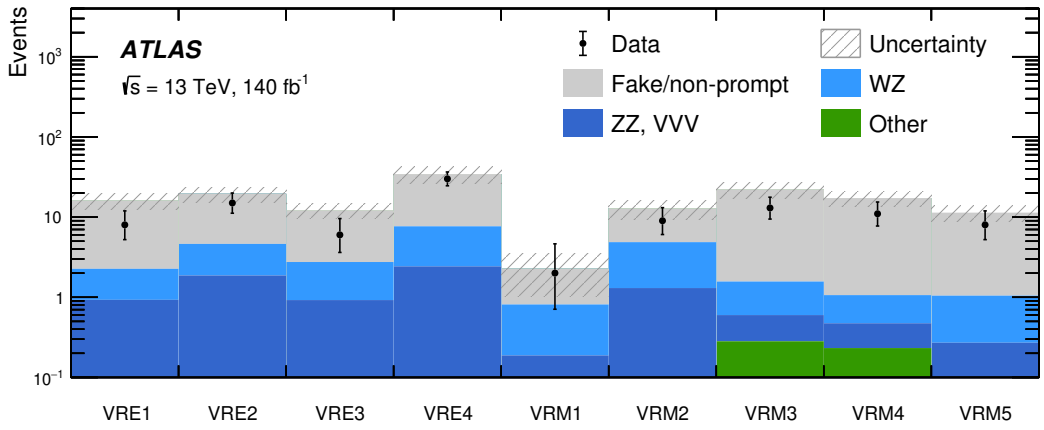


Figure 7.23: Data/background comparison in the defined validation regions [140]. Both Monte Carlo and data-driven estimates were considered for the background yields. All types of uncertainties, statistical and systematics, were applied and are shown as the hatched band.

exactly three signal leptons, $N_{\text{lep}}^{\text{sig}} = 3$, $m_{\text{T}} > 80$ GeV, and the requirement for leptons producing a SC pair to have $p_{\text{T}} > 25$ GeV. The result is shown in fig. 7.22, with the yields being separated for the number of jets in the event. An excellent description of the observed data was found using the simulated samples, with minor contributions from the data-driven estimates. Good results were also obtained by looking at the different variables distributions discussed in section 7.5.1, suggesting reliable predictions for these SM processes.

Finally, an additional set of validation regions (VRs) was defined to check the obtained background estimates in regions very close to the signal ones. The list of ap-

Table 7.8: Definitions of the VRs used to validate the background expectations. Events in the VRs satisfy the preselection requirements, as well as the requirements on $N_{\text{lep}}^{\text{sig}}$, $N_{\text{lep}}^{\text{base}}$, and $N_{\text{b-jets}}$ applied for the corresponding SRs, and differ from the SRs by the requirements shown here.

VRs	m_{T} [GeV]	m_{eff} [GeV]	$\Delta R_{\text{SC}}^{\ell\ell}$	$m_{\text{DFOC}}^{\text{min}}$ [GeV]	$m_{\text{SC}}^{\ell\ell}$ [GeV]	$m_W^{\text{max}} - m_W^{\text{min}}$ [GeV]	Additional requirements
All VRs	Veto events belonging to any SR						
Three-signal-lepton VRs							
VRE1	< 80	< 250	> 2.0	< 50	< 75	< 80	-
VRE2	< 80	< 200	-	< 50	< 75	< 80	-
VRE3	< 80	< 150	> 1.5	< 50	< 75	< 80	-
VRE4	-	< 250	-	-	-	< 70	$p_{\text{T}}^{\ell_1} < 55$ GeV, $m_{\ell\ell\ell}$ cut removed
VRM1	[70, 80]	< 250	> 2.0	< 50	< 75	< 80	-
VRM2	[45, 80]	< 150	-	< 50	< 75	< 80	$\Delta\varphi((p_{\text{T}}^{\ell_1} + p_{\text{T}}^{\ell_2}), \mathbf{p}_{\text{T}}^{\text{miss}}) > 1.0$
Two-signal-lepton VRs							
VRM3	< 70	< 250	> 1.0	-	< 75	-	-
VRM4	< 70	< 250	> 1.0	-	< 70	-	-
VRM5	< 70	< 250	> 1.5	-	< 75	-	-

plied requirements is presented in table 7.8, with each VR defined to evaluate the background close to the relative SR. These cuts were applied once again starting from the pre-selection requirements, and applying slightly more relaxed cuts from their respective signal region. Also in this case, a veto on the SRs events was applied, in order to ensure minimum signal contamination and remove remaining overlaps. The obtained yields in each validation region are shown in fig. 7.23. The combination of Monte Carlo samples for prompt lepton backgrounds and fake/non-prompt ones estimated through the matrix method was used, also considering all sources of uncertainty, statistical and systematic. The resulting data yields are within 2σ from the expected background, considering both statistical+systematic uncertainties and statistical only, confirming an overall good description of the expected backgrounds in regions close to signal ones.

7.9 Systematic uncertainties

Systematic uncertainties were used in the analysis to take into account all remaining sources of errors besides those strictly statistical from the count of events entering a certain region. These sources of uncertainty were classified into different groups depending on their origin, being related to the detector, theoretical, and others. These sources of uncertainties are accounted for by introducing, for each source, $\pm 1\sigma$ variations over the nominal value for both signal and background samples, associating weights that depend on the value of the related uncertainty.

Luminosity: a fully correlated relative uncertainty of 0.83%, as estimated for the combined integrated luminosity of Run 2, was applied on all Monte Carlo samples.

Pile-up: differences between the simulated and real data pile-up distributions were corrected through MC event reweighting. Uncertainties for these factors were obtained by varying the mean of the pile-up distribution by $\pm 4\%$.

Electron-related uncertainties: a series of experimental uncertainties related to electron measurements were considered, from the trigger efficiency to reconstruction, identification and isolation. Electron energy measurements, consisting of energy scale and resolution, were incorporated as well.

Muon-related uncertainties: similarly to electrons, dedicated uncertainties were considered for triggering, reconstruction, identification and isolation. Muon momentum scale and resolution uncertainties are introduced as well, together with uncertainties associated to muon sagitta measurements distortions, small detector mis-alignments and track-to-vertex associations.

Jet energy-related uncertainties: Jet Energy Scale (JES) uncertainties were estimated from dedicated in-situ measurements, test-beam data and MC simulations. Uncertainties related to the Jet Energy Resolution (JER) were obtained from a smearing procedure applied to MC events by matching the one measured in data, as a function of jet transverse momentum and rapidity in dijet events. A large amount of uncertainty sources are used in ATLAS for jets, but were reduced to a much smaller set using reduction schemes by dedicated studies.

Other jet uncertainties: dedicated systematics for the tagging uncertainty of b, c and light jets were considered, as measured through efficiency corrections applied to MC events and parametrised over jet momentum on flavour. Additional uncertainties considered in the analysis were related to the Jet Vertex Tagger tool efficiency, and accounted for MC generator choice and residual pile-up contaminations after their suppression.

Missing transverse momentum: the $E_{\mathrm{T}}^{\mathrm{miss}}$ variable was computed from all reconstructed physics objects, called *hard term*, supplied by additional track-based *soft terms* comprising all remaining unmatched tracks. Therefore, systematic uncertainties were obtained from the propagation of the uncertainties related to each object entering the variable calculation. Additional uncertainties were added, related to the additional soft term and accounting for data/MC differences [219].

HNL signal samples: the largest uncertainty on signal samples normalisation was estimated to be the one on the W boson cross section, taken from previous ATLAS measurements [186]. Model-dependent uncertainties related to the mixing angles and phase-space factors, as described in section 7.2, were found to be negligible and ignored. Uncertainties on acceptance variations due to the renormalisation (μ_S), factorisation (μ_F) and PDF scales choices were evaluated by multiplying the respective values by 0.5/2. Uncertainties related to the parton distribution functions and on the α_S parameter were evaluated following the PDF4LHC prescription [220]. Finally, a conservative 18% uncertainty was applied to low-mass signal points ($m_{\mathrm{HNL}} \leq 15$ GeV). This was set to account for lifetime reweighting techniques that were performed to account for the varying HNL reconstruction efficiencies dependent on τ_{HNL}, and that will be discussed in chapter 8.

Background samples: A 60% overall uncertainty was applied to Monte Carlo samples for prompt-lepton backgrounds, as derived from [221]. Conservative uncertainties of 50% were assigned to $t\bar{t}W$, $t\bar{t}Z$ and $t\bar{t}H$ processes to account for cross-section and modelling uncertainties. The same uncertainty was also applied to

other rare processes including $t\bar{t}HH$, $t\bar{t}VV$, tV, tVV, $3t$ and $4t$. Uncertainties for detector-related backgrounds, charge-flip and fake/non-prompt leptons, were the most relevant in the analysis. They were estimated in a data-driven way and their related uncertainties were detailed in sections 7.8.2 and 7.8.3.

CHAPTER

8

HNL ANALYSIS RESULTS

In this chapter, the results of the analysis presented in chapter 7 are described. The statistical framework and the applied fit strategy are discussed, followed by the observed data yields inside the signal regions. As no significant excess with respect to the expected Standard Model backgrounds was found, exclusion limits were set on the $(m_{\mathrm{HNL}}, |U_\alpha|^2)$ parameters of the model.

8.1 Statistical framework

In order to state the discovery of a new particle, an hypothesis testing procedure has to be performed, where the hypothesis of finding some signal events on top of the expected background, $\mathcal{H}_1$, has to be compared with the background-only (*null*) hypothesis, $\mathcal{H}_0$. In the absence of significant excesses over the background, exclusion limits are set on the signal model parameters. A common statistical framework in particle physics for limit setting, that is briefly summarised in the following, is the CL_S technique [222].

An a priori significance level (α) of the test to be applied to the problem must first be set, representing the probability to reject the null hypothesis $\mathcal{H}_0$ even if it is correct (type-I error). The default value used in high-energy physics to state a discovery is 2.87×10^{-7}, which corresponds to a 5σ deviation of the standard normal distribution. For the alternative model exclusion, a lower significance level $\alpha = 0.05$ (95% Confidence Level, CL) is typically used.

For each hypothesis a likelihood function $\mathcal{L}(n, \vec{\theta}_{\mathcal{H}})$ can be constructed, with n the number of observed events inside each bin of a signal region, that depends on the parameters of the model, $\vec{\theta}_{\mathcal{H}}$. A *signal strength* parameter μ can be defined, such that $\mu = 1$ for the signal hypothesis and $\mu = 0$ for the background-only hypothesis. The number of observed events n can be thought of as being extracted from a Poissonian counting experiment, having underlying distribution $\nu_{(S+B)} = \mu s + b$ for $\mu > 0$ and $\nu_B = b$ for $\mu = 0$.

The TRExFitter [139] software framework, built on top of the HistFactory [223],

RooFit [224] and RooStats [225] packages, was used in the analysis for the construction of the likelihood functions, corresponding to the two hypotheses $\mathcal{H}_0$ and $\mathcal{H}_1$. The likelihood function is calculated as the product of Poissonian distributions for all signal regions bins i, as

$$\mathcal{L}(n|\mu,\vec{\theta}) = \prod_{i\in bins} Pois(n_i|\mu\cdot s_i(\vec{\theta}) + b_i(\vec{\theta}))\cdot \prod_{j\in NP} Gaus(\vec{\theta})\cdot \prod_{i\in bins} Pois(\gamma_i). \tag{8.1}$$

Systematic uncertainties are included in the calculation through dedicated gaussian terms $Gaus(\vec{\theta})$ describing nuisance parameters (NP), while for statistical uncertainties additional factors γ_i are included for each bin i following the Beeston-Barlow "lite" technique [226].

A test-statistic variable q_μ is then introduced for the discrimination between the two alternative models. According to the Neyman-Pearson Lemma, the likelihood ratio is the most powerful discriminator for distinguishing between two hypotheses [227]. The test statistic is then taken as

$$q_\mu = -2\ln\lambda(\mu) = -2\ln\frac{\mathcal{L}(\mu,\hat{\hat{\theta}}_\mu)}{\mathcal{L}(\hat{\mu},\hat{\hat{\theta}}_{\hat{\mu}})}. \tag{8.2}$$

In the function $\lambda(\mu)$, the numerator $\mathcal{L}(\mu,\hat{\hat{\theta}}_\mu)$ is the conditional likelihood, that represents the likelihood function maximised over all nuisance parameters, while keeping the signal strength μ fixed at a given value. At the denominator, the unconditional likelihood $\mathcal{L}(\hat{\mu},\hat{\theta}_{\hat{\mu}})$ is maximised simultaneously with respect to both the signal strength and all NPs. Small values of $\lambda(\mu)$ (or equivalently large values of q_μ) indicate that the assumed signal strength μ is disfavoured by the data compared to the best-fit hypothesis. From varying values associated to the signal strength, asymptotic approximation formulae can be used for the calculation of the CL_{s+b} and CL_b values [216]. With the given inputs in the signal regions, TRExFitter is used to produce test statistic distributions under the two hypotheses with different values of μ, being $f(q|\mu)$ for the signal hypothesis and $f(q|0)$ for the background-only one

$$CL_{s+b} = \int_{q_{obs}}^{+\infty} f(q|\mu)dq \tag{8.3}$$

$$CL_b = \int_{q_{obs}}^{+\infty} f(q|0)dq. \tag{8.4}$$

Toy Monte Carlo can also be used for estimating the distribution of the q_μ test statistic. In the case of the presented analysis, tests with toy Monte Carlo were tried, yielding similar results with respect to the analytical formulae, which were therefore preferred.

From the measured data yields inside the signal regions, the value of q_{obs} is measured and one can therefore calculate CL_{s+b} and CL_b of the alternative hypothesis. The CL_s confidence limit was introduced to account for analysis cases presenting very low yields for both the signal and the background, and prevents excluding signal hypotheses to which the experiment has little sensitivity. It is defined as the ratio between the signal-plus-background and the background-only confidence levels:

$$CL_s = \frac{CL_{s+b}}{CL_b}. \tag{8.5}$$

Limits on the signal strength of the model can therefore be set from the obtained values of CL_s, considering a given desired confidence level of the test to be performed. Using a 95% confidence level, that is the default value for many particle physics analysis, the limit on the signal stregth is found by reverting

$$CL_s(\mu_{limit}) = 0.05. \tag{8.6}$$

8.2 Yields in the signal regions

The observed data yields, obtained after unblinding the signal regions and before applying any fit, are listed in table 8.1. The related plots, grouped for the corresponding final state, are shown in fig. 8.1. All considered sources of systematic uncertainties were applied, together with statistical ones. The largest component on expected background in these search regions were the fake/non-prompt leptons background, with minor contributions from WZ and other multiboson processes. Remaining sources of backgrounds considered in previous studies were found to be negligible. The total background uncertainty shown was computed with TRExFitter by building a HistFactory model through RooStats, propagating all nuisance parameters with their correlations to the total background of each bin. Tables 8.2 to 8.4 show, for each region of the analysis, the obtained significance Z, calculated from eq. (7.22), to have an estimate of the data/background disagreement. The maximum obtained tension, with a value of $Z = 1.7$ standard deviations, was found in SRE3, which was used to look for heavy neutral leptons with a mass $m_{\text{HNL}} = 40$ GeV.

Table 8.1: The observed number of data events and the expected background contributions in the SRs. The uncertainties are both statistical and systematic. The individual uncertainties can be correlated or anticorrelated and therefore do not necessarily add in quadrature to equal the total uncertainty.

	SRE1	SRE2	SRE3	SRE4	SRM1	SRM2	SRM3	SRM4	SRM5
Observed	8	10	15	10	6	9	5	7	10
Total background	4.4 ± 1.5	5.1 ± 1.5	7.9 ± 2.1	6.0 ± 1.7	3.7 ± 1.2	6.2 ± 1.9	5.1 ± 1.6	6.2 ± 1.7	7.3 ± 1.8
WZ	0.20 ± 0.13	0.25 ± 0.18	0.59 ± 0.40	0.60 ± 0.40	0.70 ± 0.43	0.71 ± 0.45	0.28 ± 0.18	0.24 ± 0.16	0.52 ± 0.33
ZZ, VVV	0.39 ± 0.25	0.88 ± 0.59	0.76 ± 0.52	0.37 ± 0.25	0.68 ± 0.42	1.1 ± 0.70	0.16 ± 0.10	0.23 ± 0.15	0.30 ± 0.19
Others	< 0.05	< 0.05	< 0.05	< 0.05	< 0.05	< 0.05	< 0.05	< 0.05	< 0.05
Fake/non-prompt	3.8 ± 1.5	3.9 ± 1.3	6.5 ± 2.0	5.0 ± 1.6	2.3 ± 1.0	4.4 ± 1.6	4.6 ± 1.6	5.7 ± 1.6	6.4 ± 1.8

Table 8.2: Calculated significances obtained in 3L EE signal regions (pre-fit inputs).

EE 3L Final State				
Region	Significance (Z)	Observed events	Exp. Background (b)	Exp. Uncertainy (σ)
SRE1	1.20633	8.0	4.37114	1.52457
SRE2	1.54163	10.0	5.09081	1.48397
SRE3	1.72664	15.0	7.85031	2.11933
SRE4	1.19424	10.0	5.95799	1.71751

As mentioned in section 7.7, the selected signal regions present some overlaps. These regions are mutually exclusive on the target final state, when considering the number of signal leptons and the flavour of the SC lepton pairs. Therefore, the groups

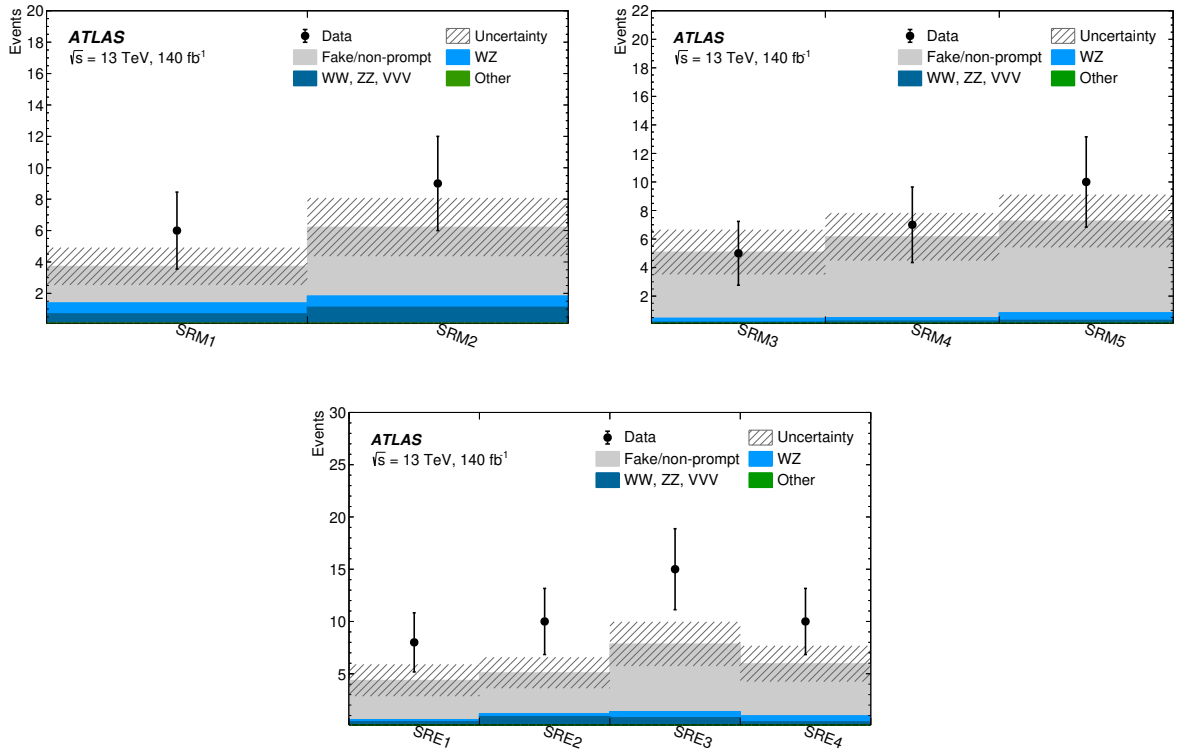


Figure 8.1: Observed data yields in the SRs, compared with the full expected background. The entire set of uncertainties, statistic and systematic, are shown.

Table 8.3: Calculated significances obtained in 3L MM signal regions (pre-fit inputs).

MM 3L Final State				
Region	Significance (Z)	Observed events	Exp. Background (b)	Exp. Uncertainy (σ)
SRM1	0.89796	6.0	3.72657	1.18977
SRM2	0.81802	9.0	6.22073	1.85462

Table 8.4: Calculated significances obtained in 2L MM signal regions (pre-fit inputs).

MM 2L Final State				
Region	Significance (Z)	Observed events	Exp. Background (b)	Exp. Uncertainy (σ)
SRM3	-0.03214	5.0	5.08798	1.56873
SRM4	0.27464	7.0	6.15551	1.66467
SRM5	0.77686	10.0	7.26418	1.84989

SM1-2, SM3-5 and SME1-4 do not overlap with each other. However, some events may enter more than one region inside each group. A count of all number of real data events, excluding double counting, was done by requiring a logical or between the different region selections. Dedicated fake/non-prompt leptons background estimation was run again in these "super-regions" to obtain their yields and related uncertainties. The resulting number of events from this study was a total of 44 data events, with a 30 ± 5 expected background. The obtained total excess was 1.7σ over the predicted background.

The TRExFitter software also allowed to estimate how each systematics uncertainty

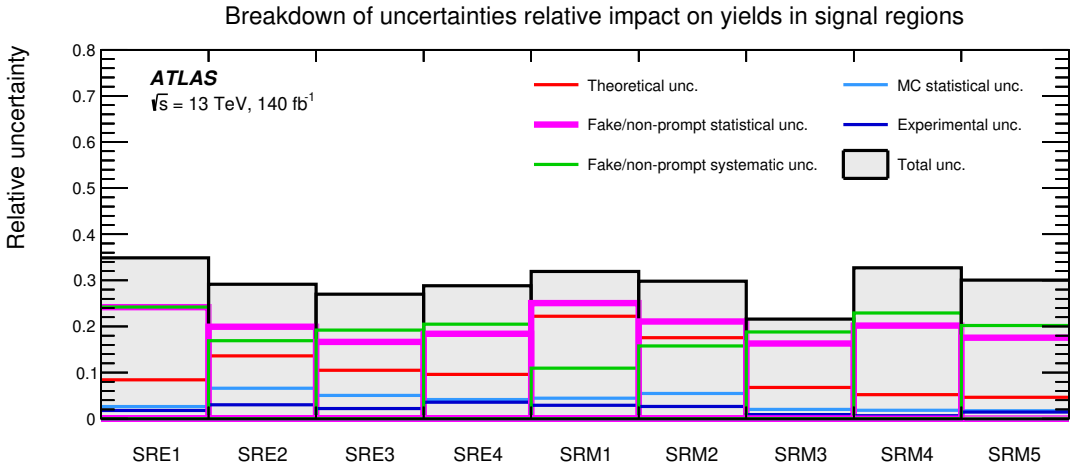


Figure 8.2: Contributions of different uncertainty categories, relative to the expected background yields, inside each SR.

affected the expected background yield in each signal region, by varying one of the dedicated parameters at time. The results are drawn in fig. 8.2, which shows the relative effect of the total expected yield in that region, only considering background samples. The sources of uncertainty were separated depending on their origin and on the type of background they affected. The dominating contribution of fake/non-prompt lepton background over other prompt lepton processes is reflected in the large relative uncertainty of the related systematics, considering both statistical and systematic uncertainties. The statistical uncertainties were originated by the limited number of real data events that were used when applying the matrix method for the data-driven background estimates. Similarly for the Monte Carlo samples these uncertainties were mostly due to the limited number of simulated events in SM samples. The remaining largest uncertainties in the SRs were the ones related to the theory and contributing to background MC samples, with remaining contributions to other experimental uncertainties.

8.3 Fit results and limits

A discovery fit was performed separately inside each SR to evaluate the compatibility of the observed data with the background-only hypothesis. The test statistic q_0^{obs} was computed using the TRExFitter framework, imposing a signal strength $\mu = 0$ for the conditional likelihood, while the best-fit value $\hat{\mu}$ from eq. (8.2) was allowed to vary freely to account for possible signal contributions in data. The expected distribution for q_0 under the background-only hypothesis was obtained using the asymptotic formulae from [216]. The observed value of the test statistic, q_0^{obs} was then used to compute the p-value, by requiring $p = P(q_0 \geq q_0^{obs}|\mu = 0)$ to estimate the data/background compatibility. The obtained p-value for each SR is reported in table 8.5. Smaller p-values were obtained in the SRE1-4 signal regions targeting $e^{\pm}e^{\pm}\mu^{\mp}$ final states, suggesting slight tensions with the expected Standard Model background. Moderate excesses in the SM1-2 regions also lead to smaller p-values, despite not as significant as the electron channel ones. In the SRM3 region, the expected background was very slightly larger than the measured data yield, leading to a measured p-value of 0.5, and the related significance was set to zero.

Table 8.5: The discovery fit results. For SRM3, where the expected background slightly exceeds the observed number of data events (see Table 8.1), the p-value is capped at 0.5, corresponding to a significance of zero.

	SRE1	SRE2	SRE3	SRE4	SRM1	SRM2	SRM3	SRM4	SRM5
p-value	0.11	0.061	0.041	0.12	0.18	0.21	0.5	0.38	0.19
Significance [σ]	1.2	1.5	1.7	1.2	0.90	0.82	0	0.30	0.87

Since no significant excesses over at least 2σ were found, model-dependent exclusion limits were set on the HNL mixing parameters $|U_\alpha|^2, \alpha = e, \mu$ for each tested value of m_{HNL}. The previously defined CL_s method was employed to test values of $|U_\alpha|^2$ resulting in signal strength parameters μ, and determining the largest value of μ such that $CL_s < 0.05$. Also in the case of limits setting, asymptotic approximations were used, with a default 95% CL. The followed procedure consisted in obtaining, for different values of μ, the two confidence levels CL_{s+b} and CL_b by applying eqs. (8.3) and (8.4). For the expected limit, the test statistic q_μ was calculated from an Asimov dataset having nuisance parameters set equal to those obtained through a background-only fit to data, and using TRExFitter to calculate the functions $f(q|\mu)$ and $f(q|\mu = 0)$. For the observed limit, the test statistic q_μ was calculated by using the measured data events. The $\pm 1\sigma$ and $\pm 2\sigma$ expected limit bands were also obtained from the asymptotic distributions of the test statistic under the background-only hypothesis, and correspond to the 68% and 95% confidence intervals of the expected exclusion. These were derived by calculating the related quantiles of the q_μ distributions and represent the variations in the expected limit due to statistical and systematic uncertainties.

Since multiple signal regions could contribute to more than one mass point, for each value of m_{HNL} the SR that was found to yield the lowest expected limit was used to establish both the expected and upper limits on μ. The chosen regions are shown in fig. 8.3, for both $\mu\mu e$ (two and three signal leptons) and $ee\mu$ (only three signal leptons) channels. As the "2LM" and "3LM" regions, featuring exactly two or three signal muons, targeted the same $\mu^\pm\mu^\pm e^\mp$ final state, the two most sensitive signal regions of each type were combined to estimate the final limits on each mass point. In the SRM5 region, that targeted high-mass HNLs with only two signal leptons, the fit did not converge because of very low statistics, and the limit could only be derived up to 50 GeV. When combined with the three signal leptons regions, however, the statistics increased and the fit converged, therefore allowing limits on the signal strength to be extracted as well. For the $e^\pm e^\pm \mu^\mp$ channel, the SRE1 yielded the best expected limit for $m_{\text{HNL}} = 8, 10$ GeV. The SRE2 was used for the points up to $m_{\text{HNL}} = 30$ GeV, the SRE3 was only used at $m_{\text{HNL}} = 40$ GeV, and the SRE5 was used in the remaining points from 50 GeV to 65 GeV. In the muon channel, for any mass point the 3LM regions obtained better limits than the 2LM ones. The SRM1 showed the best sensitivity for masses up to 40 GeV, and the SRM2 was used for the remaining 50-65 GeV points. A slight improvement was obtained through the combination of the 2LM and 3LM regions in the lower m_{HNL} mass points, up tp 12% for $m_{\text{HNL}} = 8$ GeV, about 6-8% at $m_{\text{HNL}} = 10$ GeV (depending on τ_{HNL}) and 4% for $m_{\text{HNL}} = 15, 20$ GeV.

With an increasing HNL lifetime, the decay vertex of the heavy neutral lepton through $N \rightarrow W^*\ell$ becomes more and more displaced, resulting in a loss of the signal efficiency because of the impact-parameter requirement on leptons. This loss in the

lepton reconstruction efficiency at lower masses was taken into account, after having obtained the limit for each mass point, by reweighting the signal mass samples produced with $c\tau_{\mathrm{HNL}} = 0.1$ mm for intermediate lifetime values in the $[0.1, 1]$ mm range, and using the 1 mm sample as a closure test, eventually obtaining the related systematic described in section 7.9. The obtained limits were interpolated using a cubic spline between the different samples, and repeating the procedure for each mass point between $[8 - 15]$ GeV. For masses equal or larger than 20 GeV, the HNLs are observed to decay almost exclusively through a prompt vertex, resulting in a constant efficiency. Table 8.6 shows, for each simulated signal sample with (m_{HNL}, τ_{HNL}) parameters, the product of lepton acceptance from the vertex reconstruction, and the signal region efficiency for that sample.

Table 8.6: Acceptance times efficiency ($A \times \varepsilon$) values for the considered HNL signal mass points, in the defined signal regions.

HNL mass, $c\tau$ [GeV], [mm]	SRE1	SRE2	SRE3	SRE4	SRM1	SRM2	SRM3	SRM4	SRM5
	$A \times \varepsilon$ [%]				$A \times \varepsilon$ [%]		$A \times \varepsilon$ [%]		
8, 0.1	0.34	0.32	0.27	0.06	0.47	0.30	0.23	0.23	0.25
8, 1	0.07	0.07	0.05	0.01	0.10	0.06	0.05	0.05	0.05
10, 0.1	0.59	0.57	0.45	0.10	0.83	0.54	0.25	0.26	0.28
10, 1	0.10	0.10	0.07	0.02	0.14	0.08	0.05	0.06	0.06
15, 0.1	0.84	0.81	0.65	0.17	1.30	0.85	0.27	0.30	0.31
15, 1	0.18	0.17	0.13	0.03	0.25	0.17	0.07	0.07	0.08
20, 0.1	0.97	0.94	0.78	0.22	1.49	1.01	0.31	0.33	0.34
30, 0.1	0.75	1.05	0.96	0.43	1.63	1.25	0.25	0.30	0.31
40, 0.1	0.55	0.83	1.14	0.86	1.34	1.57	0.20	0.26	0.27
50, 0.1	0.33	0.61	0.92	1.14	1.11	1.75	0.12	0.15	0.16
60, 0.1	0.22	0.41	0.66	0.84	0.76	1.33	0.02	0.04	0.05
65, 0.1	0.19	0.35	0.56	0.67	0.57	0.95	0.02	0.03	0.04

The resulting limits, after the combination of the two 2L and 3L regions in the muon channel and the signal reweighting to account for efficiency losses, are shown in fig. 8.4. The analysis was able to exclude mixing angles $|U_e|^2$ with electron neutrinos above 1.1×10^{-5} for heavy neutral leptons with $m_{\mathrm{HNL}} \in [15-30]$ GeV, and around 1.8×10^{-5} for higher masses, up to 50 GeV. For the mixing with muon neutrinos, $|U_\mu|^2$ values of 5×10^{-6} were excluded between 20 GeV and 30 GeV, lowered to $7-10\times10^{-6}$ in the range $m_{\mathrm{HNL}} \in [30 - 50]$ GeV. These results are broadly compatible with the ones obtained by the CMS experiment in a recent analysis [185] across most of the studied mass range. Slightly stronger limits were obtained by CMS in the muon channel for masses $m_{\mathrm{HNL}} > 50$ GeV, where the leptons from the $W^{\pm} \to \ell^{\pm} N$ decay become softer and a better acceptance was obtained by the other experiment. For higher values of m_{HNL}, as it approaches the W boson mass, the expected sensitivity of this analysis decreases. This is derived from a kinematic suppression of the HNL production from W bosons decay as can be observed in eq. (7.18). In the opposite scenario, the sensitivity also decreases for smaller HNL masses. The reason of this behaviour follows from eq. (7.20), with $\tau_{\mathrm{HNL}} \propto m_{\mathrm{HNL}}^{-5} \cdot |U_\alpha|^{-2}$, with an increasing lifetime for smaller values of m_{HNL}.

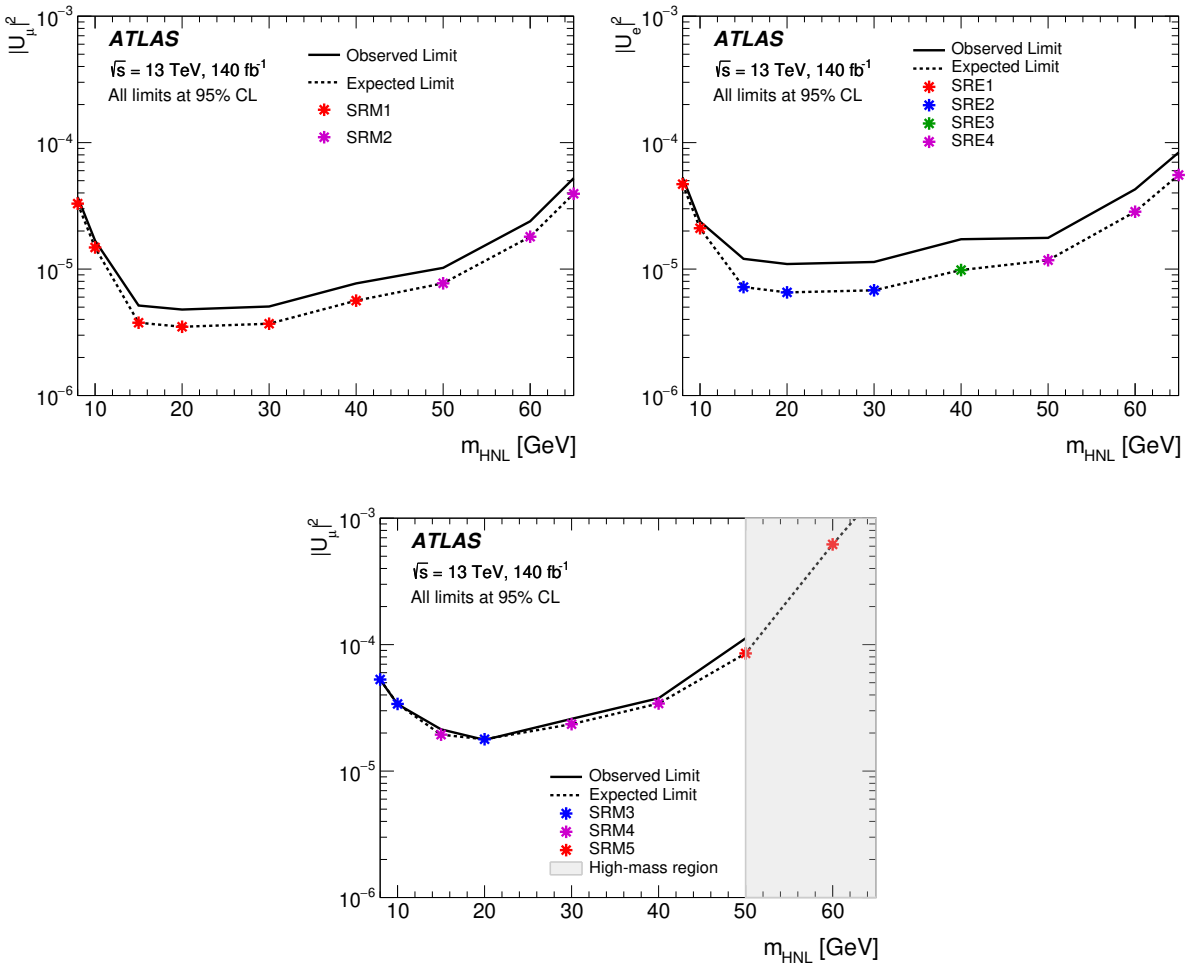


Figure 8.3: Analysis regions used for extracting limits in the $\mu\mu e$ (three or two signal leptons) and $ee\mu$ final states. In all cases, the regions were selected as the ones for which the best expected limit was obtained for the corresponding m_{HNL} value, considering all sources of backgrounds and uncertainties.

The results from this analysis are compared, in figs. 8.5 and 8.6, with other analyses performed by ATLAS targeting different m_{HNL} ranges through other production (and decay) processes. The most notable other results were obtained from searches through displaced vertices [165], and previous searches for leptons plus two or more jets [228]. At higher heavy neutral lepton masses, vector boson fusion processes were used to search for same-sign leptons final states [229][230].

8.4 Conclusions and prospects

A search for heavy neutral leptons, produced in pp collisions at the LHC with centre-of-mass energies of $\sqrt{s} = 13$ TeV and reconstructed with the ATLAS detector, was presented. In the type-I see-saw model, neutrinos acquire masses inversely proportional to those of the HNLs, hence motivating the experimentally observed neutrino masses. By accounting for three families of HNLs, a dark matter candidate and a source of CP violations causing the matter-antimatter asymmetry would be introduced. HNLs are searched through completely leptonic final states, originated by decays of W bosons. Lepton number violating processes, made possible by the potential Majorana nature of

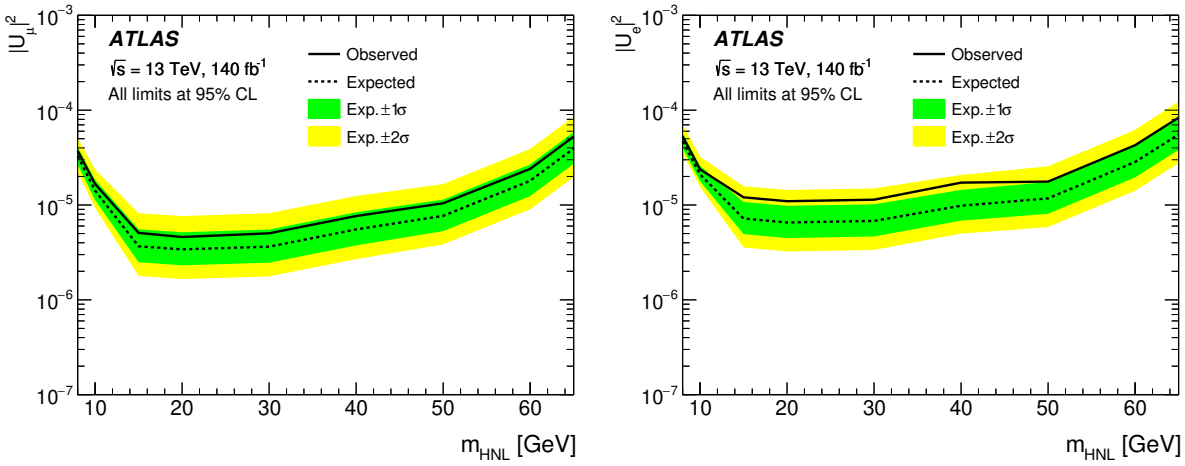


Figure 8.4: Expected and observed limits on the heavy neutral leptons mixing parameters, in the muon (left) and electron (right) channels [140].

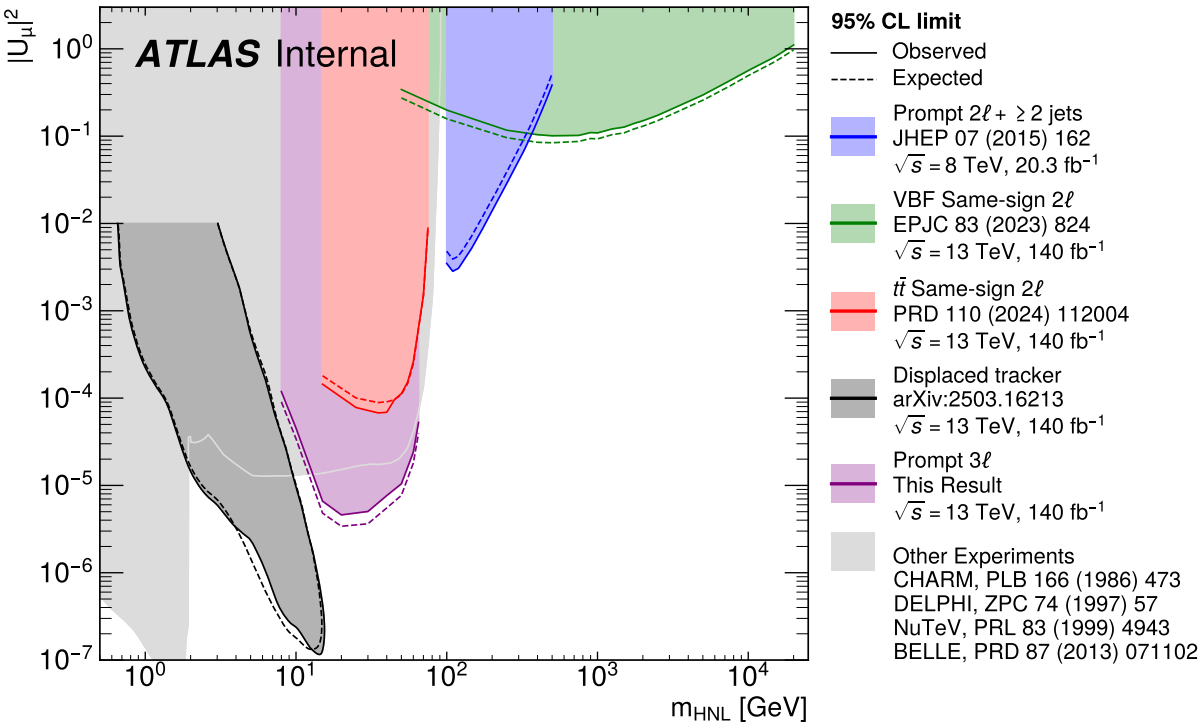


Figure 8.5: Comparison of the results obtained in this analysis with previous ones, on current Heavy Neutral Lepton mixing limits with muon neutrinos.

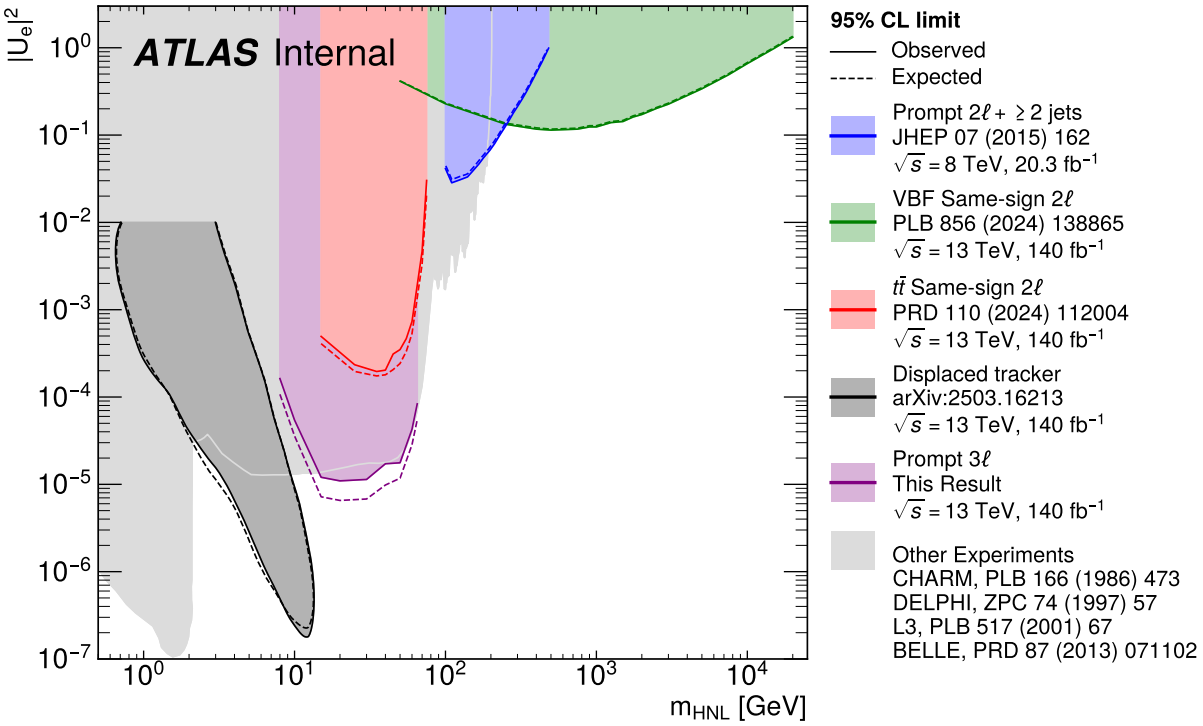


Figure 8.6: Comparison of the results obtained in this analysis with previous ones, on current Heavy Neutral Lepton mixing limits with electron neutrinos.

neutrinos, are exploited in the analysis to drastically reduce the background of Standard Model processes. The final states comprise two leptons with the same flavour and electric charge, plus a third lepton with different flavour and opposite electric charge. Only light leptons are considered, therefore restricting the search to $\mu\mu e$ and $ee\mu$ channels.

Signal regions were defined to look for possible excesses over the background in dedicated regions enriched in HNL Monte Carlo events, and with very low background yields. Because of the specific final state, the largest sources of background were found to be fake/non-prompt leptons, with minimal contribution from Standard Model processes consisting of multiboson events through τ leptons decays. Dedicated methods for estimating and validating these backgrounds in regions close to the ones used for the search were described.

As a result of this search, the observed data yields were found to be compatible with the expected background in the signal regions, with small excesses mostly in the $ee\mu$ channel with $m_{\mathrm{HNL}} = 30, 40$ GeV. We therefore proceeded in setting limits on the HNL mixing parameters as a function of the HNL mass m_{HNL}.

While the obtained result is compatible with the previous ATLAS search for the same final states, considering the improved statistic, and also with the similar CMS search, insightful information were obtained during the analysis workflow. Members of the analysis team, at the time of writing, are starting a new analysis using the Run 3 dataset, eventually combining it with the Run 2 one for increased statistics. It will be interesting to check if the small observed excess in the electron channel will be confirmed or return to be compatible with the background. A first limitation of the presented analysis was the reduced acceptance for displaced vertices due an impact parameter cut in the preliminary steps of the workflow, which led to a decreasing efficiency for

m_{HNL} values in the lower part of the considered range. In this region, a non-negligible amount of signal comprised displaced decay vertices, which were therefore cut out of the signal regions. For the next iteration of the analysis on Run 3 data, dedicated regions to cover the m_{HNL} range in common with the displaced vertex analysis will have to be considered. A different improvement to take care of is the treatment of the high mass region, in which this analysis performs slightly worse than the respective CMS one. In this case, the main problem was found to be the relatively high thresholds for leptons triggers, which led to a reduced efficiency for the event reconstruction.

Other improvements that are being discussed for the next iteration of the analysis is the inclusion of τ leptons in the final state, hence testing the sensitivity to all three HNL flavours, considering Lepton Number Conserving channels, and the exploitation of Machine Learning algorithms. These techniques were previously explored in the master thesis of the candidate [138], employing both Boosted Decision Trees and feed-forward Deep Neural Networks, showing significant improvements over cut-and-count when evaluated with Monte Carlo samples. These techniques were not pursued in the final analysis because of the significant contributions of fake/non-prompt leptons making it difficult to directly apply ML classifiers, and because of limited person-power. These algorithms will nevertheless be tested and applied in the following Run 3 analysis thanks to improved and distributed expertise in the collaboration on the usage of ML techniques.

CHAPTER

9

CONCLUSIONS AND OUTLOOK

In this thesis, I presented my contributions to two projects in experimental particle physics, the development of the HiDRa calorimeter prototype, and a search for heavy neutral leptons with the ATLAS experiment at the LHC.

The first part detailed the design, simulations and early testing of the HiDRa calorimeter, which serves as a demonstrator for the concept of the IDEA experiment at FCC. Geant4-based simulation studies were used to explore the detector response with different materials, geometries and other parameters of the design. Particular attention was posed on extrapolating single-particle performances to a full-scale IDEA design.

Parallel to the construction of the prototype, additional studies on the performances of the detector in terms of spatial resolution for electromagnetic showers were performed by means of the simulation. As an application of the excellent lateral granularity that would be in reach with the final calorimeter geometry, a classification task of simulated π^0/γ originated electromagnetic showers was presented. The distinction of the two classes was performed by means of a boosted decision tree package called XGBoost, showing good separation power.

Finally, my own analysis of the data collected during the 2024 test beam campaign was presented, which only featured about half of the total calorimeter volume, and with PMT readout. While the results from this testing were far from being conclusive, they provided useful insights on the detector operation for following data taking campaigns. The electromagnetic response exhibited a noticeable position-dependent response. After correcting for this effect linearity was restored and the stochastic term of the energy resolution approached the simulation predictions, despite significant constant terms arising from the correction procedure. For hadrons, a worse energy resolution with respect to the one predicted by simulations was obtained. Among the effects to be taken into account are non completely clear light attenuation in optical fibres, the equalisation of all PMTs due to position dependence, and also saturation issues during data taking. These effects will be further investigated through the analysis of data collected during

a second test beam campaign in September 2025, with a nearly completed calorimeter, comprising 8 towers with SiPM readout. The analysis is currently ongoing with a focus on the completed calorimeter performances.

The second main topic of the thesis reported an ATLAS search for heavy neutral leptons, with the dataset collected during the Run 2 of the LHC. The analysis targets final states consisting of three leptons and missing energy from one escaping neutrino, with the requirement of one same-flavour and same-charge lepton pair, and the third lepton having different flavour and opposite electric charge. Cuts on kinematic and custom variables were defined to obtain sets of signal regions enriched in signal events and depleted from background processes. From these selections, only minor contribution due to multiboson events entered the signal regions, as estimated through Monte Carlo samples. The dominant background contributions in the signal regions arose from fake/non-prompt leptons, whose yields in the signal regions were estimated through a dedicated data-driven technique. After unblinding the signal regions, very small excesses with a maximum value of 1.7σ were found in the $ee\mu$ channel, with some overlaps across regions. In the absence of a significant excess over the predicted background, limits were posed on the heavy neutral leptons mixings with active electron and muon neutrinos. The presented analysis allowed to set tighter limits with respect to a previous ATLAS search with a limited Run 2 dataset of 36 fb^{-1}, and broadly comparable to those of a recent search by CMS. Further improvements planned for the search with the extended dataset including Run 3 of the LHC concern the inclusion of τ lepton flavours, lepton-number-conserving topologies, and exploitation of machine learning algorithms to enhance the sensitivity.

A future line of research, whose investigation has started but is currently at very preliminary level, is the comparison of the sensitivity to heavy neutral leptons of the IDEA experiment, estimated through the detector full-simulation, with respect to the one obtained in this thesis with the ATLAS detector. The excellent calorimetric performances expected with IDEA would allow to exploit also final states comprising hadronic decays of the W boson, enhancing the statistics for the search and therefore testing smaller heavy neutral leptons mixings. A similar search was performed in [231] with a fast simulation of IDEA, that features a parametrised response of the calorimeter. Such a study with a full simulation would provide a benchmark search that explores the combined capabilities of a highly granular calorimeter and the dual-readout technique. An interesting approach would be the application of clustering algorithms that exploit single fibre information to further improve the energy resolution to jets, eventually applying modern machine learning methods.

BIBLIOGRAPHY

[1] G. Aad, T. Abajyan, B. Abbott, et al. "Observation of a new particle in the search for the Standard Model Higgs boson with the ATLAS detector at the LHC". In: *Physics Letters B* 716.1 (Sept. 17, 2012), pp. 1–29. ISSN: 0370-2693. DOI: 10.1016/j.physletb.2012.08.020. URL: https://www.sciencedirect.com/science/article/pii/S037026931200857X (visited on 12/28/2024).

[2] S. Chatrchyan, V. Khachatryan, A. M. Sirunyan, et al. "Observation of a new boson at a mass of 125 GeV with the CMS experiment at the LHC". In: *Physics Letters B* 716.1 (Sept. 17, 2012), pp. 30–61. ISSN: 0370-2693. DOI: 10.1016/j.physletb.2012.08.021. URL: https://www.sciencedirect.com/science/article/pii/S0370269312008581 (visited on 12/28/2024).

[3] H. Schopper. "LEP - The Lord of the Collider Rings at CERN 1980-2000: The Making, Operation and Legacy of the World's Largest Scientific Instrument". In: (2009). DOI: 10.1007/978-3-540-89301-1. URL: https://link.springer.com/10.1007/978-3-540-89301-1 (visited on 12/28/2024).

[4] S. Alam, M. Aubert, S. Avila, et al. "Completed SDSS-IV extended Baryon Oscillation Spectroscopic Survey: Cosmological implications from two decades of spectroscopic surveys at the Apache Point Observatory". In: *Physical Review D* 103.8 (Apr. 28, 2021), p. 083533. ISSN: 2470-0010, 2470-0029. DOI: 10.1103/PhysRevD.103.083533. URL: https://link.aps.org/doi/10.1103/PhysRevD.103.083533 (visited on 12/31/2024).

[5] D. DeCamp, B. Deschizeaux, J. .-. Lees, et al. "Determination of the number of light neutrino species". In: *Physics Letters B* 231.4 (Nov. 16, 1989), pp. 519–529. ISSN: 0370-2693. DOI: 10.1016/0370-2693(89)90704-1. URL: https://www.sciencedirect.com/science/article/pii/0370269389907041 (visited on 12/28/2024).

[6] "Hitchhiker's guide to the Standard Model of Particle Physics". Sept. 1, 2022. URL: https://cosmosmagazine.com/science/physics/particle-physics-standard-model/ (visited on 12/28/2024).

[7] P. W. Higgs. "Broken Symmetries and the Masses of Gauge Bosons". In: *Physical Review Letters* 13.16 (Oct. 19, 1964), pp. 508–509. ISSN: 0031-9007. DOI: 10.1103/PhysRevLett.13.508. URL: https://link.aps.org/doi/10.1103/PhysRevLett.13.508 (visited on 12/29/2024).

[8] F. Englert and R. Brout. "Broken Symmetry and the Mass of Gauge Vector Mesons". In: *Physical Review Letters* 13.9 (Aug. 31, 1964), pp. 321–323. ISSN: 0031-9007. DOI: 10.1103/PhysRevLett.13.321. URL: https://link.aps.org/doi/10.1103/PhysRevLett.13.321 (visited on 12/29/2024).

[9] S. Navas, C. Amsler, T. Gutsche, et al. "Review of Particle Physics". In: *Physical Review D* 110.3 (Aug. 1, 2024), p. 030001. ISSN: 2470-0010, 2470-0029. DOI: 10.1103/PhysRevD.110.030001. URL: https://link.aps.org/doi/10.1103/PhysRevD.110.030001 (visited on 01/03/2025).

[10] S. D. Bass, A. De Roeck, and M. Kado. "The Higgs boson implications and prospects for future discoveries". In: *Nature Reviews Physics* 3.9 (Sept. 2021), pp. 608–624. ISSN: 2522-5820. DOI: 10.1038/s42254-021-00341-2. URL: https://www.nature.com/articles/s42254-021-00341-2 (visited on 01/03/2025).

[11] M. Aaboud, G. Aad, B. Abbott, et al. "Observation of H→bb̄ decays and *VH* production with the ATLAS detector". In: *Physics Letters B* 786 (Nov. 10, 2018), pp. 59–86. ISSN: 0370-2693. DOI: 10.1016/j.physletb.2018.09.013. URL: https://www.sciencedirect.com/science/article/pii/S0370269318307056 (visited on 01/03/2025).

[12] A. M. Sirunyan, A. Tumasyan, W. Adam, et al. "Observation of Higgs Boson Decay to Bottom Quarks". In: *Physical Review Letters* 121.12 (Sept. 17, 2018), p. 121801. ISSN: 0031-9007, 1079-7114. DOI: 10.1103/PhysRevLett.121.121801. URL: https://link.aps.org/doi/10.1103/PhysRevLett.121.121801 (visited on 01/14/2026).

[13] S. Chatrchyan, V. Khachatryan, A. Sirunyan, et al. "Evidence for the 125 GeV Higgs boson decaying to a pair of τ leptons". In: *Journal of High Energy Physics* 2014.5 (May 22, 2014), p. 104. ISSN: 1029-8479. DOI: 10.1007/JHEP05(2014)104. URL: https://doi.org/10.1007/JHEP05(2014)104 (visited on 01/03/2025).

[14] G. Aad, B. Abbott, J. Abdallah, et al. "Evidence for the Higgs-boson Yukawa coupling to tau leptons with the ATLAS detector". In: *Journal of High Energy Physics* 2015.4 (Apr. 21, 2015), p. 117. ISSN: 1029-8479. DOI: 10.1007/JHEP04(2015)117. URL: https://doi.org/10.1007/JHEP04(2015)117 (visited on 08/16/2025).

[15] M. Aabboud, G. Aad, B. Abbott, et al. "Observation of Higgs boson production in association with a top quark pair at the LHC with the ATLAS detector". In: *Physics Letters B* 784 (Sept. 10, 2018), pp. 173–191. ISSN: 0370-2693. DOI: 10.1016/j.physletb.2018.07.035. URL: https://www.sciencedirect.com/science/article/pii/S0370269318305732 (visited on 08/16/2025).

[16] A. M. Sirunnyan, A. Tumasyan, W. Adam, et al. "Observation of t̄tH Production". In: *Physical Review Letters* 120.23 (June 4, 2018), p. 231801. ISSN: 0031-9007, 1079-7114. DOI: 10.1103/PhysRevLett.120.231801. URL: https://link.aps.org/doi/10.1103/PhysRevLett.120.231801 (visited on 08/23/2025).

[17] A. M. Sirunyan, A. Tumasyan, W. Adam, et al. "Evidence for Higgs boson decay to a pair of muons". In: *Journal of High Energy Physics* 2021.1 (Jan. 25, 2021), p. 148. ISSN: 1029-8479. DOI: 10.1007/JHEP01(2021)148. URL: https://doi.org/10.1007/JHEP01(2021)148 (visited on 01/03/2025).

[18] G. Aad, E. Aakvaag, B. Abbott, et al. "Evidence for the Dimuon Decay of the Higgs Boson in p p Collisions with the ATLAS Detector". In: *Physical Review Letters* 135.23 (Dec. 3, 2025), p. 231802. ISSN: 0031-9007, 1079-7114. DOI: 10.1103/gzdh-p159. URL: https://link.aps.org/doi/10.1103/gzdh-p159 (visited on 01/06/2026).

[19] A. M. Sirunyan, A. Tumasyan, W. Adam, et al. "A search for the standard model Higgs boson decaying to charm quarks". In: *Journal of High Energy Physics* 2020.3 (Mar. 24, 2020), p. 131. ISSN: 1029-8479. DOI: 10.1007/JHEP03(2020)131. URL: https://doi.org/10.1007/JHEP03(2020)131 (visited on 01/03/2025).

[20] M. Aaboud, G. Aad, B. Abbott, et al. "Search for the Decay of the Higgs Boson to Charm Quarks with the ATLAS Experiment". In: *Physical Review Letters* 120.21 (May 22, 2018), p. 211802. ISSN: 0031-9007, 1079-7114. DOI: 10.1103/PhysRevLett.120.211802. URL: https://link.aps.org/doi/10.1103/PhysRevLett.120.211802 (visited on 01/03/2025).

[21] J. D. Wells. "Higgs naturalness and the scalar boson proliferation instability problem". In: *Synthese* 194.2 (Feb. 1, 2017), pp. 477–490. ISSN: 1573-0964. DOI: 10.1007/s11229-014-0618-8. URL: https://doi.org/10.1007/s11229-014-0618-8 (visited on 01/04/2025).

[22] "2020 Update of the European Strategy for Particle Physics (Brochure) - CERN Document Server". URL: https://cds.cern.ch/record/2721370/files/ (visited on 01/04/2025).

[23] L. Evans and P. Bryant. "LHC Machine". In: *Journal of Instrumentation* 3.8 (Aug. 14, 2008), S08001–S08001. ISSN: 1748-0221. DOI: 10.1088/1748-0221/3/08/S08001. URL: https://iopscience.iop.org/article/10.1088/1748-0221/3/08/S08001 (visited on 12/29/2024).

[24] Atlas Collaboration, G. Aad, E. Abat, et al. "The ATLAS Experiment at the CERN Large Hadron Collider". In: *Journal of Instrumentation* 3.8 (Aug. 14, 2008), S08003–S08003. ISSN: 1748-0221. DOI: 10.1088/1748-0221/3/08/S08003. URL: https://iopscience.iop.org/article/10.1088/1748-0221/3/08/S08003 (visited on 09/07/2025).

[25] The Cms Collaboration, S. Chatrchyan, G. Hmayakyan, et al. "The CMS experiment at the CERN LHC". In: *Journal of Instrumentation* 3.8 (Aug. 14, 2008), S08004–S08004. ISSN: 1748-0221. DOI: 10.1088/1748-0221/3/08/S08004. URL: https://iopscience.iop.org/article/10.1088/1748-0221/3/08/S08004 (visited on 01/14/2026).

[26] The LHCb Collaboration, A. A. Alves, L. M. A. Filho, et al. "The LHCb Detector at the LHC". In: *Journal of Instrumentation* 3.8 (Aug. 14, 2008), S08005–S08005. ISSN: 1748-0221. DOI: 10.1088/1748-0221/3/08/S08005. URL: https://iopscience.iop.org/article/10.1088/1748-0221/3/08/S08005 (visited on 01/07/2026).

[27] The Alice Collaboration, K. Aamodt, A. A. Quintana, et al. "The ALICE experiment at the CERN LHC". In: *Journal of Instrumentation* 3.8 (Aug. 14, 2008), S08002–S08002. ISSN: 1748-0221. DOI: 10.1088/1748-0221/3/08/S08002. URL: https://iopscience.iop.org/article/10.1088/1748-0221/3/08/S08002 (visited on 01/07/2026).

[28] H. Abreu, M. Andreini, C. Antel, et al. "Technical Proposal: FASERnu". 2019. URL: https://cds.cern.ch/record/2702868 (visited on 08/16/2025).

[29] The Totem Collaboration, G. Anelli, G. Antchev, et al. "The TOTEM Experiment at the CERN Large Hadron Collider". In: *Journal of Instrumentation* 3.8 (Aug. 14, 2008), S08007–S08007. ISSN: 1748-0221. DOI: 10.1088/1748-0221/3/08/S08007. URL: https://iopscience.iop.org/article/10.1088/1748-0221/3/08/S08007 (visited on 08/16/2025).

[30] O. Adriani, L. Bonechi, M. Bongi, et al. "LHCf experiment". 2006. URL: https://cds.cern.ch/record/926196 (visited on 08/16/2025).

[31] J. Pinfold, R. Soluk, Y. Yao, et al. "Technical Design Report of the MoEDAL Experiment". 2009. URL: https://cds.cern.ch/record/1181486 (visited on 08/16/2025).

[32] "The CERN accelerator complex, layout in 2022". URL: https://cds.cern.ch/images/CERN-GRAPHICS-2022-001-1 (visited on 01/06/2025).

[33] H. Bartosik and G. Rumolo. "Performance of the LHC injector chain after the upgrade and potential development". Mar. 17, 2022. DOI: 10.48550/arXiv.2203.09202. arXiv: 2203.09202. URL: http://arxiv.org/abs/2203.09202 (visited on 01/06/2025).

[34] L. R. Evans and P. Lebrun. "Progress in construction of the LHC". In: (1998). URL: https://cds.cern.ch/record/367978 (visited on 01/06/2025).

[35] P. Grafström and W. Kozanecki. "Luminosity determination at proton colliders". In: *Progress in Particle and Nuclear Physics* 81 (Mar. 1, 2015), pp. 97–148. ISSN: 0146-6410. DOI: 10.1016/j.ppnp.2014.11.002. URL: https://www.sciencedirect.com/science/article/pii/S0146641014000878 (visited on 01/06/2025).

[36] "Standard Model Summary Plots June 2024". 2024. URL: https://cds.cern.ch/record/2903866.

[37] T. Abe, K. Akai, N. Akasaka, et al. "Achievements of KEKB". In: *Progress of Theoretical and Experimental Physics* 2013.3 (Mar. 26, 2013), 3A001–. ISSN: 2050-3911. DOI: 10.1093/ptep/pts102. URL: https://academic.oup.com/ptep/article-lookup/doi/10.1093/ptep/pts102 (visited on 01/14/2025).

[38] O. Brüning, H. Gray, K. Klein, et al. "The scientific potential and technological challenges of the High-Luminosity Large Hadron Collider program". In: *Reports on Progress in Physics* 85.4 (Apr. 1, 2022), p. 046201. ISSN: 0034-4885, 1361-6633. DOI: 10.1088/1361-6633/ac5106. URL: https://iopscience.iop.org/article/10.1088/1361-6633/ac5106 (visited on 01/15/2025).

[39] G. Apollinari, Béjar Alonso I, Brüning O, et al. "High-Luminosity Large Hadron Collider (HL-LHC) Preliminary Design Report". 2015. DOI: 10.5170/CERN-2015-005. URL: http://cds.cern.ch/record/2116337 (visited on 01/15/2025).

[40] F. L. Manghi. "ATLAS upgrade for the HL-LHC". In: *Nuclear Instruments and Methods in Physics Research Section A: Accelerators, Spectrometers, Detectors and Associated Equipment* 1069 (Dec. 1, 2024), p. 169917. ISSN: 0168-9002. DOI: 10.1016/j.nima.2024.169917. URL: https://www.sciencedirect.com/science/article/pii/S016890022400843X (visited on 01/15/2025).

[41] F. Luongo and CMS Collaboration. "The CMS tracker upgrade for the High Luminosity LHC". In: "Proceedings of The Eleventh Annual Conference on Large Hadron Collider Physics — PoS(LHCP2023)". The Eleventh Annual Conference on Large Hadron Collider Physics. Belgrade, Serbia: Sissa Medialab, Jan. 15, 2024, p. 291. DOI: 10.22323/1.450.0291. URL: https://pos.sissa.it/450/291 (visited on 01/15/2025).

[42] T. E. S. Group. "Deliberation document on the 2020 Update of the European Strategy for Particle Physics". 2020. URL: http://cds.cern.ch/record/2720131 (visited on 01/15/2025).

[43] A. Abada, M. Abbrescia, S. S. AbdusSalam, et al. "FCC Physics Opportunities". In: *The European Physical Journal C* 79.6 (June 5, 2019), p. 474. ISSN: 1434-6052. DOI: 10.1140/epjc/s10052-019-6904-3. URL: https://doi.org/10.1140/epjc/s10052-019-6904-3 (visited on 01/17/2025).

[44] A. Abada, M. Abbrescia, S. S. AbdusSalam, et al. "FCC-ee: The Lepton Collider". In: *The European Physical Journal Special Topics* 228.2 (June 1, 2019), pp. 261–623. ISSN: 1951-6401. DOI: 10.1140/epjst/e2019-900045-4. URL: https://doi.org/10.1140/epjst/e2019-900045-4 (visited on 01/17/2025).

[45] A. Abada, M. Abbrescia, S. S. AbdusSalam, et al. "FCC-hh: The Hadron Collider". In: *The European Physical Journal Special Topics* 228.4 (July 1, 2019), pp. 755–1107. ISSN: 1951-6401. DOI: 10.1140/epjst/e2019-900087-0. URL: https://doi.org/10.1140/epjst/e2019-900087-0 (visited on 01/17/2025).

[46] M. Benedikt, W. Bartmann, J.-P. Burnet, et al. "Future Circular Collider Feasibility Study Report Volume 2: Accelerators, technical infrastructure and safety". In: (2025). DOI: 10.17181/CERN.EBAY.7W4X. URL: http://cds.cern.ch/record/2928793 (visited on 05/03/2025).

[47] W. Bartmann, J.-P. Burnet, C. Carli, et al. "Future Circular Collider Feasibility Study Report Volume 1: Physics and Experiments". In: (2025). DOI: 10.17181/CERN.9DKX.TDH9. URL: http://cds.cern.ch/record/2928193 (visited on 05/02/2025).

[48] N. Bacchetta, J. .-. Blaising, E. Brondolin, et al. "CLD – A Detector Concept for the FCC-ee". In: (2019). DOI: 10.48550/ARXIV.1911.12230. URL: https://arxiv.org/abs/1911.12230 (visited on 01/18/2025).

[49] T. I. S. Group. "The IDEA detector concept for FCC-ee". Feb. 28, 2025. DOI: 10.48550/arXiv.2502.21223. arXiv: 2502.21223. URL: http://arxiv.org/abs/2502.21223 (visited on 03/03/2025).

[50] J. Pekkanen. "ALLEGRO FCC-ee detector concept & Noble liquid calorimetry". In: *Nuclear Instruments and Methods in Physics Research Section A: Accelerators, Spectrometers, Detectors and Associated Equipment* 1069 (Dec. 1, 2024), p. 169921. ISSN: 0168-9002. DOI: 10.1016/j.nima.2024.169921. URL: https://www.sciencedirect.com/science/article/pii/S0168900224008477 (visited on 01/18/2025).

[51] V. Maura, B. A. Stefanek, and T. You. "The Higgs Self-Coupling at FCC-ee". 2025. DOI: 10.48550/ARXIV.2503.13719. URL: https://arxiv.org/abs/2503.13719 (visited on 05/02/2025).

[52] A. Tumasyan, W. Adam, J. W. Andrejkovic, et al. "A search for decays of the Higgs boson to invisible particles in events with a top-antitop quark pair or a vector boson in proton-proton collisions at {$\sqrt{s} = 13$ TeV}". In: *The European Physical Journal C* 83.10 (Oct. 16, 2023), p. 933. ISSN: 1434-6052. DOI: 10.1140/epjc/s10052-023-11952-7. URL: https://doi.org/10.1140/epjc/s10052-023-11952-7 (visited on 05/29/2025).

[53] A. Blondel. "The number of neutrinos and the Z line shape". In: *Comptes Rendus. Physique* 3.9 (Aug. 25, 2002), pp. 1155–1164. ISSN: 1878-1535. DOI: 10.1016/S1631-0705(02)01393-2. URL: https://comptes-rendus.academie-sciences.fr/physique/articles/10.1016/S1631-0705(02)01393-2/ (visited on 05/03/2025).

[54] A. Blondel and E. Gianfelice. "The challenges of beam polarization and keV-scale centre-of-mass energy calibration at the FCC-ee". In: *The European Physical Journal Plus* 136.11 (Nov. 2021), p. 1103. ISSN: 2190-5444. DOI: 10.1140/epjp/s13360-021-02038-y. URL: https://link.springer.com/10.1140/epjp/s13360-021-02038-y (visited on 05/03/2025).

[55] R. Tenchini. "Asymmetries at the Z pole: The Quark and Lepton Quantum Numbers". In: L. Maiani and L. Rolandi. "Advanced Series on Directions in High Energy Physics". Vol. 26. WORLD SCIENTIFIC, Oct. 2016, pp. 161–184. DOI: 10.1142/9789814733519_0009. URL: http://www.worldscientific.com/doi/abs/10.1142/9789814733519_0009 (visited on 05/03/2025).

[56] S. Monteil and G. Wilkinson. "Heavy-quark opportunities and challenges at FCC-ee". In: *The European Physical Journal Plus* 136.8 (Aug. 13, 2021), p. 837. ISSN: 2190-5444. DOI: 10.1140/epjp/s13360-021-01814-0. URL: https://doi.org/10.1140/epjp/s13360-021-01814-0 (visited on 05/04/2025).

[57] J. Alimena, P. Azzi, M. Bauer, et al. "Searches for Long-Lived Particles at the Future FCC-ee". Sept. 28, 2022. DOI: 10.48550/arXiv.2203.05502. arXiv: 2203.05502. URL: http://arxiv.org/abs/2203.05502 (visited on 05/03/2025).

[58] G. Polesello. "Sensitivity of the FCC-ee to decay of an axion-like particle into two photons". 2025. DOI: 10.48550/ARXIV.2502.08411. URL: https://arxiv.org/abs/2502.08411 (visited on 05/03/2025).

[59] J. Gao. "CEPC Technical Design Report: Accelerator". In: *Radiation Detection Technology and Methods* 8.1 (Mar. 1, 2024), pp. 1–1105. ISSN: 2509-9949. DOI: 10.1007/s41605-024-00463-y. URL: https://doi.org/10.1007/s41605-024-00463-y (visited on 01/07/2026).

[60] "Input to the European Strategy for Particle Physics - 2026 update". Indico. URL: https://indico.cern.ch/event/1439855/contributions/6542430/ (visited on 05/29/2025).

[61] T. Behnke, J. E. Brau, B. Foster, et al. "The International Linear Collider Technical Design Report". Geneva, 2013. URL: https://cds.cern.ch/record/1601966 (visited on 01/19/2025).

[62] P. Bambade, T. Barklow, T. Behnke, et al. "The International Linear Collider: A Global Project". 2019. DOI: 10.48550/ARXIV.1903.01629. URL: https://arxiv.org/abs/1903.01629 (visited on 01/20/2025).

[63] A. Robson, P. N. Burrows, N. C. Lasheras, et al. "The Compact Linear e e Collider (CLIC): Accelerator and Detector". 2018. DOI: 10.48550/ARXIV.1812.07987. URL: https://arxiv.org/abs/1812.07987 (visited on 01/20/2025).

[64] M. Aicheler, P. Burrows, M. Draper, et al. "A Multi-TeV Linear Collider Based on CLIC Technology: CLIC Conceptual Design Report". Geneva: CERN, 2012. URL: https://cds.cern.ch/record/1500095 (visited on 01/20/2025).

[65] P. Roloff, R. Franceschini, U. Schnoor, et al. "The Compact Linear e e Collider (CLIC): Physics Potential". 2018. URL: https://cds.cern.ch/record/2652257 (visited on 01/20/2025).

[66] IMCC Collaboration. "Vol. 2 (2024): Interim report for the International Muon Collider Collaboration | CERN Yellow Reports: Monographs". In: (). URL: https://e-publishing.cern.ch/index.php/CYRM/issue/view/171 (visited on 01/22/2025).

[67] C. Accettura, D. Adams, R. Agarwal, et al. "Towards a muon collider". In: *The European Physical Journal C* 83.9 (Sept. 26, 2023), p. 864. ISSN: 1434-6052. DOI: 10.1140/epjc/s10052-023-11889-x. URL: https://link.springer.com/10.1140/epjc/s10052-023-11889-x (visited on 08/17/2025).

[68] R. Wigmans. "Calorimetry: Energy Measurement in Particle Physics". 2nd ed. Oxford University PressOxford, Sept. 14, 2017. DOI: 10.1093/oso/9780198786351.001.0001. URL: https://academic.oup.com/book/26593 (visited on 04/18/2025).

[69] M. Livan and R. Wigmans. "Calorimetry for Collider Physics, an Introduction". UNITEXT for Physics. Cham: Springer International Publishing, 2019. DOI: 10.1007/978-3-030-23653-3. URL: http://link.springer.com/10.1007/978-3-030-23653-3 (visited on 04/18/2025).

[70] C. W. Fabjan and F. Gianotti. "Calorimetry for particle physics". In: *Reviews of Modern Physics* 75.4 (Oct. 15, 2003), pp. 1243–1286. ISSN: 0034-6861, 1539-0756. DOI: 10.1103/RevModPhys.75.1243. URL: https://link.aps.org/doi/10.1103/RevModPhys.75.1243 (visited on 04/18/2025).

[71] "Particle Data Group". Particle Data Group. URL: https://pdg.lbl.gov/2024/html/authors_2024.html (visited on 03/15/2025).

[72] H. Wilkens and T. A. L. Collaboration. "The ATLAS Liquid Argon calorimeter: An overview". In: *Journal of Physics: Conference Series* 160 (Apr. 1, 2009), p. 012043. ISSN: 1742-6596. DOI: 10.1088/1742-6596/160/1/012043. URL: https://iopscience.iop.org/article/10.1088/1742-6596/160/1/012043 (visited on 04/25/2025).

[73] W. Lustermann and T. C. E. Group. "The electromagnetic calorimeter of cms, summary and status". In: *Journal of Physics: Conference Series* 160 (Apr. 1, 2009), p. 012044. ISSN: 1742-6596. DOI: 10.1088/1742-6596/160/1/012044. URL: https://iopscience.iop.org/article/10.1088/1742-6596/160/1/012044 (visited on 04/25/2025).

[74] Y. Zolnierowski. "The ATLAS liquid-argon electromagnetic calorimeter". In: *Nuclear Instruments and Methods in Physics Research Section A: Accelerators, Spectrometers, Detectors and Associated Equipment* 384.1 (Dec. 1996), pp. 230–236. ISSN: 01689002. DOI: 10.1016/S0168-9002(96)00949-7. URL: https://linkinghub.elsevier.com/retrieve/pii/S0168900296009497 (visited on 05/08/2025).

[75] A. Andresen, A. Bamberger, A. Bargende, et al. "Construction and beam test of the ZEUS forward and rear calorimeter". In: *Nuclear Instruments and Methods in Physics Research Section A: Accelerators, Spectrometers, Detectors and Associated Equipment* 309.1 (Nov. 1991), pp. 101–142. ISSN: 01689002. DOI: 10.1016/0168-9002(91)90095-8. URL: https://linkinghub.elsevier.com/retrieve/pii/0168900291900958 (visited on 05/11/2025).

[76] S. Lee, M. Livan, and R. Wigmans. "On the limits of the hadronic energy resolution of calorimeters". In: *Nuclear Instruments and Methods in Physics Research Section A: Accelerators, Spectrometers, Detectors and Associated Equipment* 882 (Feb. 21, 2018), pp. 148–157. ISSN: 0168-9002. DOI: 10.1016/j.nima.2017.10.087. URL: https://www.sciencedirect.com/science/article/pii/S0168900217311762 (visited on 06/08/2025).

[77] C. W. Fabjan, W. Struczinski, W. J. Willis, et al. "Iron liquid-argon and uranium liquid-argon calorimeters for hadron energy measurement". In: *Nuclear Instruments and Methods* 141.1 (Feb. 15, 1977), pp. 61–80. ISSN: 0029-554X. DOI: 10.1016/0029-554X(77)90747-9. URL: https://www.sciencedirect.com/science/article/pii/0029554X77907479 (visited on 06/06/2025).

[78] T. Åkesson, A. L. S. Angelis, F. Corriveau, et al. "Performance of the uranium/plastic scintillator calorimeter for the HELIOS experiment at CERN". In: *Nuclear Instruments and Methods in Physics Research Section A: Accelerators, Spectrometers, Detectors and Associated Equipment* 262.2 (Dec. 15, 1987), pp. 243–263. ISSN: 0168-9002. DOI: 10.1016/0168-9002(87)90862-X. URL: https://www.sciencedirect.com/science/article/pii/016890028790862X (visited on 06/06/2025).

[79] T. Davidek. "ATLAS Tile Calorimeter performance for single particles in beam tests". In: *Journal of Physics: Conference Series* 160 (Apr. 1, 2009), p. 012057. ISSN: 1742-6596. DOI: 10.1088/1742-6596/160/1/012057. URL: https://iopscience.iop.org/article/10.1088/1742-6596/160/1/012057 (visited on 06/07/2025).

[80] A. Bodek. "Performance of a prototype CMS hadron barrel calorimeter in a test beam". In: *IEEE Transactions on Nuclear Science* 46.3 (June 1999), pp. 407–409. ISSN: 0018-9499, 1558-1578. DOI: 10.1109/23.775552. URL: https://ieeexplore.ieee.org/document/775552/ (visited on 06/07/2025).

[81] S. Lee, M. Livan, and R. Wigmans. "Dual-readout calorimetry". In: *Reviews of Modern Physics* 90.2 (Apr. 26, 2018), p. 025002. ISSN: 0034-6861, 1539-0756. DOI: 10.1103/RevModPhys.90.025002. URL: https://link.aps.org/doi/10.1103/RevModPhys.90.025002 (visited on 06/07/2025).

[82] R. Wigmans. "The DREAM project—Towards the ultimate in calorimetry". In: *Nuclear Instruments and Methods in Physics Research Section A: Accelerators, Spectrometers, Detectors and Associated Equipment*. 11th Pisa Meeting on Advanced Detectors 617.1 (May 11, 2010), pp. 129–133. ISSN: 0168-9002. DOI: 10.1016/j.nima.2009.09.118. URL: https://www.sciencedirect.com/science/article/pii/S0168900209019007 (visited on 06/07/2025).

[83] R. Wigmans. "The new RD52 (DREAM) fiber calorimeter". In: *Journal of Physics: Conference Series* 404 (Dec. 21, 2012), p. 012068. ISSN: 1742-6588, 1742-6596. DOI: 10.1088/1742-6596/404/1/012068. URL: https://iopscience.iop.org/article/10.1088/1742-6596/404/1/012068 (visited on 06/09/2025).

[84] A. Pareti and IDEA Dual Readout Group. "Dual-readout calorimeter development for future High-Energy Physics Experiments". In: "Proceedings of Corfu Summer Institute 2023 "School and Workshops on Elementary Particle Physics and Gravity" — PoS(CORFU2023)". Corfu Summer Institute 2023 "School and Workshops on Elementary Particle Physics and Gravity". Corfu, Greece: Sissa Medialab, July 31, 2024, p. 019. DOI: 10.22323/1.463.0019. URL: https://pos.sissa.it/463/019 (visited on 11/03/2025).

[85] N. Akchurin, K. Carrell, J. Hauptman, et al. "Hadron and jet detection with a dual-readout calorimeter". In: *Nuclear Instruments and Methods in Physics Research Section A: Accelerators, Spectrometers, Detectors and Associated Equipment* 537.3 (Feb. 1, 2005), pp. 537–561. ISSN: 0168-9002. DOI: 10.1016/j.nima.2004.07.285. URL: https://www.sciencedirect.com/science/article/pii/S0168900204018091 (visited on 06/09/2025).

[86] S. Lee, A. Cardini, M. Cascella, et al. "Hadron detection with a dual-readout fiber calorimeter". In: *Nuclear Instruments and Methods in Physics Research Section A: Accelerators, Spectrometers, Detectors and Associated Equipment* 866 (Sept. 11, 2017), pp. 76–90. ISSN: 0168-9002. DOI: 10.1016/j.nima.2017.05.025. URL: https://www.sciencedirect.com/science/article/pii/S0168900217305703 (visited on 06/09/2025).

[87] N. Akchurin, F. Bedeschi, A. Cardini, et al. "Dual-readout calorimetry with a full-size BGO electromagnetic section". In: *Nuclear Instruments and Methods in Physics Research Section A: Accelerators, Spectrometers, Detectors and Associated Equipment* 610.2 (Nov. 2009), pp. 488–501. ISSN: 01689002. DOI: 10.1016/j.nima.2009.08.074. URL: https://linkinghub.elsevier.com/retrieve/pii/S0168900209016039 (visited on 06/08/2025).

[88] M. Lucchini, W. Chung, S. Eno, et al. "New perspectives on segmented crystal calorimeters for future colliders". In: *Journal of Instrumentation* 15.11 (Nov. 2, 2020), P11005–P11005. ISSN: 1748-0221. DOI: 10.1088/1748-0221/15/11/P11005. URL: https://iopscience.iop.org/article/10.1088/1748-0221/15/11/P11005 (visited on 07/05/2025).

[89] C. Gatto, V. Di Benedetto, and A. Mazzacane. "A Review of the Multiple-Readout Concept and Its Application in an Integrally Active Calorimeter". In: *Instruments* 8.4 (Nov. 14, 2024), p. 49. ISSN: 2410-390X. DOI: 10.3390/instruments8040049. URL: https://www.mdpi.com/2410-390X/8/4/49 (visited on 06/09/2025).

[90] M. A. Thomson. "Particle flow calorimetry and the PandoraPFA algorithm". In: *Nuclear Instruments and Methods in Physics Research Section A: Accelerators, Spectrometers, Detectors and Associated Equipment* 611.1 (Nov. 21, 2009), pp. 25–40. ISSN: 0168-9002. DOI: 10.1016/j.nima.2009.09.009. URL: https://www.sciencedirect.com/science/article/pii/S0168900209017264 (visited on 06/09/2025).

[91] F. Sefkow, A. White, K. Kawagoe, et al. "Experimental tests of particle flow calorimetry". In: *Reviews of Modern Physics* 88.1 (Feb. 8, 2016), p. 015003. ISSN: 0034-6861, 1539-0756. DOI: 10.1103/RevModPhys.88.015003. URL: https://link.aps.org/doi/10.1103/RevModPhys.88.015003 (visited on 06/09/2025).

[92] D. Buskulic, D. Casper, I. De Bonis, et al. "Performance of the ALEPH detector at LEP". In: *Nuclear Instruments and Methods in Physics Research Section A: Accelerators, Spectrometers, Detectors and Associated Equipment* 360.3 (June 1995), pp. 481–506. ISSN: 01689002. DOI: 10.1016/0168-9002(95)00138-7. URL: https://linkinghub.elsevier.com/retrieve/pii/0168900295001387 (visited on 06/09/2025).

[93] ATLAS Collaboration. "R=0.4 jets input comparison and Monte Carlo calibration with the ATLAS Detector". Geneva: CERN, 2022. URL: https://cds.cern.ch/record/2824558.

[94] M. Aaboud, G. Aad, B. Abbott, et al. "Jet reconstruction and performance using particle flow with the ATLAS Detector". In: *The European Physical Journal C* 77.7 (July 13, 2017), p. 466. ISSN: 1434-6052. DOI: 10.1140/epjc/s10052-017-5031-2. URL: https://doi.org/10.1140/epjc/s10052-017-5031-2 (visited on 09/12/2025).

[95] A. Sirunyan, A. Tumasyan, W. Adam, et al. "Particle-flow reconstruction and global event description with the CMS detector". In: *Journal of Instrumentation* 12.10 (Oct. 6, 2017), P10003–P10003. ISSN: 1748-0221. DOI: 10.1088/1748-0221/12/10/P10003. URL: https://iopscience.iop.org/article/10.1088/1748-0221/12/10/P10003 (visited on 06/09/2025).

[96] CMS Collaboration. "The Phase-2 Upgrade of the CMS Endcap Calorimeter". 2017. DOI: 10.17181/CERN.IV8M.1JY2. URL: http://cds.cern.ch/record/2293646 (visited on 06/09/2025).

[97] A. White, J. Yu, G. Eigen, et al. "Design, construction and commissioning of a technological prototype of a highly granular SiPM-on-tile scintillator-steel hadronic calorimeter". In: *Journal of Instrumentation* 18.11 (Nov. 1, 2023), P11018. ISSN: 1748-0221. DOI: 10.1088/1748-0221/18/11/P11018. URL: https://iopscience.iop.org/article/10.1088/1748-0221/18/11/P11018 (visited on 06/10/2025).

[98] The ILD Collaboration and c. T. Behnke. "The ILD detector at the ILC". arXiv.org. Dec. 10, 2019. URL: https://arxiv.org/abs/1912.04601v1 (visited on 06/10/2025).

[99] N. A. Graf. "The Silicon Detector Concept". In: *Physics Procedia*. Proceedings of the 2nd International Conference on Technology and Instrumentation in Particle Physics (TIPP 2011) 37 (Jan. 1, 2012), pp. 143–150. ISSN: 1875-3892. DOI: 10.1016/j.phpro.2012.02.365. URL: https://www.sciencedirect.com/science/article/pii/S187538921201677X (visited on 06/10/2025).

[100] F. Pitters. "The CLIC Detector Concept". arXiv.org. Feb. 16, 2018. DOI: 10.23727/CERN-Proceedings-2017-001. URL: https://arxiv.org/abs/1802.06008v1 (visited on 06/10/2025).

[101] L. Pezzotti. "Particle Detectors R&D: Dual-Readout Calorimetry for Future Colliders and MicroMegas Chambers for the ATLAS New Small Wheel Upgrade". PhD thesis. Apr. 8, 2021. URL: https://iris.unipv.it/handle/11571/1429275# (visited on 07/05/2025).

[102] P. Azzi and E. Perez. "Exploring requirements and detector solutions for FCC-ee". In: *The European Physical Journal Plus* 136.11 (Nov. 30, 2021), p. 1195. ISSN: 2190-5444. DOI: 10.1140/epjp/s13360-021-02141-0. URL: https://doi.org/10.1140/epjp/s13360-021-02141-0 (visited on 07/05/2025).

[103] R. Aleksan and S. Jadach. "Precision measurement of the Z boson to electron neutrino coupling at the future circular colliders". In: *Physics Letters B* 799 (Dec. 10, 2019), p. 135034. ISSN: 0370-2693. DOI: 10.1016/j.physletb.2019.135034. URL: https://www.sciencedirect.com/science/article/pii/S0370269319307567 (visited on 07/05/2025).

[104] ALICE collaboration. "Technical Design report for the ALICE Inner Tracking System 3 - ITS3 ; A bent wafer-scale monolithic pixel detector". Geneva: CERN, 2024. URL: https://cds.cern.ch/record/2890181.

[105] M. Frank, F. Gaede, M. Petric, et al. "AIDASoft/DD4hep: v01-25-01". In collab. with C. Grefe, P. Mato, A. Munnich, et al. Feb. 24, 2023. DOI: 10.5281/ZENODO.592244. URL: https://zenodo.org/record/592244 (visited on 12/02/2025).

[106] G. Cataldi, F. Grancagnolo, and S. Spagnolo. "Cluster counting in helium based gas mixtures". In: *Nuclear Instruments and Methods in Physics Research Section A: Accelerators, Spectrometers, Detectors and Associated Equipment* 386.2 (Feb. 21, 1997), pp. 458–469. ISSN: 0168-9002. DOI: 10.1016/S0168-9002(96)01164-3. URL: https://www.sciencedirect.com/science/article/pii/S0168900296011643 (visited on 11/01/2025).

[107] W. Elmetenawee, G. Chiarello, A. Corvaglia, et al. "The Tracking performance for the IDEA drift chamber". In: "Proceedings of 41st International Conference on High Energy physics — PoS(ICHEP2022)". Vol. 414. SISSA Medialab, June 15, 2023, p. 362. DOI: 10.22323/1.414.0362. URL: https://pos.sissa.it/414/362/ (visited on 12/01/2025).

[108] G. Bencivenni, L. Benussi, L. Borgonovi, et al. "The μ-RWELL detector". In: *Journal of Instrumentation* 12.6 (June 23, 2017), pp. C06027–C06027. ISSN: 1748-0221. DOI: 10.1088/1748-0221/12/06/C06027. URL: https://iopscience.iop.org/article/10.1088/1748-0221/12/06/C06027 (visited on 11/03/2025).

[109] F. Sauli. "The gas electron multiplier (GEM): Operating principles and applications". In: *Nuclear Instruments and Methods in Physics Research Section A: Accelerators, Spectrometers, Detectors and Associated Equipment*. Special Issue in memory of Glenn F. Knoll 805 (Jan. 1, 2016), pp. 2–24. ISSN: 0168-9002. DOI: 10.1016/j.nima.2015.07.060. URL: https://www.sciencedirect.com/science/article/pii/S0168900215008980 (visited on 11/03/2025).

[110] "MPPC (SiPMs) / MPPC arrays | Hamamatsu Photonics". URL: https://www.hamamatsu.com/eu/en/product/optical-sensors/mppc/mppc_mppc-array.html (visited on 07/08/2025).

[111] F. Simon. "Silicon photomultipliers in particle and nuclear physics". In: *Nuclear Instruments and Methods in Physics Research Section A: Accelerators, Spectrometers, Detectors and Associated Equipment*. Silicon Photomultipliers: Technology, Characterisation and Applications 926 (May 11, 2019), pp. 85–100. ISSN: 0168-9002. DOI: 10.1016/j.nima.2018.11.042. URL: https://www.sciencedirect.com/science/article/pii/S0168900218316176 (visited on 07/07/2025).

[112] K. Ieki. "Upgrade of the MEG liquid xenon calorimeter with VUV-light sensitive large area SiPMs". In: *Nuclear Instruments and Methods in Physics Research Section A: Accelerators, Spectrometers, Detectors and Associated Equipment*. Frontier Detectors for Frontier Physics: Proceedings of the 13th Pisa Meeting on Advanced Detectors 824 (July 11, 2016), pp. 686–690. ISSN: 0168-9002. DOI: 10.1016/j.nima.2015.11.047. URL: https://www.sciencedirect.com/science/article/pii/S0168900215014126 (visited on 07/08/2025).

[113] L. Gruber. "LHCb SciFi — Upgrading LHCb with a scintillating fibre tracker". In: *Nuclear Instruments and Methods in Physics Research Section A: Accelerators, Spectrometers, Detectors and Associated Equipment*. Proceedings of the Vienna Conference on Instrumentation 2019 958 (Apr. 1, 2020), p. 162025. ISSN: 0168-9002. DOI: 10.1016/j.nima.2019.03.080. URL: https://www.sciencedirect.com/science/article/pii/S016890021930422X (visited on 07/08/2025).

[114] F. Sefkow, F. Simon, and CALICE Collaboration. "A highly granular SiPM-on-tile calorimeter prototype". In: *Journal of Physics: Conference Series* 1162 (Jan. 2019), p. 012012. ISSN: 1742-6588, 1742-6596. DOI: 10.1088/1742-6596/1162/1/012012. URL: https://iopscience.iop.org/article/10.1088/1742-6596/1162/1/012012 (visited on 07/08/2025).

[115] Y. Haemisch, T. Frach, C. Degenhardt, et al. "Fully Digital Arrays of Silicon Photomultipliers (dSiPM) – a Scalable Alternative to Vacuum Photomultiplier Tubes (PMT)". In: *Physics Procedia*. Proceedings of the 2nd International Conference on Technology and Instrumentation in Particle Physics (TIPP 2011) 37 (Jan. 1, 2012), pp. 1546–1560. ISSN: 1875-3892. DOI: 10.1016/j.phpro.2012.03.749. URL: https://www.sciencedirect.com/science/article/pii/S187538921201869X (visited on 07/08/2025).

[116] A. Karadzhinova-Ferrer, J. Agarwala, N. Ampilogov, et al. "Novel prototype tower structure for the dual-readout fiber calorimeter". In: *Journal of Instrumentation* 17.9 (Sept. 1, 2022), T09007. ISSN: 1748-0221. DOI: 10.1088/1748-0221/17/09/T09007. URL: https://iopscience.iop.org/article/10.1088/1748-0221/17/09/T09007 (visited on 07/13/2025).

[117] "KODAK WRATTEN 2 Filters". Kodak. URL: https://www.kodak.com/en/motion/page/wratten-2-filters/ (visited on 08/10/2025).

[118] N. Ampilogov, S. Cometti, J. Agarwala, et al. "Exposing a fibre-based dual-readout calorimeter to a positron beam". In: *Journal of Instrumentation* 18.9 (Sept. 1, 2023), P09021. ISSN: 1748-0221. DOI: 10.1088/1748-0221/18/09/P09021. URL: https://iopscience.iop.org/article/10.1088/1748-0221/18/09/P09021 (visited on 07/14/2025).

[119] S. Albergo, A. Braghieri, A. Burdyko, et al. "Energy response and resolution to positrons in a capillary-tube dual-readout calorimeter prototype". In: *Journal of Instrumentation* 20.7 (July 1, 2025), P07040. ISSN: 1748-0221. DOI: 10.1088/1748-0221/20/07/P07040. URL: https://iopscience.iop.org/article/10.1088/1748-0221/20/07/P07040 (visited on 08/10/2025).

[120] A. Pareti and the IDEA dual-readout calorimeter group. "Status of dual-readout calorimetry for future high-energy physics experiments". In: *Journal of Instrumentation* 19.4 (Apr. 1, 2024), p. C04029. ISSN: 1748-0221. DOI: 10.1088/1748-0221/19/04/C04029. URL: https://iopscience.iop.org/article/10.1088/1748-0221/19/04/C04029 (visited on 11/03/2025).

[121] L. Centeno and A. Leon. "Performance studies of a dual-readout calorimeter for the IDEA detector and development of a test beam online monitoring tool". thesis. University of Sussex, May 2, 2025. URL: https://sussex.figshare.com/articles/thesis/Performance_studies_of_a_dual-readout_calorimeter_for_the_IDEA_detector_and_development_of_a_test_beam_online_monitoring_tool/28845896/1 (visited on 01/17/2026).

[122] M. Dejardin. "Role of the CMS electromagnetic calorimeter in the hunt for the Higgs boson through the two-gamma decay channel". In: "International Conference on Calorimetry for the High Energy Frontier". 2013, pp. 16–23.

[123] B. Andrieu, J. Bán, E. Barrelet, et al. "Electron/pion separation with the H1 LAr calorimeters". In: *Nuclear Instruments and Methods in Physics Research Section A: Accelerators, Spectrometers, Detectors and Associated Equipment* 344.3 (May 15, 1994), pp. 492–506. ISSN: 0168-9002. DOI: 10.1016/0168-9002(94)90870-2. URL: https://www.sciencedirect.com/science/article/pii/0168900294908702 (visited on 08/19/2025).

[124] B. Michel. "Electron-pion separation in a highly segmented electromagnetic calorimeter designed for the ALEPH experiment". In: *Nuclear Instruments and Methods in Physics Research Section A: Accelerators, Spectrometers, Detectors and Associated Equipment* 263.1 (Jan. 1, 1988), pp. 43–50. ISSN: 0168-9002. DOI: 10.1016/0168-9002(88)91015-7. URL: https://www.sciencedirect.com/science/article/pii/0168900288910157 (visited on 08/19/2025).

[125] S. Giagu, L. Torresi, and M. Di Filippo. "Tau Lepton Identification With Graph Neural Networks at Future Electron–Positron Colliders". In: *Frontiers in Physics* 10 (July 19, 2022), p. 909205. ISSN: 2296-424X. DOI: 10.3389/fphy.2022.909205. URL: https://www.frontiersin.org/articles/10.3389/fphy.2022.909205/full (visited on 08/19/2025).

[126] N. Akchurin, J. Cash, J. Damgov, et al. "High-granularity Dual-readout Calorimeter: Evolution of a Classic Prototype". In: *EPJ Web of Conferences* 320 (2025). Ed. by T. Chujo and W. Ootani, p. 00028. ISSN: 2100-014X. DOI: 10.1051/epjconf/202532000028. URL: https://www.epj-conferences.org/10.1051/epjconf/202532000028 (visited on 08/19/2025).

[127] S. Ko, H. Yoo, and S. Ha. "Reconstruction of 3D Shower Shape with the Dual-Readout Calorimeter". In: *Instruments* 6.3 (Sept. 13, 2022), p. 39. ISSN: 2410-390X. DOI: 10.3390/instruments6030039. URL: https://www.mdpi.com/2410-390X/6/3/39 (visited on 08/19/2025).

[128] R. Wigmans and M. T. Zeyrek. "On the differences between calorimetric detection of electrons and photons". In: *Nuclear Instruments and Methods in Physics Research Section A: Accelerators, Spectrometers, Detectors and Associated Equipment* 485.3 (2002), pp. 385–398. ISSN: 0168-9002. DOI: https://doi.org/10.1016/S0168-9002(01)02141-6. URL: https://www.sciencedirect.com/science/article/pii/S0168900201021416.

[129] M. Calvo Gomez, O. Deschamps, S. Monteil, et al. "A tool for γ/π^0 separation at high energies". CERN Document Server. Aug. 11, 2015. URL: https://cds.cern.ch/record/2042173 (visited on 08/23/2025).

[130] T. Chen and C. Guestrin. "XGBoost: A Scalable Tree Boosting System". June 10, 2016. DOI: 10.48550/arXiv.1603.02754. arXiv: 1603.02754. URL: http://arxiv.org/abs/1603.02754 (visited on 08/24/2025).

[131] G. Salsi. "Tecniche di "Machine Learning" per discriminazione $\gamma/\pi 0$ in un calorimetro Dual-Readout ad alta granularità per sperimentazione a futuri acceleratori". In: (Apr. 15, 2025). URL: https://unitesi.unipv.it/handle/20.500.14239/28644 (visited on 08/19/2025).

[132] "A5202". CAEN - Tools for Discovery. URL: https://www.caen.it/products/a5202/ (visited on 08/26/2025).

[133] "Citiroc 1A - Weeroc". URL: https://www.weeroc.com/read_out_chips/citiroc-1a/ (visited on 08/28/2025).

[134] "304 Stainless steel capillary Tubing 1/4 ". URL: https://www.sscoiledtubing.com/products/ss_capillary_tubing/304_capillary_tubing/astm_a269_304_stainless_steel_welded_capillary_tubings_1_4__0_035_.html (visited on 08/27/2025).

[135] "Detergent GP 17.40 SUP". NGL. URL: https://www.ngl-group.com/en/product/gp-17-40-sup/ (visited on 11/10/2025).

[136] N. Valle. "Dual readout with capillary tubes – status and prospects". In: *EPJ Web of Conferences* 320 (2025). Ed. by T. Chujo and W. Ootani, p. 00054. ISSN: 2100-014X. DOI: 10.1051/epjconf/202532000054. URL: https://www.epj-conferences.org/10.1051/epjconf/202532000054 (visited on 08/26/2025).

[137] "DT5215". CAEN - Tools for Discovery. URL: https://www.caen.it/products/dt5215/ (visited on 11/13/2025).

[138] A. Pareti. "Stima della sensibilità dell'esperimento ATLAS a neutrini massivi, basata su tecniche Machine Learning". In: (July 11, 2024). URL: https://unitesi.unipv.it/handle/20.500.14239/14767 (visited on 09/07/2025).

[139] M. Aly, T. Dado, L.-G. Gagnon, et al. "TRExFitter". Aug. 1, 2025. DOI: 10.5281/ZENODO.16684099. URL: https://zenodo.org/doi/10.5281/zenodo.16684099 (visited on 10/17/2025).

[140] ATLAS Collaboration. "Search for heavy neutral leptons in decays of W bosons produced in 13 TeV pp collisions using prompt signatures in the ATLAS detector". version: 1. Aug. 28, 2025. DOI: 10.48550/arXiv.2508.20929. arXiv: 2508.20929. URL: http://arxiv.org/abs/2508.20929 (visited on 10/09/2025).

[141] "CMS coordinate system – TikZ.net". July 11, 2024. URL: https://tikz.net/axis3d_cms/ (visited on 09/07/2025).

[142] R. M. Bianchi and A. Collaboration. "ATLAS experiment schematic or layout illustration". 2022. URL: https://cds.cern.ch/record/2837191.

[143] B. Abbott, J. Albert, F. Alberti, et al. "Production and integration of the ATLAS Insertable B-Layer". In: *Journal of Instrumentation* 13.5 (May 16, 2018), T05008–T05008. ISSN: 1748-0221. DOI: 10.1088/1748-0221/13/05/T05008. URL: https://iopscience.iop.org/article/10.1088/1748-0221/13/05/T05008 (visited on 01/15/2026).

[144] ATLAS Collaboration. "Basic ATLAS TRT performance studies of Run 1". Geneva: CERN, 2014. URL: https://cds.cern.ch/record/1669603.

[145] M. Nicolás Viaux. "The ATLAS 'New Small Wheel' Muon detector stations recently commissioned for LHC Run3". In: *Nuclear Instruments and Methods in Physics Research Section A: Accelerators, Spectrometers, Detectors and Associated Equipment* 1045 (Jan. 2023), p. 167574. ISSN: 01689002. DOI: 10.1016/j.nima.2022.167574. URL: https://linkinghub.elsevier.com/retrieve/pii/S016890022200866X (visited on 09/08/2025).

[146] T. A. Collaboration. "Operation of the ATLAS trigger system in Run 2". In: *Journal of Instrumentation* 15.10 (Oct. 2, 2020), P10004–P10004. ISSN: 1748-0221. DOI: 10.1088/1748-0221/15/10/P10004. URL: https://iopscience.iop.org/article/10.1088/1748-0221/15/10/P10004 (visited on 09/10/2025).

[147] G. Manco. "Testing the Standard Model with precision flavour measurements at the ATLAS experiment". PhD thesis. Pavia U., 2024-04-02, 2024.

[148] M. Elsing, L. Goossens, A. Nairz, et al. "The ATLAS Tier-0: Overview and operational experience". In: *Journal of Physics: Conference Series* 219.7 (Apr. 1, 2010), p. 072011. ISSN: 1742-6596. DOI: 10.1088/1742-6596/219/7/072011. URL: https://iopscience.iop.org/article/10.1088/1742-6596/219/7/072011 (visited on 09/10/2025).

[149] G. Aad, B. Abbott, D. Abbott, et al. "Electron and photon performance measurements with the ATLAS detector using the 2015–2017 LHC proton-proton collision data". In: *Journal of Instrumentation* 14.12 (Dec. 10, 2019), P12006–P12006. ISSN: 1748-0221. DOI: 10.1088/1748-0221/14/12/P12006. URL: https://iopscience.iop.org/article/10.1088/1748-0221/14/12/P12006 (visited on 09/11/2025).

[150] M. Aaboud, G. Aad, B. Abbott, et al. "Electron reconstruction and identification in the ATLAS experiment using the 2015 and 2016 LHC proton–proton collision data at $$\sqrt{s} = 13$$ $$\text {TeV}$$". In: *The European Physical Journal C* 79.8 (Aug. 3, 2019), p. 639. ISSN: 1434-6052. DOI: 10.1140/epjc/s10052-019-7140-6. URL: https://doi.org/10.1140/epjc/s10052-019-7140-6 (visited on 09/11/2025).

[151] W. Lampl, S. Laplace, D. Lelas, et al. "Calorimeter Clustering Algorithms". Geneva: CERN, 2008. URL: https://cds.cern.ch/record/1099735.

[152] R. Frühwirth. "A Gaussian-mixture approximation of the Bethe–Heitler model of electron energy loss by bremsstrahlung". In: *Computer Physics Communications* 154.2 (Aug. 1, 2003), pp. 131–142. ISSN: 0010-4655. DOI: 10.1016/S0010-4655(03)00292-3. URL: https://www.sciencedirect.com/science/article/pii/S0010465503002923 (visited on 09/11/2025).

[153] "Improved electron reconstruction in ATLAS using the Gaussian Sum Filter-based model for bremsstrahlung". Geneva: CERN, 2012. URL: https://cds.cern.ch/record/1449796.

[154] ATLAS Collaboration, G. Aad, B. Abbott, et al. "Muon reconstruction performance of the ATLAS detector in proton–proton collision data at $$\sqrt{s}$$ s =13 TeV". In: *The European Physical Journal C* 76.5 (May 2016), p. 292. ISSN: 1434-6044, 1434-6052. DOI: 10.1140/epjc/s10052-016-4120-y. URL: http://link.springer.com/10.1140/epjc/s10052-016-4120-y (visited on 09/12/2025).

[155] J. Illingworth and J. Kittler. "A survey of the hough transform". In: *Computer Vision, Graphics, and Image Processing* 44.1 (Oct. 1988), pp. 87–116. ISSN: 0734189X. DOI: 10.1016/S0734-189X(88)80033-1. URL: https://linkinghub.elsevier.com/retrieve/pii/S0734189X88800331 (visited on 09/12/2025).

[156] ATLAS Collaboration, G. Aad, B. Abbott, et al. "Muon reconstruction and identification efficiency in ATLAS using the full Run 2 pp collision data set at $$\sqrt{s}=13$$ TeV". In: *The European Physical Journal C* 81.7 (July 2021), p. 578. ISSN: 1434-6044, 1434-6052. DOI: 10.1140/epjc/s10052-021-09233-2. URL: https://link.springer.com/10.1140/epjc/s10052-021-09233-2 (visited on 09/12/2025).

[157] M. Cacciari, G. P. Salam, and G. Soyez. "The anti-k_t jet clustering algorithm". In: *Journal of High Energy Physics* 2008.4 (Apr. 16, 2008), pp. 063–063. ISSN: 1029-8479. DOI: 10.1088/1126-6708/2008/04/063. URL: http://stacks.iop.org/1126-6708/2008/i=04/a=063?key=crossref.2ffef838d94c2b899ee27950c18ee8d2 (visited on 09/12/2025).

[158] M. Cacciari, G. P. Salam, and G. Soyez. "FastJet user manual". In: *The European Physical Journal C* 72.3 (Mar. 16, 2012), p. 1896. ISSN: 1434-6052. DOI: 10.1140/epjc/s10052-012-1896-2. URL: https://doi.org/10.1140/epjc/s10052-012-1896-2 (visited on 09/12/2025).

[159] G. Aad, B. Abbott, D. C. Abbott, et al. "Jet energy scale and resolution measured in proton–proton collisions at $$\sqrt{s}=13$$ TeV with the ATLAS detector". In: *The European Physical Journal C* 81.8 (Aug. 3, 2021), p. 689. ISSN: 1434-6052. DOI: 10.1140/epjc/s10052-021-09402-3. URL: https://doi.org/10.1140/epjc/s10052-021-09402-3 (visited on 09/12/2025).

[160] G. Aad, B. Abbott, J. Abdallah, et al. "Topological cell clustering in the ATLAS calorimeters and its performance in LHC Run 1". In: *The European Physical Journal C* 77.7 (July 24, 2017), p. 490. ISSN: 1434-6052. DOI: 10.1140/epjc/s10052-017-5004-5. URL: https://doi.org/10.1140/epjc/s10052-017-5004-5 (visited on 09/12/2025).

[161] G. Aad, B. Abbott, D. C. Abbott, et al. "ATLAS b-jet identification performance and efficiency measurement with $$t{\bar{t}}$$ events in pp collisions at $$\sqrt{s}=13$$ TeV". In: *The European Physical Journal C* 79.11 (Nov. 25, 2019), p. 970. ISSN: 1434-6052. DOI: 10.1140/epjc/s10052-019-7450-8. URL: https://doi.org/10.1140/epjc/s10052-019-7450-8 (visited on 09/12/2025).

[162] G. Aad, B. Abbott, D. C. Abbott, et al. "ATLAS flavour-tagging algorithms for the LHC Run 2 pp collision dataset". In: *The European Physical Journal C* 83.7 (July 31, 2023), p. 681. ISSN: 1434-6052. DOI: 10.1140/epjc/s10052-023-11699-1. URL: https://doi.org/10.1140/epjc/s10052-023-11699-1 (visited on 09/12/2025).

[163] ATLAS Collaboration. "Transforming jet flavour tagging at ATLAS". May 26, 2025. DOI: 10.48550/arXiv.2505.19689. arXiv: 2505.19689. URL: http://arxiv.org/abs/2505.19689 (visited on 09/12/2025).

[164] G. Aad, B. Abbott, D. C. Abbott, et al. "Search for heavy neutral leptons in decays of W bosons produced in 13 TeV pp collisions using prompt and displaced signatures with the ATLAS detector". In: *Journal of High Energy Physics* 2019.10 (Oct. 30, 2019), p. 265. ISSN: 1029-8479. DOI: 10.1007/JHEP10(2019)265. URL: https://doi.org/10.1007/JHEP10(2019)265 (visited on 10/12/2025).

[165] G. Aad, E. Aakvaag, B. Abbott, et al. "Search for heavy neutral leptons in decays of W bosons using leptonic and semi-leptonic displaced vertices in $$ \sqrt{s} $$= 13 TeV pp collisions with the ATLAS detector". In: *Journal of High Energy Physics* 2025.7 (July 17, 2025), p. 196. ISSN: 1029-8479. DOI: 10.1007/JHEP07(2025)196. URL: https://doi.org/10.1007/JHEP07(2025)196 (visited on 10/09/2025).

[166] Y. Fukuda, T. Hayakawa, E. Ichihara, et al. "Evidence for Oscillation of Atmospheric Neutrinos". In: *Physical Review Letters* 81.8 (Aug. 24, 1998), pp. 1562–1567. ISSN: 0031-9007, 1079-7114. DOI: 10.1103/PhysRevLett.81.1562. URL: https://link.aps.org/doi/10.1103/PhysRevLett.81.1562 (visited on 02/08/2025).

[167] Q. R. Ahmad, R. C. Allen, T. C. Andersen, et al. "Direct Evidence for Neutrino Flavor Transformation from Neutral-Current Interactions in the Sudbury Neutrino Observatory". In: *Physical Review Letters* 89.1 (June 13, 2002), p. 011301. ISSN: 0031-9007, 1079-7114. DOI: 10.1103/PhysRevLett.89.011301. URL: https://link.aps.org/doi/10.1103/PhysRevLett.89.011301 (visited on 02/08/2025).

[168] F. An, G. An, Q. An, et al. "Neutrino Physics with JUNO". Oct. 18, 2015. DOI: 10.48550/arXiv.1507.05613. arXiv: 1507.05613. URL: http://arxiv.org/abs/1507.05613 (visited on 03/15/2025).

[169] K. Abe, R. Akutsu, A. Ali, et al. "Constraint on the matter–antimatter symmetry-violating phase in neutrino oscillations". In: *Nature* 580.7803 (Apr. 2020), pp. 339–344. ISSN: 1476-4687. DOI: 10.1038/s41586-020-2177-0. URL: https://www.nature.com/articles/s41586-020-2177-0 (visited on 03/15/2025).

[170] J. Boucrot. "Oscillations of neutral B mesons systems". In: *Nuclear Physics B - Proceedings Supplements* 75.3 (Apr. 1, 1999), pp. 261–266. ISSN: 0920-5632. DOI: 10.1016/S0920-5632(99)00362-X. URL: https://www.sciencedirect.com/science/article/pii/S092056329900362X (visited on 08/17/2025).

[171] K. M. Beshtoev. "Oscillations in the K0 mesons system at *S* (strangeness) and *CP* violations". In: *Nuclear Physics B - Proceedings Supplements*. The Proceedings of the 5th Joint International Hadron Structure '11 Conference 219-220 (Oct. 1, 2011), pp. 276–280. ISSN: 0920-5632. DOI: 10.1016/j.nuclphysbps.2011.10.110. URL: https://www.sciencedirect.com/science/article/pii/S0920563211008516 (visited on 08/17/2025).

[172] J.-L. Tastet, O. Ruchayskiy, and I. Timiryasov. "Reinterpreting the ATLAS bounds on heavy neutral leptons in a realistic neutrino oscillation model". In: *Journal of High Energy Physics* 2021.12 (Dec. 27, 2021), p. 182. ISSN: 1029-8479. DOI: 10.1007/JHEP12(2021)182. URL: https://doi.org/10.1007/JHEP12(2021)182 (visited on 03/18/2025).

[173] A. M. Abdullahi, P. Barham Alzás, B. Batell, et al. "The present and future status of heavy neutral leptons". In: *Journal of Physics G: Nuclear and Particle Physics* 50.2 (Feb. 1, 2023), p. 020501. ISSN: 0954-3899, 1361-6471. DOI: 10.1088/1361-6471/ac98f9. URL: https://iopscience.iop.org/article/10.1088/1361-6471/ac98f9 (visited on 12/31/2024).

[174] S. F. King. "Right-handed neutrinos: seesaw models and signatures". Feb. 26, 2025. DOI: 10.48550/arXiv.2502.07877. arXiv: 2502.07877. URL: http://arxiv.org/abs/2502.07877 (visited on 03/27/2025).

[175] T. Asaka, S. Blanchet, and M. Shaposhnikov. "The νMSM, dark matter and neutrino masses". In: *Physics Letters B* 631.4 (Dec. 29, 2005), pp. 151–156. ISSN: 0370-2693. DOI: 10.1016/j.physletb.2005.09.070. URL: https://www.sciencedirect.com/science/article/pii/S0370269305013675 (visited on 04/01/2025).

[176] E. K. Akhmedov, V. A. Rubakov, and A. Y. Smirnov. "Baryogenesis via Neutrino Oscillations". In: *Physical Review Letters* 81.7 (Aug. 17, 1998), pp. 1359–1362. ISSN: 0031-9007, 1079-7114. DOI: 10.1103/PhysRevLett.81.1359. URL: https://link.aps.org/doi/10.1103/PhysRevLett.81.1359 (visited on 04/01/2025).

[177] M. Drewes, B. Garbrecht, P. Hernandez, et al. "ARS Leptogenesis". Nov. 8, 2017. DOI: 10.48550/arXiv.1711.02862. arXiv: 1711.02862. URL: http://arxiv.org/abs/1711.02862 (visited on 04/30/2025).

[178] A. D. Sakharov. "Violation of *CP* in variance, *C* asymmetry, and baryon asymmetry of the universe". In: *Physics-Uspekhi* 34.5 (May 1, 1991), pp. 392–393. ISSN: 1063-7869. URL: https://ufn.ru/en/articles/1991/5/h/ (visited on 04/01/2025).

[179] D. Bödeker and W. Buchmüller. "Baryogenesis from the weak scale to the grand unification scale". In: *Reviews of Modern Physics* 93.3 (Aug. 19, 2021), p. 035004. ISSN: 0034-6861, 1539-0756. DOI: 10.1103/RevModPhys.93.035004. URL: https://link.aps.org/doi/10.1103/RevModPhys.93.035004 (visited on 04/02/2025).

[180] M. Fukugita and T. Yanagida. "Barygenesis without grand unification". In: *Physics Letters B* 174.1 (June 26, 1986), pp. 45–47. ISSN: 0370-2693. DOI: 10.1016/0370-2693(86)91126-3. URL: https://www.sciencedirect.com/science/article/pii/0370269386911263 (visited on 04/01/2025).

[181] M. A. Luty. "Baryogenesis via leptogenesis". In: *Physical Review D* 45.2 (Jan. 15, 1992), pp. 455–465. ISSN: 0556-2821. DOI: 10.1103/PhysRevD.45.455. URL: https://link.aps.org/doi/10.1103/PhysRevD.45.455 (visited on 04/02/2025).

[182] S. Davidson, E. Nardi, and Y. Nir. "Leptogenesis". In: *Physics Reports* 466.4 (Sept. 1, 2008), pp. 105–177. ISSN: 0370-1573. DOI: 10.1016/j.physrep.2008.06.002. URL: https://www.sciencedirect.com/science/article/pii/S0370157308001889 (visited on 04/01/2025).

[183] S. Alekhin, W. Altmannshofer, T. Asaka, et al. "A facility to search for hidden particles at the CERN SPS: the SHiP physics case". In: *Reports on Progress in Physics* 79.12 (Dec. 1, 2016), p. 124201. ISSN: 0034-4885, 1361-6633. DOI: 10.1088/0034-4885/79/12/124201. URL: https://iopscience.iop.org/article/10.1088/0034-4885/79/12/124201 (visited on 04/05/2025).

[184] B. Abi, R. Acciarri, M. Acero, et al. "Volume I. Introduction to DUNE". In: *Journal of Instrumentation* 15.8 (Aug. 27, 2020), T08008–T08008. ISSN: 1748-0221. DOI: 10.1088/1748-0221/15/08/T08008. URL: https://iopscience.iop.org/article/10.1088/1748-0221/15/08/T08008 (visited on 04/05/2025).

[185] A. A. Hayrapetyan, A. Tumasyan, W. Adam, et al. "Search for heavy neutral leptons in final states with electrons, muons, and hadronically decaying tau leptons in proton-proton collisions at $$ \sqrt{s} $$= 13 TeV". In: *Journal of High Energy Physics* 2024.6 (June 19, 2024), p. 123. ISSN: 1029-8479. DOI: 10.1007/JHEP06(2024)123. URL: https://doi.org/10.1007/JHEP06(2024)123 (visited on 10/10/2025).

[186] G. Aad, B. Abbott, J. Abdallah, et al. "Measurement of $W\pm$ and Z-boson production cross sections in pp collisions at s=13 TeV with the ATLAS detector". In: *Physics Letters B* 759 (Aug. 10, 2016), pp. 601–621. ISSN: 0370-2693. DOI: 10.1016/j.physletb.2016.06.023. URL: https://www.sciencedirect.com/science/article/pii/S0370269316302763 (visited on 10/17/2025).

[187] G. Aad, B. Abbott, J. Abdallah, et al. "Measurement of the W $\to \ell\nu$ and Z/γ* $\to \ell\ell$ production cross sections in proton-proton collisions at $ \sqrt {s} = 7 TeV $ with the ATLAS detector". In: *Journal of High Energy Physics* 2010.12 (Dec. 14, 2010), p. 60. ISSN: 1029-8479. DOI: 10.1007/JHEP12(2010)060. URL: https://doi.org/10.1007/JHEP12(2010)060 (visited on 10/10/2025).

[188] D. Gorbunov and M. Shaposhnikov. "How to find neutral leptons of the νMSM?" In: *Journal of High Energy Physics* 2007.10 (Oct. 3, 2007), pp. 015–015. ISSN: 1029-8479. DOI: 10.1088/1126-6708/2007/10/015. URL: http://stacks.iop.org/1126-6708/2007/i=10/a=015?key=crossref.2f9f0e9a797a4c9536cb723402b397a3 (visited on 10/10/2025).

[189] M. Gronau, C. N. Leung, and J. L. Rosner. "Extending limits on neutral heavy leptons". In: *Physical Review D* 29.11 (June 1, 1984), pp. 2539–2558. ISSN: 0556-2821. DOI: 10.1103/PhysRevD.29.2539. URL: https://link.aps.org/doi/10.1103/PhysRevD.29.2539 (visited on 10/10/2025).

[190] G. Aad, B. Abbott, D. C. Abbott, et al. "Evidence for the production of three massive vector bosons with the ATLAS detector". In: *Physics Letters B* 798 (Nov. 10, 2019), p. 134913. ISSN: 0370-2693. DOI: 10.1016/j.physletb.2019.134913. URL: https://www.sciencedirect.com/science/article/pii/S0370269319306355 (visited on 10/13/2025).

[191] "Modelling of rare top quark processes at \sqrts = 13 TeV in ATLAS". Geneva: CERN, 2020. URL: https://cds.cern.ch/record/2730584.

[192] G. Avoni, M. Bruschi, G. Cabras, et al. "The new LUCID-2 detector for luminosity measurement and monitoring in ATLAS". In: *Journal of Instrumentation* 13.7 (July 23, 2018), P07017–P07017. ISSN: 1748-0221. DOI: 10.1088/1748-0221/13/07/P07017. URL: https://iopscience.iop.org/article/10.1088/1748-0221/13/07/P07017 (visited on 10/12/2025).

[193] J. Catmore, J. Cranshaw, T. Gillam, et al. "A new petabyte-scale data derivation framework for ATLAS". In: *Journal of Physics: Conference Series* 664.7 (Dec. 23, 2015), p. 072007. ISSN: 1742-6588, 1742-6596. DOI: 10.1088/1742-6596/664/7/072007. URL: https://iopscience.iop.org/article/10.1088/1742-6596/664/7/072007 (visited on 10/12/2025).

[194] ATLAS Collaboration. "Athena". Version 22.0.1. Apr. 9, 2019. DOI: 10.5281/zenodo.2641997. URL: https://zenodo.org/records/2641997 (visited on 10/12/2025).

[195] P. Mato. "GAUDI-Architecture design document". Geneva: CERN, 1998. URL: https://cds.cern.ch/record/691746.

[196] J. Catmore, J. Elmsheuser, J. Schaarschmidt, et al. "PHYSLITE - a new reduced common data format for ATLAS". In: (2023). URL: https://cds.cern.ch/record/2857821.

[197] G. Aad, B. Abbott, J. Abdallah, et al. "The ATLAS Simulation Infrastructure". In: *The European Physical Journal C* 70.3 (Dec. 1, 2010), pp. 823–874. ISSN: 1434-6052. DOI: 10.1140/epjc/s10052-010-1429-9. URL: https://doi.org/10.1140/epjc/s10052-010-1429-9 (visited on 10/12/2025).

[198] C. ATLAS, M. Beckingham, M. Duehrssen, et al. "The simulation principle and performance of the ATLAS fast calorimeter simulation FastCaloSim". Geneva: CERN, 2010. URL: http://cds.cern.ch/record/1300517.

[199] Z. Marshall and ATLAS Collaboration. "Simulation of Pile-up in the ATLAS Experiment". In: *Journal of Physics: Conference Series* 513.2 (June 11, 2014), p. 022024. ISSN: 1742-6588, 1742-6596. DOI: 10.1088/1742-6596/513/2/022024. URL: https://iopscience.iop.org/article/10.1088/1742-6596/513/2/022024 (visited on 10/13/2025).

[200] T. Sjöstrand, S. Mrenna, and P. Skands. "A brief introduction to PYTHIA 8.1". In: *Computer Physics Communications* 178.11 (June 1, 2008), pp. 852–867. ISSN: 0010-4655. DOI: 10.1016/j.cpc.2008.01.036. URL: https://www.sciencedirect.com/science/article/pii/S0010465508000441 (visited on 10/13/2025).

[201] R. D. Ball, V. Bertone, S. Carrazza, et al. "Parton distributions with LHC data". In: *Nuclear Physics B* 867.2 (Feb. 11, 2013), pp. 244–289. ISSN: 0550-3213. DOI: 10.1016/j.nuclphysb.2012.10.003. URL: https://www.sciencedirect.com/science/article/pii/S0550321312005500 (visited on 10/13/2025).

[202] "The Pythia 8 A3 tune description of ATLAS minimum bias and inelastic measurements incorporating the Donnachie-Landshoff diffractive model". Geneva, 2016. URL: https://cds.cern.ch/record/2206965.

[203] G. Aad, B. Abbott, D. Abbott, et al. "ATLAS data quality operations and performance for 2015–2018 data-taking". In: *Journal of Instrumentation* 15.4 (Apr. 2, 2020), P04003–P04003. ISSN: 1748-0221. DOI: 10.1088/1748-0221/15/04/P04003. URL: https://iopscience.iop.org/article/10.1088/1748-0221/15/04/P04003 (visited on 10/13/2025).

[204] D. J. Lange. "The EvtGen particle decay simulation package". In: *Nuclear Instruments and Methods in Physics Research Section A: Accelerators, Spectrometers, Detectors and Associated Equipment*. BEAUTY2000, Proceedings of the 7th Int. Conf. on B-Physics at Hadron Machines 462.1 (Apr. 11, 2001), pp. 152–155. ISSN: 0168-9002. DOI: 10.1016/S0168-9002(01)00089-4. URL: https://www.sciencedirect.com/science/article/pii/S0168900201000894 (visited on 10/13/2025).

[205] E. Bothmann, G. Singh Chahal, S. Höche, et al. "Event generation with Sherpa 2.2". In: *SciPost Physics* 7.3 (Sept. 18, 2019), p. 034. ISSN: 2542-4653. DOI: 10.21468/SciPostPhys.7.3.034. URL: https://scipost.org/10.21468/SciPostPhys.7.3.034 (visited on 10/13/2025).

[206] F. Buccioni, J.-N. Lang, J. M. Lindert, et al. "OpenLoops 2". In: *The European Physical Journal C* 79.10 (Oct. 22, 2019), p. 866. ISSN: 1434-6052. DOI: 10.1140/epjc/s10052-019-7306-2. URL: https://doi.org/10.1140/epjc/s10052-019-7306-2 (visited on 10/13/2025).

[207] S. Schumann and F. Krauss. "A parton shower algorithm based on Catani-Seymour dipole factorisation". In: *Journal of High Energy Physics* 2008.3 (Mar. 13, 2008), pp. 038–038. ISSN: 1029-8479. DOI: 10.1088/1126-6708/2008/03/038. URL: http://stacks.iop.org/1126-6708/2008/i=03/a=038?key=crossref.0fd4ab847c35ee85978d7acf1fcaae19 (visited on 10/13/2025).

[208] J. Alwall, R. Frederix, S. Frixione, et al. "The automated computation of tree-level and next-to-leading order differential cross sections, and their matching to parton shower simulations". In: *Journal of High Energy Physics* 2014.7 (July 17, 2014), p. 79. ISSN: 1029-8479. DOI: 10.1007/JHEP07(2014)079. URL: https://doi.org/10.1007/JHEP07(2014)079 (visited on 10/13/2025).

[209] S. Frixione, E. Laenen, P. Motylinski, et al. "Single-top hadroproduction in association with a W boson". In: *Journal of High Energy Physics* 2008.7 (July 8, 2008), pp. 029–029. ISSN: 1029-8479. DOI: 10.1088/1126-6708/2008/07/029. URL: http://stacks.iop.org/1126-6708/2008/i=07/a=029?key=crossref.a5ad530a34e44ef37a8b94f7d2d7ece2 (visited on 10/13/2025).

[210] R. D. Ball, V. Bertone, S. Carrazza, et al. "Parton distributions for the LHC run II". In: *Journal of High Energy Physics* 2015.4 (Apr. 8, 2015), p. 40. ISSN: 1029-8479. DOI: 10.1007/JHEP04(2015)040. URL: https://doi.org/10.1007/JHEP04(2015)040 (visited on 10/13/2025).

[211] S. Frixione, G. Ridolfi, and P. Nason. "A positive-weight next-to-leading-order Monte Carlo for heavy flavour hadroproduction". In: *Journal of High Energy Physics* 2007.9 (Sept. 28, 2007), pp. 126–126. ISSN: 1029-8479. DOI: 10.1088/1126-6708/2007/09/126. URL: http://stacks.iop.org/1126-6708/2007/i=09/a=126?key=crossref.f5eb02711c0aa01e633cfb748bac6b98 (visited on 10/13/2025).

[212] N. Kidonakis and N. Yamanaka. "Higher-order corrections for tW production at high-energy hadron colliders". In: *Journal of High Energy Physics* 2021.5 (May 31, 2021), p. 278. ISSN: 1029-8479. DOI: 10.1007/JHEP05(2021)278. URL: https://doi.org/10.1007/JHEP05(2021)278 (visited on 10/13/2025).

[213] C. Degrande, O. Mattelaer, R. Ruiz, et al. "Fully automated precision predictions for heavy neutrino production mechanisms at hadron colliders". In: *Physical Review D* 94.5 (Sept. 6, 2016), p. 053002. ISSN: 2470-0010, 2470-0029. DOI: 10.1103/PhysRevD.94.053002. URL: https://link.aps.org/doi/10.1103/PhysRevD.94.053002 (visited on 10/13/2025).

[214] L. Lönnblad and S. Prestel. "Matching tree-level matrix elements with interleaved showers". In: *Journal of High Energy Physics* 2012.3 (Mar. 7, 2012), p. 19. ISSN: 1029-8479. DOI: 10.1007/JHEP03(2012)019. URL: https://doi.org/10.1007/JHEP03(2012)019 (visited on 10/13/2025).

[215] G. Aad, E. Aakvaag, B. Abbott, et al. "The performance of missing transverse momentum reconstruction and its significance with the ATLAS detector using 140 $$\hbox {fb}^{-1}$$of $$\sqrt{s}=13$$TeV pp collisions". In: *The European Physical Journal C* 85.6 (June 2, 2025), p. 606. ISSN: 1434-6052. DOI: 10.1140/epjc/s10052-025-14062-8. URL: https://doi.org/10.1140/epjc/s10052-025-14062-8 (visited on 10/14/2025).

[216] G. Cowan, K. Cranmer, E. Gross, et al. "Asymptotic formulae for likelihood-based tests of new physics". In: *The European Physical Journal C* 71.2 (Feb. 9, 2011), p. 1554. ISSN: 1434-6052. DOI: 10.1140/epjc/s10052-011-1554-0. URL: https://doi.org/10.1140/epjc/s10052-011-1554-0 (visited on 10/16/2025).

[217] "Formulae for Estimating Significance". Geneva: CERN, 2020. URL: https://cds.cern.ch/record/2736148.

[218] G. Aad, B. Abbott, D. Abbott, et al. "Tools for estimating fake/non-prompt lepton backgrounds with the ATLAS detector at the LHC". In: *Journal of Instrumentation* 18.11 (Nov. 1, 2023), T11004. ISSN: 1748-0221. DOI: 10.1088/1748-0221/18/11/T11004. URL: https://iopscience.iop.org/article/10.1088/1748-0221/18/11/T11004 (visited on 10/15/2025).

[219] "E_\textT^\textmiss performance in the ATLAS detector using 2015-2016 LHC p-p collisions". 2018. URL: https://cds.cern.ch/record/2625233.

[220] J. Butterworth, S. Carrazza, A. Cooper-Sarkar, et al. "PDF4LHC recommendations for LHC Run II". In: *Journal of Physics G: Nuclear and Particle Physics* 43.2 (Feb. 1, 2016), p. 023001. ISSN: 0954-3899, 1361-6471. DOI: 10.1088/0954-3899/43/2/023001. URL: https://iopscience.iop.org/article/10.1088/0954-3899/43/2/023001 (visited on 10/17/2025).

[221] M. Aaboud, G. Aad, B. Abbott, et al. "Measurement of $$W^{\pm }Z$$production cross sections and gauge boson polarisation in pp collisions at $$\sqrt{s} = 13~\text {TeV}$$with the ATLAS detector". In: *The European Physical Journal C* 79.6 (June 22, 2019), p. 535. ISSN: 1434-6052. DOI: 10.1140/epjc/s10052-019-7027-6. URL: https://doi.org/10.1140/epjc/s10052-019-7027-6 (visited on 10/17/2025).

[222] A. L. Read. "Presentation of search results: the CL_s technique". In: *Journal of Physics G: Nuclear and Particle Physics* 28.10 (Oct. 1, 2002), pp. 2693–2704. ISSN: 0954-3899. DOI: 10.1088/0954-3899/28/10/313. URL: https://iopscience.iop.org/article/10.1088/0954-3899/28/10/313 (visited on 10/17/2025).

[223] K. Cranmer, G. Lewis, L. Moneta, et al. "HistFactory: A tool for creating statistical models for use with RooFit and RooStats". New York: New York U., 2012. DOI: 10.17181/CERN-OPEN-2012-016. URL: https://cds.cern.ch/record/1456844.

[224] W. Verkerke and D. Kirkby. "The RooFit toolkit for data modeling". June 14, 2003. DOI: 10.48550/arXiv.physics/0306116. arXiv: physics/0306116. URL: http://arxiv.org/abs/physics/0306116 (visited on 10/17/2025).

[225] L. Moneta, K. Belasco, K. Cranmer, et al. "The RooStats Project". Feb. 1, 2011. DOI: 10.48550/arXiv.1009.1003. arXiv: 1009.1003. URL: http://arxiv.org/abs/1009.1003 (visited on 10/17/2025).

[226] J. S. Conway. "Incorporating Nuisance Parameters in Likelihoods for Multisource Spectra". Mar. 2, 2011. DOI: 10.48550/arXiv.1103.0354. arXiv: 1103.0354. URL: http://arxiv.org/abs/1103.0354 (visited on 10/18/2025).

[227] A. Rotondi, P. Pedroni, and A. Pievatolo. "Probabilità, Statistica e Simulazione: Programmi applicativi scritti in R". Vol. 131. UNITEXT. Milano: Springer Milan, 2021. DOI: 10.1007/978-88-470-4010-6. URL: https://link.springer.com/10.1007/978-88-470-4010-6 (visited on 10/18/2025).

[228] G. Aad, B. Abbott, J. Abdallah, et al. "Search for heavy Majorana neutrinos with the ATLAS detector in pp collisions at $$ \sqrt{s}=8 $$TeV". In: *Journal of High Energy Physics* 2015.7 (July 29, 2015), p. 162. ISSN: 1029-8479. DOI: 10.1007/JHEP07(2015)162. URL: https://doi.org/10.1007/JHEP07(2015)162 (visited on 10/20/2025).

[229] G. Aad, E. Aakvaag, B. Abbott, et al. "Search for heavy Majorana neutrinos in $e^{\pm}e^{\pm}$ and $e^{\pm}\mu^{\pm}$ final states via WW scattering in *pp* collisions at s=13 TeV with the ATLAS detector". In: *Physics Letters B* 856 (Sept. 1, 2024), p. 138865. ISSN: 0370-2693. DOI: 10.1016/j.physletb.2024.138865. URL: https://www.sciencedirect.com/science/article/pii/S0370269324004234 (visited on 10/20/2025).

[230] G. Aad, B. Abbott, K. Abeling, et al. "Search for Majorana neutrinos in same-sign WW scattering events from pp collisions at $$\sqrt{s}=13$$ TeV". In: *The European Physical Journal C* 83.9 (Sept. 15, 2023), p. 824. ISSN: 1434-6052. DOI: 10.1140/epjc/s10052-023-11915-y. URL: https://doi.org/10.1140/epjc/s10052-023-11915-y (visited on 10/20/2025).

[231] L. Bellagamba, G. Polesello, and N. Valle. "Searches for heavy neutral leptons at FCC-ee in final states including a muon". In: *The European Physical Journal C* 85.9 (Sept. 26, 2025), p. 1069. ISSN: 1434-6052. DOI: 10.1140/epjc/s10052-025-14749-y. URL: https://doi.org/10.1140/epjc/s10052-025-14749-y (visited on 11/26/2025).

ACKNOWLEDGEMENTS

At the end of this strenuous but at the same time fulfilling journey, I would like to express my appreciation to the people who have been by my side throughout more than three years of Ph.D. studies. First of all, I would like to express my deepest gratitude to Gabriella, Andrea, Giacomo and all the other members of the RD_FCC and ATLAS groups at the University of Pavia and the INFN Pavia unit. I never felt alone during my activity here, thanks to the continuous support and positive feedback, and could not have hoped for a better team.

My sincere gratitude also goes to Romualdo, Iacopo and all the members of the HiDRa group for the enriching experience, including the several nights spent at test beams at CERN working (and despairing) to collect meaningful data. I believe that the work carried out together has been significant in teaching me how excellent research is conducted in our field, and has allowed me to grow both as a scientist and as a person. I am also grateful to Fabrizio, Otilia and the other members of the ATLAS HNL group for their inspiring leadership in our searches for new physics, which I am sure will one day reveal itself.

I wish to thank the Ph.D. coordinator at the Department of Physics, Daniela, for her ceaseless support and guidance throughout my doctoral studies. Many thanks to all the professors, the university and the INFN personnel, whose work was essential for the successful completion of my research project. I would also like to thank the mechanics and electronics workshops for their fundamental contribution to the construction and preparation of the detector discussed in this thesis.

Finally, I would like to express my heartfelt gratitude to my parents, Daniela and Roberto, and my brother Federico, for always encouraging me and for being a constant source of inspiration in hard work and being down to earth, even when studying the Universe. Many thanks to all my family, friends and colleagues for the endless support and kindness. I am sure I will always remember these years as some of the most enriching and rewarding experiences I have ever had.